Multicomponent Metal Organic Frameworks Using Amino Acids and Peptides

A thesis presented in partial fulfilment of the requirements of the degree of

Doctor of Philosophy

in

Chemistry

at Massey University, Manawatu, New Zealand

Ghadir Dahalan

2025

For Adam and Zane

Abstract

Multicomponent metal-organic frameworks (MMOFs) are a class of metal-organic frameworks (MOFs) that consist of *multiple* structurally unique ligands and/or metal ions/clusters. There has been an interest in flexible ligands such as amino acids and peptides.[1-4] However, all studies to date have used a *single* type of amino acid, or peptide. I present the first *multicomponent* amino acids MOFs using *combinations* of amino acids-based ligands.

In this work, we explored the development of multicomponent amino acid-based MOFs using unmodified amino acids as linkers. Despite extensive synthetic efforts, the formation of 3D MMOFs from unmodified amino acids proved unsuccessful due to the inherent structural limitations of amino acids and their preferred coordination modes with metal ions.

To overcome these limitations, a new family of amino acid-derived ligands, H_2XPyr (X denotes amino acids), was designed and synthesised. These linkers enable the formation of a robust framework synthesis by incorporating the amino acid functionality, which is covalently coordinated to the pyrazole group. These frameworks retain the amino acid's chemical characteristics. Zn_2XPyr frameworks are the first successful examples of multicomponent amino acid-based MOFs constructed from this new linker family.

A complementary approach was pursued through the functionalisation of the MUF-77 framework, a member of the Massey University Framework (MUF) series previously developed by the Telfer Group.[5, 6] In this strategy, amino acids or their derivatives were installed onto the linear ditopic linkers of MUF-77, enabling precise control over the chemical microenvironment within its pores. This modular design allowed of the engineering of cooperative *catalytic dyads* within the pore structure, mimicking the spatial arrangement of functional residues within enzyme active sites.

Two approaches were adopted for designing enzyme-inspired multicomponent MOFs: the first is incorporating amino acids into new amino acid-derived linkers capable of forming robust MMOFs, and the second is installing amino acid functionalities within well-established MOF structures (MUF-77) to create catalytically active pore environments.

Contributions

All the work in this thesis was completed by Ghadir Dahalan

Except:

The bdc-Br_2 and bpdc-Br_2 syntheses were done by prior group member.

The synthesis of H_3hbtt, H_3htt, and H_3hptt was performed by prior group member.

High-resolution mass spectrometry data were collected by Dave Lun.

The TLC and HPLC conditions for the aldol reaction were developed by Dr. Subo Lee.

Assistance with SCXRD refinement of the three disordered structures:
[Zn(*l*-methionine-H)$_3$(*l*-valine-H)], [Zn_2(GlyPyr)$_3$(SerPyr)$_2$] and
[Zn_2(PhePyr)$_3$(ValPyr)$_2$] was provided by Dr. Subo Lee.

Acknowledgements

First and foremost, I would like to thank my supervisor, Professor Shane Telfer, for the opportunity to undertake this PhD and for his guidance, support, and encouragement as I grew as a researcher.

I am also deeply grateful to Professor Geoff Jameson for his continuous help and advice with SCXRD solutions.

I am grateful to the MacDiarmid Institute, and especially MESA, for workshops, symposia, and networking opportunities that helped me develop beyond the lab.

My sincere thanks go to everyone who supported my day-to-day research: Dr Pat Edwards for his steady help with NMR, and all past group members for their assistance and camaraderie. I am especially grateful to the late David Lun, whose expertise with MS and many lab instruments, and whose generosity of time, greatly supported this research. His guidance and kindness are warmly remembered. Special thanks to Subo for patiently guiding me through the instruments at the beginning and for continued support over the years, to Mohana for help with the HPLC instrument, and to Cara for her help with the PoreBlazer. I also thank Ludwig and Elnaz for making every day in the lab enjoyable.

I gratefully acknowledge the financial support of the Sir Paul Callaghan Scholarship, which enabled me to pursue my PhD studies, and the Freemasons Scholarship, which supported me through the later stages of my research.

Beyond the lab, I would like to thank my dear friend Rania for the good times we have shared since I moved to Palmerston North and for her support during difficult moments. My heartfelt thanks also go to Olfat and Dania for their help, kindness, and the many good times we had together.

Finally, my deepest thanks go to my family, my mum Hayat, my partner Muhammad, and my children Adam and Zane. Your unwavering love, patience, and belief in me have been my greatest source of strength throughout this journey.

Publications and thesis structure

Not applicable.

Publications relevant to this thesis

Not applicable.

Table of Contents

Abbreviations

AIBN	Azobisisobutyronitrile
Ala	Alanine
Aq	Aqueous
BA	Benzoic acid
Bdc	Benzene-1,4-dicarboxylic acid
BOC	tert-Butyloxycarbonyl
Boc_2O	Di-tert-butyl dicarbonate
BPin	Bis(pinacolato)diboron
Bpdc	Biphenyl-4,4′-dicarboxylic acid
btb	1,3,5-Tris(4-carboxyphenyl)benzene
btc	Benzene-1,3,5-tricarboxylate
BzCHO	Benzaldehydes
d	Doublet
dd	Doublet of doublets
ddd	Doublet of doublet of doublets
DEF	Diethylformamide
DIC	N,N′-Diisopropylcarbodiimide
DMAP	4-Dimethylaminopyridine
DMF	Dimethylformamide
DMSO	Dimethyl sulfoxide
EDC	1-Ethyl-3-(3-dimethylaminopropyl)carbodiimide
EDG	Electron donating group
EDTA	Ethylenediaminetetraacetic acid
EWG	Electron withdrawing group
Gly	Glycine
GHG	Glycine-Histidine-Glycine

ee	Enantiomeric excess
eq	Equivalents
HKUST	Hong Kong University of Science and Technology
His	Histidine
Hmtt	5,5′,10,10′,15,15′-Hexamethyltruxene-2,7,eddeed-tricarboxylic acid
HPLC	High-performance liquid chromatography
HOBt	Hydroxybenzotriazole
Hz	Hertz
Ile	Isoleucine
Im	Imidazole
J	coupling constant
L	Ligand
Leu	Leucine
LIFM-28	Lehn Institute of Functional Materials
Lys	Lysine
m	Multiplet
m/z	Mass to charge ratio
Me	Methyl
Met	methionine
MIL	Matériaux de l′Institut Lavoisier
MMOF	Multicomponent metal-organic framework
MOF	Metal-organic framework
mol %	mole percent
MUF	Massey University Framework
NBS	N-Bromosuccinimide
ndc	2,6-Napthalenedicarboxylate
NMR	Nuclear magnetic resonance
PCN	Porous coordination network

Phe	phenylalanine
PXRD	Powder X-ray diffraction
R_f	Retention factor
s	Singlet
SBU	Secondary building unit
SCXRD	Single-crystal X-ray diffraction
Ser	serine
t	Triplet
TEA	Triethylamine
TFA	Trifluoroacetic acid
TGA	Thermogravimetric analysis
THF	Tetrahydrofuran
Thr	threonine
TLC	Thin layer chromatography
UiO-67	Universitetet i Oslo
UV	Ultraviolet
Val	Valine
ZIF	Zeolitic imidazolate frameworks

Chapter 1 Introduction

1.1 Metal organic frameworks (MOFs) general overview

Over the course of the twentieth century, the chemistry of crystalline materials grew in both scope and complexity.[7-9] These materials consist of metal nodes or metal clusters that are connected by organic linkers to form a 3D network. These organic linkers are generally rigid and have anionic groups that can bind to the positively charged metals. The resulting frameworks are more porous compared to conventional crystalline materials; this feature distinguishes these materials from other coordination materials. Guidelines for naming, defining, and classifying these materials were released by IUPAC in 2013 (**Figure 1.1**).[10]

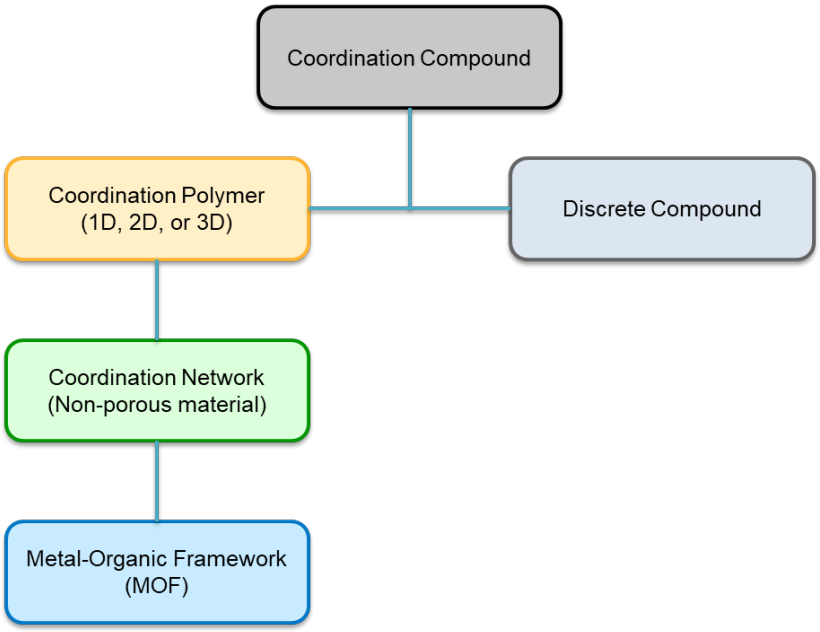

Term	Definition
Coordination Polymer	The repeating metal-ligand units extend in 1, 2, or 3 dimensions. It can be 1D chains, 2D sheets or 3D network.
Coordination Network	A special type of coordination polymer, where the repeating ligand-metal units are interconnected, not just linear chains. This goes beyond simple polymers by including cross-links, loops, or multidimensional connectivity.
Metal-Organic Frameworks	MOFs are a subclass of coordination networks with organic ligands acting as linkers. MOFs are typically porous

Figure 1.1: The top hierarchy represents the IUPAC classification of the coordination compounds. The bottom table shows the definition of these classes.

These crystalline materials have been described using various terms, including metal-organic frameworks (MOFs), microporous coordination polymers (MCPs), porous coordination networks (PCNs), porous coordination polymers (PCPs), and zeolite-like metal-organic frameworks (ZMOFs). Among these, MOF is the most widely adopted term and is strongly recommended for use.[11]

A MOF is usually given a nickname, such as MOF-5[12], or PCN-777,[13] or an abbreviated formula such as $Cu_3(BTC)_2$ (BTC = Benzen-1,3,5-tricarboxylate).[14] Another way for naming MOF is after the place of origin, such as MUF-77 (Massey University Framework),[6] HKUST-1 (Hong Kong University of Science and Technology),[14] and UMCM (University of Michigan Crystalline Material).[15]

1.2 MOF timeline

Porous coordination polymers were first described by Richard Robson in 1989.[16] Then, the first publication containing metal-organic frameworks in the title was in 1995, by Omar Yaghi.[17] The history of MOFs started with MOF-5, which was reported by Omar Yaghi in 1999.[12] The idea was simple yet innovative. Inspired by the well-known octahedral geometry of zinc acetate, researchers replaced the acetate with 1,4-benzenedicarboxylate (bdc), a linear ligand. This substitution enabled the formation of an extended 3D framework with an open network, as bdc bridges between the metal nodes (**Figure 1.2**).

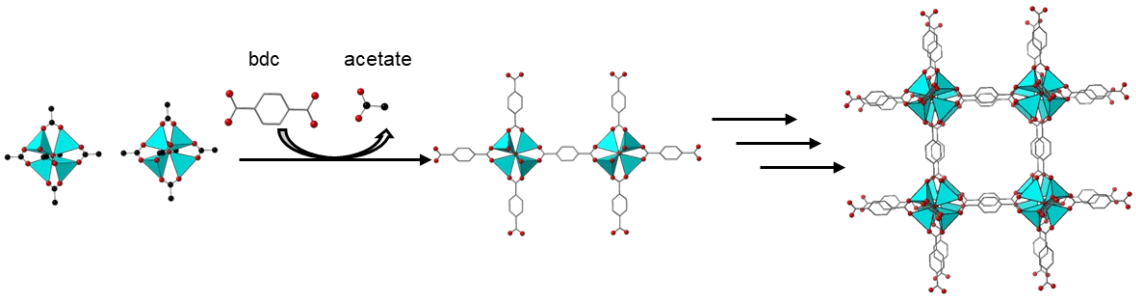

Figure 1.2: A schematic diagram illustrates the MOF-5 is derived from zinc acetate where the acetate is replaced with bridging bdc.

There are major differences between MOF-5 and zinc acetate. First of all, bdc bridges between the Zn_4O cluster, resulting in high thermal and architectural stability of the framework. Secondly, the coordination network extends in 3D, resulting in a primitive cubic net. Thirdly, it exhibits high stability upon removing the solvent that fills the pores, reflecting its permanent porosity. MOF-5 opened the way to a new era of crystalline, porous materials that are built from inorganic metals and organic linkers. The pore environment can be controlled by functionalising the organic linkers or using different metal types. This porosity makes these materials a host for many guests, which makes it useful for many applications such as gas storage,[18, 19] gas separation[20] and catalysis.[21]

1.3 Secondary building units (SBUs)

MOFs consist of metal ions or clusters that function as nodes, connected by organic linkers. Polynuclear clusters were widely employed in MOF synthesis. As their name implies, polynuclear clusters consist of multiple atoms, which could be *multiple* metal atoms or metals coordinating to *multiple* atoms, such as nitrogen and oxygen. Although SBUs are not discrete chemical entities, the concept provides a way for rationalising the MOF structure.[14] SBUs are found in permanently porous MOFs, which retain porosity even after the solvent removal from the pores, such as HKUST-1, MOF-5 and MOF-2.[14, 17, 22]

One of the most common single metal atoms SBU observed in MOFs is the ZnN_4. This SBU is common in zeolitic imidazolates frameworks (ZIF), which is a major subclass of MOFs.[23] Another classical motif is the paddlewheel $M_2(COO)_4$, where four carboxylates coordinate to two metal ions at the equatorial positions, while the axial positions are occupied by solvent molecules or N-atoms from ligands bridging between the SBUs.[24, 25] $M_4O(COO)_6$ which forms the foundation in MOF-5, is another example of a well-known SBU.[12] This unit consists of tetrahedral M_4O^{6+} cluster coordinating to six carboxylates generating an octahedral geometry (**Figure 1.3**).

Other SBUs include rod-like clusters such as $M_3O_3(COO)_3$, which form 1D channels. MOF-74 has an infinite SBU, which is formed from ligand 2,5-dihydroxyterephthalate, where the hydroxyl group provides an extra oxygen, which is essential to build this SBU.[26] Importantly, solvent removal often generates open metal sites, which is essential for many SBU stability and functionality.[27] A further example is the $M_6O_4(OH)_4(COO)_{12}$ cluster, which is the defining SBU of the UIO (Universitetet I Oslo) family of MOFs. This highly connected octahedral cluster is highly responsible for these MOFs exceptional robustness and chemical stability (**Figure 1.3**).[28] There are many other examples of SBUs, as the majority of the periodic table metals were used for the MOF synthesis.[29] In conclusion, these SBUs provide the structural diversity and design flexibility that boost the rapid expansion of the MOF chemistry field.

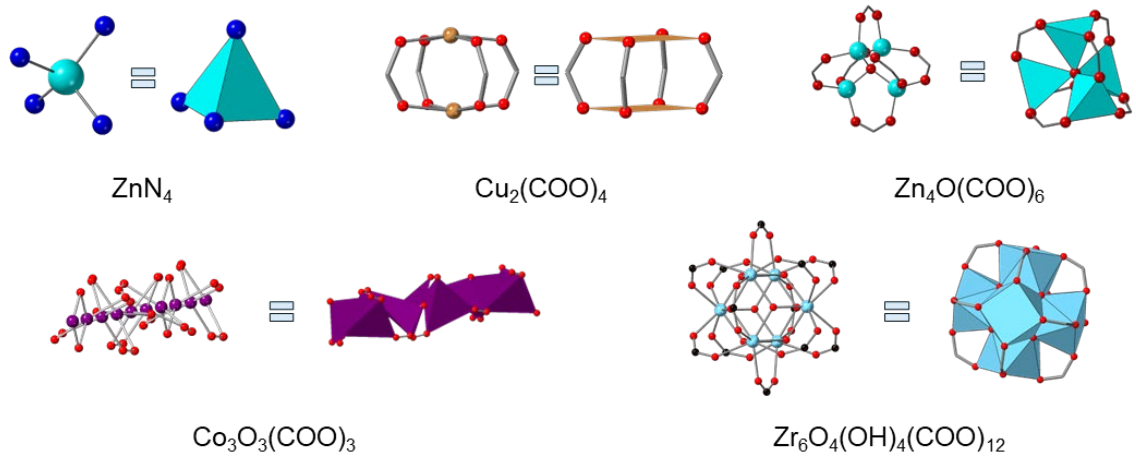

Figure 1.3: Examples of metal clusters commonly found in MOFs.

1.4 Isoreticular MOFs

MOFs synthesis is challenging and depends on many factors such as the metal type, the solvent type, the temperature, and the synthesis method. Reticular chemistry can be applied to MOFs as they consist of strong bonds that extend in a repeating net-like architecture (topology).[23, 30, 31] The isoreticular principle is essential in MOF chemistry, as it forms a MOF series with the same topology but with different properties. These structures are achieved by changing the ligands, such as the ligand's length (**Figure 1.4**), resulting in MOFs family with the same topology but with different pore sizes.[32] One example of the IRMOF series is that generated by the Yaghi group (**Figure 1.4**).[33, 34] These MOFs are isoreticular to MOF-5, and they were synthesised in two different ways. The first one is functionalising the ligands with various functional groups, as bdc was functionalised in compounds **2**, **3** and **4** resulting in IRMOF-2, 3, and 4, respectively. The other way is using longer linkers by the addition of a benzene ring to the bdc, such as ligands **8**, **10**, and **16**, which make the IRMOF-8, 10 , and 16, respectively.[33] As the linker size increases, the pore size does as well but maintaining the topology.

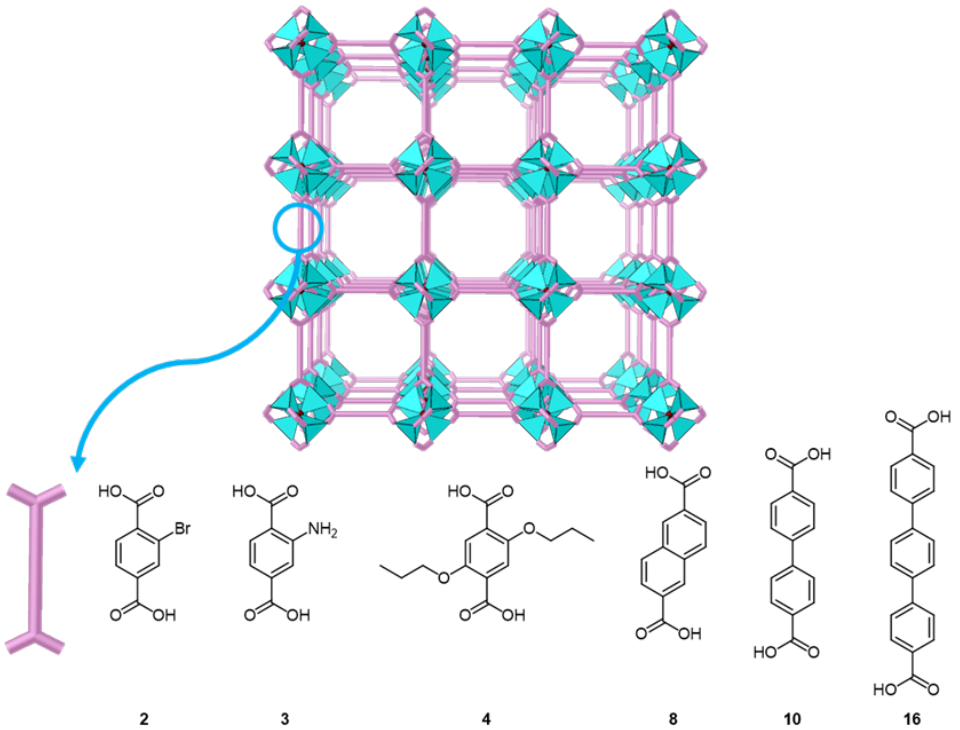

Figure 1.4: IRMOF with various linear organic ligands. **2**, **3** and **4** are functionalised bdc with different functional groups, while **8**, **10,** and **16** are longer linear linkers with the same coordination geometry as bdc.

The isoreticular principle applies not only to ligand lengths and functional groups, but different metal types can also produce isoreticular MOFs, as found in MOF-74 (**Figure 1.5**). The metal centres in this framework adopt an octahedral coordination geometry by binding to oxygen atoms from carboxylate groups or hydroxyl groups of the 2,5-dihydroxyterephthalate (DHTP) ligands.[35] These secondary building units (SBUs) assemble into helical rods, which interconnect to form a honeycomb-like 3D porous structure.[35] Solvent molecules, initially coordinated to the metal sites, are removed upon activation, generating open metal sites that face into the pore channels. In the as-synthesised material, these positions are typically occupied by DMF.

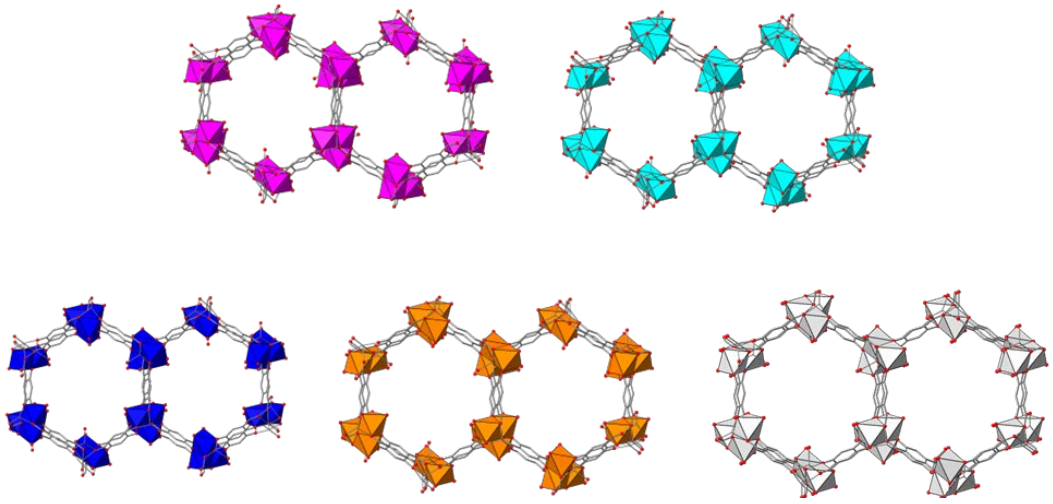

Figure 1.5: Structures of the isoreticular MOF-74 series. Atoms colour: C chain = grey, O = red, Zn(II) = teal blue, Ni(II) = silver, Co(II) = magenta, Mg(II) = orange, and Cu(II) = royal blue. Hydrogen atoms are omitted for clarity.

1.5 Multicomponent versus multivariate MOFs

The number of reported multicomponent MOFs (MMOFs) remains limited, with only a few examples extending to quaternary systems composed of four distinct building blocks. The synthesis of MMOFs is particularly challenging, as many factors influence MOF crystallisation and growth. For instance, even the simple MOF-5 framework, constructed from zinc ions and bdc linkers, can yield different topologies depending on solvent, pH, temperature, and the use of additives.[24, 36-41]Consequently, the preparation of MMOFs is even more complex, since additional variables come into play with each component introduced.

MUF-8 and MUF-84 highlight the delicacy of MMOF synthesis. Both frameworks are constructed from the same tritopic linker, ntb (4,4',4"-nitrobenzoate), combined with various bdc derivatives, yet they crystallise into distinct topologies. The determining factor is the number of secondary functional groups on the phenyl ring of the bdc linker: MUF-8 is favoured when the bdc carries multiple substituents, whereas MUF-84 forms when the bdc is unsubstituted or contains only a single substituent (**Figure 1.6**).[42]

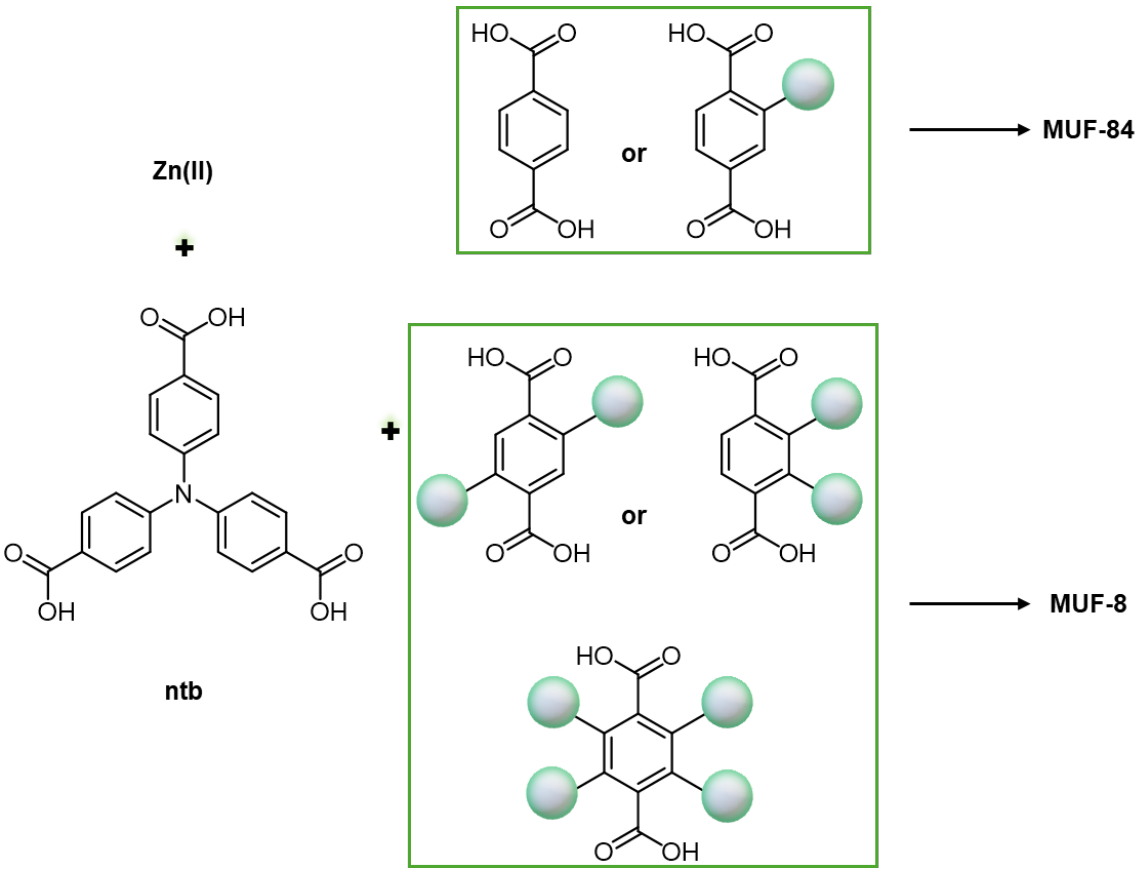

Figure 1.6: This schematic figure illustrates the effect of the bdc degree of functionalisation on the competition between ligands. Increasing the number of substitutions to 2, 3, and 4 pushes the topology towards MUF-8.

Another major limitation in MMOF synthesis is the competition between different ligands, which can lead to the formation of multiple MOF phases. For instance, MUF-7[5] is built from Zn_4O clusters and three distinct ligands, btb, bpdc, and bdc. However, each of these ligands can independently form its own MOF with Zn_4O (**Figure 1.7**): bdc yields MOF-5,[43] bpdc forms IRMOF-10,[33] and btb produces MOF-177.[44] Moreover, combinations of these ligands give rise to additional frameworks (**Figure 1.7**), such as UMCM-1 from btb, bdc, and Zn_4O,[15] or SUMOF-4 (Stockholm University Metal Organic Framework) from bdc and bpdc.[45] Despite this complexity, careful control of the synthesis conditions makes MUF-7 the thermodynamically favoured product.

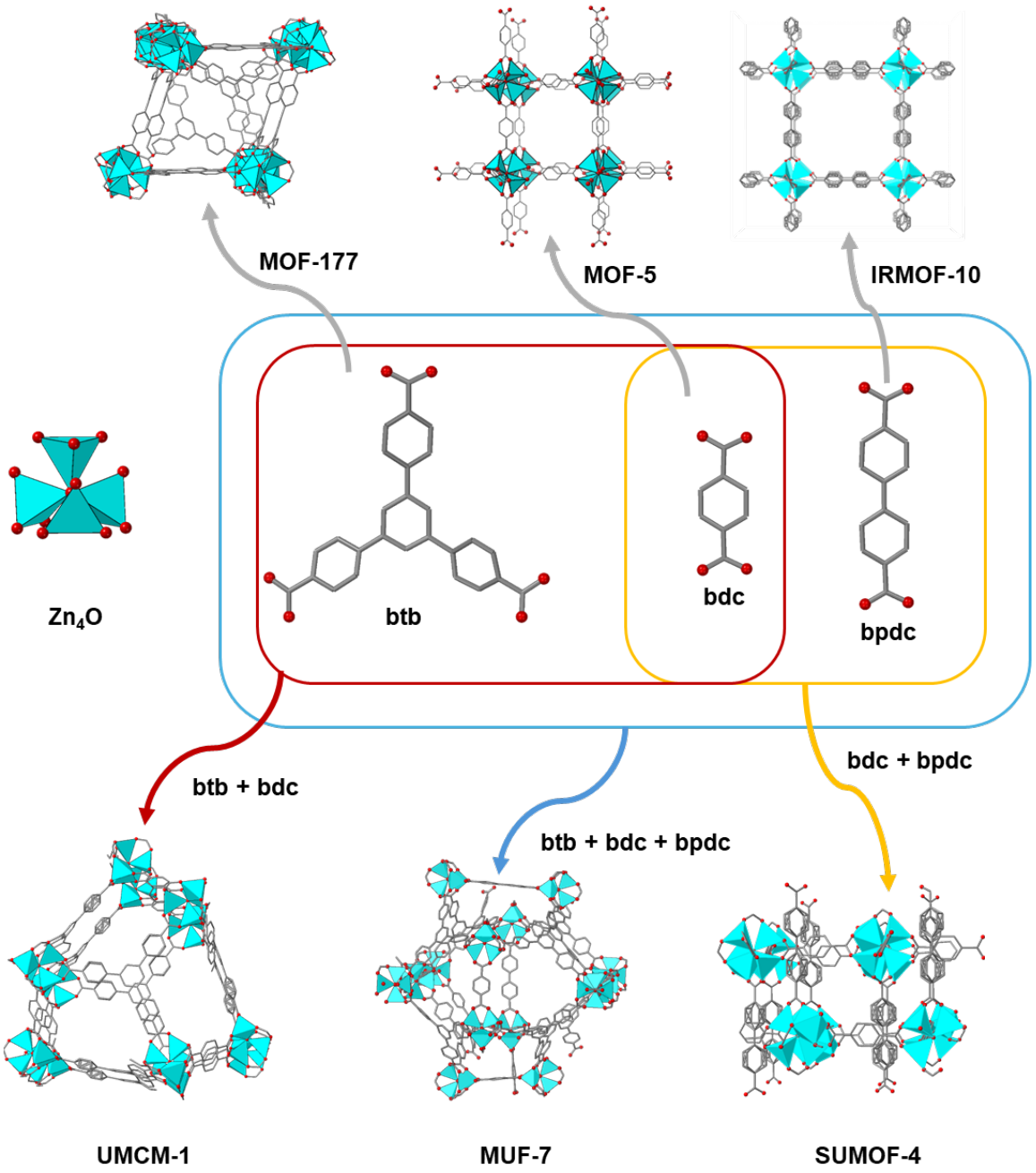

Figure 1.7: An example of ligand competition in *multicomponent* MOF synthesis. Zn_4O SBU can combine with different linkers: btb, bdc, and bpdc, to produce different frameworks. Bdc forms MOF-5, bpdc forms IRMOF-10, and btb forms MOF-177. In multiple ligand systems, btb + bdc + Zn_4O generate UMCM-1, while bdc + bpdc + Zn_4O give SUMOF-4. Incorporating all three ligands under optimised conditions results in the thermodynamically favoured MMOF, MUF-7.

The multicomponent framework FDM-8 incorporates two metal cations, Cu(II) and Zn(II), together with three organic linkers: bdc, 2,6-ndc (naphthalene-2,6-dicarboxylate), and PyC (pyrazole-4-carboxylate). This MOF is isoreticular with MUF-7, sharing the same overall topology.[46] In FDM-8, the tritopic btb linker of MUF-7 is replaced by PyC, while bpdc is substituted with the shorter 2,6-ndc (**Figure 1.8**).

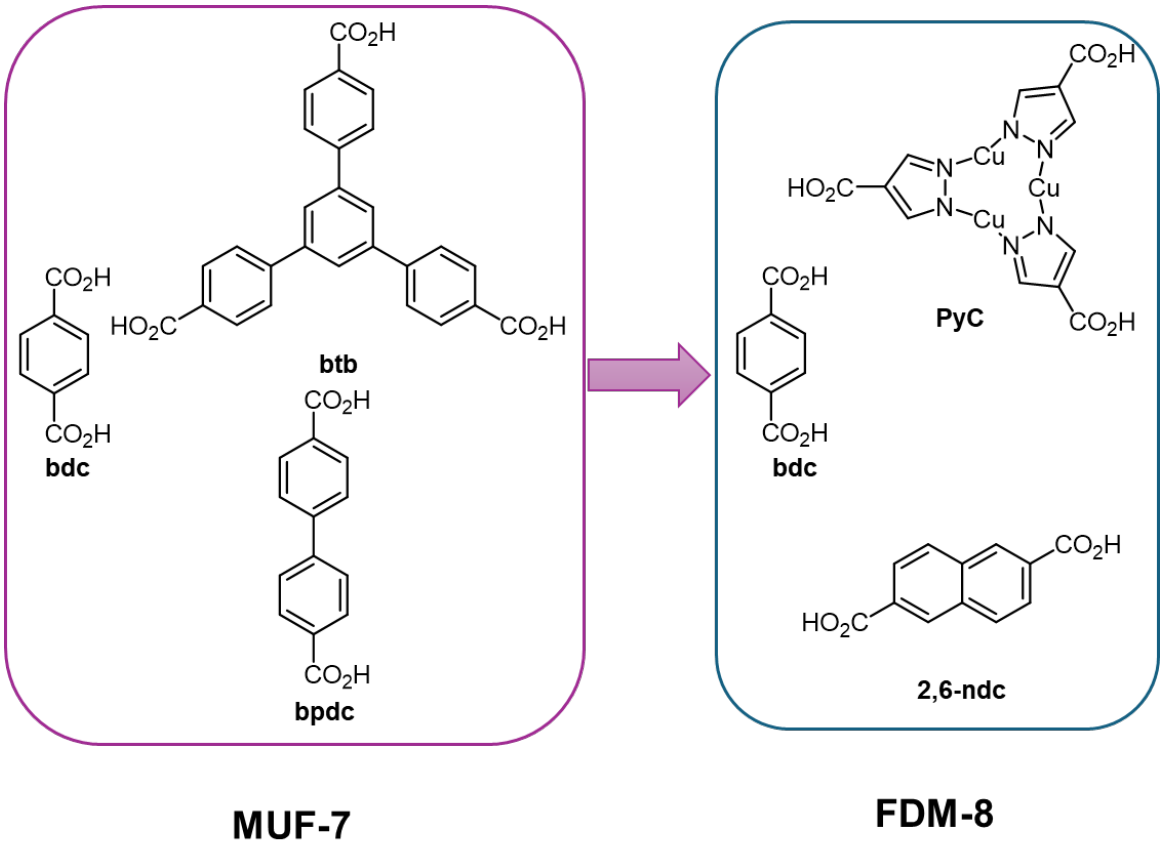

Figure 1.8: In FDM-8, the linkers differ from those in MUF-7: the btb linker is replaced by a Cu(II)-PyC complex, while the bpdc linker is substituted with the shorter ndc linker.

Multivariate MOFs (MTV-MOFs) are built of building blocks with similar coordination geometries. The first MOF-74 was reported with zinc as the metal centre. Later, isoreticular analogues (IR-MOF-74) incorporating different types of metals, such as cobalt, magnesium, and copper, were developed.[27, 35, 47-50] Then, Yaghi's group reported multi-metallic MOF-74 systems, demonstrating the incorporation of up to ten different metal ions (Ba, Ca, Cd, Co, Fe, Ni, Mg, Mn, Sr, and Zn) while retaining the same framework topology (**Figure 1.9.a**).[51] These mixed-metal MOFs exemplify multivariate MOFs, where compositional heterogeneity is introduced without altering the underlying structure. Such heterogeneity can be achieved either by combining different metals that form identical SBUs, or by incorporating chemically distinct linkers with the same coordination motifs, for instance, using bdc and bdc-Br (**Figure 1.9.b**).[32]

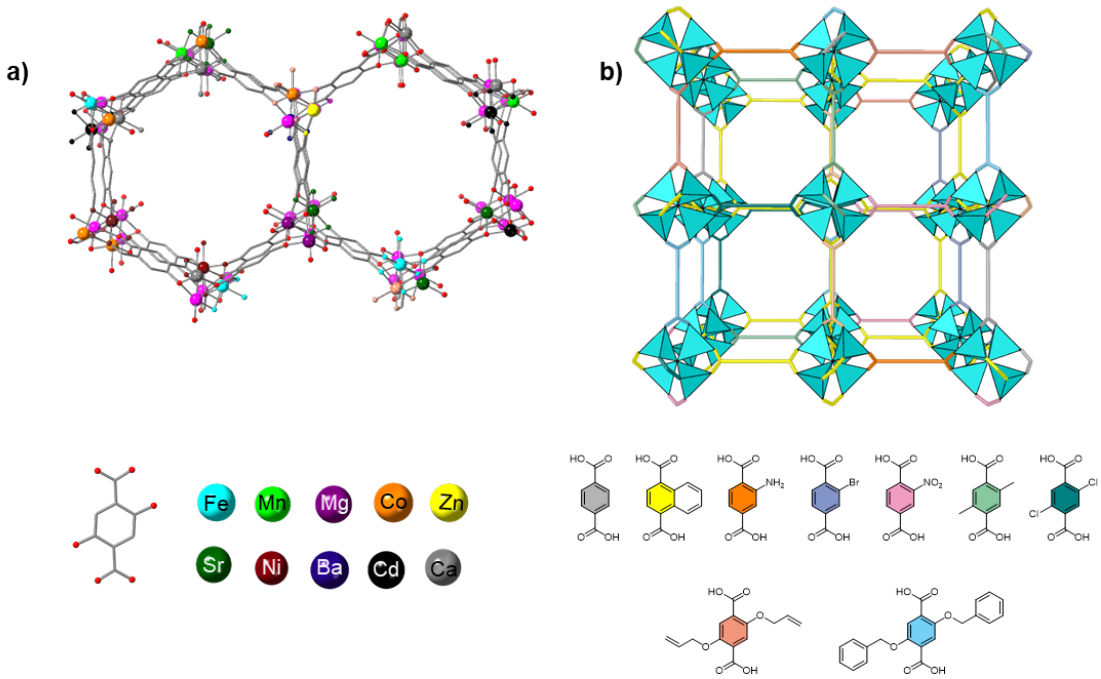

Figure 1.9: a) MTV-MOF-74, where up to 10 metals were incorporated. **b)** MTV-MOF-5, where up to 9 linkers were incorporated.

1.6 MOF characteristics

MOFs have many attractive properties that make them valuable for a wide range of applications. One of their key advantages is permanent porosity, which gives structural stability under diverse conditions, including exposure to different solvents, pH levels, and temperatures. Importantly, the pores are the sites where much of the chemistry occurs.[22] The exact structure of MOFs can be determined using X-ray diffraction, providing atomic-level precision that enables a deeper understanding of their working mechanisms.

A vast number of MOFs can be synthesised due to the diversity of available metals and ligands. Transition metals, particularly Zn(II) and Co(II), are the most commonly used in MOF synthesis; however, alkaline earth metals such as Mg(II) and lanthanide ions can also be incorporated.[52] The ligands' choice is limited only by the organic chemistry principles and the chemist's creativity. Ligands can be ditopic (two coordination sites), tritopic (three coordination sites), or have even higher number of connectivity, enabling variable ways of coordination to SBUs and leading to the formation of a wide variety of MOF structures.

MOFs are robust materials, exhibiting stability against both chemical and thermal degradation, while also being relatively inexpensive and straightforward to synthesise. Unlike many other crystalline materials, MOFs are highly designable and tunable, offering the unique advantage of post-synthetic modification.[53-55]

With all these advantages, MOFs have found applications across a wide range of fields. They can function as catalysts when their ligands are functionalised with catalytically active groups.[56-58] In addition, MOFs can exhibit luminescent properties arising either from the metal centres (e.g., lanthanides) or from aromatic ligands containing π-conjugated systems.[59] These luminescent features enable their use in sensing applications, such as the detection of ions, vapours, and variations in pH or temperature.[60]

1.7 Amino acids as ligands for MOFs synthesis

1.7.1 Rationale for using amino acids and peptides as ligands

Most of the previously reported MOFs focused on the rigid organic linkers, such as dicarboxylates (-COOH) and nitrogen heterocyclic ligands, that ensure MOFs' stability and permanent porosity.[53, 61, 62] Amino acids and peptides are appealing to use as linkers for MOFs synthesis, as they have both carboxylate groups (-COOH) and an amino group ($-NH_2$) (**Figure 1.10)**, which can coordinate to metal centres in different coordination ways, such as N,O-bidentate coordination, or monodentate via N or O. Additionally, the side chains of amino acids, such as the hydroxyl group of serine, the thiol of cysteine, and the imidazole of histidine, enhance the framework possibilities and functionality. [63-65]

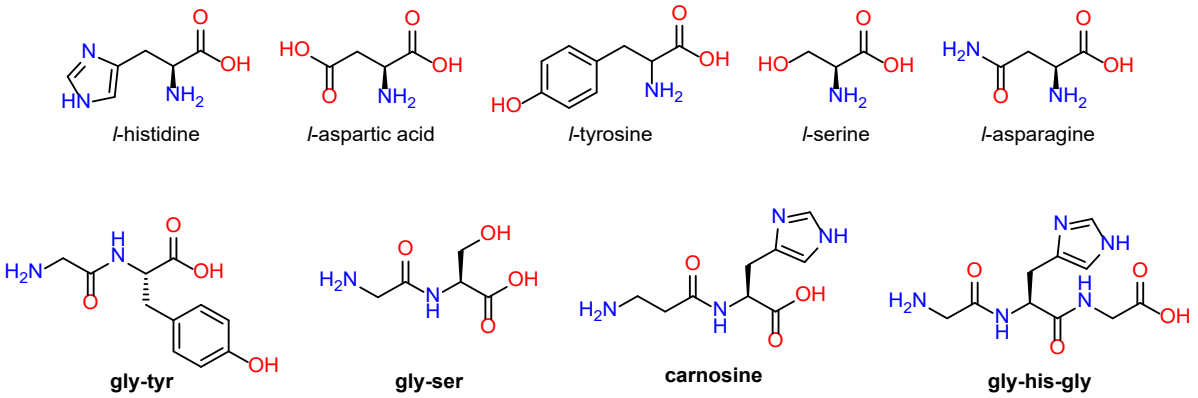

Figure 1.10: Example of amino acids and peptides that were used as MOFs building blocks.

Amino acids are inherently chiral, except for glycine. This chirality is transferred to MOFs, resulting in homochiral MOFs. Chiral MOFs are of particular importance for enantioselective uptake and chiral compounds separation. The correct enantiomer choice is vital in pharmaceuticals, as one enantiomer is therapeutically useful while the other may be harmful or ineffective.[66, 67] Amino acid-based MOFs may mimic enzymes by creating a chiral pocket that is suitable for catalysis; therefore, they can be used as asymmetric catalysts. For example, chiral MOFs were used as asymmetric catalysts for Michael addition and Aldol reaction, demonstrating the potential of using these amino acid-based MOFs as asymmetric catalysts.[68]

Moreover, amino acids are highly abundant, and available at a low cost. This advantage makes the amino acids highly appealing to use as ligands over the organic linkers.[69] Also, amino acids are biocompatible and have low toxicity, which broadens the amino acid-based MOFs applications in the biomedical field, particularly in drug delivery, biosensing, and imaging.[8, 70] Amino acids contribute to MOF chemistry sustainability, as their incorporation into MOF offers an eco-friendly pathway to functional porous materials.[53] The chirality, along with the sustainability, are two attractive features that make them unique from organic ligands, and their use in MOFs synthesis is highly valuable.

1.7.2 Solitary amino acids and/or peptides as ligands in MOFs

Amino acids possess multiple functional groups that enable diverse coordination modes beyond those typically available to conventional aromatic ligands. Their conformational flexibility allows access to structural topologies that are often inaccessible to rigid aromatic linkers.[63] For instance, histidine can act as a tridentate ligand, coordinating metals through its imidazole nitrogen, carboxylate oxygen, and amino nitrogen. Similarly, tyrosine can bind via its carboxylate, amino group, and phenolic hydroxyl group.[63]

Several amino acids have been incorporated into the synthesis of MOFs; each showed different properties. For example, glycine, the simplest amino acid, coordinates Cu(II) via its carboxylate oxygen and amino nitrogen in a square-planar geometry. This arrangement generates 2D layers that extend into 3D structures through hydrogen bonding.[71] However, because glycine lacks additional donor groups, the resulting framework is compact, with limited pore accessibility and low surface area.[63]

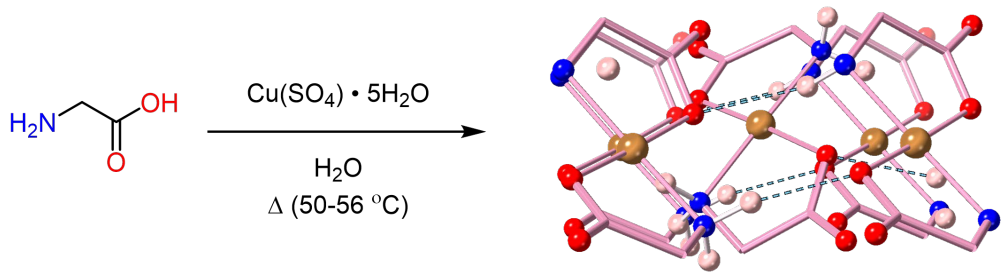

Figure 1.11: $Cu(Gly)_2$ structure synthesis from glycine and $CuSO_4$ in aqueous basic solution. Aom colours: glycine C chain = pink, H = pinkish white, O = red, N = blue, and Cu = brown.
H atoms are omitted except for those essential for H-bond (dashed bonds).

In contrast to glycine's compact assemblies, glutamic acid, bearing an extra carboxylate group, offers higher connectivity and dimensionality. Glutamate coordinates with Zn(II) in octahedral geometry via both the carboxylate O atom and the amino N atom. The carboxylate groups bridge Zn(II) ions to form a robust 3D framework (**Figure 1.12**). This material is water-stable at ambient temperature.[72] Beyond structural robustness, this framework has demonstrated catalytic activity, including the cycloaddition of CO_2 with epoxides to produce cyclic carbonates, as well as photocatalytic dye degradation under light irradiation.[73]

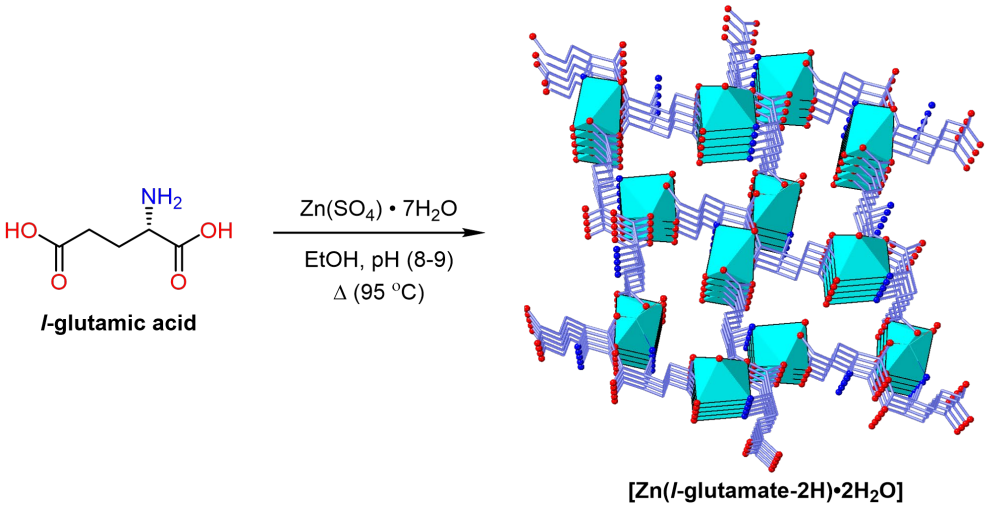

Figure 1.12: 3D framework synthesised from *l*-glutamic acid and $ZnSO_4$ in ethanol. Atom colours: glutamate C chain = blue, O = red, N = blue, and Zn = teal blue. H atoms are omitted for clarity.

A related amino acid, aspartic acid, further illustrates how not only ligand identity but also reaction conditions strongly influence framework dimensionality. The mesoporous 3D framework $[Ni_{2.5}(OH)(l\text{-Asp})_2]\cdot 6.55H_2O$ is obtained solvothermally from *l*-aspartic acid, $NiCl_2$, and triethylamine under high pH conditions.[74] In this case, extended Ni-O-Ni linkages generate an open, homochiral structure with 1D channels of approximately 8 x 5 Å (**Figure 1.13**). At lower pH, however, the synthesis yields only a 1D polymer, $[Ni_2O(l\text{-Asp})(H_2O)_2]\cdot 4H_2O$, underscoring the pivotal role of pH as a structural switch in amino acid-based MOF formation.[74] This example demonstrates that framework dimensionality can be tuned not only by amino acid side-chain functionality but also by careful control of reaction environment.

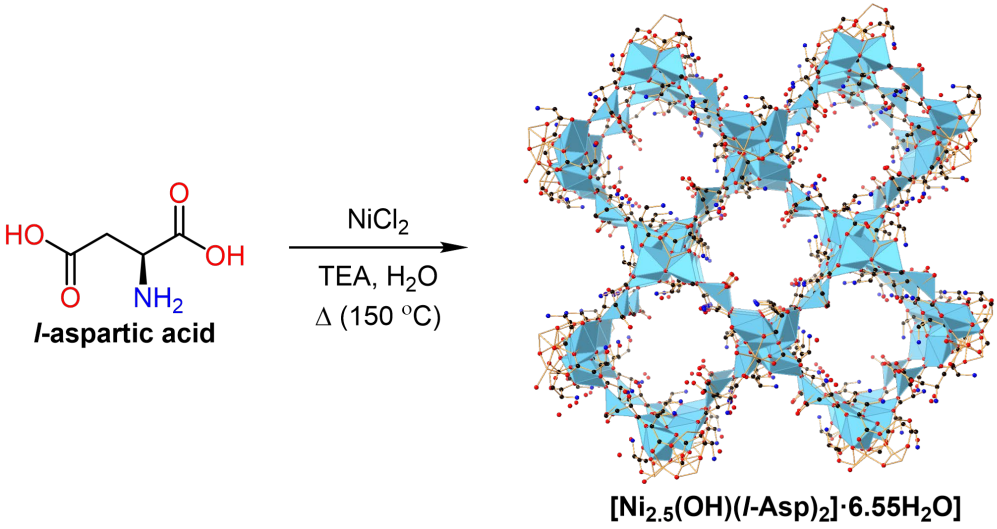

Figure 1.13: 3D framework synthesised from *l*-aspartic acid and $NiCl_2$ in aqueous medium. Atom colours: aspartate C chain = yellow, O = red, N = blue, and Ni = blue. H atoms are omitted for clarity.

Amino acids with aromatic or phenolic side chains introduce additional coordination possibilities and functional behaviour. Tyrosine, for example, with its phenolic side chain, has been shown to generate 3D frameworks with Co(II) and Zn(II). (**Figure 1.14.a**).[65, 75, 76] Co(II) ions coordinate to phenoxy oxygens, forming inequivalent tetrahedra, while other Co(II) centres bind to the amino nitrogen and carboxylate groups of *l*-tyrosine, yielding stable five-membered chelate rings within octahedral geometries.[52] The resulting lattice, constructed from both tetrahedral and octahedral Co(II) units linked via shared oxygen atoms, not only stabilises the framework but also enables functional properties: in the Co(II) analogue, ferromagnetic exchange interactions arise between adjacent dimers.[52]

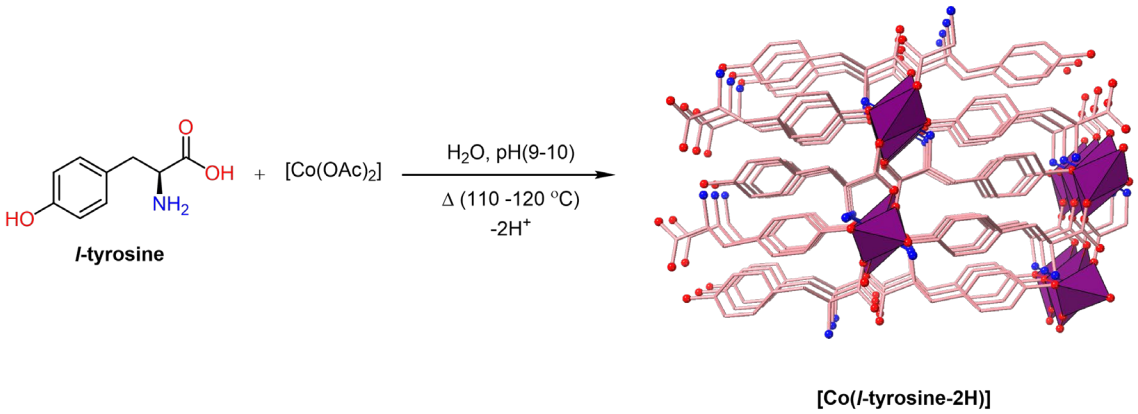

Figure 1.14: 3D framework synthesised from *l*-tyrosine and $Co(OAc)_2$ in aqueous medium. Aom colours: tyrosine C chain = pink, O = red, N = blue, and Co = purple. H atoms are omitted for clarity.

While frameworks derived from single amino acids reveal valuable structure-function relationships, their inherent size and flexibility often limit porosity and functionality. To overcome these restrictions, researchers have turned to short peptides, which extend the coordination distance and introduce sequence-specific chirality (**Figure 1.15**). These features can improve framework order and enhance porosity.[77-79] Peptide-based MOFs have been employed for enantioselective recognition/separation[77, 80] and catalysis,[79, 81]showing their ability to overcome the structural and functional limitations associated with solitary amino acid-based MOFs.[82, 83]

A representative example is carnosine (Car), a dipeptide with the sequence β-alanyl-*l*-histidine, which provides multiple binding sites: the imidazole side chain, the amino group, and the carboxyl group. Upon coordination with Zn(II), the imidazole deprotonates to form Zn-imidazolate chains, a motif analogous to zeolitic imidazolate frameworks (ZIFs). Zn(carnosine) exhibits piezoelectric behaviour: when its pores are filled with polar guest molecules, mechanical pressure induces charge alignment and generates a voltage. This electrical response is tunable depending on the guest molecules, providing a strategy for chemically adjustable, low-power energy harvesting.[4,84]

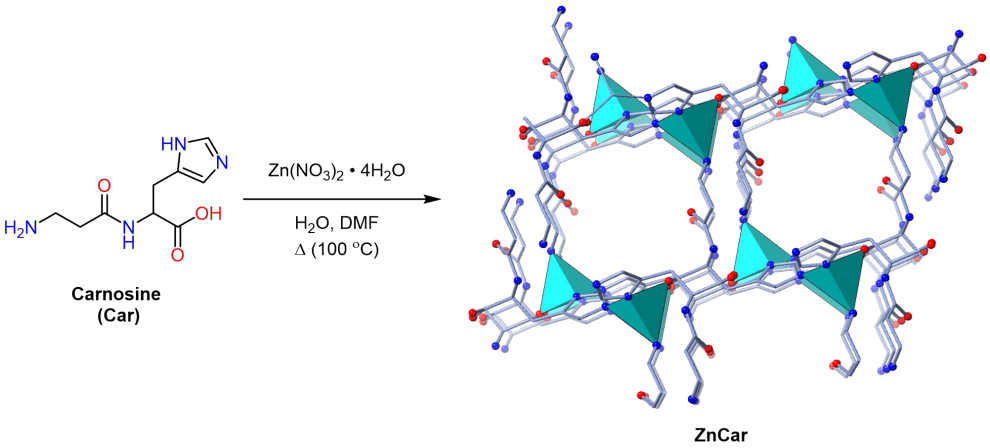

Figure 1.15: 3D framework of ZnCar synthesised from carnosine and $Zn(NO_3)_2$ in DMF. Atom colours: Carnosine C chain = mauve, O = red, N = blue, and Zn = teal blue. H atoms are omitted for clarity.

Tripeptides can offer even greater control over framework geometry and function. For example, the tripeptide Gly-*l*-His-Gly (GHG) coordinates Cu(II) to generate a homochiral 3D peptide MOF with periodic chiral channels. The histidine residue provides an imidazole side chain that acts as a directional binding site, while the glycine residues impart flexibility and extend the coordination distance (**Figure 1.16**).[79] This framework exhibits remarkable enantioselective separation ability: as a solid-phase extractant, Cu(GHG) can rapidly isolate over 50% of (+)-ephedrine from a racemic mixture within minutes.[79] This represents the first demonstration of a peptide-based MOF capable of rapid, efficient enantio-separation of polar chiral drugs.

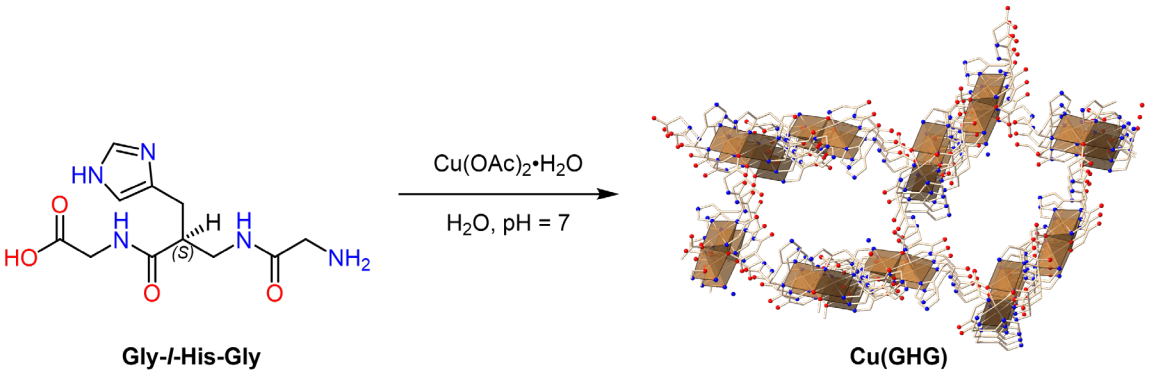

Figure 1.16: Synthesis of the homochiral, 3D, Cu(Gly–*l*-His–Gly) framework. The tripeptide GHG coordinates Cu(II) through its terminal amino and carboxylate groups and the histidine imidazole nitrogen under neutral aqueous conditions. Atom colours: GHG C chain =grey, O = red, N = blue, and Cu = brown. H atoms are omitted for clarity.

Despite these advances, single amino acid-based MOFs face challenges. Their flexibility and small size result in low porosity and limited surface area, which limit their use in gas storage and separation.[63]

Combining *multiple* distinct amino acids within the same framework may allow for functional group diversity, such as the imidazole from histidine, the hydroxyl from serine or tyrosine, and additional carboxylates from glutamate/aspartate. Therefore, the coordination environment can be enriched; moreover, it can form new structural topologies that are not accessible with a single amino acid-MOF.

1.7.3 Functionalised amino acids for MOFs synthesis

Beyond single amino acids and short peptides, researchers have developed functionalised amino acid-derived ligands, in which the amino acid backbone is covalently extended with heteroaromatic group. These ligands retain the functionality of the amino acids while extending them into more robust linkers. This approach combines the rigidity of organic linkers with the biological functionality of amino acids. The most widely adopted strategy has been the incorporation of amino acids with heteroaromatic backbones, such as pyrazoles.

Pyrazole-functionalised amino acid linkers

Amino acids functionalised with pyrazole have been used to form flexible, isoreticular frameworks with tunable pore environments, where the amino acid side chain results in functional diversity.[85] For example, glycine and alanine were coupled to the pyrazole group to form H_2GlyPyr and H_2AlaPyr, respectively. Then, these ligands were incorporated into IRZnXPyr (X denotes the amino acid type), and these MOFs have a honeycomb-like topology, with 1D pore channels (**Figure 1.17**).

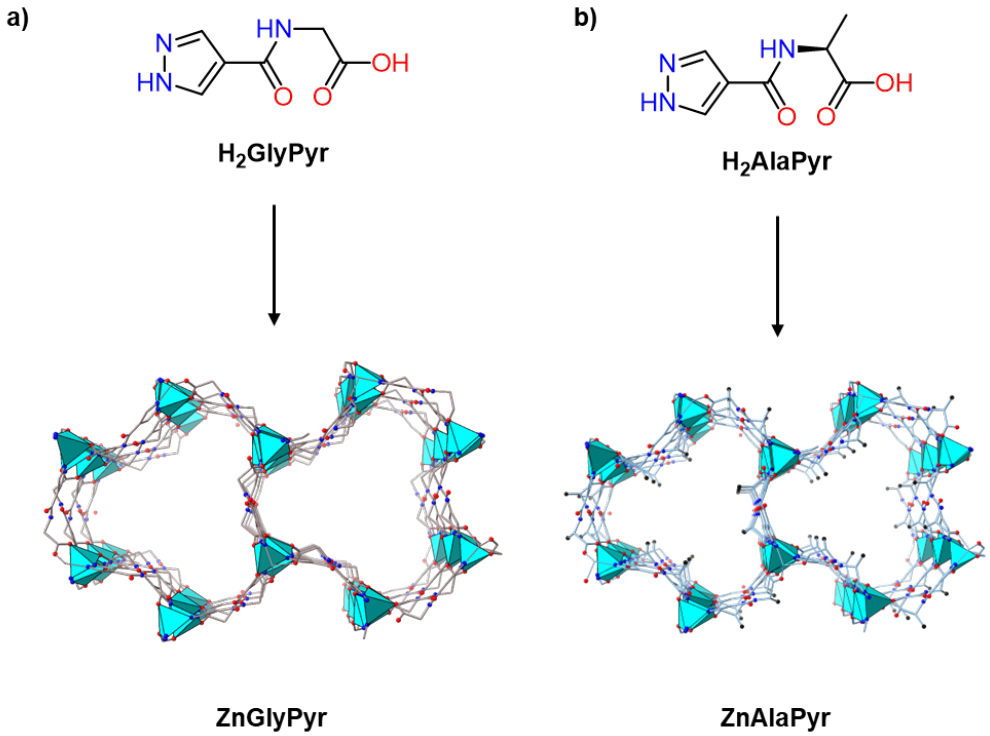

Figure 1.17: H_2GlyPyr and H_2AlaPyr ligands were incorporated into ZnGlyPyr and ZnAlaPyr, respectively. Atom colours: GlyPyr C chain = beige, AlaPyr C chain = blue, O = red, N = blue, and Zn = teal blue. H atoms are omitted for clarity.

Pyridine-carboxaldehyde based linkers

Beyond pyrazoles, amino acids have also been functionalised with 4-pyridine carboxaldehyde. For example, alanine reacts with 4-pyridine carboxaldehyde to form N-(4-pyridylmethyl)-*l*-alanine linker. These ligands were synthesised in a salt form of NaX ($X = Cl^-$, Br^-, HCO_2^-, $CH_3CO_2^-$). These ligands can be incorporated into frameworks such as AlaZnFor, in which each Zn centre coordinates to one oxygen atom from a carboxylate group and one nitrogen atom from an amino donor (**Figure 1.18**).[86] These structures exhibit rare zeolitic topologies. Interestingly, salt metathesis in aqueous media converts these 3D frameworks into 2D coordination polymers (CPs), but the transformation is reversible, allowing recyclability.

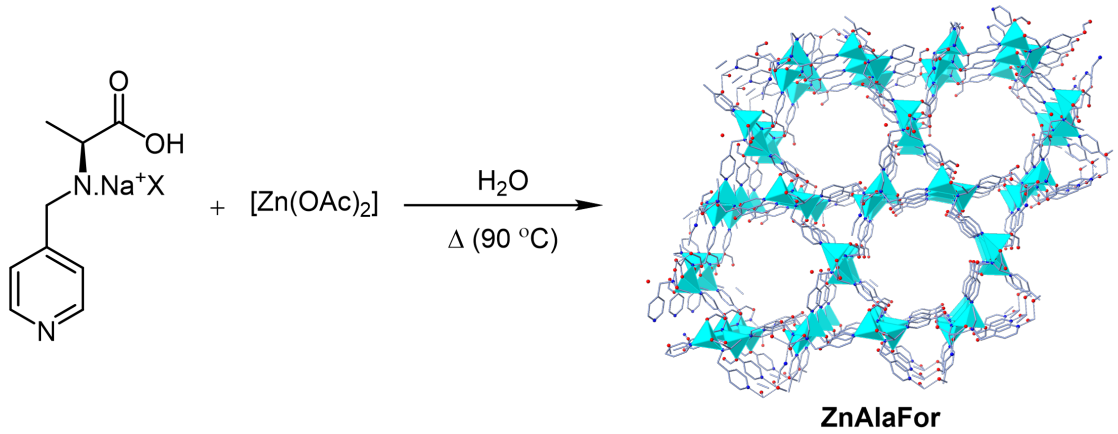

Figure 1.18: AlaZnFor synthesis pathway via solvothermal synthesis of AlaPyridine salt form where X is HCO_2^- (For). Atom colours: N-(4-pyridylmethyl)-*l*-alanine·Na HCO_2 C chain = mauve, O = red, N = blue, and Zn = teal blue. Hydrogen atoms are omitted for clarity.

Valine was used in an analogous manner to form N-(4-pyridylmethyl)-*l*-valine·NaX salts, which were successfully incorporated into zeolitic frameworks isoreticular with ZnAlaFor (**Figure 1.19**).[87] Extending this strategy further, serine, threonine, and leucine were derivatised with 4-pyridine carboxaldehyde to generate linkers of the type N-(4-pyridylmethyl)-*l*-amino acid·NaX (X = Cl^- or Br^-). The dimensionality of the resulting coordination networks was counterion-dependent: the bromide salts, in particular, afforded 3D frameworks formulated as [Cd(L)(Br)], where L denotes the amino acid-derived linker.[88]

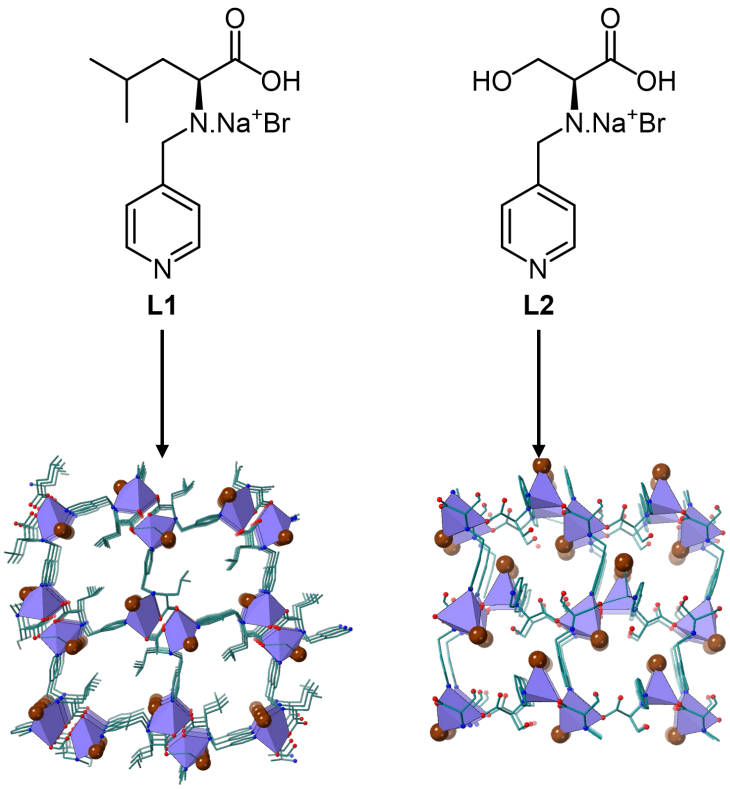

Figure 1.19: N-(4-pyridylmethyl)-*l*-leucine·NaBr (L1) and N-(4-pyridylmethyl)-*l*-serine NaBr (L2) forming [Cd(L1)(Br)] and [Cd(L2)(Br)]. Atom colours: amino acid based-linker C chain = green), O = red, N = blue, Br = brown, and Cd = mauve. H atoms are omitted for clarity.

Amino acids as modulators in Zr-MOFs

In addition to their role as structural linkers, amino acids have also been exploited as modulators in Zr-MOF synthesis. Proline, glycine, and phenylalanine, for example, have been used to introduce functional groups and regulate particle size (**Figure 1.20**). High-yield synthesis was achieved at elevated temperatures (120 °C), while lower temperatures produced crystals suitable for SCXRD. These amino acids coordinate to defect sites in the Zr-MOF structure, with loadings up to a 1:1 ratio, and significantly enhance CO_2 uptake capacity.[89]

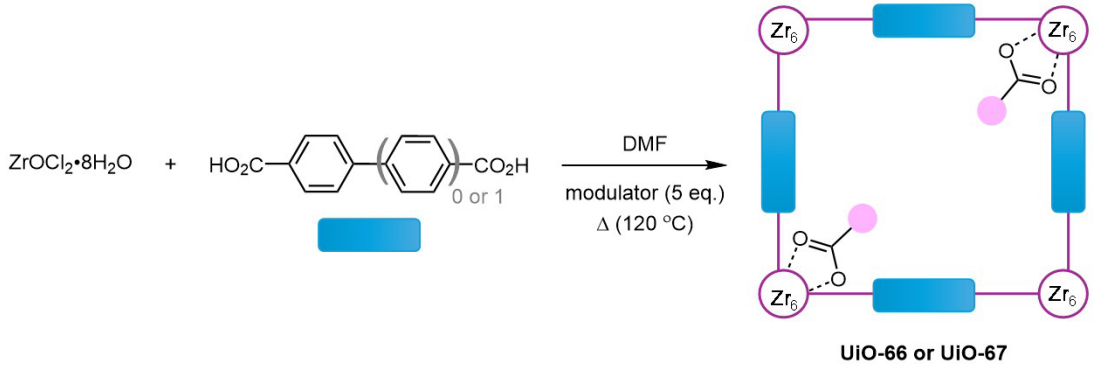

Figure 1.20: Anchoring amino acids to ZrMOFs during synthesis.

Alternative heteroaromatic scaffolds

Finally, imidazole- and imidazolium-carboxylate scaffolds were synthesised from amino acids and have been reported to assemble into 1D and 2D homochiral coordination polymers, but they do not extend into 3D MOFs (**Figure 1.21**). Nonetheless, their ability to form ordered, low-dimensional networks highlights the versatility of amino acid functionalisation.[90]

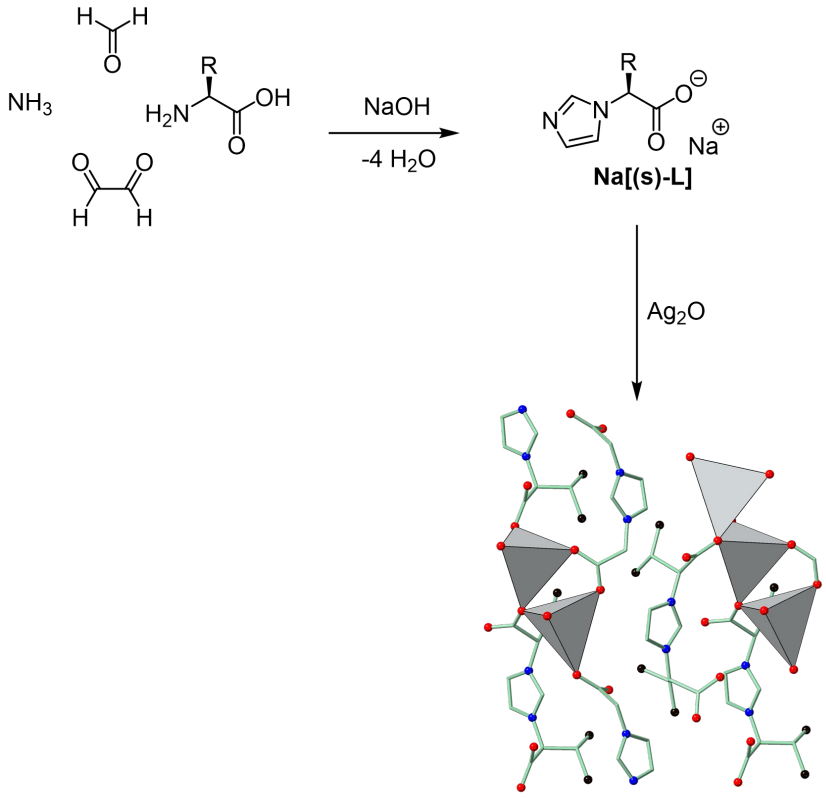

Figure 1.21: Imidazolium salts were synthesised from amino acids, and subsequent treatment with Ag_2O yielded 1D coordination polymers.
Atom colours: linker C chain = mint green, O = red, N = blue, and Ag = grey.
Hydrogen atoms are omitted for clarity.

1.7.4 Amino acids in mixed-linker MOFs

Mixed-linker strategies combine an amino acid linker with a rigid organic linker within a single MOF. The amino acid provides chirality, polarity, and H-bonding/soft-donor chemistry, while the organic linker fixes long-range connectivity and pore geometry. Two representative examples are (i) amino acid + polycarboxylate ligand (H_3Btc) and (ii) amino acid layer + N-donor pillar (bipyridine).

d-Histidine (*d*-His), trimesic acid (H_3BTC), and Zn(II) afford DHTZn under solvothermal conditions (130 °C, pH ≈ 4.4), giving a tetragonal, non-centrosymmetric 3D framework featuring five interwoven helices (**Figure 1.22**). The polycarboxylate node (BTC) supplies rigid, high-connectivity vertices; *d*-His installs chiral/polar surfaces inside channels. Working near pH ≈ 4-5 keeps the imidazole mostly protonated, avoiding connectivity capping and favouring extended 3D helices.[91]

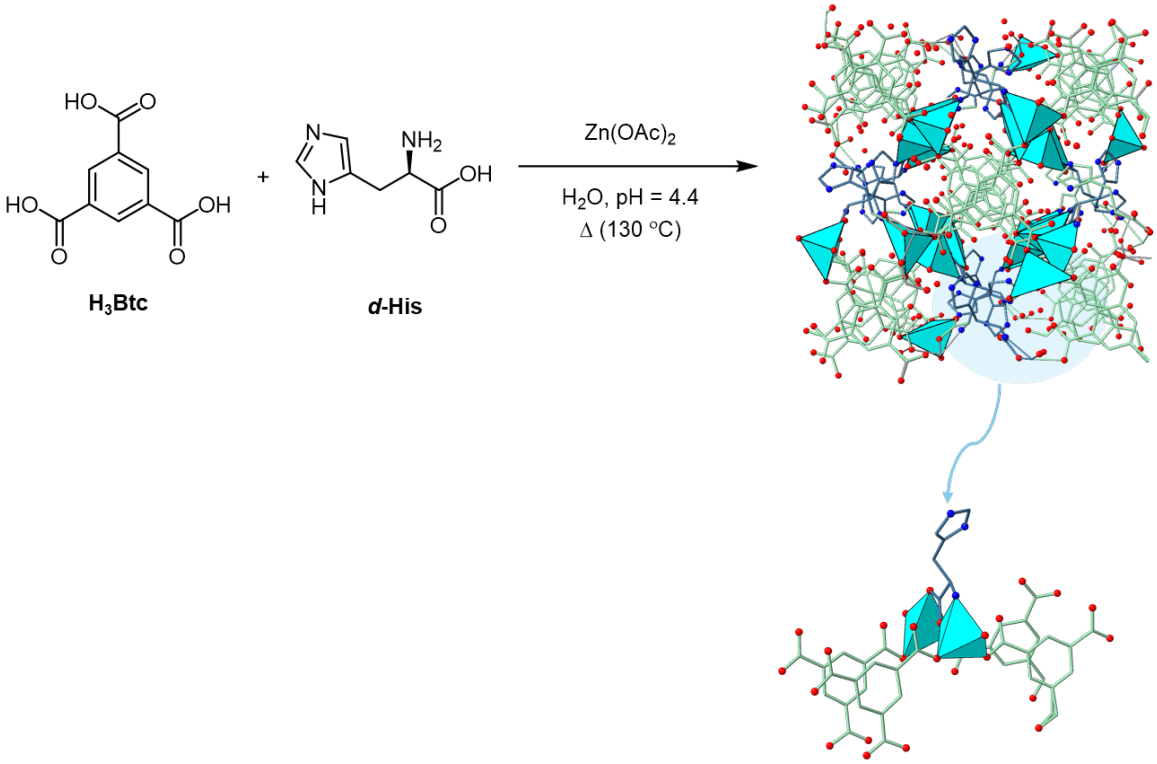

Figure 1.22: Synthesis pathway of DHisZn, via solvothermal synthesis of trimesic acid (H_3BtC), *d*-histidine with $Zn(OAc)_2$ in aqueous medium.
Atom colours: trimesic acid C chain = mint green, histidine C chain = blue, O = red, N = blue, and Zn = teal blue. Hydrogen atoms are omitted for clarity.

Using preformed Ni(*l*-asp)·$3H_2O$ with bipyridine (bipy) in equal volumes of H_2O and MeOH (150 °C) yields homochiral [Ni_2(*l*-asp)$_2$(bipy)] (**Figure 1.23**); higher water induces racemisation and the achiral analogue. Pillared layers of tridentate Asp linked by bipy form 1D channels. Enantioselective sorption of small chiral diols (up to enantiomeric excess ≈ 54%), governed by multipoint H-bonding to the aspartate-lined pocket and geometric matching of OH separations.[92]

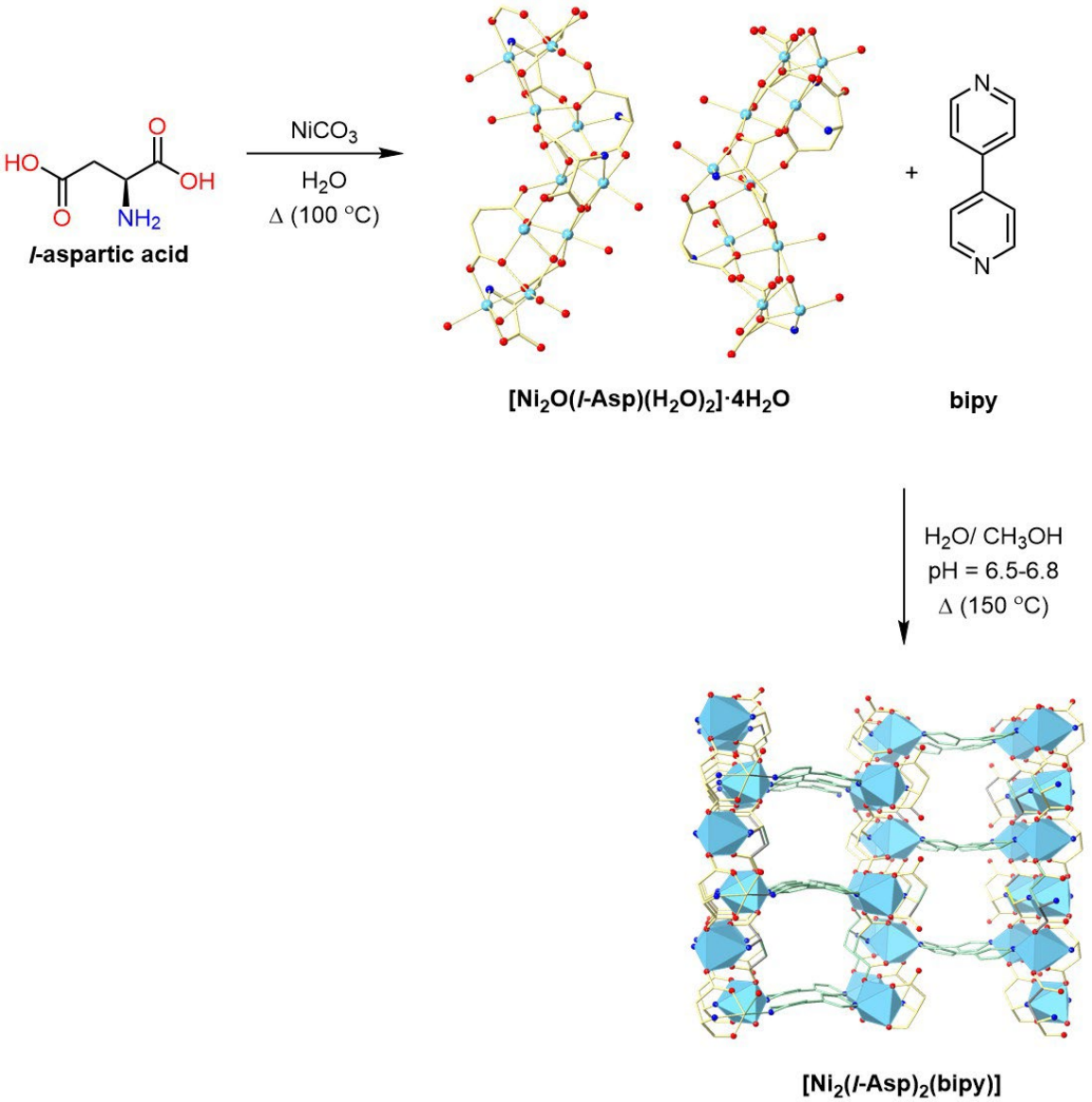

Figure 1.23: Synthesis pathway of [Ni2(*l*-Asp)2(bipy)] MOF. Atom colours: aspartate C chain = yellow, bipy C chain = green, O = red, N = blue, and Ni = blue. Hydrogen atoms are omitted for clarity.

1.8 Applications of amino acid–based MOFs

MOFs have developed from academic research to practical platforms offering a wide range of applications. The MOFs' unique properties, such as high porosity, crystallinity, and pore tunability, allow MOFs to host, separate, or transform guest molecules. Biomedical drug delivery and catalysis are promising applications for amino acid-based frameworks. In these fields, the inherent chirality, biocompatibility, and chemical diversity of amino acids provide additional advantages compared with conventional linkers.

1.8.1 MOFs as drug carriers

One of the most intensively investigated biomedical applications of MOFs is drug delivery. The exceptionally high surface areas, pore volumes, and structural tunability of MOFs make them excellent candidates for encapsulating therapeutic agents, and their crystallinity enables precise characterisation of host-guest interactions and release mechanisms.

High loading and controlled release MOFs can accommodate a broad spectrum of therapeutics, from small molecules (e.g., doxorubicin, ibuprofen) to biomacromolecules (proteins, siRNA, CRISPR components).[93-98] Framework flexibility (such as pore breathing, ligand rotation) (**Figure 1.24**) and specific host-guest interactions modulate loading and release profiles, enabling stimuli-responsive delivery (such as pH/redox triggers) that is attractive for oncology and precision medicine (**Figure 1.24**).[94, 99-101] Classic flexible systems such as MIL-53 and MIL-88 illustrate how structural dynamics couple to guest uptake/release and NO delivery [102, 103]

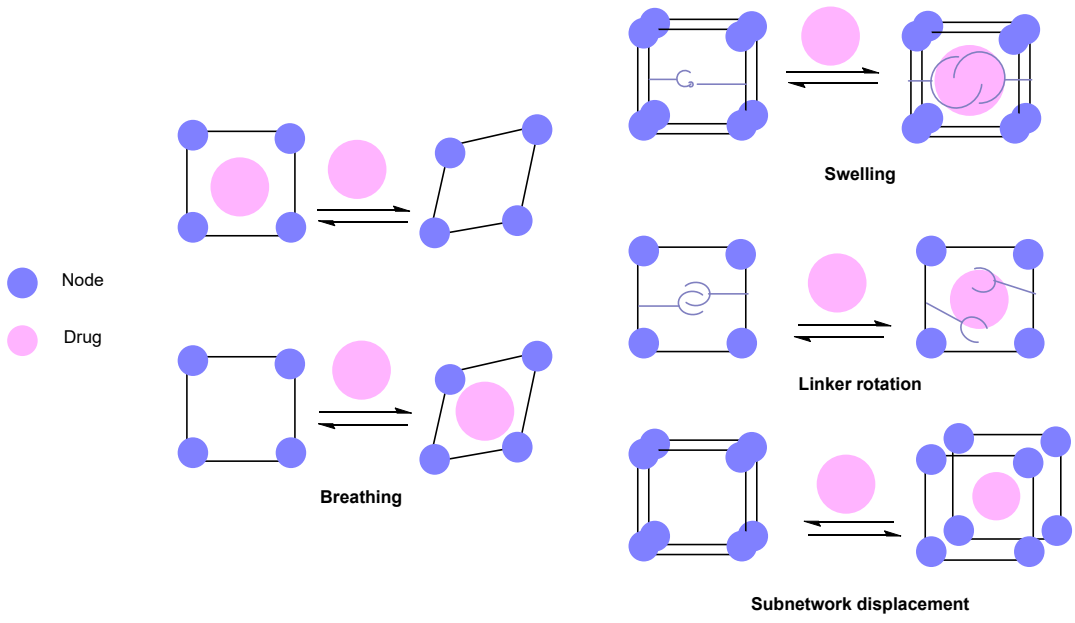

Figure 1.24: The behaviour of MOFs with flexible pores upon drug loading..

Biocompatibility and stability

Clinically relevant carriers must combine low toxicity with colloidal and chemical stability under physiological conditions. Zr-MOFs (e.g., UIO derivatives, NU-1000) and Fe-MOFs (e.g., MIL-88/MIL-100) have shown promising biocompatibility and stability. Zn-based systems, like ZIF-8, are widely used but require attention to Zn(II) release.[103, 104] Surface functionalisation (e.g., polymer/biomolecule coatings, biomimetic mineralisation) improves stability and reduces systemic toxicity while protecting labile cargo.[95, 105] Particle size is also critical: nanoscale MOFs in the ~10-100 nm range often balance efficient uptake with avoidance of rapid clearance, a design principle emphasised across recent surveys.[95, 105]

Loading strategies

Mainstream strategies include one-pot synthesis**,** biomimetic mineralisation**,** post-synthetic encapsulation, and surface loading/adsorption (**Figure 1.25**).[106-108] One-pot and biomimetic routes can yield high loadings and are gentle for fragile biomacromolecules (proteins, nucleic acids), whereas post-synthetic encapsulation offers modular pairing of drug and carrier. Surface loading, although typically results in lower capacity, can enable multi-drug or sequential release schemes when combined thoughtfully with pore encapsulation.[106, 108]

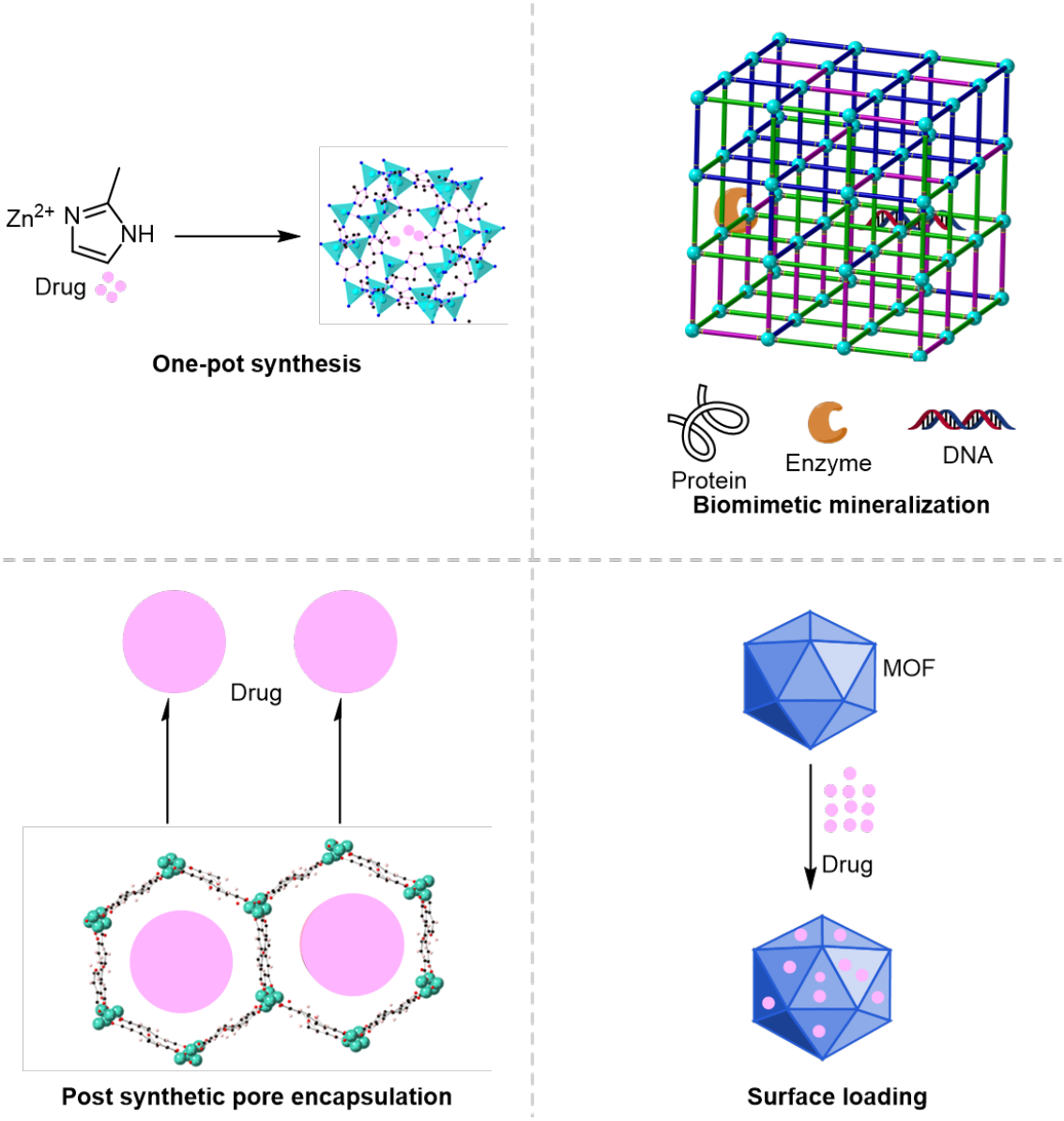

Figure 1.25: Drug loading on/into the porous MOFs. Several methods can be used to load the drug into the pores or on the surface of the MOF. These methods are one-pot synthesis, biomimetic mineralisation, post synthetic pore encapsulation, and surface loading.

The outlook for amino acid–MOFs in drug delivery

Amino acid-based MOFs add biocompatibility, chirality, and functional-group diversity (e.g., hydroxyl, imidazole, thiol) that can enhance selective recognition and binding of therapeutic cargo.[1, 2, 4, 101] Installing amino acids into robust frameworks such as MUF-77 provides a route to tailored pore microenvironments, combining the stability and permanent porosity of classical MOFs with the molecular recognition features of biological building blocks.[5, 56, 108, 109]

1.8.2 MOFs in Catalysis

In parallel with biomedical uses, MOFs are powerful platforms for catalysis because they position active sites in ordered, high-surface-area pores and allow the co-location of Lewis acidic nodes.[56, 109, 110] This dual organic-inorganic tunability enables oxidation, C-C bond formation, acid-base, and photochemical catalysis with opportunities for shape/size selectivity and microenvironment control.[56,109,110] Moreover, installing functional groups with intrinsic organocatalytic properties, such as amines, can transfer molecular catalytic behaviour into the MOF lattice.[59]

MOFs as enzyme mimics

Although enzymes are powerful catalysts, they suffer from many limitations, such as their affinity towards very specific substrates, their sensitivity to harsh conditions, and their difficulty to engineer.[111,112] These limitations prevent their broader utility. Molecular catalysts serve as a bridge between enzyme selectivity and synthetic methods, which allows expanding the possible catalytic applications scope. Conventional synthetic techniques can be used for these catalysts' synthesis. Many of these catalysts are practical to straightforward screening processes. Nonetheless, the basic structure of molecular catalysts may restrict control over the substrate environment. More complex molecular catalysts present challenges in synthesis and structural prediction.

To bridge this gap, *multicomponent* MOF such as MUF-77 provide a versatile scaffold for mimicking enzymatic function. MUF-77 offers a highly porous, crystalline framework with precise spatial control over the placement of functional groups. Its modular design enables the incorporation of catalytic residues into well-defined pore environments, facilitating the design of artificial active sites with cooperative functionalities, such as catalytic dyads or triads.

Because catalytic confinement and organised secondary interactions are central to enzyme function, MOFs can recreate aspects of these environments. By embedding open metal sites and designed linker functionality with organocatalytic properties within well-defined pores, they can provide routes to chemo-, regio-, and enantioselectivity.[56, 109, 110]

Peptide-inspired catalysts

Short peptide sequences (3–8 residues) provide catalytic motifs (e.g., imidazole, carboxylate, hydroxyl) and a chiral scaffold that enables site-selective and enantioselective transformations.[98, 113-116] Peptide or amino acid groups appended to linkers place catalytic and modulating functionalities in predictable positions within pores, combining the selectivity of peptides with the stability and addressability of reticular frameworks.

MUF-77 as a catalytic scaffold

The MUF-77 family is a particularly attractive platform due to its large tetrahedral pores and modular, multicomponent design.[5, 6] By appending amino-acid/peptide side-arms to the bdc, bpdc, or truxene linkers that assemble MUF-77, catalytic groups can be oriented to line the channels, creating peptide-like microenvironments for substrate recognition, cooperative effects, and enantioselective transformations, while retaining the chemical robustness of the parent framework.[5, 6, 56, 117]

1.8.3 Gas separations

Multicomponent amino acid/peptide MOFs that have pores on the dimension of small molecules may be useful for gas separations by molecular sieving and related effects. Competent materials are in extremely high demand.[118]

1.9 Overarching project scope

Building on the principles outlined above, this project focused on the design and synthesis of MMOFs incorporating two or more distinct amino acid ligands within a single crystalline structure. The overarching objective was to introduce complementary functional groups into confined pore environments, thereby enabling cooperative interactions that may enhance catalytic performance.

The formation of multicomponent frameworks presented significant synthetic challenges. The presence of multiple ligands increased the likelihood of competitive coordination, phase separation, or alternative topology formation. In addition, framework assembly remained highly sensitive to crystallisation parameters, such as solvent composition, concentration, pH, temperature, and additives. Accordingly, a central aim of this research was the development of reliable strategies that favour controlled co-assembly into homogeneous multicomponent architectures.

1.9.1 Two complementary approaches were pursued.

The first approach involved the direct co-assembly of two or more amino acids with metal ions under solvothermal conditions. A central challenge was promoting the incorporation of multiple ligands into a single crystalline framework rather than forming discrete phases or low-dimensional coordination polymers. In practice, direct co-assembly of unmodified amino acids proved difficult due to competitive coordination and limited structural directionality. Nevertheless, these studies provided important insight into ligand compatibility and coordination preferences, which informed subsequent design strategies.

The second approach was built on established multicomponent frameworks within the MUF-77 family. In this strategy, conventional linear linkers were covalently functionalised with amino acid or peptide side arms before MOF synthesis. These modified linkers were successfully incorporated into the multicomponent architecture, enabling controlled positioning of functional residues along the pore surfaces while retaining the underlying topology. This modular design allowed structural robustness to be preserved while introducing chemical diversity within the pore environment.

Together, these complementary strategies advanced the development of multicomponent amino acid–based frameworks. While direct assembly of simple amino acids was synthetically limited, functionalised linker approaches proved more effective in achieving structurally defined systems with enhanced potential for catalytic applications.

Chapter 2 MMOFs from amino acids

2.1 Introduction

Proteins exemplify nature's mastery in molecular design: flexible chains of amino acid that fold into intricate 3D structures that enable molecular recognition, catalysis, and changes in response to external, environmental changes.[85, 119] This versatility arises from the chemical diversity of amino acids and the peptide backbone flexibility, which allows adaptation in shape and function.[2-4] These features: structural complexity, flexibility, and functional diversity are highly desirable in crystalline materials, yet remain challenging to replicate.

Inspired by this natural complexity, researchers have incorporated amino acids or peptides into MOFs to mimic the structural sophistication and functional diversity of proteins. These amino acid-based MOFs have shown promising potential in catalysis, sensing, and drug delivery.[2-4] MOFs are crystalline materials that are built of metal nodes and organic linkers, which extend into 3D framework. This nature allows control over the pores size and their chemical environment. MOFs are useful in many applications such as catalysis, gas adsorption and separation.[12, 53, 120] Bio-MOFs, a subclass that has emerged over the past decade, use biomolecular linkers including amino acids, peptides, nucleobases, and saccharides.[2,121] These frameworks introduce chirality, flexibility, and biocompatibility, enabling functions such as catalysis,[2] sensing,[122] drug delivery,[123, 124]and proton conduction.[125]

Multicomponent MOFs (MMOFs) have been a mainstay of the Telfer Group since the discovery and report of MUF-7 in 2013 and MUF-77 in 2015 (MUF = Massey University Framework).[5,6] MUF-7 and MUF-77 are formed using conventional rigid organic carboxylate ligands, while my research forged a new pathway to MOFs that have not been reported in the literature to date at all.

This biomimetic approach diverges from the conventional use of rigid aromatic by enabling conformational adaptability, tunable functional sites, and potentially chiral environments. These features allow dynamic behaviours reminiscent of proteins, such as guest-responsive porosity, selective binding, and cooperative catalysis.[5, 6] Thus, this work moves beyond the static architectures of MUF-7 and MUF-77 toward dynamic, adaptive crystalline materials.

To date, most amino acid- or peptide-based MOFs have been constructed from a *single* type of amino acid or peptide. In contrast, this study explores the incorporation of multiple amino acids and peptides into a single MMOF framework. The aim is to employ the diversity and flexibility of biological building blocks to create dynamic, adaptive crystalline materials.

Several strategies for incorporating amino acids into MOFs were explored. This chapter focuses on the first approach: the direct reaction of multiple amino acids or peptides with metal ions. This method involved reacting a set of two or three different amino acids with metal salts such as $Zn(NO_3)_2$, and it mirrored the approach typically used to make single-component amino acid MOFs. The central challenge in this method was achieving the incorporation of *multiple* ligands into a single MOF structure rather than forming separate phases.

2.2 Results and discussion

This project began by selecting one *l*-amino acid and combining it with other type or types of *l*-amino acids to explore the formation of *multicomponent* frameworks. Throughout all experiments, enantiopure *l*-amino acids were used to ensure the formation of enantiopure MOFs. This approach was intended to maintain the stereochemical integrity of the ligands and increase the likelihood of obtaining well-defined, homochiral frameworks.

2.2.1 Tyrosine with other amino acids co-assembly in MMOFs

The first set of experiments focused on mixing *l*-tyrosine with other amino acids. *l*-Tyrosine refers to the neutral form of the amino acid, whereas *l*-tyrosine-2H denotes the fully deprotonated form. *l*-Tyrosine was chosen as a starting point due to its previously reported ability to form 3D MOF structures. Its phenolic side chain offers additional coordination possibilities beyond the amino and carboxylate groups, therefore enhancing the structural diversity. Literature reports have shown that *l*-tyrosine can coordinate with metal ions under solvothermal conditions to form MOFs, particularly when reacted with $Co(OAc)_2$ and/or $Zn(OAc)_2$[52, 126] (**Figure 1.14**).

l-Tyrosine was combined in pairs with different amino acids, resulting in the formation of several new crystalline structures. However, none of these exhibited permanent porosity or extended 3D frameworks. Instead, only three discrete *multicomponent* amino acid complexes were isolated: [Zn/Co(*l*-asparagine-H)(*l*-tyrosine-H)], [Zn(*l*-histidine-H)(*l*-tyrosine-H)·H_2O], and [Co_2(*l*-histidine-2H)(*l*-tyrosine-H)$_3$·$4H_2O$] (**Figure 2.1**).

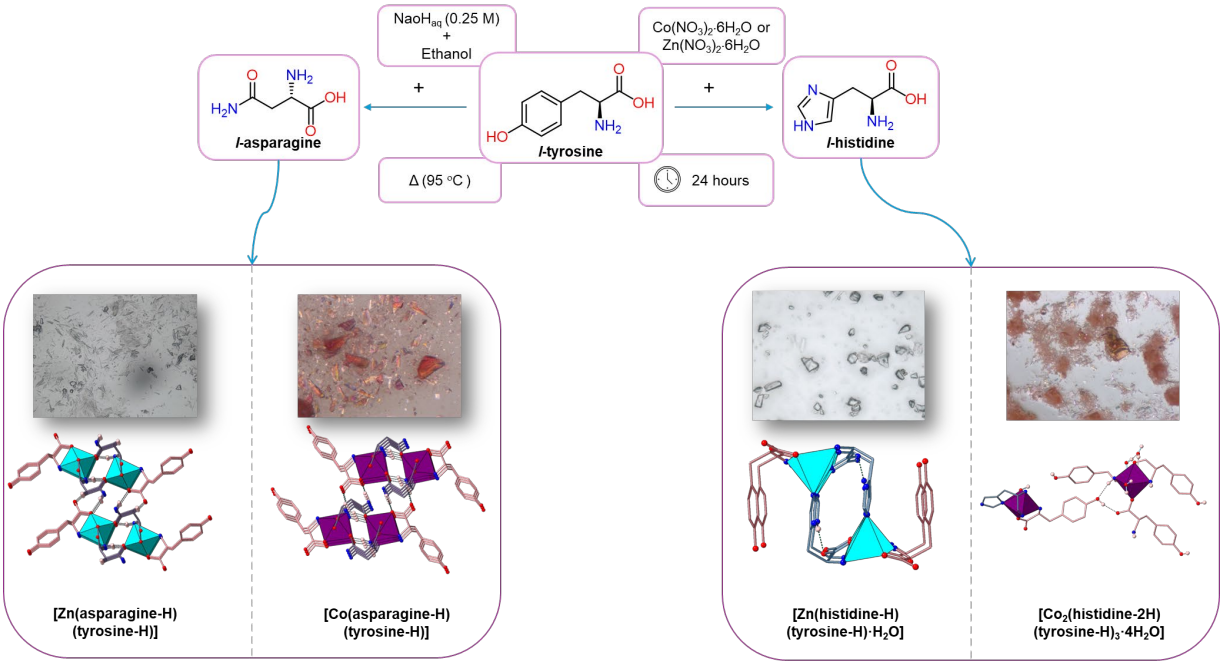

Figure 2.1: Summary of the successful experiments that resulted in the formation of crystalline *multicomponent* structures. These structures were obtained by combining *l*-tyrosine with either *l*-asparagine or *l*-histidine in the presence of $Zn(NO_3)_2$ or $Co(NO_3)_2$. Atom colours: tyrosine C chain = pastel pink, asparagine C chain = pastel purple, histidine C chain = pastel purple, O = red, N = blue, Co(II) = purple, and Zn(II) = blue. Hydrogens are omitted for clarity.

The structural details of these three new multicomponent frameworks are discussed in the following sections.

[Zn(*l*-aspragine-H)(*l*-tyrosine-H)] / [Co(*l*-aspragine-H)(*l*-tyrosine-H)]

The combination of *l*-tyrosine and *l*-asparagine under solvothermal conditions with either Zn(II) or Co(II) nitrate yielded isomorphous multicomponent structures (**Figure 2.2).**

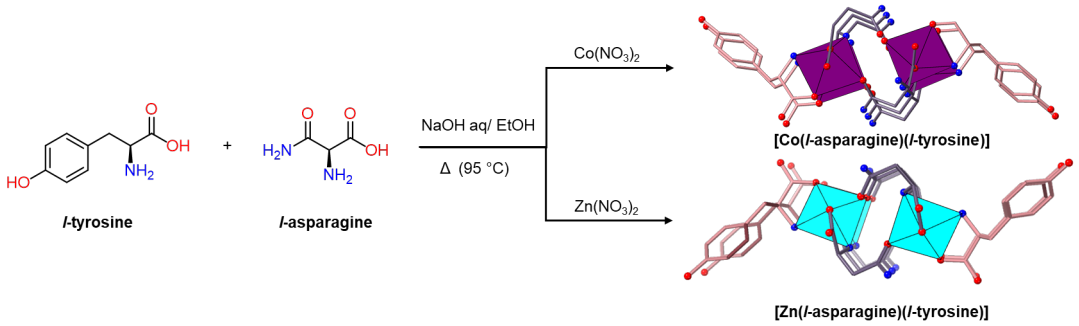

Figure 2.2: Synthetic pathway to [Co(*l*-asparagine-H)(*l*-tyrosine-H)] and [Zn(*l*-asparagine-H)(*l*-tyrosine-H)] and their SCXRD structures. Atom colours**:** tyrosine C chain = pastel pink, asparagine C chain = pastel purple, O = red, N = blue, Co(II) = purple, and Zn(II) = blue. Hydrogen atoms are omitted in structural models for clarity.

The choice of tyrosine and asparagine was guided by their complementary functionalities: tyrosine provides both amino/carboxylate and phenolic donors, while asparagine introduces both amino/carboxylate and an amide group. Together, these ligands were expected to favour the assembly to form 3D networks

SCXRD analysis reveals that both Co(II) and Zn(II) form isomorphous structures. Each metal ion exhibits a distorted octahedral coordination environment, arising from chelating ligand coordination. Each amino acid ligand is singly deprotonated; the complex arises from the coordination of one *l*-asparagine molecule through its carboxylate oxygen and amino nitrogen, while the other two *l*-asparagine molecules coordinate via one of the carboxylate group's oxygen atoms (C=O). Additionally, *l*-tyrosine coordinates with the metal through its carboxylate oxygen and amino nitrogen atoms (**Figure 2.3**).

A dense network of inter- and intramolecular hydrogen bonds stabilises the structure. The intramolecular hydrogen bonds form between the tyrosine phenolic hydrogen and the tyrosine carboxylate oxygen, as well as between the asparagine amide hydrogen and the asparagine carboxylate oxygen. An intermolecular hydrogen bond is formed between the tyrosine carboxylate's oxygen and the neighbouring asparagine amide's hydrogen (**Figure 2.3**). Collectively, these interactions generate a layered 3D structure, highlighting the key role of amide-carboxylate and phenol-carboxylate contacts in directing the formation of the structure.

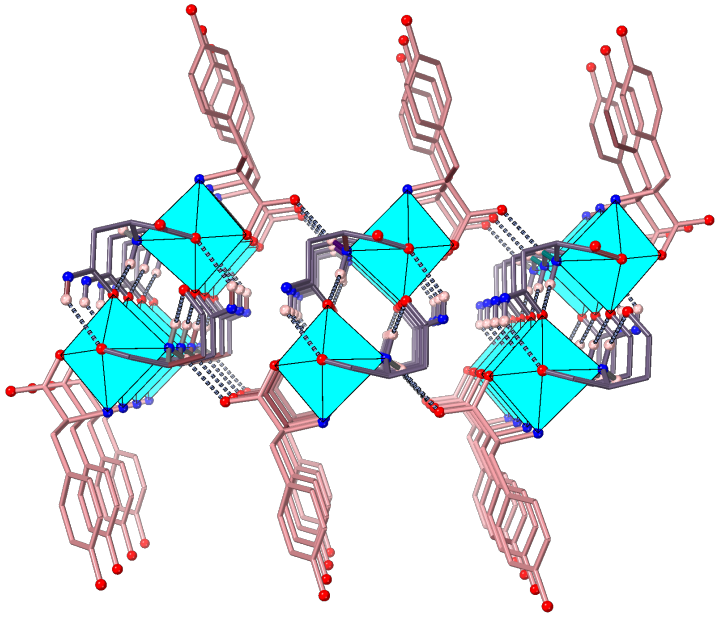

Figure 2.3: Hydrogen bonding interactions (dashed bonds) between coordinated *l*-asparagine and *l*-tyrosine ligands. Atom colours tyrosine C chain = pastel pink asparagine C chain = pastel purple, O = red, N = blue, Co(II) = purple, and Zn(II) = light blue. Hydrogen atoms are omitted in structure except the essential for H-bond.

Powder X-ray diffraction (PXRD) confirmed the bulk crystals' purity, where the calculated PXRD pattern from the corresponding SCXRD data matched the experimental PXRD of both [Co(asparagine-H)(tyrosine-H)] and [Zn(asparagine-H)(tyrosine-H)], with no other peaks appearing. A slight peak shift was observed in the Co(II) analogue, consistent with its slightly larger unit cell dimensions relative to Zn(II) (**Figure 2.33**). ^{1}H NMR spectroscopy of the acid-digested crystals confirmed a 1:1 ratio between asparagine and tyrosine (**Figure 2.34**), in agreement with the Zn(II) and Co(II) crystallographic models.

[Zn(*l*-histidine-2H)(*l*-tyrosine-H)·H_2O]

The co-assembly of *l*-tyrosine and *l*-histidine with $Zn(NO_3)_2$ in a basic aqueous medium afforded a new *multicomponen*t amino acid structure (**Figure 2.4**).

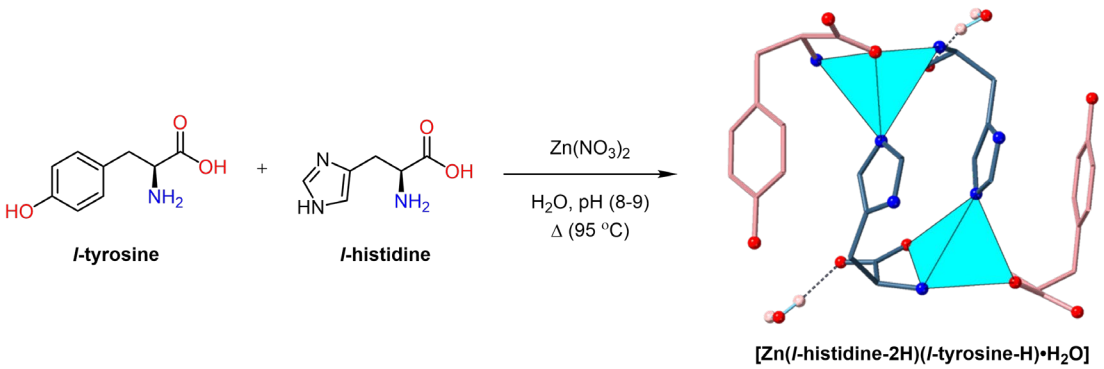

Figure 2.4: Synthetic pathway to [Zn(histidine-2H)(tyrosine-H)·H_2O]. Atom colours: tyrosine C chain = pastel pink, histidine C chain = pastel blue, O = red, N = blue and Zn(II) = teal blue. Most of the hydrogen atoms (Whitish pink) are omitted for clarity except the essential for H-bonding.

The SCXRD revealed that the compound assembles into a 1D rod-like architecture rather than an extended 3D framework **(Figure 2.5.a**).

Zn(II) adopts a trigonal bipyramidal coordination geometry, binding to five donor atoms. *l*-Histidine is doubly deprotonated, and two distinct histidine coordination modes are observed: one histidine coordinates through its carboxylate oxygen and amino nitrogen, while the second binds via the imidazole nitrogen donor. In contrast, tyrosine remains singly deprotonated and coordinates through its carboxylate oxygen and amino nitrogen, providing a bridging role that links histidine and Zn(II). The distinct use of the imidazole nitrogen highlights the versatility of histidine in diversifying structural motifs in amino acid-based MOFs (**Figure 2.5.b**).

Although the imidazole nitrogen does coordinate to Zn(II), thereby demonstrating the versatility of histidine as a donor, in this system its binding leads only to 1D rod-like assemblies rather than the extended 3D networks often observed in Zn-imidazole-carboxylate frameworks (e.g., ZnCar,[4] *d*-HTZn[91]). This suggests that the local geometry and competing coordination preferences of tyrosine limit the dimensionality of the assembly.

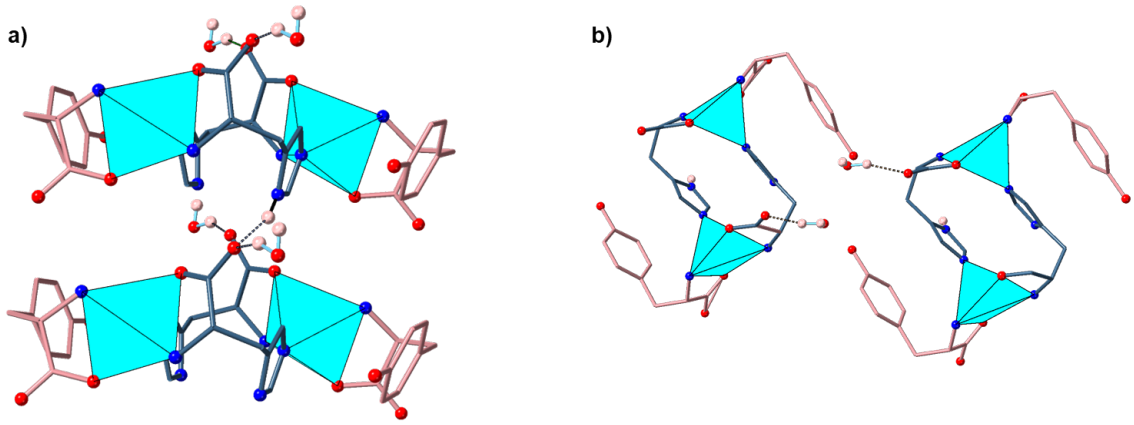

Figure 2.5: Two different views of [Zn(*l*-histidine-2H)(*l*-tyrosine-H)·H_2O]. The structure assembles into a 1D rod-like coordination polymer. Atom colours: tyrosine C chain = pastel pink, histidine C chain = pastel blue, O = red, N = blue and Zn(II) = teal blue. Most of the hydrogen atoms (Whitish pink) are omitted for clarity except those essential for H-bonding.

The phase purity of the material was confirmed by PXRD, with the experimental pattern in good agreement with the calculated from the corresponding SCXRD data and no additional reflections were observed (**Figure 2.37**). Acid digestion of the crystals in DCl/DMSO (23 µL/ 1 mL), followed by ^{1}H NMR spectroscopy, revealed a 1:1 ratio of tyrosine to histidine (**Figure 2.38**), which further supports the phase purity of the material.

[Co_2(*l*-histidine-2H)(*l*-tyrosine-H)$_3$·$4H_2O$]

Replacing Zn(II) with Co(II) under identical synthetic conditions led to the formation of a new multicomponent amino acid complex, [Co_2(*l*-histidine-2H)(*l*-tyrosine-H)$_3$·$4H_2O$] (**Figure 2.6**). The reaction of *l*-tyrosine and *l*-histidine with $Co(NO_3)_2$ in a basic aqueous solution produced two distinct crystalline phases: block-like crystals corresponding to the complex and needle-like crystals identified as free tyrosine. The isolation of both phases highlights the competitive nature of tyrosine coordination under these conditions.

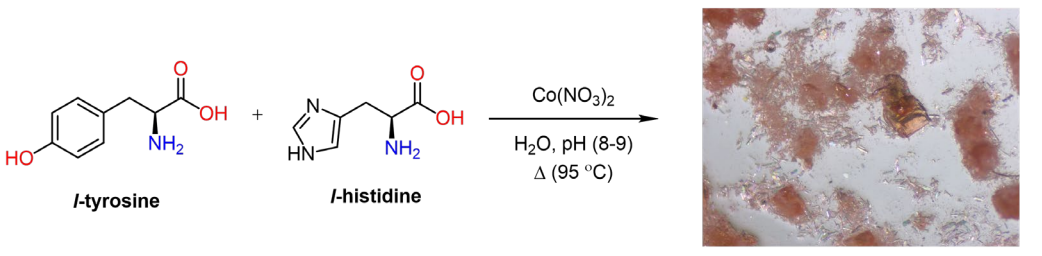

Figure 2.6: Synthetic pathway to [Co_2(*l*-histidine-2H)(*l*-tyrosine-H)$_3$·$4H_2O$].

SCXRD of the block-like crystals revealed that the structure crystallises in a H-bonded layers assembled from two crystallographically distinct Co(II) coordination environments (**Figure 2.7**). Both Co(II) centres adopt octahedral geometries but with different donor sets. In the first environment, two tyrosine ligands coordinate Co(II) through their amino and carboxylate groups, an additional tyrosine through a monodentate carboxylate, and one aqua ligand. The second environment involves coordination to histidine through three donors: the imidazole nitrogen, the amino nitrogen, and the carboxylate oxygen. This Co(II) centre is further connected by one tyrosine (via amino and carboxylate donors) and a water molecule, completing the octahedral sphere. The coexistence of these two distinct Co(II) sites introduces structural asymmetry and provides multiple hydrogen-bonding vectors for framework assembly.

The structure extends into a 3D layer through extensive H-bonding (**Figure 2.7.b**). Two principal interaction types are observed:

- **Tyrosine-derived interactions:** hydrogen bonds form between the phenolic hydroxyl group of tyrosine and the carboxylate oxygen of a neighbouring tyrosine coordinated to a different Co(II) centre. These interactions link discrete units into extended layers
- **Histidine-derived interactions:** hydrogen bonds occur between the imidazole N–H group and the carboxylate oxygen of another histidine ligand bound to an adjacent Co(II) ion, cross-linking the layers into a 3D network.

PXRD confirmed that the bulk crystalline material corresponds to the SCXRD-identified phase, with experimental patterns in close agreement with those simulated from the SCXRD (**Figure 2.37**). The reproducible synthesis and consistent PXRD data indicate that the block-like phase is stable under the applied conditions. However, the competition with free tyrosine suggests sensitivity to stoichiometry and solution chemistry.

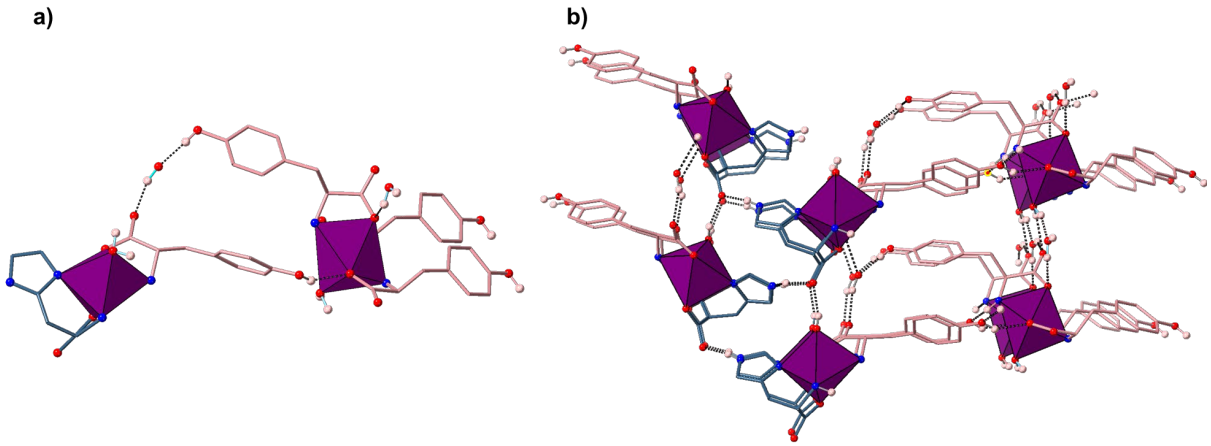

Figure 2.7: a) Monomeric unit and 2D view of the structure. **b)** 3D view of the layered structure, highlighting the two types of hydrogen bonds that assemble the monomers into the supramolecular structure. Atom colours: tyrosine C chain = pastel pink, histidine C chain = pastel blue, H = whitish pink, O = red, N = blue, and Co(II) = teal blue. Most of the hydrogen atoms are omitted for clarity except the essential for H-bonding.

Unintended tyrosine-based phases

Attempts to co-assemble *l*-tyrosine with other amino acids frequently resulted in unintended crystalline phases dominated by simple tyrosine-metal complexes, rather than the targeted multicomponent frameworks. This behaviour highlights the strong coordination tendency of tyrosine to outcompete other amino acids under solvothermal conditions.

The most common product was [Co(*l*-tyrosine)(H_2O)$_2$]·2NO_3, reproducibly obtained when tyrosine was combined with glycine or glutamic acid in basic aqueous ethanol solutions (**Figure 2.8**).

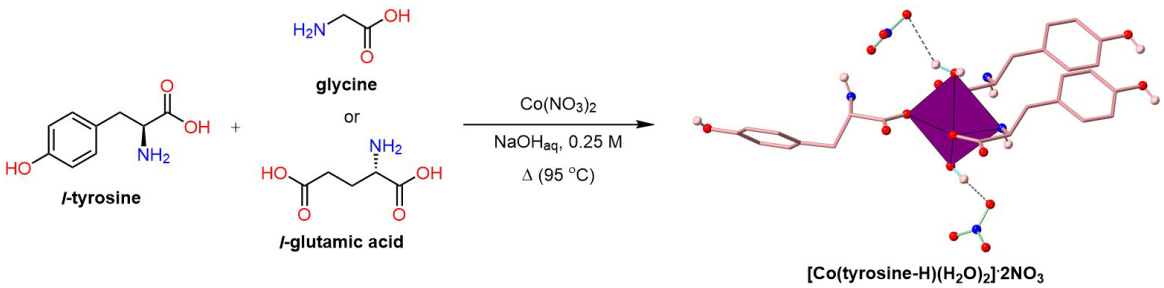

Figure 2.8: Synthetic pathway leading to the formation of [Co(*l*-tyrosine-H)(H_2O)$_2$·2NO_3]. Atom colours: tyrosine C chain = pastel pink, H = whitish pink, O = red, N = blue, and Co(II) = purple. Most of the hydrogen atoms are omitted for clarity except the essential for H-bonding

SCXRD confirmed that the structure represents a new supramolecular motif not previously reported in the CCDC (**Figure 2.9.a**). Co(II) adopts an octahedral geometry, coordinating to three tyrosine ligands (via carboxylate and amino donors) and two water molecules. The framework is assembled into a 3D motif through three types of H-bonds: (i) nitrate-water interactions, (ii) nitrate-tyrosine interactions, and (iii) tyrosine-tyrosine hydrogen bonds. PXRD confirmed phase purity by excellent agreement between the experimental and the simulated patterns from their corresponding SCXRD (**Figure 2.9.b**).

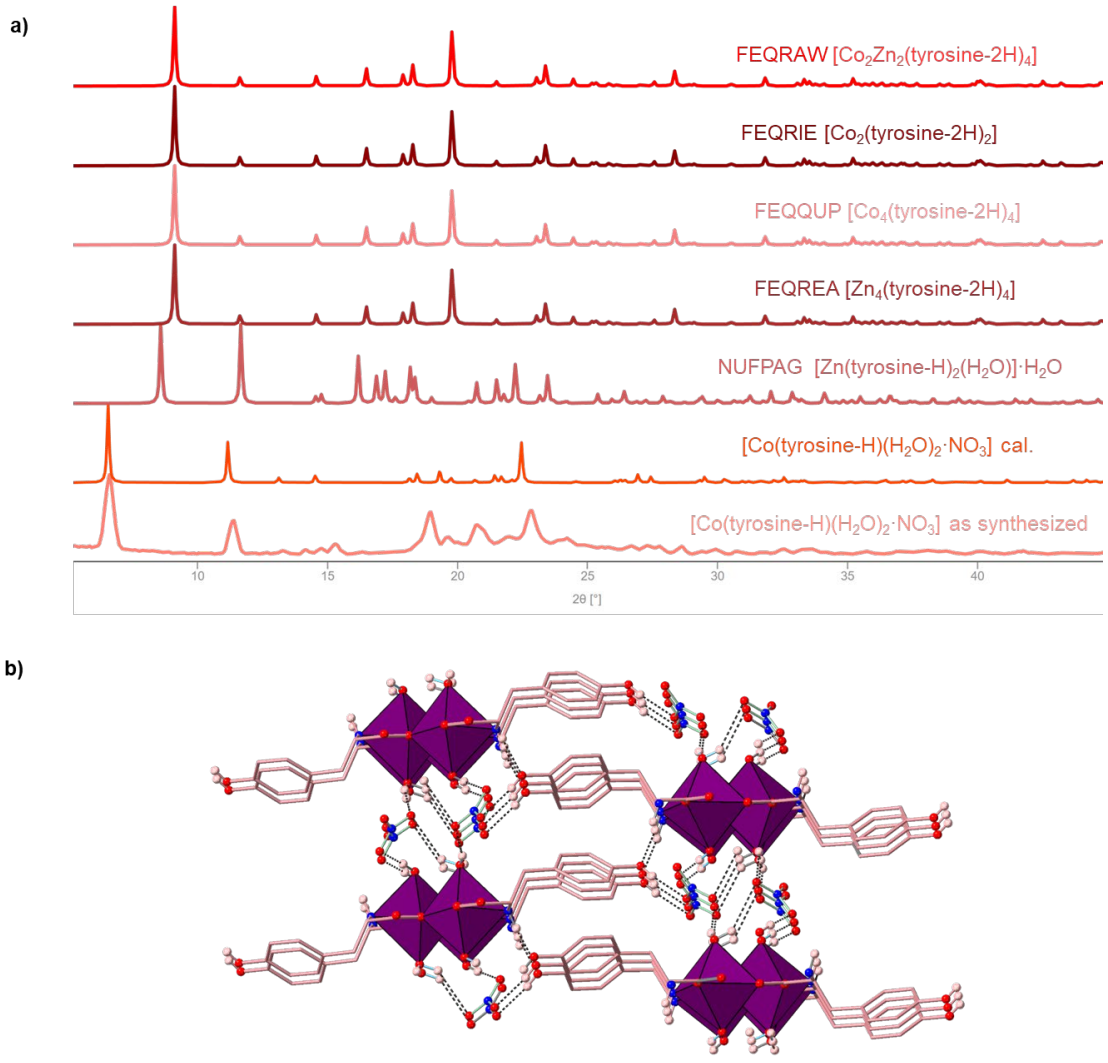

Figure 2.9: a) The experimental PXRD pattern of the obtained crystals was compared with simulated PXRD patterns of tyrosine-containing structures reported in the CCDC database **b)** The 3D supramolecular motif reveals H-bonding interactions involving nitrate (NO_3^-) group. Atom colours: tyrosine C chain = pastel pink, H = whitish pink, O = red, N = blue, and Co(II) = purple. Most of the hydrogen atoms are omitted for clarity except the essential for H-bonding.

In addition to this new phase, several known tyrosine complexes were frequently reproduced. When combined with lysine, both [Zn(tyrosine-H)$_2$·H$_2$O] and [Co(tyrosine-H)$_2$·H$_2$O] formed, featuring tyrosine in its common N,O-bidentate mode,[127] giving rise to 1D coordination polymers rather than 3D networks. When combined with serine, the previously reported [Co(tyrosine-2H)$_2$] phase was obtained (**Figure 2.10**), where tyrosine binds through carboxylate, amino, and phenolic groups, representing its less common coordination mode.[52, 127]

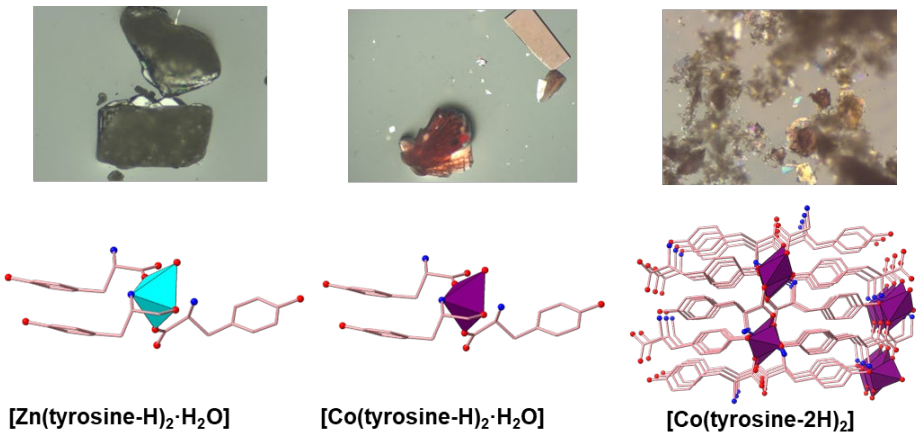

Figure 2.10: Crystal structures obtained in this study were previously reported in the CCDC.

In all cases, phase purity was verified by comparing the experimental PXRD data with the calculated PXRD patterns reported in the literature, derived from their respective SCXRD analyses (**Figure 2.11**).

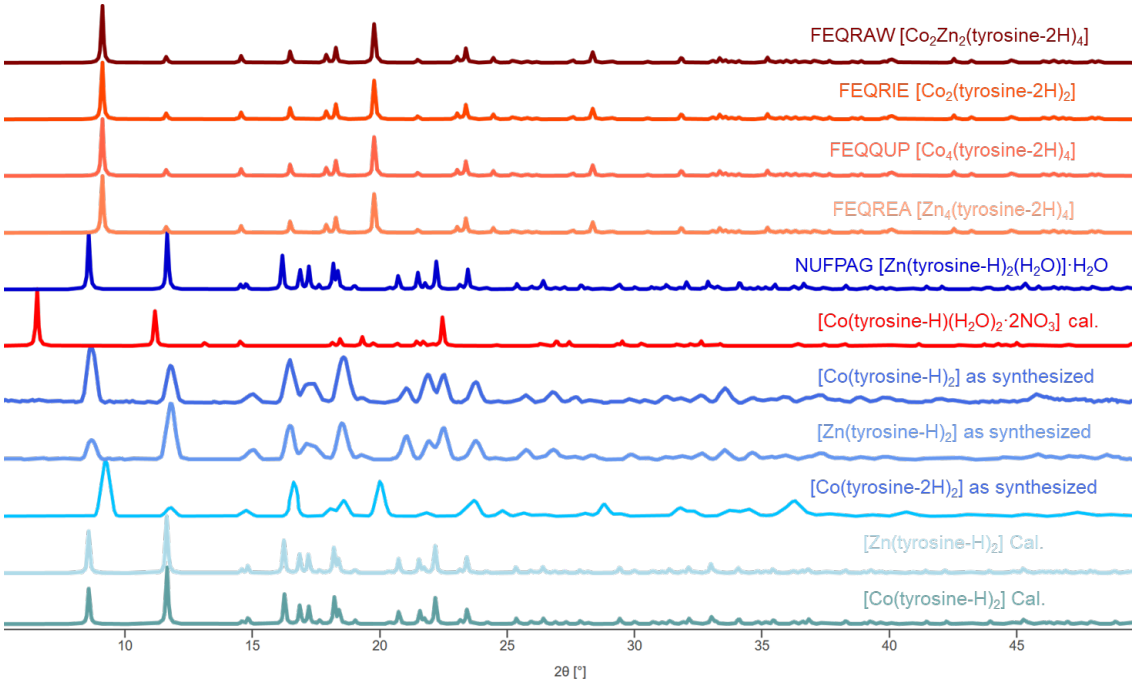

Figure 2.11: The experimental and the calculated PXRD patterns for some of the obtained crystals compared to patterns reported in the CCDC.

Beyond these crystalline phases, many attempts to combine tyrosine with glutamic acid, methionine, valine, or other amino acids produced only crystalline powders unsuitable for SCXRD, despite extensive optimisation. Details of these trials are provided in the **Appendix A**.Overall, these results show that tyrosine exhibits a strong tendency to dominate coordination chemistry, favouring self-phases rather than co-assembly into *multicomponent* frameworks. While this prevented the isolation of new MMOFs under the tested conditions, the outcomes provide important insights into the competitive behaviour of amino acid ligands and underscore the need to balance donor functionality when designing multicomponent frameworks.

2.2.2 Co-assembly of glutamic acid and other amino acids in MMOFs

Glutamic acid (Glu) was selected as a co-ligand because it is widely reported to form MOFs,[75, 128] and its three donor sites, the α-carboxylate, γ-carboxylate, and amine, offer *multiple* coordination possibilities that could, in principle, support mixed-ligand frameworks. Two principal modes dominate the literature with divalent metals: (i) bidentate N,O chelation, which commonly yields 1D coordination polymers, and (ii) simultaneous coordination through α-COO^-, γ-COO^-, and NH_2, which can support 3D networks.

Guided by these precedents, we attempted direct co-assembly of Glu with tyrosine (Tyr), asparagine (Asn), glycine (Gly), and histidine (His) with Co(II) and Zn(II), varying pH, solvent composition (H_2O/EtOH), stoichiometry, temperature, and crystallisation time to access multicomponent MOFs (MMOFs).

Across the screened conditions, crystallisation reproducibly delivered single-component glutamate frameworks, with no detectable incorporation of the second amino acid (**Figure 2.12**). This outcome was observed for Glu paired with Tyr, Gly, and His with either Co(II) or Zn(II).

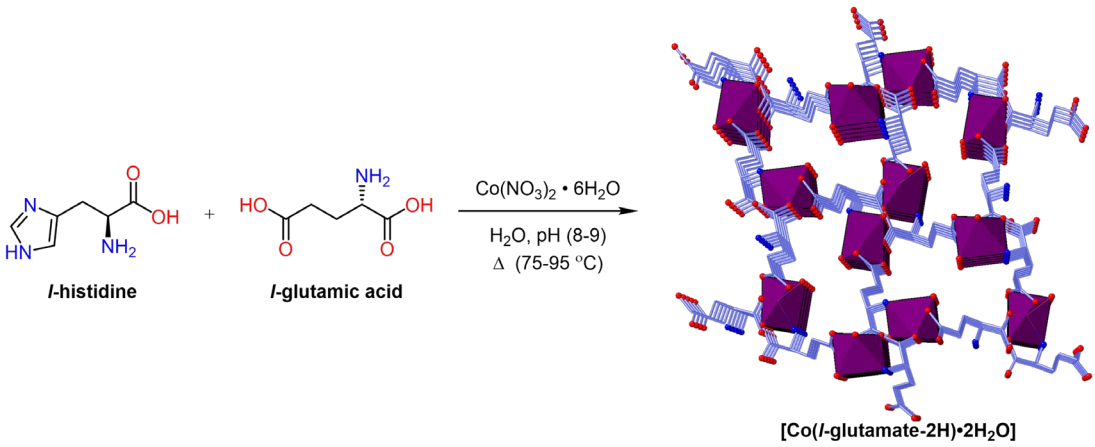

Figure 2.12: Synthetic pathway aimed at incorporating both glutamic acid and histidine into a MMOF with Co(II). Atom colours: glutamate C chain = pastel blue, O = red, N = blue, and Co(II) = purple. Hydrogen atoms are omitted for clarity except the essential for H-bonding.

The assignment of Glu-only phases is supported by PXRD, where PXRD patterns matched those simulated from reference single-component Glu structures; no other reflections attributable to mixed-ligand phases were observed.

2.2.3 Co-assembly of methionine and other amino acids in MMOFs

Methionine is an attractive amino acid for MOF construction because of its versatile coordination chemistry and unique side-chain functionality.[52] It possesses both an amino and a carboxylate group, which readily coordinate to metal centres and enable zwitterionic binding modes. In addition, the thioether group in its side chain provides a soft donor atom capable of binding to soft metal ions such as Ag(I) and Cu(II), introducing opportunities for selective metal-sulfur interactions. These multiple coordination sites allow methionine to support diverse topologies ranging from 1D coordination polymers to extended 3D frameworks.[63, 129] By combining methionine with other amino acids under different conditions, we aimed to exploit these features to generate MMOFs with enhanced structural diversity and functional properties.

[Zn(*l*-methionine-H)$_3$(*l*-valine-H)]

A basic aqueous solution of *l*-methionine, *l*-valine, and $Zn(NO_3)_2$ at room temperature afforded needle-like crystals of [Zn(*l*-methionine–H)$_3$(*l*-valine–H)] **(Figure 2.13)**.

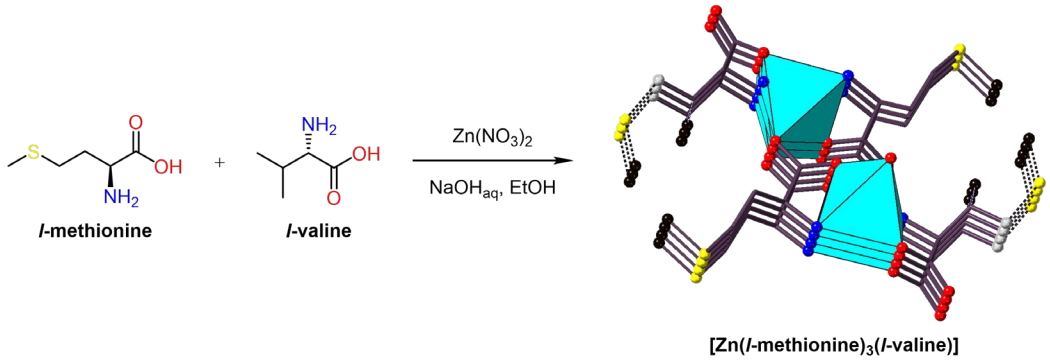

Figure 2.13: Synthetic pathway to [Zn(*l*-methionine-H)$_3$(*l*-valine-H)] at room temperature. Atom colours: C chain = dark purple, terminal C = black, O = red, N = blue, S = yellow, and Zn(II) = teal blue. Hydrogen atoms are omitted for clarity.

SCXRD showed a single Zn(II) centre in a trigonal-bipyramidal environment coordinated by amino and carboxylate donors (**Figure 2.14.a**). ^{1}H NMR spectroscopy of the digested crystals in DCl/DMSO showed a 3:1 ratio of methionine: valine (**Figure 2.42**). The asymmetric unit contains two unique amino-acid positions (**Figure 2.14.b**), which appears inconsistent with the 3:1 methionine: valine composition. The discrepancy was resolved by identifying positional disorder at one ligand site: one coordination site was fully occupied by Met, while the second was disordered ≈50:50 between Met and Val (**Figure 2.14.c,d**). Refinement of site occupancies yielded an overall 3:1 methionine:valine stoichiometry, in full agreement with the NMR data.

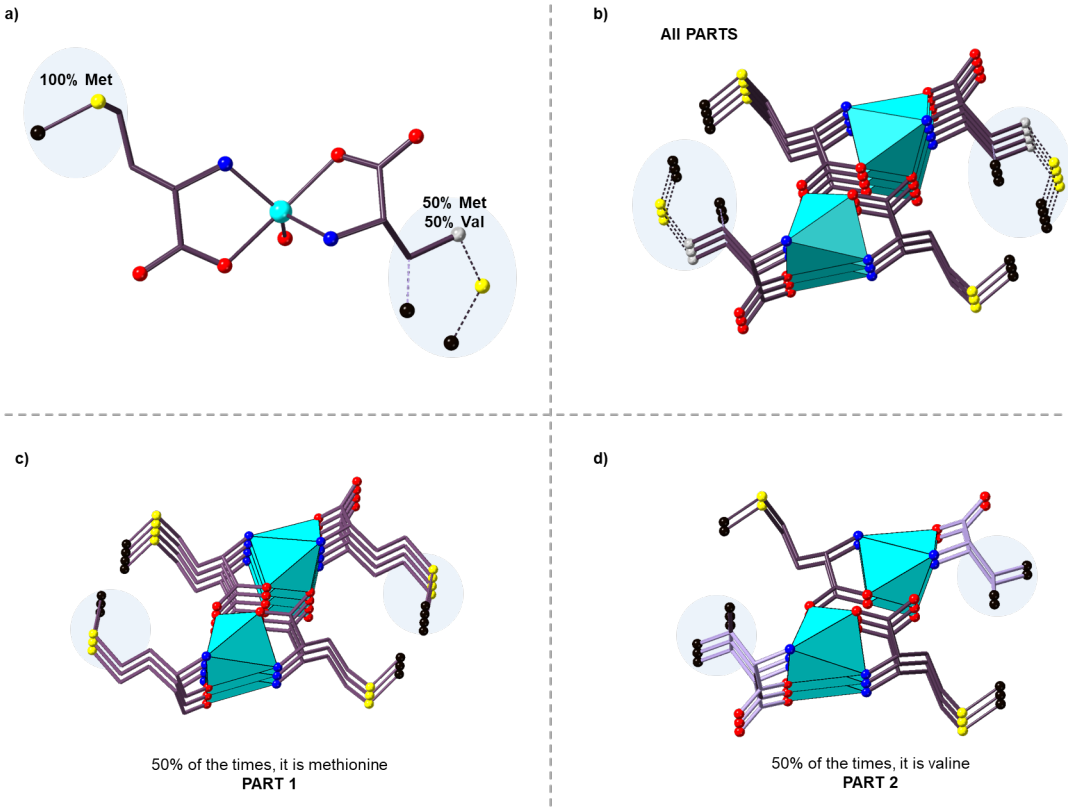

Figure 2.14: a) Local coordination environment and asymmetric unit of the Zn(II) centre. Zn(II) adopts a trigonal bipyramidal geometry with two ligand sites: one fully occupied by methionine (100% Met) and the other disordered ≈50:50 between methionine and valine. Dashed bonds indicate the Met/Val exchangeable position. **b–d)** Polymer views illustrating the 1D coordination motif and the location of the disordered site along the chain in different orientations. The disordered ligand is highlighted with pale circles. Atom colours: methionine C chain = dark purple, valine C chain =light purple, terminal C = black, O = red, N =blue, S = yellow and Zn(II) = teal blue. Hydrogen atoms are omitted for clarity.

Each methionine binds as a bidentate ligand (N,O chelation), forming a 1D coordination polymer rather than an extended 3D framework. The trigonal-bipyramidal geometry reflects mixed N/O donors, with carboxylate oxygen atoms occupying axial/equatorial positions as allowed by the chelate bite. No continuous 3D pore network was observed.

[Co(*l*-methionine-H)$_2$]

l-Methionine was combined with *l*-histidine in an attempt to co-assemble both amino acids into a MMOF. In one experiment, both amino acids were dissolved in H_2O and EtOH, and a small amount of DMF, and the mixture was heated, which yielded plate-like crystals (**Figure 2.15**). SCXRD revealed that instead of forming the targeted MMOF from methionine and histidine, the obtained crystals were [Co(*l*-methionine-H)$_2$].

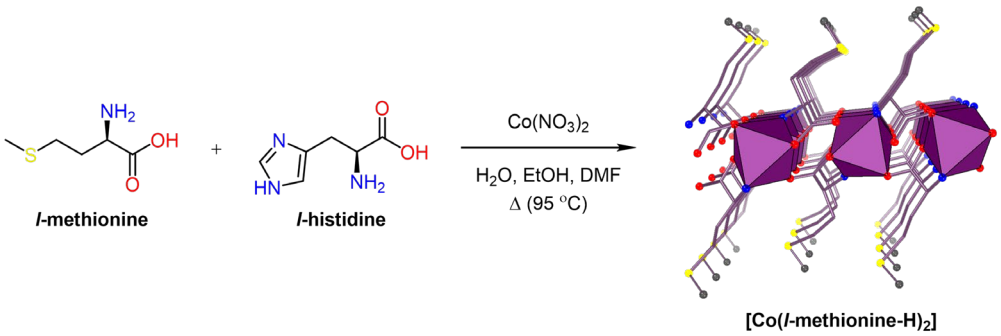

Figure 2.15: Synthetic pathway leading to the formation of [Co(*l*-methionine-H)$_2$]. Atom colours: methionine C chain = dark purple, terminal C = black, O = red, N = blue, S = yellow and Co(II) = purple. Hydrogen atoms are omitted for clarity.

The structure contains four singly deprotonated methionine ligands (methionine-H). Two ligands coordinate in a bidentate fashion through both the carboxylate oxygen (C=O) and amino nitrogen (NH), while the other two bind solely via their carboxylate oxygen (C-O) atoms (**Figure 2.16.a**). The connectivity propagates into a 1D coordination polymer rather than an extended 3D framework (**Figure 2.16.b**).

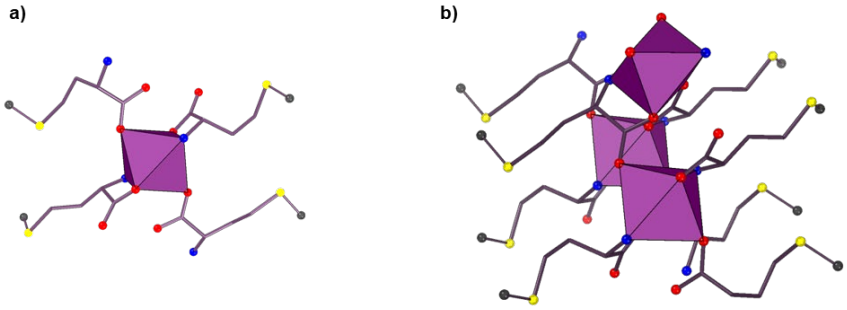

Figure 2.16: a) Co(II) coordinated by four methionine ligands: two bidentate (via carboxylate O and amino N) and two monodentate (via carboxylate O only). **b)** This connectivity yields a 1D polymer, not a 3D framework. Atom Colours: methionine C chain =dark purple, terminal C = black, O = red, N = blue, S = yellow, and Co(II) = purple. Hydrogen atoms are omitted for clarity.

The experimental PXRD pattern matches the one calculated from SCXRD, confirming phase purity (**Figure 2.44**). This structure was reproducibly obtained under several reaction conditions, including attempts with Zn(II), as summarised in **Appendix A**.

From this series, I isolated two crystalline products: [Zn(*l*-methionine-H)$_3$(*l*-valine-H)] and [Co(*l*-Met-H)$_2$]. All other trials are summarised in **Appendix A**. Collectively, the data show that direct one-pot co-assembly with methionine under basic/neutral conditions favours chelate-driven 1D polymers with site disorder (Zn/valine case) or single-ligand selectivity (Co/histidine case).

2.2.4 Leucine co-assembly with other amino acids

Leucine, a hydrophobic branched-chain amino acid, has limited direct application in MOF synthesis compared to other amino acids. Instead of serving as a primary ligand, it has mainly been explored in indirect roles. For example, leucine has been used as a modifying agent for pyridine, which was subsequently incorporated into a MOF.[63] In another case, leucine was employed to post-synthetically functionalise an existing MOF, introducing additional functional groups into the pores and creating channels that enhance water adsorption.[63, 130] Building on these precedents, leucine was incorporated into this study to broaden the scope of exploration of amino acid-based MOFs.

[Zn(*l*-leucine-H)$_2$]

l-Leucine was combined with valine and Zn(NO$_3$) in an attempt to co-assemble both amino acids into a MMOF. In a representative experiment, leucine, valine, and Zn(NO$_3$)$_2$ were dissolved in an aqueous basic solution and left at room temperature (**Figure 2.17**). Plate-like crystals were obtained and analysed by SCXRD. The structure revealed that only leucine coordinated to Zn(II), yielding [Zn(*l*-leucine-H)$_2$].

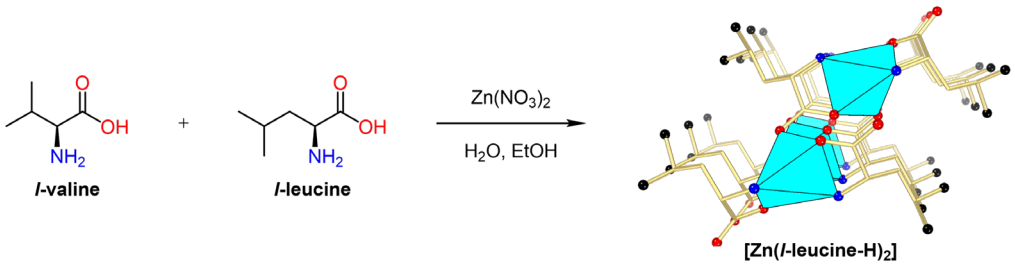

Figure 2.17: Synthetic pathway leading to the formation of [Zn(*l*-leucine-H)$_2$]. Atom colours: leucine C chain = pastel yellow, terminal C = black, O = red, N = blue, and Zn(II) = teal blue. Hydrogen atoms are omitted for clarity.

In this structure, three singly deprotonated leucine ligands coordinate to each Zn(II) centre. Two leucine ligands bind in a bidentate fashion through both the carboxylate oxygen and amino nitrogen, while the third coordinates via its carboxylate oxygen (**Figure 2.18.a**). The connectivity propagates into a 1D coordination polymer (**Figure 2.18.b**).

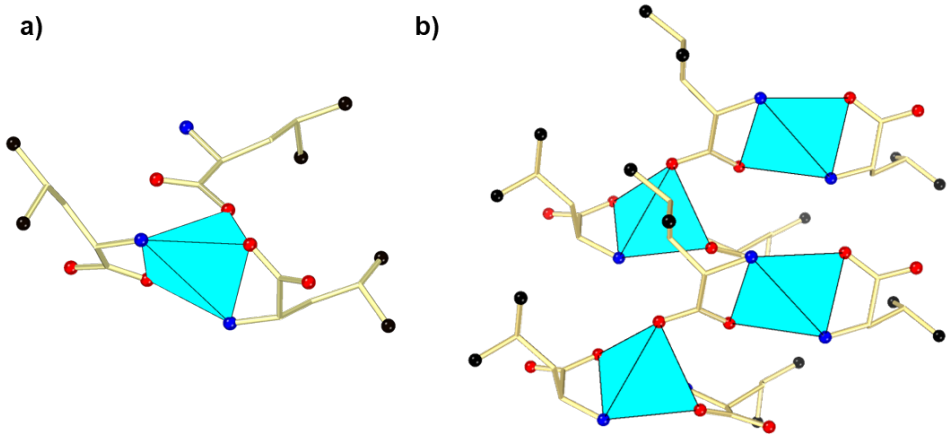

Figure 2.18: a) Zn(II) in trigonal bipyramidal geometry, coordinated by three leucine ligands: two bidentate (via carboxylate O and amino N) and one monodentate (via carboxylate O only). **b)** Extension into a 1D coordination polymer. Atom colours: leucine C chain = pastel yellow, terminal C = black, O = red, N = blue, and Zn(II) = teal blue. Hydrogen atoms are omitted for clarity.

Comparison of experimental PXRD data with the calculated pattern from SCXRD confirmed phase purity (**Figure 2.47**).

This structure was reproducibly obtained under several conditions, including attempts with Co(II); details are provided in **Appendix A**.

[Co(*l*-leucine-H)$_2$·2H$_2$O]

In an attempt to co-assemble *l*-leucine and *l*-arginine into a MMOF, mixtures of the two amino acids with Co(NO$_3$)$_2$ were left at room temperature (**Figure 2.19**). Instead of the targeted MMOF, the reaction yielded plate-like crystals of [Co(*l*-leucine-H)$_2$·2H$_2$O]. The crystals were characterised by PXRD, and SCXRD. The experimental PXRD pattern matched the one calculated from the corresponding SCXRD, with no additional reflections observed (**Figure 2.47**).

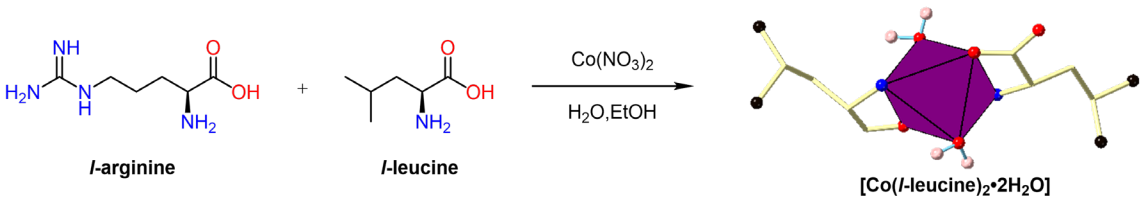

Figure 2.19: Synthetic pathway leading to the formation of [Co(*l*-leucine-H)$_2$·2H$_2$O]. Atom Colours: leucine C chain = pastel yellow, terminal C = black, H = whitish pink, O = red, N =blue, and Co(II) =purple. Hydrogen atoms are omitted for clarity, except those of coordinated H$_2$O molecules.

In the crystal structure, Co(II) adopts an octahedral coordination geometry, binding to six donor atoms. Two singly deprotonated leucine ligands coordinate in a bidentate manner through their carboxylate oxygen and amino nitrogen atoms, while two water molecules complete the coordination sphere **(Figure 2.20.a**). Co(II) is frequently observed in tetrahedral environments with amino acid ligands; however, in this case, the donor set enforces an octahedral arrangement. The structure is discrete and does not extend into either a polymeric chain or a 3D structure (**Figure 2.20.b**).

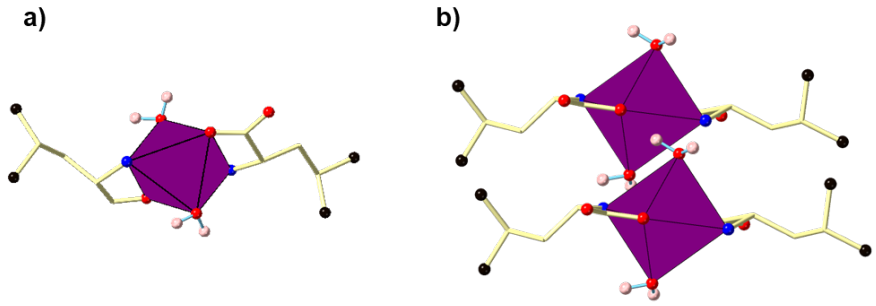

Figure 2.20: a) Octahedral coordination of Co(II) by two mono-deprotonated leucine ligands and two water molecules. **b)** The structure remains discrete, with no polymeric or 3D extension. Atom colours: leucine C chain = pastel yellow, terminal C = black H = whitish pink, O = red, N = blue, and Co(II) = purple. Hydrogen atoms are omitted for clarity, except those of coordinated H_2O molecules.

2.2.5 Glycine co-assembly with other amino acids

Glycine, the simplest amino acid, has been explored in MOF chemistry both as a ligand and as a functional modifier. It has been reported to form layered chain structures with halogen-containing species.[63] In addition, glycine has been employed as a modulating agent for UIO-66 which improved CO_2 adsorption.[63]

[Co(glycinate-H)$_3$]

One of the combinations involved glycine and *l*-valine with $Co(NO_3)_2$ in an ethanol/DMF mixture. Solvothermal synthesis produced needle-like crystals, which were analysed by SCXRD (**Figure 2.21**). Unfortunately, instead of obtaining a MMOF from both amino acids, the structure corresponded to [Co(glycinate-H)$_3$].

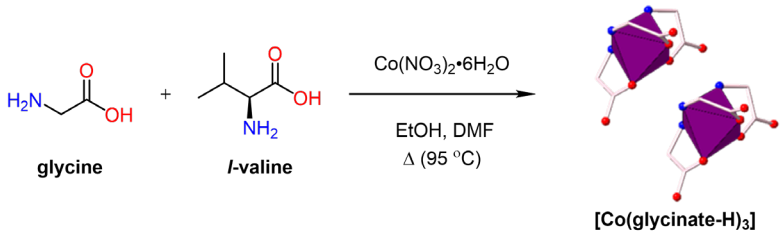

Figure 2.21: Synthetic pathway leading to the formation of [Co(glycinate-H)$_3$].Atom colours: glycine C chain = pastel pink, O = red, N = blue, and Co(II) = purple. Hydrogen atoms are omitted for clarity.

The Co(III) centre is six-coordinate and adopts a distorted octahedral geometry, defined by three bidentate glycinate ligands coordinating through their amino nitrogen and carboxylate oxygen atoms.

The structure consists of three singly deprotonated glycine ligands (glycinate-H), each coordinating through both the carboxylate oxygen and amino nitrogen atoms. The resulting complex is discrete and does not extend into either a 3D framework or a 1D polymer (**Figure 2.21**).

The experimental PXRD pattern matched the simulated pattern calculated from SCXRD, confirming phase purity of the crystals (**Figure 2.49**).

(Valine)$_2$·benzoate

In another experiment, *l*-valine, glycine, and $Co(NO_3)_2$ were dissolved in aqueous NaOH and heated overnight. Benzoic acid was introduced as a modulator to control crystal growth and improve crystal quality. This reaction produced two distinct crystal habits, block-like and sheet-like, both corresponding to a (valine)$_2$·benzoate adduct (**Figure 2.22**).

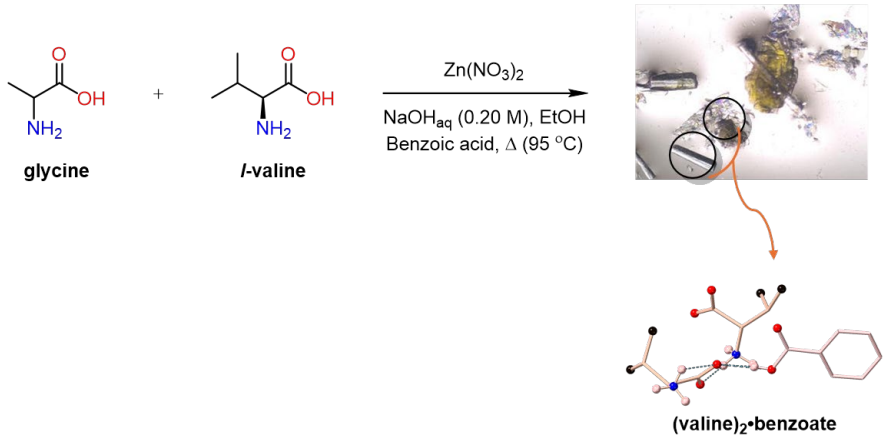

Figure 2.22: Synthetic pathway leading to the formation of (valine)$_2$·benzoate. Atom colours: valine C chain = orange, terminal C = black, benzoate = pink, O = red, N = blue. Blue dashed lines represent hydrogen bonds.

SCXRD analysis revealed that two equivalents of valine were hydrogen-bonded to benzoate. The structure consists of a discrete hydrogen-bonded complex formed by two zwitterionic *l*-valine molecules and a benzoate, stabilised through multiple N-H···O hydrogen-bonding interactions.

PXRD analysis showed good agreement between experimental and simulated patterns from the collected SCXRD (**Figure 2.51**). To further verify the product's identity and purity, the crystals were washed with acetone and analysed by ^{1}H NMR spectroscopy following dissolution in DCl/DMSO-d_6. The spectra for both crystal habits were identical, confirming the presence of (valine)$_2$·benzoic acid in a 2:1 ratio (**Figure 2.52**).

2.2.6 Cysteine and alanine co-assembly in MMOFs

Since the previous experiments did not yield MMOFs, the study was extended to include a wider range of amino acids. This broader screening aimed to test whether alternative functional groups could promote framework formation. Within this set, *l*-cysteine was of particular interest because of its thiol functionality, which imparts distinctive reactivity. Indeed, *l*-cysteine reacted readily with *l*-alanine, even under room-temperature conditions. The resulting coordination structure is presented in the following section.

[Zn/Co(H_2O)$_3$(2-methylzialodine-2,4-dicarboxylic acid)]

This compound was formed through a solvothermal reaction, which involves heating a mixture of reactants in a solvent at high pressure. In this case, the reactants were *l*-alanine and *l*-cysteine, which were combined in a basic aqueous medium and ethanol (**Figure 2.23**). However, the resulting structure was not the expected MMOF of *l*-alanine and *l*-cysteine. Unexpectedly, crystallography showed that the structure comprised Zn(II) and 2-methylzialodine-2,4-dicarboxylic acid.

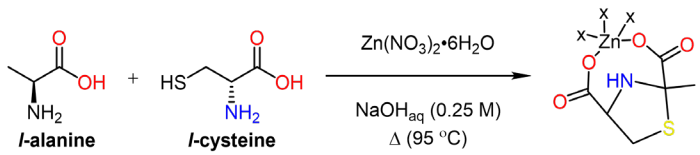

Figure 2.23: Synthetic pathway leading to the formation of [Zn(H_2O)$_3$ (2-methylzialodine-2,4-dicarboxylic acid)]. X denotes H_2O molecule.

The crystallography results matched the ^{1}H NMR spectroscopic data, confirming the phase purity and indicating that the crystals are the main product rather than a side product (**Figure 2.56**).The oxidation of alanine (amino acid) to pyruvic acid (keto acid) commonly happens in the body, and it is called oxidative deamination. Then, water hydrolyses this intermediate to pyruvic acid. The pyruvic acid reacted with the *l*-cysteine to form the 2-methylzialodine-2,4-dicarboxylic acid (**Figure 2.24**). [131, 132]

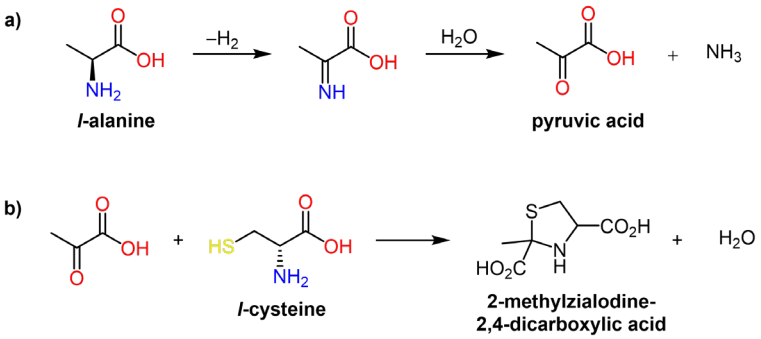

Figure 2.24: a) Oxidative deamination of alanine forms an imino acid intermediate, which hydrolyses to pyruvic acid. **b)** Pyruvic acid then reacts with cysteine to yield 2-methylthiazolidine-2,4-dicarboxylic acid.

Crystals with needle-like shape with Zn(II), or block-like shape with Co(II) were formed. Within the crystal structure, the Zn(II)/Co(II) metal ion adopts an octahedral geometry. Three coordinating water molecules are coordinating with oxygen atoms, while the other three coordinating atoms consist of one oxygen atom from each carboxylate group and one nitrogen atom from the thiazolidine ring (**Figure 2.25.a**).

Despite numerous adjustments and optimisations to the experimental conditions, MOFs or crystalline structures based on cysteine and alanine could not be obtained.

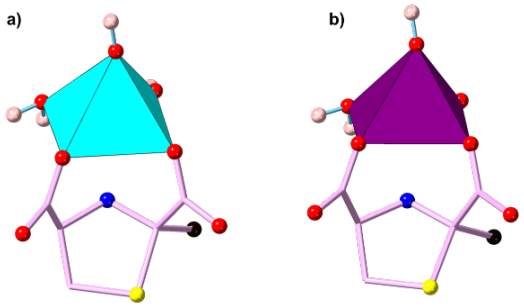

Figure 2.25: **a)** The asymmetric unit of [Zn(H_2O)$_3$(2-methylzialodine-2,4-dicarboxylic acid)] compound, the hydrogen atoms were omitted for clarity. **b)** [Co(H_2O)$_3$(2-methylzialodine-2,4-dicarboxylic acid)] compound structure. Atom colours: C chain = mauve, O = red; S = yellow, N = blue, H = whitish pink.

2.2.7 Miscellaneous crystal structures

[Zn(benzoate)$_2$]

In an attempt to co-assemble *l*-arginine and *l*-leucine into a MMOF, a mixture containing both amino acids with $Zn(NO_3)_2$ in ethanol and DMF was heated overnight (**Figure 2.26**). Benzoic acid was introduced as a modulator, since earlier experiments with benzoate had yielded crystalline powders with well-defined PXRD patterns. The modulator was intended to slow down crystal growth and promote the formation of high-quality crystals. However, instead of yielding a MMOF based on arginine and leucine or even individual MOFs derived from either amino acid, crystals of Zn(benzoate)$_2$ were obtained.

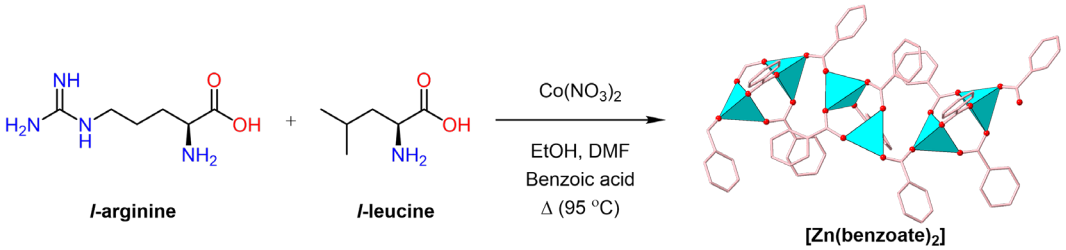

Figure 2.26: Synthetic pathway leading to the formation of Zn(benzoate)$_2$. Atom colours: benzoate C chain = pink, O = red, and Zn(II) =teal blue.

In this structure, each Zn(II) ion adopts a tetrahedral coordination geometry, being coordinated by four benzoate ligands. These benzoate ligands bridge the Zn(II) centres, leading to the formation of a 1D coordination polymer (**Figure 2.26**). This structure corresponds to a previously reported Zn(benzoate)$_2$ complex.[133]

The experimental PXRD pattern was compared to the simulated pattern calculated from the collected SCXRD, with a good match between them (**Figure 2.58**).

[Co(HCO$_2$)$_8$·8H$_2$O]

This complex was obtained via solvothermal synthesis, where the decomposition of DMF in the presence of water at elevated temperature generated formate ligands. For example, heating *l*-histidine and *l*-methionine in DMF/H$_2$O produced crystals of [Co(HCO$_2$)$_8$·H$_2$O] (**Figure 2.27**).

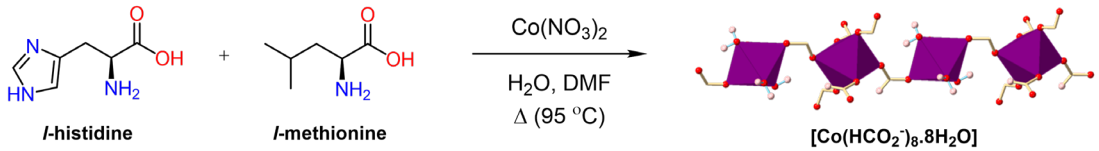

Figure 2.27: Synthetic pathway leading to the formation of $[Co(HCO_2^-)_8 \cdot H_2O]$. Atom colours: C chain = yellow, O = red, and Co(II) = purple. Hydrogen atoms are omitted for clarity, except those for H_2O molecules.

Four Co(II) ions have two types, both of which have a trigonal bipyramidal geometry. Two Co(II) coordinate to four water molecules and one shared formate group and the second coordinate to five formate groups, one of them is shared between two Co(II) (**Figure 2.28)**.

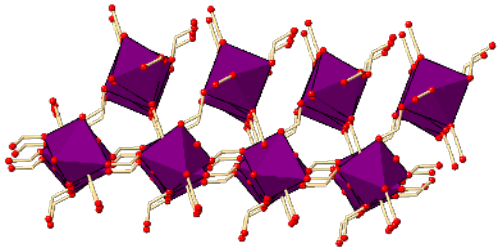

Figure 2.28: The decomposition product of DMF, formate group, coordinates with Co(II) to form a 3D structure. Atom colours: C chain = yellow, O = red, and Co(II) = purple. Hydrogen atoms are omitted for clarity except those for H_2O molecules.

The experimental PXRD pattern was compared to the simulated pattern calculated from the collected SCXRD, with a good match between them (**Figure 2.60**).

Free ligand crystal structures

Amino acids often convert into amorphous powders under harsh conditions such as high pH or elevated temperature. To avoid this, syntheses were conducted at room temperature, resulting in two distinct sets of outcomes presented here.

Alanine polymorph and Asparagine polymorph

In an effort to synthesise an MMOF from *l*-asparagine and *l*-alanine, the amino acids were dissolved in a basic aqueous solution and left at room temperature for three days. However, rather than forming a MOF from either or both components, the amino acids crystallised independently in their free forms, without coordinating to the metal centre (**Figure 2.29**).

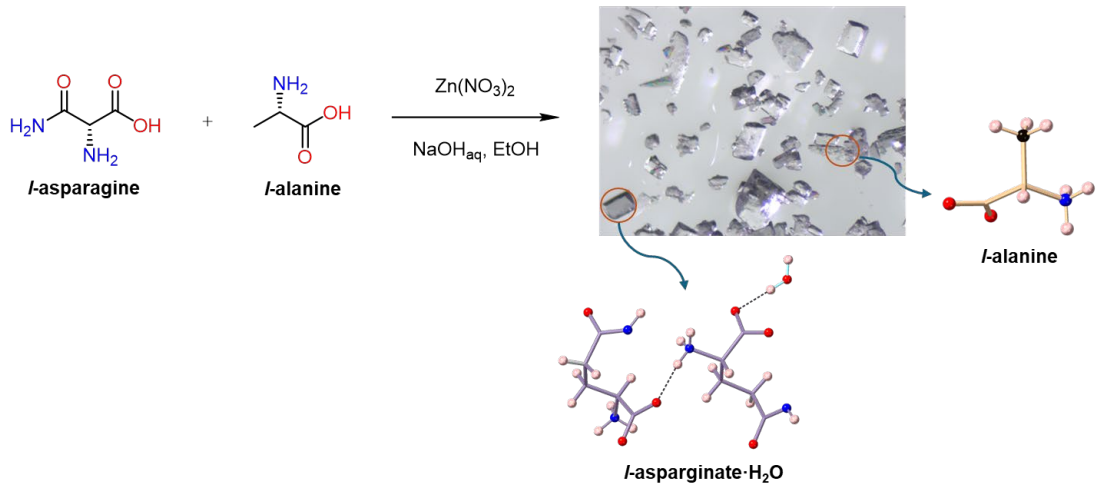

Figure 2.29: Synthetic pathway leading to the formation of different polymorphs of asparagine and alanine, instead of the desired MMOFs.
Atom colours: asparagine C chain = mauve, alanine C chain = orange, H = whitish pink terminal C = black, H = whitish pink, O = red, and N = blue.

The free ligand *l*-asparagine crystallised as block-like crystals, adopting its zwitterionic form in the solid state and forming hydrogen bonds with water molecules. This crystal structure has not been previously reported in the CCDC. In contrast, alanine crystallised as plate-like crystals in its zwitterionic form, corresponding to a known and previously reported phase in the CCDC (ALUCAL, *d*-Ala) (**Figure 2.29**).

l-Serine and *l*-glutamic acid polymorph

l-Glutamic acid and *l*-serine were dissolved in a basic aqueous solution and stirred at room temperature. Instead of forming a MMOF, the two amino acids crystallised separately as uncoordinated free ligands, with no evidence of metal coordination (**Figure 2.30**).

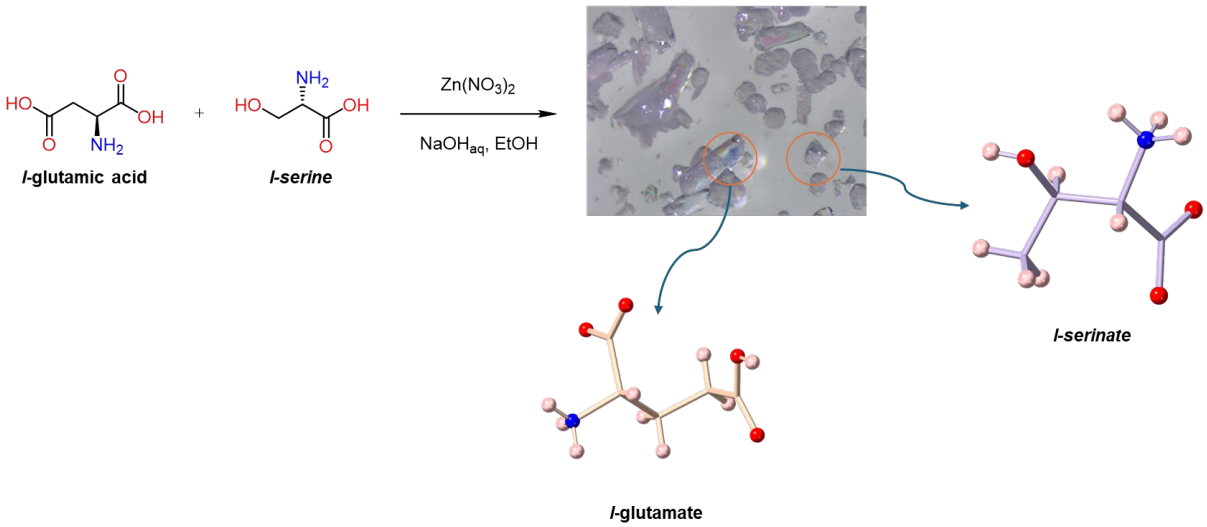

Figure 2.30: Synthetic pathway resulted in the formation of *l*-glutamic acid and *l*-serine polymorphs. Atom colours: glutamic acid C chain = pastel orange, H = whitish pink, serine C chain = green, O = red, and N = blue.

l-Glutamic acid crystallises as rectangular-shaped crystals in its zwitterionic form (LGLUAC02), while *l*-serine forms block-like crystals, also in the zwitterionic form (BUHGOA06) (**Figure 2.30**). Both structures have been previously reported, as confirmed by their entries in the CCDC database.

Across all room-temperature experiments, only one case combining valine and methionine resulted in the formation of a multicomponent structure (as described above). In the remaining cases, the amino acids either crystallised separately in their free forms or remained dissolved in solution.

2.3 Conclusion

The primary objective of this chapter was to synthesise MMOFs using multiple amino acids. Although a wide variety of combinations amino acids were explored under diverse conditions, MMOFs with well-defined SBUs and permanent porosity were not obtained. This highlights the inherent challenges of constructing robust, crystalline MMOFs from amino acid building blocks, rather than simply indicating an unsuccessful outcome.

The limited success of crystalline MMOFs synthesis can be partly attributed to the challenges of integrating amino acids into robust SBUs. Well-defined SBUs are essential for obtaining 3D, porous frameworks. SBUs such as metal-oxo clusters or metal carboxylate paddlewheels act as rigid structural nodes that allow framework extension into 3D networks.[12, 53] Although amino acids have multiple coordination sites (e.g., amino, carboxylate, and sometimes side-chain functional groups), their coordination modes are sensitive to pH, solvent type and composition, and ligands competition.[134, 135] Also, amino acids flexibility limits the formation of known SBUs, leading to 1D coordination polymers or amorphous solids instead of 3D frameworks.[136, 137]

Moreover, amino acids chelating behaviour, especially when acting as N,O-bidentate ligands, forms discrete mononuclear complexes rather than extended frameworks.[138] The amino acids side chains steric effect, and the possibility of forming multiple coordination modes further complicate the self-assembly process, which makes the control over connectivity and dimensionality more complicated.[23] Although amino acids can offer rich functionality and chirality, their structural flexibility can be a major limitation when the aim is to form crystalline MMOFs with well-defined SBUs.[139, 140]

2.4 Experimental section

2.4.1 General information:

All starting materials and solvents were used as received from commercial sources without further purification unless otherwise noted. Solvents were dried over 4 Å molecular sieves. NMR spectra were collected at room temperature using Bruker 500 MHz. The solvent protons were used as an internal standard for calibration.

X-ray diffraction data were collected using a Bruker D8 Venture diffractometer with Cuα radiation (1.54178 Å) generated by a IμS microfocus Diamond sealed tube and equipped with a Photon III 28 detector. Low-temperature cooling was achieved using an Oxford Cryostream 800. Data was collected, integrated, scaled, and averaged using the APEX3 or APEX4 software package. Single crystal data were refined using the Shelx[141] package under Olex2.[142] PXRD data were processed into 1D diffractograms using APEX3 and Diffrac. Eva. Predicted PXRD patterns were generated from cif files using Mercury.

2.4.2 [Co(*l*-asparagine-H)(*l*-tyrosine-H)] synthesis

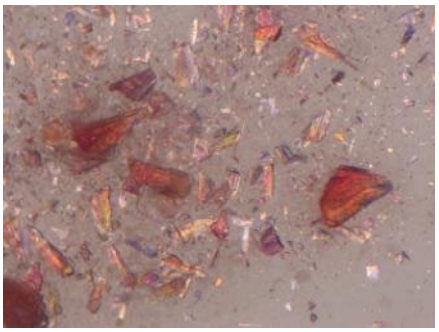

Figure 2.31: [Co(*l*-asparagine-H)(*l*-tyrosine-H)] crystals picture.

In a Teflon-lined steel autoclave, *l*-asparagine (0.07 g, 0.50 mmol) and *l*-tyrosine (0.09 g, 0.50 mmol) were dissolved in aqueous NaOH solution (0.25 M, 3.50 mL), and a similar amount of ethanol (3.50 mL) was added. The prepared samples were sonicated for 10 minutes at 70 °C. $[Co(NO_3)_2 \cdot 6H_2O]$ (0.32 g, 1.00 mmol) was added and sonicated again for another 10 minutes. Then, the Teflon-lined steel autoclave was placed into a 95 °C oven for 3 days.

For SCXRD, the crystals were kept solvated and mounted using oil. SCXRD data are presented in **Table 2.1**. The crystals were washed with ethanol, and the PXRD pattern was obtained and compared to the calculated pattern from the single crystal (**Figure 2.33**). For ^{1}H NMR spectroscopy, the crystals were washed with EtOH (x 3, 0.5 mL) and dried under a high-vacuum pump. ^{1}H NMR spectroscopy was done in a solution of DCl/DMSO (23 μL/ 1 mL) (**Figure 2.34**).

2.4.3 [Zn(*l*-asparagine-H)(*l*-tyrosine-H)] synthesis

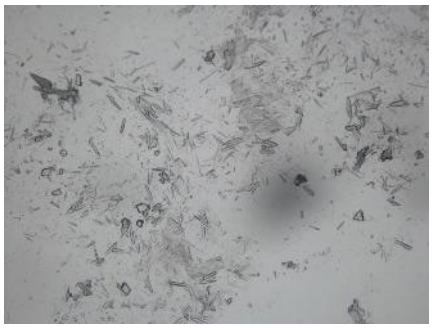

Figure 2.32: [Zn(*l*-asparagine-H)(*l*-tyrosine-H)] crystals picture.

The procedure above was repeated, but [$Zn(NO_3)_2 \cdot 6H_2O$] (0.26 g, 1.00 mmol) was added instead and sonicated for 10 minutes. Then, the bomb was placed into a 95 °C oven for 3 days.

The crystals were kept solvated and mounted in oil; the corresponding crystallographic data are presented in **Table 2.1**. PXRD patterns were collected from the washed crystals and compared with the simulated pattern calculated from the SCXRD data. The experimental and calculated PXRD patterns matched closely, confirming the phase purity of the material (**Figure 2.33**).

Both [Co(*l*-asparagine-H)(*l*-tyrosine-H)] and [Zn(*l*-asparagine-H)(*l*-tyrosine-H)] have identical ^{1}H NMR spectroscopic data (**Figure 2.34**).

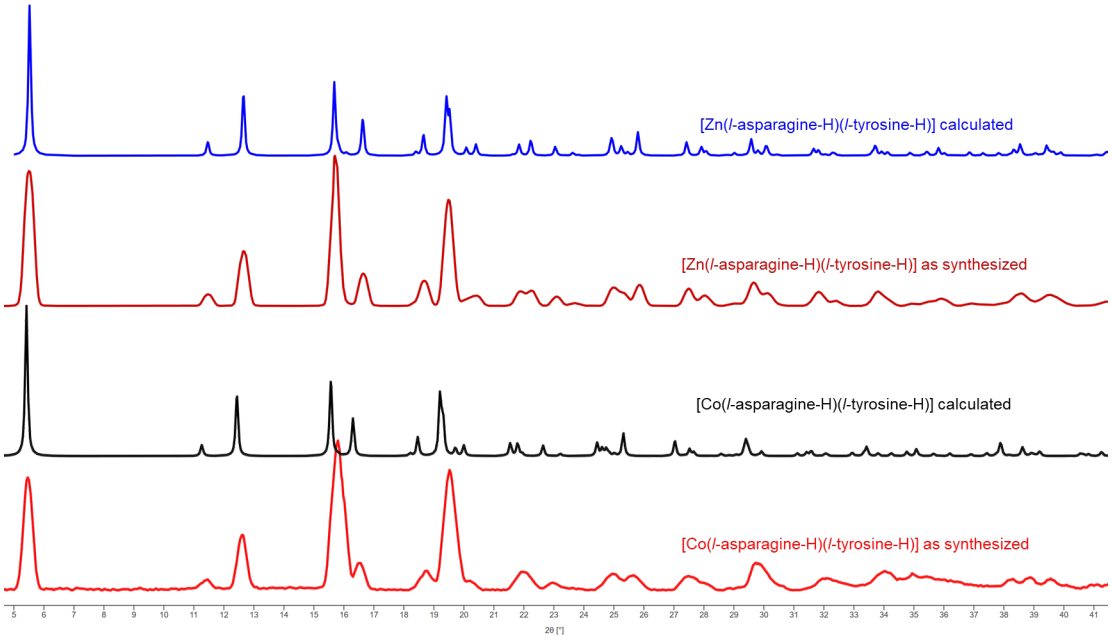

Figure 2.33: Experimental and calculated PXRD patterns for [Zn(*l*-asparagine-H)(*l*-tyrosine-H)] and [Co(*l*-asparagine-H)(*l*-tyrosine-H)]. Both Zn(II) and Co(II) structures are identical. The slight difference in the PXRD peaks positions is related to the slight difference in the unit cell.

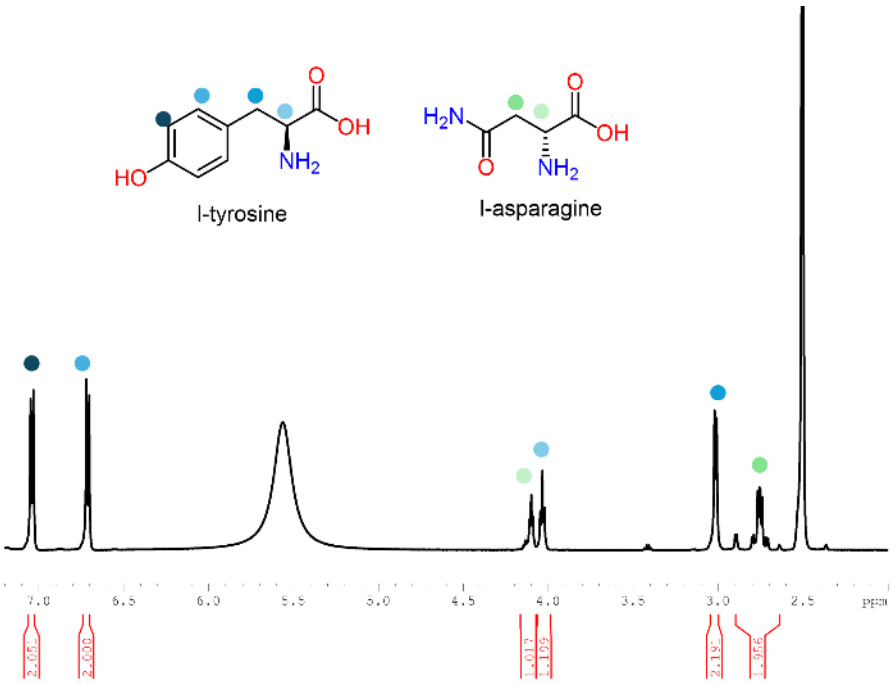

Figure 2.34: ^{1}H NMR spectrum of [Co/Zn(*l*-asparagine-H)(*l*-tyrosine-2H)] dissolved in DCl/DMSO (23 µL/ 1 mL DMSO).

2.4.4 [Zn(*l*-histidine-H)(*l*-tyrosine-H)]

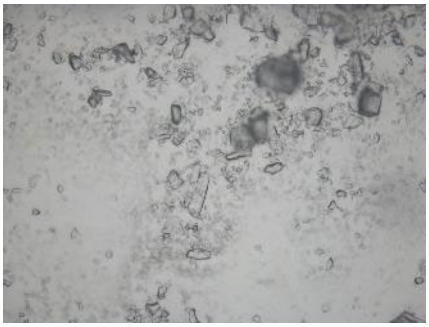

Figure 2.35: [Zn(*l*-histidine-H)(*l*-tyrosine-H)] crystals picture.

In a 20 mL vial, *l*-tyrosine (0.09 g, 0.49 mmol), *l*-histidine (0.07 g, 0.48 mmol), and $[Co(NO_3)_2 \cdot 6H_2O]$ (0.31 g, 1.19 mmol) were dissolved in H_2O (5 mL). pH was adjusted to around 8 using NaOH solution (0.25 M). Then, EtOH (2 mL) was added. The sealed vial was placed into a 95 °C oven for 24 hours.

The crystals were kept solvated and mounted in oil, and the corresponding crystallographic data are presented in **Table 2.1**. PXRD data were collected from washed crystals and compared with the simulated pattern generated from the SCXRD data, confirming phase purity (**Figure 2.37**). For ^{1}H NMR spectroscopic analysis, the crystals were washed with acetone (x 3, 1 mL), dried under high vacuum, and dissolved in DCl/DMSO-d_6 (23 µL / 1 mL) (**Figure 2.38**).

2.4.5 [Co_2(*l*-histidine-2H)(*l*-tyrosine-H)$_3$·4H_2O]

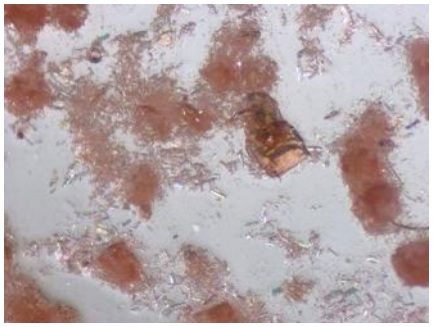

Figure 2.36: [Co_2(*l*-histidine-2H)(*l*-tyrosine-H)$_3$·4H_2O] crystals picture.

In a 20 mL vial, *l*-tyrosine (0.09 g, 0.49 mmol), *l*-histidine (0.07 g, 0.48 mmol), and [$Zn(NO_3)_2$·6H_2O] (0.34 g, 1.15 mmol) were dissolved in deionized water (5.00 mL). The pH of the solution was adjusted to around 8 using NaOH (0.25 M). Then, ethanol (2 mL) was added, and the vial was capped and heated in an oven at 95 °C for 24 hours.

After cooling to room temperature, the resulting crystals were washed with ethanol (x 5, 0.5 mL) and analysed by PXRD. The experimental PXRD pattern was consistent with the simulated pattern generated from the SCXRD data of the needle-like and block-like crystals, (**Figure 2.37**). The corresponding SCXRD data for [Co_2(*l*-histidine–2H)(*l*-tyrosine–H)$_3$·4H_2O] are presented in **Table 2.2**.

Several solvent washes (hot water, ethanol, and methanol) failed to dissolve *l*-tyrosine. As it is only soluble in basic aqueous solution, which also dissolved the crystalline product, ^{1}H NMR spectroscopic analysis was not performed.

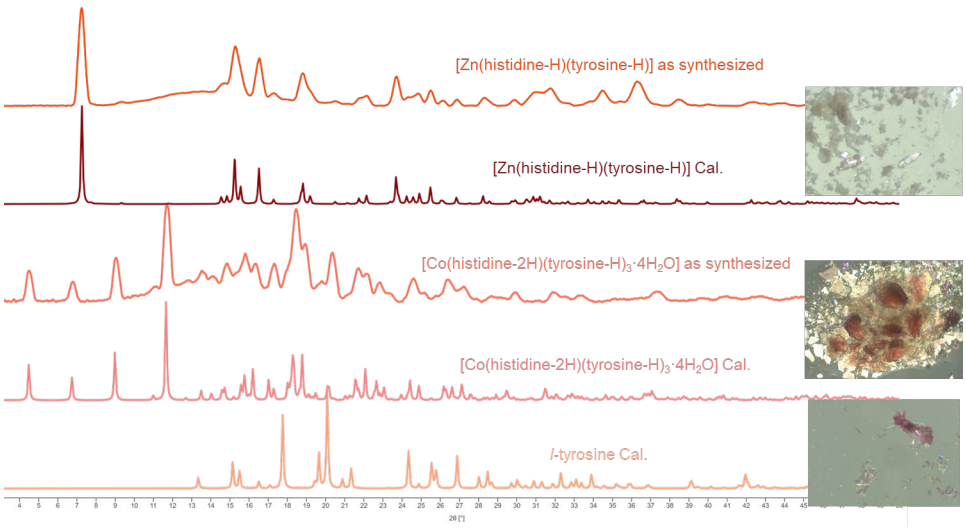

Figure 2.37: Experimental and calculated PXRD patterns for [Zn(histidine-H)(tyrosine-H)] and [Co(histidine-2H)(tyrosine-H)$_3$.4H_2O].

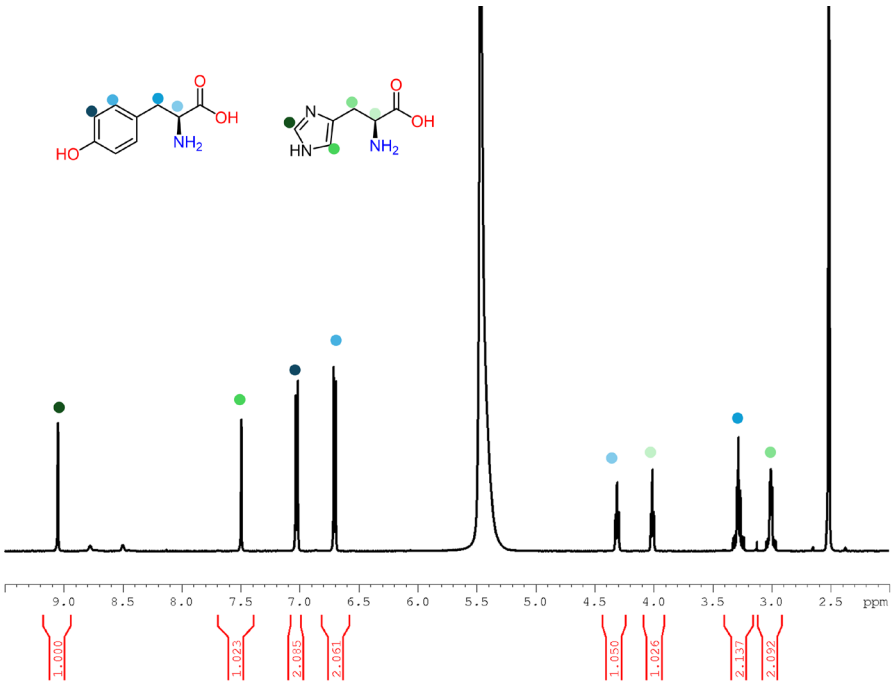

Figure 2.38: ^{1}H NMR spectrum of [Zn(*l*-histidine-H)(*l*-tyrosine-H)] digested in DCl/DMSO (23 µL/ 1 mL).

2.4.6 [Co(*l*-tyrosine-H)(H_2O)$_2$·2NO_3]

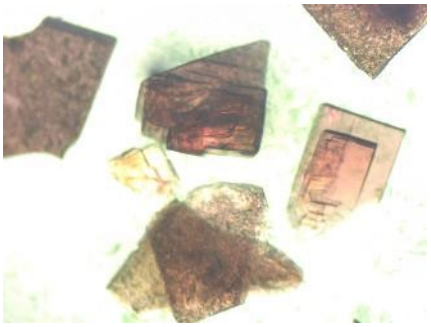

Figure 2.39: Co(*l*-tyrosine-H)(H_2O)$_2$·2NO_3 crystals.

In a 20 mL vial, *l*-tyrosine (0.04 g, 0.20 mmol), *l*-glutamic acid (0.03 g, 0.21 mmol), and [Co(NO_3)$_2$·6H_2O] (0.18 g, 0.62 mmol) were dissolved in aqueous NaOH (0.25 M, 2 mL). Ethanol (2 mL) was added, and the vial was sealed and heated at 95 °C for 24 hours. After cooling to room temperature, the resulting crystals were left in the mother liquor until analysis.

The crystals were washed with ethanol and mounted in oil, and the corresponding crystallographic data are presented in **Table 2.2**. PXRD data were also collected and compared with simulated patterns generated from related SCXRD structures in the Cambridge Crystallographic Data Centre (CCDC) (**Figure 2.11**).

2.4.7 [Zn(*l*-methionine)$_3$(*l*-valine)]

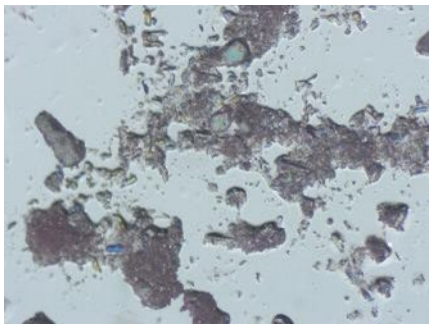

Figure 2.40: [Zn(*l*-methionine)$_3$(*l*-valine)] crystals.

In a 20 mL vial, *l*-methionine (0.18 g, 1.19 mmol) and *l*-valine (0.12 mg, 1.04 mmol) were dissolved in a mixture of aqueous NaOH (0.1 M, 3 mL) and ethanol (3 mL). [$Zn(NO_3)_2 \cdot 6H_2O$] (0.38 g, 1.27 mmol) was then added, and the mixture was stirred at room temperature for three days. The resulting crystals were left in the mother liquor until analysis.

Crystals were then mounted using oil, SCXRD are presented illustrated in **Table 2.2**. PXRD analysis was carried out and compared with the simulated pattern of the corresponding SCXRD (**Figure 2.41**).

For ^{1}H NMR spectroscopy, the crystals were washed with EtOH (x 3, 0.5 mL), dried under vacuum, then digested in DCl/ DMSO (23 µL/ 1 mL) (**Figure 2.42**).

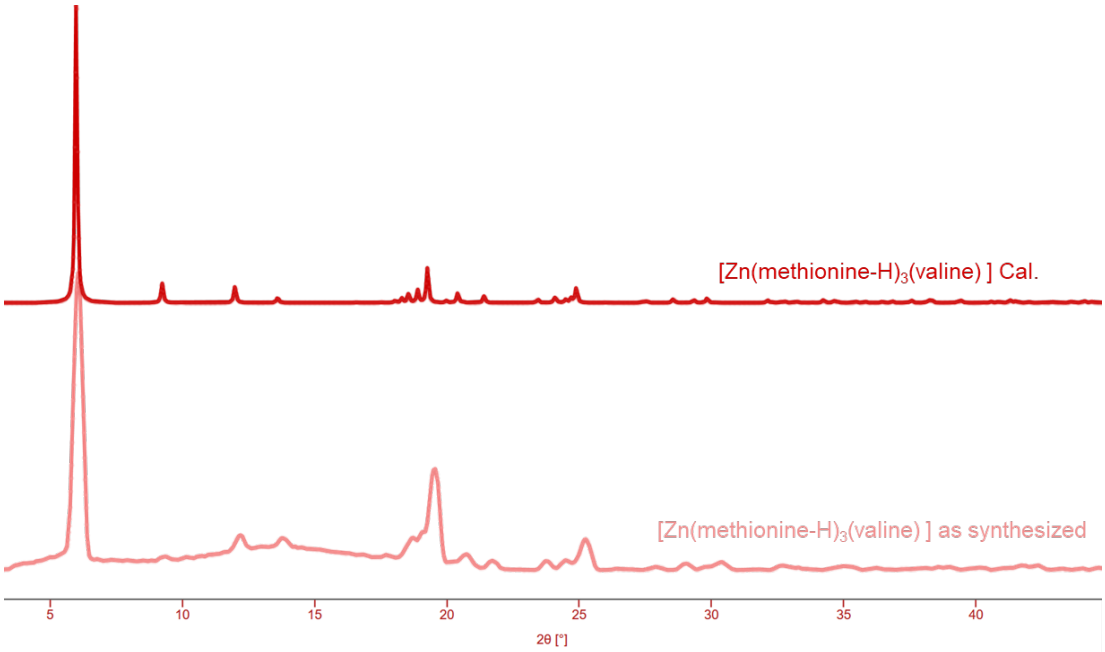

Figure 2.41: The calculated (upper) and experimental (lower) PXRD patterns of [Zn(methionine-H)(valine-H)].

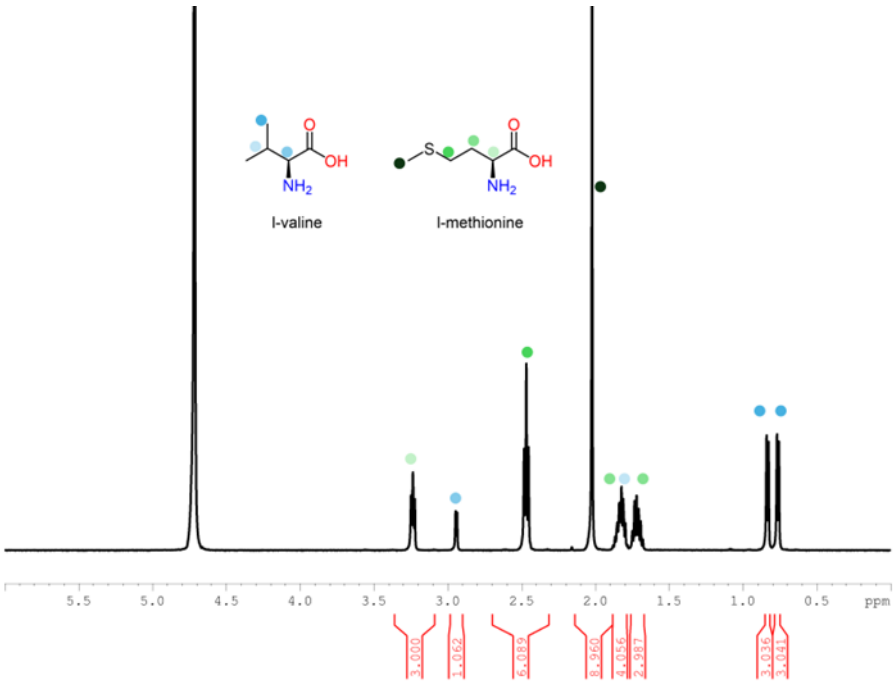

Figure 2.42: ^{1}H NMR spectrum of [Zn(*l*-methionine-H)$_3$(*l*-valine-H)] digested in DCl/DMSO (23 µL/ 1 mL).

2.4.8 [Co(*l*-methionine-H)$_2$]

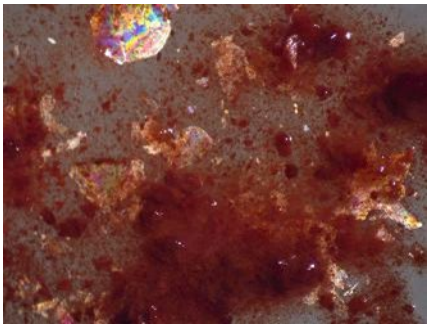

Figure 2.43: [Co(*l*-methionine-H)$_2$] crystals picture.

In a 4 mL vial, *l*-methionine (0.07 g, 0.48 mmol) and *l*-histidine (0.08 g, 0.52 mmol) were dissolved in H_2O (1 mL), EtOH (1 mL), and DMF (10 µL). Then, [$Co(NO_3)_2 \cdot 6H_2O$] (0.19 g,0.65 mmol) was added. The vial was capped and placed in a 95 °C oven for 3 days. After cooling to room temperature, the resulting crystals were left in the mother liquor until analysis.

The crystals were mounted in oil, and the corresponding crystallographic data are presented in **Table 2.3**. PXRD data were also collected and compared with the simulated pattern generated from the SCXRD structure **(Figure 2.44).**

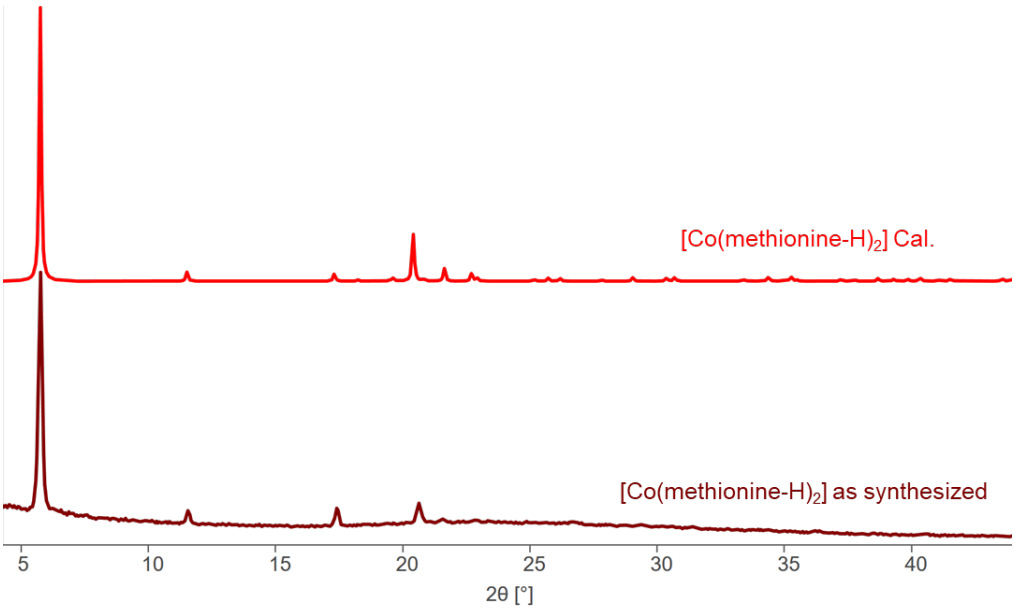

Figure 2.44: PXRD patterns of the [Co(*l*-methionine-H)$_2$] as-synthesised crystals overlaid with the simulated pattern generated from the corresponding SCXRD.

2.4.9 [Zn(*l*-leucine-H)$_2$]

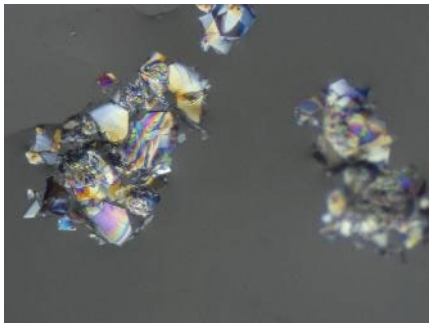

Figure 2.45: [Zn(*l*-leucine-H)$_2$] crystals picture.

In 20 mL vial, *l*-leucine (0.06 g, 0.49 mmol), *l*-valine (0.07 mg, 0.41 mmol) were dissolved in H_2O (2 mL) and EtOH (2 mL). Then, [$Zn(NO_3)_2 \cdot 6H_2O$] (0.03 mg, 0.97 mmol) was added, and the reaction mixture was stirred at r.t. After crystallisation, the crystals were left in the mother liquor until analysis.

The crystals were mounted in oil, and the corresponding crystallographic data are presented in **Table 2.3**. PXRD data were also collected and compared with the simulated pattern calculated from the SCXRD data, confirming the phase purity of the product (**Figure 2.47**).

2.4.10 [Co(*l*-leucine-H)$_2$.2H$_2$O]

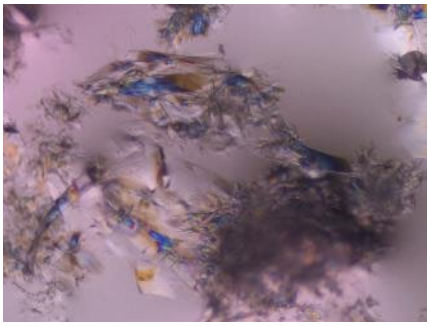

Figure 2.46: [Co(*l*-leucine-H)$_2$.2H$_2$O] crystals picture.

In 20 mL vials, *l*-leucine (0.06 g, 0.49 mmol), *l*-arginine (0.07 mg, 0.41 mmol) were dissolved in H$_2$O (2 mL) and EtOH (2 mL). Then, [Co(NO$_3$)$_2$·6H$_2$O] (0.33 g, 1.13 mmol) was added, and the reaction mixture was stirred at r.t. for 2 days. The crystals were left in the mother liquor until analysis and were mounted in oil for SCXRD. The crystallographic data obtained are summarised in **Table 2.3**.

Subsequently, PXRD patterns were collected and compared with the simulated patterns calculated from the SCXRD data to confirm the phase purity of the bulk material (**Figure 2.47**).

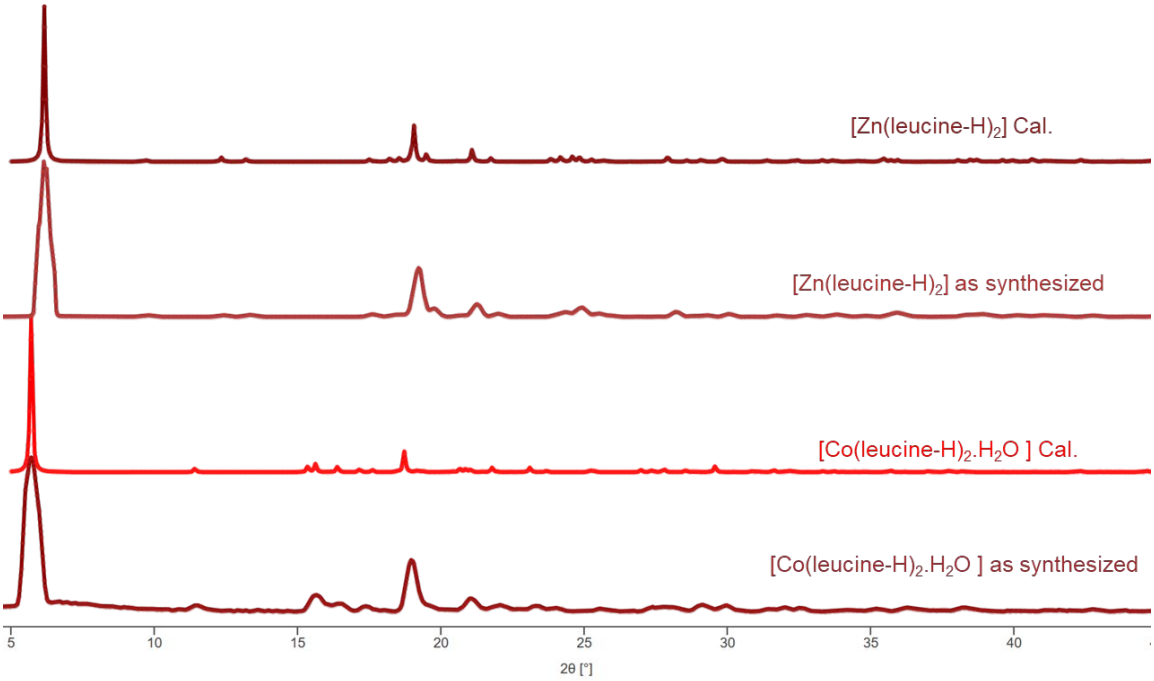

Figure 2.47: Experimental and calculated PXRD patterns for [Zn(*l*-leucine-H)$_2$] and [Co(*l*-leucine-H)$_2$·H$_2$O].

2.4.11 [Co(glycinate-H)$_3$]

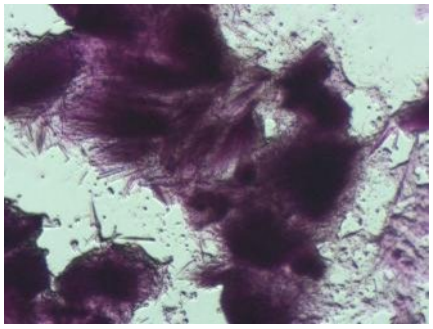

Figure 2.48: Co(glycinate-H)$_3$ crystals picture.

In a 4 mL glass vial, *l*-glycine (0.03 g , 0.46 mmol) and *l*-valine (0.05 g, 0.46 mmol) were dissolved in ethanol (1.00 mL) and DMF (20 µL). [$Co(NO_3)_2 \cdot 6H_2O$] (0.19 g, 0.65 mmol) was then added, and the mixture was heated at 95 °C overnight. The crystals were left in the mother liquor until analysis and were mounted in oil for SCXRD. The crystallographic data obtained are summarised in **Table 2.4**. Subsequently, PXRD patterns were collected and compared with the simulated patterns calculated from the SCXRD data to confirm the phase purity of the bulk material **(Figure 2.49)**.

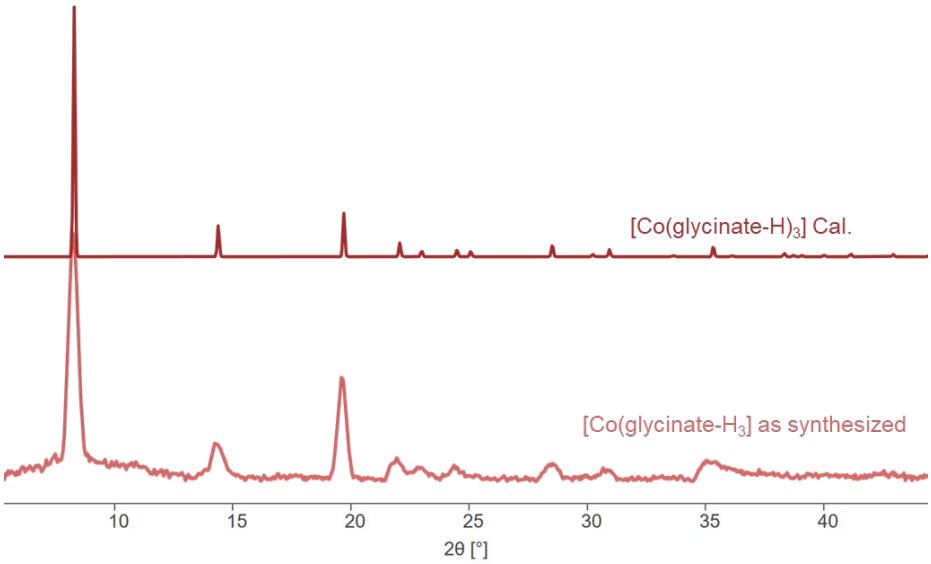

Figure 2.49: PXRD patterns of the [Co(glycine-H)$_3$] as-synthesised crystals (dark red) overlaid with the simulated pattern generated from the corresponding SCXRD (peach).

2.4.12 (Valine)$_2$·benzoate

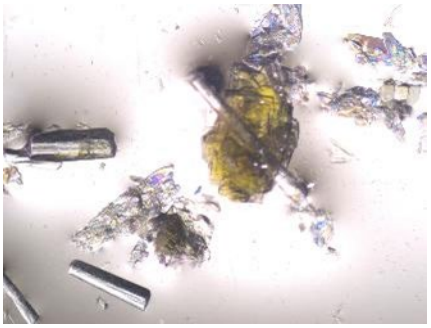

Figure 2.50: Valine)$_2$·benzoate crystals picture.

In a 4 mL vial, l-glycine (0.04 g, 0.50 mmol), *l*-valine (0.06 g, 0.52 mmol), and [$Co(NO_3)_2 \cdot 6H_2O$] (0.16 g, 0.53 mmol) were dissolved in ethanol (1 mL) and DMF (20 µL). Benzoic acid (0.12 g, 1.00 mmol) was added to this solution, the vial was sealed, and the mixture was heated at 95 °C. After cooling to room temperature, two distinct crystal habits, block-like and plate-like, were observed in the mother liquor. SCXRD analyses of both morphologies were performed, and the corresponding crystallographic data are summarised in **Table 2.4**. PXRD patterns were also collected for each morphology, confirming that both exhibited identical structures, indicating phase purity (**Figure 2.51**).

For ^{1}H NMR spectroscopic analysis, crystals were washed with acetone (x 3, 0.5 mL) and dried under a high-vacuum pump. Then, the dried crystals were dissolved in DCl/DMSO-d_6 (23 µL/1 mL) **(Figure 2.52)**.

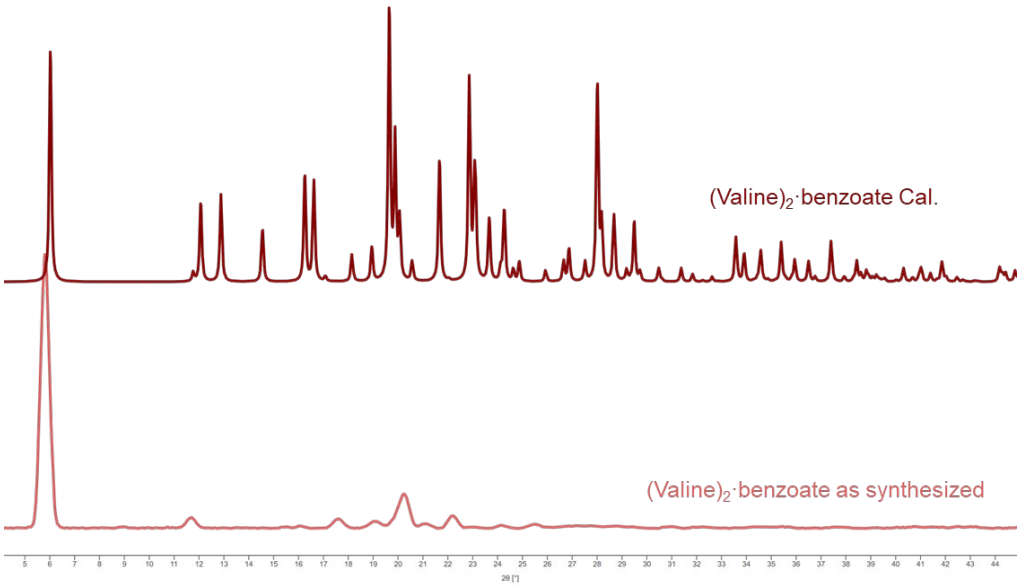

Figure 2.51: PXRD patterns of the (valine)$_2$·benzoic acid as-synthesised crystals (dark red) overlaid with the simulated pattern generated from the corresponding SCXRD (peach).

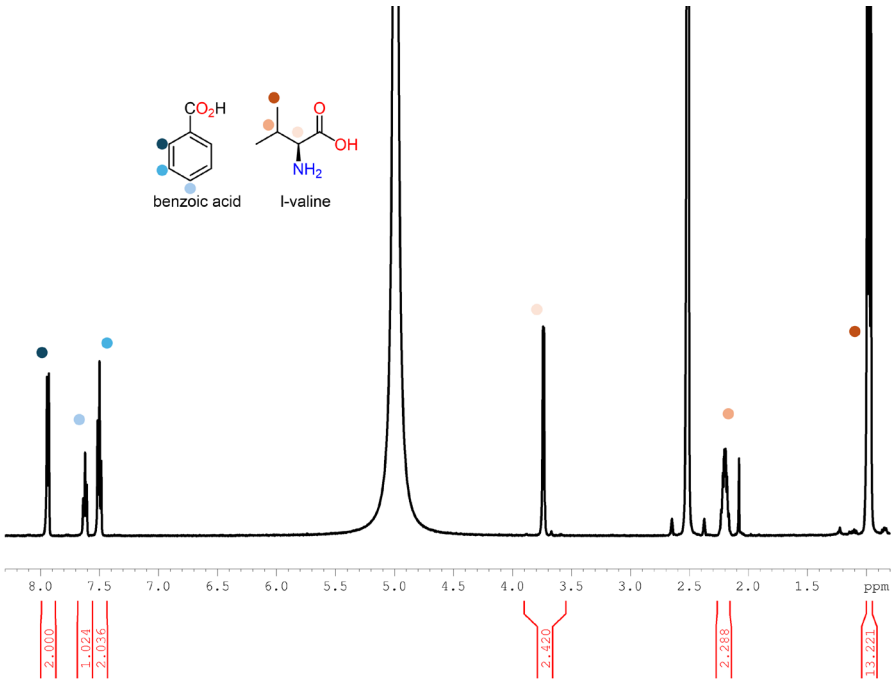

Figure 2.52: ^{1}H NMR spectrum of (valine)$_2$·benzoate digested in DCl/DMSO (23 µL/ 1 mL).

2.4.13 [Zn(H$_2$O)$_3$(2-methylzialodine-2,4-dicarboxylic acid)]

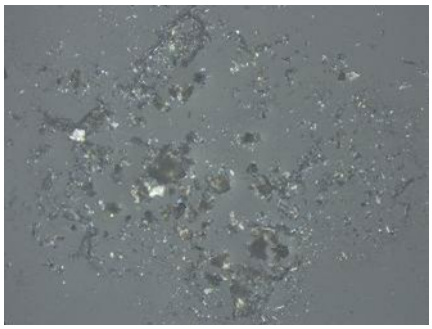

Figure 2.53: [Zn(H$_2$O)$_3$(2-methylzialodine-2,4-dicarboxylic acid)] crystals picture.

In a Teflon-lined steel autoclave, *l*-alanine (0.09 g, 1.00 mmol) and *l*-cysteine (0.12 g, 1.00 mmol) were dissolved in NaOH (0.25 M, 3.5 mL) and ethanol (3.5 mL). [Zn(NO$_3$)$_2$·6H$_2$O] (0.24 g, 1.00 mmol) was added. The reaction mixture was heated at 95 °C for 24 hours. After cooling to room temperature, crystals were obtained and left in the mother liquor until analysis. SCXRD data were collected from a crystal mounted in oil, and the SCXRD is summarised in **Table 2.4**. PXRD data were also collected and compared with the simulated pattern calculated from the SCXRD data, confirming the phase purity of the bulk sample **(Figure 2.55)**. For ^{1}H NMR spectroscopy, the crystals were washed with acetone (x 3, 0.5 mL) and dried under a high vacuum pump. The crystals were then dissolved in DCl/DMSO-d$_6$ solution (23 µL/ 1 mL) (**Figure 2.56**).

2.4.14 [Co(H$_2$O)$_3$(2-methylzialodine-2,4-dicarboxylic acid)]

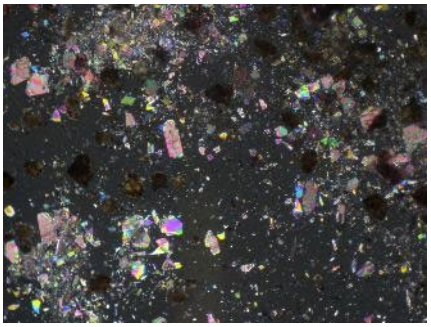

Figure 2.54: [Co(H$_2$O)$_3$(2-methylzialodine-2,4-dicarboxylic acid)] crystals picture.

The procedure was repeated but [Co(NO$_3$)$_2$·6H$_2$O] (0.40 g, 1.2 mmol) was instead added. After cooling to room temperature, crystals were obtained and left in the mother liquor until analysis. SCXRD data were collected from a crystal mounted in oil. PXRD data were also collected and compared with the simulated pattern calculated from the SCXRD data, confirming the phase purity of the bulk sample **(Figure 2.55)**. This structure is identical to the [Zn(H$_2$O)$_3$(2-methylzialodine-2,4-dicarboxylic acid)].

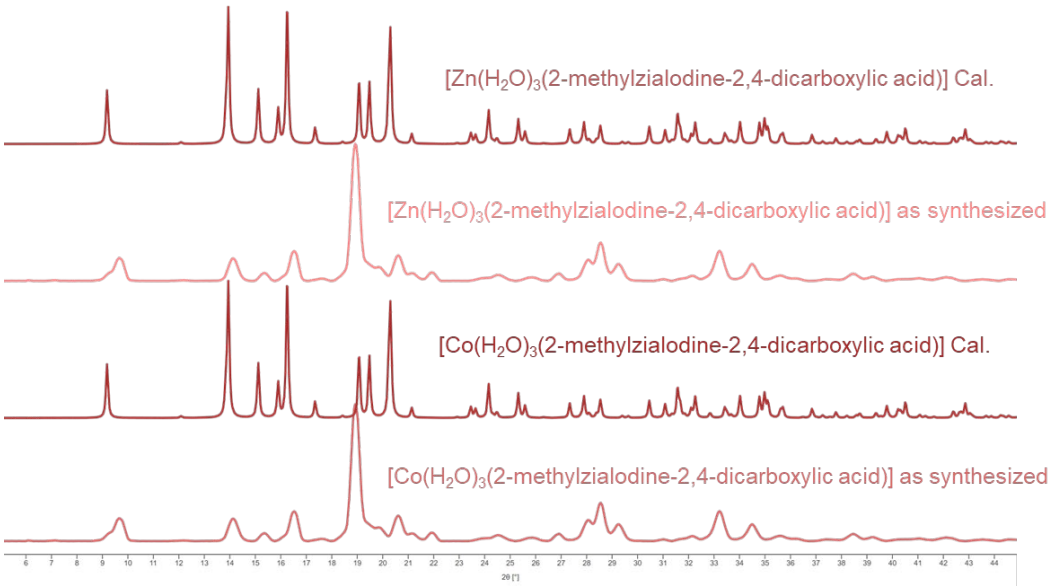

Figure 2.55: PXRD patterns of the [Zn(H$_2$O)$_3$(2-methylzialdone-2,4-dicarboxylic acid)] and [Co(H$_2$O)$_3$(2-methylzialdone-2,4-dicarboxylic acid)] as-synthesised crystals (dark red) overlaid with the simulated patterns generated from the corresponding SCXRD (peach).

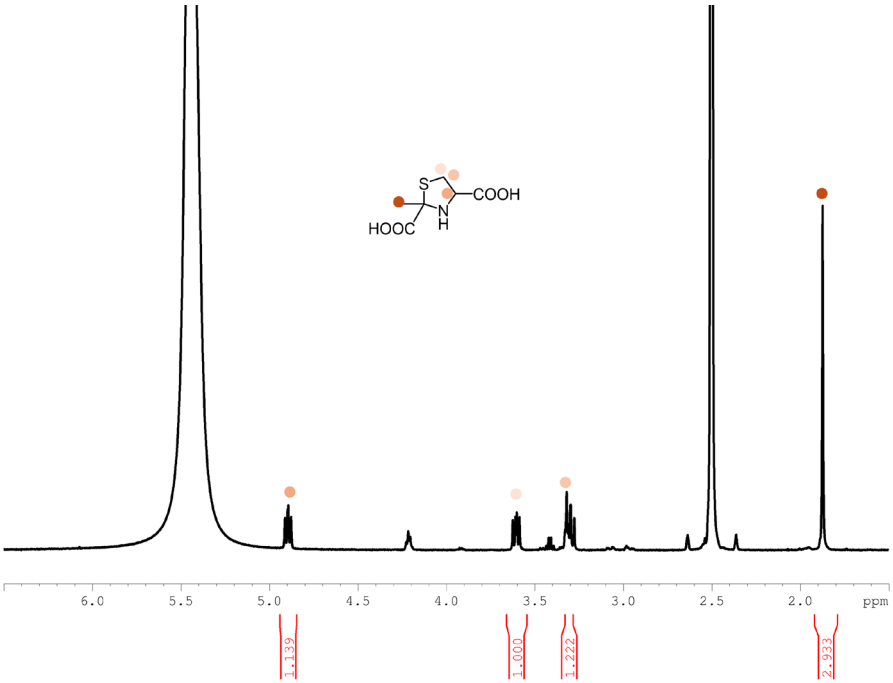

Figure 2.56: ^{1}H NMR spectrum of [Zn(H$_2$O)$_3$(2-methylzialdone-2,4-dicarboxylic acid)] digested in DCl/DMSO (23 µL/ 1 mL).

2.4.15 [Zn_2(benzoate)$_4$]

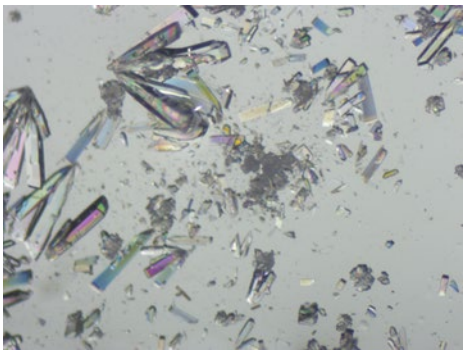

Figure 2.57: Zn(benzoate)$_2$ crystals picture.

In 4 mL vials, *l*-arginine (0.09 g, 0.50 mmol), *l*-leucine (0.07 g, 0.52 mmol), and benzoic acid (0.12 g, 1.00 mmol) were dissolved in EtOH (1.00 mL) and DMF (20 µL). Then, [$Zn(NO_3)_2 \cdot 6H_2O$] (0.14 g, 0.47 mmol) was added. Then, the vial was sealed and placed in an oven at 95 °C for 3 days. After cooling to room temperature, crystals were obtained and left in the mother liquor until analysis. SCXRD data were collected from a crystal mounted in oil, and the crystallographic information is presented in **Table 2.5**. PXRD patterns were also collected and compared with the simulated pattern calculated from the SCXRD data **(Figure 2.58)**.

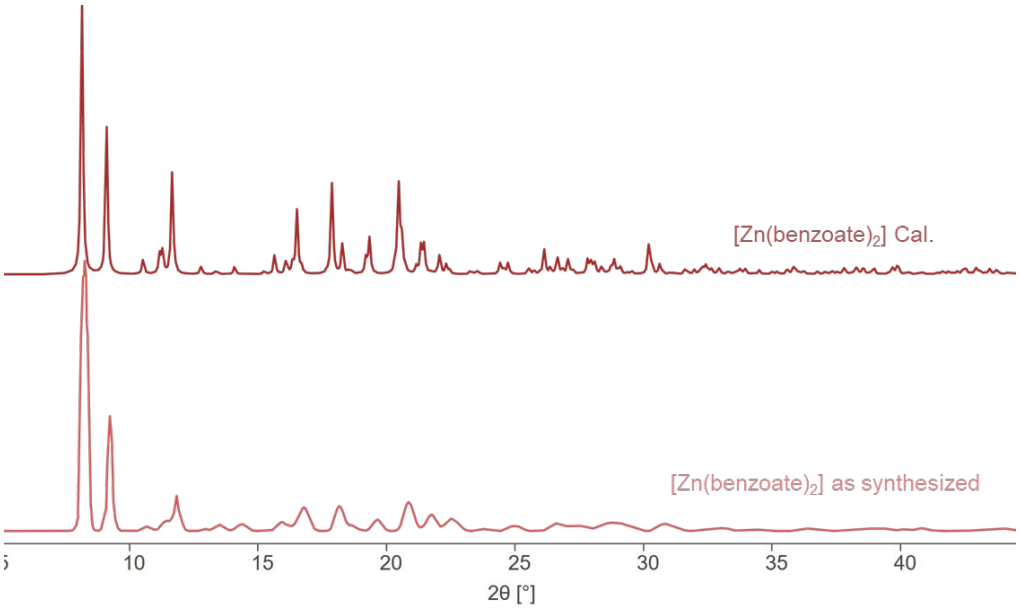

Figure 2.58: PXRD pattern of the [Zn(benzoate)$_2$] as-synthesised crystals (dark red) overlaid with the simulated pattern calculated from the corresponding SCXRD (peach).

2.4.16 $[Co(HCO_2)_8{\cdot}8H_2O]$

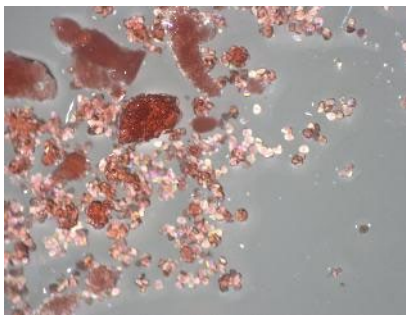

Figure 2.59: $[Co(HCO_2)_8{\cdot}8H_2O]$ crystals picture.

In a Teflon-lined steel autoclave, *l*-histidine (0.08 g, 0.52 mmol), *l*-asparagine (0.13 g, 1.00 mmol), and $[Co(NO_3)_2{\cdot}6H_2O]$ (0.29 g, 1.00 mmol) were dissolved in deionised water (1 mL) and DMF (1 mL). The vessel was sealed and heated at 95 °C for 72 hours. After cooling to room temperature, the resulting crystals were left in the mother liquor for subsequent characterisation.

SCXRD and PXRD analyses were performed. The experimental PXRD pattern was compared with the simulated pattern generated from the corresponding SCXRD data **(Figure 2.60)**.

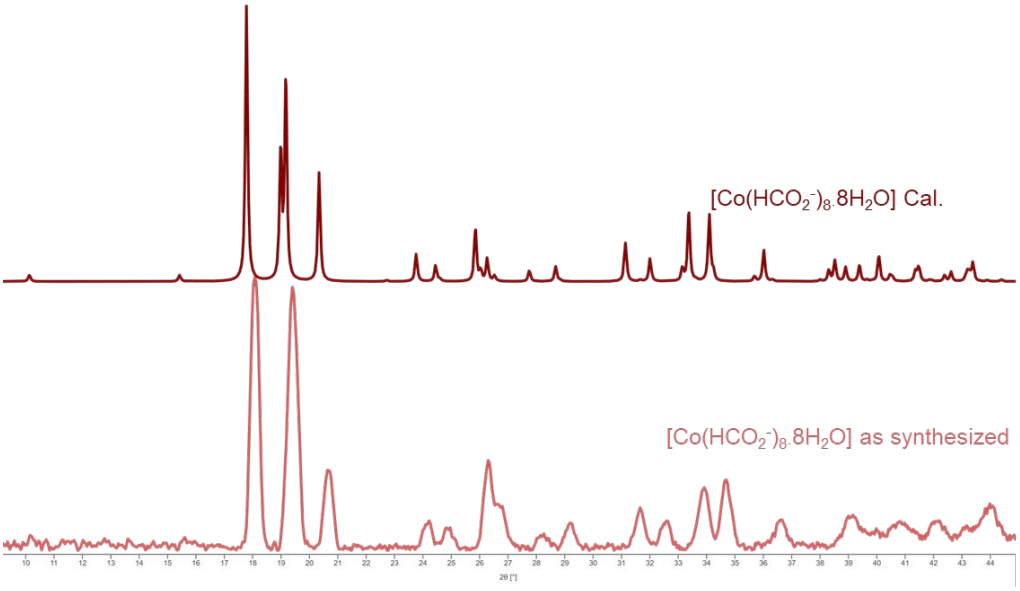

Figure 2.60: PXRD patterns of the $[Co(HCO_2)_8{\cdot}8H_2O]$ as-synthesised crystals (dark red) overlaid with the simulated pattern generated from the corresponding SCXRD (peach).

2.4.17 Free ligands crystal structures

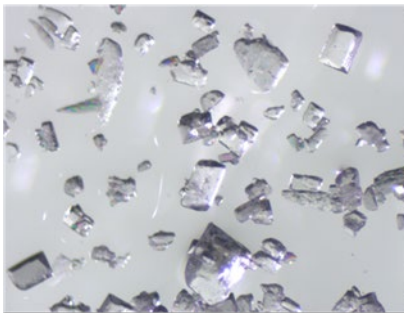

Figure 2.61: Asparagine and alanine polymorphs crystals picture.

Asparagine and alanine polymorphs: In a 20 mL vial, *l*-asparagine (0.07 g, 0.54 mmol) and *l*-alanine (0.05 g, 0.61 mmol) were dissolved in $NaOH_{aq}$ (0.1 M, 2 mL) and EtOH (2 mL). Then, $Zn(NO_3)_2 \cdot 6H_2O$ (0.12 mg, 0.64 mmol) was added. The mixture was left at room temperature for 3 days. After crystallisation, the resulting solids were washed with ethanol (x 2, 2 mL).

SCXRD analyses were carried out on two distinct crystal phases, and the corresponding crystallographic data are summarised in **Table 2.5** and **Table 2.6**. PXRD data were also collected and compared with the simulated pattern generated from the SCXRD data (**Figure 2.63**).

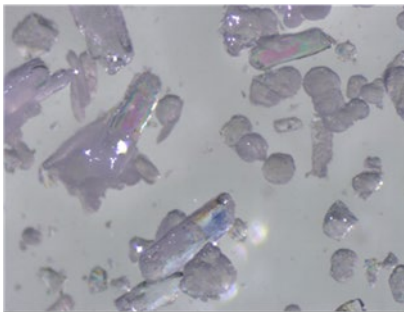

Figure 2.62: Glutamic acid and serine polymorphs crystals picture.

Glutamic acid and serine polymorphs: In a 20 mL vial, *l*-glutamic acid (0.06 g, 0.47 mmol) and *l*-serine (0.07 g,0.65 mmol) were dissolved in $NaOH_{aq}$ (0.1 M, 2 mL) and EtOH (2 mL). Then, $Zn(NO_3)_2 \cdot 6H_2O$ (0.13 g, 0.68 mmol) was added. The mixture was stirred at room temperature for 3 days. After crystallisation, the resulting solids were washed with ethanol (x 2, 2 mL).

SCXRD analyses were performed on two distinct crystalline phases, and the corresponding crystallographic data are summarised in **Table 2.6**. PXRD data were also collected, compared with the simulated pattern generated from the SCXRD data, confirming the structural consistency of the polymorphs (**Figure 2.63**).

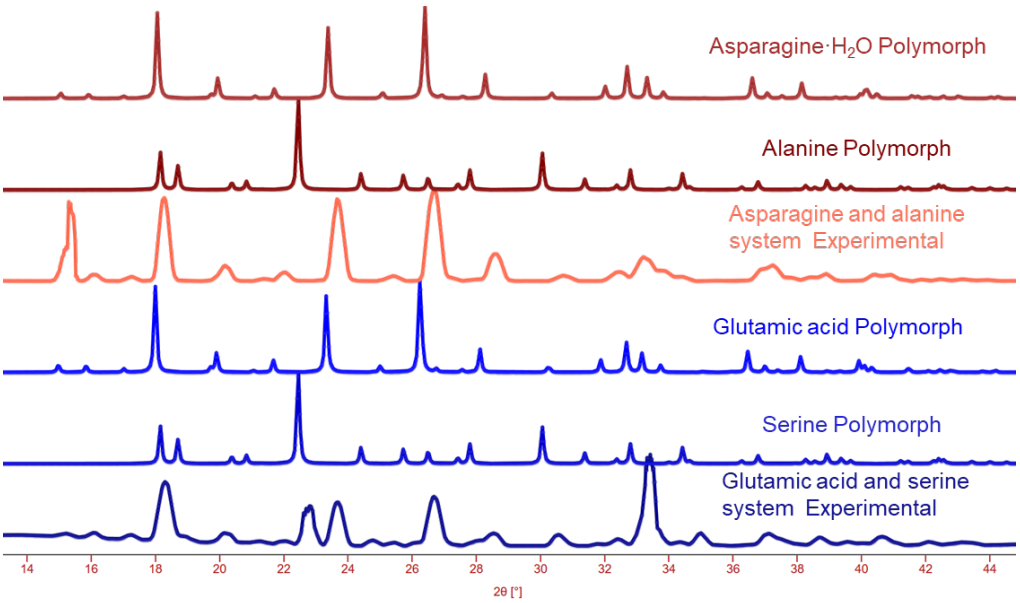

Figure 2.63: Comparison of calculated and experimental PXRD patterns for crystals obtained from alanine/asparagine and serine/glutamic acid reactions, each yielding two distinct polymorphic phases corresponding to the individual amino acid polymorph.

2.4.18 SCXRD measurements

X-ray diffraction data were collected using a Bruker D8 Venture diffractometer with Cu_{α} radiation (1.54180 Å) generated by an IμS microfocus Diamond sealed tube and equipped with a Photon III 28 detector. For PXRD, the data were processed into 1D diffractograms using APEX4 and Diffract Eva. Predicted PXRD patterns were generated from crystals information files using Mercury. Single crystal data was refined using the Shelx package under Olex2.

Note: For some structures, the Flack parameter was refined to approximately 0.3. However, considering the use of enantiopure amino acid linkers and the absence of crystallographic indications of inversion twinning, the absolute configuration is assigned as refined.

Table 2.1: SCXRD data summary.

Name	[Zn(asparagine-H)(tyrosine-H)]	[Co(asparagine-H)(tyrosine-H)]	[Zn(histidine-H)(tyrosine-H)·H_2O]
Empirical formula	$C_{13}H_{15}N_3O_6Zn$	$C_{13}H_{17}CoN_3O_6$	$C_{15}H_{20}N_4O_6Zn$
Formula weight	374.65	370.22	417.72
Temperature/K	295	295	295
Crystal system	monoclinic	monoclinic	monoclinic
Space group	$P2_1$	$P2_1$	C2
a/Å	7.7123(3)	7.7370(4)	23.4304(9)
b/Å	6.0353(3)	5.9822(3)	6.0038(2)
c/Å	15.9843(7)	16.0678(8)	12.4990(5)
α/°	90	90	90
β/°	90.9630(10)	90.860(2)	103.2540(10)
γ/°	90	90	90
Volume/Å^3	743.90(6)	743.60(7)	1711.42(11)
Z	2	2	4
ρ_{calc} g/cm^3	1.673	1.653	1.621
μ/mm^{-1}	2.638	9.393	2.376
F(000)	384.0	382.0	864.0
Crystal size/mm	0.41 × 0.18 × 0.16	0.61 × 0.31 × 0.07	0.48 × 0.19 × 0.06
Radiation	CuKα (λ = 1.54178)	CuKα (λ = 1.54178)	CuKα (λ = 1.54178)
Index ranges	$-9 \le h \le 9$, $-6 \le k \le 7$, $-18 \le l \le 19$	$-9 \le h \le 9$, $-7 \le k \le 6$, $-19 \le l \le 19$	$-27 \le h \le 27$, $-6 \le k \le 6$, $-14 \le l \le 14$
Reflections collected	11854	10003	12343
Independent reflections	2841 [R_{int} = 0.0232, R_{sigma} = 0.0230]	2557 [R_{int} = 0.0618, R_{sigma} = 0.0652]	2764 [R_{int} = 0.0321, R_{sigma} = 0.0315]
Data/restraints/ parameters	2841/1/222	2557/1/209	2764/1/239
Goodness-of-fit on F^2	1.068	1.100	1.071
2Θ range for data refinement/°	5.53 to 139.201	5.5 to 121.535	7.266 to 123.962
Final R indexes [I>=2σ (I)]	R_1 = 0.0229, wR_2 = 0.0616	R_1 = 0.0795, wR_2 = 0.2052	R_1 = 0.0277, wR_2 = 0.0707
Final R indexes [all data]	R_1 = 0.0229, wR_2 = 0.0616	R_1 = 0.1013, wR_2 = 0.2322	R_1 = 0.0283, wR_2 = 0.0712
Largest diff. peak/hole / e Å^{-3}	0.52/-0.46	0.43/-0.74	0.25/-0.39
Flack Parameter	0.114(8)	0.274(7)	0.072(12)

Table 2.2: SCXRD data summary.

Name	$[Co_2$(histidine-H)(tyrosine-H)$_3 \cdot 4H_2O]$	$[Co$(tyrosine-H)$(H_2O)_3 \cdot 2NO_3]$	$[Zn$(methionine-H)$_3$(valine-H)$]$
Empirical formula	$C_{33}H_{46}Co_2N_6O_{15}$	$C_9H_{14}CoN_2O_8$	$C_{10}H_{16.5}N_2O_4S_{1.5}Zn$
Formula weight	884.62	337.15	342.21
Temperature/K	152	286	180
Crystal system	monoclinic	orthorhombic	monoclinic
Space group	$P2_1$	$P2_12_12_1$	$P2_1$
a/Å	5.9799(4)	5.9602(2)	9.6062(19)
b/Å	8.0992(6)	8.1630(3)	5.2751(10)
c/Å	38.775(3)	26.5541(10)	14.660(3)
α/°	90	90	90
β/°	91.024(3)	90	101.419(8)
γ/°	90	90	90
Volume/Å^3	1877.6(2)	1291.94(8)	728.1(3)
Z	2	4	2
ρ_{calc}g/cm^3	1.565	1.733	1.561
μ/mm^{-1}	7.605	10.835	4.454
F(000)	920.0	692.0	353.0
Crystal size/mm^3	0.05 × 0.05 × 0.04	0.3 × 0.15 × 0.07	0.3 × 0.23 × 0.05
Radiation	CuKα (λ = 1.54178)	CuKα (λ = 1.54178)	CuKα (λ = 1.54178)
Index ranges	$-7 \le h \le 6$, $-9 \le k \le 9$, $-46 \le l \le 44$	$-7 \le h \le 7$, $-10 \le k \le 10$, $-32 \le l \le 32$	$-10 \le h \le 11$, $-6 \le k \le 6$, $-16 \le l \le 16$
Reflections collected	22492	26981	7262
Independent reflections	6313 [R_{int} = 0.0866, R_{sigma} = 0.1013]	2534 [R_{int} = 0.0916, R_{sigma} = 0.0458]	2242 [R_{int} = 0.0540, R_{sigma} = 0.0513]
Data/restraints/ parameters	6313/1/516	2534/0/185	2242/25/196
Goodness-of-fit on F^2	1.064	1.078	1.121
2Θ range for data refinement	4.558 to 123.962	6.658 to 139.201	6.15 to 124.550
Final R indexes [I>=2σ (I)]	R_1 = 0.0732, wR_2 = 0.1820	R_1 = 0.0485, wR_2 = 0.1206	R_1 = 0.0747, wR_2 = 0.2064
Final R indexes [all data]	R_1 = 0.1104, wR_2 = 0.2081	R_1 = 0.0493, wR_2 = 0.1215	R_1 = 0.0861, wR_2 = 0.2247
Largest diff. peak/hole / e Å^{-3}	0.43/-0.87	0.78/-0.71	1.03/-0.91
Flack Parameter	0.210(7)	0.092(7)	0.29(3)

Table 2.3: SCXRD data summary.

Name	Co(*l*-methionine-H)$_2$]	[Zn(*l*-leucine-H)$_2$],	[Co*l*-leucine-H)$_2$·2H$_2$O]
Empirical formula	$C_{10}H_{18}CoN_2O_4S_2$	$C_{12}H_{24}N_2O_4Zn$	$C_{12}H_{26}CoN_2O_6$
Formula weight	353.31	325.70	352.27
Temperature/K	295	293	180
Crystal system	monoclinic	monoclinic	monoclinic
Space group	$P2_1$	$P2_1$	$P2_1$
a/Å	9.4453(14)	9.523(12)	4.9023(9)
b/Å	5.0510(8)	5.333(10)	30.531(6)
c/Å	15.130(3)	14.65(5)	5.8969(10)
α/°	90	90	90
β/°	91.223(10)	106.99(12)	105.560(7)
γ/°	90	90	90
Volume/Å^3	721.6(2)	712(3)	850.3(3)
Z	2	2	2
ρ_{calc}g/cm^3	1.626	1.520	1.376
μ/mm^{-1}	12.143	2.515	8.154
F(000)	366.0	344.0	372.0
Crystal size/mm^3	0.3 × 0.2 × 0.1	0.61 × 0.31 × 0.03	0.3 × 0.15 × 0.03
Radiation	CuKα (λ = 1.54178)	CuKα (λ = 1.54184)	CuKα (λ = 1.54178)
2Θ range for data refinement°	5.842 to 139.201	6.308 to 121.535	5.79 to 126.550
Index ranges	-11 ≤ h ≤ 11, -6 ≤ k ≤ 5, -18 ≤ l ≤ 18	-11 ≤ h ≤ 11, -6 ≤ k ≤ 6, -17 ≤ l ≤ 18	-5 ≤ h ≤ 5, -35 ≤ k ≤ 34, -6 ≤ l ≤ 6
Reflections collected	7862	9251	14932
Independent reflections	2518 [R_{int} = 0.0562, R_{sigma} = 0.0593]	2661 [R_{int} = 0.0523, R_{sigma} = 0.0462]	2747 [R_{int} = 0.0924, R_{sigma} = 0.0651]
Data/restraints/ parameters	2518/7/180	2661/1/176	2747/1/196
Goodness-of-fit on F^2	1.538	1.101	1.095
2Θ range for data collection/°	5.842 to 145.294	6.308 to 150.68	5.79 to 131.198
Final R indexes [I>=2σ (I)]	R_1 = 0.1199, wR_2 = 0.3322	R_1 = 0.0443, wR_2 = 0.1133	R_1 = 0.1176, wR_2 = 0.3238
Final R indexes [all data]	R_1 = 0.1362, wR_2 = 0.3616	R_1 = 0.0579, wR_2 = 0.1248	R_1 = 0.1356, wR_2 = 0.3378
Largest diff. peak/hole / e Å^{-3}	0.88/-1.50	0.65/-0.77	1.77/-0.82
Flack Parameter	0.390(12)	0.13(2)	0.231(10)

Table 2.4: SCXRD data summary.

Name	[Co(glycinate-H)$_3$]	(Valine)$_2$·benzoate	[Zn(H$_2$O)$_3$(2-methylzialodine-2,4-dicarboxylic acid)]
Empirical formula	$C_{22}H_{55}Co_2N_6O_{17}$	$C_{12}H_{17}NO_4$	$C_6H_{13}NO_7SZn$
Formula weight	563.24	239.26	308.60
Temperature/K	180	295	100
Crystal system	triclinic	orthorhombic	orthorhombic
Space group	P_1	$P2_12_12_1$	$P2_12_12_1$
a/Å	4.968(2)	5.4665(5)	5.9399(4)
b/Å	12.295(7)	7.6605(7)	12.5991(8)
c/Å	12.295(5)	28.887(3)	14.4132(10)
α/°	60.00	90	90
β/°	90	90	90
γ/°	90	90	90
Volume/Å^3	650.4(5)	1209.67(19)	1078.65(12)
Z	1	4	4
ρ_{calc}g/cm^3	1.438	1.314	1.900
μ/mm^{-1}	10.544	0.820	5.232
F(000)	289.0	512.0	632.0
Crystal size/mm^3	0.09 × 0.04 ×0.0	0.34 × 0.17 × 0.03	0.3× 0.03× 0.02
Radiation	CuKα (λ = 1.54178)	CuKα (λ = 1.54178)	CuKα (λ = 1.54178)
2Θ range for data refinement/°	8.304 to 121.535	6.12 to 134.245	9.322 to 98.787
Index ranges	-5 ≤ h ≤ 5, -12 ≤ k ≤ 13, -14 ≤ l ≤ 13	-6 ≤ h ≤ 6, -9 ≤ k ≤ 8, -35 ≤ l ≤ 35	-7 ≤ h ≤ 7, -15 ≤ k ≤ 15, -17 ≤ l ≤ 17
Reflections collected	5886	11610	28119
Independent reflections	3577 [R_{int} = 0.1015, R_{sigma} = 0.2436]	2332 [R_{int} = 0.0330, R_{sigma} = 0.0272]	2167 [Rint = 0.1384, Rsigma = 0.0529]
Data/restraints/ parameters	3577/3/211	2332/0/158	2167/1/152
Goodness-of-fit on F^2	1.004	1.418	1.080
2Θ range for data refinement/°	8.304 to 121.535	6.12 to 139.209	9.322 to 98.787
Final R indexes [I>=2σ (I)]	R_1 = 0.1244, wR_2 = 0.3112	R_1 = 0.0616, wR_2 = 0.1493	R1 = 0.0832, wR2 = 0.2078
Final R indexes [all data]	R_1 = 0.2249, wR_2 = 0.3782	R_1 = 0.0620, wR_2 = 0.1503	R1 = 0.1067, wR2 = 0.2510
Largest diff. peak/hole / e Å^{-3}	0.88/-0.80	0.30/-0.54	0.98/-0.65
Flack Parameter	0.288(18)	0.09(5)	0.12(3)

Table 2.5: SCXRD data summary.

Name	[Zn(benzoate)$_2$]	[Co(HCO$_2^-$)$_8$·8H$_2$O]	asparagine·H$_2$O
Empirical formula	$C_{28}H_{20}O_8Zn_2$	$C_8H_{24}Co_4O_{24}$	$C_4H_{10}N_2O_4$
Formula weight	615.18	739.99	150.14
Temperature/K	273	292.00	294.00
Crystal system	monoclinic	triclinic	orthorhombic
Space group	$P2_1/c$	P-1	$P2_12_12_1$
a/Å	10.721(5)	11.2537(5)	5.5820(2)
b/Å	13.077(6)	11.2537(5)	9.8193(3)
c/Å	19.195(9)	11.7326(8)	11.7975(3)
α/°	90	108.0200(10)	90
β/°	95.301(19)	118.0080(10)	90
γ/°	90	100.83	90
Volume/Å^3	2680(2)	1145.08(11)	646.64(3)
Z	4	2	4
ρ_{calc}g/cm^3	1.525	2.146	1.542
μ/mm^{-1}	2.619	23.340	1.193
F(000)	1248.0	744.0	320.0
Crystal size/mm^3	0.28 × 0.23 × 0.02	0.03 × 0.02 × 0.02	0.12 × 0.07 × 0.05
Radiation	CuKα (λ = 1.54178)	CuKα (λ = 1.54178)	CuKα (λ = 1.54178)
Index ranges	-12 ≤ h ≤ 12, -14 ≤ k ≤ 15, -22 ≤ l ≤ 22	-13 ≤ h ≤ 13, -13 ≤ k ≤ 13, -14 ≤ l ≤ 14	-6 ≤ h ≤ 6, -11 ≤ k ≤ 12, -14 ≤ l ≤ 13
Reflections collected	38469	25494	6531
Independent reflections	4382 [R_{int} = 0.0408, R_{sigma} = 0.0234]	4418 [R_{int} = 0.0973, R_{sigma} = 0.0850]	1261 [R_{int} = 0.0293, R_{sigma} = 0.0207]
Data/restraints/ parameters	4382/0/343	4418/4/341	1261/0/96
Goodness-of-fit on F^2	1.097	1.284	1.117
2Θ range for data refinement/°	8.192 to 143.245	9.002 to 139.291	11.726 to 143.245
Final R indexes [I>=2σ (I)]	R_1 = 0.0453, wR_2 = 0.1120	R_1 = 0.1450, wR_2 = 0.3552	R_1 = 0.0264, wR_2 = 0.0713
Final R indexes [all data]	R_1 = 0.0559, wR_2 = 0.1172	R_1 = 0.1922, wR_2 = 0.4255	R_1 = 0.0268, wR_2 = 0.0717
Largest diff. peak/hole / e Å^{-3}	0.22/-0.42	1.13/-2.27	0.16/-0.15
Flack Parameter	-	-	0.04(7)

Table 2.6: SCXRD data summary.

Name	alanine polymorph	serine polymorph	glutamic acid polymorph
Empirical formula	$C_3H_7NO_2$	$C_3H_7NO_3$	$C_5H_9NO_4$
Formula weight	89.10	105.10	147.13
Temperature/K	294	295	180
Crystal system	orthorhombic	orthorhombic	orthorhombic
Space group	$P2_12_12_1$	$P2_12_12_1$	$P2_12_12_1$
a/Å	5.7833(15)	5.6146(6)	7.0268(10)
b/Å	6.0297(18)	8.5823(9)	8.7658(9)
c/Å	12.357(4)	9.3433(11)	10.2629(12)
α/°	90	90	90
β/°	90	90	90
γ/°	90	90	90
Volume/Å^3	430.9(2)	450.22(9)	632.15(13)
Z	4	4	4
ρ_{calc}g/cm^3	1.373	1.550	1.546
μ/mm^{-1}	0.980	1.208	1.167
F(000)	192.0	224.0	312.0
Crystal size/mm^3	0.12 × 0.11 × 0.06	0.13 × 0.08 × 0.09	0.12 × 0.11 × 0.07
Radiation	CuKα (λ = 1.54178)	CuKα (λ = 1.54178)	CuKα (λ =1.54178)
Index ranges	$-6 \le h \le 6$, $-6 \le k \le 6$, $-14 \le l \le 14$	$-6 \le h \le 6$, $-9 \le k \le 9$, $-10 \le l \le 10$	$-5 \le h \le 5$, $-5 \le k \le 9$, $-8 \le l \le 10$
Reflections collected	3262	1903	976
Independent reflections	682 [R_{int} = 0.0485, R_{sigma} = 0.0375]	659 [R_{int} = 0.0324, R_{sigma} = 0.0367]	526 [R_{int} = 0.0230, R_{sigma} = 0.0454]
Data/restraints/ parameters	682/0/57	659/0/74	526/4/96
Goodness-of-fit on F^2	1.118	1.128	1.178
2Θ range for data refinement/°	14.336 to 125.595	14.012 to 123.595	13.282 to 123.595
Final R indexes [I>=2σ (I)]	R_1 = 0.0549, wR_2 = 0.1402	R_1 = 0.0449, wR_2 = 0.1175	R_1 = 0.0610, wR_2 = 0.1469
Final R indexes [all data]	R_1 = 0.0629, wR_2 = 0.1491	R_1 = 0.0464, wR_2 = 0.1197	R_1 = 0.0611, wR_2 = 0.1469
Largest diff. peak/hole / e Å^{-3}	0.20/-0.30	0.27/-0.28	0.41/-0.35
Flack Parameter	0.3(2)	0.27(16)	0.0(3)

Chapter 3 MMOFs from amino acids pyrazole ligands

3.1 Introduction

The inherent coordination modes of amino acids restrict the scope of amino acid-based MOFs. Because amino acids coordinate primarily through their amino and carboxylate groups, they tend to form mononuclear nodes with limited connectivity, thereby narrowing the accessible topologies.[85] As shown in Chapter 2, metals often assemble into mononuclear centres in both single- and multi-amino acid structures, further constraining the diversity of MOF architectures.

To broaden this structural landscape, reticular chemistry commonly employs SBUs, which provide greater rigidity, directionality, and predictability. These features facilitate the construction of permanently porous frameworks with well-defined connectivity.[32, 143, 144] A complementary approach is to expand the coordination modes of amino acid-derived linkers through careful molecular design to accommodate diverse SBUs.

Beyond topology, linkers' functionalisation allows precise control over their size and shape, enabling the functionalisation of their pores with diverse functional groups. The pore functionalisation allows the mimicry of the proteins' active site, thus enhancing the potential of MOFs for applications in catalysis and separations.[145, 146] Moreover, the presence of multiple functional groups within the framework can act cooperatively, contributing to more efficient catalytic transformations and optimised drug release.[145-147]

To overcome these topological constraints and introduce functional diversity, a new family of linkers, denoted H_2XPyr, was designed and synthesised. In these linkers, amino acids (X) are covalently attached to a pyrazole moiety via an amide bond. Each linker terminates in both carboxyl and pyrazole groups, providing expanded coordination possibilities for framework construction (**Figure 3.1**).[85, 145] This design draws inspiration from Rosseinsky's work, where the synthesised ligands maintain flexibility around the sp^3 carbon torsion angle while introducing new coordination chemistry to support diverse SBUs.[85, 145]

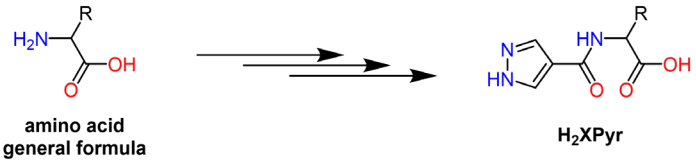

Figure 3.1: The amino acids undergo three distinct organic modification steps to covalently attach to the pyrazole moiety via an amide bond. The resulting H_2XPyr ligand features terminal carboxyl and pyrazole groups, enabling the construction of extended frameworks with enhanced coordination diversity.

Flexible MOFs, a subclass of crystalline materials in which metal ions or clusters are coordinated to organic linkers, can undergo dynamic structural transformations in response to external stimuli. This flexibility underpins their potential across a wide range of applications. These flexible MOFs can also be derived from peptides, where the torsion angle around the amino acid Cα confers a high degree of adaptability.[85] However, the chemical diversity of natural peptides is inherently limited, restricting the variety of attainable MOFs.[4,148-152]

Guest-dependent breathing behaviour in ZnXPyr frameworks has been demonstrated through systematic solvent exchange studies, in which exposure to a library of liquid guests produced significant and reversible changes in unit cell volume while retaining overall connectivity and symmetry.[85] These structural transformations were attributed to small adjustments in linker torsion angles that are amplified through the topology, providing direct evidence of stimulus-responsive flexibility.[85]

Building on this flexible ZnXPyr architecture, the H_2XPyr platform provides a route to MMOFs with uniform topology yet systematically varied pore chemistry. As shown in this chapter, substitution of the amino acid side chain within the H_2XPyr backbone preserves framework connectivity while modulating the chemical environment of the pores. MMOFs based on H_2XPyr ligands therefore, represent a strategy for constructing flexible MOFs with controlled chemical diversity and ordered functionality.

A useful biological analogy is the polypeptide: proteins are built from polypeptide chains sharing a common amino acid backbone, with side chains positioned precisely according to their chemical properties during the assembly process.[145, 153] By contrast, MTV-MOFs introduce diversity in a far less controlled fashion, with functional groups distributed randomly. While this disorder can still influence properties such as drug release,[145, 147] catalytic efficiency[145, 146], and molecular separations[145], it lacks the ordered precision characteristic of biological systems. Achieving MMOFs with a uniform and controlled arrangement of multiple functional groups along a common linker backbone remains a significant challenge.[145, 154]

H_2XPyr ligands address this challenge. Their dual coordination modes (carboxylate and pyrazole) promote the formation of stable SBUs while preserving the ZnXPyr topology, even in the presence of multiple ligands. This approach provides a pathway toward MMOFs that combine structural robustness with systematically ordered chemical diversity.

3.2 Results and discussion

3.2.1 Expanding the H_2XPyr linkers library

Four new amino acid-based pyrazole linkers were synthesised. The general synthetic route for obtaining H_2XPyr involves coupling the amino acid tert-butyl ester with compound **3A**, followed by de-esterification of the ligand intermediate to yield the final ligand **(H_2XPyr)** (**Figure 3.2**).[85] The synthesis of compound **3A** is described in **Appendix B (B.1).**

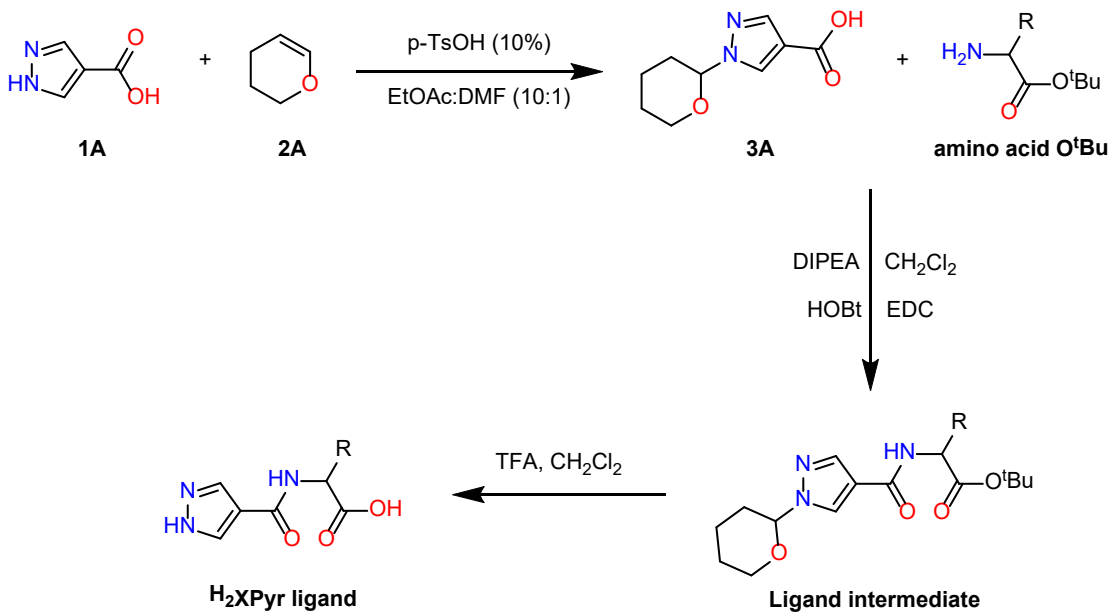

Figure 3.2: General synthetic procedure to the H_2XPyr linkers. R denotes the amino acid functional group.

The ligands H_2ValPyr, H_2SerPyr, H_2PhePyr, and H_2TyrPyr, were synthesised (**Figure 3.3**) starting from commercially available amino acid tert-butyl esters, specifically, *l*-valine-O^{t}Bu, *l*-serine-O^{t}Bu, *l*-phenylalanine-O^{t}Bu, and *l*-tyrosine-O^{t}Bu. The full synthesis procedures for the new 4 linkers are described in the experimental section **3.4**.

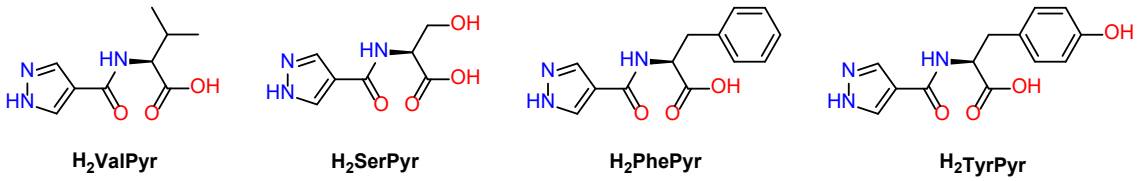

Figure 3.3: Structures of the four new ligands prepared by coupling pyrazole with the amino acids valine, serine, phenylalanine, and tyrosine.

3.2.2 Incorporation of novel H_2XPyr into Isoreticular ZnXPyr frameworks (IR-ZnXPyr)

The newly synthesised ligands (H_2ValPyr, H_2SerPyr, H_2PhePyr, and H_2TyrPyr) were successfully incorporated into ZnXPyr frameworks that are isoreticular to the flexible MOFs previously reported by Rossinsky. The resulting family of frameworks is hereafter referred to as IR-ZnXPyr. To achieve their synthesis, various synthetic parameters, including temperature and concentration, were carefully optimised. This systematic approach facilitated the isolation of well-defined crystalline products, and notably, high-quality single-crystal X-ray diffraction (SCXRD) data were obtained for ZnValPyr and ZnPhePyr·DMF (**Figure 3.4**).

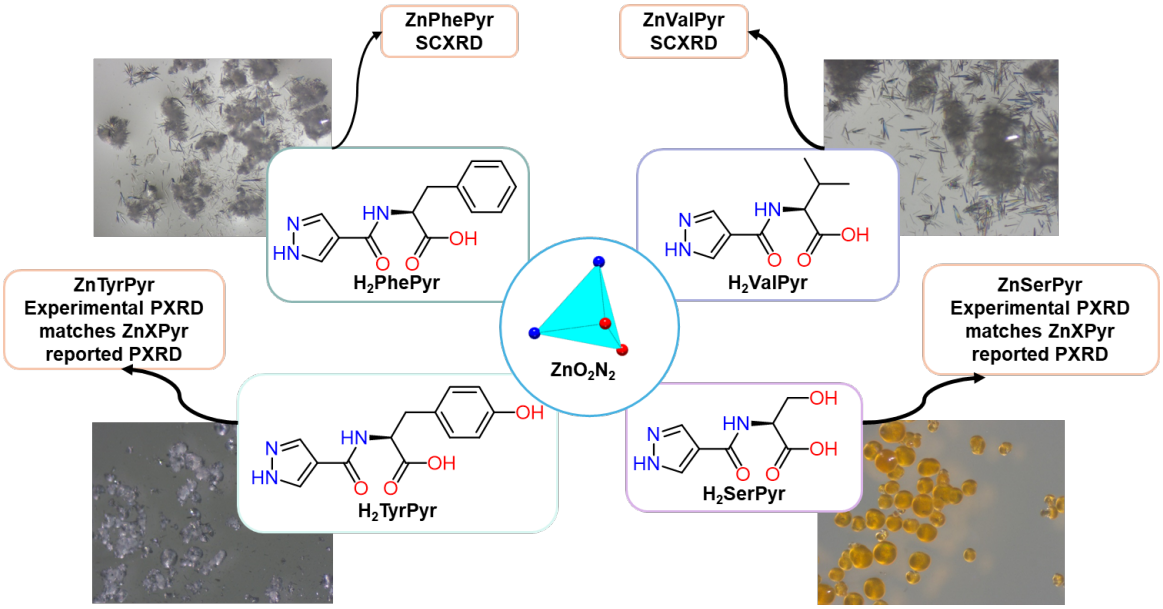

Figure 3.4: Overview of crystalline ZnXPyr materials synthesised from the newly developed linkers, H_2XPyr. The structures feature the well-known ZnO_2N_2 SBU, formed during the reaction of the ligand with $Zn(NO_3)_2$ in DMF under heated conditions.

ZnValPyr and ZnPhePyr·DMF synthesis and characterisation

ZnValPyr and ZnPhePyr·DMF were synthesised by dissolving the corresponding ligand (H_2ValPyr or H_2PhePyr) with $Zn(NO_3)_2$ in DMF, followed by heating overnight. Both reactions produced needle-like crystals with comparable crystal habits (**Figure 3.5**). The synthesis solvent was decanted and replaced with fresh DMF for both samples. The synthetic procedure was adapted from the literature method reported for the preparation of ZnAlaPyr.[85]

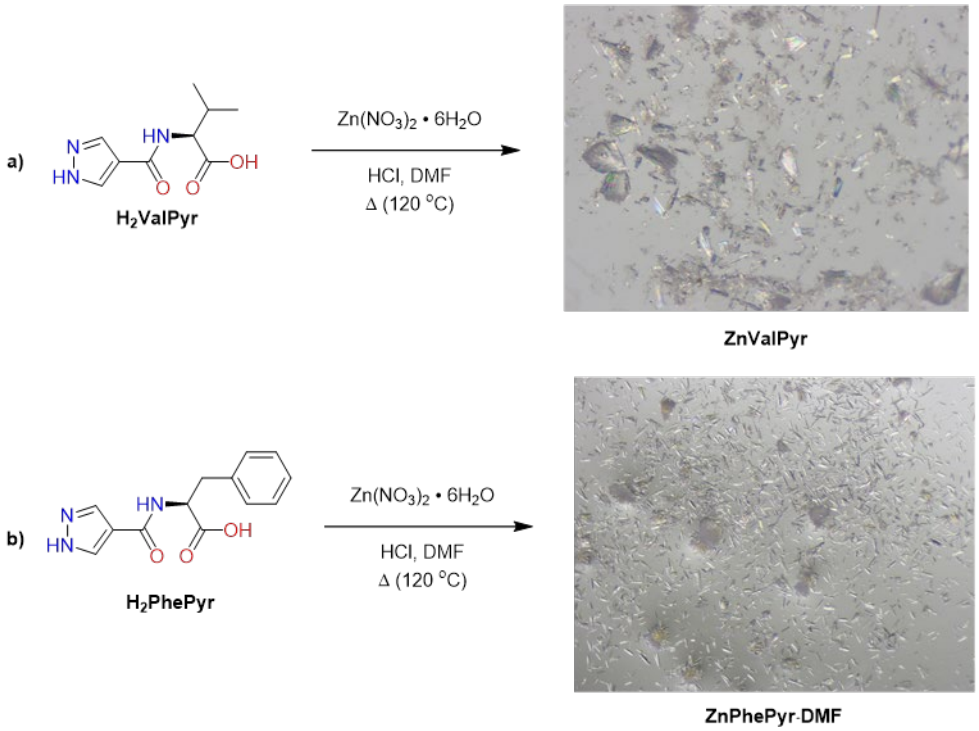

Figure 3.5: **a)** Synthesis of ZnValPyr from H_2ValPyr in DMF.
b) Synthesis of ZnPhePyr·DMF from H_2PhePyr in DMF.

PXRD patterns were collected and compared with the simulated pattern generated from the reported SCXRD of ZnGlyPyr.[85] The experimental patterns of ZnValPyr and ZnPhePyr·DMF closely matched the ZnGlyPyr reference, confirming that both frameworks are isoreticular members of the ZnXPyr family (**Figure 3.6**).

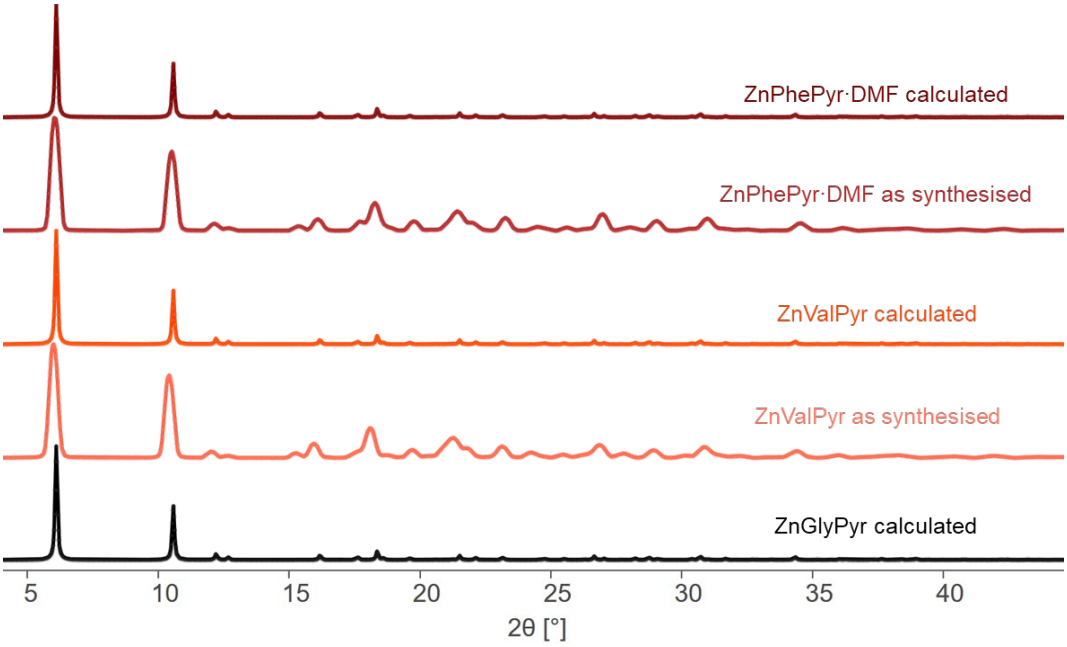

Figure 3.6: ZnValPyr and ZnPhePyr·DMF experimental pattern and the calculated PXRD patterns corresponding to their SCXRD were compared to the ZnGlyPyr calculated pattern.

SCXRD data were collected at 180 K, which showed that ZnValPyr (**Table 3.2**) and ZnPhePyr·DMF (**Table 3.2**) crystallise in the trigonal space group R3. In both structures, the carboxyl and pyrazole groups are deprotonated and coordinate to Zn(II) to give tetrahedral ZnO_2N_2 environments, with each Zn(II) bound to two carboxylate O donors and two pyrazole N donors. These local coordination modes propagate into 1D helical rod SBUs that form the backbone of the extended 3D framework (**Figure 3.7**).

The carboxylate and pyrazole groups coordinate alternatively to form an infinite ribbon. The ribbon bridges between the ZnO_2N_2 SBUs to form inorganic rods, which run parallel to the crystallographic c axis (**Figure 3.7**).

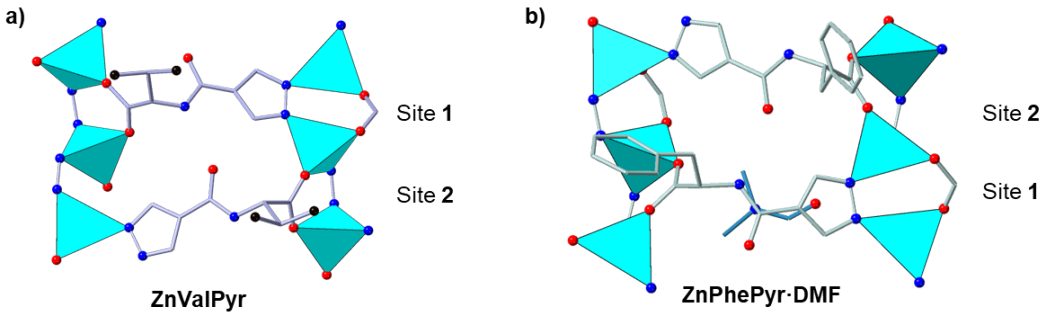

Figure 3.7: a,b) Both carboxyl and pyrazole groups are coordinated to the Zn(II) to from tetrahedra. The tetrahedra are bridged by the alternating ligands to form inorganic rods. Half of these rods are right-handed, and the other half are left-handed. Atom colours: ValPyr C chain = mauve, PhePyr C chain = green, terminal C = black, DMF C chain = pastel blue, O = red, N = blue, and Zn(II) = teal blue. Hydrogen atoms are omitted for clarity.

Both frameworks adopt the *etb* topology, defined by six rods and six ribbons that generate a 1D pore surrounded by three peripheral pockets (**Figure 3.8**). The alkyl side chain of valine and the phenyl rings of phenylalanine project toward the constriction between the central channel and the peripheral pockets, influencing the internal dimensions of the pore. In ZnValPyr, the isopropyl groups partially narrow the passageways (20.19 A), whereas in ZnPhePyr·DMF, the bulkier phenyl rings cause a greater reduction in pore size (volume = 7865.96 A^3) and wall-to-wall distance (14.89 A). Additionally, DMF molecules occupy sites between opposing phenyl rings within each peripheral pocket, further restricting the openings connecting the pockets to the central channel. As a result, ZnPhePyr·DMF exhibits a smaller effective pore size than ZnValPyr (**Figure 3.8**).

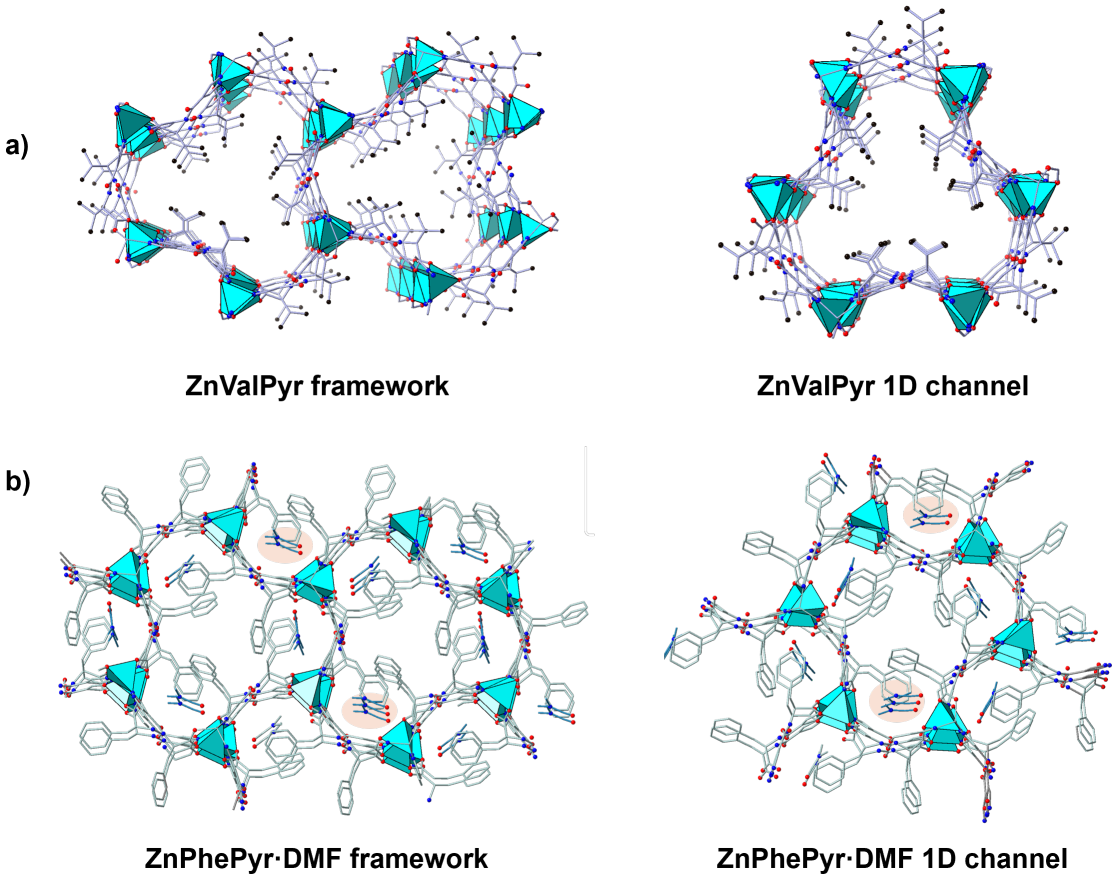

Figure 3.8: **a)** Crystal structure of ZnValPyr showing a porous 3D framework with isopropyl chains positioned at the pore entrances. The structure features 1D channels composed of three peripheral pockets. **b)** Crystal structure of ZnPhePyr exhibiting a honeycomb-like framework. The 1D shaped pores and peripheral pockets are reduced in size due to the presence of bulky phenyl rings. Atom colours: ValPyr C chain = mauve, PhePyr C chain = green, terminal C = black, DMF C chain = pastel blue, O = red, N = blue, and Zn(II) = teal blue. Hydrogen atoms are omitted for clarity.

3.2.3 MMOFs synthesis based on IR-ZnXPyr

The objective of this study was to develop MMOFs using the H_2XPyr linker series, which features various functional groups integrated into a common pyrazole-amino acid scaffold. To advance this aim, two previously described linkers, H_2GlyPyr and H_2AlaPyr, originally synthesised by Rosseinsky, were reproduced from their precursors and incorporated into the study. As the simplest representatives of the H_2XPyr family, these ligands were selected for co-assembly with newly synthesised linkers to construct MMOFs. The full synthesis procedures for H_2GlyPyr and H_2AlaPyr are provided in **Appendix B** (**B.2**, **B.3**).

The synthesis strategy followed a systematic approach. In the first stage, H_2GlyPyr was individually combined with each of the newly developed linkers. Parallel experiments were then performed using H_2AlaPyr. In the second stage, the complexity was increased by introducing bulkier amino acid side chains, which presented additional challenges for MMOF formation. These cases required tighter control over reaction parameters and more extended optimisation periods. This section details the synthesis and characterisation of the novel MMOFs obtained from H_2XPyr ligands.

3.2.4 H_2GlyPyr and other H_2XPyr co-assembly into IR-ZnXPyr

Combinations of these ligands were incorporated into the MMOF structures. Reactions of H_2GlyPyr with (i) H_2ValPyr, (ii) H_2PhePyr, and (iii) H_2SerPyr each yielded distinct crystalline materials, all successfully characterised by SCXRD (**Figure 3.9**). Multicomponent MOF formation was further confirmed by ^{1}H NMR spectroscopy of the base digested crystals in NaOD/D_2O. Despite repeated attempts under varied synthetic conditions, single crystals could not be obtained for the GlyPyr/TyrPyr combination.

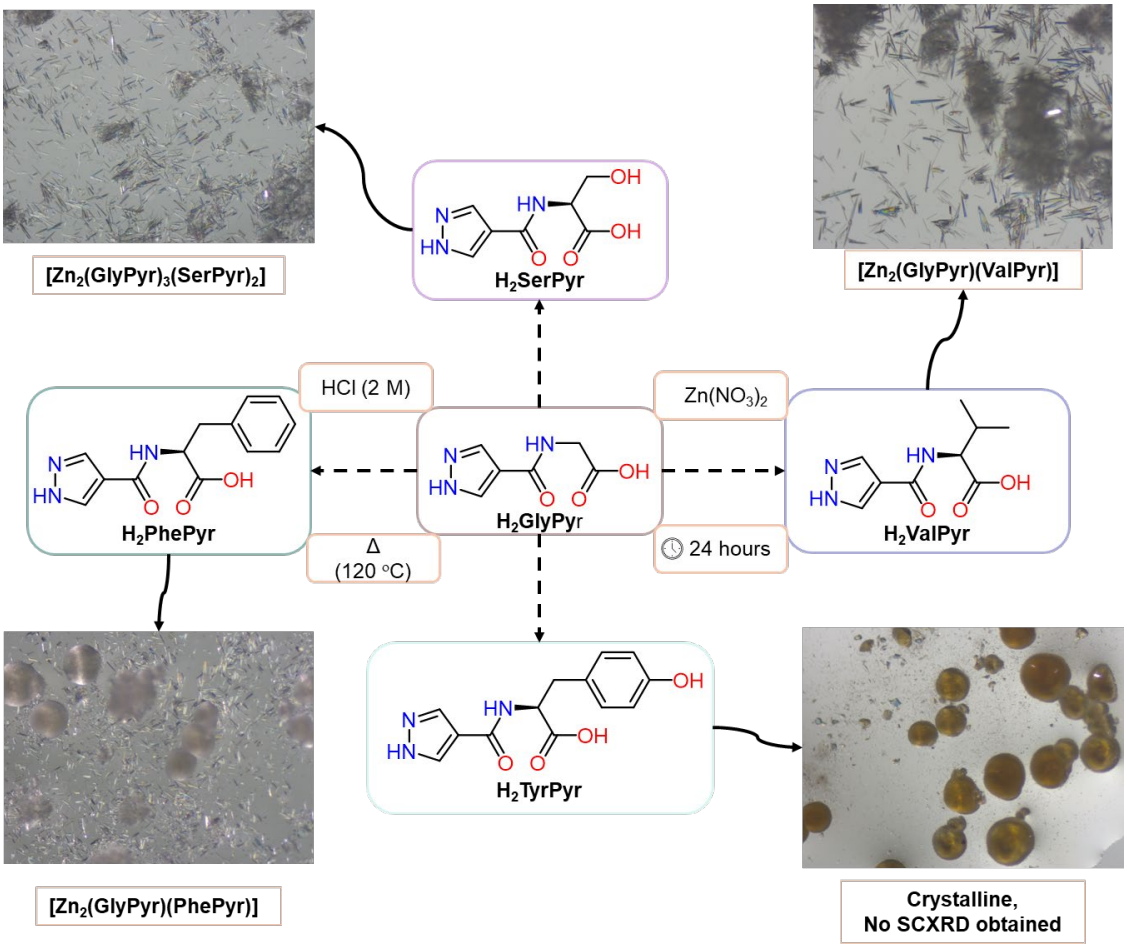

Figure 3.9: An overview of crystalline materials obtained from the reaction of H_2GlyPyr with the other new linkers, H_2XPyr, and $Zn(NO_3)_2$ in DMF.

[Zn_2(GlyPyr)(ValPyr)], [Zn_2(GlyPyr)(PhePyr)] and [$Zn_2(GlyPyr)_3$(SerPyr)$_2$]: synthesis and characterisation

Each MMOF was synthesised by reacting H_2GlyPyr with H_2ValPyr, H_2PhePyr, or H_2SerPyr in DMF along with $Zn(NO_3)_2$ and HCl, the latter used as a modulator to slow crystal growth and ensure phase-pure materials. The resulting products were: [Zn_2(GlyPyr)(ValPyr)], [Zn_2(GlyPyr)(PhePyr)], and [$Zn_2(GlyPyr)_3$(SerPyr)$_2$], respectively (**Figure 3.10**). After crystal formation, the solvent was replaced with fresh DMF to halt further growth and remove excess reagents. The crystals were characterised by PXRD, SCXRD, and ^{1}H NMR spectroscopy.

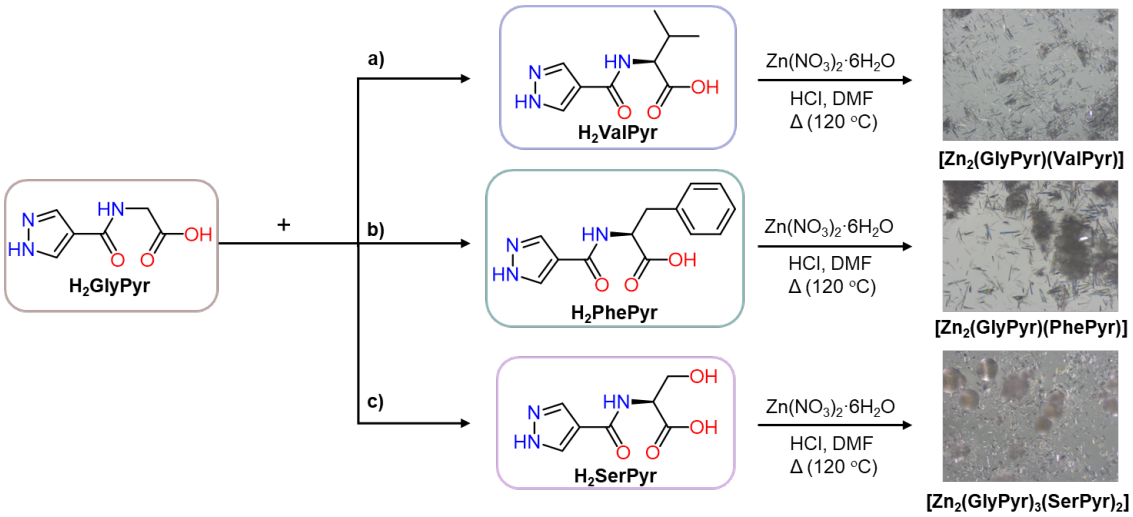

Figure 3.10: Synthesis of $[Zn_2(GlyPyr)(ValPyr)]$, $[Zn_2(GlyPyr)(PhePyr)]$ and $[Zn_2(GlyPyr)_3(SerPyr)_2]$ from mixing $H_2GlyPyr$, with $H_2ValPyr$, $H_2PhePyr$ or $H_2SerPyr$, respectively, along with $Zn(NO_3)_2$ in DMF.

The experimental PXRD patterns of all three MMOFs matched the corresponding calculated patterns derived from their SCXRD data and also agreed with the reported ZnGlyPyr pattern derived from its corresponding SCXRD[85] (**Figure 3.11**), confirming both the phase purity of the bulk crystals and their isoreticular relationship within the ZnXPyr family.

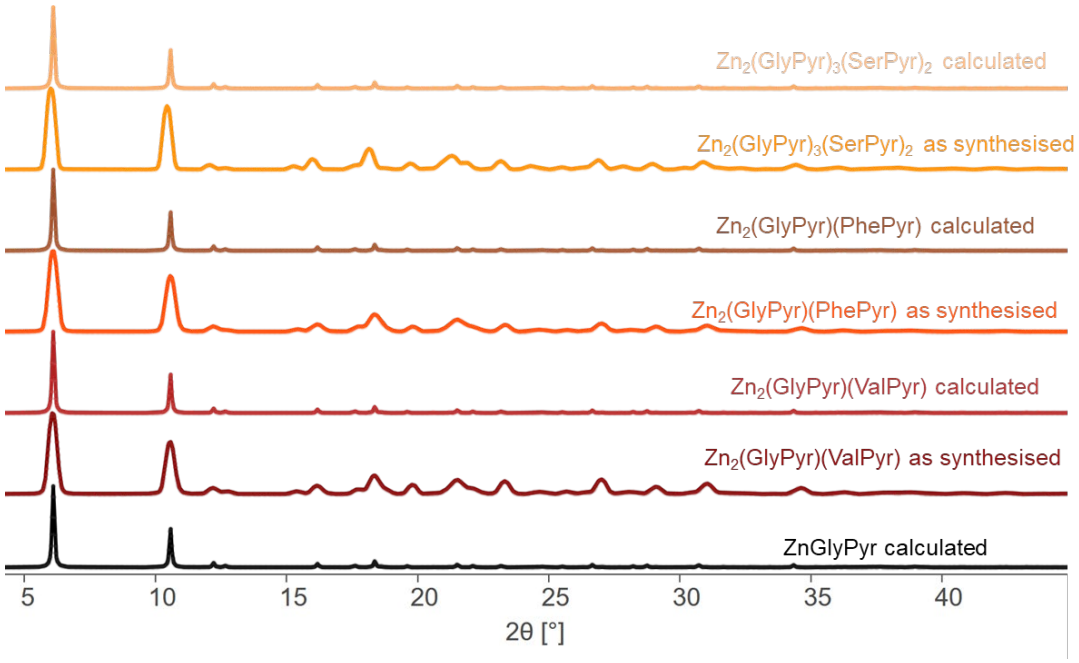

Figure 3.11: The experimental and the calculated PXRD patterns for the three obtained frameworks compared to the previously reported ZnGlyPyr.

The ^{1}H NMR spectra of dissolved [Zn_2(GlyPyr)(ValPyr)] and [Zn_2(GlyPyr)(PhePyr)] in NaOD/D_2O revealed a 1:1 ratio between GlyPyr and ValPyr (**Figure 3.23**), and between GlyPyr and PhePyr, respectively **(Figure 3.24)**. In contrast, the ^{1}H NMR spectrum of [Zn_2(GlyPyr)$_3$(SerPyr)$_2$] revealed a GlyPyr:SerPyr ratio of 3:2 (**Figure 3.25**). These results further confirm the phase purity of the bulk crystals, as the ^{1}H NMR spectrum integrations of the digested sample gave integer (rounded) ratios, consistent with the expected stoichiometry of the framework. If multiple phases were present, these integrations would deviate from whole numbers due to contributions from structurally distinct components.

Structural analysis

In this section, [Zn_2(GlyPyr)(ValPyr)] and [Zn_2(GlyPyr)(PhePyr)] are discussed in parallel to highlight their similarities and differences, while [Zn_2(GlyPyr)$_3$(SerPyr)$_2$] is addressed separately in the section.

Consistent with the previously discussed crystals, both [Zn_2(GlyPyr)(ValPyr)] and [Zn_2(GlyPyr)(PhePyr)] exhibited good stability in DMF. The crystals were stored in solvent and mounted using oil for analysis. SCXRD data for [Zn_2(GlyPyr)(ValPyr)] were collected at room temperature (**Table 3.3**). In contrast, the data for [Zn_2(GlyPyr)(PhePyr)] were collected at 180 K (**Table 3.3**).

Both MOFs crystallise in the trigonal R3 space group. In each structure, the pyrazole and carboxylate groups were deprotonated and coordinated with Zn(II) to form ZnO_2N_2 tetrahedra (**Figure 3.12**). Ligands (GlyPyr and ValPyr, or PhePyr) are coordinated in an antiparallel manner, and connecting the tetrahedra, to form inorganic rods (**Figure 3.12**).

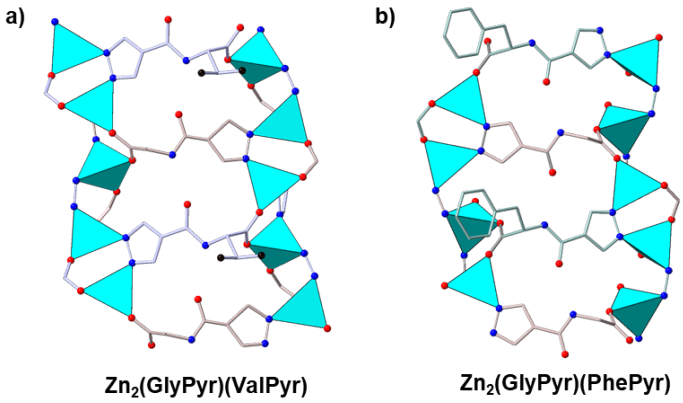

Figure 3.12: ZnO_2N_2 tetrahedra are connected by GlyPyr and ValPyr (**a**) or PhePyr (**b**), that are coordinated to Zn(II) in an antiparallel manner. The connected tetrahedra form inorganic rods for the 3D framework. Atom colours: ValPyr C chain =mauve, terminal C= black, PhePyr C chain = pastel green, GlyPyr C chain = beige, O = red, and N =blue. Hydrogen atoms are omitted for clarity.

These inorganic rods assemble into a 3D framework with a honeycomb-like topology (*etb*). At the narrow junctions between each peripheral pocket and the 1D channel, either a valine isopropyl group in [Zn_2(GlyPyr)(ValPyr)] or a phenyl group in [Zn_2(GlyPyr)(PhePyr)] is positioned. Owing to the alternating incorporation of GlyPyr, each pair of junction sites bears one bulky group (isopropyl or phenyl group) and the other one remains an unoccupied site. Consequently, each framework features a 1D pore symmetrically decorated with either isopropyl or phenyl groups at alternating pinch points, depending on the ligand used (**Figure 3.13**).

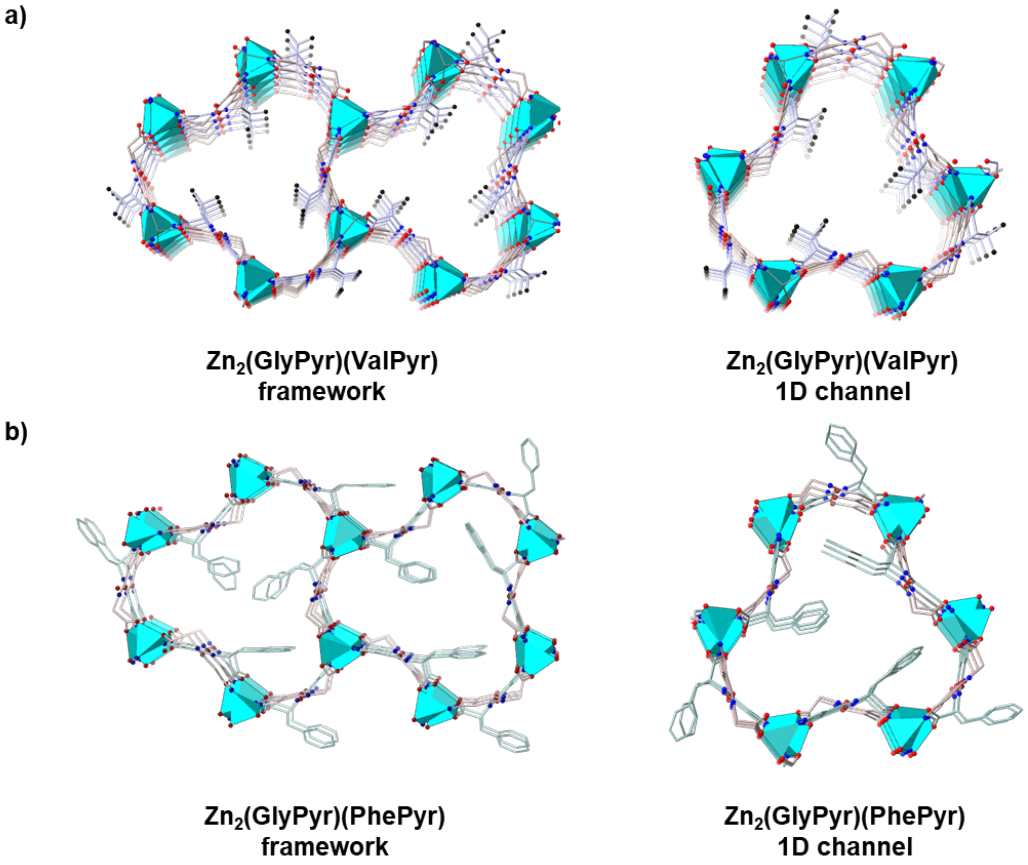

Figure 3.13: a) Crystal structure of the [Zn_2(GlyPyr)(ValPyr)], ValPyr is protruding in and out the pocket and the zoom in overview of the 1D channel, which consists of the three peripheral pockets and one main channel. **b)** Crystal structure of [Zn_2(GlyPyr)(PhePyr)], PhePyr is protruding in and out the pocket and the zoom in overview of the 1D channel, which consists of the three peripheral pockets and one main channel. Atom colours: ValPyr C chain =mauve, terminal C = black, PhePyr C chain = pastel green, GlyPyr C chain = beige, O = red, and N = blue. Hydrogen atoms are omitted for clarity.

$[Zn_2(GlyPyr)_3(SerPyr)_2]$ crystals were stored in solvent and mounted using oil for analysis. SCXRD data were collected at 150 K (**Table 3.3**). The MOF crystallises in the trigonal R3 space group, consistent with the previously explained structures. The pyrazole and carboxylate groups were deprotonated and coordinated with Zn(II) to form ZnO_2N_2 tetrahedra (**Figure 3.14)**.

The inconsistency between the ^1H NMR spectroscopic ratio and the SCXRD asymmetric unit indicates structural disorder. ^1H NMR spectroscopic analysis shows a 3:2 ratio of GlyPyr to SerPyr, while the SCXRD asymmetric unit contains two distinct XPyr sites. This suggests that one site is fully occupied by GlyPyr, while the second site is partially occupied, 60% by GlyPyr and 40% by SerPyr (**Figure 3.14**). This model makes the SCXRD data and the NMR consistent.

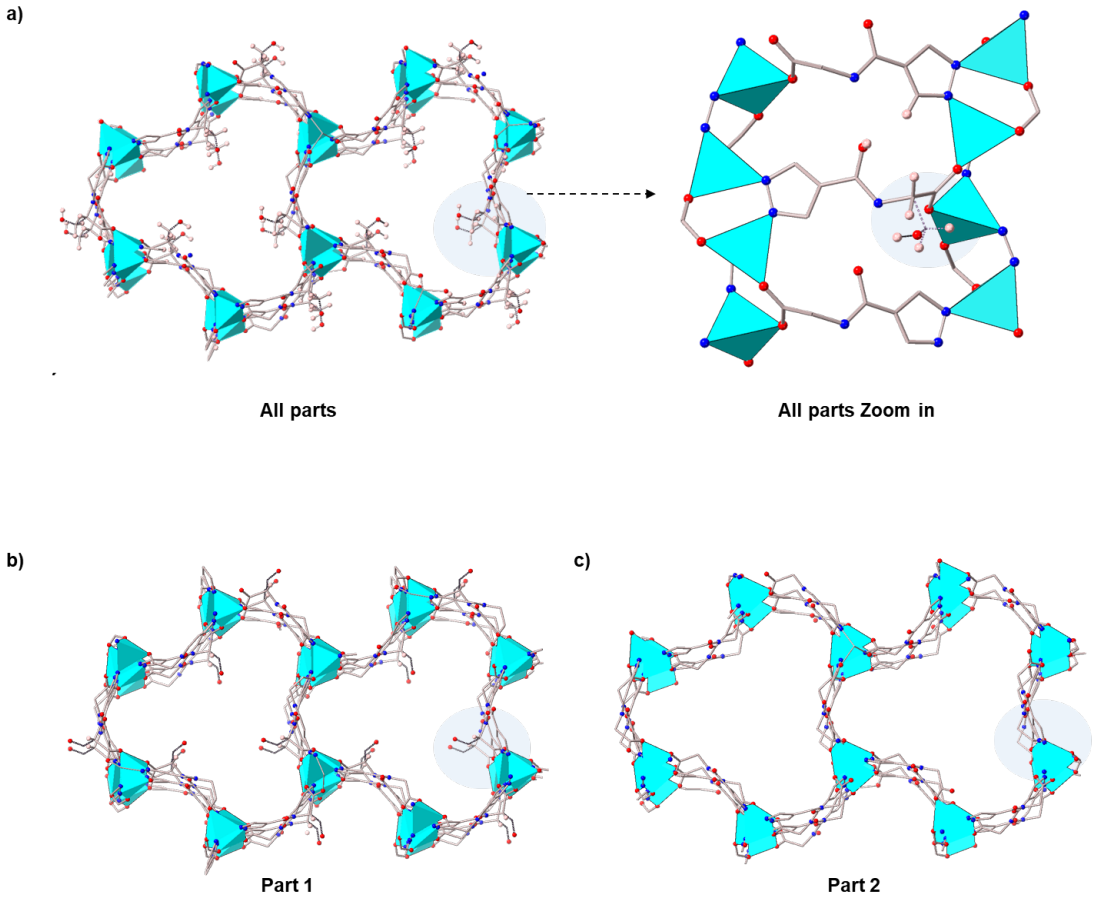

Figure 3.14: a) Representation of all sites in the crystal structure where one site is fully occupied by GlyPyr and the other is disordered between GlyPyr and SerPyr. The presence of both ligands at the same site results in an additional hydrogen atom associated with this mixed occupancy. **b**) In 40% of the structure, the disordered site is occupied by SerPyr, while the other remains GlyPyr. **c**) In 60% of the structure, both sites are occupied by GlyPyr. Atom colours: GlyPyr C chain = beige, C of terminal C = black, SerPyr C chain = beige, dashed, O = red, and N = blue. Most of hydrogen atoms are omitted for clarity.

3.2.5 H_2AlaPyr and other H_2XPyr co-assembly into IR-ZnXPyr

H_2AlaPyr was also combined with other H_2XPyr ligands including H_2ValPyr, H_2SerPyr, H_2PhePyr, or H_2TyrPyr and $Zn(NO_3)_2$ in DMF. IR-ZnXPyr frameworks were successfully obtained in two of these combinations (**Figure 3.15**). SCXRD data were obtained for the combinations of H_2AlaPyr with H_2ValPyr or with H_2PhePyr.

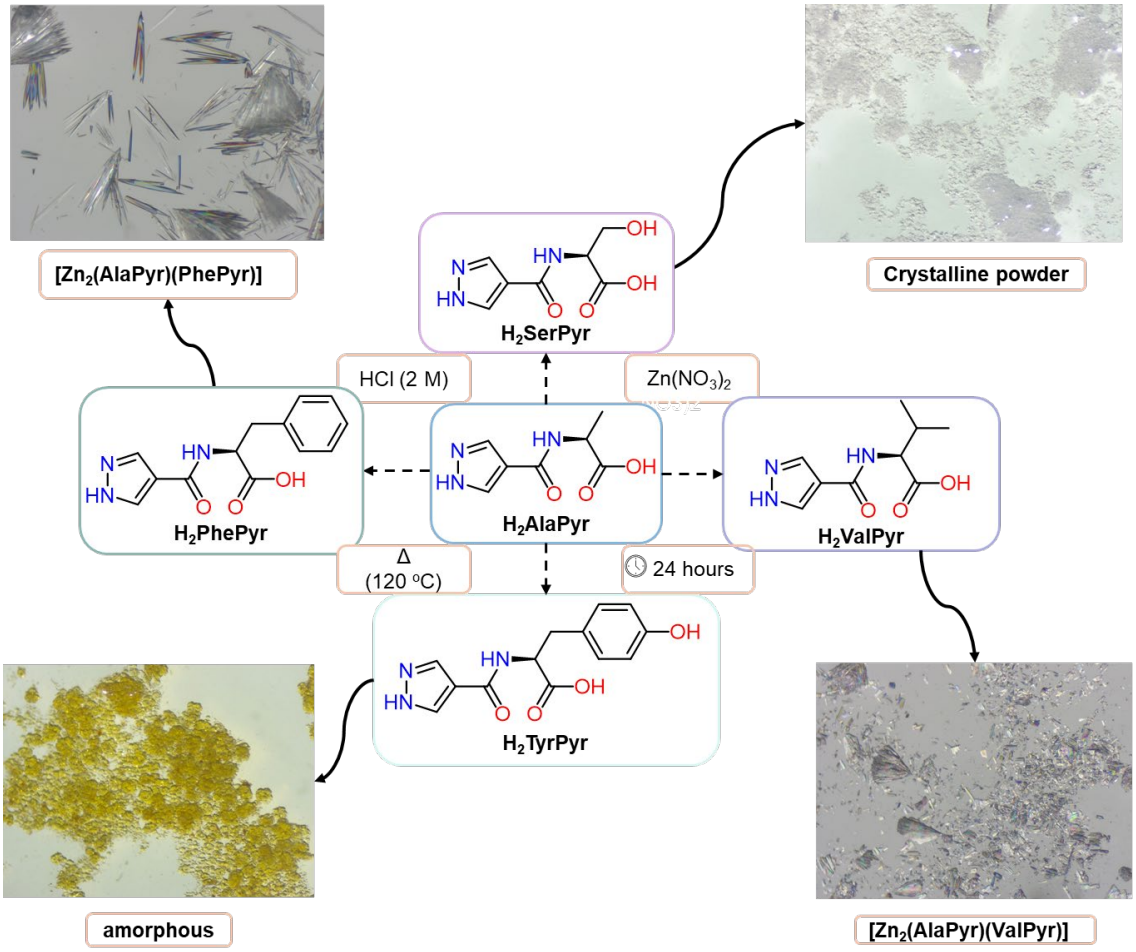

Figure 3.15: An overview of crystalline materials (ZnXPyr) obtained from the new linkers, H_2XPyr, in combination with H_2AlaPyr, along with $Zn(NO_3)_2 \cdot 6H_2O$ in DMF.

[Zn_2(AlaPyr)(ValPyr)] and [Zn_2(AlaPyr)(PhePyr)] synthesis and characterisation

H_2AlaPyr with H_2ValPyr or H_2PhePyr was heated with $Zn(NO_3)_2$ in DMF and HCl (as a crystal-growth modulator) to yield phase-pure [Zn_2(AlaPyr)(ValPyr)] and [Zn_2(AlaPyr)(PhePyr)] (**Figure 3.16**), respectively. After crystallisation, DMF was replaced with fresh solvent to stop further growth and remove excess reagents. The crystals were analysed by PXRD, SCXRD, and ^{1}H NMR spectroscopy.

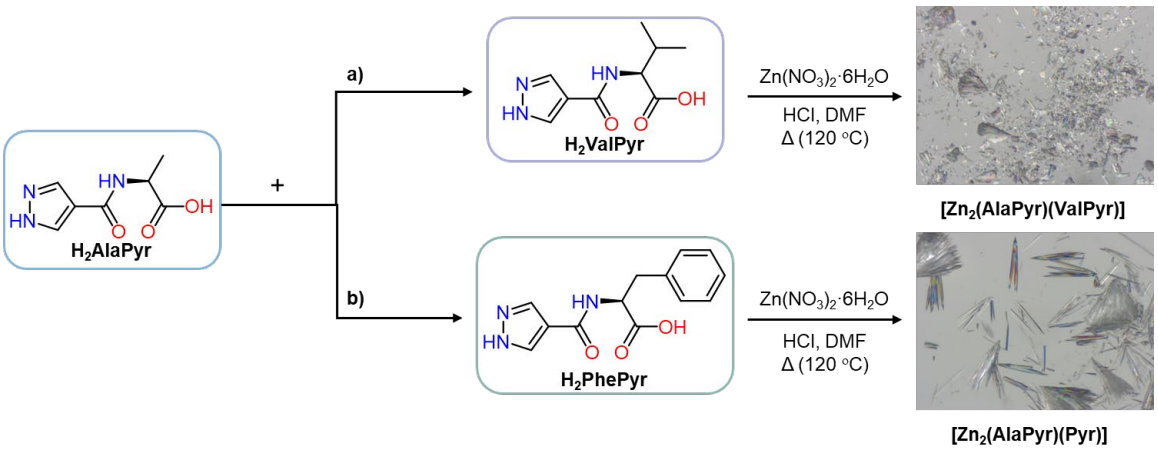

Figure 3.16: Synthesis of [Zn_2(AlaPyr)(ValPyr)] and [Zn_2(AlaPyr)(PhePyr)] from H_2AlaPyr with H_2ValPyr or H_2PhePyr in DMF.

The experimental PXRD patterns of these crystals matched the calculated patterns derived from their corresponding SCXRD data, as well as the reported calculated pattern of ZnGlyPyr obtained from its published SCXRD structure (**Figure 3.17**). This confirms the phase purity of the bulk samples.

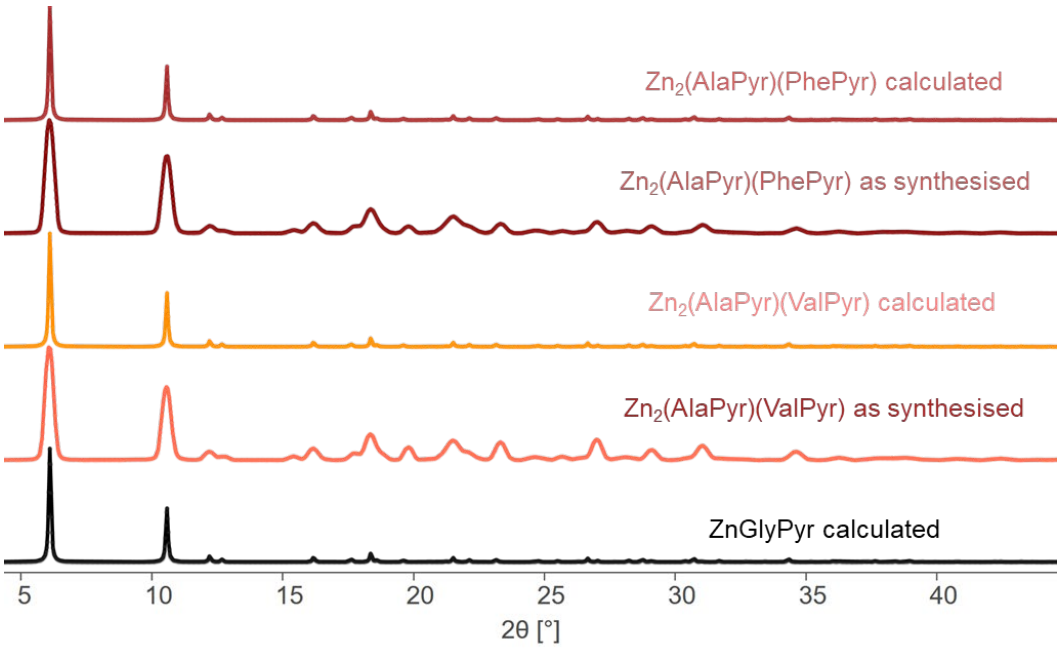

Figure 3.17: The experimental PXRD pattern of [Zn_2(AlaPyr)(ValPyr)] and [Zn_2(AlaPyr)(PhePyr)] matched their calculated patterns from collected SCXRD, and the reported pattern for ZnGlyPyr. This further confirms the phase purity of the framework.

The ^{1}H NMR spectra of separately dissolved crystals of [Zn_2(AlaPyr)(ValPyr)] and crystals of [Zn_2(AlaPyr)(PhePyr)] in NaOD/D_2O revealed a 1:1 ratio between AlaPyr and ValPyr (**Figure 3.26**), and between AlaPyr and PhePyr, respectively **(Figure 3.27)**, further confirming the phase purity of the samples (vide infra).

Structural analysis

The crystals remained stable while stored in solvent but became amorphous upon air exposure. This loss of crystallinity can be attributed to desolvation, which is the removal of solvent molecules occupying the pores or coordinating to metal centres within the framework. Solvent molecules in these MOFs stabilises the framework through weak interactions such as H-bonding or strong bonds as coordination to Zn(II). Upon air exposure, solvent molecules gradually evaporate, leading to the framework collapse.[54, 155] Accordingly, crystals were kept in solvent and mounted in a small amount of oil. SCXRD showed MMOFs with AlaPyr and ValPyr/PhePyr in 1:1 ratio. Both MOFs crystallised in the trigonal R3 space group. ZnO_2N_2 tetrahedra formed from Zn(II) coordinated by two carboxylate oxygen and two pyrazole nitrogen atoms. AlaPyr and ValPyr or PhePyr coordinated in an antiparallel manner, linking tetrahedra into helical rods that assemble into the 3D framework (**Figure 3.18)**.

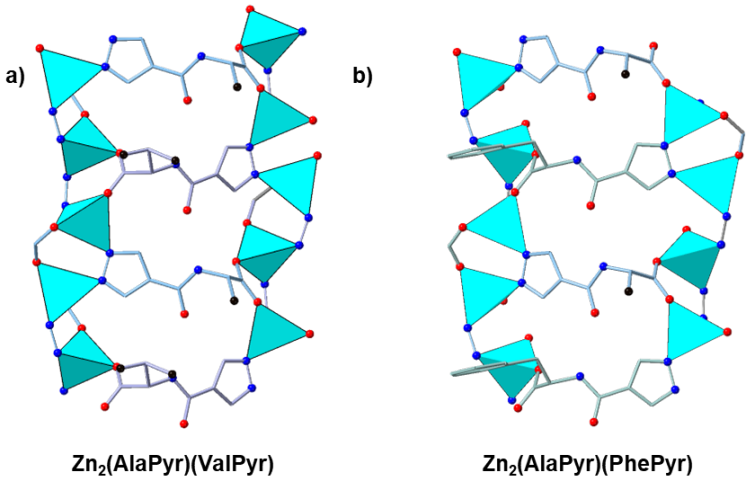

Figure 3.18: a,b) ZnO_2N_2 tetrahedra are connected by AlaPyr and ValPyr **(a)** or PhePyr **(b),** that are coordinated to Zn(II) in an antiparallel manner. Atom colours: ValPyr C chain = mauve, AlaPyr C chain = blue, terminal C = black, PhePyr C chain = pastel green, O = red, and N = blue. Hydrogens are omitted for clarity.

In both structures, an alanine methyl group projects on one side of each peripheral pocket, while a valine isopropyl chain or a phenyl group occupies the opposite side. This arrangement reduces wall-to-wall distances within the peripheral pockets and decreases pore volume (**Figure 3.19**).

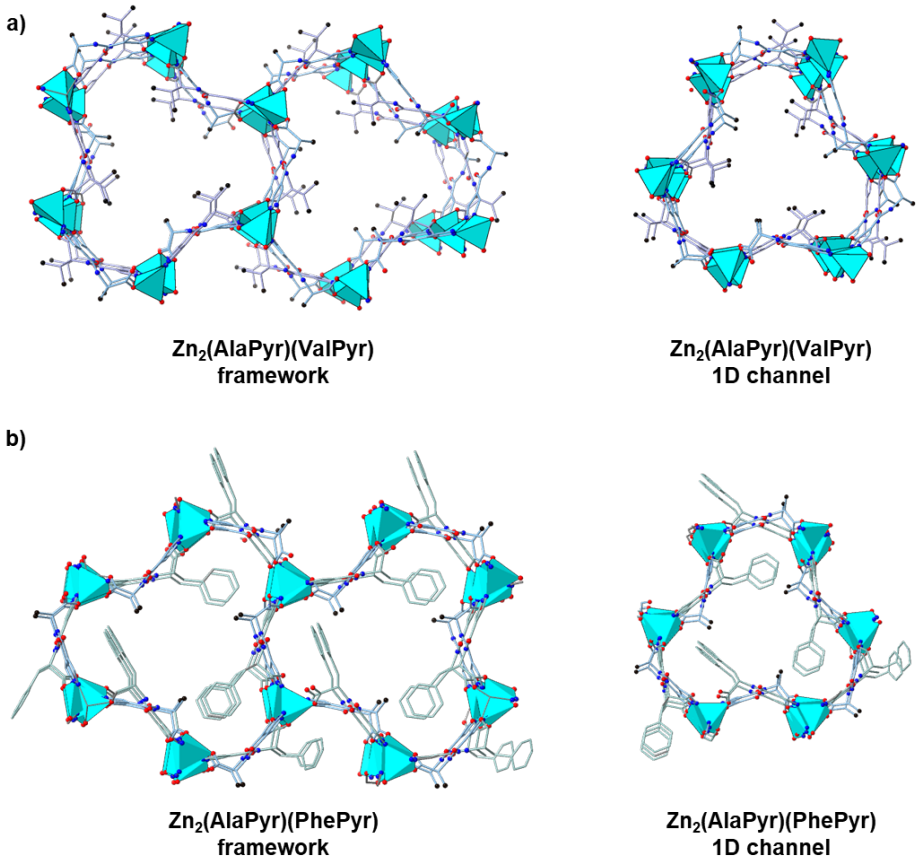

Figure 3.19: a) Crystal structure of the [Zn_2(AlaPyr)(ValPyr)], ValPyr and AlaPyr are protruding in and out the pocket and zoom in overview of the 1D channel, which consists from the three peripheral pockets and one main channel. **b)** Crystal structure of the [Zn_2(AlaPyr)(PhePyr)], PhePyr and AlaPyr are protruding in and out the pocket and the zoom in overview of the 1D channel, which consists of the three peripheral pockets and one main channel. Atom colours: ValPyr C chain = mauve, AlaPyr C chain = blue, terminal C = black, PhePyr C chain = pastel green, O = red, and N = blue. Hydrogens are omitted for clarity.

3.2.6 H_2ValPyr co-assembly with other H_2XPyr linkers into IR-ZnXPyr

Despite numerous attempts to incorporate H_2ValPyr into IR-ZnXPyr with other H_2XPyr ligands, only one MMOF structure was obtained. The successful case is detailed in here.

[Zn_2(PhePyr)$_3$(ValPyr)$_2$]

This structure was prepared via solvothermal synthesis by heating H_2ValPyr and H_2PhePyr with $Zn(NO_3)_2$ in DMF (**Figure 3.20**). The product formed needle-like crystals, consistent with prior materials. After crystallisation, DMF was refreshed; PXRD, SCXRD, and ^{1}H NMR spectroscopy were then performed.

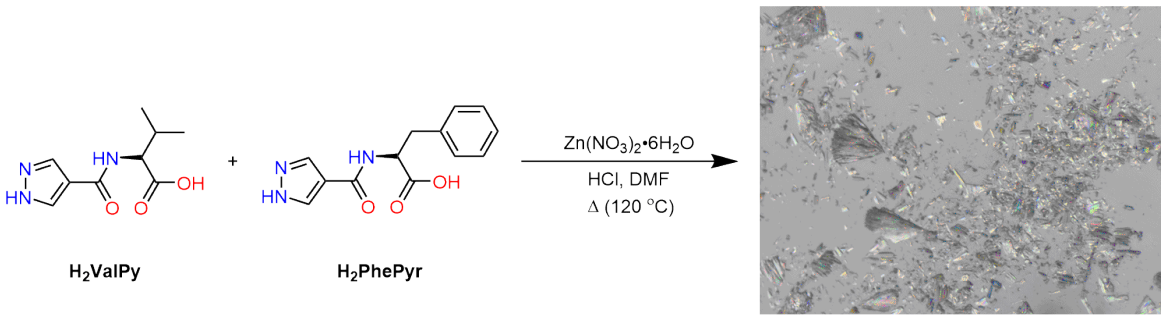

Figure 3.20: Synthetic pathway to $[Zn_2(PhePyr)_3(ValPyr)_2]$, which was obtained by heating the two linkers and the $Zn(NO_3)_2$ in DMF.

The structure crystallised in trigonal R3. As in related MOFs, pyrazole and carboxylate groups deprotonated and coordinated to Zn(II), forming ZnO_2N_2 tetrahedra. ValPyr and PhePyr linkers alternated along the nodes, forming infinite ribbons; ZnO_2N_2 units linked into inorganic rods, generating a 3D framework (**Figure 3.22**).

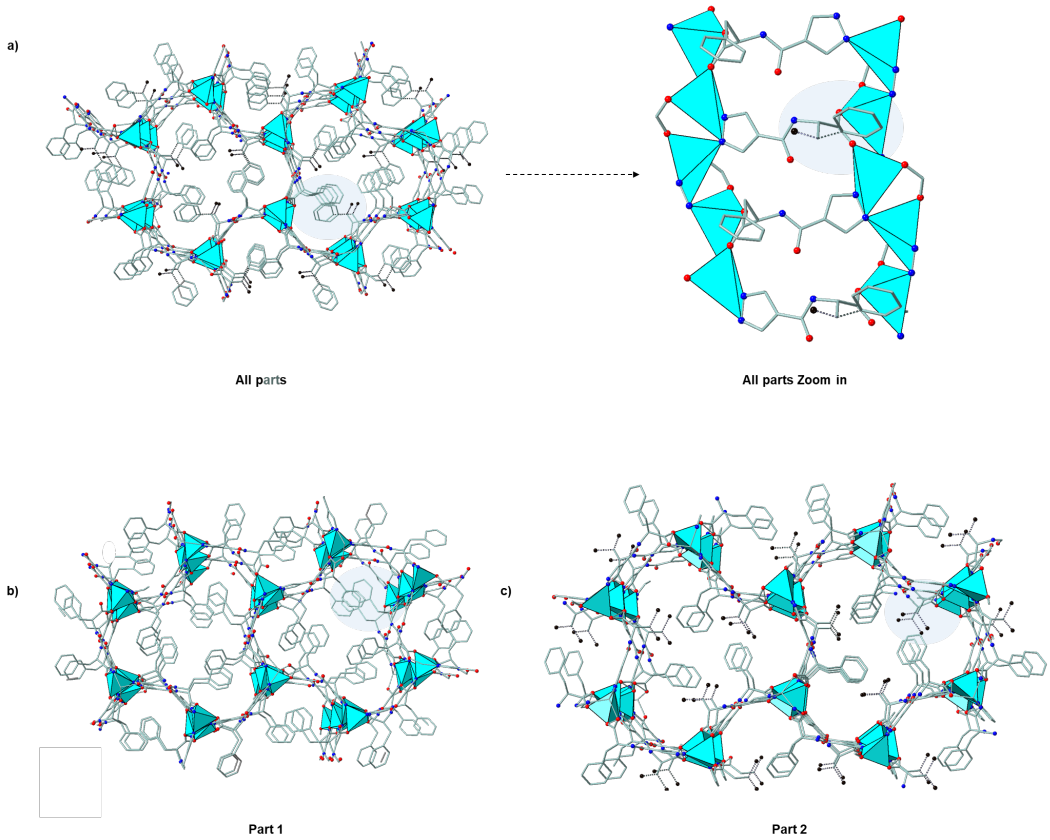

Figure 3.21: a) Disordered crystal structure of $Zn_2(PhePyr)_3(ValPyr)_2$**.** The structure displays two distinct coordination environments: one site is fully occupied by PhePyr, while the second site is disordered, being 60% occupied by PhePyr and 40% by ValPyr. Both components are shown, with dashed bonds indicating disordered positions. **b)** Major component (60% occupancy): both sites occupied by PhePyr, corresponding to part 1**. c)** Minor component (40% occupancy): one site occupied by PhePyr and the other by ValPyr, corresponding to part 2. Atom colours: PhePyr C chain = pastel green, ValPyr isopropyl chain = mauve, terminal C = black ,O = red, and N = blue. Hydrogen atoms are omitted for clarity.

The experimental PXRD pattern matched both the simulated pattern derived from the corresponding SCXRD data and the calculated pattern based on the reported ZnGlyPyr structure, indicating that the framework is isoreticular with ZnXPyr and confirming the phase purity of the sample (**Figure 3.22**).

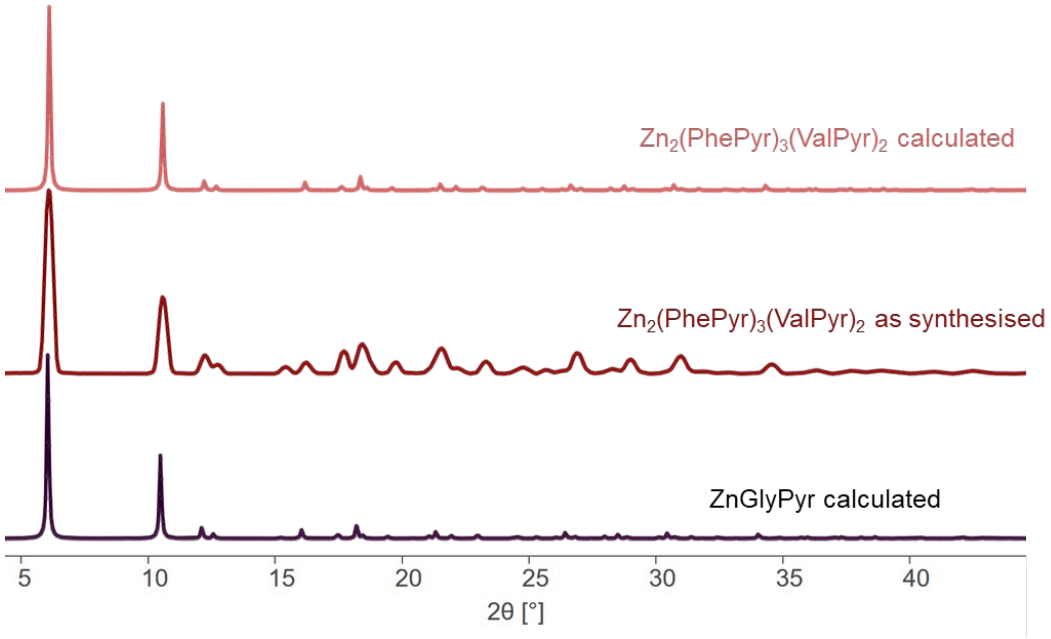

Figure 3.22: The experimental PXRD pattern of [$Zn_2(PhePyr)_3(ValPyr)_2$] closely matches the SCXRD-simulated pattern and the reported ZnGlyPyr pattern, supporting isoreticularity and phase purity.

The ^{1}H NMR spectrum of the digested MOF in NaOD/D_2O showed a PhePyr:ValPyr ratio of 3:2 (**Figure 3.28**). However, this ligand ratio did not align with the asymmetric unit determined by SCXRD, which revealed two distinct XPyr sites, suggesting structural disorder within the framework.

To reconcile ^{1}H NMR spectroscopic data and SCXRD (**Table 3.4**), a mixed-occupancy model was adopted: one XPyr site is fully occupied by PhePyr, while the second site is disordered (60% PhePyr, 40% ValPyr), consistent with the observed 3:2 NMR ratio between PhePyr and ValPyr, and the crystallographic model (**Figure 3.21)**.

The topology is honeycomb-like, with 1D main channels and three peripheral pockets. One site is consistently phenyl groups, while the opposite site alternates between phenyl and isopropyl groups (**Figure 3.21.a**).

3.3 Conclusion

This chapter demonstrated a systematic expansion of amino acid-derived pyrazole ligands (H_2XPyr, where X = Val, Ser, Phe, or Tyr) and their successful incorporation into MOFs structures isoreticular to ZnXPyr, and multicomponent frameworks. Through rational linker design, combining amino acids with a pyrazole functionality via amide coupling, the H_2XPyr family introduced dual coordination modes (carboxylate and pyrazole) and retained conformational flexibility around the Cα centre.[85, 149, 151] These attributes were critical in achieving structural fidelity across the ZnXPyr series, enabling predictable framework assembly and controlled multicomponent incorporation.

Single-crystal X-ray diffraction confirmed that all frameworks, both single- and multicomponent, retain the same underlying ZnO_2N_2 tetrahedral secondary building unit (SBU) and the characteristic *etb* topology. This structural consistency demonstrates that the H_2XPyr linker design successfully decouples chemical diversity from topological variability, a long-standing challenge in the synthesis of amino acid-based frameworks.[32,144] The MMOFs obtained, including [Zn_2(GlyPyr)(ValPyr)], [Zn_2(GlyPyr)(PhePyr)], [Zn_2(GlyPyr)$_3$(SerPyr)$_2$], [Zn_2(AlaPyr)(ValPyr)], [Zn_2(AlaPyr)(PhePyr)], and [Zn_2(PhePyr)$_3$(ValPyr)$_2$], exemplify the incorporation of multiple linkers within a single topology, an achievement that parallels the hierarchical organisation of side chains in proteins.

These findings extend the principles of reticular chemistry beyond purely inorganic or rigid organic systems toward biomimetic frameworks capable of controlled heterogeneity. Unlike multivariate MOFs (MTV-MOFs), where functional group distribution is random,[154] the H_2XPyr-based MMOFs display topologically ordered functionality (except [Zn_2(PhePyr)$_3$(ValPyr)$_2$], and [Zn_2(GlyPyr)$_3$(SerPyr)$_2$]), offering precise control over pore environment and chemical heterogeneity. Such control is essential for the rational design of frameworks with cooperative catalytic sites, selective adsorption pockets, or tailored host-guest recognition.[4, 145, 150]

In the broader context of amino acid-based MOFs, these results demonstrate that introducing a secondary coordinating group (pyrazole) is an effective strategy for overcoming the limitations imposed by native amino acid coordination chemistry namely, low connectivity, flexibility, and pH sensitivity. By stabilising well-defined SBUs and maintaining isoreticular topology, this work provides a robust platform for engineering functionally diverse yet structurally uniform MOFs.[85, 149, 151] Future efforts can exploit this linker family to develop MMOFs with spatially programmed functionalities, bridging the gap between protein-inspired materials and reticular chemistry.

These findings demonstrate that amino acid-derived pyrazole ligands enable the formation of both single- and multicomponent MOFs, offering a platform for further investigation into their structural and functional characteristics. Functionalising linkers controls pore decoration, introducing varied groups that allow MOFs to imitate protein-like functions, making them suited for catalysis and separation (e.g., hexane-isomer discrimination).[145, 146] The synthesised MOFs, in contrast to Rosseinsky's multicomponent frameworks, are chiral and enantiopure, as they are constructed exclusively from enantiomerically pure amino acid-derived linkers. This intrinsic chirality distinguishes them from achiral systems such as ZnGlyPyr and racemic frameworks like [Zn_2(*l*-AlaPyr)(*d*-AlaPyr)] and offers potential for enantioselective guest uptake and separation. Multiple functionalities in the framework can act together to optimise drug release and catalytic processes.

Looking ahead, spatial programming of H_2XPyr linkers (e.g., controlling which points host specific groups) offers a clear path to designed cooperativity and guest-responsive behaviour in flexible MOFs, advancing the integration of biomimetic function with reticular control.[85, 146, 147, 154]

3.4 Experimental section

3.4.1 General information:

All general synthetic procedures, instrumentation details, and characterisation methods (except for the silica column chromatography) are described in the **2.4.1**. Column chromatography was performed on silica gel (grade 60, mesh size 230-400, ScharlauPore volume and pore dimensions were calculated with PoreBlazer, using the XYZ coordinates generated from the single-crystal X-ray diffraction (SCXRD) CIF files.[156]

3.4.2 Synthesis of compound H_2ValPyr (5A)

Synthesis of compound 4A

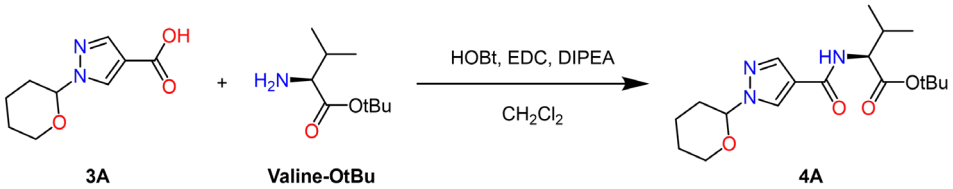

Scheme 3.1: Synthesis of compound **4A.**

Compound **3A** (0.48 g, 2.44 mmol) was dissolved in DCM (5 mL). Then, *l*-hydroxybenzotriazole hydrate (HOBt) (0.49 g, 2.93 mmol, 1.2 eq), EDC (0.45 g, 1.93 mmol, 1.2 eq.), and DIPEA (1.3 mL, 7.65 mmol, 3 eq.) were added to the solution. The solution was then stirred at room temperature. Then, *l*-valine tert-butyl ester (0.61 g, 1.2 eq.) was added to the reaction mixture, and the mixture was stirred at room temperature overnight (**Scheme 3.1**). TLC showed the reaction completion. H_2O (x 2, 10 mL) was added to the reaction mixture, and the product was partitioned to the DCM layer. The organic layers were collected and dried over magnesium sulfate and concentrated on a rotary evaporator under reduced pressure at 40 °C. The obtained pale-yellow crude product was purified by column chromatography using EtOAc: DCM: cyclohexane (2:2:1) over silica gel. R_f: 0.54. Yield: 0.39 g, 1.10 mmol, 46%.

^{1}H NMR (500 MHz, $CDCl_3$) δ 8.13 (s, 1H), 7.88 (s, 1H), 6.45 (t, J = 7.56 Hz, 1H), 5.42 (dd, J = 5.42, 5.40 Hz, 1H), 4.63 – 4.60 (m, 1H), 3.75 – 3.69 (m, 1H), 2.26 – 2.20 (m, 3H), 2.1 – 2.01 (m, 3H), 1.74 – 1.62 (m, 3H),1.49 (s, 9H), 0.98 (dd, J = 6.94, 6.62 Hz, 6H) ppm.

HRMS (FTMS + p ESI Full) calculated for $[M + H]^+(C_{18}H_{29}N_3O_4)^+$ *m/z* 352.2231, found *m/z* 352.2221.

Synthesis of ligand 5A

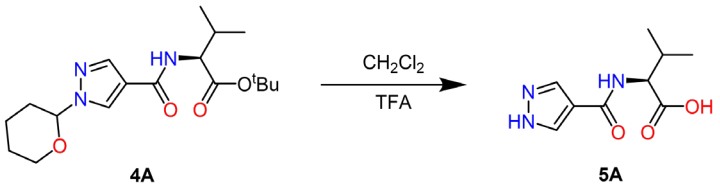

Scheme 3.2: Synthesis of compound **5A**.

Compound **4A** (0.15 g, 0.43 mmol) was dissolved in DCM (7 mL). The solution was cooled using an ice bath. To the above-stirred solution, trifluoroacetic acid (TFA) (4.9 mL, 43.0 mmol,100 eq.) was added dropwise (**Scheme 3.2**). The reaction mixture was stirred at room temperature for 8 hours. The solution colour turned to a dark brown. The reaction was stopped and the solvent was removed on a rotary evaporator under reduced pressure, which afforded a dark brown gel. The product was separated from the impurity using H_2O (2 mL) and DCM (2 mL), where the impurity partitioned the DCM layer, while the product remained in the H_2O layer. The H_2O was removed under reduced pressure, yielding a colourless oil. The product was precipitated as a powder by sonicating it with DCM. Yield: 0.08 g, 0.37 mmol, 86%.

^{1}H NMR (500 MHz, D_2O) δ (ppm) 8.17 (s, 2H), 4.40 (d, J = 6.31 Hz, 1H), 2.29–2.23 (m, 1H), 1.03 (dd, J = 3.15, 3.15 Hz, 6H). ^{13}C NMR (126 MHz, D_2O) δ (ppm) 175.8, 134.95, 115.99, 58.80, 29.80, 18.5, 17.3.

HRMS (FTMS + p ESI Full) calculated for $[M + H]^+(C_9H_{14}N_3O_3)^+$ *m/z* 212.1030, found *m/z* 212.1026.

3.4.3 Synthesis of compound H_2SerPyr (7A)

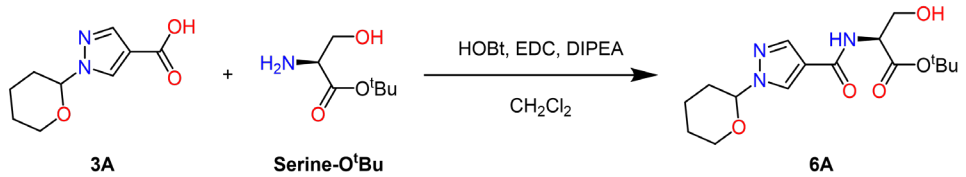

Scheme 3.3: Synthesis of compound **6A**.

Synthesis of compound 6A

Compound **3A** (0.28 g, 1.52 mmol) was dissolved in DCM (10 mL). Then, *l*-hydroxybenzotriazole hydrate (HOBt) (0.25 g, 1.82 mmol, 1.2 eq), EDC (0.28 g, 1.82 mmol, 1.2 eq.), and DIPEA (845.0 µL, 4.56 mmol, 3 eq.) were added to the solution. The reaction mixture was stirred at room temperature for 10 minutes. Then, *l*-serine tert-butyl ester hydrochloride (0.36 g, 1.2 eq.) was added to the reaction mixture. The mixture stirred at room temperature overnight (**Scheme 3.3**). Then, H_2O (x 2, 10 mL) was added to the reaction mixture. The product partitioned to the DCM layer. The organic layers were collected dried over anhydrous magnesium sulfate and concentrated on a rotary evaporator. The obtained pale-yellow oil was purified by column chromatography using MeOH in EtOAc:(10%) over silica gel. R_f: 0.45. Yield: 0.15 g, 0.44 mmol, 30%.

^{1}H NMR (500 MHz, $CDCl_3$) δ (ppm) 8.08 (s, 1H), 7.84 (s, 1H), 6.81 (t, J = 8.83 Hz, 1H), 5.39 (dd, J = 5.99 , 6.30 Hz, 1H), 4.69 – 4.66 (m, 1H), 3.74 – 3.68 (m, 1H), 2.08 – 2.02 (m, 3H), 1.71 – 1.63 (m, 3H),1.51 (s, 9H).

HRMS (FTMS + p ESI Full) calculated for $[M + H]^+(C_{16}H_{26}N_3O)^+$ *m/z* 340.1867, found *m/z* 340.1859.

Synthesis of ligand 7A

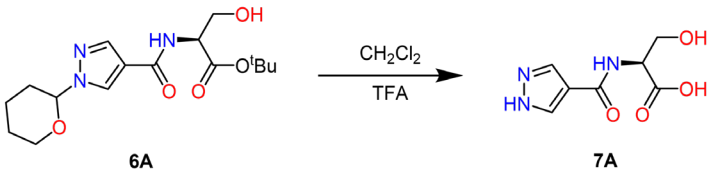

Scheme 3.4: Synthesis of compound **7A**.

Compound **6A** (0.10 g, 0.29 mmol) was dissolved DCM (6 mL) and cooled with an ice bath. Trifluoroacetic acid (TFA) (2.3 mL, 29.46 mmol, 100 eq.) was added dropwise. After the addition was finished, the ice bath was removed, and the reaction mixture was warmed to room temperature and stirred for 3 hours (**Scheme 3.4**). The reaction mixture turned dark brown. The solvent was removed on a rotary evaporator under reduced pressure, which afforded a dark brown gel. H_2O (2 mL) and DCM (2 mL) were added to the brown gel. The impurity partitioned to the DCM layer, while the product partitioned to the H_2O layer. The H_2O was removed to obtain colourless oil. The product was precipitated as a powder by sonicating it with DCM. Yield: 0.05 g, 0.23 mmol, 78%.

^{1}H NMR (500 MHz, D_2O) δ (ppm) 8.14 (s, 2H), 4.65 (t, J = 9.46 Hz, 1H), 3.98–3.90 (m, 2H) ppm. ^{13}C NMR (126 MHz, D_2O) δ (ppm) 173.71, 165.56, 134.89, 116.13, 60.83, 54.47.

HRMS (FTMS + p ESI Full) calculated for $[M + H]^+(C_7H_{10}N_3O_4)^+$ *m/z* 200.0666, found *m/z* 200.0665.

3.4.4 Synthesis of compound H_2PhePyr (9A)

Synthesis of compound 8A

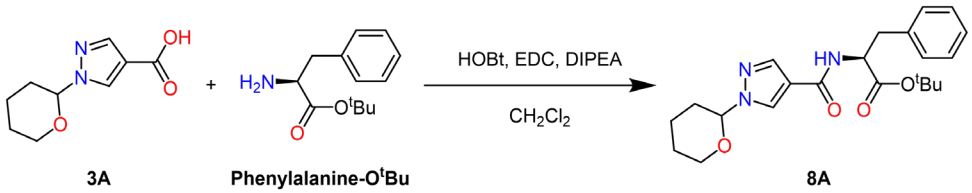

Scheme 3.5: Synthesis of compound **8A**.

Compound **3A** (0.50 g, 2.55 mmol) was dissolved in DCM (50 mL). Then, *l*-hydroxybenzotriazole hydrate (HOBt) (0.41 g, 3.06 mmol, 1.2 eq), EDC (0.48 g, 3.06 mmol, 1.2 eq.), and DIPEA (665.0 µL, 7.65 mmol, 3 eq.) were added to the solution at room temperature. The reaction mixture was stirred at room temperature, then, phenylalanine tert-butyl ester hydrochloride (0.68 g, 1.2 eq.) was added to the reaction mixture (**Scheme 3.5**). The mixture was stirred at room temperature overnight. After completion of the reaction, water (50 mL) was added to the reaction mixture.

Then the product was extracted with DCM (x 3, 100 mL) and the organic layers were washed with H_2O (x 3, 50 mL), dried over anhydrous sodium sulfate, and concentrated on a rotary evaporator under reduced pressure at 40 °C. The obtained pale-yellow oil was purified by column chromatography using EtOAc: DCM: cyclohexane (2: 2: 1) over silica gel. R_f: 0.52. Yield: 1.00 g, 1.12 mmol, 44%.

^{1}H NMR (500 MHz, $CDCl_3$) δ (ppm) 8.03 (s, 1H), 7.76 (s, 1H), 7.20-7.29 (m, 5H), 6.23 (t, *J* = 6.94 Hz, 1H), 5.36 (dd, *J* = 17.35, 3.80 Hz, 1H), 4.91-4.90 (m, 1H), 4.05 (dd, *J* = 3.09, 3.71 Hz, 1H), 3.73-3.67 (m, 1H), 3.19 (m, 1H), 2.14-2.07 (m, 3H), 1.72-1.62 (m, 3H), 1.43 (s, 9H).

HRMS (FTMS + p ESI Full) calculated for $[M + H]^+(C_{22}H_{30}N_3O_4)^+$ *m/z* 400.2231, found *m/z* 400.2221.

Synthesis of ligand 9A

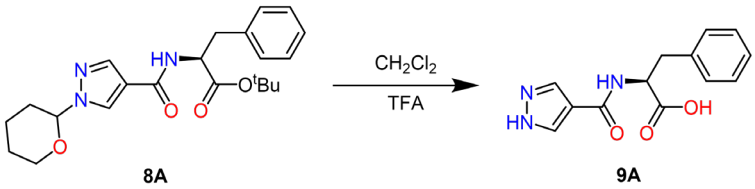

Scheme 3.6: Synthesis of compound **9A**.

Crude Compound **8A** (0.24 g, 0.58 mmol) was dissolved using DCM (10 mL) and cooled with an ice bath. Then, trifluoroacetic acid (TFA) (4.50 mL, 29.46 mmol, 100 eq.) was added dropwise (**Scheme 3.6**). After the addition was finished, the ice bath was removed, and the reaction mixture was stirred at room temperature for 8 hours. The reaction mixture turned to dark brown. The solvent was removed by rotary evaporation under reduced pressure, yielding a dark brown gel. The product was partitioned between H_2O (2 mL) and DCM (2 mL). The impurity partitioned to the DCM layer, while the product partitioned to the H_2O layer. The H_2O was removed to obtain colourless oil. The product was precipitated as a powder by sonicating it with DCM. Yield: 0.12 g, 0.46 mmol, 80%.

^{1}H NMR (500 MHz, D_2O) δ (ppm) 7.95 (s, 2H), 7.29 (dd, *J* = 7.25, 6.94 Hz, 2H), 7.23 (t, *J* = 17.33 Hz, 2H), 3.29 (dd, *J* = 5.36, 5.36 Hz, 1H), 3.08 (q, *J* = 23.33 Hz, 1H).

^{13}C NMR (126 MHz, D_2O) δ (ppm) 175.03, 165.01, 154.09, 134.95, 130.34, 128.34, 116.22, 115.28, 53.90, 35.76.

HRMS (FTMS + p ESI Full) calculated for $[M]^-(C_{13}H_{12}N_3O_3)^-$ *m/z* 258.0873, found *m/z* 258.0880.

3.4.5 Synthesis of compound H_2TyrPyr (11A)

Synthesis of compound 10A

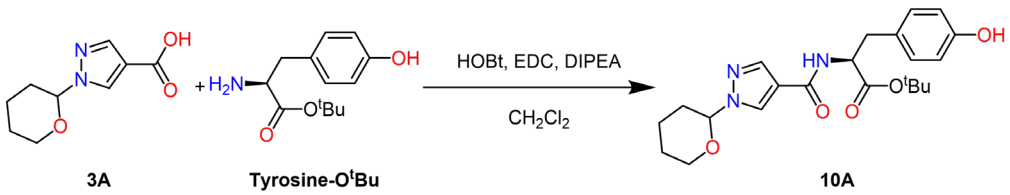

Scheme 3.7: Synthesis of compound **10A**.

Compound **3A** (0.50 g, 2.55 mmol) was dissolved in DCM (30 mL). Then, *l*-hydroxybenzotriazole hydrate (HOBt) (0.41 g, 3.06 mmol, 1.2 eq), EDC (0.48 g, 3.06 mmol, 1.2 eq.), and DIPEA (665.0 µL, 7.65 mmol, 3 eq.) were added. The reaction mixture was stirred at room temperature for 10 minutes, after which, tyrosine tert-butyl ester (0.73 g, 1.2 eq.) was added to the reaction mixture and the mixture stirred at room temperature overnight (**Scheme 3.7**). After the reaction completion, water (50 mL) was added to the reaction mixture. The solution was extracted with DCM (x 3, 50 mL), and the organic layers were collected, washed with H_2O (x 3, 20 mL), then dried over anhydrous sodium sulfate, and concentrated on a rotary evaporator under reduced pressure at 40 °C. The obtained pale-yellow crude product was purified by column chromatography using ethyl acetate (EtOAc) over silica gel. R_f: 0.52. Yield: 1.00 g, 1.07 mmol, 42%.

^{1}H NMR (500 MHz, $CDCl_3$) δ (ppm) 8.05 (s, 1H), 7.78 (s, 1H), 7.015 (d, *J* = 12.32 Hz, 2H), 6.72 (d, *J* = Hz, 2H), 6.72 (t, *J* = Hz, 1H), 6.24 (dd, *J* = 8.38 Hz, 1H), 5.39 (dd, *J* = 5.95, 3.72 Hz,1H), 4.90-4.86 (m, 1H), 4.04 (d, *J* = 7.42 Hz, 1H), 3.15 (m, 2H), 3.73-3.67 (m, 1H), 3.19 (m, 2H), 2.08-2.01 (m, 3H), 1.72-1.62 (m, 3H), 1.45 (s, 9H).

HRMS (FTMS + p ESI Full) calculated for $[M + H]^+(C_{22}H_{30}N_3O_4)^+$ *m/z* 416.2180, found *m/z* 416.2169.

Synthesis of ligand 11A

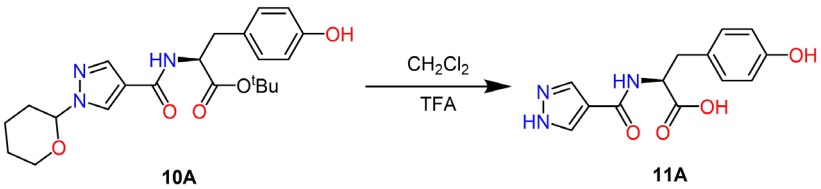

10A 11A

Scheme 3.8: Synthesis of compound **11A**.

Compound **10A** (0.17 g, 0.41 mmol) was dissolved in DCM (15 mL) and cooled with an ice bath. To the above-stirred solution, TFA (3.1 mL, 4.7 mmol, 100 eq.) was added drop by drop over 10 minutes. After the addition was finished, the ice bath was removed, and the reaction mixture was warmed to r.t. and stirred for 3 hours (**Scheme 3.8**). The reaction mixture turned dark brown. The solvent was removed on a rotary evaporator under reduced pressure, which afforded a dark brown gel. The product was partitioned between H_2O (2 mL) and DCM (2 mL). The impurity partitioned to the DCM layer, while the product partitioned to the H_2O layer. The H_2O was removed to obtain colourless oil. The product was precipitated as a powder by sonicating it with Et_2O. Yield: 0.60 g, 0.21 mmol, 53%.

^{1}H NMR (500 MHz, D_2O) δ (ppm) 7.96 (s, 2H), 7.12 (d, J = 8.51 Hz, 2H), 6.78 (d, J = 9.45 Hz, 2H), 5.67 (dd, J = 5.67, 5.67 Hz, 1H), 3.00 (J = 23.01 Hz, 1H).

^{13}C NMR (126 MHz, D_2O) δ 175.26, 165.22, 154.4, 136.87, 134.83, 129.38, 129.18, 127.03, 54.16, 36.63.

HRMS (FTMS + p ESI Full) calculated for $[M]^-(C_{13}H_{12}N_3O_3)^-$ *m/z* 274.0822, found *m/z* 274.0831.

3.4.6 MOF Synthesis

The general synthetic procedure for the IR-ZnXPyr structures is described, with all corresponding weights summarised in **Table 3.1** below.

In a 4 mL vial, H_2XPyr1 (**LK1**, x mg, x µmol), H_2XPyr2 (**LK2**, x mg, x µmol) and $Zn(NO_3)_2{\cdot}6H_2O$ (**M**, x mg, x µmol) were dissolved in DMF (2 mL). Then, HCl (2 M, 25 µL) was added. Then, the vial was capped and heated in an oven at 120 °C for 24 hours. The vial was taken out, the solvent was decanted and replaced with fresh DMF.

Table 3.1: Summary of the linkers, metal weights, and moles for the obtained IR-ZnXPyr.

IR-ZnXPyr Formula	**LK1**	**LK2**	**LK1** mg, µmol	**LK2** mg, µmol	**M** mg, µmol
ZnValPyr	H_2ValPyr	×	8.8, 41.7	×	13.4, 53.7
ZnPhePyr·DMF	H_2PhePyr	×	11.9,45.9	×	13.4, 53.7
[Zn_2(GlyPyr)(ValPyr)]	H_2GlyPyr	H_2ValPyr	8.0, 47.3	9.0, 44.7	13.5, 42.6
[Zn_2(GlyPyr)(PhePyr)]	H_2GlyPyr	H_2PhePyr	9.0, 43.8	7.0, 35.2	12.3, 41.3
[Zn_2(GlyPyr)$_3$(SerPyr)$_2$]	H_2GlyPyr	H_2SerPyr	7.4, 53.2	9.8, 38.1	12.3, 41.3
[Zn_2(AlaPyr)(ValPyr)]	H_2AlaPyr	H_2ValPyr	7.3, 39.9	8.6, 40.7	13.4, 53.7
[Zn_2(AlaPyr)(PhePyr)]	H_2AlaPyr	H_2PhePyr	7.3, 39.9	8.6, 33.5	16.4, 55.1
[Zn_2(PhePyr)$_3$(ValPyr)$_2$]	H_2PhePyr	H_2ValPyr	11.5,44.7	8.2, 38.8	15.4, 55.6

3.4.7 MOFs crystals ^{1}H NMR spectroscopic data

The MOF crystals were washed thoroughly with acetone (x 3, 0.5 mL) and dried under high vacuum before digestion. ^{1}H NMR spectroscopy of the dissolved crystals in NaOD/D_2O (23 µL/ 1 mL) was then performed.

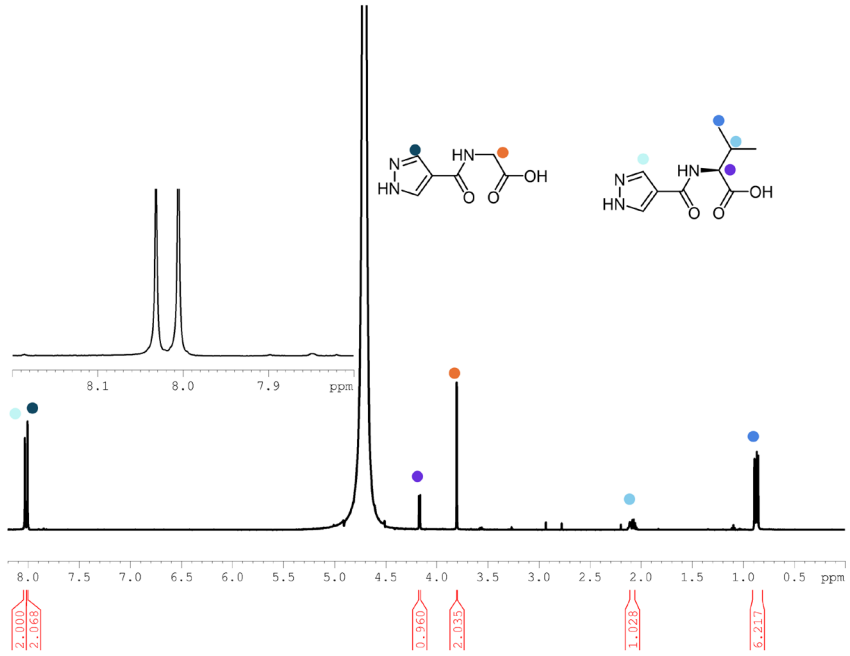

Figure 3.23: ^{1}H NMR spectrum of [Zn_2(GlyPyr)(ValPyr)] crystals digested in NaOD/D_2O.

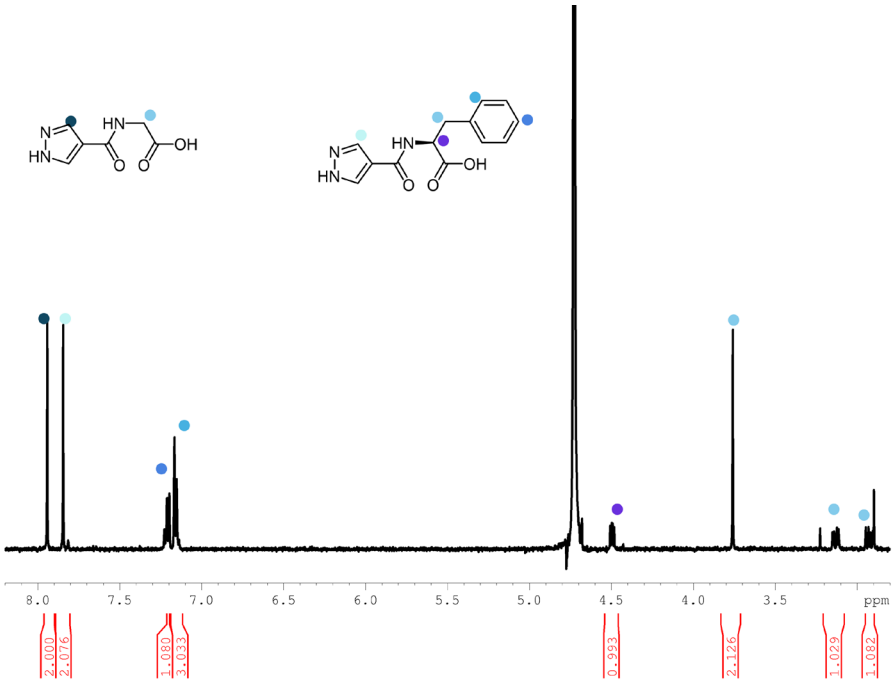

Figure 3.24: ^{1}H NMR spectrum of [Zn_2(GlyPyr)(PhePyr)] crystals digested in NaOD/D_2O.

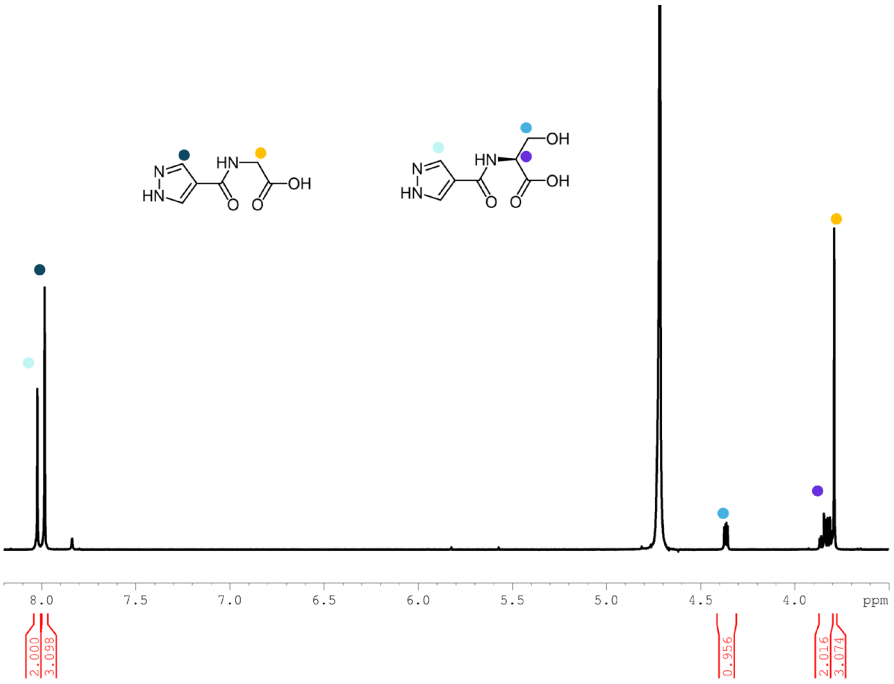

Figure 3.25:^{1}H NMR spectrum for [Zn_2(GlyPyr)$_3$(SerPyr)$_2$] crystals digested in NaOD/D_2O .

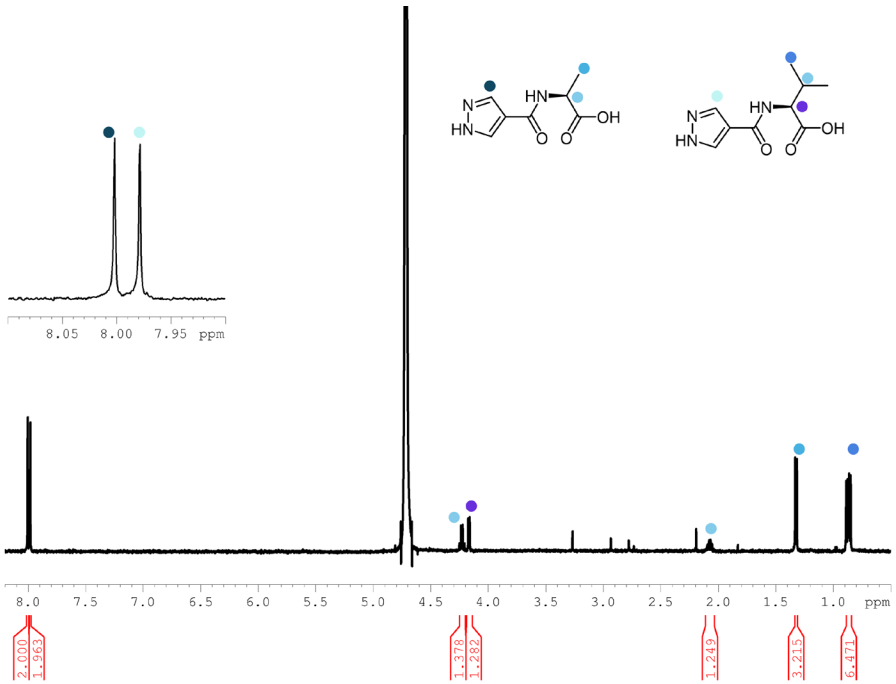

Figure 3.26: ^{1}H NMR spectrum of [Zn_2(AlaPyr)(ValPyr)] crystals dissolved in NaOD/D_2O.

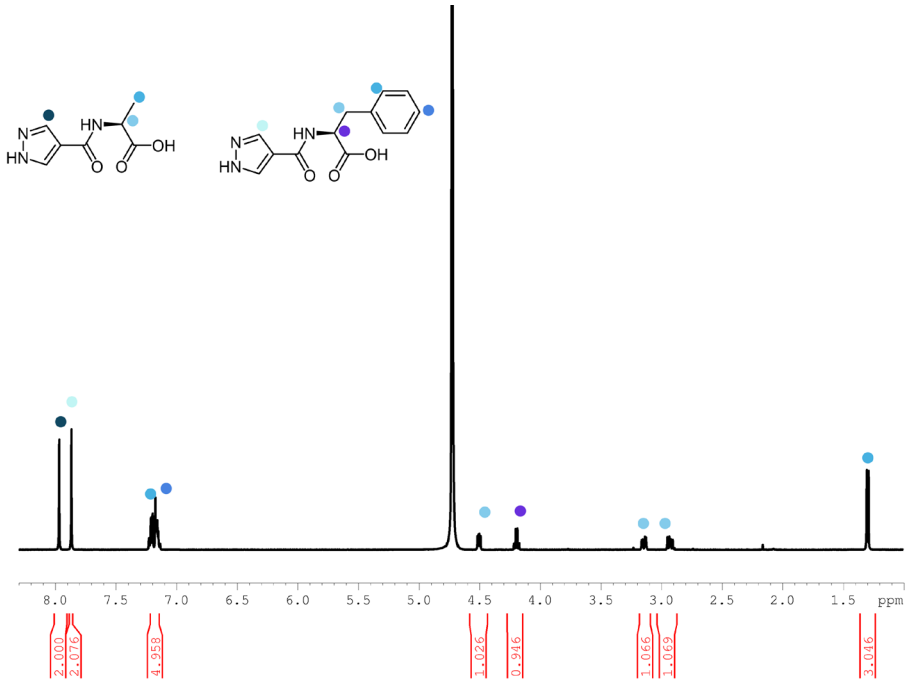

Figure 3.27: ^{1}H NMR spectrum of [Zn_2(AlaPyr)(PhePyr)] crystals dissolved in NaOD/D_2O .

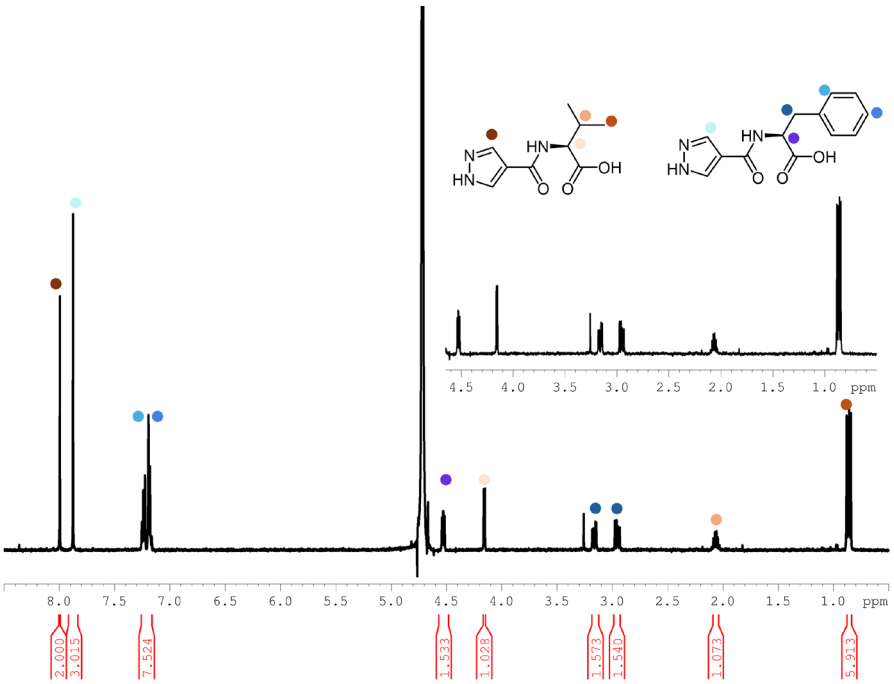

Figure 3.28: ^{1}H NMR spectrum of the dissolved $[Zn_2(PhePyr)_3(ValPyr)_2]$ crystals in $NaOD/D_2O$.

3.4.8 SCXRD measurements

Table 3.2: Summary of SCXRD data.

Name	ZnValPyr	ZnPhePyr·DMF
Empirical formula	$C_{18}H_{22}N_6O_6Zn_2$	$C_{29}H_{27}N_7O_7Zn_2$
Formula weight	549.15	716.31
Temperature/K	295.00	180
Crystal system	trigonal	trigonal
Space group	R3	R3
a/Å	29.789(2)	29.789(2)
b/Å	29.789(2)	29.789(2)
c/Å	10.2355(12)	10.2355(12)
α/°	90	90
β/°	90	90
γ/°	120	120
Volume/Å^3	7866.0(15)	7866.0(15)
Z	9	9
ρ_{calc}g/cm^3	1.043	1.361
μ/mm^{-1}	1.954	2.122
F(000)	2520.0	3294.0
Crystal size/mm^3	0.95 × 0.27 × 0.14	0.08 × 0.07 × 0.02
Radiation	CuKα (λ = 1.54178)	CuKα (λ = 1.54178)
Index ranges	$-34 \le h \le 31$, $-33 \le k \le 33$, $-11 \le l \le 11$	$-29 \le h \le 32$, $-32 \le k \le 12$, $-8 \le l \le 10$
Reflections collected	23409	4023
Independent reflections	5591 [R_{int} = 0.0639, R_{sigma} = 0.0534]	3267 [R_{int} = 0.0380, R_{sigma} = 0.1086]
Data/restraints/ parameters	5591/1/293	3267/46/391
Goodness-of-fit on F^2	1.057	1.050
2Θ range for data refinement/°	5.934 to 123.962	5.934 to 117.068
Final R indexes [I>=2σ (I)]	R_1 = 0.0822, wR_2 = 0.2324	R_1 = 0.0810, wR_2 = 0.2088
Final R indexes [all data]	R_1 = 0.1006, wR_2 = 0.2537	R_1 = 0.1202, wR_2 = 0.2455
Largest diff. peak/hole / e Å^{-3}	1.73/-0.69	1.12/-0.60
Flack Parameter	0.06(2)	0.07(7)

Table 3.3: Summary of SCXRD data.

Name	[Zn_2(GlyPyr)(ValPyr)]	[Zn_2(GlyPyr)(PhePyr)],	[Zn_2(GlyPyr)$_3$(SerPyr)$_2$]
Empirical formula	$C_{15}H_{16}N_6O_6Zn_2$	$C_{19}H_{16}N_6O_6Zn_2$	$C_{12.8}H_{11.6}N_6O_{6.8}Zn_2$
Formula weight	507.08	545.04	488.01
Temperature/K	295.00	180.00	150.00
Crystal system	trigonal	trigonal	trigonal
Space group	R3	R3	R3
a/Å	29.3041(6)	29.789(2)	29.789(2)
b/Å	29.3041(6)	29.789(2)	29.789(2)
c/Å	10.1807(3)	10.2355(12)	10.2355(12)
α/°	90	90	90
β/°	90	90	90
γ/°	120	120	120
Volume/Å^3	7571.2(4)	7866.0(15)	7866.0(15)
Z	9	9	9
ρ_{calc}g/cm^3	1.001	1.036	0.927
μ/mm^{-1}	1.997	1.963	1.927
F(000)	2304.0	2430.0	2194.0
Crystal size/mm^3	0.16 × 0.15 × 0.052	0.16 × 0.14 × 0.08	0.03 × 0.02 × 0.02
Radiation	CuKα (λ = 1.54178)	CuKα (λ = 1.54178)	CuKα (λ = 1.54178)
Index ranges	-34 ≤ h ≤ 35, -34 ≤ k ≤ 35, -11 ≤ l ≤ 12	-32 ≤ h ≤ 33, -32 ≤ k ≤ 29, -10 ≤ l ≤ 11	-33 ≤ h ≤ 33, -33 ≤ k ≤ 32, -11 ≤ l ≤ 10
Reflections collected	27163	13418	23885
Independent reflections	6088 [R_{int} = 0.0559, R_{sigma} = 0.0447]	4488 [R_{int} = 0.0958, R_{sigma} = 0.0921]	5173 [R_{int} = 0.1350, R_{sigma} = 0.1067]
Data/restraints/ parameters	6088/3/264	4488/4/246	5173/4/244
Goodness-of-fit on F^2	1.095	1.873	1.528
2Θ range for data refinement/°	6.032 to 132.326	5.934 to 119.248	5.934 to 119.248
Final R indexes [I>=2σ (I)]	R_1 = 0.0695, wR_2 = 0.2043	R_1 = 0.1248, wR_2 = 0.3136	R_1 = 0.1500, wR_2 = 0.3836
Final R indexes [all data]	R_1 = 0.0864, wR_2 = 0.2232	R_1 = 0.1665, wR_2 = 0.3340	R_1 = 0.2091, wR_2 = 0.4338
Largest diff. peak/hole / e Å^{-3}	0.89/-0.84	1.27/-1.36	1.99/-3.59
Flack Parameter	0.085(16)	0.13(4)	0.16(4)

Table 3.4: Summary of SCXRD data.

Name	$[Zn_2(AlaPyr)(ValPyr)]$	$[Zn_2(AlaPyr)(PhePyr)]$	$[Zn_2(PhePyr)_3(ValPyr)_2]$
Empirical formula	$C_{16}H_{18}N_6O_6Zn_2$	$C_{20}H_{18}N_6O_6Zn_2$	$C_{28.8}H_{29.27}N_6O_6Zn_2$
Formula weight	521.10	569.14	686.19
Temperature/K	260.00	290.00	294.00
Crystal system	trigonal	trigonal	trigonal
Space group	R3	R3	R3
a/Å	29.2374(7)	29.789(2)	29.789(2)
b/Å	29.2374(7)	29.789(2)	29.789(2)
c/Å	10.1945(4)	10.2355(12)	10.2355(12)
α/°	90	90	90
β/°	90	90	90
γ/°	120	120	120
Volume/Å^3	7547.0(5)	7866.0(15)	7866.0(15)
Z	9	9	9
ρ_{calc}g/cm^3	1.032	1.081	1.304
μ/mm^{-1}	2.014	1.974	2.065
F(000)	2376.0	2592.0	3169.0
Crystal size/mm^3	0.95 × 0.27 × 0.15	0.27 × 0.26 × 0.17	0.27 × 0.2 × 0.09
Radiation	CuKα (λ = 1.54178)	CuKα (λ = 1.54178)	CuKα (λ = 1.54178)
Index ranges	$-35 \le h \le 34$, $-32 \le k \le 33$, $-11 \le l \le 12$	$-32 \le h \le 29$, $-32 \le k \le 32$, $-11 \le l \le 11$	$-33 \le h \le 32$, $-33 \le k \le 32$, $-11 \le l \le 11$
Reflections collected	18744	32152	19744
Independent reflections	5880 [R_{int} = 0.0573, R_{sigma} = 0.0612]	5007 [R_{int} = 0.0457, R_{sigma} = 0.0302]	5143 [R_{int} = 0.0715, R_{sigma} = 0.0618]
Data/restraints/ parameters	5880/4/264	5007/5/260	5143/272/323
Goodness-of-fit on F^2	1.060	1.118	1.005
2Θ range for data refinement/°	6.046 to 143.245	5.934 to 119.248	5.934 to 121.535
Final R indexes [I>=2σ (I)]	R_1 = 0.0791, wR_2 = 0.2273	R_1 = 0.0809, wR_2 = 0.2336	R_1 = 0.0807, wR_2 = 0.2200
Final R indexes [all data]	R_1 = 0.1116, wR_2 = 0.2612	R_1 = 0.0902, wR_2 = 0.2473	R_1 = 0.1002, wR_2 = 0.2434
Largest diff. peak/hole / e Å^{-3}	0.81/-0.91	0.80/-1.38	0.53/-0.69
Flack Parameter	0.08(2)	0.120(15)	0.20(2)

Chapter 4 MUF-77 using linkers functionalised with amino acids

4.1 Introduction

4.1.1 MUF-77, a quaternary multicomponent MOF

MUF-77 (Massey University Framework) is a quaternary multicomponent MOF, which is built from three chemically *distinct* carboxylate ligands and a Zn_4O SBU. When the ligands are functionalised with catalytically active groups, MUF-77 can act a heterogeneous, recyclable catalyst.[6] By introducing functional groups to the MUF-77 linkers, it is possible to modulate the pore environment and consequently influence the material's catalytic properties.[56]

4.1.2 MUF-77 synthetic methods

MUF-77, with the general formula $[Zn_4O(hxtt)_{4/3}(bpdc)_{1/2}(bdc)_{1/2}]$, where x denotes the alkyl substituents on the truxene methylene bridges (e.g., m for methyl, e for ethyl), can be synthesised via two distinct methods developed by our research group. The first method involves a solvothermal approach, in which the three ligands are dissolved along with $Zn(NO_3)_2$ and benzoic acid in DEF (**Figure 4.1**). Under the right required conditions, this method yields crystals with well-defined dodecahedral shape, typically reaching sizes of up to 0.5 mm. These crystals are transparent, which is indicative of good crystallinity. A transition to opacity generally signifies a loss of crystallinity.[5]

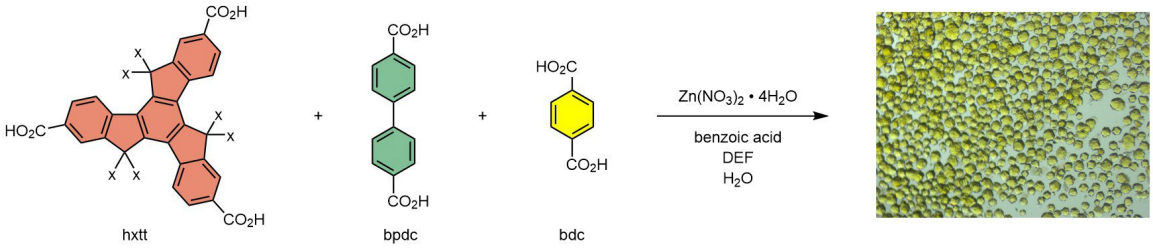

Figure 4.1: The general synthetic pathway for MUF-77 involves dissolving the tritopic linker with alkyl chain substituents (denoted as x), bpdc and bdc in DEF. The solution is then heated at 85 °C for 24 hours.

Crystal nucleation and growth are strongly influenced by both the concentration of benzoic acid, used as a modulator, and the reaction temperature. Increased amounts of benzoic acid slow down crystal growth, promoting better crystallinity, while elevated temperatures accelerate the crystallization process, often producing well-formed crystals within 1-2 hours. The optimal synthesis conditions were determined to be heating at 85 °C for 24 hours, yielding highly crystalline MUF-77 suitable for further applications.[5, 6]

The second method is a room-temperature synthesis in which $Zn(NO_3)_2$ is replaced with $Zn(OAc)_2$ as the metal source. In this procedure, the reaction is carried out in a 50:1 (v/v) DMF: water mixture, with the two linear linkers (bdc, and bpdc) used in a 1:1 ratio, and the tritopic linker added in 2.5 equivalents. Increasing the basicity under these conditions results in the rapid formation of small nanocrystals, with a size up to 500 µm, which is obtained within few minutes of synthesis.[59]

4.1.3 MUF-77 pore modulation

MUF-77 is assembled from three different linkers, each occupying a specific crystallographic position. The framework crystallises in the cubic space group Pm-3. Each Zn_4O SBU coordinates with four tritopic linkers in equatorial positions, while bdc and bpdc occupy the axial positions. The combination of SBUs and linkers results in two types of pores: mesopores, which measure 24 Å and 22 Å, and a micropore measuring 10 Å (**Figure 4.2**).

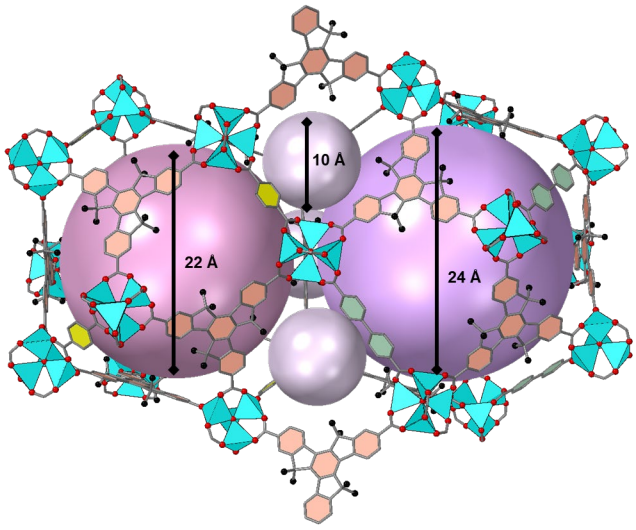

Figure 4.2: The tritopic linker (orange) and two ditopic linkers (green and yellow) coordinate with Zn_4O clusters to form the porous MUF-77 framework featuring two mesopores (24 Å and 22 Å) and one micropore (10 Å).

MUF-77 frameworks have a highly porous nature, with BET surface areas of up to 3600 m^2/g.[6] The framework porosity depends on the linker' functionalisation and the space they occupy in the pore. For example, changing the alkyl chain on the tritopic linkers from hexamethyl- to hexahexyl- or hexadecyl- truexene causes a drop in the BET surface area to 2170 and 1170 m^2/g, respectively. The high surface area of the framework lays the foundation for MUF-77 applications.

The isoreticular principle applies to MUF-77, where the ligands can be replaced with ones of the same size and geometry, or by functionalising the ligands with different functional groups. MUF-77 shows high stability in solvents, after solvent removal and at high temperatures, in comparison with other zinc-carboxylate MOFs. As MUF-77 is a multicomponent MOF, the precise linkers arrangements allow the pores properties tuning by functionalising each ligand (**Figure 4.3**).

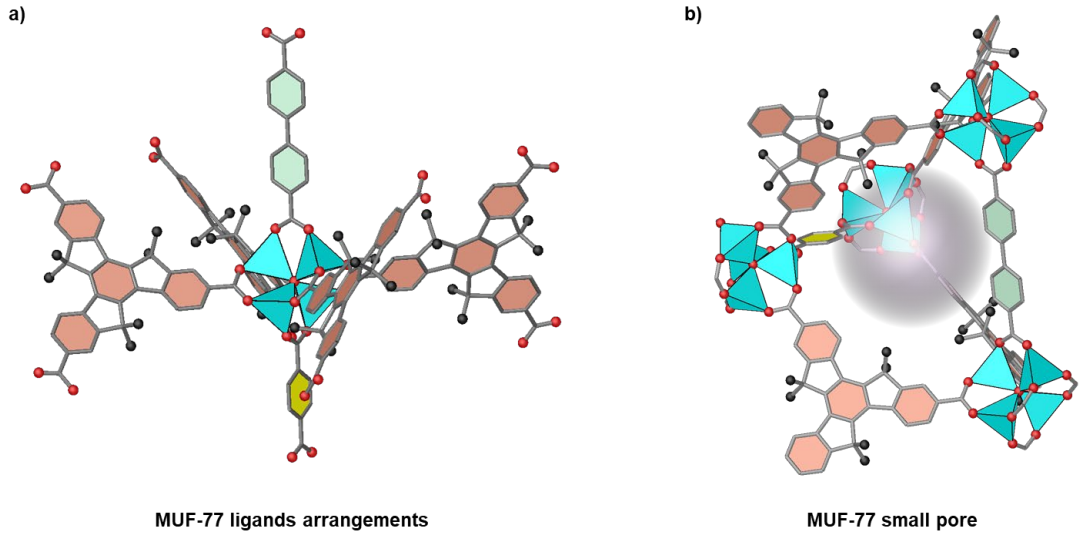

Figure 4.3: a) MUF-77 ligands arrangement in specific crystallographic positions. **b)** MUF-77 micropore showing the three different linkers at specific places.

Although multicomponent synthesis is challenging, MUF-77 synthetic methodology has been developed to favour this framework assembly from all three linkers, rather than other structures that might arise from one or two linkers. This approach enables precise MUF-77 pore characteristics modulation through the incorporation of various functionalised ligands in a highly predictable manner.

4.1.4 Catalysis using MUF-77 pore

Enzymes, nature's catalysts, have been known for centuries in applications such as using yeast in bread making and bacterial strains in cheese production. Enzymes are necessary tools in both research and industry.[157] Enzymes are especially important in stereoselective pharmaceutical production.[158, 159]

Enzymes are proteins that fold into complex 3D structures.[160] The region that is catalytically active is buried within the enzyme structure, and it is called the active site. This region is formed from a group of amino acids that work cooperatively to facilitate the chemical transformation. The active site is a selective microenvironment that allows the reactions to be carried out at fast rate and high stereoselectivity (enantiomeric excess ≥ 99.9%).[161-163]

Catalytic triads are a feature of the active site of some enzymes. An example is the combination of serine, histidine, and aspartic acid which found in serine proteases.[164] In these systems, the side chains of the three amino acids are oriented toward the active site pocket, where they are precisely positioned in a way to work cooperatively, with one acting as a nucleophile, one as a base, and the third to stabilize the charge or help in the charge transfer **(Figure 4.4)**.[165]

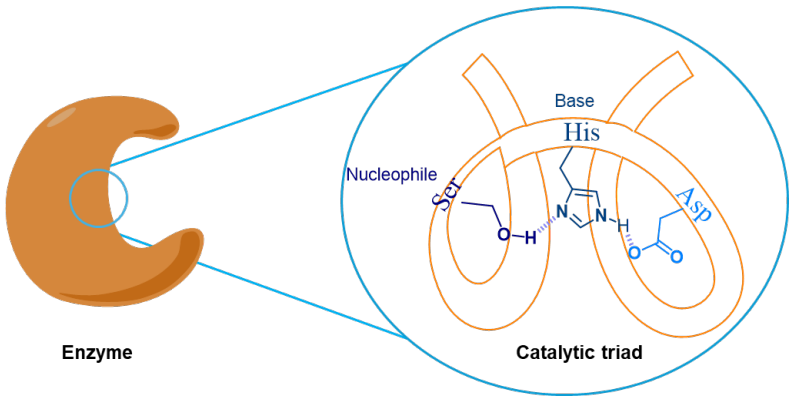

Figure 4.4: This cartoon illustrates how the catalytic triad is buried within the enzyme's structure. Although the three key amino acids are distant in the primary sequence, they come together in the folded protein to work cooperatively in catalysing the reaction. Each residue plays a distinct role: serine acts as the nucleophile, histidine functions as the base, and aspartic acid serves as the acid.

Catalytic triads may be replicated in synthetic materials. In the case of MUF-77, amino acid residues could be positioned so that their functional side chains point into the pore, mimicking the orientation and cooperation observed in enzymatic triads.

A key example of amino acid functionalisation in MUF-77 is the incorporation of proline, a naturally occurring amino acid and a widely studied chiral organocatalysts. Proline is not part of a catalytic dyad or triad; rather, it operates as a single catalytic residue, most notably via enamine and iminium ion mechanisms. Proline forms a cornerstone in organocatalysis.[166, 167] Proline was used in the early 1970s for the catalysis of the Hajos-Parrish-Eder-Sauer-Wiechert reaction, then the scope of the catalyst was broadened to other reactions including Mannich reaction,[168] α-amination of aldehydes,[169] and Michael addition.[170] Aldol reaction was then catalysed with proline with exceptionally high enantioselectivity of 95%.[171]

The Telfer group has functionalised the ditopic linkers with proline in the MUF-77 framework.[56] The bdc or bpdc linker was modified with proline and the resulting MOF was subsequently used to catalyse the aldol reaction with acetone (**Figure 4.5**). To modulate the pore chemical environment containing the catalyst, an additional modulating group was attached to the opposite ditopic linker. These modulators were achiral; increasing the size of these groups led to a decrease in both the reaction rate and enantiomeric excess (ee). This effect is attributed to increased pore filling, which impedes substrate flow into the pores. Control over the chemical environment near the catalyst significantly affects the product's enantiomeric excess.[56]

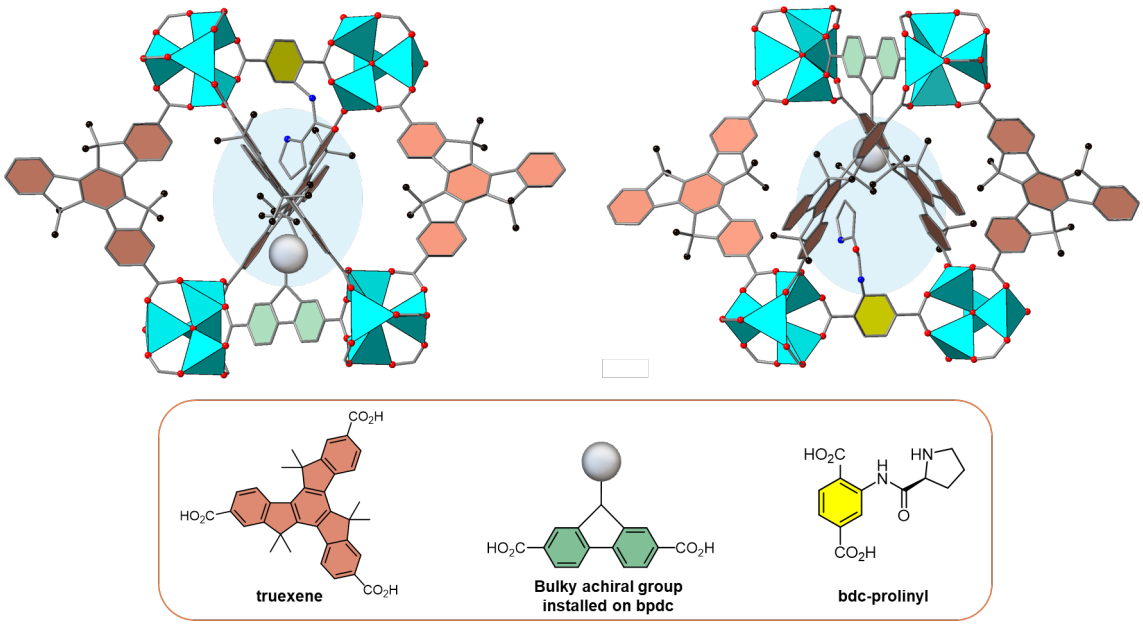

Figure 4.5: This graphical representation shows the two views of the small, micropore in MUF-77. The bdc linker (yellow) is functionalised with chiral, catalytically active proline, while the bpdc linker (green) bears a bulky achiral group (white sphere). These functional groups create a defined microenvironment within the pore, where the bulky group, positioned near the proline, can influence the catalytic reaction.

These results demonstrate that MUF-77 can serve not only as a scaffold for heterogeneous, recyclable catalysis, but also as a platform for designing enzyme-like catalytic sites with controlled geometry, sterics, and functionality.

The ligands developed in this study are inspired by the most efficient catalysts in nature, enzymes. Certain residues participate directly in the catalytic process, while others act as structural elements that influence the reaction outcome, for example, by controlling product enantioselectivity.[161, 173]

4.1.5 Functionalising MUF-77 linear linkers with amino acids

Building on the established synthesis and structural predictability of MUF-77, the second approach of this project focused on expanding its chemical functionality through the introduction of amino acid-derived side arms. This strategy retained the MUF-77 scaffold but incorporated new chemical functionality by grafting amino acids or amino alcohols onto the linear linkers using conventional organic synthesis techniques (**Figure 4.6**).

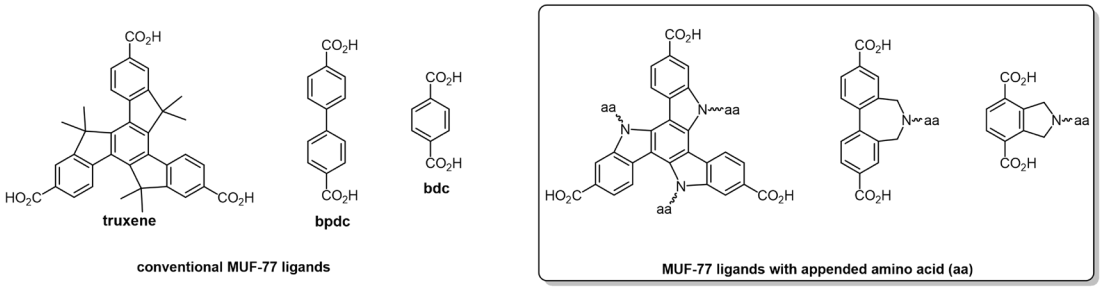

Figure 4.6: The three MUF-77 linkers can be functionalised with amino acids (aa) or its derivatives. The focus of this research was to functionalise the linear linkers (bdc/bpdc).

By positioning different functional groups at precise crystallographic sites, MUF-77 offers a unique opportunity to mimic this arrangement synthetically. For example, a lysine-derived amine could act as a nucleophile or base, while a nearby histidine mimic could serve as a general acid/base, reminiscent of the His-Lys dyad found in some hydrolases. Such multifunctional site design is difficult to achieve using small-molecule catalysts but becomes accessible through the modular assembly of multicomponent MOFs.

MUF-77's three linkers can be selectively functionalised with different amino acids or their derivatives (**Figure 4.6**). These functional groups are positioned along the internal pore surfaces in a predictable, ordered manner, allowing control over polarity, sterics, and hydrogen bonding interactions. This spatial precision facilitates the design of catalytic pockets, in which multiple residues may operate synergistically, potentially enabling biomimetic catalytic cycles within a robust, crystalline framework.

4.2 Results and discussion

4.2.1 Bdc functionalised with amino alcohols

A series of linkers was synthesised by appending amino acids to linear linkers (bdc/ bpdc). In this design, some appended amino acids possess intrinsic catalytic activity, whereas others do not; however, both types can function synergistically to facilitate reactions. Enantiopure amino acids and their derivatives are commercially available in a wide range and at relatively low cost, making them attractive building blocks for functionalised linker synthesis.

Attachment of amino acids or their derivatives to linear linkers was most effectively achieved via their amino functional group. However, the carboxyl group of the amino acid can compete with the carboxylate groups of the linkers for coordination to the metal centres. To minimise this competitive binding, the carboxyl group was either protected as a methyl ester or circumvented entirely by employing amino alcohols in place of amino acids.
This section focuses on the synthesis of bdc-based linkers functionalised with amino alcohols (**Figure 4.7.a**). These linkers were prepared in four sequential organic steps to afford a common backbone shared by all members of the family (**Figure 4.7.b**). In this synthetic route, the primary amine forms a symmetric five-membered ring attached to the bdc backbone, while the remaining portion of the amino alcohol projects outward from the aromatic core. This family of linkers is denoted ^{5}N-Bdc-X-OH, where "^{5}N" refers to the five-membered ring and "X-OH" specifies the amino alcohol incorporated. Details of the bdc backbone synthesis and general procedures are provided in **Appendix C**, while the synthesis of a representative ligand (^{5}N-bdc-Ala-OH) is described **4.4.1** section.

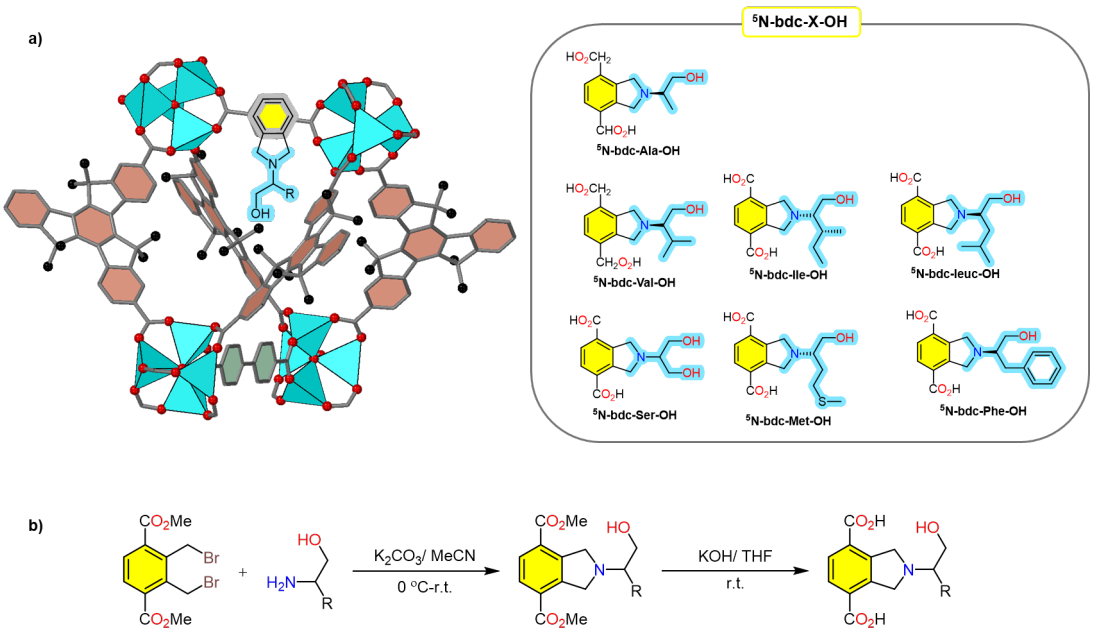

Figure 4.7: a) General synthetic route for preparing amino alcohol-functionalised bdc backbones. **b)** The tetrahedral pore of MUF-77, constructed from hmtt (tritopic truxene ligand), bpdc, and amino alcohol-functionalised bdc linkers. The novel amino alcohol-based ligands (^{5}N-bdc-X-OH) were incorporated alongside bpdc and hmtt to assemble MUF-77 frameworks.

^{5}N-Bdc-X-OH ligands family demonstrated limited thermal stability, undergoing decomposition at 85 °C over a 24 h period. This instability posed significant challenges for MOF synthesis. The issue was first identified during attempts to introduce these ligands into the MUF-77 framework using the solvothermal procedure previously reported by our group. Under these conditions, ligand incorporation was incomplete and declined further with increased heating duration. Prolonged residence in the oven not only reduced incorporation efficiency but also promoted the formation of decomposition products and other unidentified side-products. Consequently, the original solvothermal conditions were deemed unsuitable for the reliable integration of these ligands into MUF-77.

For example, when ^{5}N-bdc-Ser-OH was incorporated alongside H_3hmtt and H_2bpdc using the original MUF-77 solvothermal synthesis, ^{1}H NMR spectroscopic analysis of the digested crystals revealed that the integration value for ^{5}N-bdc-Ser-OH was reduced by approximately 30% relative to the expected ratio. Furthermore, additional peaks appeared in the aromatic region, consistent with the presence of decomposed bdc-derived species (**Figure 4.8**). This suggests that partial degradation of the functionalised linker occurred under the solvothermal conditions, with the resulting fragments incorporated into the framework in place of the desired parent bdc linker.

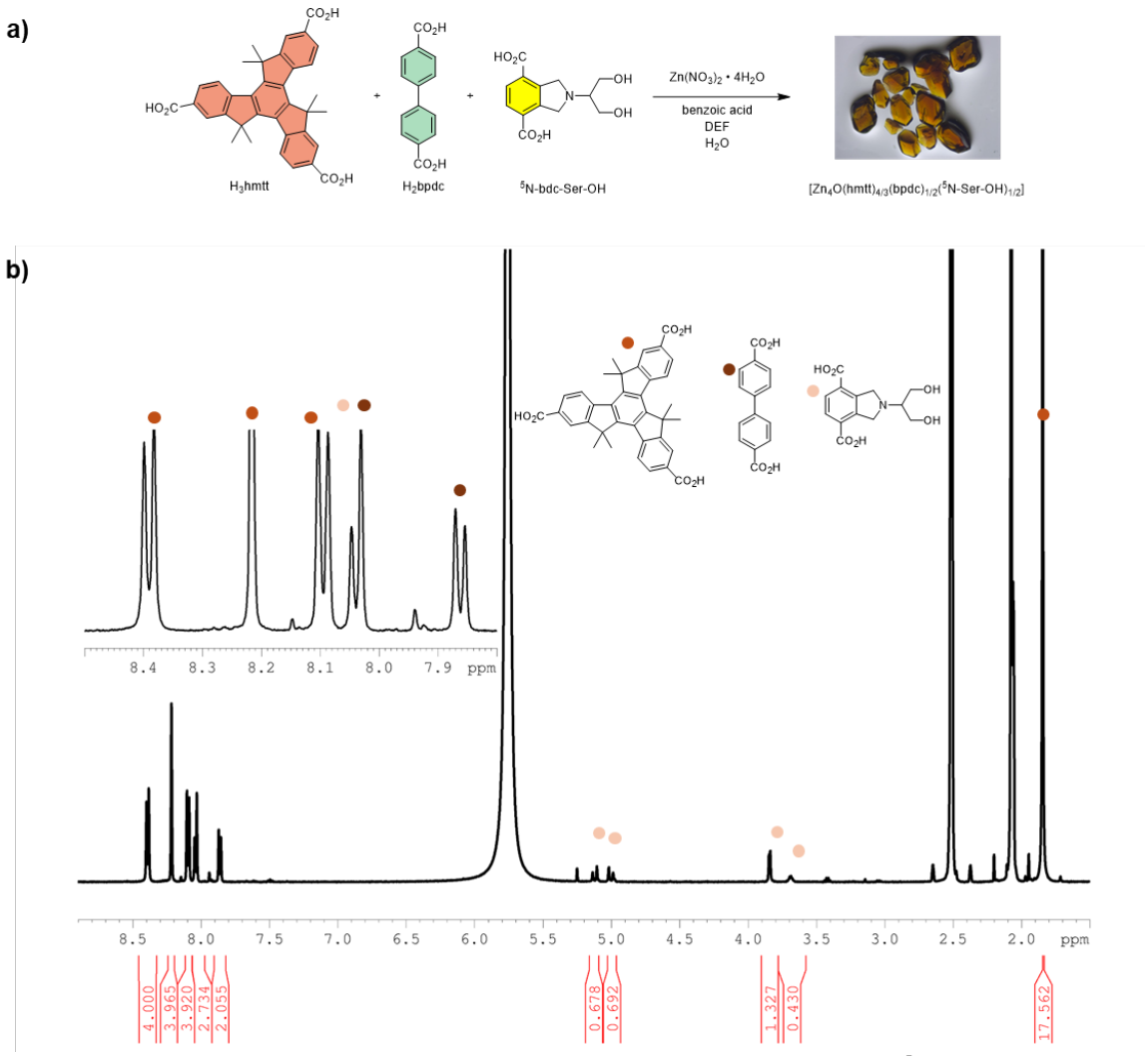

Figure 4.8 a) The original solvothermal synthetic pathway by which ^{5}N-bdc-Ser-OH was incorporated into MUF-77 **b)** ^{1}H NMR spectrum analysis of digested MUF-77 crystals in DCl/DMSO-d_6 (23 µL/1 mL), in which ^{5}N-bdc-Ser-OH was incorporated alongside other ligands using the original MUF-77 solvothermal procedure, revealed that the integration of ^{5}N-bdc-Ser-OH was reduced by approximately 30%.

To investigate this instability further, one representative ligand, ^{5}N-bdc-Ser-OH, was selected for thermogravimetric analysis (TGA), as all ligands in this series exhibited similar incorporation issues. This ligand was chosen based on its higher synthetic yield. To mimic synthesis-relevant conditions, the ligand was subjected to an isothermal hold at 100 °C. Only a minor mass loss was detected, which can be attributed primarily to the evaporation of residual moisture.

However, the temperature may still influence ligand stability in the presence of additional factors such as Zn(II) ions, benzoic acid, and the reaction solvent. To address this, the strategy was to shorten the reaction time. Several modifications to the synthetic procedure were explored, including increasing the proportion of H_2O, reducing the amount of benzoic acid, and pre-deprotonating the ligand with a weak base.

Several modifications were done to the solvothermal procedure and were evaluated with the aim of reducing the reaction time. Increasing the proportion of H_2O relative to DEF was initially tested, as higher water content can sometimes accelerate coordination and crystals growth. However, this adjustment prolonged the crystallisation time, and in some cases, completely inhibited MUF-77 crystals formation.

Benzoic acid is a modulator that control the crystals growth, so benzoic acid removal can accelerate the crystals growth. However, benzoic acid removal unexpectedly inhibited MUF-77 crystal growth.

Finally, triethylamine (2.5 eq, relative to the functionalised ligand) was added to the ligand solution immediately before synthesis. This modification markedly accelerated crystallisation, with visible MUF-77 crystals forming within 30 min of heating at 85 °C. The resulting crystals were analysed by PXRD, which confirmed phase purity, and by ^{1}H NMR spectroscopy of digested samples, which verified incorporation of the functionalised linker.

To confirm structural consistency, the experimental PXRD pattern of MUF-77 synthesised from H_3hmtt, H_2bpdc, and ^{5}N-bdc-X-OH was compared to the calculated PXRD pattern of the parent MUF-77. For example, the framework $[Zn_4O(hmtt)_{4/3}(bpdc)_{1/2}(^5N\text{-bdc-Ser-OH})_{1/2}]$ was successfully synthesised using this modified procedure (**Figure 4.9.a**). The experimental PXRD pattern was consistent with the calculated parent MUF-77 pattern, showing no additional reflections and confirming that the bulk sample retained the intended MUF-77 topology without the formation of side products (**Figure 4.9.b**).

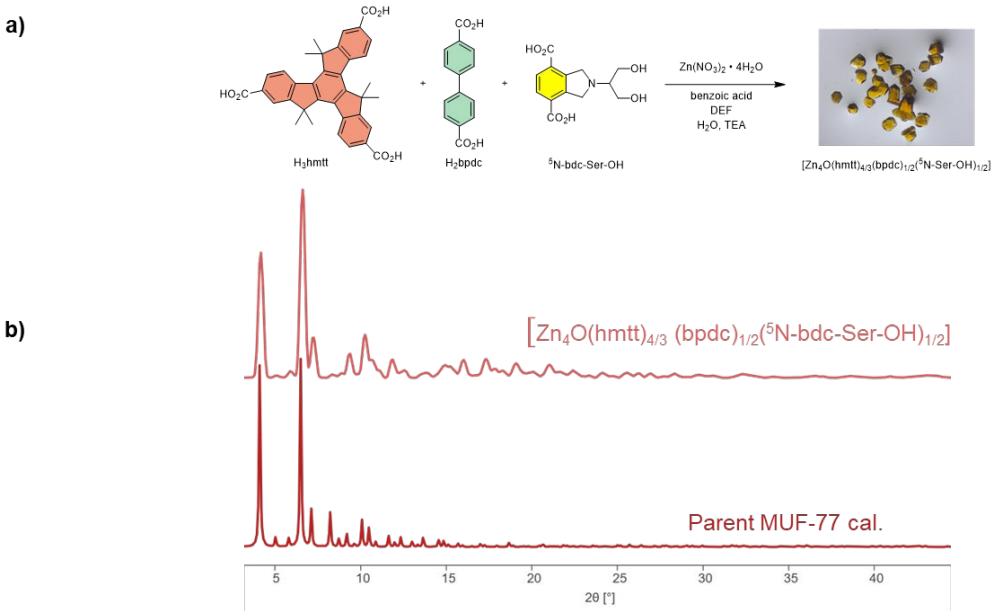

Figure 4.9: a) Synthesis pathway of $[Zn_4O(hmtt)_{4/3}(bpdc)_{1/2}(^5N\text{-Ser-OH})_{1/2}]$ using the slightly modified MUF-77 synthesis procedure.
b) $[Zn_4O(hmtt)_{4/3}(bpdc)_{1/2}(^5N\text{-Ser-OH})_{1/2}]$ experimental PXRD compared to the calculated PXRD pattern.

The crystals were then washed thoroughly with acetone (x 5, 0.5 mL) and dried under high vacuum prior to further analysis. ^{1}H NMR spectroscopy was performed on digested samples in (DCl/DMSO-d_6, 23 µL/1 mL). Signal integration was carried out according to the reference MUF-77 formula $[Zn_4O(hxtt)_{4/3}(bpdc)_{1/2}(bdc)_{1/2}]$ (**4.4.6**). In the case of the ^{5}N-bdc-Ser-OH containing MUF-77, the aromatic signal for the functionalised bdc linker integrated to 1H, in excellent agreement with the theoretical value (**Figure 4.10**). This analysis demonstrates that the modified synthesis procedure enabled the incorporation of the intact ^{5}N-bdc-Ser-OH ligand in the expected stoichiometric ratio while maintaining the overall structural topology of MUF-77.

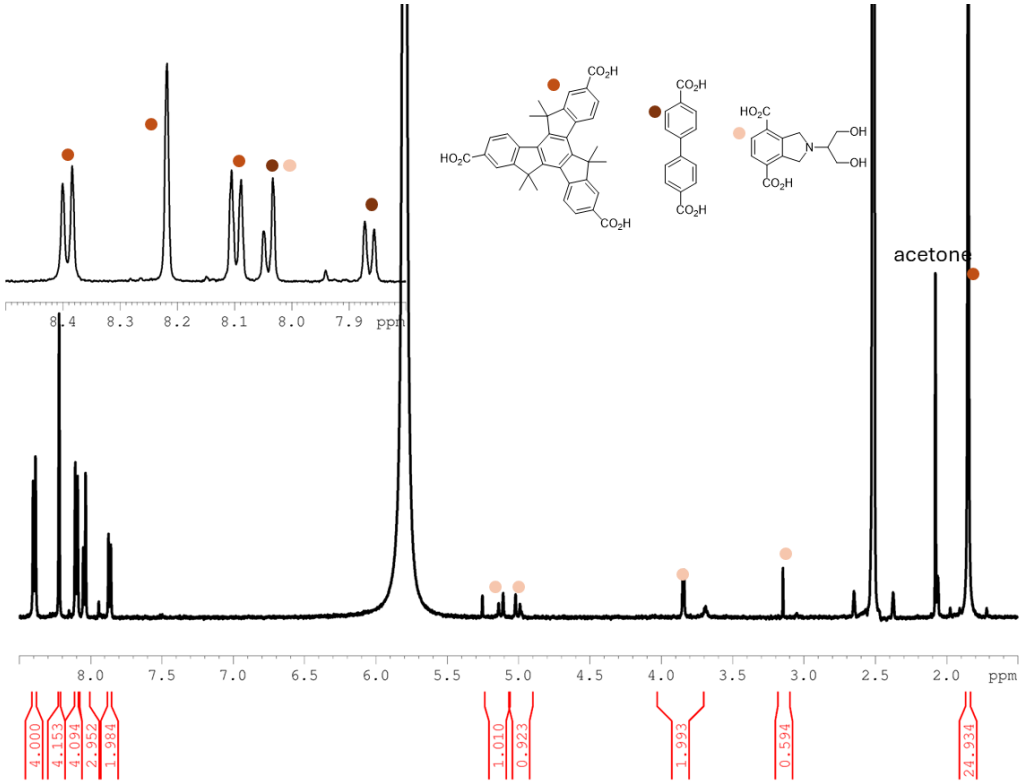

Figure 4.10: ^{1}H NMR spectrum of digested $[Zn_4O(hmtt)_{4/3}(bpdc)_{1/2}(^{5}N\text{-}Ser\text{-}OH)_{1/2}]$ crystals in DCl/DMSO-d_6 (23 µL/1 mL), in which ^{5}N-bdc-Ser-OH was incorporated alongside other ligands using the slightly modified MUF-77 solvothermal procedure.

4.2.2 General overview of bdc-based amino alcohol linkers (L1–L7)

All seven amino alcohol-functionalised bdc linkers (**L1–L7**) were incorporated into the MUF-77 framework using a modified solvothermal procedure. Each linker was combined with H_2bpdc, H_3hmtt, $Zn(NO_3)_2 \cdot 4H_2O$, and benzoic acid in DEF. The reaction conditions were slightly adjusted to reduce reaction time and to preserve the five-membered ring integrity of the functional groups. TEA was used to promote crystal growth and shorten the reaction time.

Each resulting MOF exhibited the general formula $[Zn_4O(hmtt)_{4/3}(\mathbf{L})_{1/2}(bpdc)_{1/2}]$, confirmed by PXRD and SCXRD.

In crystallography, positional disorder arises when atoms or groups of atoms do not occupy a single, well-defined position but instead are distributed over two or more alternative sites within the crystal lattice. As a result, the electron density for such atoms is not localised to one position, but appears smeared or split across multiple locations, reflecting that these atoms occupy different positions in different unit cells.[174, 175]

There are two types of positional disorder, which can be static or dynamic. In static disorder, atoms are in one of several possible positions, so the diffraction pattern represents an average over these fixed positions across the crystal. In contrast, dynamic disorder occurs when atoms move rapidly between alternative sites due to thermal motion. Distinguishing between the two typically needs temperature-dependent measurements: a reduction in atomic displacement parameters upon cooling suggests dynamic behaviour, whereas unchanged disorder indicates a static origin.[177, 178]

SCXRD unambiguously established the connectivity of the framework in $[Zn_4O(hmtt)_{4/3}(bpdc)_{1/2}(L)_{1/2}]$, with all carboxylate groups from hmtt, bpdc, and ^{5}N-bdc-X-OH linkers coordinating to Zn(II) centres as expected.

Refinement suggested positional disorder, partly imposed by the crystallographic symmetry at the bdc site, which requires the side group to be distributed over two equivalent orientations. Additional disorder likely arises from (i) rotational motion of the bdc linker about its long axis and (ii) flexibility of the serine moiety itself. Bdc and CH_2 group of the ring are disordered over two positions with partial occupancy of ~0.5, while the pendant side chains are disordered over four positions with partial occupancy of ~0.25. This type of positional disorder is commonly observed in flexible side chains of amino acid-derived ligands, where multiple orientations are averaged in the crystal lattice.

The chemical presence of the alanyl, valinyl, iso-leucinyl, leucinyl, serinyl, and methioninyl functionalities was instead confirmed by acid digestion of the MOFs in DCl/DMSO-d_6 (23 µL/ 1 mL) followed by ^{1}H NMR spectroscopy, which clearly verified the incorporation of these residues despite their crystallographic disorder.

The MUF-77 topology was retained in all cases, as demonstrated by both SCXRD and PXRD analyses. The calculated PXRD patterns matched well with the experimental data, confirming structural consistency across the series (**Figure 4.44**).

4.2.2.1 $[Zn_4O(hmtt)_{4/3}(bpdc)_{1/2}(^5N\text{-bdc-Ala-OH})_{1/2}]$

^{5}N-bdc-Ala-OH linker (**L1**) was synthesised using the general synthetic procedure (**Figure 4.7**) mentioned above. **L1** was incorporated into MUF-77 framework, to give cubic crystals with a good yield (**Figure 4.11**).

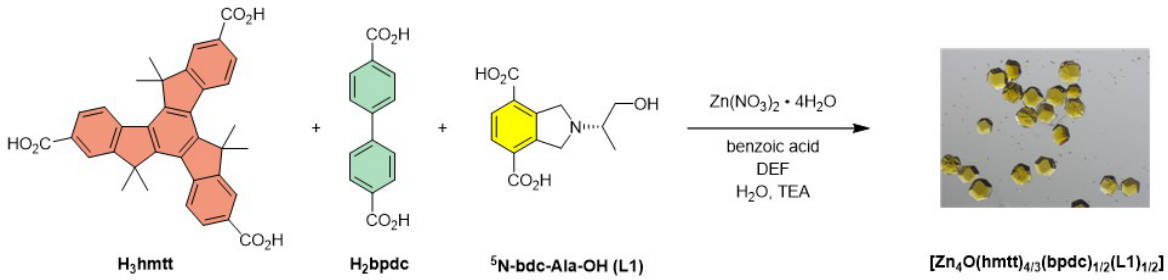

Figure 4.11: Synthetic pathway to $[Zn_4O(hmtt)_{4/3}(bpdc)_{1/2}(^5N\text{-bdc-Ala-OH})_{1/2}]$ using the modified synthesis procedure.

The phase purity of $[Zn_4O(hmtt)_{4/3}(bpdc)_{1/2}(\mathbf{L1})_{1/2}]$ was confirmed by the agreement between its experimental PXRD pattern and the reported calculated pattern,[5] with no additional reflections observed (**Figure 4.44**). Furthermore, ^{1}H NMR spectroscopy of digested crystals in DCl/DMSO-d_6 (23 µL/1 mL), verified the integrity of the ligands (**Figure 4.46**).

The resulting structure retains the topology and the characteristic pore architecture of the MUF-77 family, comprising one micropore and two mesopores. The micropore is tetrahedral in shape and is formed by the intersection of four tritopic hmtt linkers, which bridge between one **L1** and one bpdc linker positioned opposite each other. The larger dodecahedral mesopores are assembled by eight hmtt linkers connected to six linear linkers arranged in opposing pairs. In this variant, the shorter **L1** linker produces slightly smaller mesopores compared to those built entirely with bpdc, due to its reduced length (**Figure 4.12**).

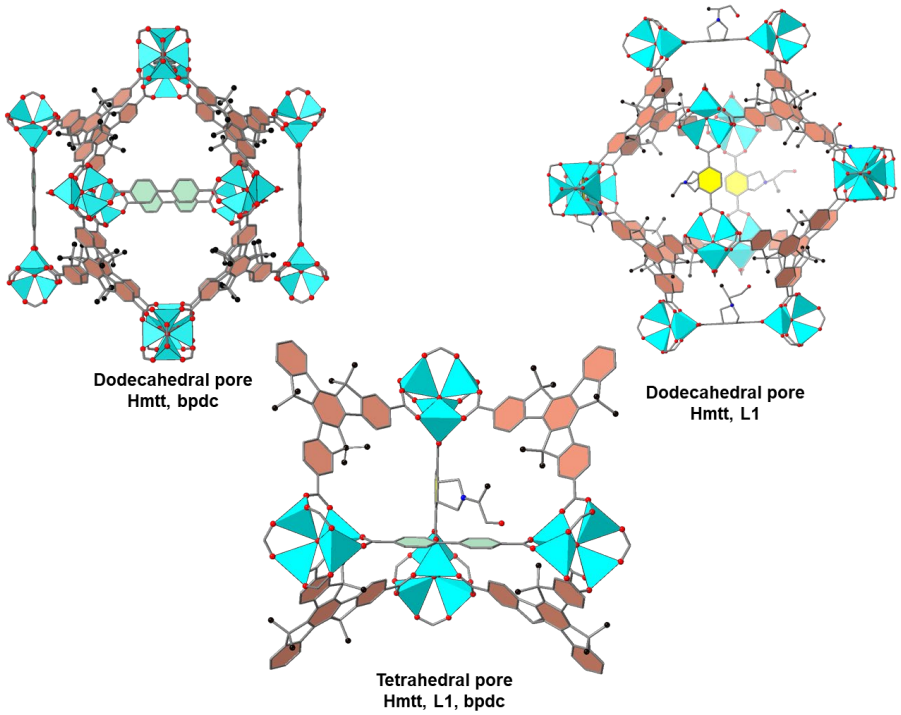

Figure 4.12: This graphical representation shows the pore structure specific to this material, showing **L1** functionalised with *l*-alaninol groups. The alanyl side chain could not be directly resolved via SCXRD due to positional disorder, but its presence was proved by ^{1}H NMR spectroscopy.

4.2.2.2 $[Zn_4O(hmtt)_{4/3}(bpdc)_{1/2}(^5N\text{-bdc-Val-OH})_{1/2}]$

^{5}N-bdc-Val-OH linker (**L2**) was synthesised using the general synthetic procedure (**Figure 4.7**) mentioned above. Then, **L2** was placed into MUF-77 framework (**Figure 4.13**).

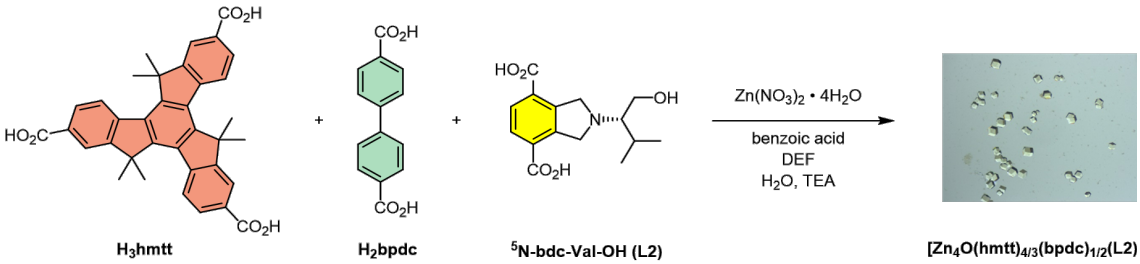

Figure 4.13: Synthetic pathway to $[Zn_4O(hmtt)_{4/3}(bpdc)_{1/2}(^5N\text{-bdc-Val-OH})_{1/2}]$ using the modified synthesis procedure.

The phase purity of $[Zn_4O(hmtt)_{4/3}(bpdc)_{1/2}(\mathbf{L2})_{1/2}]$ was confirmed by the agreement between its experimental PXRD pattern and the reported calculated pattern of the parent MUF-77 (**Figure 4.44**). In addition, ^{1}H NMR spectroscopy of digested crystals in DCl/DMSO-d_6 (23 µL/1 mL) verified the integrity of the ligands (**Figure C.65**).

The overall framework retains the characteristic MUF-77 topology, including the three distinct pore types previously described. As with **L1**, the use of a shorter bdc-type linker alongside bpdc results in slightly asymmetric mesopore sizes. The pore structure specific to this variant, where **L2** introduces a branched valinyl group, offering a different steric profile compared to the methyl group of **L1**. This subtle variation may influence the local pore environment or guest interactions (**Figure 4.14**).

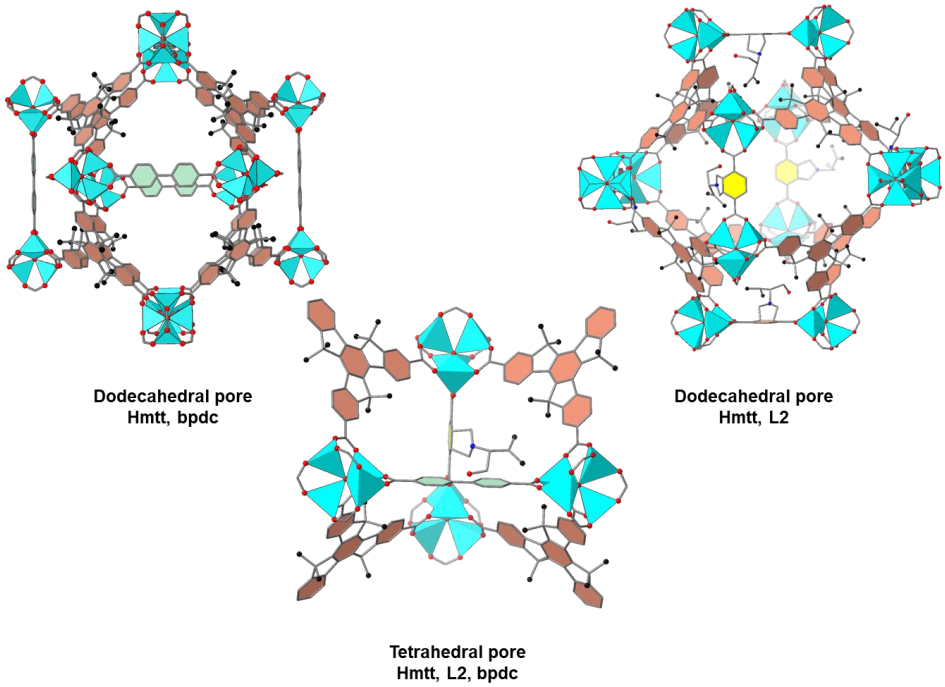

Figure 4.14: This graphical representation shows the pore structure specific to this material, showing **L2** functionalised with *l*-valinol groups. The valinyl side chain could not be directly resolved via SCXRD due to positional disorder, but its presence was proved by ^{1}H NMR spectroscopy. The valinyl side chain alters the local chemical environment within the pores, potentially enabling hydrogen bonding or catalytic activity. This modification introduces unique chemical functionality without altering the overall framework topology.

4.2.2.3 $[Zn_4O(hmtt)_{4/3}(bpdc)_{1/2}(^{5}N\text{-bdc-Leu-OH})_{1/2}]$

^{5}N-bdc-Leu-OH linker (**L3**) was synthesised using the general synthetic procedure (**Figure 4.7**) mentioned above. Then, **L3** was incorporated into MUF-77 framework (**Figure 4.15**).

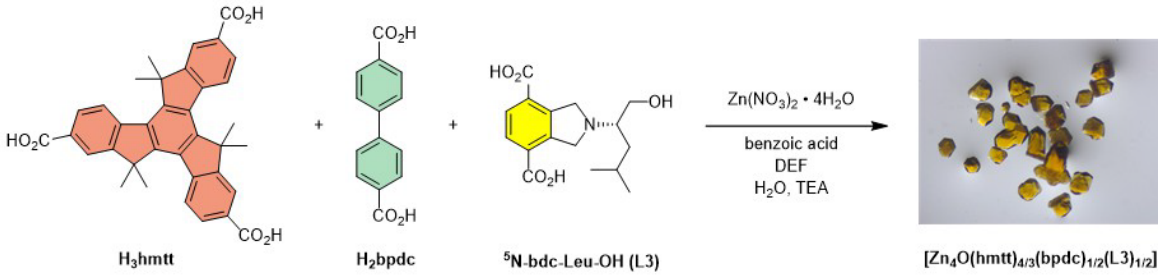

Figure 4.15: The synthetic pathway to $[Zn_4O(hmtt)_{4/3}(bpdc)_{1/2}(^{5}N\text{-bdc-Leu-OH})_{1/2}]$ using the modified synthesis procedure.

The phase purity of the framework with the general formula $[Zn_4O(hmtt)_{4/3}(bpdc)_{1/2}(\mathbf{L3})_{1/2}]$ was confirmed by the agreement between its experimental PXRD pattern and the calculated PXRD pattern of the reported parent MUF-77 (**Figure 4.44**). Furthermore, ^{1}H NMR spectroscopy of digested crystals in DCl/DMSO-d_6 verified the integrity of the ligands and further supports the crystals phase purity (**Figure C.66**).

Coordination of the doubly deprotonated **L3** linker to the Zn(II) centres occur via carboxylate oxygens, alongside the co-linkers bpdc and hmtt (**Figure 4.16**). As observed with other amino alcohol-functionalised bdc linkers in this series, the leucyl side chain of **L3** could not be resolved in the crystal structure due to positional disorder.

The framework adopts the established MUF-77 topology, comprising one tetrahedral micropore and two dodecahedral mesopores, with the latter formed by eight tritopic hmtt linkers and six linear linkers (either **L3** or bpdc). The pore structure (**Figure 4.16**), which include of the branched, hydrophobic leucinyl group, subtly alters the internal pore environment while preserving the overall connectivity.

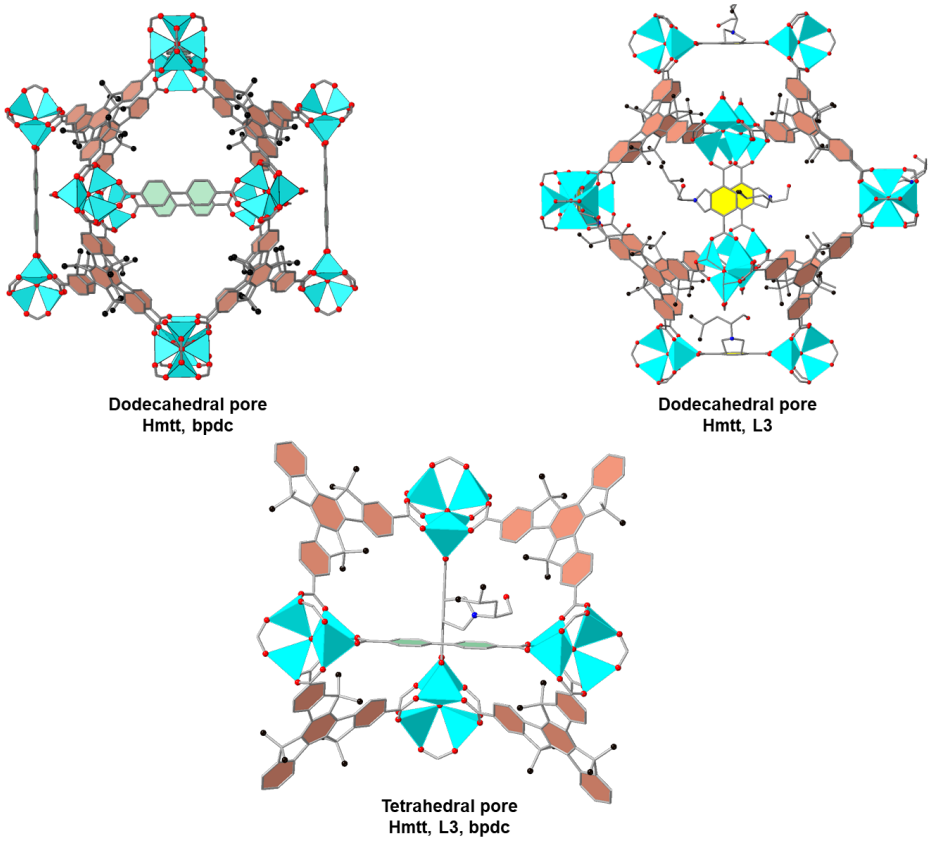

Figure 4.16: This graphical representation shows the pore structure specific to this material, showing **L3** functionalised with *l*-leucinol groups. The leucinyl side chain could not be directly resolved via SCXRD due to positional disorder, but its presence was confirmed by ^{1}H NMR spectroscopy of the acid-digested MUF-77 crystals.

4.2.2.4 $[Zn_4O(hmtt)_{4/3}(bpdc)_{1/2}(^5N\text{-bdc-Ile-OH})_{1/2}]$

^{5}N-bdc-Ile-OH linker (**L4**) was synthesised using the general synthetic procedure (**Figure 4.7**) mentioned above. **L4** was incorporated into MUF-77 framework by solvothermal synthesis where **L4**, H_2bpdc and H_3hmtt were dissolved along with $Zn(NO_3)_2$, benzoic acid and TEA in DEF (**Figure 4.17**).

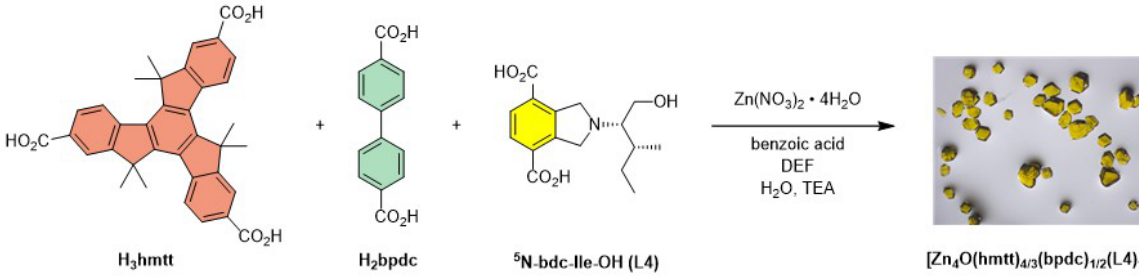

Figure 4.17: Synthetic pathway to $[Zn_4O(hmtt)_{4/3}(bpdc)_{1/2}(^5N\text{-bdc-Ile-OH})_{1/2}]$ using the modified synthesis procedure.

The phase purity of the framework with the general formula $[Zn_4O(hmtt)_{4/3}\ (bpdc)_{1/2}(\mathbf{L4})_{1/2}]$ was confirmed, consistent with the previously described materials, by PXRD (**Figure 4.44**) and ^{1}H NMR (**Figure C.67**).

The overall framework retains the characteristic MUF-77 topology, including the three distinct pore types previously described. As with the previous ligands, the use of a shorter bdc-type linker alongside bpdc results in slightly asymmetric mesopore sizes. The pore structure specific to this variant, where **L4** introduces a branched iso-leucinyl group, offering a different steric profile compared to the methyl group of **L1** and valyl group of **L2** (**Figure 4.18**).

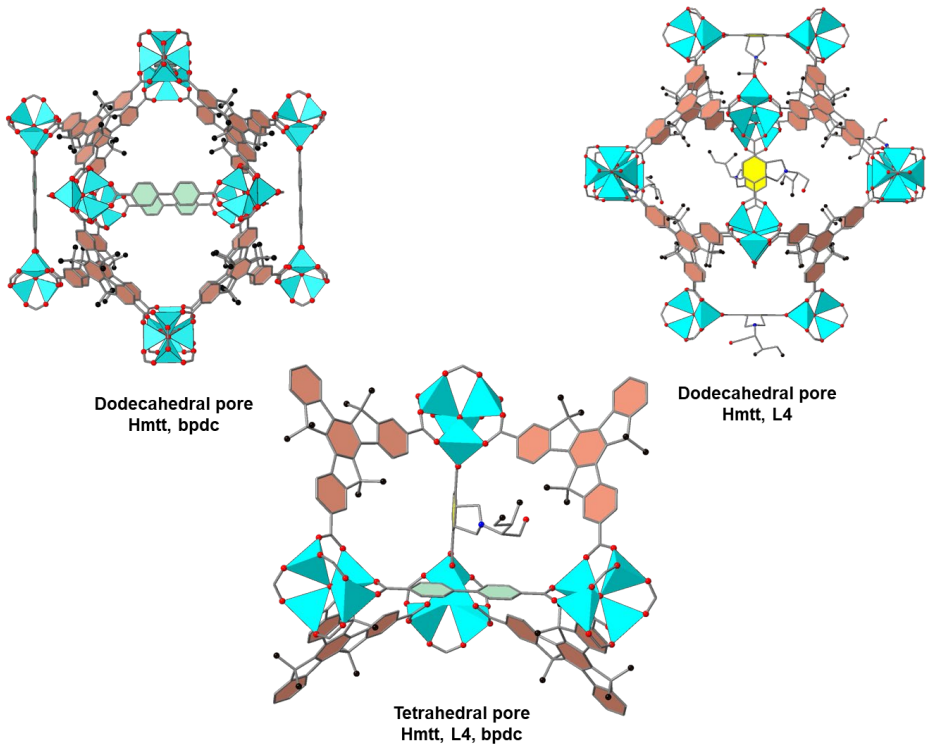

Figure 4.18: This graphical representation shows the pore structure specific to this material, showing **L4** functionalised with *l*-isoleucinol groups. The isoleucinyl side chain could not be directly resolved via SCXRD due to positional disorder, but its presence was confirmed by ^{1}H NMR spectroscopy of the acid-digested MUF-77 crystals.

4.2.2.5 [$Zn_4O(hmtt)_{4/3}(bpdc)_{1/2}(^5$N-bdc-Ser-OH$)_{1/2}$]

^{5}N-bdc-Ser-OH linker (**L5**) was synthesised using the general synthetic procedure (**Figure 4.7**) mentioned above. Then, **L5** was incorporated into MUF-77 framework (**Figure 4.19**).

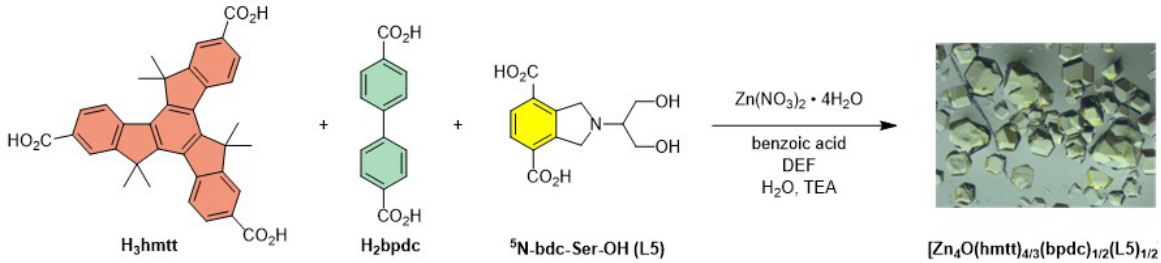

Figure 4.19: Synthetic pathway to [$Zn_4O(hmtt)_{4/3}(bpdc)_{1/2}(^5$N-bdc-Ser-OH$)_{1/2}$] using the modified synthesis procedure.

Phase purity of the resulting material was confirmed by PXRD analysis (**Figure 4.44**), which showed good agreement with the simulated pattern of the MUF-77 architecture, consistent with successful incorporation of **L5** into the framework proved by ^{1}H NMR (**Figure C.68**).

The resulting framework retains the characteristic MUF-77 architecture, comprising one micropore and two mesopores formed by combinations of tritopic hmtt and linear linkers.

The pore structure of MUF-77 is modified with **L5**, where the presence of a polar hydroxymethyl side chain (from serinol) introduces a distinct local chemical environment within the pores (**Figure 4.20**).

Although the hydroxyl-containing side chain of **L5** could not be resolved in the SCXRD model due to positional disorder, refined to an occupancy of ~0.25, its incorporation is supported by ^{1}H NMR spectroscopy after acid digestion in DCl/DMSO-d_6 (23 µL/ 1ml) (**Figure 4.10**). The introduction of a hydrophilic functional group into the pore walls has the potential to enhance hydrogen bonding with guest molecules, distinguishing this framework from its hydrophobic and less polar analogues.

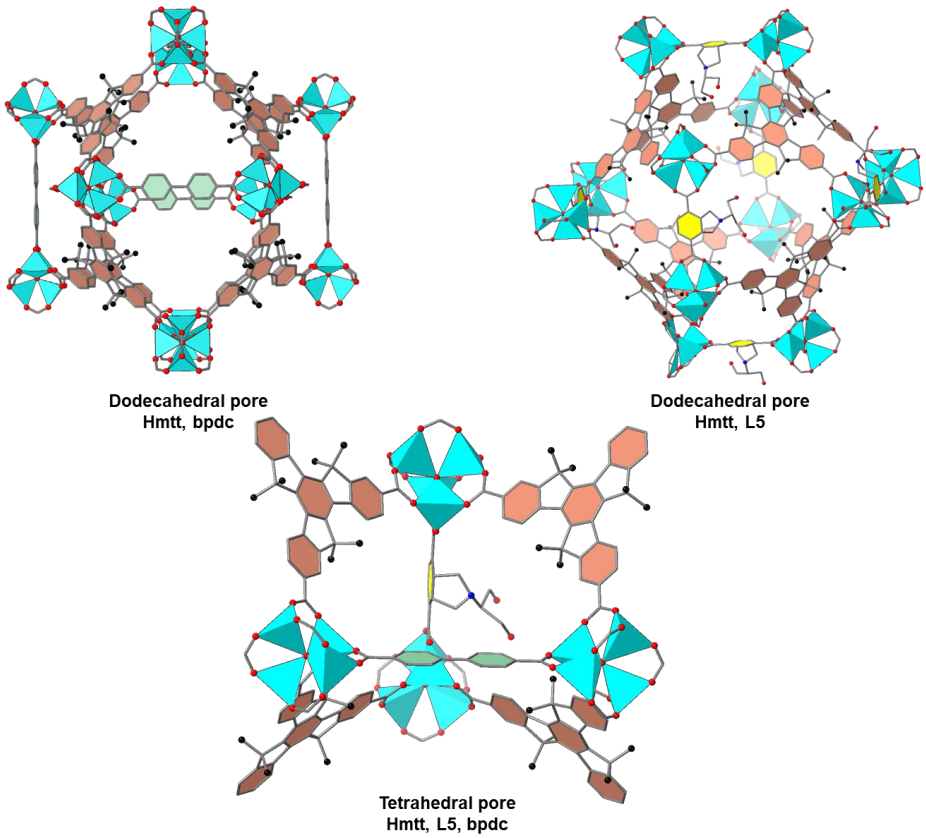

Figure 4.20: This graphical representation shows the pore structure specific to this material, showing **L5** functionalised with serinol groups. The serinyl side chain could not be directly resolved via SCXRD due to positional disorder, but its presence was confirmed by ^{1}H NMR spectroscopy of the acid-digested MUF-77 crystals.

4.2.2.6 $[Zn_4O(hmtt)_{4/3}(bpdc)_{1/2}(^5N\text{-bdc-Met-OH})_{1/2}]$

^{5}N-bdc-Met-OH linker (**L6**) was synthesised using the general synthetic procedure (**Figure 4.7**) mentioned above. Then, **L6** was incorporated into MUF-77 framework (**Figure 4.21**).

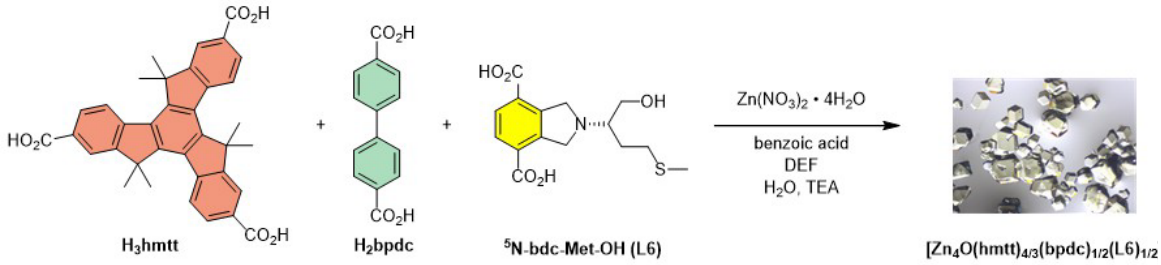

Figure 4.21: Synthetic pathway to $[Zn_4O(hmtt)_{4/3}(bpdc)_{1/2}(^5N\text{-bdc-Met-OH})_{1/2}]$ using the modified synthesis procedure.

As with other members of this series, the resulting material adopts the characteristic MUF-77 topology, comprising one micropore and two mesopores formed by the combination of tritopic and linear linkers (**Figure 4.22**).

The framework composition and phase purity were confirmed by PXRD (**Figure 4.44**) and ^{1}H NMR spectroscopy following acid digestion (**Figure C.69**). The methioninol-derived side chain of **L6**, containing a thioether functional group, could not be resolved in the SCXRD data due to positional disorder. The pore structure of MUF-77 was modified with **L6**, where the sulfur-containing side chain introduces a weakly polar environment within the pore channels, offering opportunities for soft donor interactions with guest species (**Figure 4.22**).

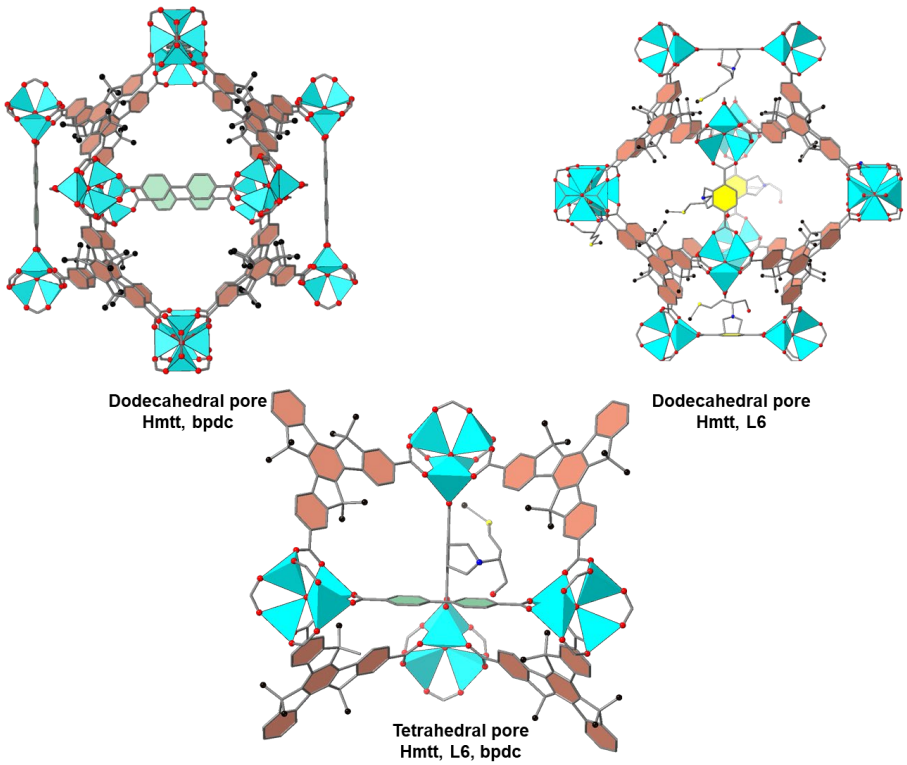

Figure 4.22: This graphical representation shows the pore structure specific to this material, showing **L6** functionalised with *l*-methioninol groups. The methioninyl side chain could not be directly resolved via SCXRD due to positional disorder, but its presence was confirmed by ^{1}H NMR spectroscopy of the acid-digested MUF-77 crystals.

4.2.2.7 $[Zn_4O(hmtt)_{4/3}(bpdc)_{1/2}(^5N\text{-bdc-Phe-OH})_{1/2}]$

^{5}N-bdc-Phe-OH linker (**L7**) was synthesised using the general synthetic procedure (**Figure 4.7**) mentioned above. Then, **L7** was incorporated into the MUF-77 framework (**Figure 4.23**).

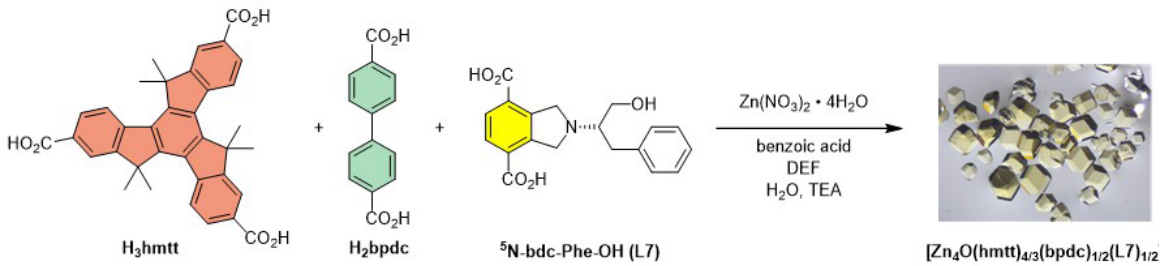

Figure 4.23: Synthetic pathway to $[Zn_4O(hmtt)_{4/3}(bpdc)_{1/2}(^5N\text{-bdc-Phe-OH})_{1/2}]$ using the modified synthesis procedure.

Phase purity of the material was confirmed by PXRD analysis (**Figure 4.44**), which showed good agreement with the simulated pattern of the MUF-77 structure. As with other variants, the resulting material adopts the standard MUF-77 topology, comprising micropores and two types of mesopores constructed from hmtt and linear linkers. The phenyl-bearing side chain of **L7** could not be resolved by SCXRD due to positional disorder, but its presence was confirmed by ^{1}H NMR spectroscopy of the acid digested crystals (**Figure C.70**).

The pore environment of MUF-77 modified with **L7**, where the bulky, aromatic phenyl side chain introduces enhanced hydrophobicity and potential π-interactions within the pore (**Figure 4.24**).

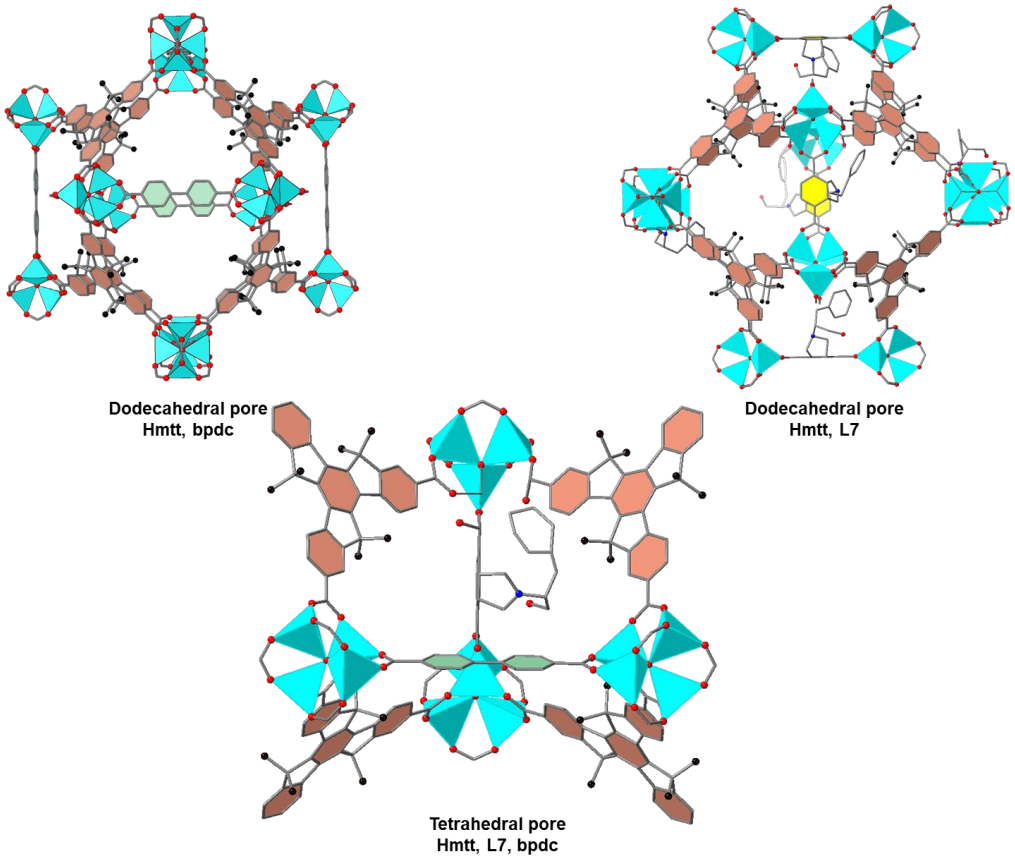

Figure 4.24: This graphical representation shows the pore structure specific to this material, showing **L7** functionalised with *l*-phenylalaninol groups. The phenylalaninyl side chain could not be directly resolved via SCXRD due to positional disorder, but its presence was confirmed by ^{1}H NMR spectroscopy of the acid-digested MUF-77 crystals.

4.2.3 Bpdc functionalised with amino acids

The second family of linkers developed in this study is based on the other linear linker, bpdc, functionalised with amino acids whose carboxyl groups are protected as methyl esters (**Figure 4.25.a)**. This design allows the incorporation of catalytically relevant amino acid side chains while preventing the free carboxyl group from competing with the linker's carboxylate functionalities for coordination to the metal nodes. The methyl ester protection also enhances synthetic compatibility during linker preparation and ensures retention of the amino acid's structural integrity throughout MOF assembly.

In enzymes, amino acids with diverse side chains contribute to the cooperative environment of the active site, influencing both catalytic activity and substrate recognition. Inspired by this principle, the bpdc-based linkers were designed to present amino acid residues into the pore space, where they could interact with guest molecules either through direct participation in catalysis or through secondary interactions that modulate reaction pathways and selectivity.

These linkers were synthesised through a stepwise functionalisation of O^{t}Bu-bpdc, in which the amine of the amino acid methyl ester was coupled to one end of the biphenyl backbone, then cyclise to form seven-membered-N-ring, leaving the protected carboxyl intact (**Figure 4.25.a**). The resulting materials share a common biphenyl scaffold but differ in the identity of the appended amino acid side chain (**Figure 4.25.b**), enabling systematic tuning of pore polarity, hydrophobicity, and potential catalytic properties. This family is denoted ^{7}N-bpdc-X, where "X" specifies the amino acid residue that has been incorporated (**Figure 4.25**). Details of the bpdc backbone synthesis and linkers general procedures are provided in **Appendix C**, while the synthesis of a representative ligand (^{7}N-bpdc-Ala) is described **4.4.1** section.

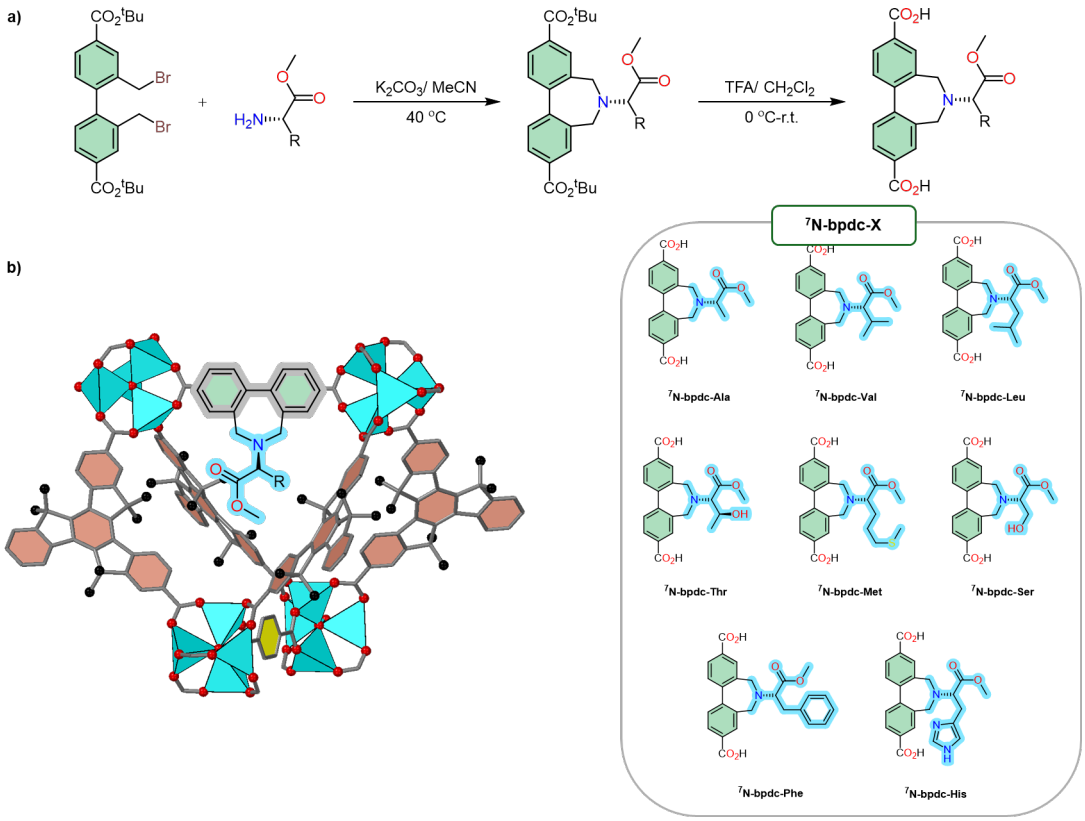

Figure 4.25: a) The synthetic pathway by which ^{7}N-bpdc-X linkers were synthesised. **b)** A series of newly synthesised amino acid-derived bpdc ligands (highlighted in pastel green) were incorporated into MUF-77, alongside H_2bdc and the tritopic ligand H_3hmtt.

This family of linkers suffered from low stability when the original solvothermal procedure was used where the ligands were heated at 85 °C overnight. When these ligands were incorporated into MUF-77, and a subsequent ^{1}H NMR spectroscopy experiment was done for the digested crystals in DCl/DMSO-d_6 (23 µL/1 mL), the ligand integration was either off or the ligand was degraded.

For example, when ^{7}N-bpdc-Leu was incorporated alongside H_3hmtt and H_2bdc using the original MUF-77 solvothermal synthesis, ^{1}H NMR spectroscopic analysis of the digested crystals revealed that the integration value for the linker was reduced by approximately 50% relative to the expected ratio. Furthermore, additional signals appeared in the aromatic region that could not be assigned to any of the intended linkers, which indicated a side reaction had happened.

To investigate this instability further, ^{7}N-bpdc-Leu, was selected for thermogravimetric analysis (TGA), as all ligands in this series exhibited similar incorporation issues. This ligand was chosen based on its higher synthetic yield. The experimental approach that was employed is the isothermal heat-and-hold at 120 °C, this temperature was selected as lower temperature took longer time to plateau. The mass loss observed was minimal and primarily attributable to moisture evaporation. Subsequent ^{1}H NMR spectroscopy confirmed that the ligand's chemical integrity was preserved.

Although temperature alone did not affect the ligand's integrity, other factors, such as the solvent (DEF) and the presence of Zn(II), together with elevated temperatures, influenced the ligand's stability. Similar to the previous linker family (^{5}N-bdc-X-OH), the use of TEA (2.5 eq.) shortened the reaction time and produced MUF-77 crystals. These crystals were characterised by PXRD and ^{1}H NMR spectroscopy of the digested crystal in DCl/DMSO-d_6 (23 μL/ mL). The agreement between the experimental PXRD pattern and the calculated pattern of the parent MUF-77 confirmed the phase purity of the crystals, while ^{1}H NMR spectroscopy verified the integrity of the ligands and further supports the phase purity.

4.2.4 General overview of bpdc-based amino acids (^{7}N-bpdc-X linkers)

All amino acids-functionalised bpdc linkers (**L8–L15**) were incorporated into the MUF-77 framework using a modified solvothermal procedure. Each linker was combined with H_2bdc, H_3hmtt, $Zn(NO_3)_2 \cdot 4H_2O$, and benzoic acid in DEF. The reaction conditions were slightly adjusted to reduce reaction time and to preserve the seven-membered ring integrity of the functional groups. Low equivalents of TEA were used to promote crystal growth and shorten the reaction time.

Each resulting MOF exhibited the general formula $[Zn_4O(hmtt)_{4/3}(L)_{1/2}(bdc)_{1/2}]$, as confirmed by ^{1}H NMR spectroscopy after acid digestion. Consistent with previous MUF-77 analogues, the hmtt, bdc, and ^{7}N-bpdc-X linkers coordinated to Zn(II) centres through their carboxylate oxygens.

In the SCXRD analysis, the bpdc backbone, the seven-membered heterocyclic ring, and amino acid side chains are positionally disordered, similar to that observed in previously synthesised linker families (^{5}N-bdc-X-OH). Bpdc backbone and seven-membered ring are disordered over two positions with approximately equal occupancies of ~0.5, whereas the side chains are distributed over four orientations with occupancies of ~0.25 each.

The MUF-77 topology was retained in all cases; this was proved by SCXRD, and PXRD. The experimental PXRD pattern was collected and compared to the calculated pattern from the corresponding SCXRD. The agreement between both PXRD patterns confirms the bulk phase purity (**Figure 4.45**). MUF-77 comprises three distinct pore types: one micropore formed from four tritopic hmtt linkers and two mesopores built from eight hmtt linkers and six linear linkers (bdc/ bpdc). The slightly different lengths of the bpdc and bdc derivatives led to subtle variations in the mesopore dimensions.

The following subsections provide specific details for each individual framework.

4.2.4.1 $[Zn_4O(hmtt)_{4/3}(^{7}N\text{-bpdc-Ala})_{1/2}(bdc)_{1/2}]$

Alanine was chosen as the first amino acid for functionalising bpdc because its small methyl side chain minimises steric hindrance, and the absence of additional functional groups reduces the likelihood of interfering with MOF formation.

^{7}N-Bpdc-Ala (**L8**) was synthesised using the general procedure mentioned above (**Figure 4.25a**). This ligand was incorporated into MUF-77 framework successfully, using the procedure below **(Figure 4.26)**.

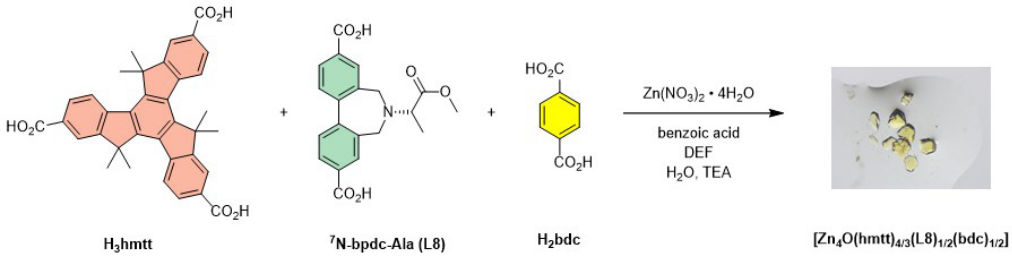

Figure 4.26: Synthetic pathway to $[Zn_4O(hmtt)_{4/3}(^7N\text{-bpdc-Ala})_{1/2}(bdc)_{1/2}]$ using the modified synthesis procedure.

The phase purity of the framework with the general formula $[Zn_4O(hmtt)_{4/3}(\mathbf{L8})_{1/2}(bdc)_{1/2}]$ was confirmed by the agreement between its experimental PXRD pattern and the calculated PXRD pattern of the reported parent MUF-77(**Figure 4.45**). Furthermore, ^1H NMR spectroscopy of digested crystals in DCl/DMSO-d_6 verified the integrity of the ligands and further supported the phase purity (**Figure 4.47**).

The resulting structure retains the topology and the characteristic pore architecture of the MUF-77 family, comprising one micropore and two mesopores. The micropore is tetrahedral in shape and is formed by the intersection of four tritopic hmtt linkers, which bridge between one **L8** and one bdc linker positioned opposite each other. The larger dodecahedral mesopores are assembled by eight hmtt linkers connected to six linear linkers arranged in opposing pairs. In this variant, the more extended **L8** linker produces slightly larger mesopores compared to those built entirely with bdc, due to its increased length (**Figure 4.27**).

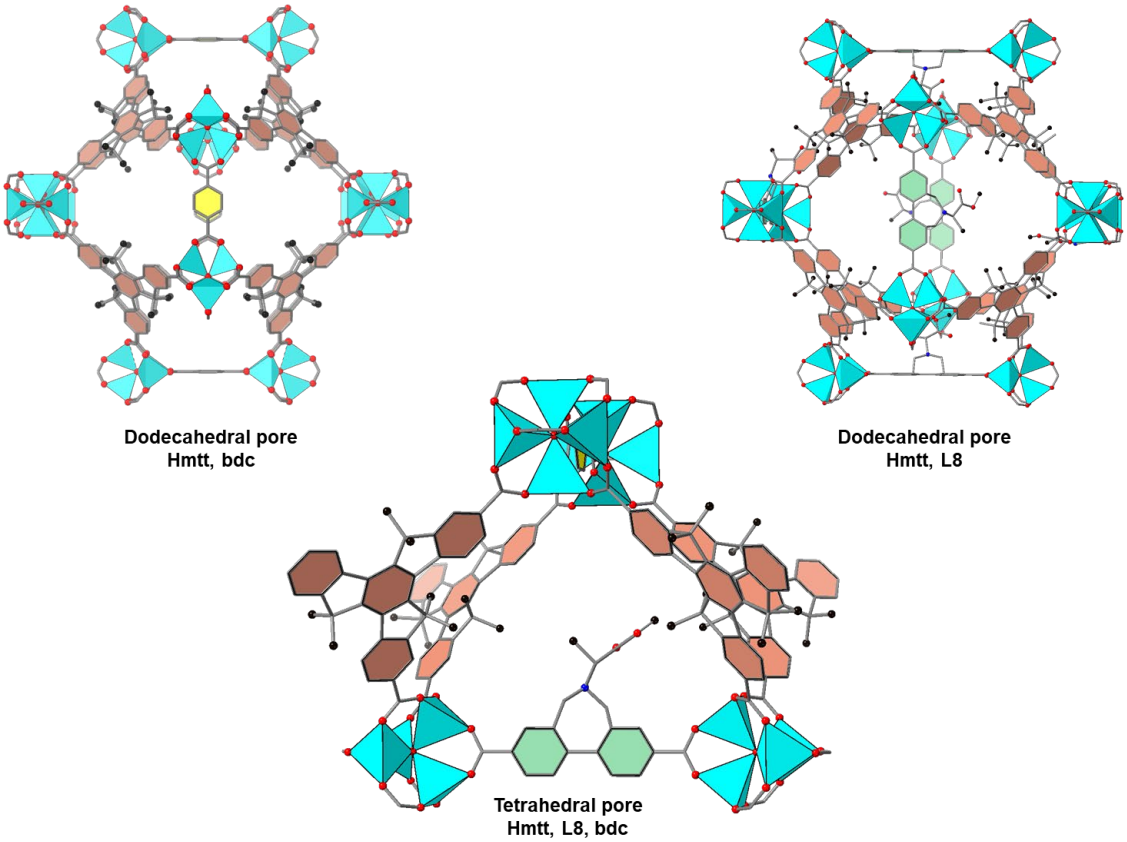

Figure 4.27: This graphical representation shows the pore structure specific to this material, showing **L8** functionalised with *l*-alanine OMe groups. The alanine side chain could not be directly resolved via SCXRD due to positional disorder, but its presence was confirmed by ^{1}H NMR spectroscopy of the acid-digested MUF-77 crystals.

4.2.4.2 [$Zn_4O(hmtt)_{4/3}$ (^{7}N-bpdc-Val)$_{1/2}(bdc)_{1/2}$]

Valine was also considered for functionalising bpdc; while it does not contribute directly to catalytic dyads or triads like alanine due to the lack of reactive side chains, its bulkier isopropyl group provides an opportunity to investigate steric effects on MUF-77 formation and structural stability.

^{7}N-Bpdc-Val (**L9**) was synthesised using the general procedure mentioned above (**Figure 4.25.b**). **L9** was incorporated into MUF-77 framework successfully, using the procedure below **(Figure 4.28).**

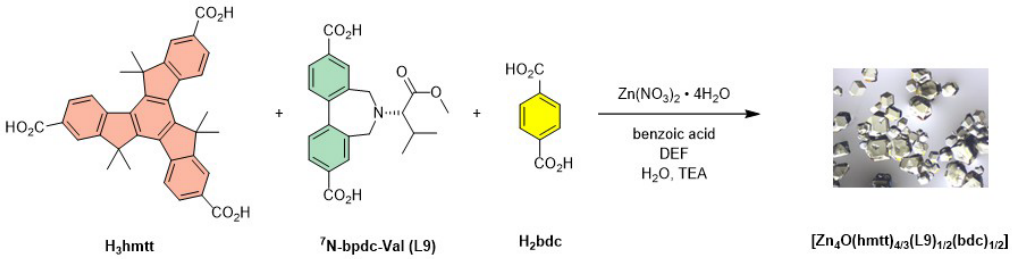

Figure 4.28: Synthetic pathway to $[Zn_4O(hmtt)_{4/3}(^7N\text{-bpdc-Val})_{1/2}(bdc)_{1/2}]$ using the modified synthesis procedure.

The phase purity of the framework with the general formula $[Zn_4O(hmtt)_{4/3}(\mathbf{L9})_{1/2}(bdc)_{1/2}]$ was confirmed by the agreement between its experimental PXRD pattern and the calculated PXRD pattern of the reported parent MUF-77 (**Figure 4.45**). Furthermore, ^{1}H NMR spectroscopy of digested crystals in DCl/DMSO-d_6 (**Figure C.71**) verified the integrity of the ligands and further supports the phase purity.

The resulting structure retains the topology and the characteristic pore architecture of the MUF-77 family, comprising one micropore and two mesopores (**Figure 4.29**). The incorporation of the branched valine side chain modifies the steric environment within the framework, subtly influencing the accessibility and shape of the pore apertures.

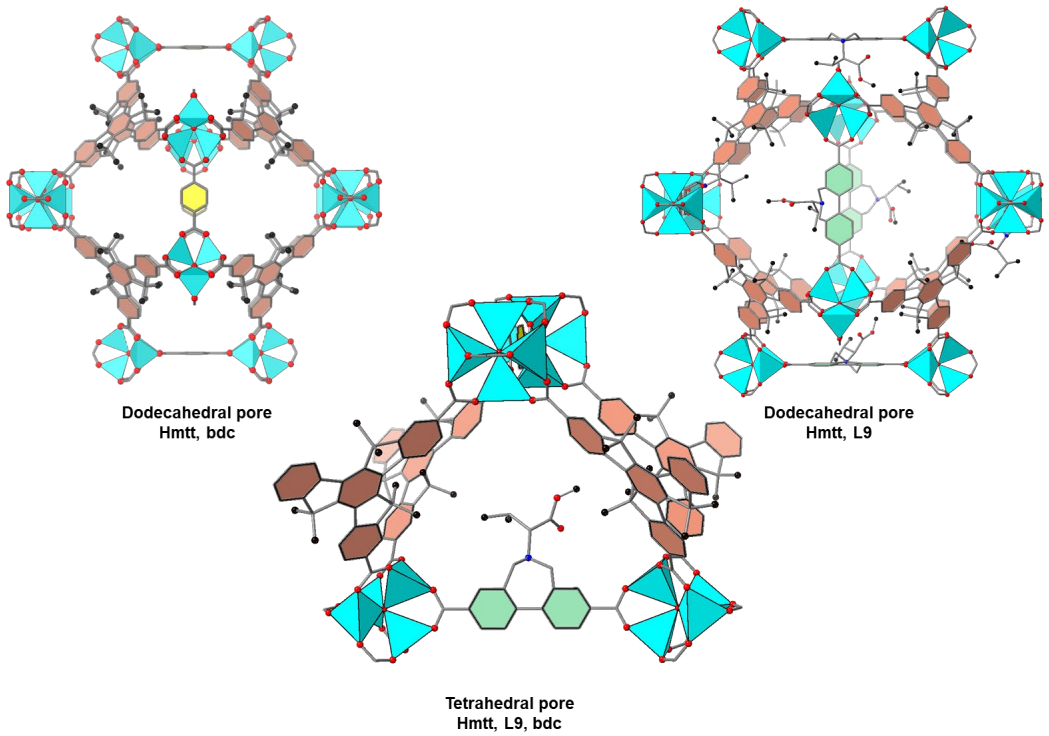

Figure 4.29: This graphical representation shows the pore structure specific to this material, showing **L9** functionalised with *l*-valine OMe groups. The valine side chain could not be directly resolved via SCXRD due to positional disorder, but its presence was confirmed by ^{1}H NMR spectroscopy of the acid-digested MUF-77 crystals.

4.2.4.3 $[Zn_4O(hmtt)_{4/3}(^7N\text{-bpdc-Leu})_{1/2}(bdc)_{1/2}]$

Leucine was selected as an additional amino acid for functionalising bpdc to further examine steric effects. Although, like alanine and valine, it does not contribute directly to catalytic dyads or triads, its larger isobutyl side chain offers a means to systematically assess how progressive increases in steric bulk influence MOF formation.

^{7}N-Bpdc-Leu (**L10**) was synthesised using the general procedure mentioned above (**Figure 4.25.b**). **L10** was incorporated into MUF-77 framework successfully, using the modified procedure below **(Figure 4.30).**

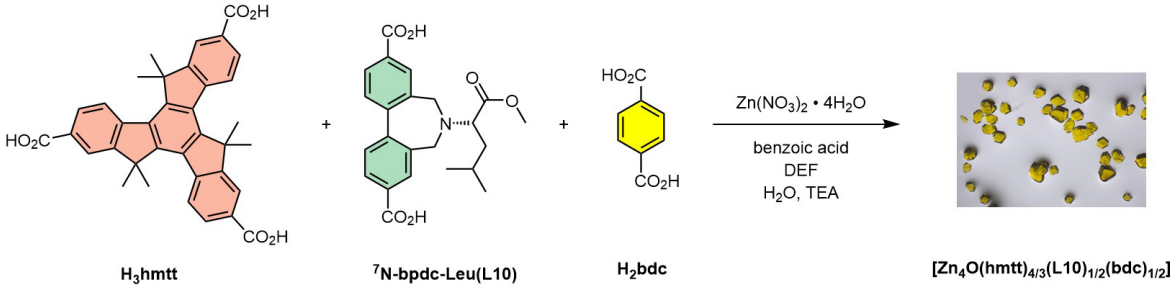

Figure 4.30: Synthetic pathway to $[Zn_4O(hmtt)_{4/3}(^7N\text{-bpdc-Leu})_{1/2}(bdc)_{1/2}]$ using the modified synthesis procedure.

The phase purity of the framework with the general formula $[Zn_4O(hmtt)_{4/3}(\mathbf{L10})_{1/2}(bdc)_{1/2}]$ was confirmed by the agreement between its experimental PXRD pattern and the calculated PXRD pattern of the reported parent MUF-77 (**Figure 4.45**). Furthermore, ^{1}H NMR spectroscopy of digested crystals in DCl/DMSO-d_6 (**Figure C.72**) verified the integrity of the ligands and further supports the phase purity.

The resulting structure retains the topology and the characteristic pore architecture of the MUF-77 family, comprising one micropore and two mesopores (**Figure 4.31**). The incorporation of the branched leucine side chain modifies the steric environment within the framework, subtly influencing the accessibility and shape of the pore apertures.

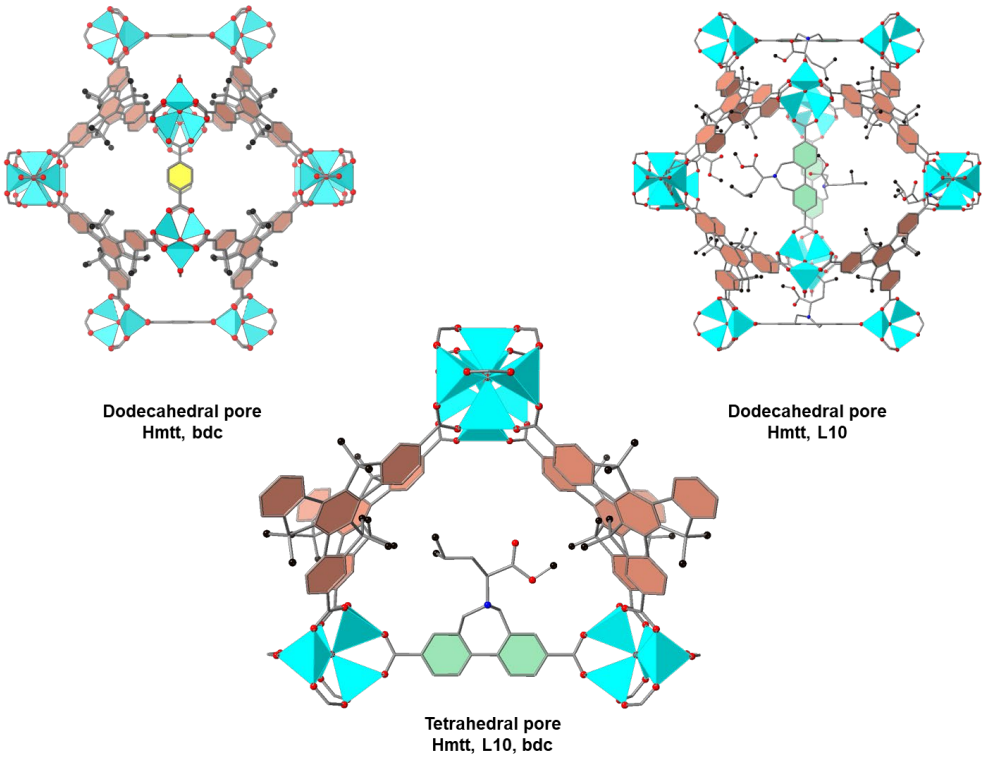

Figure 4.31: This graphical representation shows the pore structure specific to this material, showing **L10** functionalised with *l*-leucine OMe group. The leucinyl side chain could not be directly resolved via SCXRD due to positional disorder, but its presence was confirmed by ^{1}H NMR spectroscopy of the acid-digested MUF-77 crystals.

4.2.4.4 $[Zn_4O(hmtt)_{4/3}(^{7}N\text{-}bpdc\text{-}Ser)_{1/2}(bdc)_{1/2}]$

Serine is an amino acid, that has reactive β-hydroxymethyl side chain. Compared with threonine, serine has lower steric hindrance as it does not have the β-methyl chain. This gives more accessibility to the hydroxyl group to form H-bonding. This accessibility allows serine-derived ligands to form strong H-bonding networks within MOFs, potentially stabilising flexible structures or tuning pore polarity to enhance guest uptake.

In enzymatic systems, serine's nucleophilic hydroxyl group plays a vital role in serine protease catalytic triad, where it hydrolyses the peptide bond through nucleophilic attack and is activated by a histidine-aspartate dyad.[176] Serine acts as a nucleophile in dyad or triad arrangements, a principle that can be rationally transferred into ligand design. Due to the H-bonding ability of the serine side chain, serine-derived ligands can generate asymmetric environments, useful for enantioselective transformations.[177]

Bpdc functionalisation with serine can introduce enhanced H-bonding capability to MUF-77 and introduce the potential for cooperative dyad/triad catalysis inspired by serine proteases. These properties make serine a promising functional group for the MUF-77.

^{7}N-Bpdc-Ser (**L11**) was synthesised using the general procedure mentioned above (**Figure 4.25.b**). **L11** was incorporated into MUF-77 framework successfully, using the modified procedure below **(Figure 4.32).**

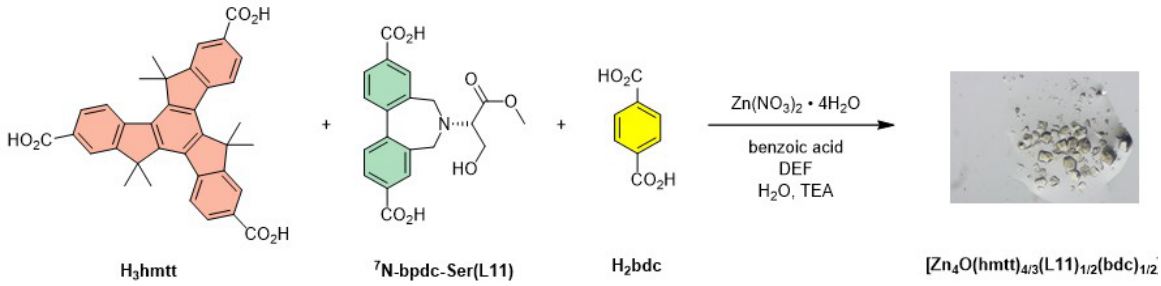

Figure 4.32: Synthetic pathway to $[Zn_4O(hmtt)_{4/3}(^{7}N\text{-bpdc-Ser})_{1/2}(bdc)_{1/2}]$ using the modified synthesis procedure.

The phase purity of the framework with the general formula $[Zn_4O(hmtt)_{4/3}(\mathbf{L11})_{1/2}(bdc)_{1/2}]$ was confirmed by the agreement between its experimental PXRD pattern and the calculated PXRD pattern of the reported parent MUF-77 (**Figure 4.46**). Furthermore, ^{1}H NMR spectroscopy of digested crystals in DCl/DMSO-d_6 (**Figure C.73**) verified the integrity of the ligands and further supports the phase purity.

The resulting structure retains the topology and the characteristic pore architecture of the MUF-77 family, comprising one micropore and two mesopores (**Figure 4.33)**. In contrast to the hydrophobic branched side chains of valine and leucine, the polar hydroxymethyl side chain of serine introduces H-bonding potential within the pores. The pore chemical environment change can potentially enhance interactions with polar guest molecules.

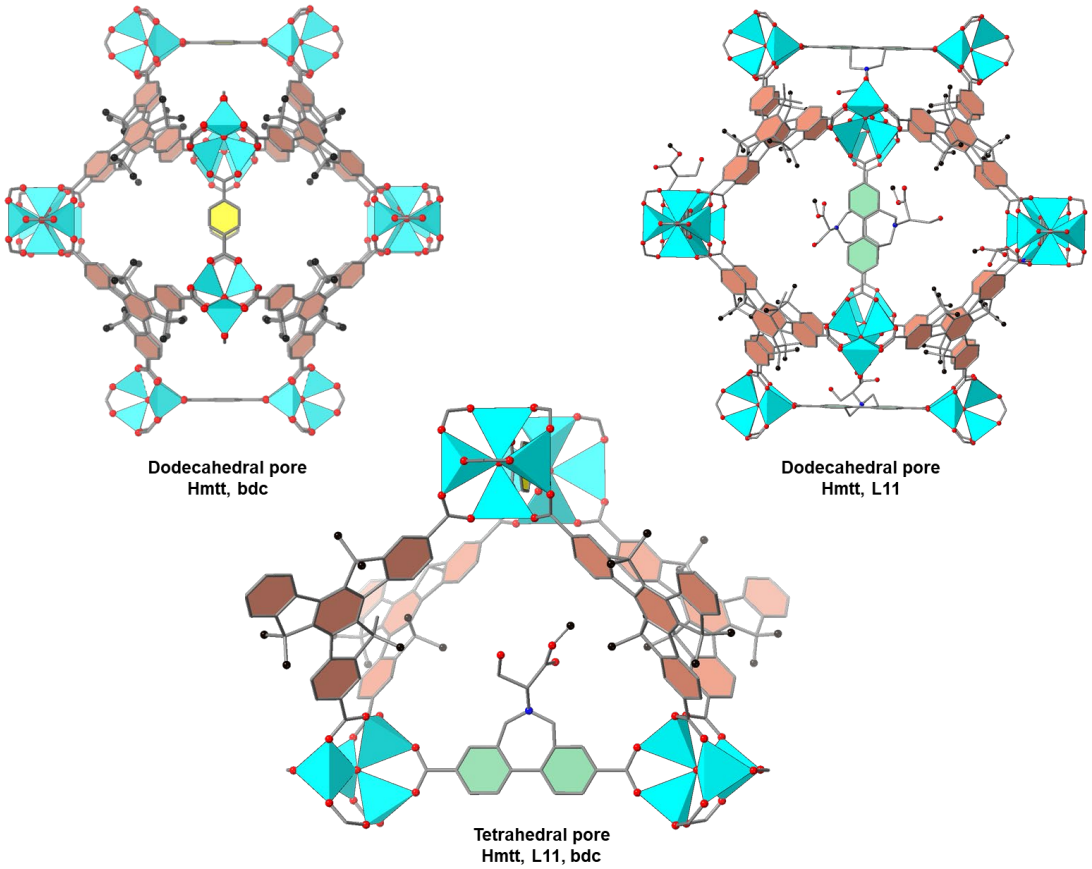

Figure 4.33: This graphical representation shows the pore structure specific to this material, showing **L11** functionalised with *l*-serine OMe group. The serinyl side chain could not be directly resolved via SCXRD due to positional disorder, but its presence was confirmed by ^{1}H NMR spectroscopy of the acid-digested MUF-77 crystals.

4.2.4.5 [$Zn_4O(hmtt)_{4/3}(^{7}N\text{-}bpdc\text{-}Thr)_{1/2}(bdc)_{1/2}$]

Threonine has a balance between the steric and electronic features, which makes it an attractive amino acid for functionalising ligands in coordination frameworks and organocatalysts. Threonine has a β-hydroxyl group adjacent to a stereogenic center, which enables both H-bonding capability. The β-methyl group participates to steric differentiation that can create well-defined pockets in MOFs.

^{7}N-Bpdc-Thr (**L12**) was synthesised using the general procedure mentioned above (**Figure 4.25.a**). **L12** was incorporated into MUF-77 framework successfully, using the procedure below (**Figure 4.34**).

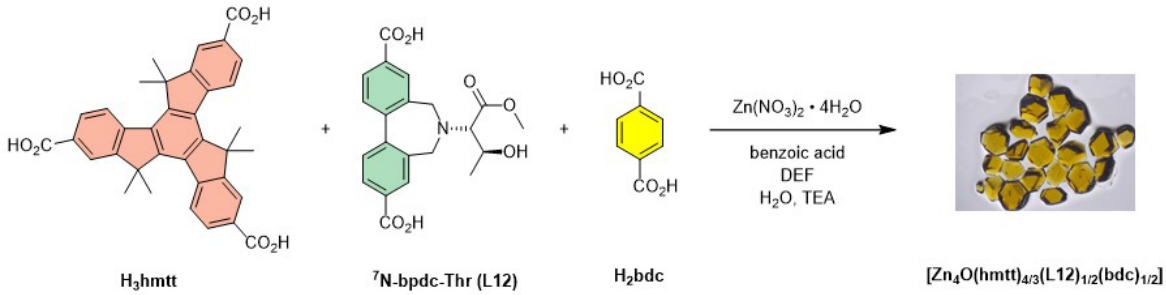

Figure 4.34: Synthetic pathway to $[Zn_4O(hmtt)_{4/3}(^7N\text{-bpdc-Thr})_{1/2}(bdc)_{1/2}]$ using the modified synthesis procedure.

The phase purity of the framework with the general formula $[Zn_4O(hmtt)_{4/3}(\mathbf{L12})_{1/2}(bdc)_{1/2}]$ was confirmed by the agreement between its experimental PXRD pattern and the calculated PXRD pattern of the reported parent MUF-77 (**Figure 4.45**). Furthermore, ^{1}H NMR spectroscopy of digested crystals in DCl/DMSO-d_6 (**Figure C.74**) verified the integrity of the ligands and further confirms the phase purity.

The resulting structure retains the topology and the characteristic pore architecture of the MUF-77 family, comprising one micropore and two mesopores (**Figure 4.35)**. The β-methyl and hydroxyl-bearing side chain of threonine combines moderate steric bulk with polarity, introducing hydrogen-bonding sites while partially constricting the pore apertures compared to serine.

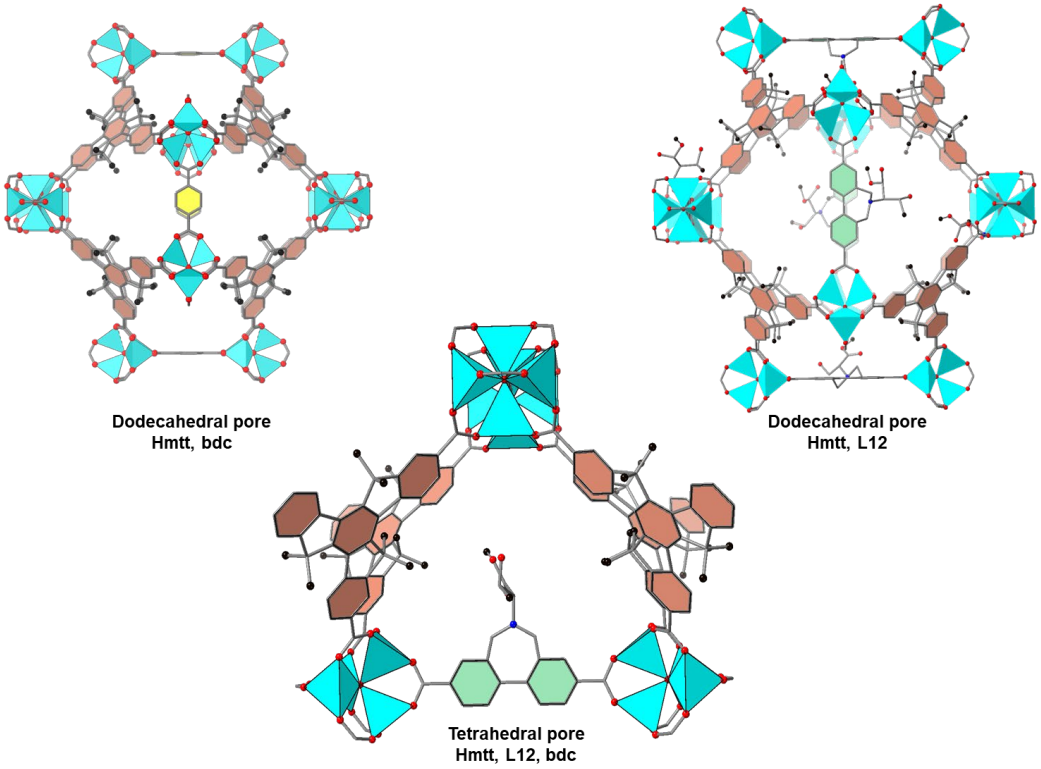

Figure 4.35: This graphical representation shows the pore structure specific to this material, showing **L12** functionalised with *l*-threonine OMe group. The threoninyl side chain could not be directly resolved via SCXRD due to positional disorder, but its presence was confirmed by ^{1}H NMR spectroscopy of the acid-digested MUF-77 crystals.

4.2.4.6 $[Zn_4O(hmtt)_{4/3}(^{7}N\text{-bpdc-Met})_{1/2}(bdc)_{1/2}]$

^{7}N-Bpdc-Met (**L13**) was synthesised using the general procedure mentioned above (**Figure 4.23.b**). **L13** was incorporated into MUF-77 framework successfully, using the procedure below (**Figure 4.36**).

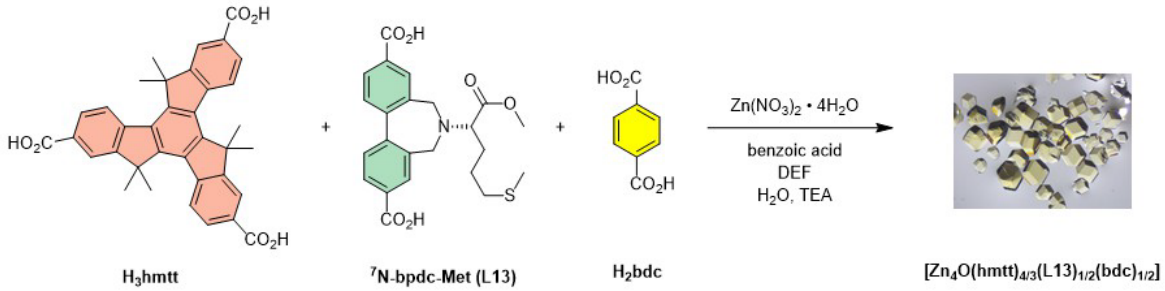

Figure 4.36: Synthetic pathway to $[Zn_4O(hmtt)_{4/3}(^{7}N\text{-bpdc-Met})_{1/2}(bdc)_{1/2}]$ using the modified synthesis procedure.

The phase purity of the framework with the general formula $[Zn_4O(hmtt)_{4/3}(\mathbf{L13})_{1/2}(bdc)_{1/2}]$ was confirmed by the agreement between its experimental PXRD pattern and the calculated PXRD pattern of the reported parent MUF-77 (**Figure 4.45**). Furthermore, ^{1}H NMR spectroscopy of digested crystals in DCl/DMSO-d_6 (**Figure C.75**) verified the integrity of the ligands.

The resulting structure retains the topology and characteristic pore architecture of the MUF-77 family, comprising one micropore and two mesopores (**Figure 4.37**). The elongated thioether side chain of methionine introduces greater conformational flexibility and hydrophobicity within the pores, subtly modifying aperture dimensions while creating a less polar internal surface compared to frameworks incorporating polar amino acid residues.

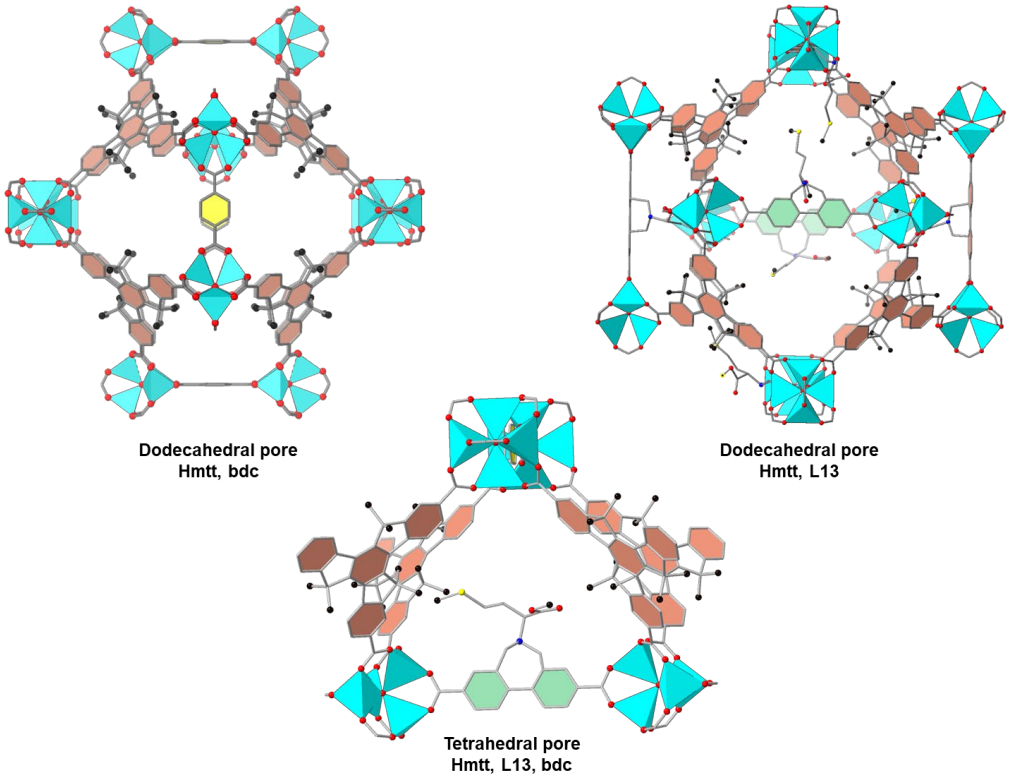

Figure 4.37: This graphical representation shows the pore structure specific to this material, showing **L13** functionalised with *l*-methionine OMe group. The methioninyl side chain could not be directly resolved via SCXRD due to positional disorder, but its presence was confirmed by ^{1}H NMR spectroscopy of the acid-digested MUF-77 crystals.

4.2.4.7 $[Zn_4O(hmtt)_{4/3}(^7N\text{-bpdc-Phe})_{1/2}(bdc)_{1/2}]$

Phenylalanine (Phe), an aromatic amino acid, plays a significant role in catalysis, particularly in the context of MOFs. Its hydrophobic benzyl side chain facilitates π–π stacking interactions. Hydrophobic interactions arise from the tendency of nonpolar aromatic surfaces to cluster together in order to minimize contact with polar solvents such as water, creating a nonpolar microenvironment within the pore. In MOF-based catalysis, Phe can be incorporated to modulate the electronic environment and steric properties of the active site, thereby influencing catalytic efficiency and selectivity.

For instance, the integration of Phe into MOF composites has been explored to enhance the selective adsorption of gases such as CO_2 and CH_4, demonstrating its potential in gas separation technologies.[178] Additionally, Phe-functionalised MOFs have been utilized in chiral recognition systems, showcasing their ability to differentiate between enantiomers in complex mixtures.[179] These applications underscore the versatility of phenylalanine in catalysis, particularly within MOF structures, where its aromatic properties and ability to engage in non-covalent interactions can be harnessed to achieve desired catalytic outcomes.

Functionalising bpdc ligand with Phe, provides a rigid and hydrophobic environment that can influence substrate binding and selectivity, which may direct the substrate in a specific position which can enhance the catalysis.

^{7}N-Bpdc-Phe (**L14**) was synthesised using the general procedure mentioned above (**Figure 2.25.a**). **L14** was incorporated into MUF-77 framework successfully, using the procedure below (**Figure 4.38**).

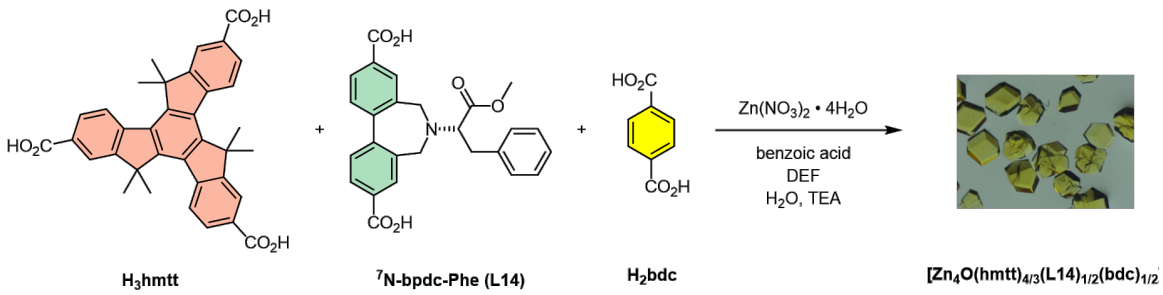

Figure 4.38: Synthetic pathway to $[Zn_4O(hmtt)_{4/3}(^7N\text{-bpdc-Phe})_{1/2}(bdc)_{1/2}]$ using the modified synthesis procedure.

The phase purity of the framework with the general formula $[Zn_4O(hmtt)_{4/3}(\mathbf{L14})_{1/2}(bdc)_{1/2}]$ was confirmed by the agreement between its experimental PXRD pattern and the calculated PXRD pattern of the reported parent MUF-77 (**Figure 4.46**). Furthermore, ^{1}H NMR spectroscopy of digested crystals in DCl/DMSO-d_6 (**Figure C.76**) verified the integrity of the ligands and the crystals phase purity.

The resulting structure retains the topology and characteristic pore architecture of the MUF-77 family, comprising one micropore and two mesopores (**Figure 4.39**). The bulky aromatic side chain of phenylalanine significantly increases steric bulk within the pores, while the phenyl ring introduces the potential for π–π interactions with aromatic guest molecules, creating a more hydrophobic and structurally constrained internal environment.

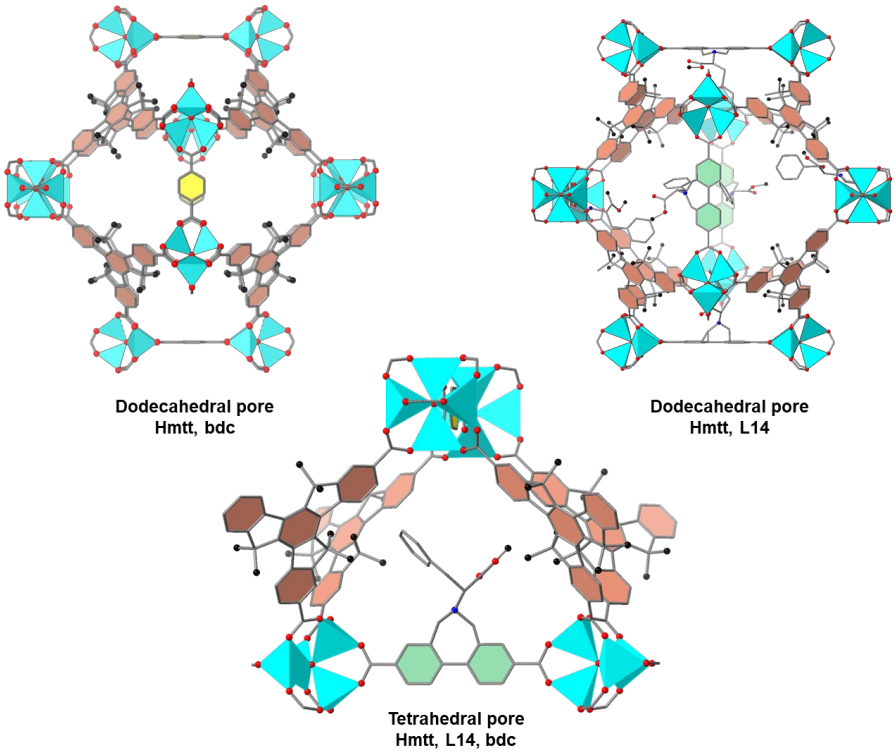

Figure 4.39: This graphical representation shows the pore structure specific to this material, showing **L14** functionalised with *l*-phenylalanine OMe group. The phenylalaninyl side chain could not be directly resolved via SCXRD due to positional disorder, but its presence was confirmed by ^{1}H NMR spectroscopy of the acid-digested MUF-77 crystals.

4.2.4.8 $[Zn_4O(hmtt)_{4/3}(^7N\text{-bpdc-His})_{1/2}(bdc)_{1/2}]$

By functionalising bpdc with histidine, we aimed to introduce H-bonding sites and, enhancing the ligand's capability to form cooperative interactions within the resulting MOFs, to form enzyme-like microenvironments for catalysis.

^{7}N-Bpdc-His (**L15**) was synthesised using the general procedure mentioned above (**Figure 4.25.a**). **L15** was incorporated into MUF-77 framework successfully, using the procedure below (**Figure 4.40**).

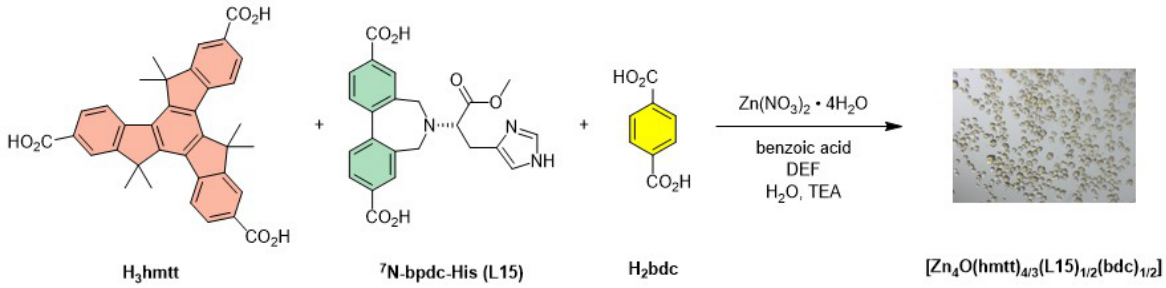

Figure 4.40: Synthetic pathway to $[Zn_4O(hmtt)_{4/3}(^7N\text{-bpdc-His})_{1/2}(bdc)_{1/2}]$ using the modified synthesis procedure.

The phase purity of the framework with the general formula $[Zn_4O(hmtt)_{4/3}(\mathbf{L15})_{1/2}(bdc)_{1/2}]$ was confirmed by the agreement between its experimental PXRD pattern and the calculated PXRD pattern of the reported parent MUF-77 (**Figure 4.46**). Furthermore, ^{1}H NMR spectroscopy of digested crystals in DCl/DMSO-d_6 verified the integrity of the ligands and further confirms the phase purity (**Figure C.77**).

The resulting structure retains the topology and characteristic pore architecture of the MUF-77 family, comprising one micropore and two mesopores (**Figure 4.41**).

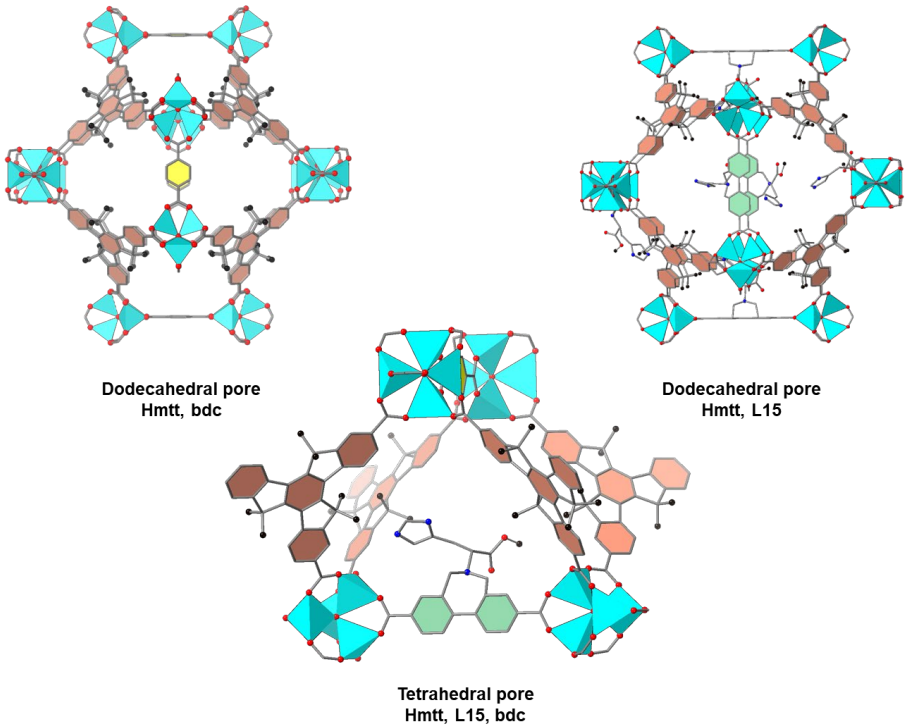

Figure 4.41: This graphical representation shows the pore structure specific to this material, showing **L15** functionalised with *l*-histidine OMe group. The histidinyl side chain could not be directly resolved via SCXRD due to positional disorder, but its presence was confirmed by ^{1}H NMR spectroscopy of the acid-digested MUF-77 crystals.

4.3 Conclusion

In this chapter, the linear linkers of MUF-77 were systematically functionalised with a series of amino alcohol and amino acid derivatives and successfully incorporated into the framework while preserving the characteristic MUF-77 topology. Both bdc- and bpdc-based linker families were developed, enabling controlled installation of diverse side chains within the pore environment without disrupting structural integrity.

The resulting frameworks retained the quaternary architecture of MUF-77, while introducing chemically distinct functionalities such as hydroxyl, thioether, aromatic, and imidazole-containing groups. Although the appended side chains frequently exhibited positional disorder in SCXRD analyses, their incorporation and phase purity were consistently confirmed by PXRD and ^{1}H NMR spectroscopy of digested samples. Functionalisation of the internal pore environment tunes the polarity, hydrogen-bonding, hydrophobicity, and potential catalytic behaviour while preserving crystallinity.

These results demonstrate that the MUF-77 platform tolerates different functionalities on its linear linkers, allowing structural robustness and functional modification to be achieved. This strategy provides a route for engineering pore-confined amino acid functionalities and establishes the structural foundation for subsequent investigations into cooperative and biomimetic catalysis.

4.4 Experimental section

All general synthetic procedures, instrumentation details, and characterisation methods (except for thermogravimetric analysis) are described in the **2.4.1** and **3.4.1**. Thermogravimetric analyses were performed on a TA Instruments Q50 device. Structural graphics were prepared in Discovery Studio Visualizer using atomic coordinates obtained from the refined CIF files. The coordinates correspond to the experimentally determined framework atoms; disordered components are shown as the major occupancy orientation.

The synthesis of all bdc and bpdc backbones is provided in **Appendix C**. Representative procedures for ^{5}N-bdc-X-OH and ^{7}N-bpdc-X are described in this section, with the remaining derivatives reported in **Appendix C.**

4.4.1 ^{5}N-Bdc-Ala-OH synthesis

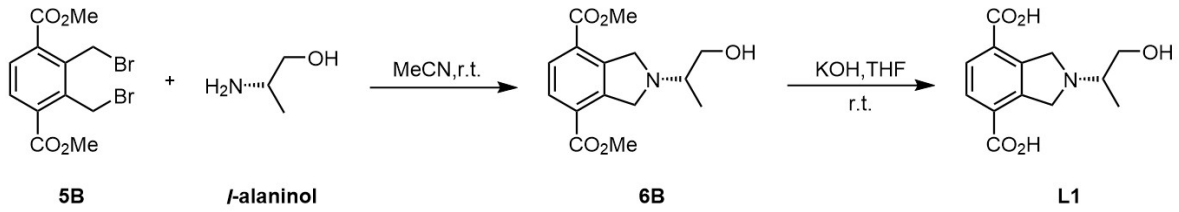

Figure 4.42: Synthetic pathway to **L1**.

Compound 6B synthesis

Compound **5B** (0.17 g, 0.44 mmol), and K_2CO_3 (0.26 g, 1.68 mmol) were suspended in MeCN (10 mL). *l*-Alaninol (50.11 mg, 0.67 mmol) was dissolved in MeCN (1 mL). Then, it was added gradually to the reaction mixture in 3 batches. The reaction mixture was stirred at room temperature for 24 hours. The base was filtered off, and the solvent was removed. Then, it was loaded onto a flash silica column chromatography. The product was eluted with methanol/EtOAc (1:9). R_f (1:9, methanol: EtOAc) = 0.78. Yield: 0.12 g, 0.41 mmol, 93%.

^{1}H NMR (500 MHz, $CDCl_3$) δ (ppm) 7.94 (s, 2H), 4.40-4.32 (m, 4H), 3.93 (s, 6H), 3.70 (dd, *J* = 10.8, 4.3 Hz, 1H), 3.52 (dd, *J* = 10.8, 7.0 Hz, 1H), 3.10-3.04 (m, 1H), 2.58 (brs, 1H), 1.16 (d, *J* = 6.6 Hz, 3H).

HRMS (FTMS + p ESI Full) calculated for $[M+H]^+$ $(C_{15}H_{20}N_1O5)^+$ *m/z* 294.1336, found *m/z* 294.1330.

Ligand L1 synthesis

Compound **6B** (0.10 g, 0.30 mmol) was dissolved in 2 mL 1:1(V/V) THF/KOH (aq., 1M) and the solution was stirred at r.t. overnight. Then, THF was removed under reduced pressure. The pH was adjusted to around 4 using HCl_{aq} (0.1 M). The product was precipitated out gradually. Yield: 70.00 mg, 0.26 mmol, 88%.

^{1}H NMR (500 MHz, D_2O/NaOD) δ (ppm) 7.58 (s, 2H), 4.21 (s, 4H), 3.84 (dd, *J* = 11.9, 4.3 Hz, 1H), 3.76 (dd, *J* = 11.9, 5.4 Hz, 1H), 2.71-2.67 (m, 1H), 1.83-1.75 (m, 1H), 1.71-1.62 (m, 1H), 0.96 (t, *J* = 7.5 Hz, 3H). ^{13}C NMR (126 MHz, D_2O/NaOD) δ (ppm) 175.54, 139.35, 133.80, 126.99, 65.55, 60.72, 56.51, 21.29, 8.87.

HRMS (FTMS + p ESI Full) calculated for $[M]^-(C_{13}H_{14}N_1O_5)^-$ *m/z* 264.0866, found *m/z* 264.0869.

4.4.2 ^{7}N-Bpdc-Ala (L8) synthesis

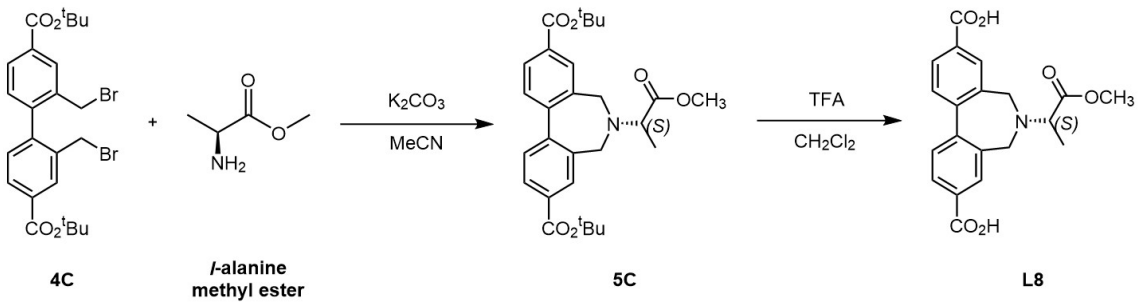

Figure 4.43: Synthetic pathway to **L8**.

l-Alanine esterification

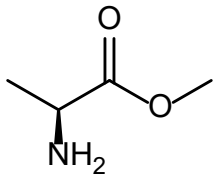

$SOCl_2$ (0.8 mL, 2 eq.) was added dropwise to the mixture of *l*-alanine (0.50 g, 5.52 mmol) and methanol (10 mL) in an ice water bath with stirring. Then, the temperature was gradually warmed up to r.t. and the mixture was stirred overnight. The solvent was removed by evaporation under reduced pressure. The product was an oil, then after drying under high vacuum the product precipitated as a powder.[180] Yield: 0.54 g, 5.54 mmol, 95%. ^{1}H NMR spectroscopy was done in DMSO-d_6.

^{1}H NMR (500 MHz, DMSO-d_6) δ (ppm) 1.35(s, 3H), 3.49 (d, J = 7.22, 3H), 4.2 (d, J = 7.22, 1H).

Compound 5C synthesis

Compound **4C** (350.00 mg, 0.68 mmol, 1 eq.), and K_2CO_3 (529.50 mg, 3.83 mmol, 5.7 eq.) were suspended in MeCN (10 mL). *l*-Alanine methyl ester (203.50 mg, 1.97 mmol, 3 eq.) was dissolved in MeCN (1 mL) and gradually added to the reaction mixture in 3 batches. The reaction mixture was stirred at 35 °C for 24 hours. The base was filtered off, and the solvent was removed. A column was done using EtOAc in cyclohexane (1:10) to remove the unreacted starting material. The product was then eluted using EtOAc in cyclohexane (1:5). R_f (5:1, cyclohexane: EtOAc) = 0.54. Yield: 260.00 mg, 0.54 mmol, 80%.

^{1}H NMR (500 MHz, DMSO-d_6) δ (ppm): 1.33 (d, J = 7.22, 3H), 1.58 (br s, 18H), 3.49 (d, J = 12.6 Hz, 2H), 3.53 (s, 3H), 3.57 (d, J = 12.92 Hz, 2H), 7.17 (q, J = 25.8 Hz, 1H), 7.67 (d, J = 9.3 Hz, 2H), 7.90 (s, 2H), 8.002 (dd, J = 1.7 Hz, J = 1.7 Hz, 2H).

HRMS (FTMS + p ESI Full) calculated for $[M + H]^+(C_{28}H_{36}NO_6)^+$ 482.2512, found *m/z* 482.2511.

Ligand L8 synthesis

Compound **5C** (200.0 mg, 0.42 mmol) was dissolved in CH_2Cl_2 (3.0 mL). Then, TFA (4.74 g, 3.2 mL, 10.50 mmol) was added and the solution was stirred at rt overnight. TLC was performed using EtOAc/n-hexane (1:1), which indicated the consumption of the starting material. Then, the reaction was stopped, and the product was extracted with an aqueous NaOH solution (0.10 M). The extract was placed in an ice bath, and HCl solution (1.00 M) was added gradually to precipitate out the product. The precipitated product 4 was filtered out and dried using a vacuum oven. Yield: 120.00 mg, 3.29 mmol, 92%.

^{1}H NMR (500 MHz, DMSO-d_6) δ (ppm) 1.64 (d, *J* = 6.38, 3H), 3.49 (d, *J* = 12.6 Hz, 2H), 3.53 (s, 3H), 3.57 (d, *J* = 12.92 Hz 2H), 7.17 (q, *J* = 25.8 Hz, 1H), 7.8 (d, *J* = 8.29 Hz, 2H), 8.002 (dd, *J* = 1.45, 3.11 Hz, 2H) , 8.22 (s, 2H) ppm. ^{13}C NMR (126 MHz, D_2O/NaOD) δ: 181.92, 175.57, 135.96, 134.08, 130.60, 128.92, 127.53, 51.94, 48.83. 17.10 ppm.

HRMS **(**FTMS + p ESI Full) calculated for $[M]^-(C_{20}H_{19}NO_6)^-$ *m/z* 368.1129, found *m/z* 368.1135.

4.4.3 MOFs synthesis

MUF-77 general synthesis procedure:

All syntheses were performed in 4 mL vials sealed with septum caps. H_3hmtt (4.0 µmol), the H_2bpdc or its derivative (4.8-6.8 µmol), the H_2bdc or its derivative (8.0-11.0 µmol), benzoic acid (8.0 mg) and $Zn(NO_3)_2 \cdot 4H_2O$ (16.5 mg) were weighed into the reaction vials (**Table 4.1**). Then, DEF (1.0 mL) and H_2O (50.0 µL) were added. The vials were heated for 10 minutes at 85 °C in an isothermal oven. TEA (2.5-3.0 µL) was added, the MOF synthesis mixture was briefly sonicated, and then placed back into the oven.

After 15-30 minutes, a small amount of fluffy powder precipitated, which was filtered through a syringe filter. MOF formation was observed within 1-2 hours after filtration. Once MOF crystals were obtained in satisfactory amounts, the mother liquid was decanted, and the crystals were washed with acetone (5 × 1 mL). Each MOF synthesis yields approximately 7-15 mg of MOF crystal.

Table 4.1: Ligands, weights and molar mass used for the MOF synthesis. The measured ligands ratios of the synthesised MOFs.

MOF nomenclature	H_3hmtt mg/µmol	(^{5}N-bdc-X-OH)/ H_2bdc mg/µmol	(^{7}N-bpdc-X)/ H_2bpdc mg/µmol	^{1}H NMR ratio
$[Zn_4O(hmtt)_{4/3}(bpdc)_{1/2}(^5N\text{-}bdc\text{-}AlaOH)_{1/2}]$	2.2 3.9	2.0 7.5	1.4 5.8	1.33: 0.5: 0.5
$[Zn_4O(hmtt)_{4/3}(bpdc)_{1/2}(^5N\text{-}bdc\text{-}ValOH)_{1/2}]$	2.2 3.9	2.3 7.8	1.4 5.8	1.33: 0.5: 0.5
$[Zn_4O(hmtt)_{4/3}(bpdc)_{1/2}(^5N\text{-}bdc\text{-}Leu\text{-}OH)_{1/2}]$	2.4 4.3	2.4 7.8	1.3 5.4	1.33: 0.5: 0.5
$[Zn_4O(hmtt)_{4/3}(bpdc)_{1/2}(^5N\text{-}bdc\text{-}Ile\text{-}OH)_{1/2}]$	2.2 3.9	2.5 8.1	1.2 4.9	1.33: 0.5: 0.5
$[Zn_4O(hmtt)_{4/3}(bpdc)_{1/2}(^5N\text{-}bdc\text{-}Ser\text{-}OH)_{1/2}]$	2.3 4.1	2.2 7.8	1.4 5.8	1.33: 0.5:0.5
$[Zn_4O(hmtt)_{4/3}(bpdc)_{1/2}(^5N\text{-}bdc\text{-}MetOH)_{1/2}]$	2.3 4.1	2.9 8.9	1.2 4.9	1.33: 0.5: 0.5
$[Zn_4O(hmtt)_{4/3}(bpdc)_{1/2}(^5N\text{-}bdc\text{-}Phe\text{-}OH)_{1/2}]$	2.4 4.3	2.7 7.8	1.3 5.4	1.33: 0.5: 0.5
$[Zn_4O(hmtt)_{4/3}(^7N\text{-}bpdc\text{-}Ala)_{1/2}(bdc)_{1/2}]$	2.4 4.3	1.4 8.4	1.9 5.1	1.33: 0.5: 0.5
$[Zn_4O(hmtt)_{4/3}(^7N\text{-}bpdc\text{-}Val)_{1/2}(bdc)_{1/2}]$	2.3 4.1	1.3 7.8	2.2 5.5	1.33: 0.5: 0.5
$[Zn_4O(hmtt)_{4/3}(^7N\text{-}bpdc\text{-}Leu)_{1/2}(bdc)_{1/2}]$	2.3 4.1	1.2 7.2	2.7 6.6	1.33: 0.5: 0.5
$[Zn_4O(hmtt)_{4/3}(^7N\text{-}bpdc\text{-}Ser)_{1/2}(bdc)_{1/2}]$	2.2 3.9	1.2 7.2	2.0 5.2	1.33: 0.5: 0.5
$[Zn_4O(hmtt)_{4/3}(^7N\text{-}bpdc\text{-}Thr)_{1/2}(bdc)_{1/2}]$	2.2 3.9	1.2 7.2	2.1 5.3	1.33: 0.5: 0.5
$[Zn_4O(hmtt)_{4/3}(^7N\text{-}bpdc\text{-}Met)_{1/2}(bdc)_{1/2}]$	2.2 3.9	1.3 7.8	2.6 5.9	1.33: 0.5: 0.5
$[Zn_4O(hmtt)_{4/3}(^7N\text{-}bpdc\text{-}Phe)_{1/2}(bdc)_{1/2}]$	2.3 4.1	1.2 7.2	2.3 5.2	1.33: 0.5: 0.5
$[Zn_4O(hmtt)_{4/3}(^7N\text{-}bpdc\text{-}His)_{1/2}(bdc)_{1/2}]$	2.2 3.9	1.3 7.8	2.6 5.9	1.33: 0.5: 0.5

4.4.4 Experimental PXRD data and SCXRD for all the previously synthesised MUF-77

In this section, the experimental PXRD data for all the previously synthesised MUF-77 are presented, followed by an example of the collected SCXRD data for each linker family.

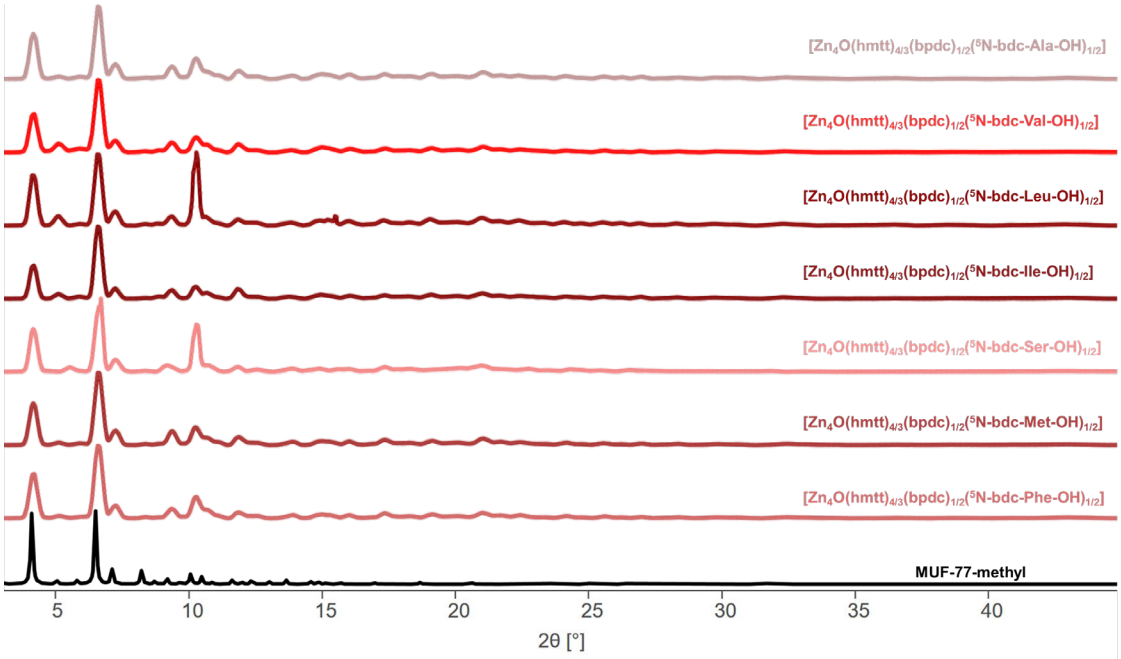

Figure 4.44: Experimental PXRD pattern for MUF-77 synthesised from hmtt, bpdc and ^{5}N-bdc-X-OH ligands.

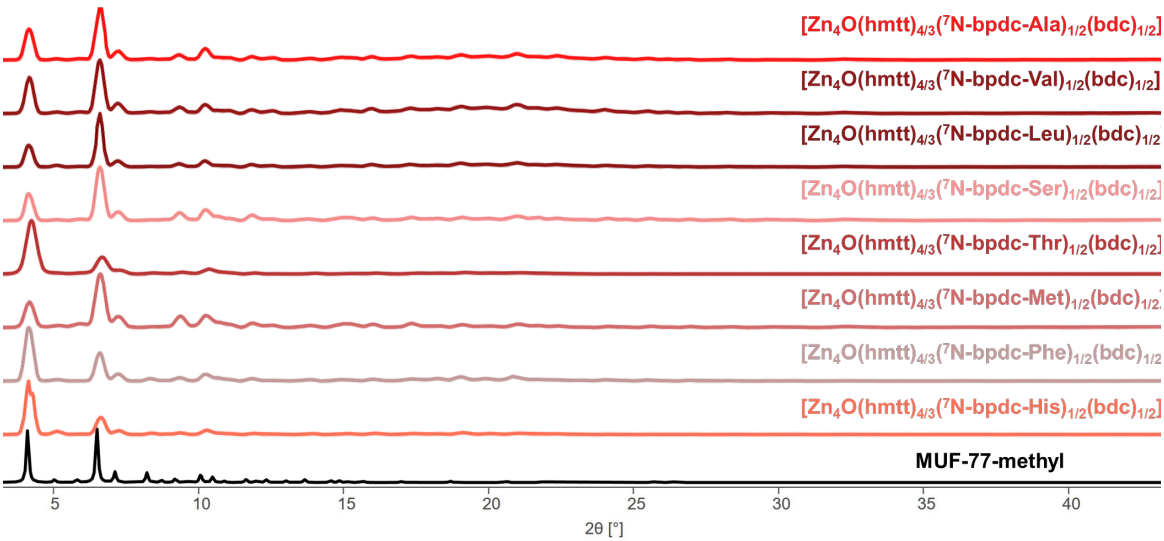

Figure 4.45: Experimental PXRD pattern for MUF-77 synthesised from hmtt, bdc and ^{7}N-bpdc-X-OH ligands.

4.4.5 SCXRD measurements:

Table 4.2: SCXRD data summary.

Name	$[Zn_4O(hmtt)_{4/3}(^7N\text{-bpdc-Ala})_{1/2}(bdc)_{1/2}]$	$[Zn_4O(hmtt)_{4/3}(bpdc)_{1/2}(^5N\text{-bdc-AlaOH})_{1/2}]$
Empirical formula	$C_{57}H_{36}O_{13}Zn_4$	$C_{57}H_{36}O_{13}Zn_4$
Formula weight	1557.02	1190.34
Temperature/K	120	298.00
Crystal system	cubic	cubic
Space group	*Pm-3*	*Pm-3*
a/Å	29.954(3)	29.8726(18)
b/Å	29.954(3)	29.8726(18)
c/Å	29.954(3)	29.8726(18)
α/°	90	90
β/°	90	90
γ/°	90	90
Volume/Å^3	26876(9)	26657(5)
Z	336	6
ρ_{calc}g/cm^3	2.250	0.445
μ/mm^{-1}	8.573	0.771
F(000)	17472.0	3612.0
Crystal size/mm^3	0.3 × 0.2 × 0.3	0.03 × 0.03 × 0.03
Radiation	CuKα (λ = 1.54178)	CuKα (λ = 1.54178)
Index ranges	$-35 \le h \le 35$, $-36 \le k \le 33$, $-33 \le l \le 25$	$-33 \le h \le 34$, $-32 \le k \le 33$, $-29 \le l \le 22$
Reflections collected	104593	100228
Independent reflections	9015 [R_{int} = 0.0454, R_{sigma} = 0.0247]	7595 [R_{int} = 0.0403, R_{sigma} = 0.0198]
Data/restraints/parameters	9015/0/195	7595/0/195
Goodness-of-fit on F^2	1.064	2.786
2Θ range for data refinement/°	2.95 to 143.245	2.958 to 125.535
Final R indexes [I>=2σ (I)]	R_1 = 0.0723, wR_2 = 0.2039	R_1 = 0.1204, wR_2 = 0.3432
Final R indexes [all data]	R_1 = 0.0911, wR_2 = 0.2283	R_1 = 0.1320, wR_2 = 0.3520
Largest diff. peak/hole / e Å^{-3}	0.40/-0.68	1.45/-1.18

Note: The ring and the appended amino acid/ alcohol moieties could not be modelled.

4.4.6 MUF-77 ^{1}H NMR spectroscopic analysis

The crystals were washed thoroughly with acetone (x 5, 0.5 mL) and dried under high vacuum before digestion. ^{1}H NMR spectroscopy of the dissolved crystals in DCl/DMSO-d_6 (23 µL/ 1 mL) was then performed to confirm phase purity. Signal integration followed the established method based on the MUF-77 formula $[Zn_4O(hxtt)_{4/3}(bpdc)_{1/2}(bdc)_{1/2}]$, which establishes an expected linker ratio of 4/3:1/2:1/2 (hmtt:bpdc:bdc). One of the three aromatic signals of the truxene linker, each corresponding to three protons, was used as the reference and set to 4H (since 4/3 × 3H = 4H). Under this calibration, the expected integrals of bpdc and bdc are reduced to half their absolute values.

Representative examples of MUF-77 analogues synthesised with the amino acid–functionalised linker family (^{5}N-bdc-X-OH and ^{7}N-bpdc-X, where X denotes the amino acid substituent) are shown in **Figure 4.46** and **Figure 4.47.** The ^{1}H NMR spectrum of $[Zn_4O(hmtt)_{4/3}(bpdc)_{1/2}(5N\text{-}bdc\text{-}Ala\text{-}OH)_{1/2}]$ (**Figure 4.46**) and that of $[Zn_4O(hmtt)_{4/3}$ (^{7}N-bpdc-Ala)$_{1/2}(bdc)_{1/2}]$ (**Figure 4.47**) are presented as representative examples. The remaining spectra for other members of the series are provided in **Appendix C**.

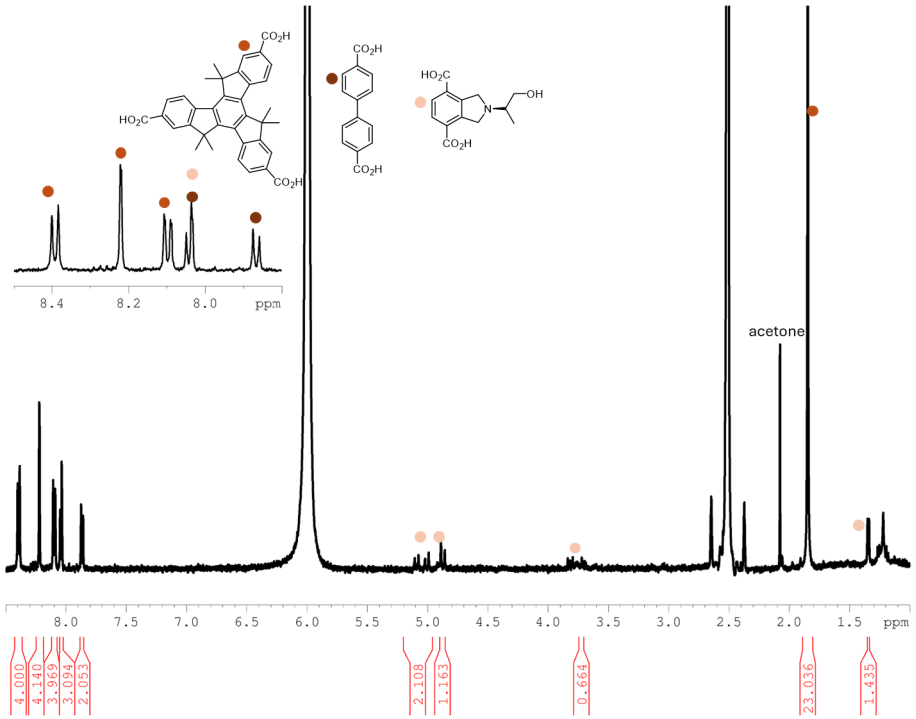

Figure 4.46: ^{1}H NMR spectrum of [$Zn_4O(hmtt)_{4/3}(bpdc)_{1/2}(^{5}$N-bdc-Ala-OH)$_{1/2}$] that was dissolved in0 DCL/DMSO-d_6.

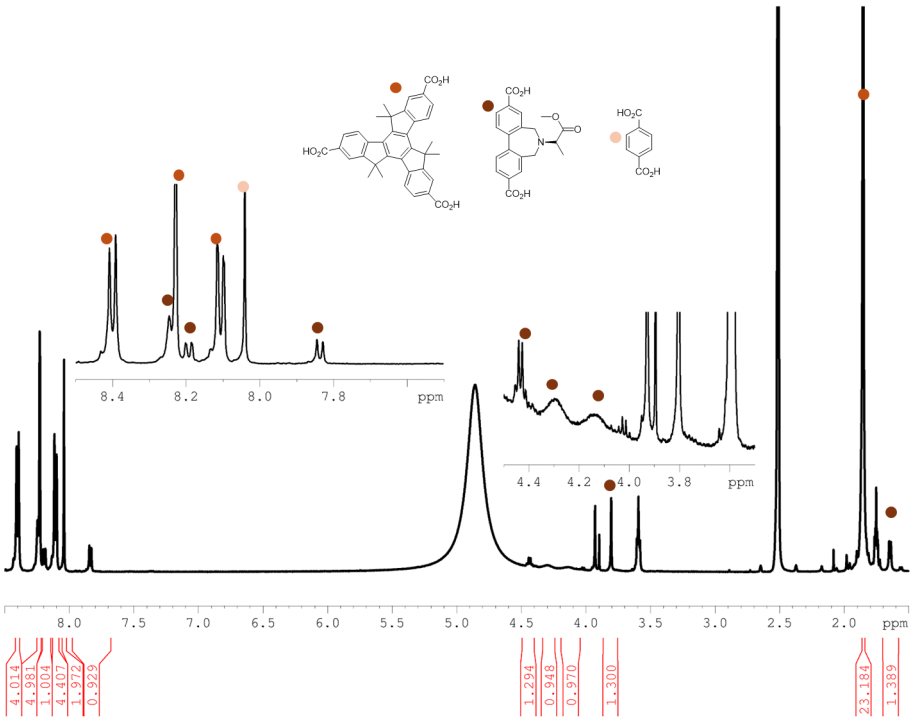

Figure 4.47: ^{1}H NMR spectrum of [$Zn_4O(hmtt)_{4/3}(bdc)_{1/2}(^{7}$N-bpdc-Ala)$_{1/2}$] that was dissolved in DCL/DMSO-d_6.

Chapter 5 Steps towards a catalytic triad

5.1 Introduction

Enzymes provide a natural model of catalysts, as their extraordinary efficiency and selectivity arise not from a single functional group, but from the cooperative action of multiple residues arranged within a confined microenvironment. To frame the catalytic potential of MUF-77, this chapter provides an overview of cooperative catalysis before focusing on interdependent motifs such as catalytic dyads and triads

5.1.1 Cooperative catalysis

Multicomponent MOFs enable cooperative catalysis by incorporating linkers with different functionalities that act together to accelerate reactions, a concept particularly suited to cascade or sequential processes where the removal of one component reduces but does not abolish activity.[181] LIFM-28 is a representative example, in which Cu(I) sites catalysed aerobic alcohol oxidation and click reactions, while amine linkers promoted Knoevenagel condensation, enabling multiple transformations within a single framework (**Figure 5.1**).[182, 183]

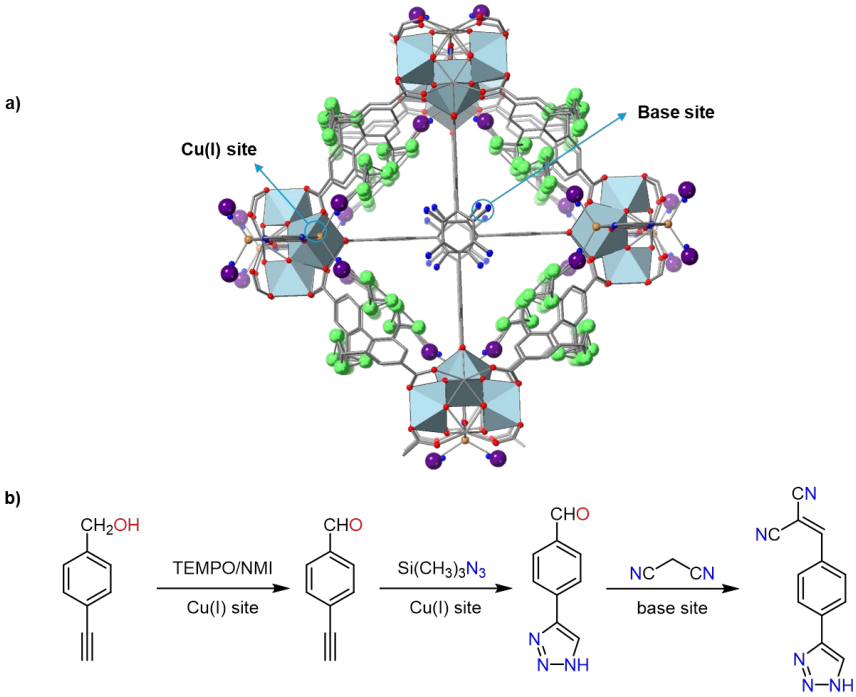

Figure 5.1: Synergistic catalysis using LIFM-28, where multiple catalysts are incorporated.

Similarly, IR-UIO-68, prepared by post synthetic incorporation of metal–salen linkers (Cr, Mn, Cu, Fe, V), displayed high activity and enantioselectivity across diverse reactions, including cyanosilylation, epoxide ring-opening, and oxidative kinetic resolution.[184] In particular, Mn and Cr centres cooperatively catalysed an epoxidation–ring-opening cascade with excellent selectivity (ee up to 99.5%), while Cu centres facilitated Friedel-Crafts and Henry reactions.[185] These examples highlight how synergistic, multicomponent MOFs can outperform homogeneous analogues by integrating multiple, spatially organized catalytic sites within a single material.

5.1.2 Catalytic dyad/triad

In cooperative catalysis, two catalysts work together to enhance reactivity, but the removal of one does not completely inhibit the process. Enzymes, however, demonstrate a more complicated form of cooperation known as a catalytic dyad/triad. In a dyad, both residues are essential; removing one abolishes catalytic activity. This mechanism relies on the precise positioning of residues in close proximity, enabling substrate activation.[165]

In translating this principle to MUF-77, functionalised linkers can be positioned within the pore microenvironment to form dyad- or triad-like motifs. Such arrangements allow enzyme-inspired precision, where reactive residues interact cooperatively within a synthetic framework system (**Figure 5.2**).

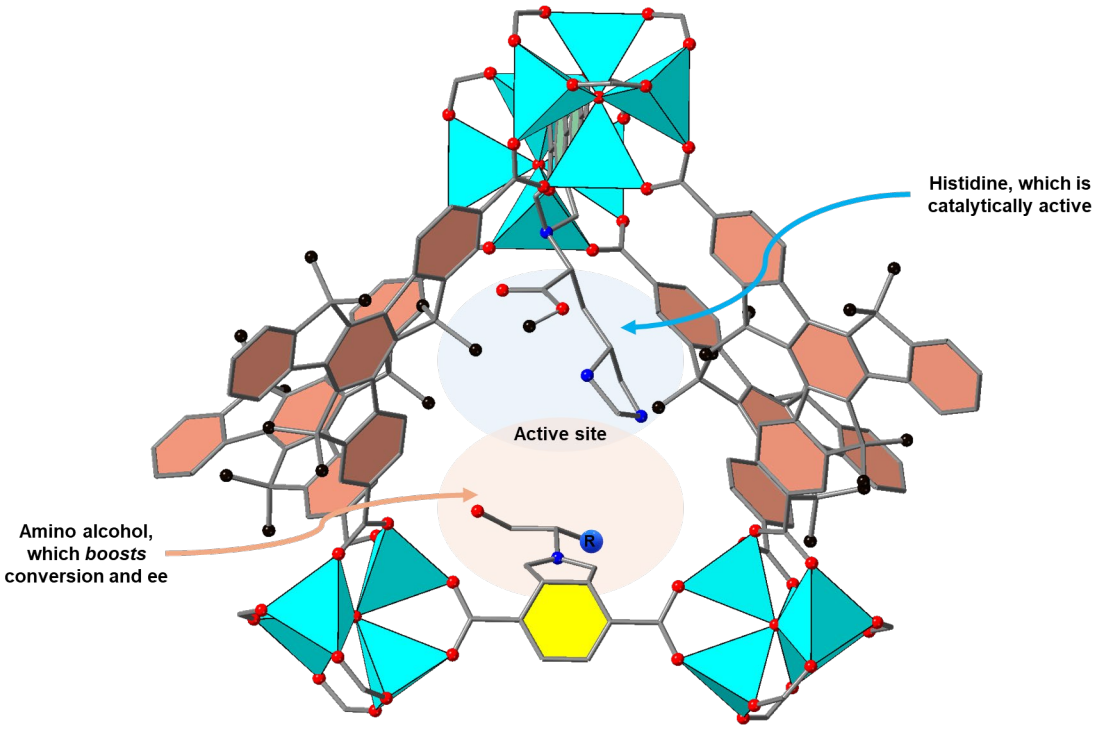

Figure 5.2: Graphical illustration of catalytic dyad/triad mimicry within the tetrahedral pore of MUF-77.

MUF-77 offers an ideal platform for mimicking enzymatic principle, because its pore environment can be engineered with functionalised linkers,[5, 6, 56] enabling the installation of amino acid residues in precise orientations. By controlling the amino acids groups on the linkers, it is possible to recreate the cooperative arrangements of enzyme active sites within a synthetic framework.

5.1.3 Benchmark reactions modelled after enzymatic catalysis

To illustrate this concept, this study focused on the well-established reactions: the Michael and aldol reactions (one-residue iminium/enamine mimic), cyanohydrin formation (two-residue diketopiperazine/dyad mimic), and hydrolysis (three-residue triad mimic). These reactions were chosen for several reasons:

- ❖ They are well studied and provide clear models for biomimicry
- ❖ They depend on the cooperative work of nucleophilic, basic, and stabilizing residues that can be emulated by amino acid functional groups in MUF-77.
- ❖ They allow systematic progression from simple (one residue) to complex (dyad/triad) catalytic motifs.

5.1.4 Model reactions for enzyme-mimicry

One-Residue Catalysis: Iminium and Enamine Mechanisms

Iminium and enamine catalysis form the foundation of many organocatalytic strategies. While enamine catalysis, exemplified by Class I aldolases, is more common in nature, several enzymes employ iminium intermediates in their catalytic cycles. For example, iminium reductases and Pictet–Spenglerases transiently generate iminium ions during substrate transformation, highlighting their role as reactive intermediates in biological systems.[186, 187]

The concept of iminium catalysis has been extensively adopted in organocatalysis, particularly in the 21st century, where both primary and secondary amines have been utilized as catalysts. Secondary amines, such as proline derivatives, are especially prevalent due to their ability to stabilize iminium intermediates. In general, iminium catalysis proceeds via the reaction of an amine catalyst with a carbonyl substrate to form an iminium ion **(Figure 5.3)**. The iminium intermediate is significantly more electrophilic than the parent aldehyde or ketone, thereby facilitating nucleophilic attack. In general, iminium catalysis involves condensation of an amine catalyst with a carbonyl substrate, producing an iminium ion that is more electrophilic than the parent carbonyl and thus more susceptible to nucleophilic attack. The stereoselectivity of these reactions depends strongly on steric and H-bonding interactions surrounding the catalytic site.[187]

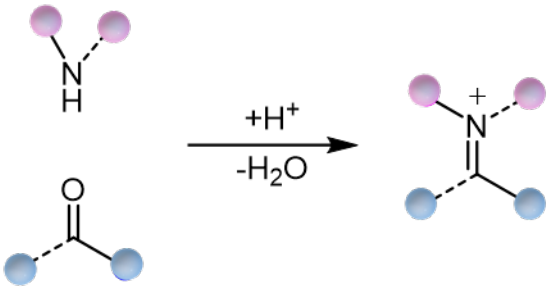

Figure 5.3: General pathway for iminium catalysis.

Michael Reactions

The Michael addition has been a benchmark transformation for exploring enzyme-inspired iminium catalysis. One example is 4-oxalocrotonate tautomerase (4-OT), a bacterial enzyme involved in aromatic hydrocarbon degradation. Through active-site engineering, 4-OT was repurposed to catalyse enantioselective Michael additions, such as the conjugate addition of nitromethane to α, β-unsaturated aldehydes to afford γ-nitroaldehydes (**Figure 5.4**). The reaction proceeds via iminium ion formation between the carbonyl substrate and the catalytic amine, with the pharmaceutically relevant R-enantiomer obtained preferentially.[187]

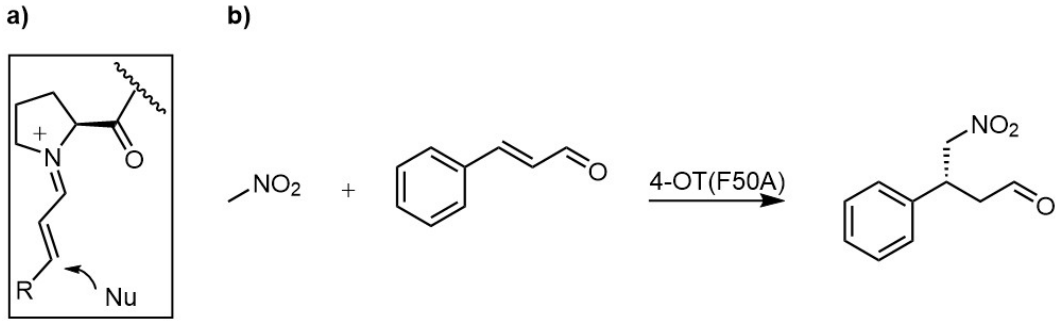

Figure 5.4: a) Engineered mechanism of 4-OT catalysing the Michael addition.
b) For example: addition of nitromethane to an α,β-unsaturated aldehyde.

Another enzyme, deoxyribose-5-phosphate aldolase (DERA), natively catalyses the asymmetric aldol reaction of acetaldehyde with D-glyceraldehyde-3-phosphate to yield 2-deoxy-D-ribose-5-phosphate. Structural studies have revealed that the lysine in the active site forms a Schiff base with the donor substrate, thereby generating an enamine intermediate. Repurposing DERA has enabled it to catalyse Michael additions, again involving an iminium intermediate with the substrate carbonyl (**Figure 5.5**).[187]

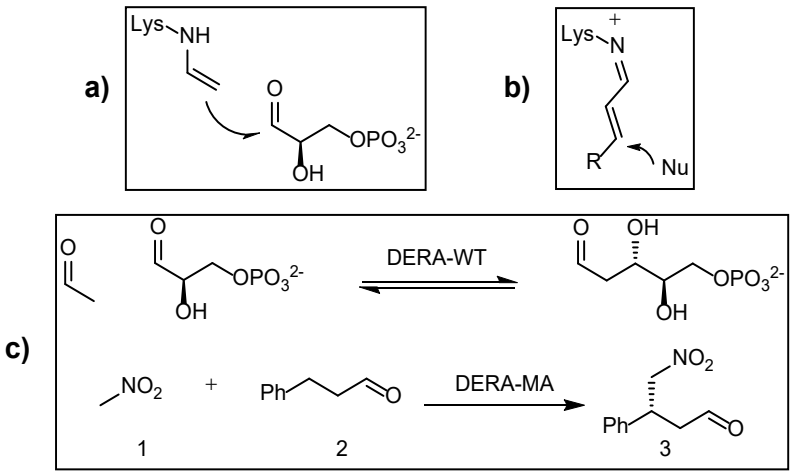

Figure 5.5: a,b) Natural aldol reaction catalysed by DERA.
c) Repurposed DERA mechanism for Michael reactions.

Computational enzyme design has also expanded this field. RA95.0, a de novo designed enzyme, was initially constructed for retro-aldol cleavage of methodol using lysine as a Schiff base in a hydrophobic pocket. After multiple rounds of directed evolution, the variant RA95.5-8 exhibited a > 4000-fold increase in activity and was successfully redirected to catalyse Michael additions of nucleophiles to α, β-unsaturated ketones (**Figure 5.6**). This activity arises from iminium intermediate formation with the lysine terminal amine, demonstrating how rational design and evolution can optimise iminium catalysis.

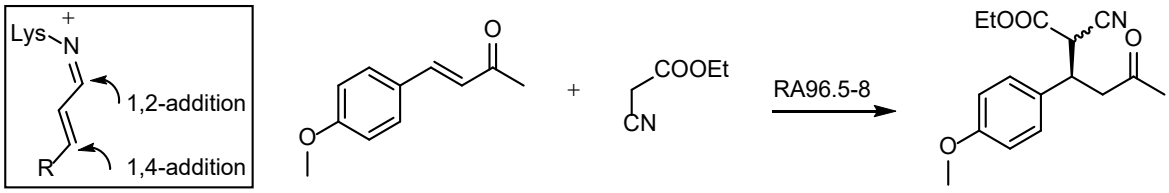

Figure 5.6: RA95.5-8 catalysing the addition of nucleophiles to α,β-unsaturated ketones via iminium intermediates.

Aldol Reactions

The aldol reaction is another benchmark transformation that can proceed through iminium or enamine intermediates. While natural enzymes such as Class I aldolases utilize lysine residues to form Schiff bases with substrates, organocatalysts based on proline or short peptides have also been developed. Proline-containing peptides catalyse aldol reactions through enamine formation at the N-terminus pyrrolidine group, while lysine-containing scaffolds mimic aldolase-type catalysis.Short peptides provide a versatile platform for asymmetric aldol catalysis, as they combine covalent enamine activation with noncovalent stabilisation through secondary structures. Numerous proline- and lysine-based peptides have been reported to catalyse aldol reactions between benzaldehyde derivatives and ketones such as acetone or cyclohexanone, with selectivity often favouring the anti-diastereomer, reminiscent of the natural proline-catalysed aldol reaction (**Figure 5.7**).[188]

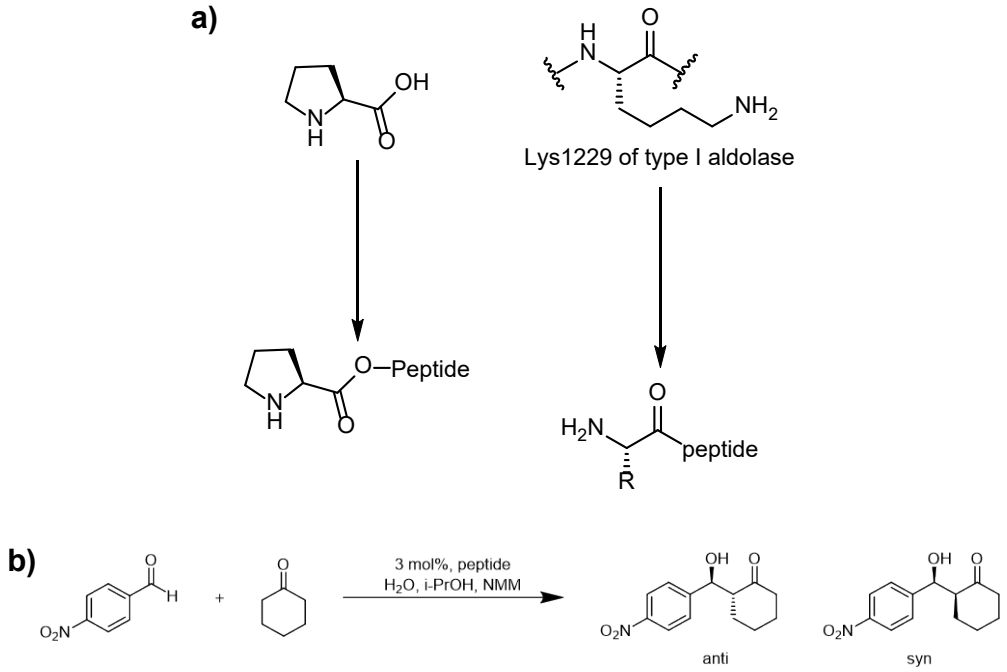

Figure 5.7: a) Amine-based catalyst design inspired by natural aldolases.
b) Example of an asymmetric aldol reaction catalysed by peptide-based catalysts.

While single-residue aldol catalysis has been dominated by proline, histidine has also been found to be an effective aldol reaction catalyst. (S)-Histidine-based dipeptides have been bifunctional organocatalysts for the direct aldol reaction. Tsogoeva and Wei demonstrated that H-Leu-His-OH catalyses the acetone condensation with aromatic aldehydes, affording products in high yield (96%) and high ee (76%).[189] Their work highlights the role of the imidazole side chain of histidine in catalysis, and how a second amino acid residue modulates

selectivity and reactivity. This precedent illustrates histidine's value as a catalytic residue even in short peptide scaffolds.

Two-Residue Catalysis: Cyanohydrin Formation

Cyanohydrins are important synthetic intermediates that can be converted into a wide range of valuable compounds, including α-hydroxy acids, amino alcohols, and β-amino acids (**Figure 5.8**). The stereogenic centre formed during cyanohydrin synthesis is generally preserved through subsequent transformations, making enantioselective cyanohydrin formation a benchmark reaction for asymmetric catalysis.[190]

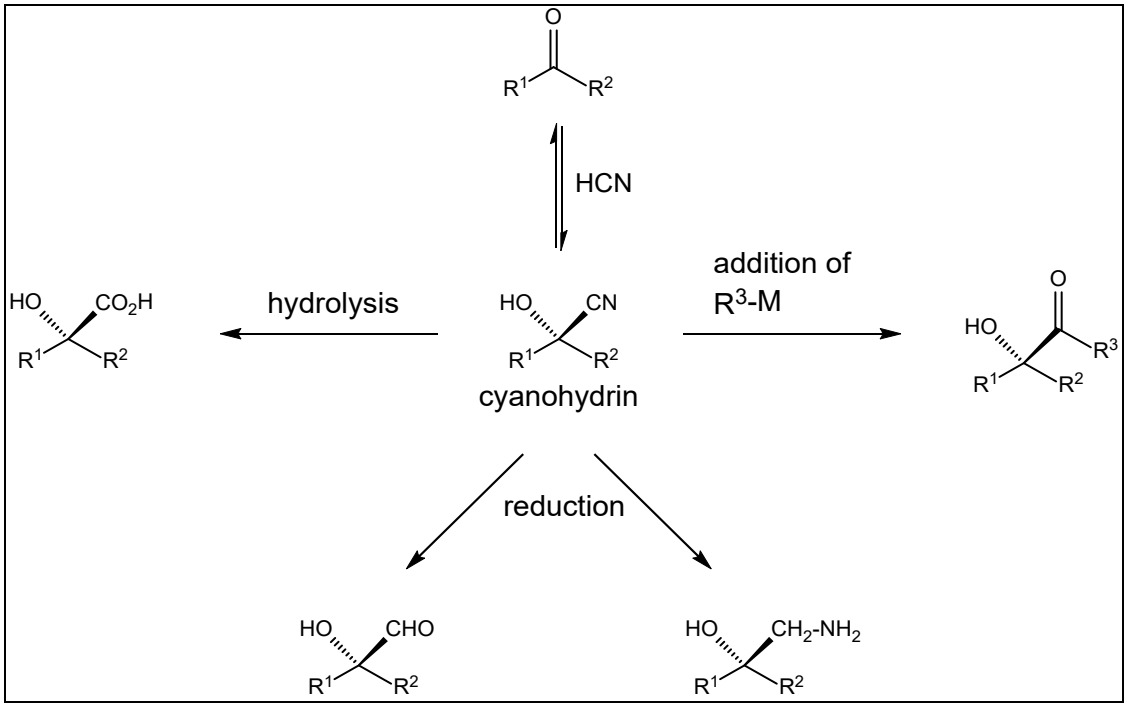

Figure 5.8: Cyanohydrin as a versatile intermediate for further transformations.

The first example of an amino acid-derived catalyst for cyanohydrin synthesis was reported by Inoue in 1981.[190] This study described the asymmetric addition of hydrogen cyanide (HCN) to aldehydes using a diketopiperazine catalyst composed of two amino acids, (S)-phenylalanine and (S)-histidine. In this system, the imidazole group of histidine acts as a catalytic base to activate the nucleophile, while the phenylalanine residue contributes to stereocontrol. The reaction produced (R)-cyanohydrins with up to 97% enantiomeric excess (ee) (**Figure 5.9**).

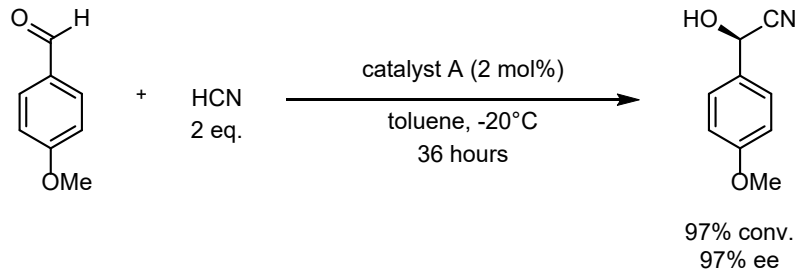

Figure 5.9: Asymmetric addition of HCN to aldehydes catalysed by a diketopiperazine-based catalyst.

Synthetic analogues based on this diketopiperazine scaffold have been developed to probe structure-activity relationships. For example, Catalyst A, derived from S-histidine and S-phenylalanine, catalysed the cyanohydrin reaction in high yield with excellent enantioselectivity. Catalyst B, in which phenylalanine was replaced by S-valine, was significantly less selective, producing lower ee values (**Figure 5.10**). This reduction in activity and selectivity was attributed to steric shielding of the imidazole group, which hindered its catalytic role.

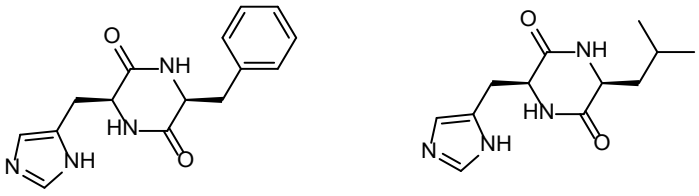

Figure 5.10: Diketopiperazine catalysts A (His-Phe) and B (His-Val) used in asymmetric cyanohydrin formation.

Further analogues were synthesised by replacing phenylalanine with aromatic or heteroaromatic residues. Most of these variants were catalytically inactive, often due to their high solubility, which prevented the formation of active catalytic assemblies. The only exception was a 2-thienyl derivative, which displayed moderate activity but lower enantioselectivity compared to Catalyst A.[191] Another cyclic dipeptide composed of histidine and alanine also catalysed the cyanohydrin reaction, but with a much lower optical yield (~20% ee).[190]

A key feature of diketopiperazine catalysis is the requirement for a heterogeneous or amorphous phase. Catalytic activity was observed when the reaction medium formed a gel-like material (e.g., in benzene or toluene) or when the catalyst remained insoluble in solvents such as ether. In contrast, crystalline solid forms of the catalyst were inactive. Moreover, the presence of a proton source, such as water or methanol, within the catalytic microenvironment was essential for activity. Interestingly, product addition was found to accelerate the reaction, suggesting a cooperative or autocatalytic effect.[191]

Despite these advances, the use of diketopiperazine catalysts in asymmetric cyanohydrin synthesis remains limited. The reliance on hazardous HCN as the cyanide source and the relatively small number of effective catalyst variants have constrained further development in this area.[191, 192]

While single- and two-residue models illustrate the foundations of biomimetic catalysis, true enzyme-like precision often requires three residues arranged cooperatively in space. This principle is exemplified in hydrolytic triads.

Three-Residue Catalysis: Hydrolysis Reactions

Unmodified amino acids and short peptides are less commonly used as catalysts than as chiral building blocks. However, peptide-based catalysis offers unique opportunities to bridge the gap between small-molecule catalysts and enzymes.[192] Peptide catalysts fall broadly into two groups: (i) small, rigid amino acids or cyclopeptides, and (ii) larger peptides capable of folding into secondary or tertiary structures. Short peptides are particularly promising since they can form secondary structures in aqueous and organic solvents, creating catalytically active sites while retaining flexibility.[192]

The catalytic ability of short peptides has been demonstrated mainly in hydrolysis reactions. Amyloid-derived peptides catalyse aldehyde hydrolysis, with only a few residues directly responsible, while the scaffold provides a cooperative chiral environment. [193] Self-assembled nanotubes enhance activity by exposing residues to the solvent, enabling recognition and catalysis through charge interactions, hydrophobic effects, and steric constraints. Even short β-folds have been shown to promote stereoselective aldehyde hydrolysis (**Figure 5.11**).[193]

A notable case is the KLVFFA sequence from amyloid-β, which assembles into β-sheet nanotubes. A leucine-modified variant (KL) preferentially hydrolysed one enantiomer of a racemic aldehyde mixture, giving modest enantioselectivity (~13% ee for the R enantiomer). Congo Red dye assays confirmed covalent anchoring via imine formation (**Figure 5.11**).[193] Although the selectivity was low, these results showed that short peptides can generate enantioselective catalytic environments in self-assembled systems.

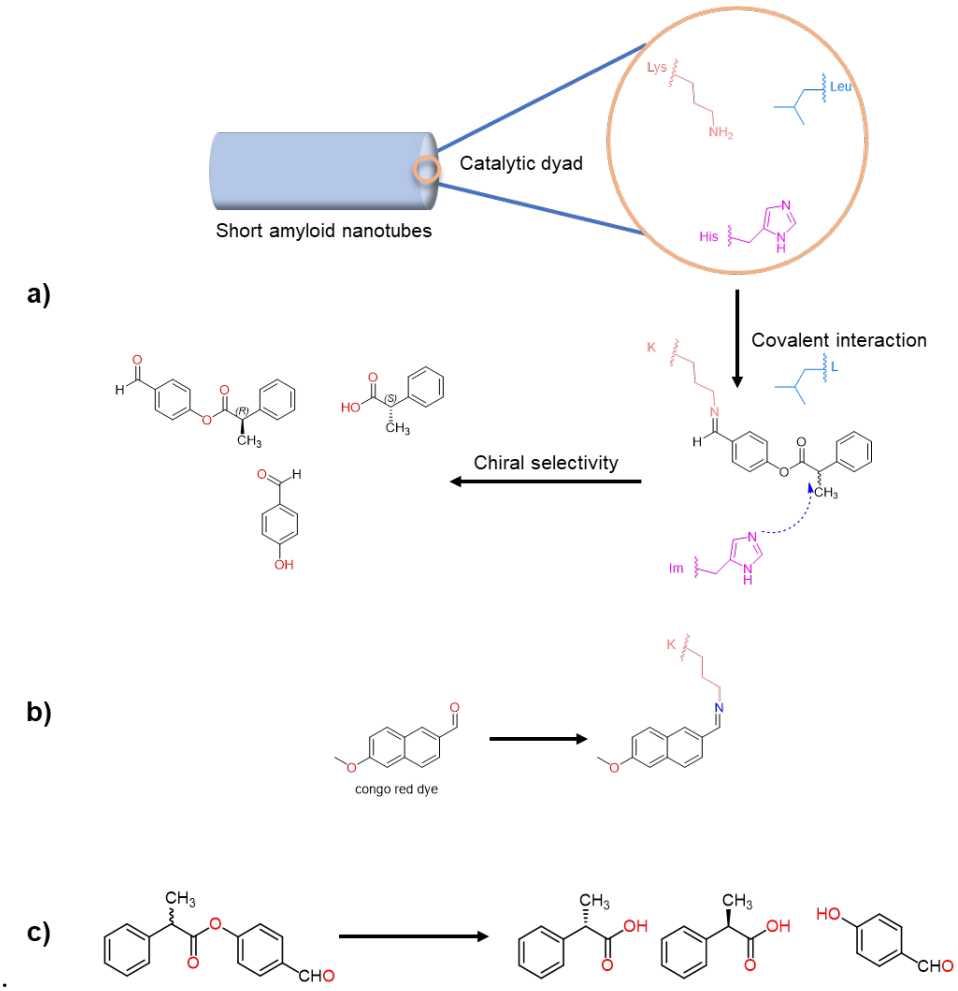

Figure 5.11: **a)** Catalytic dyad in short amyloid peptides enabling covalent substrate anchoring and hydrolysis. **b)** Congo Red dye binding assay demonstrating imine formation by KL peptide assemblies. **c)** Hydrolysis reaction catalysed by short peptide nanotube.

Further modifications introduced imidazole into KL (Im-KLVFFAL, "cat-KL"), yielding a minimal catalytic triad with imidazole as the hydrolytic residue, leucine as a hydrophobic core, and lysine as the enantioselective anchor. While less selective than natural lipases, cat-KL provided proof of concept for rational peptide-based catalysts.[193] Mutational studies reinforced this: replacing lysine with arginine abolished imine intermediate formation, lowering conversion and enantioselectivity. Substrate scope studies also showed that esters without carbonyl groups gave activity but negligible selectivity, underlining the importance of carbonyl recognition (**Figure 5.12**).[193]

a)

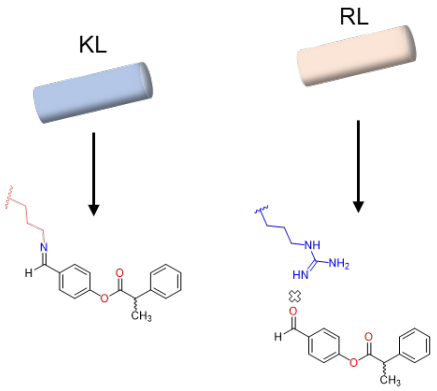

b)

Catalyst Type	Substrate	Time (Hour/s)	%ee
Cat-KL	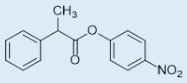	1.5	10.7 ± 4.2
Cat-RL	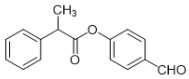	10	12.2 ± 0.6
Cat-KL	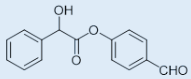	1	13.3 ± 1.5
Cat-KL	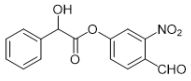	2	24.2 ± 3.8
Cat-KL	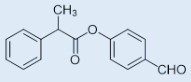	6	29.7 ± 1.2

Figure 5.12: a) Effect of lysine to arginine mutation on catalytic activity and enantioselectivity. **b)** Hydrolysis activity and enantioselectivity across different peptide-based catalysts.

Finally, stereochemical variations confirmed the role of chirality. Altering the R/S configuration of lysine and leucine reduced performance, while a doubly mutated R–R peptide showed minimal conversion and ee. Thus, the stereogenicity of key residues is critical for substrate binding and cooperative interactions that generate functional active sites.[193]

5.1.5 Engineering enzyme-like active sites in MUF-77

The overarching strategy of this work was to engineer enzyme-like active sites within MUF-77 by progressively introducing amino acid functional groups and pore-modifying units. The approach was designed to move in stages: beginning with single-residue systems to establish baseline catalytic activity (**Figure 5.13**), then advancing toward dyad and triad motifs (**Figure 5.2**) capable of cooperative catalysis. Amino acid residues such as lysine and histidine were chosen because of their ability to participate in enamine/iminium chemistry and general base catalysis, while truxene derivatives bearing long alkyl chains were targeted to mimic hydrophobic residues. Ideally, these frameworks would remain catalytically inactive until all two/three members of the dyad/triad were present, mirroring the interdependence of residues within natural enzyme active sites.

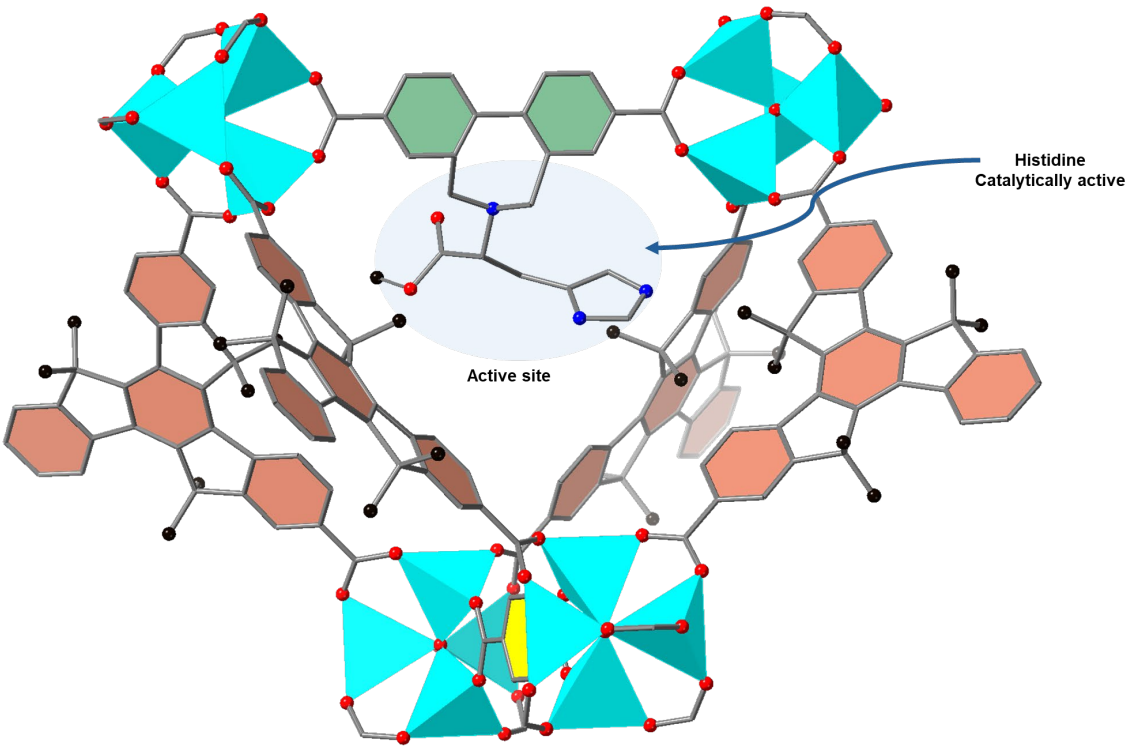

Figure 5.13: Graphical representation of the active site in the tetrahedral microporous cavity of MUF-77.

The initial plan was to begin with a single-residue system by incorporating bpdc-Lys-BOC into MUF-77 using the general linker installation procedure described previously (**Figure 5.14**). The Boc-protected amine was selected to ensure the targeted -NH_2 forms the seven-membered ring, with the intention of subsequently removing the protecting group under thermolytic conditions.

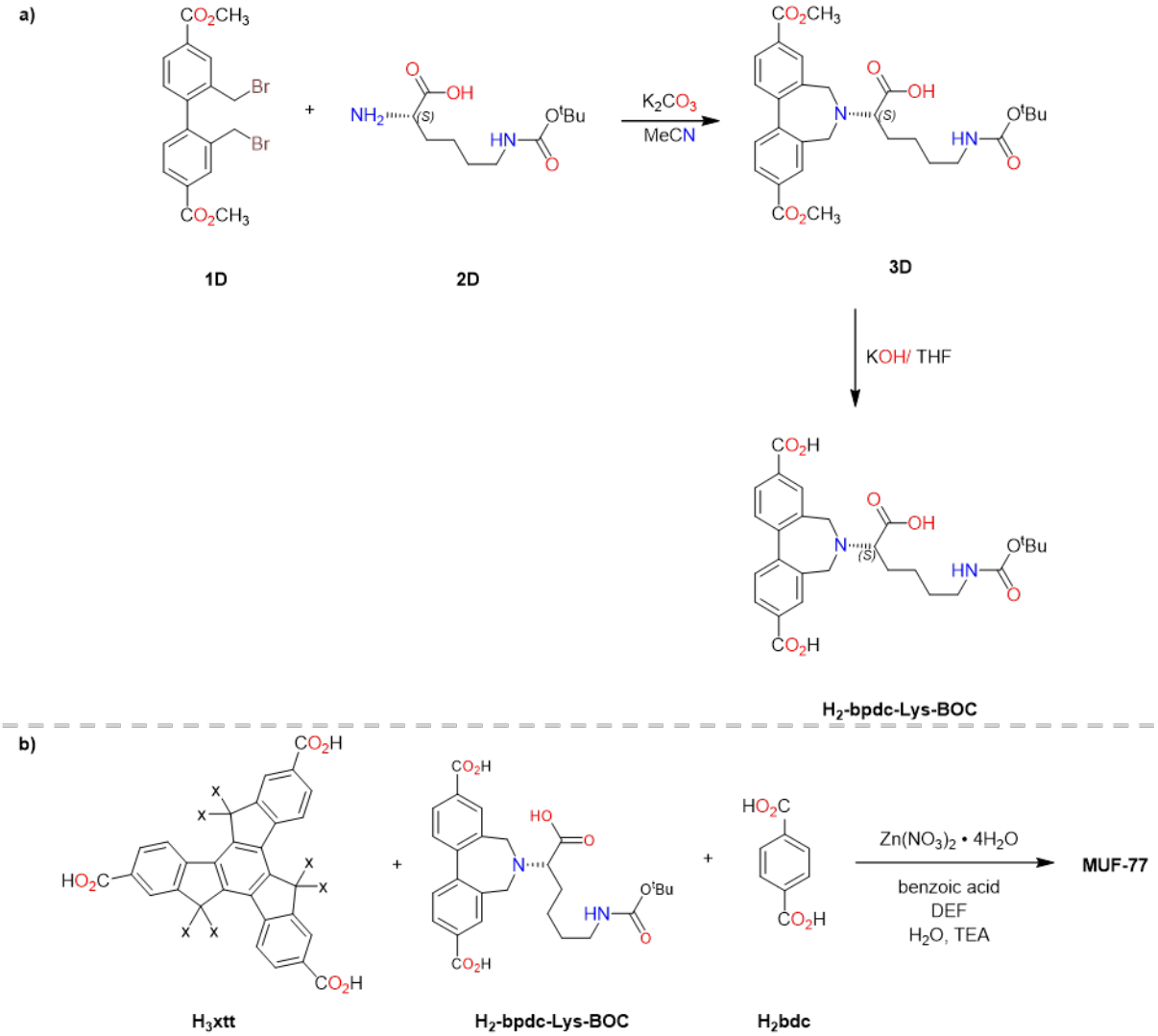

Figure 5.14: a) The most reliable procedure identified for the synthesis of ^{7}N-bpdc-Lys(BOC), which provided interpretable results
b) The proposed strategy for incorporating ligand (H_2bpdc-Lys-BOC) into the MUF-77 framework.

BOC-deprotection was expected to proceed cleanly within the solid framework, releasing CO_2 and isobutylene without compromising MUF-77 integrity (**Figure 5.15**), as demonstrated earlier with bpdc-Pro and bdc-Pro derivatives.[56]

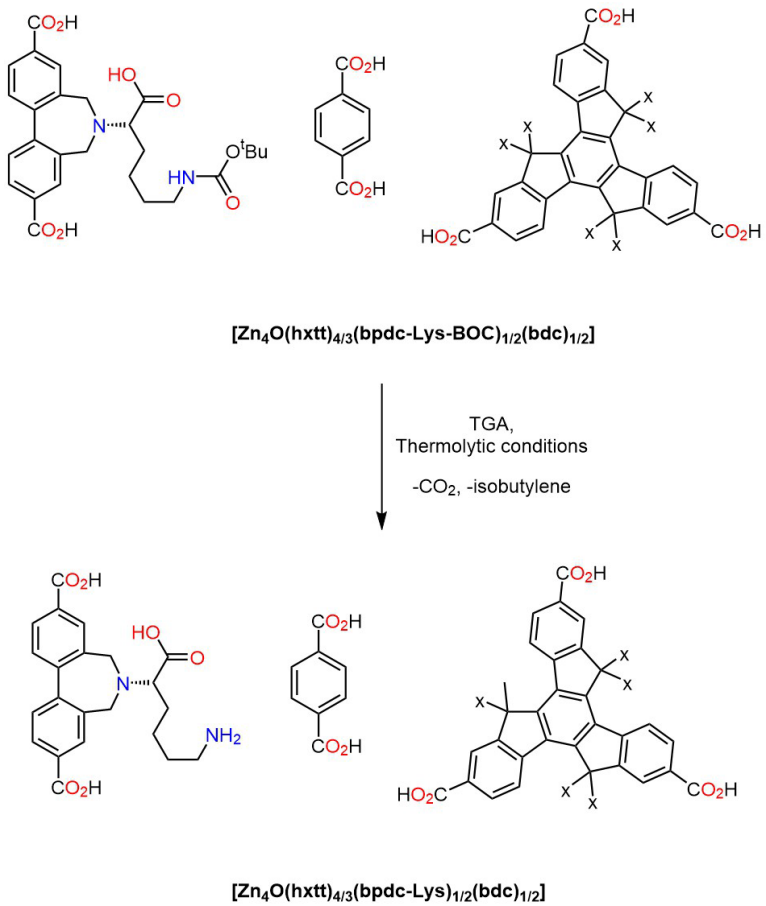

Figure 5.15: The planned removal of the Boc protecting group via thermolysis, enabling exposure of the free lysine amine within the pores.

Upon deprotection, the free terminal amine of lysine would provide a catalytically active handle inside the pores, capable of forming iminium or enamine intermediates. This would allow MUF-77 to mediate benchmark transformations such as the Michael addition and aldol reactions, directly mimicking the activity of natural aldolases.

However, despite repeated attempts, the synthesis of bpdc-Lys-BOC itself proved challenging, and the ligand could not be obtained in a pure, isolable form. As a result, this initial strategy could not be pursued further, and the focus shifted to alternative residues that could be more readily synthesised and incorporated into MUF-77.

The revised strategy employed bpdc-His, which was more straightforward to synthesise and incorporate. Histidine offers both general base catalysis and enamine chemistry, making it a suitable candidate for probing the aldol reaction. Once established, this single-residue platform can be expanded to dyad and triad systems by combining histidine with additional amino acid residues to mimic more sophisticated enzyme-like active sites.

In practice, both bpdc and bdc linkers were functionalised with residues including histidine, phenylalanine, and leucine analogues, and successfully incorporated into MUF-77 as described in **4.2.4.8**, **4.2.4.7**, **4.2.4.3,** respectively. In parallel, procedures for truxene modification with different alkyl chains were established.

5.2 Results and discussion

This chapter describes the catalytic screening of MUF-77 systems, focusing on aldol and Michael benchmark reactions, alongside comparative reactions. These reactions were selected as enzyme-inspired models (**5.1.3**), and their evaluation provides the first test of MUF-77 functionalised with amino acid residues as a biomimetic catalyst.

The screening began with a simple MUF-77 system to establish baseline reactivity before moving toward catalytic dyad/triad arrangement. The initial studies used MUF-77 functionalised with ^{7}N-bpdc-His linkers (**Figure 5.16**) to probe the catalytic potential of histidine residues within the framework.

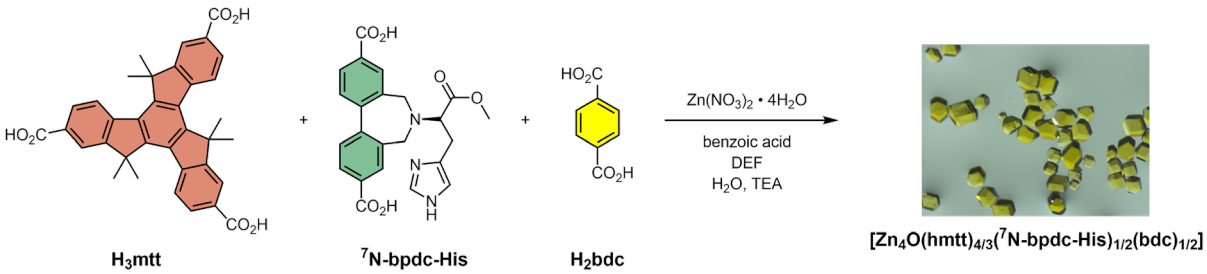

Figure 5.16: Synthetic pathway to $[Zn_4O(hmtt)_{4/3}(^{7}N\text{-bpdc-His})_{1/2}(bdc)_{1/2}]$ using the modified synthesis procedure.

5.2.1 Screening different reactions using $[Zn_4O(hmtt)_{4/3}(bdc)_{1/2}(^7N\text{-}bpdc\text{-}His)_{1/2}]$ system

The framework was tested across a series of benchmark reactions under standardised conditions to identify systems displaying measurable catalytic activity and to highlight inactive transformations for exclusion from further studies.

5.2.2 Standard reaction conditions

All catalytic screenings employed standardised protocols previously established by our group to ensure reproducibility and direct comparison across reactions. These protocols, compiled in our internal manual of standardised procedures that specify:

- TLC conditions for rapid monitoring of reaction progress
- NMR procedures for structural verification
- HPLC methods for product quantification and enantiomeric excess analysis

For each benchmark reaction, the standardised protocols provide detailed information on substrates, mobile phases, flow rates, detection wavelengths, and retention times, enabling consistent analysis across different catalysts and conditions.

A summary of these standardised conditions for the aldol is presented in the experimental section, while the Michael addition is presented in **Appendix D**.

5.2.3 Summary of the reaction screening results

This system was evaluated across the aldol reaction and Michael addition. The aldol reaction was the only reaction that showed measurable catalytic activity, while no significant conversion was observed for the Michael addition under the standard screening conditions.

Catalyst preparation

MUF-77 crystals were synthesised using the procedure described above (**Figure 5.16**). After synthesis, the mother liquor (DEF) was decanted, and the crystals were washed with acetone (x 5, 0.5 mL). The phase purity of the MUF-77 crystals and the integrity of the incorporated ligands were confirmed by SCXRD, PXRD, and ^{1}H NMR spectroscopy. Phase purity indicates that no side products were formed, as evidenced by the match between the experimental PXRD pattern and the calculated reference pattern, with no additional reflections observed. If any of the functionalised linkers failed to yield MUF-77 crystals under these conditions, the outcome was considered an unsuccessful synthesis.

This MUF-77 system was then evaluated for catalytic activity across the benchmark reactions described above. Among these, only the aldol reaction produced a measurable product under the screening conditions. Consequently, this system was further investigated using a broader range of aldehyde substrates to explore its catalytic scope (**Figure 5.17**).

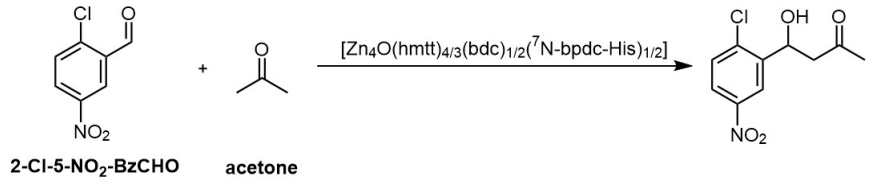

Figure 5.17: The aldol reaction of 2-Cl-5-NO_2-benzaldehyde (BzCHO) with acetone catalysed with MUF-77 (bpdc-His) system.

In this MUF-77(bpdc–His) system, the catalytic activity originates from the histidine-functionalised bpdc linker incorporated into the framework. The imidazole side chain of histidine, positioned within the pore environment (**Figure 5.13**), can act as a Lewis base to promote enamine formation with the carbonyl substrate, thereby enabling C-C bond formation. Embedding this residue in the rigid MUF-77 scaffold restricts its conformational flexibility compared to the homogeneous ester analogue, while simultaneously orienting the functional group within a defined pore environment.

Screening of Different Aldehyde Substrates

Several preliminary optimisation experiments were conducted to choose the best reaction conditions for the aldol reaction catalysed by MUF-77(bpdc–His). The aim was to maximise catalytic activity and ensure the reproducibility before evaluating substrate scope.

Homogeneous catalysis was done using the ester form of the ligand, which resulted in high conversion and a measurable ee (8.3%). This shows that the ligand is catalytically active and exerts some stereocontrol. This result confirms that the immobilised functionality in MUF-77(bpdc–His) is inherently active and capable of asymmetric induction.

Next, the choice of the truxene was evaluated by comparing the performance of MUF-77 crystals synthesised using hmtt with those synthesised using hhtt. In this experiment, H_3hhtt, H_2bdc, and ^{7}N-bpdc-His were incorporated into MUF-77 using the optimized procedure, yielding dodecahedral crystals (**Figure 5.18**). However, this MOF exhibited significantly lower conversion compared to the analogous framework synthesised from hmtt.

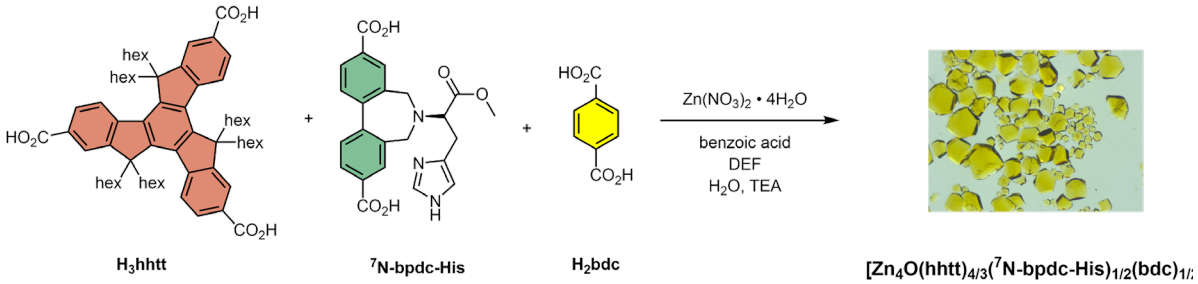

Figure 5.18: Synthetic pathway to $[Zn_4O(hhtt)_{4/3}(^7N\text{-bpdc-His})_{1/2}(bdc)_{1/2}]$ using the modified synthesis procedure.

Before screening a broader range of aldehydes, the aldol reaction of 2-Cl-5-NO_2-benzaldehyde (BzCHO) with acetone was performed in various organic solvents to identify the most suitable reaction medium (**Table 5.1**). The goal was to maximize catalytic activity while ensuring consistent product formation under the same conditions.

The solvents screened included MeCN, THF, Et_2O, DCE, toluene, and EtOAc. Reaction progress was monitored using TLC, and the conversion was quantified via HPLC. The solvent providing the highest conversion was then selected as the standard reaction medium for subsequent aldehyde screenings.

Table 5.1: Solvent Screening	
Solvent types	Qualitative conversion and ee (%)
Dioxane	Low conversion, 2.13%
DCE	Low conversion, 2.17%
THF MeCN	Good conversion, 2.5%
toluene	No product
EtOAc	Low conversion, 2.51%
Et_2O	Background reaction was noticed

THF was identified as the best solvent for the aldol reaction under this system. After selecting THF, reactions were tested at different temperatures. Room temperature provided the highest conversion.

Table 5.2: Temperature screening	
Temperature	Qualitative conversion and ee (%)
r.t.	Good conversion, 2.5%
38 °C	Good conversion, 2.5%
0 °C	No conversion

5.2.4 Screening of Different Aldehyde Substrates

MUF-77(bpdc–His) system catalytic activity was further investigated. The aldol reaction was examined using a series of aromatic aldehydes with varying substitution types and positions (**Figure 5.19**). This screening aimed firstly to evaluate the substrate scope, and the substitution patterns influence on the catalytic efficiency under standard conditions. Secondly and more importantly, to evaluate the MUF-77(bpdc-His) catalytic activity, which ideally exhibit relatively low activity on its own.[7]N-Bpdc-His linker is designed to work as part of a dyad catalytic system, where combining it with a second, active site can enhance overall catalytic performance.

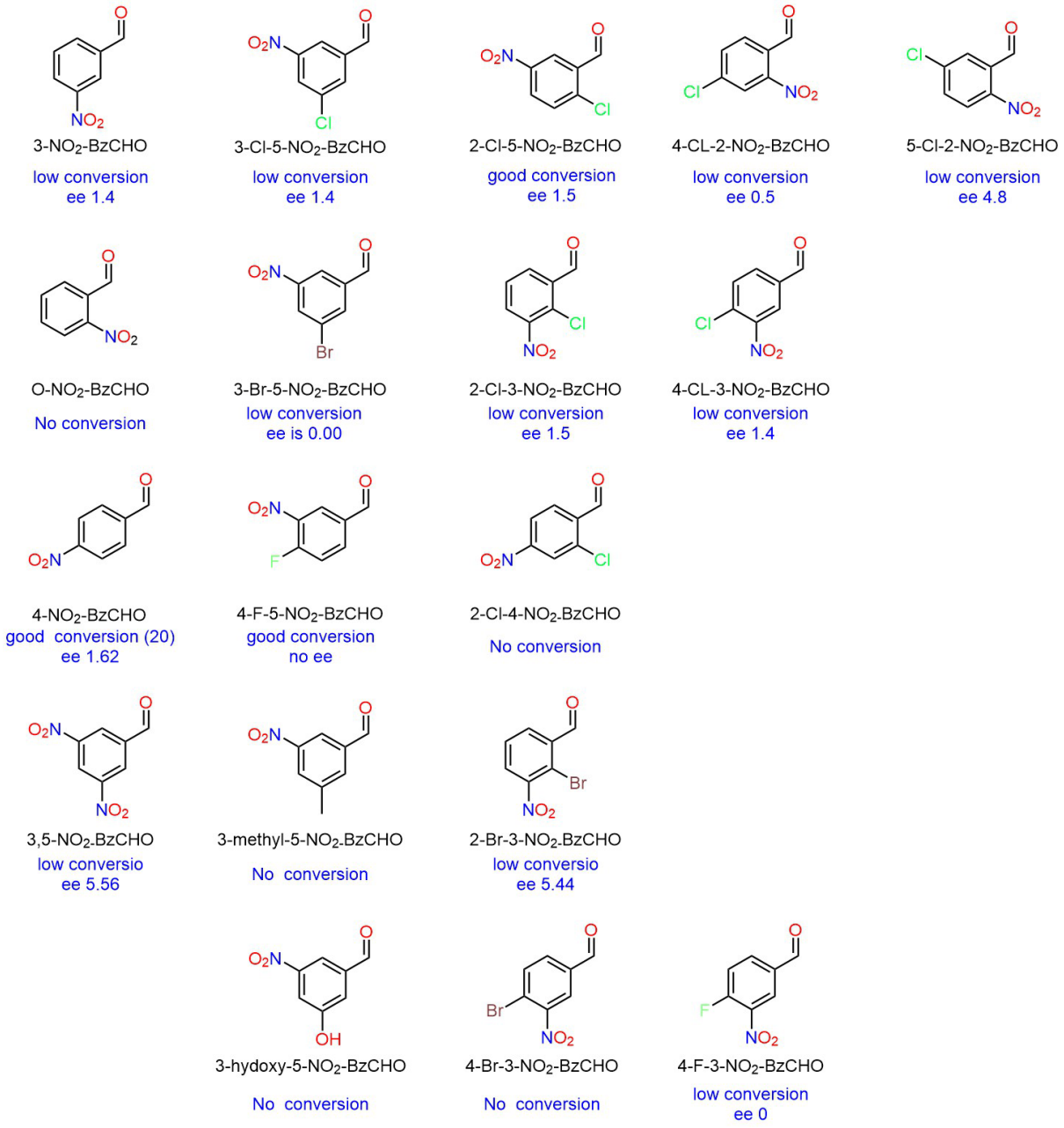

Figure 5.19: The substrate scope of the aldol reaction was examined using a series of aromatic aldehydes catalysed by the MUF-77(bpdc–His) system

We can conclude from the previous results that the aldehydes with strong electron-withdrawing groups (EWGs) such as -F, -NO_2, and -Br generally gave better conversions (such as 4-NO_2-BzCHO and 4-F-5-NO_2-BzCHO) compared to those with electron-donating groups (EDGs) like -CH_3 or -OH, which often showed low or no conversion (such as 3-OH-5-NO_2-BzCHO). EWGs withdraw the electron density from the aromatic ring and the carbonyl group, making the carbonyl carbon more electrophilic and therefore more reactive toward nucleophilic attack.

Also, the substituent positions have a strong influence on the catalytic activity. Para- and meta-substituted aldehydes (such as 4-NO_2-BzCHO, 2-Cl-3-NO_2-BzCHO) give better conversions than ortho-substituted analogues such as 2-Cl-4-NO_2-BzCHO, which showed no conversion.

The size of the substituents influences the catalytic activity, for example bulky substituents at the ortho position near the aldehyde center inhibited the catalytic activity, depicting the need for a balance between electronic activation and steric accessibility for efficient catalysis. Finally, the presence of two strong EWGs (such as 3-Br-5-NO_2) did not guarantee high conversion or enantioselectivity, indicating that steric factors and substitution geometry play equally important roles.

Overall, while some substrates afforded good conversions, the enantioselectivities (ee) remained consistently low (mostly below 5%). These findings suggest that under the current conditions, the MUF-77(bpdc–His) catalyst effectively promotes the reaction but provides limited stereocontrol.

5.2.5 Homogenous catalysis vs. heterogenous catalysis

Under homogeneous conditions, the reaction proceeded with high conversion and measurable enantioselectivity (ee ≈ 8.3%), while the MUF-77(bpdc–His) heterogeneous catalyst exhibited comparable overall conversions but low enantioselectivity (**Figure 5.20**). The difference in ee values is negligible and can likely be attributed to experimental uncertainty.

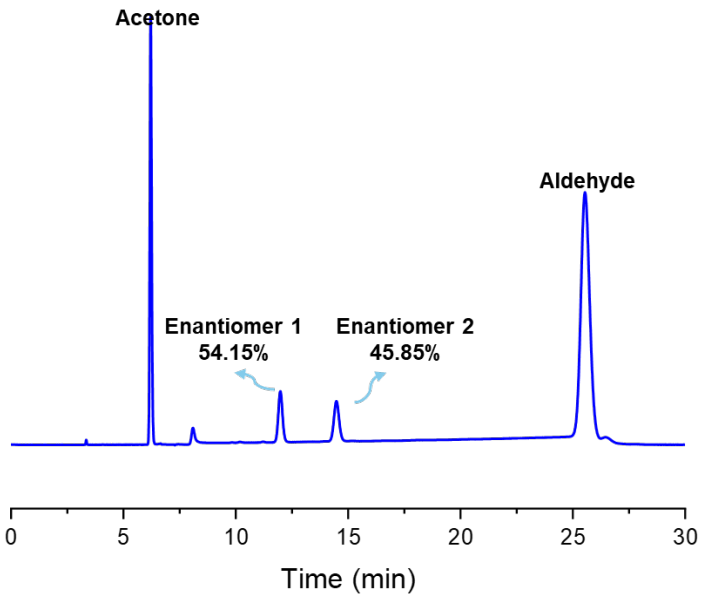

Figure 5.20: HPLC chromatogram for the aldol reaction of 2-Cl-5-NO_2-BzCHO catalysed by MUF-77(bpdc-His).

5.2.6 Toward mimicking catalytic triads

From the screening results, it is evident that the MUF-77(bpdc–His) system shows only moderate catalytic activity in the aldol reaction and fails to provide significant stereocontrol. The overall enantioselectivity remains very low (typically below 5%), even with the presence of EWG. The low enantioselectivity and the strong influence of steric and electronic factors indicate that the system alone does not provide optimal stereocontrol.

These results suggest that MUF-77(bpdc–His) provides an excellent platform for designing a dyad catalyst. By incorporating two complementary catalytic functionalities within the MOF framework, the dyad system could:

- **Enhance Catalytic Conversion:** By providing a more efficient catalytic environment that can better accommodate diverse substrates while maintaining high reactivity.
- **Improve Stereocontrol:** By introducing chiral or cooperative elements capable of guiding the reaction pathway toward a preferred enantiomer, thereby boosting the enantioselectivity.

The structural versatility of MUF-77(bpdc–His) and its demonstrated catalytic reactivity make it an ideal candidate for engineering such a cooperative dyad system, potentially mimicking enzymatic catalysis to achieve both high reaction rates and excellent stereoselectivity.

To mimic the dyad used for catalysing the aldol reaction, ^{7}N-bpdc-His, ^{5}N-bdc-Leu-OH, and H_3hhtt were incorporated into MUF-77 under optimised solvothermal conditions. The PXRD analysis confirmed that the experimental pattern matched the calculated pattern of the previously reported MUF-77 (**Figure 5.21**).

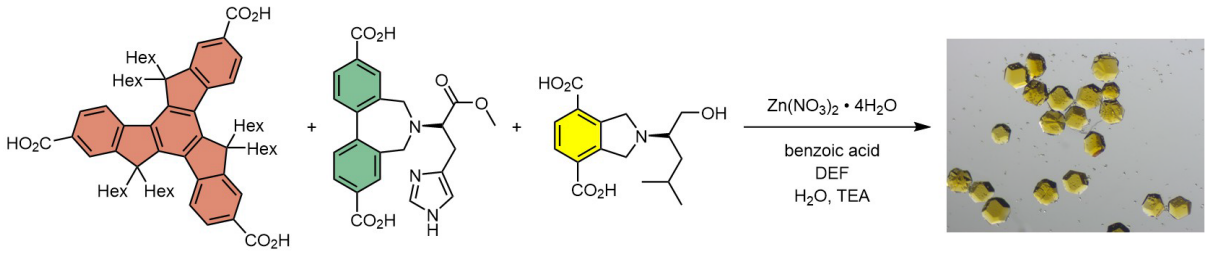

Figure 5.21: Synthetic pathway to MUF-77 using H_3hhtt, ^{7}N-bpdc-His, and ^{5}N-bdc-Leu-OH.

However, ^{1}H NMR spectroscopy of the digested crystals in DCl/DMSO-d_6 (23 µL/1 mL) revealed the occurrence of a side reaction during MOF synthesis. While H_3hhtt remained intact, the linear linkers integrations deviated from the expected values, and numerous additional peaks appeared in the aromatic region, which could not be assigned to any of the intended ligands (**Figure 5.22**).

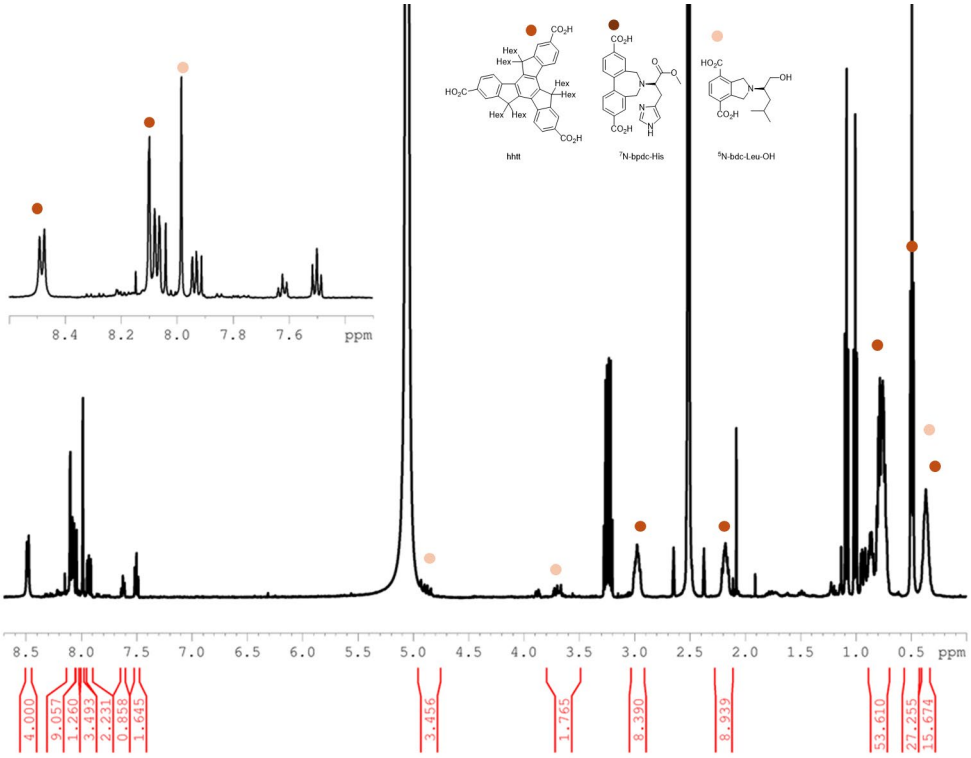

Figure 5.22: ^{1}H NMR spectrum of crystals from the attempted incorporation of hhtt, ^{7}N-bpdc-His, and ^{5}N-bdc-Leu-OH into MUF-77 using the optimised synthesis procedure, after dissolution in DCl/DMSO-d_6 (23 µL/1 mL).

A second attempt was made using ^{5}N-bdc-Val-OH in place of ^{5}N-bdc-Leu-OH, with ^{7}N-bpdc-His and H_3hhtt under similar solvothermal conditions (**Figure 5.23**). PXRD analysis again confirmed the formation of MUF-77, as the experimental pattern matched the calculated one.

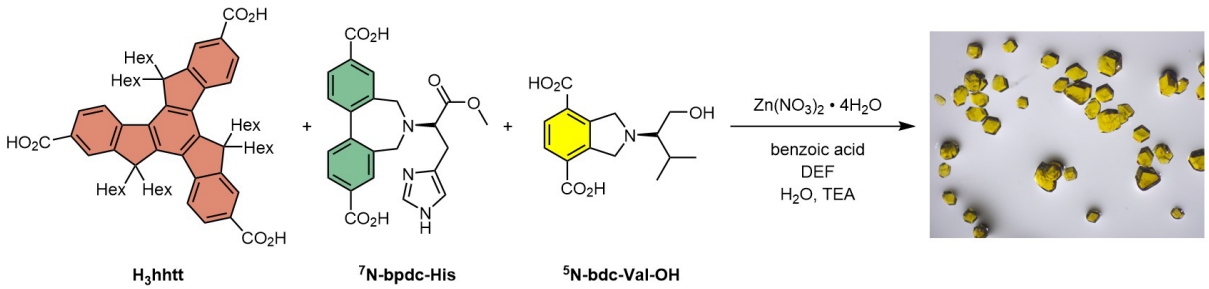

Figure 5.23: Synthetic pathway to MUF-77 using H_3hhtt, ^{7}N-bpdc-His, and ^{5}N-bdc-Val-OH.

Nonetheless, ^{1}H NMR spectroscopy of the digested crystals in DCl/DMSO-d_6 (23 µL/1 mL) again indicated a side reaction during synthesis. H_3hhtt remained intact, but the integration for ^{7}N-bpdc-His and ^{5}N-bdc-Val-OH deviated from the expected values, and multiple unassignable peaks were observed in the aromatic region.

Finally, ^{5}N-bdc-Ala-OH, a less bulky ligand, was tested alongside ^{7}N-bpdc-His and H_3hhtt. This reaction yielded well-formed dodecahedral crystals (**Figure 5.24**). The crystals experimental PXRD matched the MUF-77 calculated PXRD pattern.

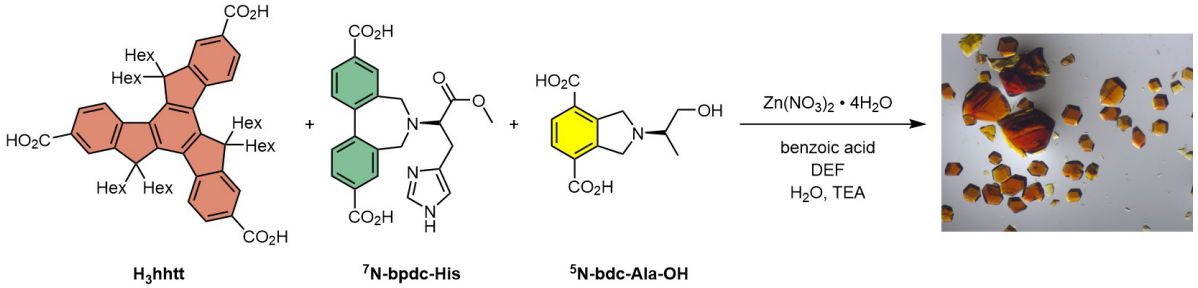

Figure 5.24: Synthetic pathway to MUF-77 using H_3hhtt, ^{7}N-bpdc-His, and ^{5}N-bdc-Ala-OH.

However, ^{1}H NMR spectroscopy of the digested crystals in DCl/DMSO-d_6 (23 µL/1 mL) again revealed a side reaction: both H_3hhtt and ^{5}N-bdc-Ala-OH remained intact, but the integration for ^{7}N-bpdc-His deviated from expected values, and numerous additional peaks appeared in the aromatic region, indicating unexpected chemical reactions during synthesis.

Since the attempts with ^{5}N-bdc-Leu-OH, ^{5}N-bdc-Val-OH and ^{5}N-bdc-Ala-OH resulted in side reactions, the simplest and least bulky bdc analogue, naphthalene-1,4-dicarboxylic acid, was chosen next. It was anticipated that its simpler structure might minimize steric effects and improve compatibility with bpdc-His. This ligand with H_3hmtt, and ^{7}N-bpdc-His, formed well-defined dodecahedral crystals (**Figure 5.25**) with a PXRD pattern matching that of MUF-77.

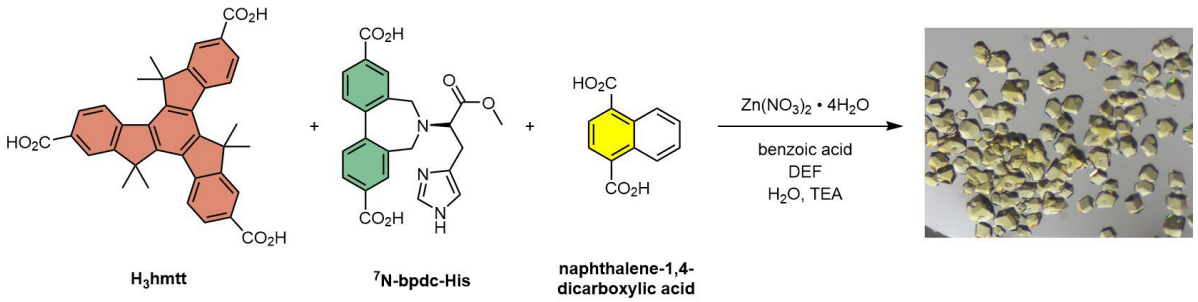

Figure 5.25: Synthetic pathway to MUF-77 using H_3hmtt, ^{7}N-bpdc-His, and naphthalene-1,4-dicarboxylic acid.

However, the ^{1}H NMR spectroscopic analysis again revealed side reactions, indicating that even simple bdc derivative could not fully prevent the undesired reactivity involving ^{7}N-bpdc-His during MOF synthesis.

These results demonstrate that, despite varying the bdc ligand from bulky to the simplest derivative, side reactions persist during MOF synthesis, suggesting that the issue lies beyond steric effects alone.

H_2bpdc-His was successfully incorporated into MUF-77 together with bdc and hmtt/hhtt. Subsequently, bulkier substituents were introduced at the truxene core to investigate the influence of different truxene alkyl chains on the catalytic conversion and enantioselectivity (ee). However, this modification led to the formation of BMUF ($M[Zn_4O(hmtt)_2(bdc)_{0.5}]$, M denotes a monovalent cationic species) rather than MUF-77. The BMUF family comprises MOFs derived from either two MUF-77 linkers or, in some cases, only one. Using H_3hbtt or H_3heptt in combination with H_2bdc and ^{7}N-bpdc-His under the optimized MUF-77 synthesis conditions yielded needle-like and plate-like crystals, respectively (**Figure 5.26).**

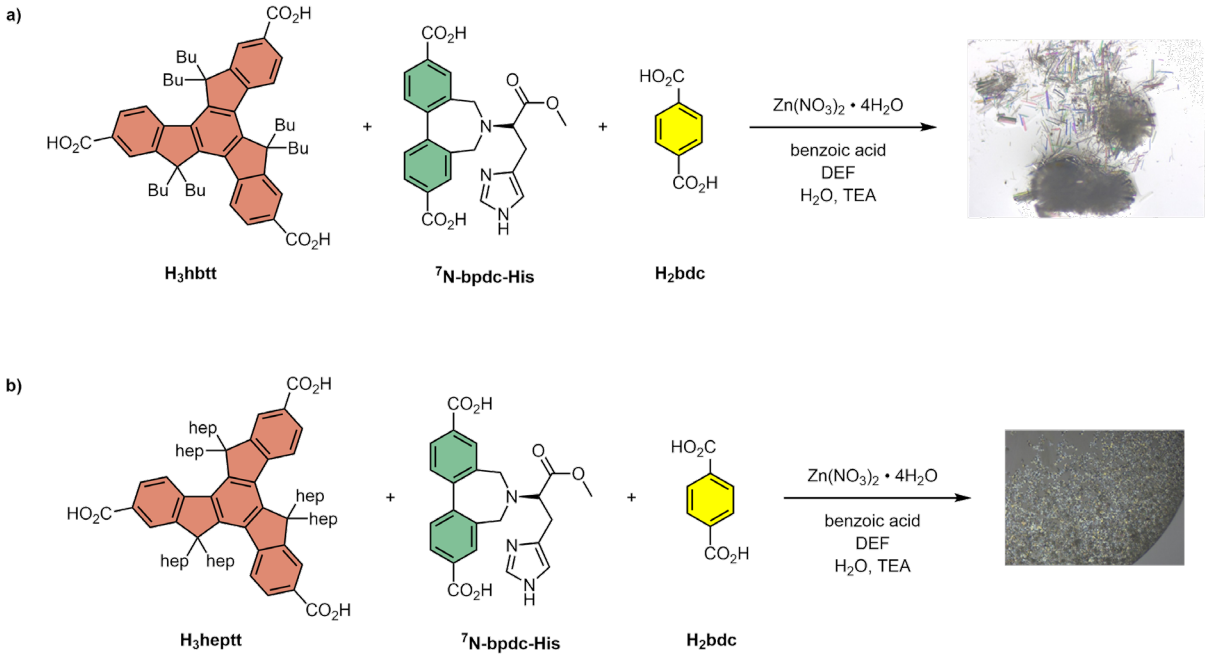

Figure 5.26: a) Attempted synthesis of MUF-77 using H_3hbtt, H_2bdc, and ^{7}N-bpdc-His under the optimised synthesis procedure. **b)** Attempted synthesis of MUF-77 using H_3heptt, H_2bdc, and ^{7}N-bpdc-His under the optimised synthesis procedure.

These crystals exhibited a PXRD pattern matching that of BMUF-4 (M[Zn_4O(hmtt)$_2$(bdc)$_{0.5}$]), a multicomponent MOF composed of truxene and bdc. Despite several modifications, such as increasing the ^{7}N-bpdc-His feed and reducing the H_2bdc feed, ^{7}N-bpdc-His failed to incorporate into the MUF-77 framework with the other ligands (**Figure 5.27).**

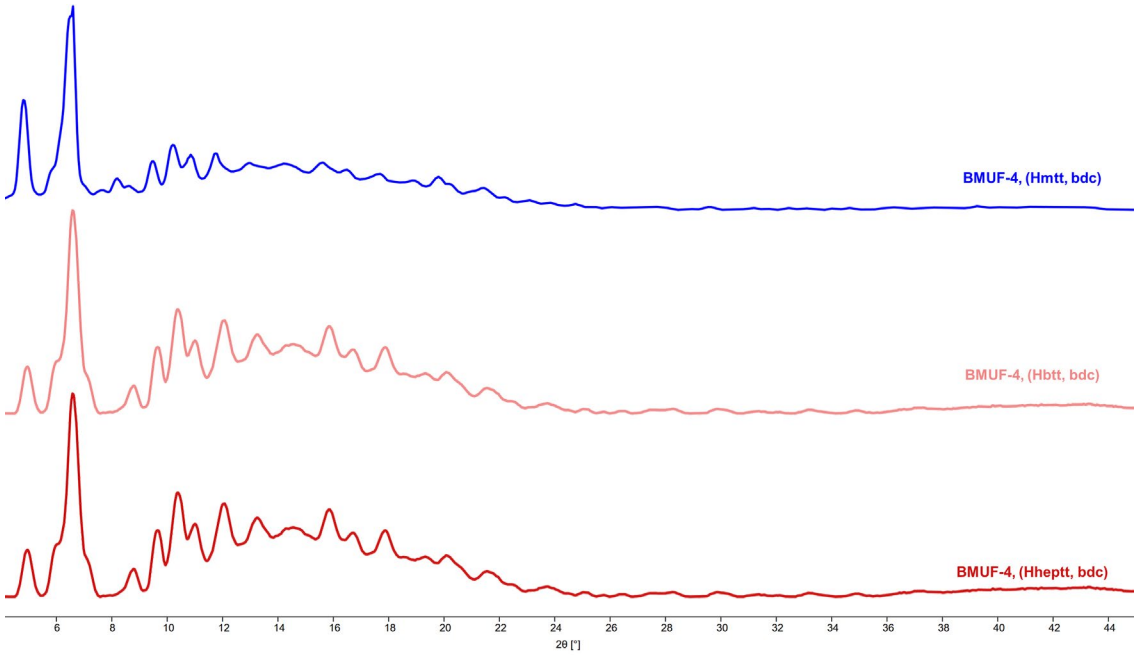

Figure 5.27: $[Zn_4O(Hbtt)_2(bdc)_{0.5}]$ and $[Zn_4O(Hheptt)_2(bdc)_{0.5}]$ experimental PXRD compared to the experimental $[Zn_4O(Hmtt)_2(bdc)_{0.5}]$.

5.3 Conclusion

The ^{7}N-bpdc-His linker was successfully incorporated into the MUF-77 framework, and phase purity was confirmed by comparing the experimental PXRD pattern with the simulated pattern derived from the corresponding SCXRD data. The resulting MUF-77(bpdc–His) material exhibited measurable catalytic activity in the aldol reaction, demonstrating that the framework can function as a biomimetic catalyst. The observed catalytic activity was modest. While low activity is not inherently desirable in practical catalytic systems, minimal intrinsic activity of an individual residue is advantageous in the context of dyad or triad design. In enzyme-inspired cooperative systems, catalysis should arise from synergistic interactions between multiple residues rather than from a single independently active site. Ideally, the MUF-77(bpdc-His) framework would exhibit negligible intrinsic activity, such that catalytic enhancement occurs only upon incorporation of the full dyad or triad assembly, demonstrating a cooperative “turn-on” effect.

Given the modest conversion and stereocontrol, the next step was to probe potential cooperative effects. A catalytic triad was therefore constructed by combining ^{7}N-bpdc-His with ^{5}N-bdc-X-OH and truxene linkers, aiming to enhance both conversion and enantioselectivity. These syntheses also yielded phase-pure MUF-77 materials, as confirmed by PXRD analysis. However, ^{1}H NMR spectroscopy of acid-digested samples consistently revealed competing side reactions involving the ^{7}N-bpdc-His linker, irrespective of the steric properties of the secondary linker. Likewise, attempts to introduce bulkier substituents on the truxene core resulted in BMUF-type phases rather than the desired MUF-77 topology.

These findings highlight that the MUF-77 framework can discriminate between different substrates and that the catalytic centres remain accessible and responsive to their chemical environment. Overall, the results demonstrate both the potential and the limitations of integrating amino-acid-derived linkers for cooperative catalysis. Future work to replicate cooperative catalytic dyads or triads should therefore prioritise alternative linker chemistries or modified synthetic conditions to promote synergistic catalytic environments capable of achieving both high activity and enantioselectivity.

5.4 Experimental section

5.4.1 MOFs synthesis:

The general procedure that was described in **4.4.3** is used for the synthesis of the MOFs in the **Table 5.3** below. The MOFs experimental PXRD were measured and compared to the calculated PXRD pattern from the SCXRD of MUF-77.

Table 5.3: Ligands, weights and molar mass used for the MOF synthesis. The measured ligands ratios of the synthesised MOFs.

MOF nomenclature	H3hXtt mg/ µmol	5N-bdc-X-OH/ bdc mg/ µmol	^{7}N-bpdc-His mg/ µmol	^{1}H NMR ratios
$[Zn_4O(hmtt)_{4/3}(bdc)_{1/2}$ $(^{7}N\text{-bpdc-His})_{1/2}]$	2.3 4.1	1.3 8.0	2.8 5.2	1.33: 0.5: 0.5
$[Zn_4O(hhtt)_{4/3}(bdc)_{1/2}$ $(^{7}N\text{-bpdc-His})_{1/2}]$	3.9 3.8	1.3 8.0	2.9 5.2	1.33:0.5: 0.5
$[Zn_4O(hhtt)_{4/3}(^{5}N\text{-bdc-Leu-OH})_{1/2}$ $(^{7}N\text{-bpdc-His})_{1/2}]$	4.2 3.9	2.4 8.0	2.8 5.2	Not the right ratio
$[Zn_4O(hhtt)_{4/3}(^{5}N\text{-bdc-Val-OH})_{1/2}$ $(^{7}N\text{-bpdc-His})_{1/2}]$	4.0 3.8	2.2 8.0	2.8 5.2	Not the right ratio
$[Zn_4O(hhtt)_{4/3}(^{5}N\text{-bdc-Ala-OH})_{1/2}$ $(^{7}N\text{-bpdc-His})_{1/2}]$	3.9 3.8	1.9 8.0	2.7 5.2	Not the right ratio
$[Zn_4O(hmtt)_{4/3}$(naphthyl-1,4-dicarboxylate)$_{1/2}(^{7}N\text{-bpdc-His})_{1/2}]$	2.3 4.1	1.9 8.0	2.9 5.2	Not the right ratio
$[Zn_4O(hbtt)_2(bdc)_{1/2}]$	3.2 4.0	1.3 8.0	2.8 5.2	NMR was not performed
$[Zn_4O(hheptt)_2(bdc)_{1/2}]$	3.5 4.0	1.3 8.0	2.8 5.2	NMR was not performed

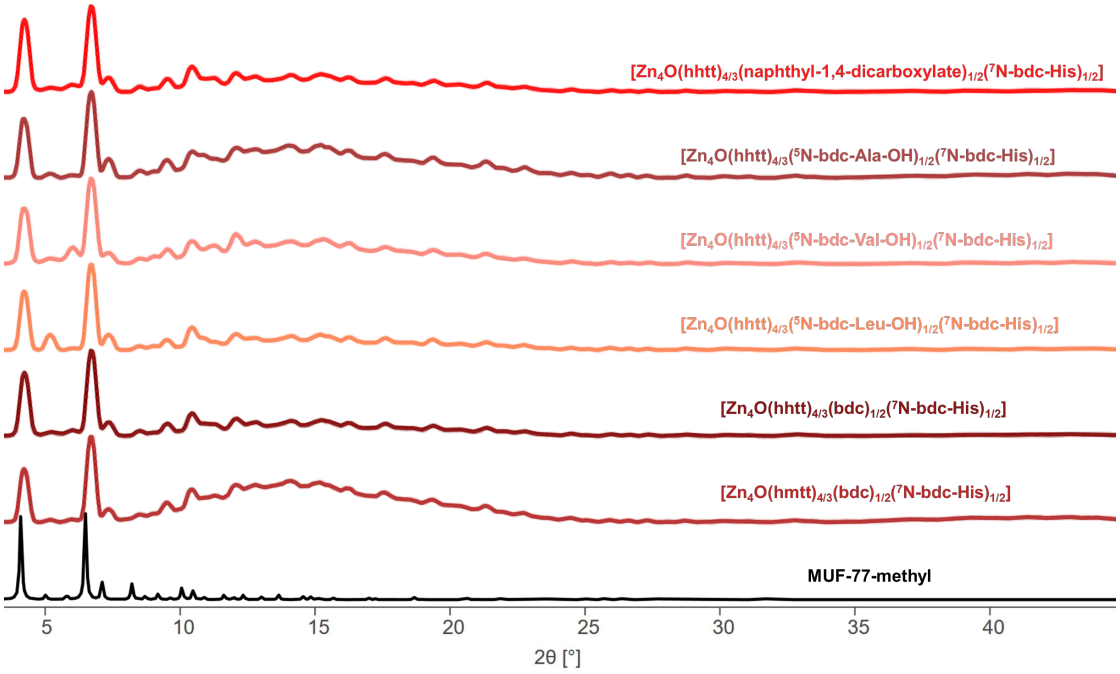

Figure 5.28: Experimental PXRD patterns of the synthesised MOFs compared to the calculated MUF-77 PXRD pattern.

5.4.2 MOFs ^{1}H NMR spectroscopic data

The samples were prepared for ^{1}H NMR spectroscopy as described in **4.4.6.**

$[Zn_4O(hhtt)_{4/3}(bdc)_{1/2}(^7N\text{-}bdc\text{-}His)_{1/2}]$ ^1H NMR spectrum

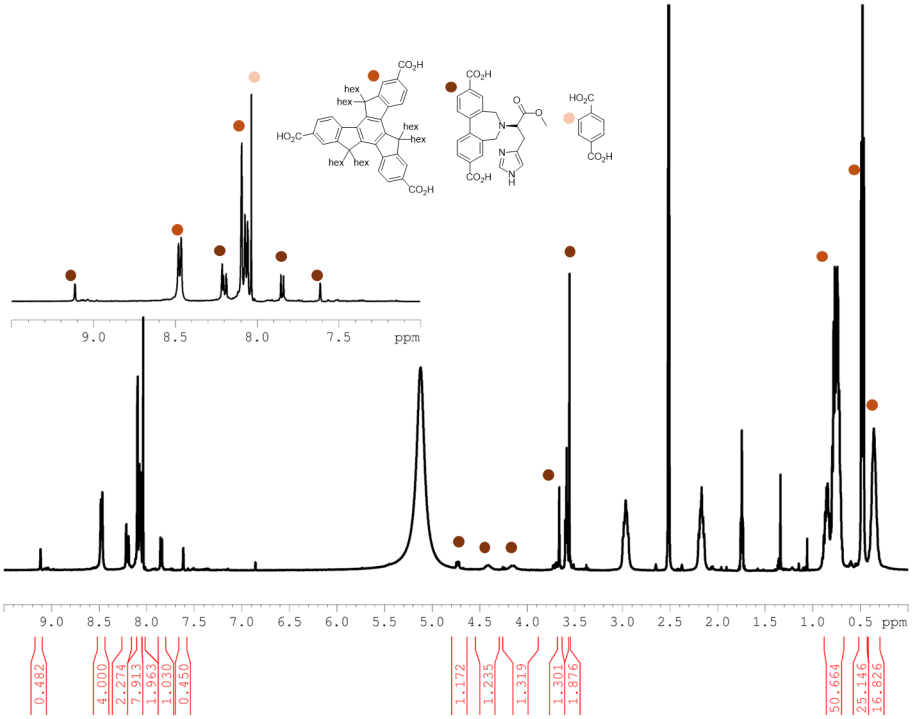

Figure 5.29: ^1H NMR spectrum of $[Zn_4O(hhtt)_{4/3}(bdc)_{1/2}(^7N\text{-}bdc\text{-}His)_{1/2}]$ in DCl/DMSO-d_6 (23 µL/1 mL)

5.4.3 Catalysis samples preparation

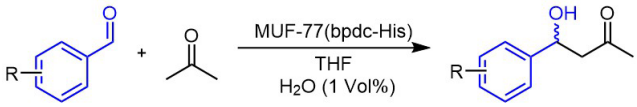

Figure 5.30: Schematic representation of the aldol reaction catalysis.

All stock solutions were prepared in 300.0 µL of the selected solvent. Substrates (12.0 µmol, see **Table 5.4**) were weighed into 2 mL vials, dissolved with acetone (50 eq.), and brought to 300 µL with THF, or with another solvent as required for solvent studies. For catalysis, reactions were run at room temperature in 2 mL vials by mixing 15.0 µL of stock solution with MUF-77 (~100 µg, ~5%).

TLC conditions for all Aldol reactions: n-hex/EtOAc, 1:1, $R_f = 0.66$.

HPLC conditions: reverse phase system; ChiPralPak AD-H (Amylose) column; 0.5 mL/min; MeCN/ H_2O (55/45, v/v); $\lambda = 280$ nm.

Table 5.4: Substrate types and weights

Substrate	Weights (mg)
3-NO_2-BzCHO	1.8
O-NO_2-BzCHO	1.9
4-NO_2-BzCHO	1.8
3,5-diNO_2-BzCHO	2.4
3-Cl-5-NO_2-BzCHO	2.2
3-Br-5-NO_2-BzCHO	2.8
4-F-5-NO_2-BzCHO	2.0
3-methyl-5-NO_2-BzCHO	2.0
3-hydroxy-5-NO_2-BzCHO	2.1
2-Cl-5-NO_2-BzCHO	2.2
2-Cl-3-NO_2-BzCHO	2.2
2-Cl-4-NO_2-BzCHO	2.2
2-Br-3-NO_2-BzCHO	2.8
4-Cl-3-NO_2-BzCHO	2.2
4-F-3-NO_2-BzCHO	2.0

Chapter 6 -Summary and Perspectives

This thesis explored the development of *multicomponent* MOFs (MMOFs) derived from amino acids and amino acid–pyrazole linkers, progressing from structural studies toward catalytic applications inspired by enzymatic active sites. The project progressed from designing new ligands, building novel frameworks, testing catalytic performance, and probing cooperative effects toward dyad and triad active-site mimics.

6.1 Simple amino acid MOFs to pyrazole-derived frameworks

The first results chapter (Chapter 2) described the synthesis of amino acid-based MMOFs, as amino acids are structurally diverse, chiral except for glycine, and have potential catalytic functionality. However, these systems did not form any 3D permanently porous frameworks. They instead produced 1D or 2D compounds without permanent porosity. Because amino acids are flexible in their coordination modes, they do not form SBUs, which are known for forming MOFs, and they favor low-dimensional structures over extended frameworks.

These challenges were tackled in the following chapter (Chapter 3). This chapter introduced pyrazole-based amino acid ligands (H_2XPyr). These ligands are combining carboxylate and pyrazole groups with variable side chains (Val, Ser, Phe, Tyr). Then, they were reliably incorporated into the IR-ZnXPyr framework, a family of isoreticular MOFs with ZnO_2N_2 SBUs forming honeycomb-like frameworks and 1D pores. MMOFs were achieved by co-assembling multiple H_2XPyr within the same framework, introducing chemical functionality while retaining crystallinity and porosity. Although some structural disorder arose from positional ligand distributions, this work established a platform for tunable pore chemistry and bio-inspired functionalisation**.**

6.2 MUF-77: Towards enzyme-mimetic catalysis

The following two chapters focused on MUF-77, a robust, quaternary MOF selected for catalytic studies. By incorporating histidine-functionalised linkers (^{7}N-bpdc–His)**,** MUF-77 was used for catalysis, which was inspired by the enzyme active sites where multiple residues work cooperatively in confined environments.

Aldehyde screening found several key points:

- ❖ Aldol reactions proceeded with moderate to good conversion, particularly for aldehydes bearing EWGs (-NO_2, -F, -Br). EDGs or ortho-substitution reduced activity, reflecting electronic activation and steric accessibility effects.
- ❖ Enantioselectivity (ee) remained low (<5%) under heterogeneous conditions, even for substrates giving high conversion. Homogeneous catalysis with the free ligand improved ee (≈8.3%), suggesting substrate mobility and conformational flexibility in solution favor chiral induction.
- ❖ Attempts to introduce secondary residues (e.g., leucine, valine, alanine linkers) into MUF-77 to form dyad or triad motifs were only partially successful. Although PXRD confirmed framework formation, side reactions involving ^{7}N-bpdc-His limited linker compatibility and prevented cooperative catalysis from emerging.

Despite these challenges, MUF-77 demonstrated that MOFs could mediate benchmark C–C bond-forming reactions and provide a tunable platform for designing enzyme-like active sites within crystalline solids.

6.3 Lessons learned and design principles

This research revealed several design principles controlling the construction of multicomponent amino acid-based MOFs.

1) Ligand design dictates framework dimensionality.

The structural outcome of amino acid–based assemblies is strongly governed by linker architecture. Unmodified amino acids, due to their conformational flexibility and limited ability to generate well-defined secondary building units (SBUs), predominantly yielded low-dimensional or discrete structures. In contrast, incorporation of rigid, directional scaffolds such as pyrazole-functionalised amino acid linkers consistently enabled the formation of extended three-dimensional frameworks. These findings highlight the necessity of combining biological functionality with structural directionality when targeting robust multicomponent architectures.

2) Multicomponent assembly is synthetically demanding but functionally powerful.

The synthesis of MMOFs proved intrinsically challenging due to ligand competition, coordination variability, and sensitivity to crystallisation conditions. However, when successfully achieved, multicomponent frameworks enabled the spatial integration of multiple functional groups within a single crystalline lattice. This controlled heterogeneity provides opportunities for cooperative behaviour, particularly in the context of enzyme-mimetic catalysis.

3) Enzyme mimicry requires spatial precision beyond functional group incorporation

The results demonstrate that mimicking catalytic dyads or triads demands more than the presence of multiple reactive residues. Precise positioning, linker compatibility, and synthetic control are essential to avoid phase impurities and undesired side reactions. Achieving such spatial organisation remains challenging under conventional solvothermal conditions, indicating that future advances may require alternative synthetic strategies.

Future progress may therefore benefit from room-temperature synthesis of nanocrystalline MUF-77 analogues (**Figure 6.1.a**),[59] which could prevent thermally induced side reactions and provide improved control over compositional homogeneity. In addition, the use of alternative protecting groups, such as tert-butyl esters (**Figure 6.1.b**), may enhance linker stability during framework assembly and reduce undesired reactivity. These considerations emphasise that successful enzyme-mimetic design depends not only on functional group selection but also on precise synthetic control.

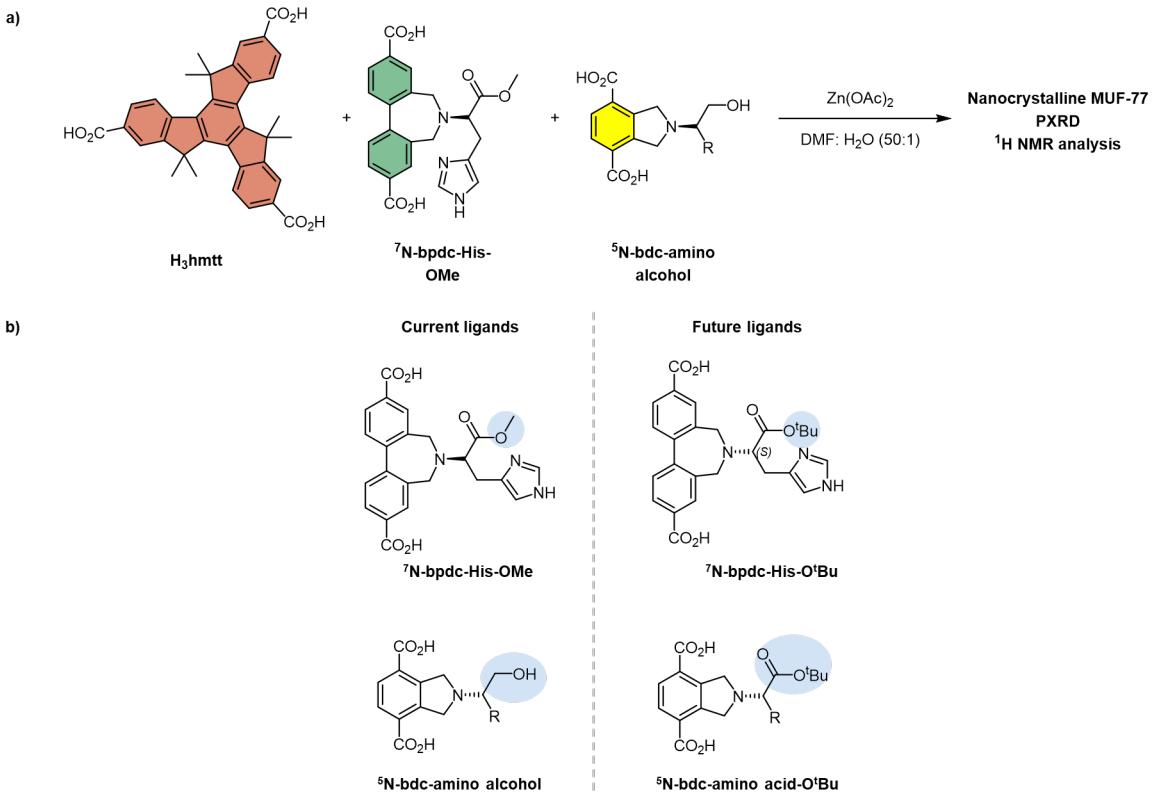

Figure 6.1: Strategies proposed to minimise side reactions during MUF-77 synthesis: **a)** room-temperature synthesis of nanocrystalline MUF-77 to reduce thermally induced side reactions observed under solvothermal conditions; **b)** modification of amino acid protecting groups, such as the use of tert-butyl esters, to enhance linker stability during framework assembly.

References

(1) Bonnefoy, J.; Legrand, A.; Quadrelli, E. A.; Canivet, J.; Farrusseng, D. Enantiopure peptide-functionalized metal–organic frameworks. *J. Am. Chem. Soc.* **2015**, *137* (29), 9409-9416.

(2) Liu, B.; Jiang, M.; Zhu, D.; Zhang, J.; Wei, G. Metal-organic frameworks functionalized with nucleic acids and amino acids for structure- and function-specific applications: A tutorial review. *Chem. Eng. J.* **2022**, *428*, 131118.

(3) Dong, J.; Liu, Y.; Cui, Y. Artificial metal-peptide assemblies: Bioinspired assembly of peptides and metals through space and across length scales. *J. Am. Chem. Soc.* **2021**, *143* (42), 17316-17336.

(4) Katsoulidis, A. P.; Park, K. S.; Antypov, D.; Martí-Gastaldo, C.; Miller, G. J.; Warren, J. E.; Robertson, C. M.; Blanc, F.; Darling, G. R.; Berry, N. G.; et al. Guest-adaptable and water-stable peptide-based porous materials by imidazolate side chain control. *Angew. Chem. Int. Ed. Engl.* **2014**, *53* (1), 193-198.

(5) Liu, L.; Konstas, K.; Hill, M. R.; Telfer, S. G. Programmed pore architectures in modular quaternary metal–organic frameworks. *J. Am. Chem. Soc.* **2013**, *135* (47), 17731-17734.

(6) Liu, L.; Telfer, S. G. Systematic ligand modulation enhances the moisture stability and gas sorption characteristics of quaternary metal-organic frameworks. *J. Am. Chem. Soc.* **2015**, *137* (11), 3901-3909.

(7) Ockwig, N. W.; Delgado-Friedrichs, O.; O'Keeffe, M.; Yaghi, O. M. Reticular chemistry: Occurrence and taxonomy of nets and grammar for the design of frameworks. *Acc. Chem. Res.* **2005**, *38* (3), 176-182.

(8) Cai, H.; Huang, Y.-L.; Li, D. Biological metal–organic frameworks: Structures, host–guest chemistry and bio-applications. *Coord. Chem. Rev.* **2019**, *378*, 207-221.

(9) Binaeian, E.; Nabipour, H.; Ahmadi, S.; Rohani, S. The green synthesis and applications of biological metal–organic frameworks for targeted drug delivery and tumor treatments. *J. Mat. Chem. B* **2023**, *11* (48), 11426-11459, 10.1039/D3TB01959D.

(10) Gropp, C.; Canossa, S.; Wuttke, S.; Gándara, F.; Li, Q.; Gagliardi, L.; Yaghi, O. M. Standard practices of reticular chemistry. *ACS Cent. Sci.* **2020**, *6* (8), 1255-1273.

(11) Batten, S. R.; Champness, N. R.; Chen, X.-M.; Garcia-Martinez, J.; Kitagawa, S.; Öhrström, L.; O'Keeffe, M.; Suh, M. P.; Reedijk, J. Coordination polymers, metal–organic frameworks and the need for terminology guidelines. *CrystEngComm* **2012**, *14* (9), 3001-3004, 10.1039/C2CE06488J.

(12) Eddaoudi, M.; Li, H.; Yaghi, O. M. Highly porous and stable metal−organic frameworks: structure, design, and sorption properties. *J. Am. Chem. Soc.* **2000**, *122* (7), 1391-1397.

(13) Feng, D.; Wang, K.; Su, J.; Liu, T.-F.; Park, J.; Wei, Z.; Bosch, M.; Yakovenko, A.; Zou, X.; Zhou, H.-C. A highly stable zeotype mesoporous zirconium metal–organic framework with ultra large pores. *Angew. Chem. Int. Ed.* **2015**, *54* (1), 149-154.

(14) Chui, S. S.; Lo, S. M.; Charmant, J. P.; Orpen, A. G.; Williams, I. D. A chemically functionalizable nanoporous material. *Science* **1999**, *283* (5405), 1148-1150.
(15) Koh, K.; Wong-Foy, A. G.; Matzger, A. J. Coordination copolymerization mediated by Zn4O(CO2R)6 Metal clusters: A balancing act between statistics and geometry. *J. Am. Chem. Soc.* **2010**, *132* (42), 15005-15010.
(16) Hoskins, B. F.; Robson, R. Infinite polymeric frameworks consisting of three dimensionally linked rod-like segments. *J. Am. Chem. Soc.* **1989**, *111* (15), 5962-5964.
(17) Yaghi, O. M.; Li, H. Hydrothermal synthesis of a metal-organic framework containing large rectangular channels. *J. Am. Chem. Soc.* **1995**, *117* (41), 10401-10402.
(18) Suh, M. P.; Park, H. J.; Prasad, T. K.; Lim, D. W. Hydrogen storage in metal-organic frameworks. *Chem. Rev.* **2012**, *112* (2), 782-835.
(19) Sumida, K.; Rogow, D. L.; Mason, J. A.; McDonald, T. M.; Bloch, E. D.; Herm, Z. R.; Bae, T.-H.; Long, J. R. Carbon dioxide capture in metal–organic frameworks. *Chem. Rev.* **2012**, *112* (2), 724-781.
(20) Li, J.-R.; Sculley, J.; Zhou, H.-C. Metal–organic frameworks for separations. *Chem. Rev.* **2012**, *112* (2), 869-932.
(21) Chughtai, A. H.; Ahmad, N.; Younus, H. A.; Laypkov, A.; Verpoort, F. Metal-organic frameworks: Versatile heterogeneous catalysts for efficient catalytic organic transformations. *Chem. Soc. Rev.* **2015**, *44* (19), 6804-6849.
(22) Howarth, A. J.; Peters, A. W.; Vermeulen, N. A.; Wang, T. C.; Hupp, J. T.; Farha, O. K. Best practices for the synthesis, activation, and characterization of metal–organic frameworks. *Chem. Mater.* **2017**, *29* (1), 26-39.
(23) Park, K. S.; Ni, Z.; Côté, A. P.; Choi, J. Y.; Huang, R.; Uribe-Romo, F. J.; Chae, H. K.; O'Keeffe, M.; Yaghi, O. M. Exceptional chemical and thermal stability of zeolitic imidazolate frameworks. *Proc Natl Acad Sci U S A* **2006**, *103* (27), 10186-10191.
(24) Lee, S. J.; Telfer, S. G. Multicomponent metal-organic frameworks. *Angew. Chem. Int. Ed.* **2023**, *62* (44), e202306341.
(25) Lee, S. J. D., C.; Baux, A.; Liu, L.; Jameson, G. B.; Richardson, C.; Pak, J. J.; Trousselet, F.; Coudert, F.-X.; Telfer, S. G. M. Multicomponent metal–organic frameworks as defect tolerant materials. *Chem. Mater.* **2016**, *28*, 368-375.
(26) Schoedel, A.; Li, M.; Li, D.; O'Keeffe, M.; Yaghi, O. M. Structures of metal–organic frameworks with rod secondary building units. *Chem. Rev.* **2016**, *116* (19), 12466-12535.
(27) Valvekens, P.; Vandichel, M.; Waroquier, M.; Van Speybroeck, V.; De Vos, D. Metal-dioxidoterephthalate MOFs of the MOF-74 type: Microporous basic catalysts with well-defined active sites. *J. Catal.* **2014**, *317*, 1-10.
(28) Cavka, J. H.; Jakobsen, S.; Olsbye, U.; Guillou, N.; Lamberti, C.; Bordiga, S.; Lillerud, K. P. A new zirconium inorganic building brick forming metal organic frameworks with exceptional stability. *J. Am. Chem. Soc.* **2008**, *130* (42), 13850-13851.

(29) Griffin, S. L.; Champness, N. R. A periodic table of metal-organic frameworks. *Coord. Chem. Rev.* **2020**, *414*, 213295.
(30) Yin, Z.; Wan, S.; Yang, J.; Kurmoo, M.; Zeng, M.-H. Recent advances in post-synthetic modification of metal–organic frameworks: New types and tandem reactions. *Coord. Chem. Rev.* **2019**, *378*, 500-512.
(31) Mandal, S.; Natarajan, S.; Mani, P.; Pankajakshan, A. Post-synthetic modification of metal–organic frameworks toward applications. *Adv. Funct. Mater.* **2021**, *31* (4), 2006291.
(32) Yaghi, O. M.; Diercks, C. S.; Kalmutzki, M. J. Introduction to reticular chemistry. **2019**;
(33) Eddaoudi, M.; Kim, J.; Rosi, N.; Vodak, D.; Wachter, J.; O'Keeffe, M.; Yaghi, O. M. Systematic design of pore size and functionality in isoreticular MOFs and their application in methane storage. *Science* **2002**, *295* (5554), 469-472.
(34) Mai, Z.; Liu, D. Synthesis and applications of isoreticular metal–organic frameworks IRMOFs-n (n = 1, 3, 6, 8). *Cryst. Growth Des.* **2019**, *19* (12), 7439-7462.
(35) Rosi, N. L.; Kim, J.; Eddaoudi, M.; Chen, B.; O'Keeffe, M.; Yaghi, O. M. Rod packings and metal-organic frameworks constructed from rod-shaped secondary building units. *J. Am. Chem. Soc.* **2005**, *127* (5), 1504-1518.
(36) Carton, A.; Mesbah, A.; Aranda, L.; Rabu, P.; François, M. New metastable hybrid phase, Zn2(OH)2(C8H4O4), exhibiting unique oxo-penta-coordinated Zn(II) atoms. *Solid State Sci.* **2009**, *11* (4), 818-823.
(37) Carton, A.; Abdelouhab, S.; Renaudin, G.; Rabu, P.; François, M. Structure of zinc hydroxy-terephthalate: Zn3(OH)4(C8H4O4). *Solid State Sci.* **2006**, *8* (8), 958-963.
(38) Saffon-Merceron, N.; Barthélémy, M.-C.; Laurent, C.; Fabing, I.; Hoffmann, P.; Vigroux, A. Two new metal–organic framework structures derived from terephthalate and linear trimetallic zinc building units. *Inorg. Chim. Acta* **2015**, *426*, 15-19.
(39) Hawxwell, S. M.; Adams, H.; Brammer, L. Two-dimensional metal-organic frameworks containing linear dicarboxylates. *Acta Crystallogr. B* **2006**, *62* (Pt 5), 808-814.
(40) Loiseau, T.; Muguerra, H.; Férey, G.; Haouas, M.; Taulelle, F. Synthesis and structural characterization of a new open-framework zinc terephthalate Zn3(OH)2(bdc)2·2DEF, with infinite Zn–(μ3-OH)–Zn chains. *J. Solid State Chem.* **2005**, *178*, 621-628.
(41) Jiang, Z.; An, Y.; Zhu, X.; Tian, C.; Bai, J.; Li, Y. Solvent-dependent synthesis from layer to microporous pillared-layer framework for selective sorption of gas light hydrocarbons. *Z. Anorg. Allg. Chem.* **2015**, *641* (15), 2599-2603.
(42) Lee, S. J.; Doussot, C.; Telfer, S. G. Architectural diversity in multicomponent metal–organic frameworks constructed from similar building blocks. *Cryst. Growth Des.* **2017**, *17* (6), 3185-3191.
(43) Li, H.; Eddaoudi, M.; O'Keeffe, M.; Yaghi, O. M. Design and synthesis of an exceptionally stable and highly porous metal-organic framework. *Nature* **1999**, *402*, 276-279.

(44) Chae, H. K.; Siberio-Pérez, D. Y.; Kim, J.; Go, Y.; Eddaoudi, M.; Matzger, A. J.; O'Keeffe, M.; Yaghi, O. M.; Materials, D.; Discovery, G. A route to high surface area, porosity and inclusion of large molecules in crystals. *Nature* **2004**, *427* (6974), 523-527.
(45) Yao, Q.; Su, J.; Cheung, O.; Liu, Q.; Hedin, N.; Zou, X. Interpenetrated metal–organic frameworks and their uptake of CO2 at relatively low pressures. *J. Mater. Chem.* **2012**, *22* (20), 10345-10351, 10.1039/C2JM15933C.
(46) Tu, B.; Diestel, L.; Shi, Z. L.; Bandara, W.; Chen, Y.; Lin, W.; Zhang, Y. B.; Telfer, S. G.; Li, Q. Harnessing bottom-up self-assembly to position five distinct components in an ordered porous framework. *Angew. Chem. Int. Ed. Engl.* **2019**, *58* (16), 5348-5353.
(47) Dietzel, P. D.; Panella, B.; Hirscher, M.; Blom, R.; Fjellvåg, H. Hydrogen adsorption in a nickel based coordination polymer with open metal sites in the cylindrical cavities of the desolvated framework. *Chem. Commun. (Camb.)* **2006**, (9), 959-961.
(48) Dietzel, P. D.; Morita, Y.; Blom, R.; Fjellvåg, H. An in situ high-temperature single-crystal investigation of a dehydrated metal-organic framework compound and field-induced magnetization of one-dimensional metal-oxygen chains. *Angew. Chem. Int. Ed. Engl.* **2005**, *44* (39), 6354-6358.
(49) Dietzel, P. D. C.; Blom, R.; Fjellvåg, H. Base-induced formation of two magnesium metal-organic framework compounds with a bifunctional tetratopic ligand. *Eur. J. Inorg. Chem.* **2008**, *2008* (23), 3624-3632.
(50) Sanz, R.; Martínez, F.; Orcajo, G.; Wojtas, L.; Briones, D. Synthesis of a honeycomb-like Cu-based metal-organic framework and its carbon dioxide adsorption behaviour. *Dalton Trans.* **2013**, *42* (7), 2392-2398.
(51) Wang, L. J.; Deng, H.; Furukawa, H.; Gándara, F.; Cordova, K. E.; Peri, D.; Yaghi, O. M. Synthesis and characterization of metal–organic framework-74 containing 2, 4, 6, 8, and 10 different metals. *Inorg. Chem.* **2014**, *53* (12), 5881-5883.
(52) Zhou, B.; Silva, N. J. O.; Shi, F.-N.; Palacio, F.; Mafra, L.; Rocha, J. CoII/ZnII–(l-tyrosine) magnetic metal–organic frameworks. *Eur. J. Inorg. Chem.* **2012**, *2012* (32), 5259-5268.
(53) Furukawa, H.; Cordova, K. E.; O'Keeffe, M.; Yaghi, O. M. The chemistry and applications of metal-organic frameworks. *Science* **2013**, *341* (6149), 1230444.
(54) Li, J.-R.; Kuppler, R. J.; Zhou, H.-C. Selective gas adsorption and separation in metal–organic frameworks. *Chem. Soc. Rev.* **2009**, *38* (5), 1477-1504, 10.1039/B802426J.
(55) Slater, A. G.; Cooper, A. I. Function-led design of new porous materials. *Science* **2015**, *348* (6238), aaa8075.
(56) Liu, L.; Zhou, T.-Y.; Telfer, S. G. Modulating the performance of an asymmetric organocatalyst by tuning its spatial environment in a metal–organic framework. *J. Am. Chem. Soc.* **2017**, *139* (39), 13936-13943.

(57) Anbu, N.; Dhakshinamoorthy, A. Regioselective ring opening of styrene oxide by carbon nucleophiles catalyzed by metal–organic frameworks under solvent-free conditions. *J. Ind. Eng. Chem.* **2018**, *58*, 9-17.
(58) Chen, Y.; Ma, S. Biomimetic catalysis of metal–organic frameworks. *Dalton Trans.* **2016**, *45* (24), 9744-9753, 10.1039/C6DT00325G.
(59) Cornelio, J.; Zhou, T. Y.; Alkaş, A.; Telfer, S. G. Systematic tuning of the luminescence output of multicomponent metal-organic frameworks. *J. Am. Chem. Soc.* **2018**, *140* (45), 15470-15476.
(60) Zhao, S.-N.; Wang, G.; Poelman, D.; Voort, P. V. D. Luminescent lanthanide MOFs: a unique platform for chemical sensing. *Mater.* **2018**, *11* (4), 572.
(61) Yaghi, O. M.; O'Keeffe, M.; Ockwig, N. W.; Chae, H. K.; Eddaoudi, M.; Kim, J. Reticular synthesis and the design of new materials. *Nature* **2003**, *423* (6941), 705-714.
(62) Kitagawa, S.; Kitaura, R.; Noro, S.-i. Functional porous coordination polymers. *Angew. Chem. Int. Ed.* **2004**, *43* (18), 2334-2375.
(63) Subramaniyam, V.; Ravi, P. V.; Pichumani, M. Structure co-ordination of solitary amino acids as ligands in metal-organic frameworks (MOFs): A comprehensive review. *J. Mol. Struct.* **2022**, *1251*, 131931.
(64) Sha, M.; Xu, W.; Wu, Y.; Jiao, L.; Chen, Y.; Huang, J.; Tang, Y.; Gu, W.; Zhu, C. Histidine-engineered metal-organic frameworks with enhanced peroxidase-like activity for sensitive detection of metallothioneins. *Sens. Actuators B: Chem.* **2022**, *366*, 131927.
(65) Lemke, T.; Edte, M.; Gebauer, D.; Peter, C. Three reasons why aspartic acid and glutamic acid sequences have a surprisingly different influence on mineralization. *J. Phys. Chem. B* **2021**, *125* (36), 10335-10343.
(66) Seo, J. S.; Whang, D.; Lee, H.; Jun, S. I.; Oh, J.; Jeon, Y. J.; Kim, K. A homochiral metal–organic porous material for enantioselective separation and catalysis. *Nature* **2000**, *404* (6781), 982-986.
(67) Batten, S. R.; Chen, B.; Vittal, J. J. Coordination polymers/MOFs: structures, properties and applications. *ChemPlusChem.* **2016**, *81* (8), 669-670.
(68) Wu, C.-D.; Hu, A.; Zhang, L.; Lin, W. A homochiral porous metal−organic framework for highly enantioselective heterogeneous asymmetric catalysis. *J. Am. Chem. Soc.* **2005**, *127* (25), 8940-8941.
(69) Horcajada, P.; Serre, C.; Vallet-Regí, M.; Sebban, M.; Taulelle, F.; Férey, G. Metal-organic frameworks as efficient materials for drug delivery. *Angew. Chem. Int. Ed. Engl.* **2006**, *45* (36), 5974-5978.
(70) Férey, G. Hybrid porous solids: past, present, future. *Chem. Soc. Rev.* **2008**, *37* (1), 191-214, 10.1039/B618320B.

(71) Gschwind, F.; Jansen, M. Poly[di-μ-glycinato-copper(II)]: A two-dimensional coordination polymer. *Acta crystallogr., Sect. E: Struct. Rep. Online* **2011**, *67* (Pt 9), m1218-1219.
(72) Proch, S.; Villanueva, J. M. R.; Irrgang, T.; Döring, C.; Kempe, R. Refinement of the crystal structure of aquazinc(II) glutamate hydrate, $Zn(H_2O)(C_5H_7NO_4) \cdot H_2O$. *Z. Kristallogr. – New Cryst. Struct.* **2008**, *223* (1), 55-56.
(73) P. Wu, W.; C. Liu, W.; W. Qiu, S.; Q. Ma, A.; Dai, W.; Qian, Y.; Kumar, A. Application of a water stable zinc(II) glutamate metal organic framework for photocatalytic degradation of organic dyes. *Bull. Chem. Soc. Ethiop.* **2019**, *33* (1), 43-50.
(74) Geng, J.; Li, Y.; Lin, H.; Liu, Q.; Lu, J.; Wang, X. A new three-dimensional zinc(II) metal-organic framework as a fluorescence sensor for sensing the biomarker 3-nitrotyrosine. *Dalton Trans.* **2022**, *51* (30), 11390-11396.
(75) Kathalikkattil, A. C.; Babu, R.; Roshan, R. K.; Lee, H.; Kim, H.; Tharun, J.; Suresh, E.; Park, D.-W. An Icy-topology amino acid MOF as eco-friendly catalyst for cyclic carbonate synthesis from CO_2: Structure-DFT corroborated study. *J. Mater. Chem. A* **2015**, *3* (45), 22636-22647, 10.1039/C5TA05688H.
(76) Zhou, B.; Silva, N. J. O.; Shi, F.-N.; Palacio, F.; Mafra, L.; Rocha, J. CoII/ZnII–(*l*-tyrosine) magnetic metal–oganic frameworks. *Eur. J. Inorg. Chem.* **2012**, *2012* (32), 5259-5268.
(77) Navarro-Sánchez, J.; Argente-García, A. I.; Moliner-Martínez, Y.; Roca-Sanjuán, D.; Antypov, D.; Campíns-Falcó, P.; Rosseinsky, M. J.; Martí-Gastaldo, C. Peptide metal-organic frameworks for enantioselective separation of chiral drugs. *J. Am. Chem. Soc.* **2017**, *139* (12), 4294-4297.
(78) Deng, H.; Grunder, S.; Cordova, K. E.; Valente, C.; Furukawa, H.; Hmadeh, M.; Gándara, F.; Whalley, A. C.; Liu, Z.; Asahina, S.; et al. Large-pore apertures in a series of metal-organic frameworks. *Science* **2012**, *336* (6084), 1018-1023.
(79) Mantion, A.; Massüger, L.; Rabu, P.; Palivan, C.; McCusker, L. B.; Taubert, A. Metal-peptide frameworks (MPFs): "Bioinspired" metal organic frameworks. *J. Am. Chem. Soc.* **2008**, *130* (8), 2517-2526.
(80) Pérez-Cejuela, H. M.; Herrero-Martínez, J. M.; Simó-Alfonso, E. F. Recent advances in affinity MOF-based sorbents with sample preparation purposes. *Molecules* **2020**, *25* (18).
(81) Ghorbani-Choghamarani, A.; Taherinia, Z. Chiral cobalt-peptide metal-organic framework (Co-P-MOF): As an efficient and reusable heterogeneous catalyst for the asymmetric sulfoxidative cross-coupling reaction using poly sulfinylpiperazine. *Synth. Met.* **2020**, *263*, 116362.
(82) Said, M. Y.; Kang, C. S.; Wang, S.; Sheffler, W.; Salveson, P. J.; Bera, A. K.; Kang, A.; Nguyen, H.; Ballard, R.; Li, X.; et al. Exploration of structured symmetric cyclic peptides as ligands for metal-organic frameworks. *Chem. Mater.* **2022**, *34* (21), 9736-9744.

(83) Loosen, A.; de Azambuja, F.; Parac-Vogt, T. N. Which factors govern the adsorption of peptides to Zr(iv)-based metal–organic frameworks? *Mater. Adv.* **2022**, *3* (5), 2475-2487, 10.1039/D1MA01027A.
(84) Chen, Y.; Guerin, S.; Yuan, H.; O'Donnell, J.; Xue, B.; Cazade, P. A.; Haq, E. U.; Shimon, L. J. W.; Rencus-Lazar, S.; Tofail, S. A. M.; et al. Guest molecule-mediated energy harvesting in a conformationally sensitive peptide-metal organic framework. *J. Am. Chem. Soc.* **2022**, *144* (8), 3468-3476.
(85) Yan, Y.; Carrington, E. J.; Pétuya, R.; Whitehead, G. F. S.; Verma, A.; Hylton, R. K.; Tang, C. C.; Berry, N. G.; Darling, G. R.; Dyer, M. S.; et al. Amino acid residues determine the response of flexible metal–organic frameworks to guests. *J. Am. Chem. Soc.* **2020**, *142* (35), 14903-14913.
(86) Kundu, T.; Sahoo, S. C.; Saha, S.; Banerjee, R. Salt metathesis in three dimensional metal-organic frameworks (MOFs) with unprecedented hydrolytic regenerability. *Chem. Comm.* **2013**, *49* (46), 5262-5264.
(87) Zhang, H.-y.; Yu, H.-j.; Xu, H.-x.; Ren, J.-s.; Qu, X.-g. Structural diversity of lanthanide–amino acid complexes under near physiological pH conditions and their recognition of single-stranded DNA. *Polyhedron* **2007**, *26* (18), 5250-5256.
(88) Kundu, T.; Sahoo, S. C.; Banerjee, R. Variable water adsorption in amino acid derivative-based homochiral metal organic frameworks. *Cryst. Growth Des.* **2012**, *12* (9), 4633-4640.
(89) Gutov, O. V.; Molina, S.; Escudero-Adán, E. C.; Shafir, A. Modulation by amino acids: toward superior control in the synthesis of zirconium metal–organic frameworks. *Chem. Eur. J.* **2016**, *22* (38), 13582-13587.
(90) Carrasco, C. J.; Montilla, F.; Álvarez, E.; Conejo, M. d. M.; Pastor, A.; Galindo, A. Recent developments in amino acid-derived imidazole-, imidazolium- and N-heterocyclic carbene-carboxylate complexes. *Inorg. Chim. Acta* **2023**, *557*, 121717.
(91) Sasikala, V.; Vignesh, S.; Kalyana Sundar, J.; El Sayed Massoud, E. Construction of three-dimensional polymeric d-histidine based metal-organic framework (MOF) for selective sorption of CO2 and copper ion sensing applications. *Chem. Phys. Lett.* **2022**, *790*, 139331.
(92) Vaidhyanathan, R.; Bradshaw, D.; Rebilly, J.-N.; Barrio, J. P.; Gould, J. A.; Berry, N. G.; Rosseinsky, M. J. A family of nanoporous materials based on an amino acid backbone. *Angew. Chem. Int. Ed.* **2006**, *45* (39), 6495-6499.
(93) Vasconcelos, I. B.; Silva, T. G. d.; Militão, G. C. G.; Soares, T. A.; Rodrigues, N. M.; Rodrigues, M. O.; Costa, N. B. d.; Freire, R. O.; Junior, S. A. Cytotoxicity and slow release of the anti-cancer drug doxorubicin from ZIF-8. *RSC Adv.* **2012**, *2* (25), 9437-9442, 10.1039/C2RA21087H.
(94) Lei, B.; Wang, M.; Jiang, Z.; Qi, W.; Su, R.; He, Z. Constructing redox-responsive metal–organic framework nanocarriers for anticancer drug delivery. *ACS Appl. Mater. Interfaces* **2018**, *10* (19), 16698-16706.

(95) Cheng, G.; Li, W.; Ha, L.; Han, X.; Hao, S.; Wan, Y.; Wang, Z.; Dong, F.; Zou, X.; Mao, Y.; et al. Self-assembly of extracellular vesicle-like metal-organic framework nanoparticles for protection and intracellular delivery of biofunctional proteins. *J. Am. Chem. Soc.* **2018**, *140* (23), 7282-7291.
(96) Zhou, A.; Jiang, L.; Yue, J.; Tong, Y.; Zhang, Q.; Lin, Z.; Liu, B.; Wu, C.; Suo, L.; Hu, Y.-S.; et al. Water-in-salt electrolyte promotes high-capacity FeFe(CN)6 cathode for aqueous Al-ion battery. *ACS Appl. Mater. Interfaces* **2019**, *11* (44), 41356-41362.
(97) Hidalgo, T.; Alonso-Nocelo, M.; Bouzo, B. L.; Reimondez-Troitiño, S.; Abuin-Redondo, C.; de la Fuente, M.; Horcajada, P. Biocompatible iron(iii) carboxylate metal-organic frameworks as promising RNA nanocarriers. *Nanoscale* **2020**, *12* (8), 4839-4845.
(98) Sanchez-Roselló, M.; Puchlopek, A. L.; Morgan, A. J.; Miller, S. J. Site-selective catalysis of phenyl thionoformate transfer as a tool for regioselective deoxygenation of polyols. *J. Org. Chem.* **2008**, *73* (5), 1774-1782.
(99) Nasrollahi, M.; Nabipour, H.; Valizadeh, N.; Mozafari, M. Chapter 5 - The role of flexibility in MOFs. In *Metal-organic frameworks for biomedical applications*, Mozafari, M. Ed.; Woodhead Publishing, **2020**; pp 93-110.
(100) Schneemann, A.; Bon, V.; Schwedler, I.; Senkovska, I.; Kaskel, S.; Fischer, R. A. Flexible metal-organic frameworks. *Chem. Soc. Rev.* **2014**, *43* (16), 6062-6096.
(101) Mallakpour, S.; Nikkhoo, E.; Hussain, C. M. Application of MOF materials as drug delivery systems for cancer therapy and dermal treatment. *Coord. Chem. Rev.* **2022**, *451*, 214262.
(102) Loiseau, T.; Serre, C.; Huguenard, C.; Fink, G.; Taulelle, F.; Henry, M.; Bataille, T.; Férey, G. A rationale for the large breathing of the porous aluminum terephthalate (MIL-53) upon hydration. *Chem. Eur. J.* **2004**, *10* (6), 1373-1382.
(103) McKinlay, A. C.; Eubank, J. F.; Wuttke, S.; Xiao, B.; Wheatley, P. S.; Bazin, P.; Lavalley, J. C.; Daturi, M.; Vimont, A.; De Weireld, G.; et al. Nitric oxide adsorption and delivery in flexible MIL-88(Fe) metal–organic frameworks. *Chem. of Mater.* **2013**, *25* (9), 1592-1599.
(104) Horcajada, P.; Chalati, T.; Serre, C.; Gillet, B.; Sebrie, C.; Baati, T.; Eubank, J. F.; Heurtaux, D.; Clayette, P.; Kreuz, C.; et al. Porous metal–organic-framework nanoscale carriers as a potential platform for drug delivery and imaging. *Nat. Mater.* **2010**, *9* (2), 172-178.
(105) Li, Y.; Zheng, Y.; Lai, X.; Chu, Y.; Chen, Y. Biocompatible surface modification of nano-scale zeolitic imidazolate frameworks for enhanced drug delivery. *RSC Adv.* **2018**, *8* (42), 23623-23628, 10.1039/C8RA03616K.
(106) Zheng, H.; Zhang, Y.; Liu, L.; Wan, W.; Guo, P.; Nyström, A. M.; Zou, X. One-pot synthesis of metal–organic frameworks with encapsulated target molecules and their applications for controlled drug delivery. *J. Am. Chem. Soc.* **2016**, *138* (3), 962-968.

(107) Liang, K.; Ricco, R.; Doherty, C. M.; Styles, M. J.; Bell, S.; Kirby, N.; Mudie, S.; Haylock, D.; Hill, A. J.; Doonan, C. J.; et al. Biomimetic mineralization of metal-organic frameworks as protective coatings for biomacromolecules. *Nat. Commun.* **2015**, *6* (1), 7240.
(108) Lawson, H. D.; Walton, S. P.; Chan, C. Metal-organic frameworks for drug delivery: A design perspective. *ACS Appl. Mater. Interfaces* **2021**, *13* (6), 7004-7020.
(109) Zhu, L.; Liu, X.-Q.; Jiang, H.-L.; Sun, L.-B. Metal–organic frameworks for heterogeneous basic catalysis. *Chem. Rev.* **2017**, *117* (12), 8129-8176.
(110) Dhakshinamoorthy, A.; Alvaro, M.; Garcia, H. Commercial metal–organic frameworks as heterogeneous catalysts. *Chem. Comm.* **2012**, *48* (92), 11275-11288, 10.1039/C2CC34329K.
(111) Bornscheuer, U. T.; Huisman, G. W.; Kazlauskas, R. J.; Lutz, S.; Moore, J. C.; Robins, K. Engineering the third wave of biocatalysis. *Nature* **2012**, *485* (7397), 185-194.
(112) Arnold, F. H. Design by directed evolution. *Acc. Chem. Res.* **1998**, *31* (3), 125-131.
(113) Griswold, K. S.; Miller, S. J. A peptide-based catalyst approach to regioselective functionalization of carbohydrates. *Tetrahedron* **2003**, *59* (45), 8869-8875.
(114) Giuliano, M. W.; Miller, S. J. Site-selective reactions with peptide-based catalysts. *Top. Curr. Chem.* **2016**, *372*, 157-201.
(115) Alford, J. S.; Abascal, N. C.; Shugrue, C. R.; Colvin, S. M.; Romney, D. K.; Miller, S. J. Aspartyl oxidation catalysts that dial In functional group selectivity, along with regio- and stereoselectivity. *ACS Cent. Sci.* **2016**, *2* (10), 733-739.
(116) Sato, K.; Kuriyama, M.; Shimazawa, R.; Morimoto, T.; Kakiuchi, K.; Shirai, R. Direct asymmetric aldol reactions catalyzed by l-proline-2,4,6-trinitroanilide. *Tetrahedron Lett.* **2008**, *49* (15), 2402-2406.
(117) Lun, D. J.; Waterhouse, G. I.; Telfer, S. G. A general thermolabile protecting group strategy for organocatalytic metal-organic frameworks. *J. Am. Chem. Soc.* **2011**, *133* (15), 5806-5809.
(118) Lin, R.-B.; Xiang, S.; Xing, H.; Zhou, W.; Chen, B. Exploration of porous metal–organic frameworks for gas separation and purification. *Coord. Chem. Rev.* **2019**, *378*, 87-103.
(119) Li, Y.; Gao, H.; Jin, Y.; Zhao, R.; Huang, Y. Peptide-derived coordination frameworks for biomimetic and selective separation. *Anal Bioanal Chem.* **2023**, *415* (18), 4079-4092.
(120) Introduction to metal–organic frameworks. *Chem. Rev.* **2012**, *112* (2), 673-674.
(121) Liu, J.; Li, Y.; Lou, Z. Recent Advancements in MOF/Biomass and Bio-MOF Multifunctional Materials: A Review. *Sustainability* **2022**, *14* (10), 5768.
(122) Tousian, B.; Khosravi, A. R.; Ghasemi, M. H.; Kadkhodaie, M. Biomimetic functionalized metal organic frameworks as multifunctional agents: Paving the way for cancer vaccine advances. *Mater. Today Bio.* **2024**, *27*, 101134.
(123) Mugaka, B. P.; Zhang, S.; Li, R. Q.; Ma, Y.; Wang, B.; Hong, J.; Hu, Y. H.; Ding, Y.; Xia, X. H. One-pot preparation of peptide-doped metal-amino acid framework for general encapsulation and targeted delivery. *ACS Appl. Mater. Interfaces* **2021**, *13* (9), 11195-11204.

(124) Binaeian, E.; Nabipour, H.; Ahmadi, S.; Rohani, S. The green synthesis and applications of biological metal–organic frameworks for targeted drug delivery and tumor treatments. *J. Mater. Chem. B* **2023**, *11* (48), 11426-11459, 10.1039/D3TB01959D.
(125) Wang, H.-S.; Wang, Y.-H.; Ding, Y. Development of biological metal–organic frameworks designed for biomedical applications: from bio-sensing/bio-imaging to disease treatment. *Nanoscale Adv.* **2020**, *2* (9), 3788-3797, 10.1039/D0NA00557F.
(126) Zhang, J.-H.; Tang, B.; Xie, S.-M.; Wang, B.-J.; Zhang, M.; Chen, X.-L.; Zi, M.; Yuan, L.-M. Determination of enantiomeric excess by solid-phase extraction using a chiral metal-organic framework as sorbent. *Molecules* **2018**, *23* (11), 2802.
(127) Wojciechowska, A.; Daszkiewicz, M.; Bieńko, A. Polymeric Zn(II) and Cu(II) complexes with exobidentate bridging l-tyrosine: Synthesis, structural and spectroscopic properties. *Polyhedron* **2009**, *28* (8), 1481-1489.
(128) Erzina, M.; Guselnikova, O.; Elashnikov, R.; Trelin, A.; Zabelin, D.; Postnikov, P.; Siegel, J.; Zabelina, A.; Ulbrich, P.; Kolska, Z.; et al. BioMOF coupled with plasmonic CuNPs for sustainable CO2 fixation in cyclic carbonates at ambient conditions. *J. CO2 Util.* **2023**, *69*, 102416.
(129) Patra, A. K.; Dhar, S.; Nethaji, M.; Chakravarty, A. R. Visible light-induced nuclease activity of a ternary mono-phenanthroline copper(ii) complex containing l-methionine as a photosensitizer. *Chem. Comm.* **2003**, (13), 1562-1563, 10.1039/B303442A.
(130) Kundu, T.; Sahoo, S. C.; Banerjee, R. Variable water adsorption in amino acid derivative based homochiral metal organic frameworks. *Cryst. Growth Des.* **2012**, *12* (9), 4633-4640.
(131) Abdulbagi, M.; Wang, L.; Siddig, O.; Di, B.; Li, B. D-Amino acids and D-amino acid-Containing peptides: Potential disease biomarkers and therapeutic targets? *Biomolecules* **2021**, *11* (11).
(132) Amino, Y.; Takino, Y.; Kaneko, M.; Ookura, F.; Yamamoto, M.; Kashiwagi, T.; Iwasaki, K. Synthesis, characterization, and evaluation of thiazolidine derivatives of cysteine for suppressing eumelanin production. *Chem. Pharm. Bull. (Tokyo)* **2016**, *64* (12), 1681-1691.
(133) Bijini, B. R.; Prasanna, S.; Deepa, M.; Nair, C. K. S.; Rajendra Babu, K. Crystal structure, spectral, thermal and dielectric studies of a new zinc benzoate single crystal. *Spectrochimica acta. Part A, Molecular and biomolecular spectroscopy* **2012**, *97*, 1002-1006.
(134) Vaidhyanathan, R.; Iremonger, S. S.; Dawson, K. W.; Shimizu, G. K. An amine-functionalized metal organic framework for preferential CO(2) adsorption at low pressures. *Chem Commun (Camb)* **2009**, (35), 5230-5232.
(135) Kumar, R.; Ismail, A. F. Fouling control on microfiltration/ultrafiltration membranes: Effects of morphology, hydrophilicity, and charge. *J. Appl. Polym. Sci.* **2015**, *132* (21).
(136) Ma, Y.; Du, H.; Zheng, S.; Zhou, Z.; Zhang, H.; Ma, Y.; Passerini, S.; Wu, Y. High-entropy approach vs. traditional doping strategy for layered oxide cathodes in alkali-metal-ion batteries: A comparative study. *Energy Storage Mater.* **2025**, *79*, 104295.

(137) Koch, T.; Blaurock, S.; Somoza, F. B.; Voigt, A.; Kirmse, R.; Hey-Hawkins, E. Unexpected P-Si or P-C bond cleavage in the reaction of Li2[(C5Me4)SiMe2-PR] (R = Cyclohexyl, 2,4,6-Me3C6H2) and Li[(C5H4)CMe2-PHR] (R = Ph, tBu) with ZrCl4 or [TiCl3(thf)3]: Formation and molecular structure of the ansa-metallocenes [{(η-C5Me4)2SiMe2}ZrCl2] and [{(η-C5H4)2CMe2}MCl2] (M = Ti, Zr). *Organometallics* **2000**, *19* (20), 4186-4186.
(138) Sigel, H.; Martin, R. B. Coordinating properties of the amide bond. Stability and structure of metal ion complexes of peptides and related ligands. *Chem. Rev.* **1982**, *82* (4), 385-426.
(139) Ma, L.; Abney, C.; Lin, W. Enantioselective catalysis with homochiral metal-organic frameworks. *Chem. Soc. Rev.* **2009**, *38* (5), 1248-1256.
(140) Devic, T.; Horcajada, P.; Serre, C.; Salles, F.; Maurin, G.; Moulin, B.; Heurtaux, D.; Clet, G.; Vimont, A.; Grenèche, J. M.; et al. Functionalization in flexible porous solids: effects on the pore opening and the host-guest interactions. *J. Am. Chem. Soc.* **2010**, *132* (3), 1127-1136.
(141) Sheldrick, G. M. SHELXT - integrated space-group and crystal-structure determination. *Acta Crystallogr. A Found. Adv.* **2015**, *71* (Pt 1), 3-8.
(142) Dolomanov, O. V.; Bourhis, L. J.; Gildea, R. J.; Howard, J. A. K.; Puschmann, H. OLEX2: A complete structure solution, refinement and analysis program. *J. App. Cryst.* **2009**, *42* (2), 339-341.
(143) Emergence of metal-organic frameworks. In *Introduction to Reticular Chemistry*, **2019**; pp 1-27.
(144) Kim, J.; Choe, W. Topology-guided roadmap for reticular chemistry of metal-organic polyhedra. *Chem. Asian. J.* **2022**, *8* (3), 617-631.
(145) Markad, D.; Kershaw Cook, L. J.; Pétuya, R.; Yan, Y.; Gilford, O.; Verma, A.; Mali, B. P.; Robertson, C. M.; Berry, N. G.; Darling, G. R.; et al. Recognition and order of multiple sidechains by metal-organic framework enhances the separation of hexane isomers. *Angew. Chem. Int. Ed. Engl.* **2024**, *63* (50), e202411960.
(146) Xia, Q.; Li, Z.; Tan, C.; Liu, Y.; Gong, W.; Cui, Y. Multivariate metal–organic frameworks as multifunctional heterogeneous asymmetric catalysts for sequential reactions. *J. Am. Chem. Soc.* **2017**, *139* (24), 8259-8266.
(147) Dong, Z.; Sun, Y.; Chu, J.; Zhang, X.; Deng, H. Multivariate metal–organic frameworks for dialing-in the binding and programming the release of drug molecules. *J. Am. Chem. Soc.* **2017**, *139* (40), 14209-14216.
(148) Imaz, I.; Rubio-Martínez, M.; An, J.; Solé-Font, I.; Rosi, N. L.; Maspoch, D. Metal-biomolecule frameworks (MBioFs). *Chem. Commun. (Camb.)* **2011**, *47* (26), 7287-7302.
(149) Rabone, J.; Yue, Y. F.; Chong, S. Y.; Stylianou, K. C.; Bacsa, J.; Bradshaw, D.; Darling, G. R.; Berry, N. G.; Khimyak, Y. Z.; Ganin, A. Y.; et al. An adaptable peptide-based porous material. *Science* **2010**, *329* (5995), 1053-1057.

(150) Martí-Gastaldo, C.; Antypov, D.; Warren, J. E.; Briggs, M. E.; Chater, P. A.; Wiper, P. V.; Miller, G. J.; Khimyak, Y. Z.; Darling, G. R.; Berry, N. G.; et al. Side-chain control of porosity closure in single- and multiple-peptide-based porous materials by cooperative folding. *Nat. Chem.* **2014**, *6* (4), 343-351.
(151) Katsoulidis, A. P.; Antypov, D.; Whitehead, G. F. S.; Carrington, E. J.; Adams, D. J.; Berry, N. G.; Darling, G. R.; Dyer, M. S.; Rosseinsky, M. J. Chemical control of structure and guest uptake by a conformationally mobile porous material. *Nature* **2019**, *565* (7738), 213-217.
(152) Imaz, I.; Rubio-Martínez, M.; An, J.; Solé-Font, I.; Rosi, N. L.; Maspoch, D. Metal–biomolecule frameworks (MBioFs). *Chem. Comm.* **2011**, *47* (26), 7287-7302, 10.1039/C1CC11202C.
(153) Kreuzer, H.; Massey, A. *Biology and biotechnology : Science, applications, and issues*; Washington, D.C. : ASM Press, 2005.
(154) Deng, H.; Doonan, C. J.; Furukawa, H.; Ferreira, R. B.; Towne, J.; Knobler, C. B.; Wang, B.; Yaghi, O. M. Multiple functional groups of varying ratios in metal-organic frameworks. *Science* **2010**, *327* (5967), 846-850.
(155) Erhart, O.; Georgiev, P. A.; Krautscheid, H. Desolvation process in the flexible metal–organic framework [Cu(Me-4py-trz-ia)], adsorption of dihydrogen and related structure responses. *CrystEngComm* **2019**, *21* (43), 6523-6535, 10.1039/C9CE00992B.
(156) Sarkisov, L.; Harrison, A. Computational structure characterisation tools in application to ordered and disordered porous materials. *Mol. Sim.* **2011**, *37* (15), 1248-1257.
(157) Iyer, P. V.; Ananthanarayan, L. Enzyme stability and stabilization—aqueous and non-aqueous environment. *Process Biochem.* **2008**, *43* (10), 1019-1032.
(158) Chapman, J.; Ismail, A. E.; Dinu, C. Z. Industrial applications of enzymes: recent advances, techniques, and outlooks. *Catal.* **2018**, *8* (6), 238.
(159) Whitesides, G. M.; Wong, C.-H. Enzymes as catalysts in synthetic organic chemistry [new synthetic methods (53)]. *Angew. Chem. Int. Ed. Engl.* **1985**, *24* (8), 617-638.
(160) Anfinsen, C. B. Principles that govern the folding of protein chains. *Science* **1973**, *181* (4096), 223-230.
(161) Bartlett, G. J.; Porter, C. T.; Borkakoti, N.; Thornton, J. M. Analysis of catalytic residues in enzyme active sites. *J. Mol. Biol.* **2002**, *324* (1), 105-121.
(162) Hollmann, F.; Otten, L. G. Enantioselectivity of enzymes. In *Wiley Encyclopedia of Chemical Biology*, **2009**; pp 1-7.
(163) García-Urdiales, E.; Alfonso, I.; Gotor, V. Enantioselective enzymatic desymmetrizations in organic synthesis. *Chem. Rev.* **2005**, *105* (1), 313-354.
(164) Rauwerdink, A.; Kazlauskas, R. J. How the same core catalytic machinery catalyzes 17 different reactions: the Serine-Histidine-Aspartate catalytic triad of α/β-hydrolase fold enzymes. *ACS Catal.* **2015**, *5* (10), 6153-6176.

(165) Hedstrom, L. Serine protease mechanism and specificity. *Chem. Rev.* **2002**, *102* (12), 4501-4524.
(166) Hajos, Z. G.; Parrish, D. R. Asymmetric synthesis of bicyclic intermediates of natural product chemistry. *The Journal of Organic Chemistry* **1974**, *39* (12), 1615-1621.
(167) Eder, U. S., G.; Wiechert, R. New type of asymmetric cyclization to optically active steroid CD partial structures. *Angew. Chem. Int. Ed. Engl.* **1971**, (10), 496–497.
(168) List, B.; Pojarliev, P.; Biller, W. T.; Martin, H. J. The proline-catalyzed direct asymmetric three-component Mannich reaction: Scope, optimization, and application to the highly enantioselective synthesis of 1,2-amino alcohols. *J. Am. Chem. Soc.* **2002**, *124* (5), 827-833.
(169) List, B. Direct catalytic asymmetric α-amination of aldehydes. *J. Am. Chem. Soc.* **2002**, *124* (20), 5656-5657.
(170) List, B.; Pojarliev, P.; Martin, H. J. Efficient proline-catalyzed Michael additions of unmodified ketones to nitro olefins. *Org. Lett.* **2001**, *3* (16), 2423-2425.
(171) List, B.; Lerner, R. A.; Barbas, C. F. Proline-catalyzed direct asymmetric aldol reactions. *J. Am. Chem. Soc.* **2000**, *122* (10), 2395-2396.
(172) Li, A.; Ye, L.; Yang, X.; Wang, B.; Yang, C.; Gu, J.; Yu, H. Reconstruction of the catalytic pocket and enzyme–substrate interactions to enhance the catalytic efficiency of a short-chain dehydrogenase/reductase. *ChemCatChem.* **2016**, *8* (20), 3229-3233.
(173) Holliday, G. L.; Mitchell, J. B.; Thornton, J. M. Understanding the functional roles of amino acid residues in enzyme catalysis. *J. Mol. Biol.* **2009**, *390* (3), 560-577.
(174) Müller, P. Practical suggestions for better crystal structures. *Crystallogr. Rev.* **2009**, *15* (1), 57-83.
(175) Giacovazzo, C.; Monaco, H. L.; Artioli, G.; Viterbo, D.; Milanesio, M.; Gilli, G.; Gilli, P.; Zanotti, G.; Ferraris, G.; Catti, M. *Fundamental crystallography*; Oxford University Press, **2011**.
(176) Kang, H. G.; Klessig, D. F. Salicylic acid-inducible arabidopsis CK2-like activity phosphorylates TGA2. *Plant Mol. Biol.* **2005**, *57* (4), 541-557.
(177) Hsiao, C. N.; Liu, L.; Miller, M. J. Cysteine- and serine-derived thiazolidinethiones and oxazolidinethiones as efficient chiral auxiliaries in aldol condensations. *J. Org. Chem.* **1987**, *52* (11), 2201-2206.
(178) Moyosore, A.; Ahmad, H.; Latif, M. A. M.; Borzehandani, M. Y.; AbdulRahman, M. B.; Abdelmalek, E. Potential of phenylalanine-, tryptophan-, and tyrosine-MOF-5 composites for selective carbon dioxide and methane adsorption. *Macromol. Theory Simul.* **2025**, *34* (1), 2400051.
(179) Lan, L.; Kuang, X.; Sun, X.; Wei, Q.; Kuang, R. MOF-enhanced chiral ECL recognition system: Dual-function in phenylalanine enantiomer detection and coreaction acceleration. *Anal. Chem.* **2023**, *95* (49), 18295-18302.

(180) Li, J.; Sha, Y. A convenient synthesis of amino acid methyl esters. *Molecules* **2008**, *13* (5), 1111-1119.
(181) Feng, L.; Wang, K.-Y.; Day, G. S.; Zhou, H.-C. The chemistry of multi-component and hierarchical framework compounds. *Chem. Soc. Rev.* **2019**, *48* (18), 4823-4853, 10.1039/C9CS00250B.
(182) Cao, C.-C.; Chen, C.-X.; Wei, Z.-W.; Qiu, Q.-F.; Zhu, N.-X.; Xiong, Y.-Y.; Jiang, J.-J.; Wang, D.; Su, C.-Y. Catalysis through dynamic spacer installation of multivariate functionalities in metal–organic frameworks. *J. Am. Chem. Soc.* **2019**, *141* (6), 2589-2593.
(183) Chen, C.-X.; Zheng, S.-P.; Wei, Z.-W.; Cao, C.-C.; Wang, H.-P.; Wang, D.; Jiang, J.-J.; Fenske, D.; Su, C.-Y. A Robust Metal–Organic Framework Combining Open Metal Sites and Polar Groups for Methane Purification and CO2/Fluorocarbon Capture. *Chem. Eur. J.* **2017**, *23* (17), 4060-4064.
(184) Thacker, N. C.; Lin, Z.; Zhang, T.; Gilhula, J. C.; Abney, C. W.; Lin, W. Robust and porous β-diketiminate-functionalized metal-organic frameworks for earth-abundant-metal-catalyzed C-H amination and hydrogenation. *J. Am. Chem. Soc.* **2016**, *138* (10), 3501-3509.
(185) Li, C.; Tang, H.; Fang, Y.; Xiao, Z.; Wang, K.; Wu, X.; Niu, H.; Zhu, C.; Zhou, H.-c. Bottom-up assembly of a highly efficient metal–organic framework for cooperative catalysis. *Inorg. Chem.* **2018**, *57* (21), 13912-13919.
(186) Ginovska, B.; Gutiérrez, O. Y.; Karkamkar, A.; Lee, M.-S.; Lercher, J. A.; Liu, Y.; Raugei, S.; Rousseau, R.; Shaw, W. J. Bioinspired catalyst design principles: Progress in emulating properties of enzymes in synthetic catalysts. *ACS Catal.* **2023**, *13* (18), 11883-11901.
(187) Xu, G.; Poelarends, G. J. Unlocking new reactivities in enzymes by iminium catalysis. *Angew. Chem. Int. Ed. Engl.* **2022**, *61* (30), e202203613.
(188) Metrano, A. J.; Chinn, A. J.; Shugrue, C. R.; Stone, E. A.; Kim, B.; Miller, S. J. Asymmetric catalysis mediated by synthetic peptides, Version 2.0: Expansion of scope and mechanisms. *Chem. Rev.* **2020**, *120* (20), 11479-11615.
(189) Tsogoeva, S.; Wei, S. (S)-Histidine-based dipeptides as organic catalysts for direct asymmetric aldol reactions. *Tetrahedron: Asymmetry* **2005**, *16*, 1947-1951.
(190) Oku, J.-i.; Ito, N.; Inoue, S. Asymmetric cyanohydrin synthesis catalyzed by synthetic dipeptides. *Makromol. Chem.* **1982**, *183* (3), 579-586.
(191) North, M. Synthesis and applications of non-racemic cyanohydrins. *Tetrahedron: Asymmetry* **2003**, *14* (2), 147-176.
(192) Jarvo, E. R.; Miller, S. J. Amino acids and peptides as asymmetric organocatalysts. *Tetrahedron* **2002**, *58* (13), 2481-2495.
(193) Singh, A.; Goswami, S.; Singh, P.; Das, D. Exploitation of catalytic dyads by short peptide-based nanotubes for enantioselective covalent catalysis. *Angew. Chem. Int. Ed. Engl.* **2023**, *62* (51), e202315716.

(194) Bindman, N. A.; Bobeica, S. C.; Liu, W. R.; van der Donk, W. A. Facile removal of leader peptides from lanthipeptides by incorporation of a hydroxy acid. *J. Am. Chem. Soc.* **2015**, *137* (22), 6975-6978.

Appendix A for Chapter 2

This section reviews the general procedures used in attempts to synthesize multicomponent MOFs (MMOFs) from amino acids. Each experimental group will be illustrated by focusing on one amino acid, such as tyrosine, combined with other amino acids in the synthesis.

A.1 Tyrosine with other amino acids

General procedure 1:

The samples below were prepared by dissolving the *l-tyrosine* (aa1) with other *l*-amino acids (aa2) at a ratio of 1:1 in H_2O (3 mL). The metal nitrate (M) was added to the previously prepared solution. Then, the pH was adjusted to a range between 8-9, by using NaOH solution (1 M). Then, EtOH (3 mL) was added. The samples were placed in a 95 °C oven for 3 days. The results are shown in the table below.

Table A.1: Weights (mg) of Tyrosine (aa1), secondary amino acids (aa2), and metal nitrates (M), along with the outcomes of their combination following the described procedure.

Metal (M) type	aa2	M Wt.	aa1 Wt.	aa2 Wt.	Results
$Co(NO_3)_2 \cdot 6H_2O$	Pro	230.90	100.80	61.20	**Crystals**: PXRD pattern matches FEQQUP
	Gly	385.00	92.10	40.30	Two **crystal** phases: 5.4.3.1 **Needles**: new phase of tyrosine complex $[Co(l\text{-tyrosine-H})(H_2O)_2 \cdot 2NO_3]$ **Blocks**: PXRD pattern matches NUFPAG
	Ser	374.00	86.80	55.30	**Crystals**: PXRD pattern matches NUFPAG
	Val	353.90	103.40	64.30	Crystalline **powder** ^1H NMR spectroscopy ratio of aa1: aa2 is 5 to 1
	Arg	316.60	90.80	117.70	**Crystals**: PXRD pattern matches NUFPAG
	Ala	327.50	100.10	109.10	**Crystals:** PXRD pattern matches NUFPAG
	Pro	337.00	95.80	48.80	No precipitate
$Zn(NO_3)_2 \cdot 6H_2O$	Pro	263.70	90.20	62.50	PXRD pattern matches FEQRAW
	Gly	249.00	95.70	44.00	**Powder**: PXRD pattern matches NUFPAG
	Ser	230.10	100.10	74.20	**Crystals**: PXRD pattern matches NUFPAG
	Val	314.70	97.40	67.40	Crystalline **powder**
	Arg	282.50	98.80	103.00	No precipitate
	Ala	276.80	94.70	98.40	**Powder:** ZnO
	Pro	328.50	105.40	46.80	No precipitate

l-Tyrosine and *l*-valine combination was *modulated* by decreasing the concentration of both amino acids. The samples below were prepared by dissolving the *l*-tyrosine (aa1, 0.25 mmol) with another *l*-valine (aa2, 0.25 mmol) at a ratio of 1:1 in H_2O (3 mL). The metal nitrate (2 eq.) was added to the previously prepared solution. Then, the pH was adjusted to a range between (8-9) by using NaOH solution (1 M). Then, EtOH (3 mL) was added. The samples were placed in a 95 °C oven for 3 days. The results are shown in the table below.

Table A.2: Weights (mg) of tyrosine (aa1), valine (aa2), and metal nitrates (M), along with the outcomes of their combination following the described procedure.

Metal (M) type	M Wt.	aa1 Wt.	aa2 Wt.	Results
$Co(NO_3)_2 \cdot 6H_2O$	257.80	55.20	27.90	Powder: PXRD pattern matches NUFPAG
$Zn(NO_3)_2 \cdot 6H_2O$	240.70	40.00	30.80	Powder: PXRD pattern matches NUFPAG

Tyrosine and valine combination was *modified* by increasing the temperature. The samples below were prepared by dissolving the *l*-tyrosine (aa1) with *l*-valine acids (aa2) at a ratio of 1:1 in H_2O (3 mL). The metal nitrate was added to the previously prepared solution. Then, the pH was adjusted by using NaOH solution (1 M) to a range between 8-9. Then, EtOH (3 mL) was added. The samples were placed in a 120 °C oven for 3 days. The results are shown in the table below.

Table A.3: Weights (mg) of Tyrosine (aa1), valine (aa2), and metal nitrates (M), along with the outcomes of their combination following the described procedure

Metal (M) type	M Wt.	aa1 Wt.	aa2 Wt.	Results
$Co(NO_3)_2 \cdot 6H_2O$	229.20	65.20	43.00	No precipitate
$Zn(NO_3)_2 \cdot 6H_2O$	212.70	58.30	38.10	No precipitate

General procedure 1 conclusion:

These observations suggest that dissolving tyrosine in the presence of other amino acids under basic aqueous-alcoholic conditions can result in the formation of distinct polymorphs of tyrosine-containing complexes, or potentially MOFs incorporating tyrosine. To further investigate this behaviour, a series of exploratory experiments were carried out, the details of which are presented in the following tables.

General procedure 2:

The samples in the table below were prepared by dissolving the *l*-tyrosine (aa1, 0.25 mmol) with other *l*-amino acids (aa2, 0.25 mmol) at a ratio of 1:1 in methanol (1 mL). The metal nitrate was then added to the solution. Then, triethylamine (10 μL) was added. The samples were placed in a 95 °C oven for 3 days.

Table A.4: Weights (mg) of Tyrosine (aa1), the second amino acid (aa2), and metal nitrates (M), along with the outcomes of their combination following the described procedure

Metal (M) type	aa2	M Wt.	aa1 Wt.	aa2 Wt.	Results
$Co(NO_3)_2 \cdot 6H_2O$	Pro.	338.20	31.90	31.20	amorphous
	Gly.	138.80	40.00	25.30	
	Ser.	128.80	47.60	35.00	
	Val.	137.60	48.10	24.40	
	Arg.	154.50	78.40	47.70	
	Ala.	192.30	51.30	44.90	
	Pro.	141.90	45.80	28.00	tyrosine free ligand
$Zn(NO_3)_2 \cdot 6H_2O$	Pro.	179.80	41.90	37.20	No precipitate
	Gly.	129.30	42.50	31.50	
	Ser.	128.50	46.40	26.90	
	Val.	144.50	42.50	24.20	
	Arg.	176.00	51.50	48.10	
	Ala.	131.30	60.20	52.50	amorphous
	Pro.	136.00	54.40	24.60	No precipitate

General procedure 3:

The samples below were prepared by suspending the *l*-tyrosine (aa1, 0.5 mmol) with other *l*-amino acids (aa2, 0.5 mmol) at a ratio of 1:1 in water (1.2 mL). The metal nitrate was then added to the solution. Then, DMF (50 μL) was added. The samples were placed in a 95 °C oven for 3 days.

Table A.5: Weights (mg) of Tyrosine (aa1), the second amino acid (aa2), and metal nitrates (M), along with the outcomes of their combination following the described procedure

Metal (M) type	aa2	M Wt.	aa1 Wt.	aa2 Wt.	Results
$Co(NO_3)_2 \cdot 6H_2O$	Pro	134.40	40.10	35.70	tyrosine free ligand
	Gly	124.40	41.60	42.40	
	Ser	117.20	42.80	41.30	
	Val	140.60	43.60	32.60	
	Arg	122.50	43.10	53.00	
	Ala	125.10	45.10	29.60	
$Zn(NO_3)_2 \cdot 6H_2O$	Pro	122.30	35.90	35.00	tyrosine free ligand
	Gly	108.40	44.30	44.50	
	Ser	153.50	61.50	35.30	
	Val	120.20	42.50	46.10	
	Arg	122.40	55.80	47.20	
	Ala	104.00	39.90	27.20	

A.2 Glutamic acid with other amino acids

In this section, only few experiments were done. All the experiments that were done, resulted in glutamic acid crystallising independently. For this reason, the experiments were stopped.

General procedure 1:

In a 4 mL vial, glutamic acid (aa1, 0.5 mmol) and the second amino acid (aa2, 0.5 mmol) were weighed. Then, they were dissolved in DMF (1 mL) and H_2O (50 µl). Then, metal nitrate (0.1 mmol) was added, and the vessels were heated in a 95 °C oven for 3 days.

Table A.6: Weights (mg) of glutamic acid (aa1), the second amino acid (aa2), and metal nitrates (M), along with the outcomes of their combination following the described procedure

Metal type	aa2	M Wt.	aa1 Wt.	aa2 Wt.	Results
$Co(NO_3)_2 \cdot 6H_2O$	Tyr	148.30	74.50	89.80	Amorphous powder
	Asn	150.60	76.90	65.20	[Co(glutamate)$_2$]
$Zn(NO_3)_2 \cdot 6H_2O$	Tyr	145.80	72.50	87.00	Amorphous powder
	Asn	130.80	75.40	64.80	[Zn(glutamate)$_2$]

General procedure 2:

In Teflon-lined steel autoclave, *l*-glutamic acid (aa1, 1 mmol) and the other amino acid (aa2, 1 mmol) were weighed. Then, they were dissolved in NaOH solution (0.25 M, 3 mL) and EtOH (3 mL). Then, the vessels were sonicated for 30 minutes at 75 °C. Then, metal nitrate (0.1 mmol) was added and the vessels were heated in a 95 °C oven for 3 days.

Table A.7: Weights (mg) of glutamic acid (aa1), the second amino acid (aa2), and metal nitrates (M), along with the outcomes of their combination following the described procedure

Metal type	aa2	M Wt.	aa1 Wt.	aa2 Wt.	Results
$Co(NO_3)_2 \cdot 6H_2O$	Tyr	480.00	150.00	180.00	**Crystals:** [Co(glutamate)$_2$]
	Asn	590.80	140.80	120.90	
$Zn(NO_3)_2 \cdot 6H_2O$	Tyr	560.00	145.30	179.80	**Crystals:** [Zn(glutamate)$_2$]
	Asn	600.30	150.90	130.70	

General procedure 3:

In a 1 mL vial, glutamic acid (aa1, 1 mmol) and the other amino acid (aa2, 1 mmol) were weighed. Then, they were dissolved in MeOH (1 mL) and H_2O (10 µL). Then, the vessels were sonicated for 30 minutes at 75 °C. Then, metal nitrate (0.1 mmol) was added, and the vessels were heated in an 85 °C oven for 3 days.

Table A.8: Weights (mg) of glutamic acid (aa1), the second amino acid (aa2), and metal nitrates (M), along with the outcomes of their combination following the described procedure

Metal type	aa2	M Wt.	aa1 Wt.	aa2 Wt.	Results
$Co(NO_3)_2 \cdot 6H_2O$	Tyr	46.00	14.80	20.00	**Powder** [Co(glutamate)$_2$]
	Asn	56.70	13.80	17.80	
$Zn(NO_3)_2 \cdot 6H_2O$	Tyr	56.00	14.50	17.98	**Powder** [Zn(glutamate)$_2$]
	Asn	60.30	12.80	16.90	

A.3 Valine with other amino acids

General procedure 1:

In 20 mL vials, the samples below were prepared by dissolving the *l*-valine (aa1, 0.5 mmol) with other *l*-amino acids (aa2, 0.5 mmol) and metal nitrate at a ratio of 1:1 in H_2O (2 mL), and the pH was adjusted using NaOH solution (1 M) to around the neutral region. Then, EtOH (3 mL) was added. The vials were placed into a 95 °C oven for 3 days.

Table A.9: Weights (mg) of valine (aa1), the second amino acid (aa2), and metal nitrates (M), along with the outcomes of their combination following the described procedure

Metal type	aa2	M Wt.	aa1 Wt.	aa2 Wt.	Results
$Co(NO_3)_2 \cdot 6H_2O$	Ser	353.40	59.60	59.40	No precipitate
	His	311.60	58.40	64.30	
	Lys	329.00	60.20	86.00	
	Asn	297.50	59.10	76.50	
	Gly	379.50	57.60	44.00	
	Ala	340.50	52.60	39.30	
$Zn(NO_3)_2 \cdot 6H_2O$	Ser	283.50	55.70	61.60	Crystalline powder
	His	348.80	62.70	72.30	powder, ZnO
	Lys	226.20	54.30	78.80	No precipitate
	Asn	272.30	65.00	76.50	
	Gly	288.90	64.30	55.90	
	Ala	244.70	58.00	33.10	

In Teflon-lined steel autoclave, valine (aa1, 0.5 mmol) and the other amino acid (aa2, 0.5 mmol) were dissolved in EtOH (1 mL), H_2O (1 mL) and DMF (20 µL). The metal nitrate was added (1 mmol), then the vials were placed at 110°C for 3 days.

Table A.10: Weights (mg) of valine (aa1), leucine (aa2), and metal nitrates (M), along with the outcomes of their combination following the described procedure

Metal type	aa2	M Wt.	aa1 Wt.	aa2 Wt.	Results
$Co(NO_3)_2 \cdot 6H_2O$	Leu	189.30	59.20	62.10	Valine Polymorph
$Zn(NO_3)_2 \cdot 6H_2O$		184.30	57.70	63.30	

The experiments above were modified in the table below,

Table A.11: Weights (mg) of valine (aa1), leucine (aa2), and metal nitrates (M), along with the outcomes of their combination following the described procedure

Metal type	aa2	Modification type	°C	M Wt.	aa1 Wt.	aa2 Wt.	Results
$Co(NO_3)_2 \cdot 6H_2O$	Leu	Lower conc.	85	115.00	28.90	30.80	No precipitate
		Same conc.	120	117.30	28.90	42.70	
		Lower conc.	95	105.80	23.10	42.70	
$Zn(NO_3)_2 \cdot 6H_2O$		Lower conc.	85	119.90	28.90	31.70	No precipitate
		Same conc.	120	146.70	29.20	35.20	
		Lower conc.	95	129.90	34.40	29.50	

General procedure 2:

Three experiments were *modified* by increasing the reaction temperature. In 20 mL vials, the samples below were prepared by dissolving the *l*-valine (aa1, 0.5 mmol) with other *l*-amino acids (aa2, 0.5 mmol) at a ratio of 1:1 in H_2O (2 mL), and the pH was adjusted to around pH 7, using NaOH solution (1 M). Then, EtOH (3 mL) was added. The metal nitrate (2 eq.) was dissolved in the solution. The samples were placed into a 120 °C oven for 3 days.

Table A.12: Weights (mg) of valine (aa1), the second amino acid (aa2), and metal nitrates (M), along with the outcomes of their combination following the described procedure

Metal type	aa2	M Wt.	aa1 Wt.	aa2 Wt.	Results
$Co(NO_3)_2{\cdot}6H_2O$	Lys	349.90	59.70	66.60	No precipitate
	Asn	401.60	65.20	53.30	
	Gly	278.00	62.20	37.10	
$Zn(NO_3)_2{\cdot}6H_2O$	Lys	258.10	64.40	57.80	No precipitate
	Asn	270.40	53.30	55.10	
	Gly	258.00	64.00	57.80	Crystalline powder

General procedure 3:

l-Valine (aa1, 0.5 mmol) and the other amino acids (aa2, 0.5 mmol) were dissolved in H_2O (2 mL), and the pH was adjusted to around 7, using NaOH solution (1 M). Then, EtOH (6 mL) was added. Two different temperatures were tried. The details and general results are demonstrated in the table below.

Table A.13: Weights (mg) of valine (aa1), the second amino acid (aa2), and metal nitrates (M), along with the outcomes of their combination following the described procedure

Metal type	°C	aa2	M Wt.	aa1 Wt.	aa2 Wt.	Results
$Co(NO_3)_2{\cdot}6H_2O$	120	Ser	353.40	59.60	49.60	No precipitate
		Gly	278.00	64.40	57.80	
	95	Ser	272.90	30.50	27.40	
		Gly	263.40	28.00	18.80	
$Zn(NO_3)_2{\cdot}6H_2O$	120	Ser	283.50	61.60	55.70	No precipitate
		Gly	285.106	64.40	57.80	
	95	Ser	217.60	30.40	28.80	
		Gly	232.90	30.70	19.90	Crystalline powder

General procedure 4:

In the experiments below, *l*-valine (0.5 mmol), the other amino acids and the metal nitrate (1 mmol) were dissolved in H_2O (2 mL), and the pH was adjusted to around 7, using NaOH solution (1 M). Then, EtOH (6 mL) was added. The vials were placed in a 95 °C oven for 3 days.

Table A.14: Weights (mg) of valine (aa1), serine (aa2), and metal nitrates (M), along with the outcomes of their combination following the described procedure

Metal type	aa2	M Wt.	aa1Wt.	aa2 Wt.	Results
$Co(NO_3)_2{\cdot}6H_2O$	Ser	263.50	27.30	23.50	No precipitate
$Zn(NO_3)_2{\cdot}6H_2O$		242.80	27.60	20.70	Crystalline powder

Another *modification* was done; the amino acids concentration was decreased. In Teflon-lined steel autoclave, *l*-valine (aa1, 0.25 mmol), the other *l*-amino acid (aa2, 0.25 mmol) and the metal nitrate (1 mmol) were dissolved in H_2O (2 mL), then the pH was adjusted to around 8 using NaOH (1 M). EtOH (3 ml) was added, and the vessels were placed in a 120 °C oven for 3 days.

Table A.15: Weights (mg) of valine (aa1), the second amino acids (aa2), and metal nitrates (M), along with the outcomes of their combination following the described procedure

Metal type	aa2	M Wt.	aa1Wt.	aa2 Wt.	Results
$Co(NO_3)_2{\cdot}6H_2O$	Ser	220.80	32.00	28.90	No precipitate
	Gly	294.40	27.50	25.00	
$Zn(NO_3)_2{\cdot}6H_2O$	ser	197.70	27.90	28.30	
	Gly	190.00	35.00	25.00	

In a Teflon-lined steel autoclave, *l*-valine (0.5 mmol) and the other amino acid were dissolved in basic H_2O (0.2 M $NaOH_{aq}$, 1 mL). The metal nitrate was added (1 mmol), then the vessels were placed at 110°C for 3 days.

Table A.16: Weights (mg) of valine (aa1), the second amino acids (aa2), and metal nitrates (M), along with the outcomes of their combination following the described procedure

Metal (M) type	aa2	M Wt.	aa1 Wt.	aa2 Wt.	Results
$Co(NO_3)_2 \cdot 6H_2O$	His	133.90	82.90	67.80	Amorphous powder
	Asn	275.50	48.50	66.20	No precipitate
	Ser	169.90	61.10	56.20	
	Lys	157.50	55.00	91.35	
	Thr	237.90	57.90	59.60	
	Leu	194.60	60.70	63.70	Crystalline powder
$Zn(NO_3)_2 \cdot 6H_2O$	His	151.50	48.00	48.50	Amorphous powder
	Asn	229.80	66.50	65.70	ZnO
	Ser	161.70	59.60	61.30	Crystalline powder
	Lys	222.40	58.20	76.90	No precipitate
	Thr	153.60	60.80	72.60	
	Leu	143.10	67.30	64.30	

Two different combinations were modified by three different ways:

In Teflon-lined steel autoclave, *l*-valine (aa1, 0.5 mmol) and the other amino acids (aa2,0.5 mmol) were dissolved in basic H_2O (0.2 M $NaOH_{aq}$, 1 mL). The metal nitrate was added (1 mmol), then the vessels were placed at a 110 °C oven for 3 days.

Table A.17: Component weights (mg) of valine (aa1), the second amino acid (aa2), and metal nitrates (M), with outcomes based on the procedure and listed modification types

Metal (M) type	aa2	Modification type	M Wt.	aa1 Wt.	aa2 Wt.	Results
$Co(NO_3)_2 \cdot 6H_2O$	Thr	conc.	120.80	33.30	40.70	Crystalline powder Threonine Polymorph
		temp. 85 °C	114.10	55.60	53.60	
		molarity	116.40	48.60	51.50	No precipitate
	Leu	conc.	158.30	28.80	32.60	Crystalline powder
		temp. 85 °C	159.40	52.80	60.70	No precipitate
		molarity	158.10	48.90	47.50	
$Zn(NO_3)_2 \cdot 6H_2O$	Thr	conc.	110.00	33.50	26.10	No precipitate
		temp. 85 °C	143.90	51.20	52.10	
		molarity	128.10	48.00	49.90	
	Leu	conc.	105.70	32.60	35.60	[Zn(leucine-H)$_2$]
		temp. 85 °C	127.60	44.90	49.10	
		molarity	116.20	47.20	49.10	No precipitate

General procedure 6: Using different organic solvents for synthesis

In 4 mL vial, *l*-valine (aa1, 0.5 mmol) and the alanine (aa2, 0.5 mmol) were dissolved in methanol (1 mL), and other solvent (20 µL). Then, the metal salt (1 mmol) was added. Then, the vials were placed in a 95°C oven for 3 days.

Table A.18: Component weights (mg) of valine (aa1), alanine (aa2), and metal nitrates (M), with outcomes based on the procedure using the listed solvent types

Metal type	solvent	M Wt.	aa1Wt.	aa2 Wt.	Results
$Co(NO_3)_2 \cdot 6H_2O$	DMF	136.60	28.30	25.00	Crystalline powder
	H_2O	117.20	29.50	25.10	No precipitate
	TEA	137.70	24.60	23.60	Crystalline powder
$Zn(NO_3)_2 \cdot 6H_2O$	DMF	126.50	27.70	24.10	No precipitate
	H_2O	116.90	27.00	25.00	
	TEA	108.30	26.70	24.60	

The samples in the table below were prepared by dissolving the l-valine (aa1, 0.5 mmol) and amino acid (aa2, 0.5 mmol) in organic solvents mentioned in the table below. The samples were heated in 95 °C dry bath for 3 days.

Table A.19: Component weights (mg) of valine (aa1), the second amino acid (aa2), and metal nitrates (M), with outcomes based on the procedure and listed solvent types.

Metal (M) type	aa2	Solvent system	M Wt.	aa1 Wt.	aa2 Wt.	Results
$Co(NO_3)_2 \cdot 6H_2O$	Ser	MeOH (3 mL), H_2O (100 µL), DMF (50 µL)	346.40	125.10	105.40	Crystalline powder
	Gly		299.90	108.40	86.40	
	Ser	EtOH (3 mL), H_2O (100 µL), DMF (50 µL)	263.30	107.40	104.80	amorphous
	Gly		265.90	103.00	73.20	
$Zn(NO_3)_2 \cdot 6H_2O$	Ser	MeOH (3 mL), H_2O (100 µL), DMF (50 µL)	225.70	131.10	115.20	amorphous
	Gly		257.70	82.20	76.10	
	Ser	EtOH (3 mL), H_2O (100 µL), DMF (50 µL)	237.90	106.60	110.50	amorphous
	Gly		257.90	112.10	81.80	

In a 4 mL vial, *l*-valine (0.5 mmol) and the other amino acids (0.5 mmol) were dissolved in methanol (1 mL), and DMF (20 µL). Then, the metal salt (1 mmol) was added. Then, the vials were placed in a 95°C oven for 3 days.

Table A.20: Component weights (mg) of valine (aa1), the second amino acid (aa2), and metal nitrates (M), with outcomes based on the procedure.

Metal (M) type	aa2	M Wt.	aa1 Wt.	aa2 Wt.	Results
$Co(NO_3)_2 \cdot 6H_2O$	Gly	141.10	62.00	34.40	No precipitate
	Ser	141.00	59.30	52.70	
	Thr	127.80	86.60	86.60	Crystalline powder
	Tyr	172.20	51.30	95.50	Tyrosine-free ligand
	Arg	174.40	53.90	90.90	No precipitate
	Leu	164.30	49.10	70.00	
	Lys	133.50	54.90	92.30	
	His	146.60	60.60	65.00	
	Asn	125.60	53.30	72.20	
	Ala	124.20	63.80	42.40	Crystalline powder
$Zn(NO_3)_2 \cdot 6H_2O$	Gly	131.40	53.10	36.60	No precipitate
	Ser	146.60	54.10	56.50	
	Thr	145.50	53.70	44.50	
	Tyr	147.50	49.90	82.50	Tyrosine-free ligand
	Arg	153.30	65.50	78.30	No precipitate
	Leu	127.70	51.10	67.90	Crystalline powder
	Lys	132.10	58.30	109.00	No precipitate
	His	143.20	70.40	73.20	
	Asn	132.10	54.70	61.60	
	Ala	128.30	49.30	48.20	

Threonine and valine combination was modified by changing the type of the alcohol that was used. MeOH was *changed* to EtOH. In a 4 mL vial, valine (0.5 mmol) was dissolved in EtOH (1 mL) and DMF (20 µL). The metal nitrate was added (1 mmol), then the vials were placed at 95 °C for 3 days.

Table A.21: Component weights (mg) of valine (aa1), threonine (aa2), and metal nitrates (M), with outcomes based on the procedure and listed modification types

Metal type	aa2	Modification type	°C	M Wt.	aa1 Wt.	aa2 Wt.	Results
$Co(NO_3)_2 \cdot 6H_2O$	Thr	Lower conc.	95	145.10	29.10	26.30	Crystalline powder matching previously collected PXRD
		Same conc.	85	158.50	65.40	48.60	
		Lower conc.	85	150.30	30.40	26.80	
$Zn(NO_3)_2 \cdot 6H_2O$		Lower conc.	95	148.40	30.60	26.70	No precipitate
		Same conc.	85	129.40	54.30	56.10	
		Lower conc.	85	119.50	26.30	28.70	

The procedure above was modified by several ways as documented in the table below.

Table A.22: Component weights (mg) of valine (aa1), threonine (aa2), and metal nitrates (M), with outcomes based on the procedure and listed modification types

Metal type	Modification type	Benzoic acid (BA)	M Wt.	aa1 Wt.	aa2 Wt.	Results
$Co(NO_3)_2 \cdot 6H_2O$	Lower feed ratios Used MeOH	64.80	120.70	31.60	27.40	Crystalline powder
	Same feed ratios	65.60	112.00	59.10	50.90	
	No DMF added, EtOH was used	58.30	109.10	25.20	28.00	
	No DMF added, MeOH was used	×	100.60	58.30	59.40	
	MeOH (0.5 mL), NaOH (0.1 M, 0.5 mL)	×	99.20	60.40	55.40	
	EtOH (0.5 mL), NaOH (0.1 M, 0.5 mL)	×	99.80	56.60	60.40	
$Zn(NO_3)_2 \cdot 6H_2O$	Lower feed ratios Used MeOH	66.40	174.70	27.00	26.40	No precipitate
	Same feed ratios	65.40	118.00	63.60	56.10	
	No DMF added, EtOH was used	68.50	128.40	27.10	28.50	

In 4 mL vials, valine (aa1, 1 mmol), the other amino acids (aa2, 1.00 mmol) were dissolved in $NaOH_{aq}$ (0.1 M, 3 mL) and EtOH (3 mL). The metal nitrate was added (2 mmol), then the vials were placed at 110 °C for 3 days.

Table A.23: Component weights (mg) of valine (aa1), the second amino acid (aa2), and metal nitrates (M), with outcomes based on the procedure.

Metal type	aa2	M Wt.	aa1 Wt.	aa2 Wt.	Results
$Co(NO_3)_2 \cdot 6H_2O$	Thr	409.80	129.80	131.90	No precipitate
	Met	434.60	126.40	157.70	
	Leu	235.30	126.40	134.20	[Co(leucine-H)$_2$]
$Zn(NO_3)_2 \cdot 6H_2O$	Thr	467.50	113.80	140.90	No precipitate
	Met	384.50	125.10	149.60	[Zn(methionine-H)$_2$]
	Leu	315.30	134.30	149.60	No precipitate

General Procedure:

In 20 mL vials, valine (aa1, 0.5 mmol) and amino acid 2 (0.5 mmol) were dissolved in 3 mL of NaOH solution (0.1 M). Then, the metal salt was added (1.00 mmol). The vials were stirred at room temperature for 3 days.

Table A.24: Component weights (mg) of valine (aa1), the second amino acid (aa2), and metal nitrates (M), with outcomes based on the procedure.

Metal type	aa2	M Wt.	aa1 Wt.	aa2 Wt.	Results
$Co(NO_3)_2 \cdot 6H_2O$	Thr	198.40	60.50	73.50	No precipitate
	Leu	193.10	60.30	62.10	
	Lys	194.10	57.80	96.90	
	Asn	218.30	54.90	79.70	
$Zn(NO_3)_2 \cdot 6H_2O$	Thr	186.90	60.50	56.00	No precipitate
	Leu	163.70	61.60	57.50	**Crystals :** PXRD pattern is different from previously collected [Co(leucine)$_2$] and valine polymorph. ^{1}H NMR spectroscopy was done, which showed that these crystals are just leucine
	Lys	181.50	67.20	89.10	No precipitate
	Asn	223.50	56.50	80.00	Asparagine polymorph

A.4 Methionine with other amino acids

General procedure 1: Using different mixing conditions in an aqueous basic solution for synthesis

The samples were prepared by dissolving the methionine (aa1, 0.5 mmol), the other amino acids (0.5 mmol), and the metal nitrate were dissolved in H_2O (2 mL), and the pH was adjusted to around 7, using NaOH solution (1 M). Then, EtOH (2 mL) was added. The vials were placed in a 95 °C oven for 48 hours.

Table A.25: Component weights (mg) of methionine (aa1), the second amino acid (aa2), and metal nitrates (M), with outcomes based on the procedure.

Metal (M) type	aa2	M Wt.	aa1 Wt.	aa2Wt.	Results
$Co(NO_3)_2 \cdot 6H_2O$	His	323.20	82.30	75.60	No Ppt.
	Lys	296.60	75.30	89.60	
	Val	256.70	72.00	60.00	
	Tyr	247.70	73.60	93.40	Crystals, PXRD matches NUFPAG
	Asn	290.50	78.80	76.40	No Ppt.
	Ser	283.00	73.30	60.20	
	Arg	299.00	73.30	60.20	
$Zn(NO_3)_2 \cdot 6H_2O$	His	325.60	83.50	77.90	No Ppt.
	lys	233.60	76.60	73.50	
	Val	250.70	79.70	75.00	
	Tyr	247.20	75.00	99.70	
	Asn	265.10	80.90	77.60	
	Ser	223.20	73.40	66.50	
	Arg	223.30	74.70	88.20	

In the table below, I repeated the above procedure, but the sample was placed in a 120 °C oven for 3 days.

Table A.26: Component weights (mg) of methionine (aa1), the second amino acid (aa2), and metal nitrates (M), with outcomes based on the procedure.

Metal (M) type	Aa 2	M Wt.	aa1 Wt.	aa2 Wt.	Results
$Co(NO_3)_2 \cdot 6H_2O$	His	215.50	80.30	89.30	No precipitate
	Lys	213.40	84.40	74.60	
	Val	225.40	79.40	82.40	
$Zn(NO_3)_2 \cdot 6H_2O$	His	208.90	76.60	81.50	[Co(methionine-H)$_2$]
	lys	243.80	75.80	80.30	
	Val	198.50	72.90	59.80	

In the table below, the first procedure was repeated, but the feed of the methionine and the other amino acids (1 mmol) was increased, except when aa2 is tyrosine, its feed was kept the same (0.5 mmol). The samples were placed in a 95 °C oven for 3 days.

Table A.27: Component weights (mg) of methionine (aa1), the second amino acid (aa2), and metal nitrates (M), with outcomes based on the procedure above.

Metal (M) type	aa2	M Wt.	aa1 Wt.	aa2 Wt.	Results
$Co(NO_3)_2 \cdot 6H_2O$	Tyr	266.20	138.00	91.80	Crystalline powder has some small purple crystals, has tyrosine MOF (different phase)
	Ser	259.10	145.30	114.00	No ppt
	Val	293.10	137.80	120.70	No PPT
	His	277.40	132.60	120.70	Crystalline powder
	Arg	267.20	148.30	174.30	CoO
	Ala	267.20	148.30	174.30	No ppt
	Gly	251.50	144.90	79.90	crystalline powder
$Zn(NO_3)_2 \cdot 6H_2O$	Tyr	257.10	154.30	89.70	Crystalline powder, multicomponent tyrosine: methionine 1:2
	Ser	221.80	148.60	115.80	Crystals, [Zn(methionine-H)$_2$]
	Val	260.40	144.50	166.20	No PPT
	His	266.40	144.50	166.20	Crystalline powder
	Arg	248.30	141.20	167.50	Low crystallinity powder
	Ala	240.40	131.60	86.30	[Zn(methionine-H)$_2$]
	Gly	225.10	143.60	82.60	ZnO glycine: methionine, 1:1

l-Methionine (aa1) and *l*-tyrosine (aa2) combination was modified by trying two different temperatures. The feed of aa2 was decreased. *l*-Tyrosine (0.25 mmol) and *l*-methionine (0.5 mmol) were dissolved in H_2O (3 mL). Then, metal nitrate was added (0.5 mmol) and the pH was adjusted to around 9, using NaOH solution (1 M). Then, EtOH (2 mL) was added. The samples that were heated at 95 °C were prepared in 20 mL vials, while samples that were heated at 120 °C were prepared in Teflon-lined steel autoclave.

Table A.28: Component weights (mg) of methionine (aa1), tyrosine (aa2), and metal nitrates (M), with outcomes based on the procedure above.

Metal type	°C	aa2	M Wt.	aa1 Wt.	aa2 Wt.	Results
$Co(NO_3)_2{\cdot}6H_2O$	95	Tyr.	326.60	79.10	48.50	crystalline powder
	120		340.20	89.70	47.20	No precipitate
$Zn(NO_3)_2{\cdot}6H_2O$	95		350.00	75.00	49.50	crystalline powder
	120		285.50	86.60	52.00	

In 20 mL vial, methionine (aa1, 0.5 mmol) and tyrosine (aa2, 0.5 mmol) were dissolved in H_2O (3 mL). Then, metal nitrate was added, and the pH was adjusted using NaOH solution (1 M). Then, DMF (150 µL) and EtOH (3 mL) were added. The vials were placed in a 95 °C oven for 3 days.

Table A.29: Component weights (mg) of methionine (aa1), tyrosine (aa2), and metal nitrates (M), with outcomes based on the procedure above.

Metal type	aa2	M Wt.	aa1 Wt.	aa2 Wt.	Results
$Co(NO_3)_2{\cdot}6H_2O$	Tyr.	169.1	67.20	42.90	Crystalline powder: PXRD matches *l*-tyrosine
$Zn(NO_3)_2{\cdot}6H_2O$		121.8	68.80	43.30	

In Teflon-lined steel autoclave, *l*-methionine (aa1, 0.5 mmol) and the other amino acids (aa2, 0.5 mmol) were dissolved in $NaOH_{aq}$ (0.1 M,1 mL). Then, EtOH (3 mL) was added. Then, the metal salt was added (1 mmol). The vials were placed at 110 °C oven for 3 days.

Table A.30: Component weights (mg) of methionine (aa1), the second amino acid (aa2), and metal nitrates (M), with outcomes based on the procedure above.

Metal (M) type	aa2	M Wt.	aa1 Wt.	aa2Wt.	Results
$Co(NO_3)_2{\cdot}6H_2O$	Tyr	247.50	67.00	42.60	Tyrosine free ligand
	Asn	202.30	64.50	73.80	No precipitate
	Ser	219.50	76.00	55.70	
$Zn(NO_3)_2{\cdot}6H_2O$	Tyr	235.50	77.30	71.10	Tyrosine free ligand
	Asn	205.40	83.50	83.50	No precipitate
	Ser	185.00	47.80	82.70	

In 4 mL vials, *l*-methionine (aa1, 1.00 mmol) and aa2 were dissolved in $NaOH_{aq}$ (0.1 M, 3 mL) and EtOH (3 mL). The metal nitrate was added (2 mmol), then the vials were placed at 110 °C for 3 days.

Table A.31: Component weights (mg) of methionine (aa1), the second amino acid (aa2), and metal nitrates (M), with outcomes based on the procedure above.

Metal (M) type	aa2	M Wt.	aa1 Wt.	aa2 Wt.	Results
$Co(NO_3)_2 \cdot 6H_2O$	Leu	449.80	149.20	126.30	No precipitate
	Thr	381.90	147.00	126.30	
$Zn(NO_3)_2 \cdot 6H_2O$	Leu	445.00	135.80	141.40	No precipitate
	Thr	404.30	137.60	125.00	[Zn(methionine-H)$_2$]

General procedure: using organic solvents in synthesis

The samples below were prepared in 4 mL vials. *l*-Methionine (aa1, 0.25 mmol) and the amino acid 2 (aa2, 0.25 mmol) were dissolved in MeOH (1 mL) and H_2O (50 µL). Then, metal nitrate (0.5 mmol) was added. The samples were placed in a 95 °C oven for 3 days.

Table A.32: Component weights (mg) of methionine (aa1), the second amino acid (aa2), and metal nitrates (M), with outcomes based on the procedure above.

Metal (M) type	aa2	M Wt.	aa1 Wt.	aa2 Wt.	Results
$Co(NO_3)_2 \cdot 6H_2O$	His	166.70	36.40	40.10	No precipitate
	Lys	127.40	36.70	52.10	
	Val	163.40	40.60	55.40	
	Ala	143.30	33.70	33.70	
	Gly	150.00	35.70	20.50	
	Ser	142.40	38.70	37.40	
	Asn	144.00	36.60	46.20	
	Thr	150.00	38.00	31.70	Amorphous
	Arg	151.80	46.00	34.20	No precipitate
	Tyr	159.80	75.70	49.10	
$Zn(NO_3)_2 \cdot 6H_2O$	His	178.50	38.60	40.90	No precipitate
	Lys	146.60	33.90	57.80	
	Val	137.50	34.50	53.70	
	Ala	130.10	34.70	28.60	
	Gly	148.50	34.70	19.00	
	Ser	139.90	38.20	30.60	
	Asn	146.90	36.00	36.60	
	Thr	112.90	36.70	32.20	
	Arg	139.20	50.10	34.20	
	Tyr	152.10	74.50	44.00	

The samples in the table below were prepared in 4 mL vials. *l*-methionine (aa1, 0.25 mmol) and the amino acid 2 (aa2, 0.25 mmol) were dissolved in MeOH (1 mL) and DMF (50 µL). Then, metal nitrate (0.5 mmol) was added. The samples were placed in a 95 °C oven for 3 days.

Table A.33: Component weights (mg) of methionine (aa1), the second amino acid (aa2), and metal nitrates (M), with outcomes based on the procedure above.

Metal (M) type	aa2	M Wt.	aa1 Wt.	aa2 Wt.	Results
$Co(NO_3)_2 \cdot 6H_2O$	Ser	134.90	37.90	29.00	No precipitate
	Val	144.80	35.10	28.30	
	His	148.70	36.60	41.90	
	Arg	139.20	46.00	33.60	
	Ala	145.50	32.20	21.40	
	Gly	184.40	33.80	33.80	
	Asn	146.30	32.40	37.40	
	Tyr	189.40	74.00	43.20	
$Zn(NO_3)_2 \cdot 6H_2O$	Ser	147.20	33.50	29.50	No precipitate
	Val	142.70	33.50	29.50	
	His	137.50	36.80	40.20	
	Arg	135.70	40.20	40.30	
	Ala	142.00	34.00	21.30	
	Gly	131.80	31.20	19.10	
	Asn	132.70	39.40	37.50	
	Tyr	146.10	75.60	45.60	

In a 4 mL vial, *l*-methionine (aa1, 0.25 mmol) and the amino acid 2 (aa2, 0.25 mmol) were dissolved in MeOH (1 mL) and TEA (10 µL). Then, metal nitrate (0.5 mmol) was added. The samples were placed in a 95 °C oven for 3 days.

Table A.34: Component weights (mg) of methionine (aa1), the second amino acid (aa2), and metal nitrates (M), with outcomes based on the procedure above.

Metal (M) type	aa2	M Wt.	aa1 Wt.	aa2 Wt.	Results
$Co(NO_3)_2 \cdot 6H_2O$	His	164.90	38.10	41.30	No precipitate
	lys	155.70	37.00	51.40	
	Val	189.30	37.20	34.10	
	Ala	151.30	36.50	22.60	
	Gly	216.50	36.90	21.00	
	Ser	124.30	34.50	27.90	
	Asn	182.60	39.50	37.00	
	Thr	149.60	30.90	33.70	
	Arg	209.80	32.40	42.50	
$Zn(NO_3)_2 \cdot 6H_2O$	His	114.30	36.60	46.30	No precipitate
	Lys	116.50	36.10	54.70	
	Val	118.00	39.60	35.20	
	Ala	131.70	37.90	22.20	
	Gly	148.30	39.10	21.60	
	Ser	160.90	32.70	30.10	
	Asn	167.20	35.40	33.70	
	Thr	166.00	34.70	28.80	
	Arg	120.40	37.80	41.00	

In 4 mL vial, *l*-methionine (0.5 mmol) and the amino acid 2 (aa2, 0.5 mmol) were dissolved in H_2O (1 mL), EtOH (1 mL), and DMF (10 µL). Then, the metal nitrate was added. The vials were placed in a 95 °C oven for 3 days.

Table A.35: Component weights (mg) of methionine (aa1), the second amino acid (aa2), and metal nitrates (M), with outcomes based on the procedure above.

Metal (M) type	aa2	M Wt.	aa1 Wt.	aa2 Wt.	Results
$Co(NO_3)_2 \cdot 6H_2O$	Asn	235.90	75.10	80.10	No precipitate
	Leu	273.60	76.70	68.50	
	Val	213.80	73.40	57.10	
	Thr	231.50	79.70	57.65	
	Ser	175.90	76.90	53.10	
	Lys	242.20	76.30	92.20	
	His	187.80	71.60	81.10	[Co(*l*-methionine-H)]
	Gly	175.90	77.50	31.70	No precipitate
$Zn(NO_3)_2 \cdot 6H_2O$	Asn	208.50	77.50	79.50	No precipitate
	Leu	237.70	74.40	69.60	
	Val	221.90	78.90	65.30	
	Thr	186.20	84.20	61.50	
	Ser	199.60	81.60	55.60	
	Lys	236.60	75.30	97.00	
	His	236.02	71.00	80.00	
	Gly	175.60	74.80	40.70	

In a 4 mL vial, *l*-methionine (1 mmol) and the second amino acid (1 mmol) were dissolved in MeOH (1 mL) and DMF (50 µL). Then, metal nitrate was added (1 mmol). The vials were placed in a 95°C oven for 3 days.

Table A.36: Component weights (mg) of methionine (aa1), the second amino acid (aa2), and metal nitrates (M), with outcomes based on the procedure above.

Metal (M) type	aa2	M Wt.	aa1 Wt.	aa2 Wt.	Results
$Co(NO_3)_2 \cdot 6H_2O$	His	227.10	146.70	151.80	No precipitate
	Lys	219.20	152.90	171.30	
	Leu	290.80	143.90	133.40	
	Gly	252.10	148.80	75.05	
	Val	225.00	137.30	122.20	
	Ala	235.00	138.40	81.00	Crystalline powder
	Asn	257.00	129.00	153.80	No precipitate
	Ser	193.90	168.10	109.90	
	Thr	205.30	140.90	104.90	Amorphous powder
	Glu	201.30	155.70	143.10	Crystalline powder
$Zn(NO_3)_2 \cdot 6H_2O$	His	181.60	152.10	157.50	amorphous
	Lys	151.90	144.80	161.90	Crystalline powder
	Leu	185.50	150.10	136.80	
	Gly	165.90	142.30	73.96	
	Val	155.80	155.60	121.80	
	Ala	180.50	142.10	82.20	
	Asn	177.80	151.80	144.90	
	Ser	166.90	156.90	110.90	
	Thr	170.60	146.70	109.90	
	Glu	185.70	147.60	144.60	

Three different combinations were tried to modify as in the previous experiments, these combinations yielded crystalline powder.

In a 4 mL vial, *l*-methionine (0.5 mmol) and the second amino acid (0.5 mmol) were dissolved in MeOH (1 mL). Then, TEA (10 µL) and H_2O (50 µL) were added. Then, metal nitrate was added (1 mmol). The vials were placed in a 95 °C oven for 3 days.

Table A.37: Component weights (mg) of methionine (aa1), the second amino acid (aa2), and metal nitrates (M), with outcomes based on the procedure above.

Metal (M) type	aa2	M Wt.	aa1 Wt.	aa2 Wt.	Results
$Co(NO_3)_2 \cdot 6H_2O$	Asn	149.00	72.30	53.10	No precipitate
	Ala	125.60	64.50	57.80	crystalline powder, but a gel-like material surrounds it. This made the PXRD pattern look noisy.
	Gly	143.90	70.20	35.00	No precipitate
$Zn(NO_3)_2 \cdot 6H_2O$	Asn	126.30	81.30	67.10	crystalline powder
	Ala	132.70	60.10	56.50	No precipitate
	Gly	122.20	65.90	37.40	

Two different combinations were tried, which are methionine and valine and methionine and histidine. The *original* procedure is: In a 4 mL vial, methionine (0.5 mmol) was dissolved in methanol (1 mL) and DMF (20 µL). The metal nitrate was added (1 mmol), then the vials were placed at 95°C for 3 days.

Table A.38: Component weights (mg) of methionine (aa1), the second amino acid (aa2), and metal nitrates (M), with outcomes based on the procedure above and the listed modifications.

Metal type	aa2	Modification type	M Wt.	aa1 Wt.	aa2 Wt.	Results
$Co(NO_3)_2 \cdot 6H_2O$	His	Dissolved in EtOH	105.20	77.90	71.10	Amorphous powder
		Dissolved in MeOH	78.30	75.80	70.00	Crystalline powder [Co(methionine-H)$_2$]
		Dissolved in MeOH (0.5 mL), and $NaOH_{aq}$ solution (0.1 M, 0.5 mL).	68.30	71.20	81.30	
		Dissolved in EtOH (0.5 mL), and $NaOH_{aq}$ solution (0.1 M, 0.5 mL).	89.50	73.60	73.00	
$Zn(NO_3)_2 \cdot 6H_2O$	Val.	Dissolved in EtOH	90.30	75.10	61.70	Crystalline powder [Zn(methionine-H)$_2$]
		Dissolved in MeOH	115.30	82.60	54.90	
		Dissolved in MeOH (0.5 mL), and $NaOH_{aq}$ solution (0.1 M, 0.5 mL).	88.80	71.80	59.60	
		Dissolved in EtOH (0.5 mL), and $NaOH_{aq}$ solution (0.1 M, 0.5 mL).	86.10	87.10	57.10	

In 4 mL vial, *l*-methionine (aa1, 0.5 mmol) and the other amino acids (aa2, 0.5 mmol) were dissolved in methanol (1 mL), TEA (10 µL) and H_2O (50 µL) were added. Then, the metal salt (1 mmol) was added. The vials were placed at 95°C oven for 3 days.

Table A.39: Component weights (mg) of methionine (aa1), the second amino acid (aa2), and metal nitrates (M), with outcomes based on the procedure above.

Metal (M) type	aa2	M Wt.	aa1 Wt.	aa2Wt.	Results
$Co(NO_3)_2 \cdot 6H_2O$	Ser	189.00	78.20	55.70	No precipitate
	His	143.00	71.00	67.60	
	Lys	210.20	68.40	89.20	
	Leu	143.60	64.60	76.90	
	Val	204.50	51.60	67.70	
	Thr	177.20	73.40	56.90	
	Glu	153.20	69.10	65.40	
$Zn(NO_3)_2 \cdot 6H_2O$	Ser	176.60	67.50	56.30	No precipitate
	His	142.70	68.30	71.60	
	Lys	158.90	67.00	95.60	
	Leu	134.10	68.20	66.40	
	Val	142.90	52.20	63.40	
	Thr	192.90	80.70	55.80	
	Glu	153.40	77.30	54.20	

A.5 Arginine with other amino acids

General procedure 1:

The samples below were prepared by dissolving the *l*-arginine (aa1, 0.5 mmol) with other *l*-amino acids (aa2, 0.5 mmol) at a ratio of 1:1 in water (3 mL). Then, 2 eq. of the metal was added. Then, the pH was adjusted to around 8 using NaOH (1 M). EtOH (2 mL) was added. The samples were placed into a 120 °C oven for 3 days

Table A.40: Component weights (mg) of arginine (aa1), the second amino acid (aa2), and metal nitrates (M), with outcomes based on the procedure above.

Metal (M) type	aa2	M Wt.	aa1 Wt.	aa2 Wt.	Results
$Co(NO_3)_2 \cdot 6H_2O$	Gly	267.70	80.10	58.70	No precipitate
	Ser	316.80	73.20	57.70	
	Val	215.30	79.30	60.20	
	His	253.40	86.60	59.90	not a MOF like PXRD
	Lys	215.30	88.50	102.50	No precipitate
	Asn	231.60	88.60	72.40	crystalline PXRD
$Zn(NO_3)_2 \cdot 6H_2O$	Gly	198.60	83.00	58.40	No precipitate
	Ser	227.50	72.30	51.10	
	Val	213.50	80.50	53.40	
	His	198.20	78.20	54.90	zinc oxide
	Lys	220.30	75.60	91.50	No precipitate
	Asn	254.60	84.10	75.50	ZnO

In a 4 mL vial, the samples below were prepared by dissolving the l-arginine (aa1, 0.5 mmol) and the other l-amino acids at a ratio of 1:1 in water (1 mL). Then, the metal nitrate was added. Then, EtOH (0.5 mL) was added. The samples were placed in a 95 °C oven for 3 days.

Table A.41: Component weights (mg) of arginine (aa1), the second amino acid (aa2), and metal nitrates (M), with outcomes based on the procedure above.

Metal (M) type	aa2	M Wt.	aa1 Wt.	aa2 Wt.	Results
$Co(NO_3)_2 \cdot 6H_2O$	Pro	258.20	90.60	60.00	No precipitate
	Ser	214.20	81.00	53.80	
	Val	269.70	78.50	62.00	
	His	237.60	87.50	70.40	
	Lys	242.00	70.90	95.90	Cobalt oxide
	Ala	245.70	85.80	43.10	low-angle peaks , crystalline powder
	Asn	271.50	77.40	53.80	no precipitate
$Zn(NO_3)_2 \cdot 6H_2O$	Pro	268.40	86.10	71.70	zinc oxide
	Ser	178.40	70.30	62.90	No precipitate
	Val	189.70	75.40	70.20	zinc oxide
	His	226.10	88.30	78.40	low crystalinity
	Lys	228.40	85.70	95.30	zinc oxide
	Ala	252.30	84.50	50.70	
	Asn	178.40	73.90	73.30	

In 4 mL vials, arginine (aa1, 0.5 mmol) and the other amino acid (aa2, 0.5 mmol) were dissolved in $NaOH_{aq}$ (0.05 M, 1 mL) and EtOH (1 mL). The metal nitrate was added (1 mmol), then the vials were placed at 95 °C oven for 3 days.

Table A.42: Component weights (mg) of arginine (aa1), the second amino acid (aa2), and metal nitrates (M), with outcomes based on the procedure above.

Metal (M) type	aa2	M Wt.	aa1 Wt.	aa2 Wt.	Results
$Co(NO_3)_2 \cdot 6H_2O$	Tyr	105.00	90.40	89.70	Tyrosine-free ligand
	Thr	122.80	85.80	58.90	No precipitate
	Val	117.30	83.40	64.10	
	His	144.80	85.50	70.00	
	Ala	144.50	89.00	44.90	
	Ser	106.70	78.10	64.30	
	Leu	149.90	78.60	66.60	
	Asn	174.20	80.90	75.00	
	Lys	120.00	80.10	97.00	
	Met	136.30	79.40	74.90	
	Gly	140.00	77.60	45.90	
$Zn(NO_3)_2 \cdot 6H_2O$	Tyr	137.20	94.20	88.50	Tyrosine-free ligand
	Thr	109.40	77.60	57.10	No precipitate
	Val	116.40	84.40	61.50	
	His	124.50	74.40	70.90	
	Ala	120.00	74.90	45.40	
	Ser	120.30	79.20	71.00	
	leu	110.30	75.10	65.60	$[Co(leucine)_2]$
	Asn	132.00	84.60	72.30	No precipitate
	Lys	136.00	75.50	90.00	
	Met	145.30	76.90	73.50	
	Gly	133.30	84.40	46.60	

In 4 mL vials, Arginine (aa1, 0.5 mmol) and the other amino acid (aa2, 0.5 mmol) were dissolved in basic $NaOH_{aq}$ solution (0.1 M, 0.5 mL) and MeOH (0.50 mL). The metal nitrate was added (1 mmol), then the vials were placed at 95 °C oven for 3 days.

Table A.43: Component weights (mg) of arginine (aa1), the second amino acid (aa2), and metal nitrates (M), with outcomes based on the procedure above.

Metal (M) type	aa2	M Wt.	aa1 Wt.	aa2 Wt.	Results
$Co(NO_3)_2 \cdot 6H_2O$	Tyr	136.30	98.10	95.00	Very small crystals
	Thr	138.80	86.40	61.90	No precipitate
	Val	143.30	86.90	61.90	Fine precipitate
	His	134.90	86.20	74.90	No precipitate
	Ala	119.60	74.20	47.60	very low amount and I could not get a PXRD pattern
	Ser	150.20	78.50	54.20	No precipitate
	Leu	163.20	86.90	68.90	[Co(leucine-H)$_2$]
	Asn	128.20	79.10	80.60	No precipitate
	Lys	108.60	85.40	83.40	No precipitate
	Met	120.40	82.70	75.70	[Co(methionine-H)$_2$]
	Gly	109.10	75.80	31.50	No precipitate
$Zn(NO_3)_2 \cdot 6H_2O$	Tyr	175.50	84.00	91.10	No precipitate
	Thr	132.00	76.50	58.00	
	Val	129.70	82.50	61.80	
	His	158.30	78.50	76.20	
	Ala	135.70	87.60	55.10	
	Ser	147.80	85.40	81.00	
	leu	124.80	81.30	69.40	[Zn(leucine-H)$_2$]
	Asn	125.40	80.10	79.90	No precipitate
	Lys	124.40	85.60	94.60	
	Met	91.50	88.10	77.80	
	Gly	82.10	73.70	31.50	

General procedure 2:

In 4 mL vials, the samples below were prepared by dissolving the l-arginine (aa1, 0.25 mmol) with other l-amino acids (aa2, 0.25 mmol) at a ratio of 1:1 in THF (1 mL), and H_2O (100 µL). Then, triethylamine (10 µL) was added. The metal (2 eq.) was added. The samples were placed into a 95 °C oven for 3 days.

Table A.44: Component weights (mg) of arginine (aa1), the second amino acid (aa2), and metal nitrates (M), with outcomes based on the procedure above.

Metal (M) type	aa2	M Wt.	aa1 Wt.	aa2 Wt.	Results
$Co(NO_3)_2 \cdot 6H_2O$	Ser	165.90	42.90	30.50	No precipitate
	Val	147.20	40.40	29.00	
	His	124.90	42.10	42.80	
	Lys	204.20	44.50	44.10	
	Asn	181.00	43.70	37.50	
$Zn(NO_3)_2 \cdot 6H_2O$	Ser	125.80	42.40	41.20	No precipitate
	Val	118.80	44.50	29.00	
	His	119.10	44.20	44.10	
	Lys	137.10	46.20	42.50	
	Asn	124.80	56.00	42.50	

In 4 mL vials, arginine (0.5 mmol) was dissolved in MeOH (1 mL) and DMF (20 µL). The metal nitrate was added (1 mmol), then the vials were placed at 95°C for 3 days.

Table A.45: Component weights (mg) of arginine (aa1), the second amino acid (aa2), and metal nitrates (M), with outcomes based on the procedure above.

Metal (M) type	aa2	M Wt.	aa1 Wt.	aa2 Wt.	Results
$Co(NO_3)_2 \cdot 6H_2O$	-	149.30	86.60	-	Crystalline powder
	-	131.10	87.00	-	
	Tyr	127.40	87.00	87.70	Crystalline powder
	Thr	114.20	84.00	60.60	
	Val	111.90	81.10	58.30	Amorphous powder
	His	110.00	89.40	74.90	
	Ala	133.10	83.60	45.70	Crystalline powder
	Ser	108.80	82.30	54.70	No precipitate
	leu	147.70	83.30	68.70	Amorphous powder
	Asn	115.12	83.30	68.70	
	Lys	135.40	83.20	88.40	Crystalline powder
	Met	111.30	84.30	75.50	
	Gly	123.30	85.60	60.60	Amorphous powder
$Zn(NO_3)_2 \cdot 6H_2O$	-	154.40	86.70	-	No precipitate
	-	122.1	84.60	-	
	Tyr	112.20	82.60	90.80	Crystalline powder
	Thr	115.10	82.50	59.80	Amorphous powder
	Val	112.00	81.50	57.20	No precipitate
	His	111.60	85.30	74.30	Amorphous powder
	Ala	120.30	82.40	60.30	No precipitate
	Ser	124.30	80.70	56.60	
	leu	117.80	84.30	69.00	Amorphous powder
	Asn	117.70	84.30	69.00	No precipitate
	Lys	107.30	84.70	86.40	
	Met	141.40	86.90	69.40	Crystalline powder
	Gly	117.90	81.00	60.30	No precipitate

In 4 mL vials, Arginine (aa1, 0.5 mmol) and amino acid 2 (aa2, 0.5 mmol) were dissolved in EtOH (1 mL) and DMF (20 μL). The metal nitrate was added (1 mmol), then the vials were placed at 95°C for 3 days.

Table A.46: Component weights (mg) of arginine (aa1), the second amino acid (aa2), and metal nitrates (M), with outcomes based on the procedure above.

Metal (M) type	aa2	M Wt.	aa1 Wt.	aa2 Wt.	Results
$Co(NO_3)_2 \cdot 6H_2O$	-	111.30	44.30	-	Crystalline powder
	-	102.30	44.80	-	
	Tyr	141.10	76.10	62.00	Tyrosine-free ligand
	Thr	122.80	76.13	62.00	
	Val	124.40	88.30	62.00	Amorphous powder
	His	157.50	82.70	70.50	
	Ala	126.80	72.60	45.30	No precipitate
	Ser	159.20	84.30	60.80	
	leu	147.20	83.90	56.10	Amorphous powder
	Asn	147.20	77.00	75.70	No precipitate
	Lys	141.60	76.60	91.30	Amorphous powder
	Met	141.90	73.20	73.80	Crystalline powder
	Gly	123.50	79.80	44.50	
$Zn(NO_3)_2 \cdot 6H_2O$	-	124.10	44.10	-	Crystalline powder
		103.30	43.30	-	
	Tyr	142.90	87.60	93.70	No precipitate
	Thr	120.80	75.90	61.10	Amorphous powder
	Val	117.00	78.60	59.00	
	His	131.40	74.40	71.90	No precipitate
	Ala	142.90	76.60	51.30	
	Ser	101.90	85.40	52.80	
	leu	121.80	76.30	60.80	[Zn(leucine-H)$_2$]
	Asn	113.10	73.90	73.40	No precipitate
	Lys	133.80	76.00	90.90	
	Met	120.90	77.70	83.50	Crystalline powder
	Gly	126.70	84.90	45.30	Amorphous powder

In 4 mL vials, *l*-arginine (aa1, 0.5 mmol) and the other amino acid (aa2, 0.5 mmol) were dissolved in EtOH (1 mL). The metal nitrate was added (1 mmol), then the vials were placed at 95 °C oven for 3 days.

Table A.47: Component weights (mg) of arginine (aa1), the second amino acid (aa2), and metal nitrates (M), with outcomes based on the procedure above.

Metal (M) type	aa2	M Wt.	aa1 Wt.	aa2 Wt.	Results
$Co(NO_3)_2 \cdot 6H_2O$	Tyr	105.60	90.20	93.60	Tyrosine-free ligand
	Thr	100.00	87.00	59.20	No precipitate
	Val	134.00	87.50	54.60	Amorphous powder
	His	132.40	90.30	77.10	No precipitate
	Ala	118.40	83.60	49.00	
	Ser	104.40	85.40	57.30	
	Leu	125.50	91.90	66.00	Crystalline powder
	Asn	103.10	85.10	75.50	Crystalline powder
	Lys	140.50	83.70	89.50	No precipitate
	Met	115.00	74.30	84.30	[Co(methionine-H)$_2$]
	Gly	110.00	88.90	35.70	No precipitate
$Zn(NO_3)_2 \cdot 6H_2O$	Tyr	112.00	86.70	90.10	Tyrosine-free ligand
	Thr	107.30	87.20	61.80	No precipitate
	Val	107.00	87.20	56.20	
	His	116.50	87.70	73.30	
	Ala	100.80	72.90	57.00	
	Ser	115.40	79.10	55.40	
	leu	111.10	84.30	69.30	[Co(leucine)$_2$]
	Asn	108.60	83.00	73.40	No precipitate
	Lys	123.30	90.90	90.10	
	Met	137.20	86.10	80.50	[Zn(methionine-H)$_2$]
	Gly	107.60	85.60	32.90	No precipitate

In 4 mL vials, *l*-arginine (aa1, 0.5 mmol), the other amino acid (aa2, 0.5 mmol) and the benzoic acid were dissolved in EtOH (1 mL) and DMF (20 µL). The metal nitrate was added (1 mmol), then the vials were placed at 95 °C oven for 3 days.

Table A.48: Component weights (mg) of arginine (aa1), the second amino acid (aa2), and metal nitrates (M), with outcomes based on the procedure above.

Metal (M) type	aa2	BA	M Wt.	aa1 Wt.	aa2 Wt.	Results
$Co(NO_3)_2 \cdot 6H_2O$	-	68.20	178.60	86.30	-	No precipitate
	Leu	121.60	144.00	86.60	68.20	
	Met	131.90	190.30			Crystals:
$Zn(NO_3)_2 \cdot 6H_2O$	-	71.00	127.00	71.80	-	No precipitate
	Leu	113.50	140.50	84.50	64.80	
	Met	123.80	145.80	68.30	70.30	

General procedure 3:

In 4 mL vials, *l*-arginine (aa1, 0.5 mmol) and the other *l*-amino acid (aa2, 0.5 mmol) were dissolved in H_2O (1 mL) and EtOH (1 mL). Then, the samples were stirred at rt for 3 days.

Table A.49: Component weights (mg) of arginine (aa1), the second amino acid (aa2), and metal nitrates (M), with outcomes based on the procedure above.

Metal (M) type	aa2	M Wt.	aa1 Wt.	aa2 Wt.	Results
$Co(NO_3)_2 \cdot 6H_2O$	Leu	330.10	82.60	72.00	[Co(leucine-H)$_2$]
	Val	156.80	70.00	60.40	No precipitate
	Met	139.90	76.60	67.50	[Co(methionine-H)$_2$]
$Zn(NO_3)_2 \cdot 6H_2O$	Leu	290.00	78.40	66.20	[Zn(leucine-H)$_2$]
	Val	151.00	81.50	57.80	No precipitate
	Met	181.90	78.10	66.90	[Zn(methionine-H)$_2$]

A.6 Glycine with valine

General procedure 1:

l-Valine (0.476 mmol, aa1), glycine (0.72 mmol, aa2), and the metal nitrates (0.31 g, 1.19 mmol) were dissolved in H_2O (3 mL). pH was adjusted to around 7 using NaOH solution (1 M). Then, EtOH (2 mL) was added. Then, the vial was placed into a 95°C oven for 3 days.

Table A.50: Component weights (mg) of valine (aa1), glycine (aa2), and metal nitrates (M), with outcomes based on the procedure above.

Metal (M) type	M Wt.	aa1 Wt.	aa2 Wt.	Results
$Co(NO_3)_2 \cdot 6H_2O$	280.30	51.80	54.40	Crystalline powder
$Zn(NO_3)_2 \cdot 6H_2O$	308.70	72.80	59.80	No Precipitate

Valine (0.5 mmol, aa1), glycine (0.8 mmol, aa2), and the metal nitrates (1.2 mmol) were dissolved in H_2O (3 mL). Then, EtOH (2 mL) was added. Then, the vial was placed into a 95°C oven for 3 days.

Table A.51: Component weights (mg) of valine (aa1), glycine (aa2), and metal nitrates (M), with outcomes based on the procedure above.

Metal (M) type	M Wt.	aa1 Wt.	aa2 Wt.	Results
$Co(NO_3)_2 \cdot 6H_2O$	296.30	29.60	21.10	No precipitate
$Zn(NO_3)_2 \cdot 6H_2O$	217.40	30.80	19.40	

General procedure 2:

Valine (0.5 mmol, aa1), glycine (0.8 mmol, aa2), and the metal nitrates (1.2 mmol) were dissolved in MeOH (1 mL). Then, TEA (10.00 µL) was added. Then, the vial was placed into a 95°C oven for 3 days.

Table A.52: Component weights (mg) of valine (aa1), glycine (aa2), and metal nitrates (M), with outcomes based on the procedure above.

Metal (M) type	M Wt.	aa1 Wt.	aa2 Wt.	Results
$Co(NO_3)_2 \cdot 6H_2O$	149.00	30.30	24.80	No precipitate
$Zn(NO_3)_2 \cdot 6H_2O$	127.30	29.70	24.70	

In 4 mL vials, *l*-valine (aa1, 0.5 mmol), glycine (aa2, 0.5 mmol) and benzoic acid (1 mmol) were dissolved in the solvent mentioned in the table below. Then, the metal nitrate (1 mmol) was added. The vials were placed into 95 °C oven.

Table A.53: Component weights (mg) of valine (aa1), glycine (aa2), and metal nitrates (M), with outcomes based on the procedure above and the listed modifications.

Metal type	Modification type	BA	M Wt.	aa1 Wt.	aa2 Wt.	Results
$Co(NO_3)_2 \cdot 6H_2O$	1 mL $NaOH_{aq}$(0.1 M) and EtOH (1 mL)	130.10	120.50	60.40	46.50	Crystalline powder
	3 mL $NaOH_{aq}$(0.1 M) and EtOH (3 mL)	123.10	155.00	61.10	37.00	
	1 mL $NaOH_{aq}$(0.1 M) and EtOH (1 mL)	×	167.60	56.10	42.60	No precipitate
	EtOH (1 mL), DMF (20 µL)	×	175.50	51.50	33.50	Thin needles-like crystals
	MeOH (1 mL), DMF (20 µL)	×	176.80	56.20	34.70	
$Zn(NO_3)_2 \cdot 6H_2O$	1 mL $NaOH_{aq}$(0.1 M) and EtOH (1 mL)	120.50	148.90	56.10	38.40	No precipitate
	3 mL $NaOH_{aq}$(0.1 M) and EtOH (3 mL)	173.50	135.20	54.20	32.30	
	1 mL $NaOH_{aq}$(0.1 M) and EtOH (1 mL)	×	125.40	34.00	65.00	
	EtOH (1 mL), DMF (20 µL)	×	176.40	52.20	38.70	
	MeOH (1 mL), DMF (20 µL)		133.80	56.90	42.90	

In 4 mL vials, *l*-valine (aa1, 0.50 mmol) and glycine (aa2, 0.50 mmol) were dissolved in EtOH (2 mL) and DMF (5 µL). The metal nitrate was added (1 mmol). The mixture was stirred at rt. for 3 days.

Table A.54 : Component weights (mg) of valine (aa1), glycine (aa2), and metal nitrates (M), with outcomes based on the procedure above.

Metal (M) type	M Wt.	aa1 Wt.	aa2 Wt.	Results
$Co(NO_3)_2 \cdot 6H_2O$	189.90	54.20	34.40	Valine polymorph
$Zn(NO_3)_2 \cdot 6H_2O$	174.60	50.80	36.10	

A.7 Alanine with cysteine co-assembly into MMOFs

General procedure 1

In Teflon-lined steel autoclave, *l*-alanine (1 mmol, aa1) and *l*-cysteine (1 mmol, aa2) were weighed and dissolved in aqueous NaOH (0.25 M, 3.5 mL) and EtOH (3.5 mL). Then, 1 mmol of the metal added as shown in the table below. Then, it was heated for 3 days at 95 °C.

Table A.55: Component weights (mg) of alanine (aa1), cysteine (aa2), and metal nitrates (M), with outcomes based on the procedure above.

Metal (M) type	M Wt.	aa1 Wt.	aa2 Wt.	Results
$Co(NO_3)_2 \cdot 6H_2O$	190.00	89.00	120.00	Crystals
$Zn(NO_3)_2 \cdot 6H_2O$	168.00	79.80	114.80	

General procedure 2

In Teflon-lined steel autoclave, *l*-alanine (1 mmol, aa1) and *l*-cysteine (1 mmol, aa2) were weighed and dissolved in aqueous NaOH (0.15 M, 3.5 mL) and EtOH (3.5 mL). Then, 1 mmol of the metal added as shown in the table below. Then, two different temperatures were tried, which are 75 °C and r.t.

Table A.56: Component weights (mg) of alanine (aa1), cysteine (aa2), and metal nitrates (M), with outcomes based on the procedure above.

Metal (M) type	M Wt.	aa1 Wt.	aa2 Wt.	Temp.	Results
$Co(NO_3)_2 \cdot 6H_2O$	200.00	89.60	120.90	75	Crystals
	260.30	85.60	132.20	r.t.	Powder
$Zn(NO_3)_2 \cdot 6H_2O$	128.90	87.90	118.20	75	Crystals
	258.90	83.40	114.30	r.t.	Powder

General procedure 3

In Teflon-lined steel autoclave, *l*-alanine (1 mmol, aa1) and *l*-cysteine (1 mmol, aa2) were weighed and dissolved in H_2O (3.5 mL) and EtOH (3.5 mL). Then, 1 mmol of the metal added as shown in the table below. Two different base concentrations were tried, one is 0.15 M NaOH and the other with no base. Then, the vials were heated at 95 °C for 3 days.

Table A.57: Component weights (mg) of alanine (aa1), cysteine (aa2), and metal nitrates (M), with outcomes based on the procedure above.

Metal (M) type	M Wt.	aa1 Wt.	aa2 Wt.	base	Results
$Co(NO_3)_2{\cdot}6H_2O$	198.20	44.50	60.50	0.15 M	crystals
	195.40	41.20	59.50	×	
$Zn(NO_3)_2{\cdot}6H_2O$	165.40	42.90	57.80	0.15 M	crystals
	164.80	42.50	56.80	×	

A.8 Tyrosine, asparagine and histidine

General procedure 1:

l-Tyrosine (aa1, 0.40 mmol), histidine (aa2, 0.56 mmol), asparagine (aa3, 0.55 mmol) and metal nitrate (M, 1.48 mmol) were dissolved in H_2O (3 mL). PH was adjusted to 7.38 using NaOH solution (1M). Then, EtOH (2 mL) was added. Then, the vial was placed into a 95°C oven for 3 days.

Table A.58: Component weights (mg) of tyrosine (aa1), histidine (aa2), asparagine (aa3) and metal nitrates (M), with outcomes based on the procedure above

Metal (M) type	M Wt.	aa1 Wt.	aa2 Wt.	aa3 Wt.	Results
$Co(NO_3)_2{\cdot}6H_2O$	431.3	72.70	65.40	82.23	[Co(asparagine)(tyrosine)]
$Zn(NO_3)_2{\cdot}6H_2O$	328.3	74.30	66.80	83.25	ZnO

***Modified experiments*:** The procedure above was *ed* by increasing the histidine feed to 1 mmol.

Table A.59: Component weights (mg) of tyrosine (aa1), histidine (aa2), asparagine (aa3) and metal nitrates (M), with outcomes based on the procedure above

Metal (M) type	M Wt.	aa1 Wt.	aa2 Wt.	aa3 Wt.	Results
$Co(NO_3)_2{\cdot}6H_2O$	442.20	91.20	164.10	76.30	No precipitate
$Zn(NO_3)_2{\cdot}6H_2O$	332.10	96.10	162.10	89.60	

Modified experiments: General procedure was modified by increasing the temperature to 120 °C.

Table A.60: Component weights (mg) of tyrosine (aa1), histidine (aa2), asparagine (aa3) and metal nitrates (M), with outcomes based on the procedure above

Metal (M) type	M Wt.	aa1 Wt.	aa2 Wt.	aa3 Wt.	Results
$Co(NO_3)_2{\cdot}6H_2O$	315.60	99.00	90.80	77.10	Tyrosine-free ligand
$Zn(NO_3)_2{\cdot}6H_2O$	312.40	87.30	91.70	80.20	Crystalline powder 3:2:1

***Modification type*:** The ratio between the three ligands tyrosine (aa1), histidine (aa2),, asparagine(aa3) was maintained to 1: 0.5: 0.25.

Table A.61: Component weights (mg) of tyrosine (aa1), histidine (aa2), asparagine (aa3) and metal nitrates (M), with outcomes based on the procedure above

Metal (M) type	M Wt.	aa1 Wt.	aa2 Wt.	aa3 Wt.	Results
$Co(NO_3)_2{\cdot}6H_2O$	342.20	176.40	73.10	41.40	Tyrosine free ligand
$Zn(NO_3)_2{\cdot}6H_2O$	335.40	181.40	81.80	37.90	

The first procedure was modified by using a 95 °C dry bath instead of the oven.

Table A.62: Component weights (mg) of tyrosine (aa1), histidine (aa2), asparagine (aa3) and metal nitrates (M), with outcomes based on the procedure above

Metal (M) type	M Wt.	aa1 Wt.	aa2 Wt.	aa3 Wt.	Results
$Co(NO_3)_2{\cdot}6H_2O$	216.90	45.50	43.70	38.50	No precipitate
$Zn(NO_3)_2{\cdot}6H_2O$	273.40	44.00	39.10	45.40	

In 4 mL vials, tyrosine (aa1, 0.40 mmol), histidine (aa2, 0.56 mmol), asparagine (aa3, 0.55 mmol) and metal nitrate (M, 1.48 mmol) were dissolved in MeOH (3 mL), H_2O (100 μL) and DMF (50 μL). Then, the vial was placed into a 95°C oven for 3 days.

Table A.63: Component weights (mg) of tyrosine (aa1), histidine (aa2), asparagine (aa3) and metal nitrates (M), with outcomes based on the procedure above.

Metal (M) type	M Wt.	aa1 Wt.	aa2 Wt.	aa3 Wt.	Results
$Co(NO_3)_2{\cdot}6H_2O$	411.70	88.00	123.80	73.10	Amorphous powder
$Zn(NO_3)_2{\cdot}6H_2O$	279.20	83.50	134.50	83.40	Crystalline powder

In 4 mL vials, tyrosine (aa1, 0.40 mmol), histidine (aa2, 0.56 mmol), asparagine (aa3, 0.55 mmol) and metal nitrate (M, 1.48 mmol) were dissolved in EtOH (3 mL), H_2O (100 μL) and DMF (50 μL). Then, the vial was placed into a 95°C oven for 3 days.

Table A.64: Component weights (mg) of tyrosine (aa1), histidine (aa2), asparagine (aa3) and metal nitrates (M), with outcomes based on the procedure above

Metal (M) type	M Wt.	aa1 Wt.	aa2 Wt.	aa3 Wt.	Results
$Co(NO_3)_2 \cdot 6H_2O$	348.20	90.00	98.80	78.80	Amorphous powder
$Zn(NO_3)_2 \cdot 6H_2O$	269.00	95.50	108.60	75.20	Crystalline powder

Appendix B for Chapter 3

B.1 Synthesis of compound 3A, the H_2XPyr Precursor

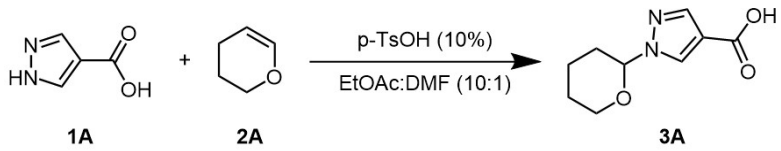

Scheme B.1: Synthesis of compound **3A**

4-Pyrazolecarboxylic acid (**1A**) (1.09 g, 9.70 mmol, 1 eq.) and p-toluenesulfonic acid monohydrate (p-TsOH) (0.2 g, 0.97 mmol, 0.1 eq.) were suspended in EtOAc (40 mL) and DMF (400 µL). Then, 3,4-Dihydro-2H-pyran (**2A**) (1.8 mL, 2 eq.) was added to the above suspension slowly and the mixture stirred overnight at room temperature (**Scheme B.1**). The reaction was stopped, and the solvent was removed using reduced pressure. The substance was diluted with EtOAc (50 mL) and washed with hot water (20 mL × 2). The organic layers were collected and dried over anhydrous sodium sulfate. Then, the solvent was removed under reduced pressure. The product was then recrystallised in EtOAc and obtained as a white solid. Yield:1.66 g, 8.44 mmol, 87%.[85]

^{1}H NMR (500 MHz, $CDCl_3$) δ (ppm) 8.18 (s, 1H), 8.00 (s, 1H), 5.43 (dd, *J* = 9.0, 3.0 Hz, 1H), 4.09 – 4.05 (m, 1H), 3.76 – 3.69 (m, 1H), 2.15 – 2.01 (m, 3H), 1.74 – 1.61 (m, 3H).

B.2 Synthesis of compound H_2GlyPyr (6)

Synthesis of compound 12A

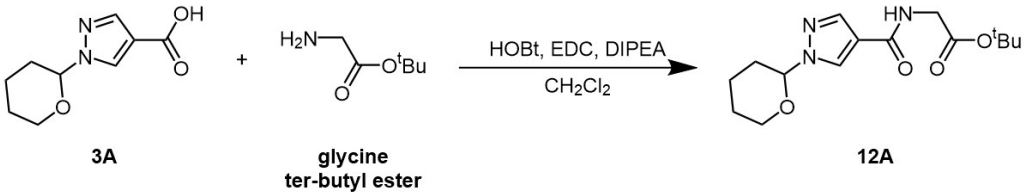

Scheme B.2: Synthesis of compound **12A**.

Compound **3A** (0.70 g, 3.6 mmol) was dissolved in DCM (10 mL). Then, *l*-hydroxybenzotriazole hydrate (HOBt) (0.58 mg, 4.26 mmol, 1.2 eq), EDC (0.67 g, 4.26 mmol, 1.2 eq.), and DIPEA (1.92 mL, 10.98 mmol, 3 eq.) were added. The reaction mixture was stirred at room temperature. Then, glycinate tert-butyl ester hydrochloride (0.56 g, 1.2 eq.) was added to the reaction mixture (**Scheme B.2**). The mixture was stirred at room temperature overnight. After completion of the reaction, water (50 mL) was added to the reaction mixture. The solution was extracted with DCM and the organic layer was washed with H_2O (5 mL). The DCM layer was dried over anhydrous sodium sulfate, and concentrated on a rotary evaporator under reduced pressure at 40°C. The pale-yellow oil was purified by column chromatography using EtOAc over silica gel. Yield: 0.59 g, 1.91 mmol, 52%.[85]

^{1}H NMR (500 MHz, $CDCl_3$) δ (ppm) 8.07 (s, 1H), 7.84 (s, 1H), 6.26 (t, J = 5.0 Hz, 1H), 5.36 (dd, J = 7.8, 4.2 Hz, 1H), 4.14 – 4.03 (m, 3H), 3.69 – 3.67 (m, 1H), 2.03 – 1.99 (m, 3H), 1.70 – 1.63 (m, 3H), 1.49 (s, 9H)

Synthesis of compound 13A

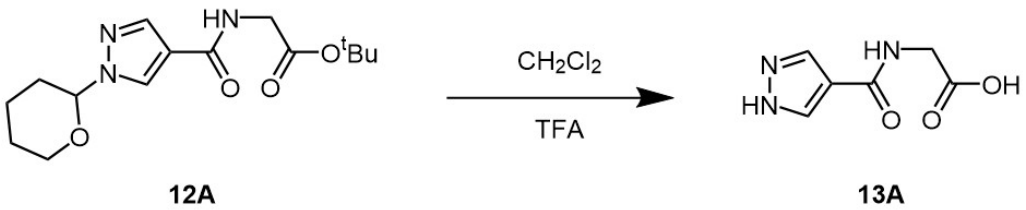

Scheme B.3: Synthesis of compound **13A**

Compound **12A** (0.59 g, 1.91 mmol) was dissolved in DCM (35 mL) and cooled using an ice bath. Then, trifluoroacetic acid (TFA) (15 mL, 100 eq.) was added dropwise over 15 minutes. After the addition was finished, the ice bath was removed, and the reaction mixture was stirred at room temperature for 8 hours. The reaction mixture turned to brown. The TLC showed most of the starting material was consumed and a new spot appeared. The solvent was removed on a rotary evaporator under reduced pressure, which afforded a dark brown oil. The product was partitioned between H_2O (2 mL) and DCM (2 mL). The impurity partitioned to the DCM layer, while the product partitioned to the H_2O layer. The H_2O was removed, to obtain colourless oil under reduced pressure at 50°C. The product was precipitated as a powder by sonicating it with DCM. Yield: 0.26 g, 1.53 mmol, 80%.[85] ^{1}H NMR (500 MHz, D_2O) δ (ppm) 8.06 (s, 2H), 4.05 (s, 2H).

B.3 Synthesis of compound H_2AlaPyr (15A)

Synthesis of compound 14A

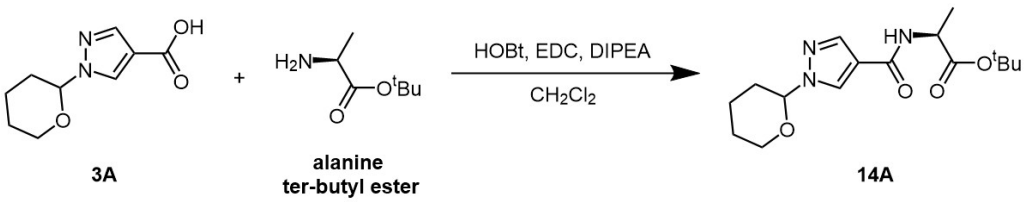

Scheme B.4: Synthesis of compound **14A**

Compound **3A** (0.50 mg, 2.5 mmol) was dissolved in DCM (10 mL). Then, 1-hydroxybenzotriazole hydrate (HOBt) (0.43 g, 3.05 mmol, 1.2 eq), EDC (0.50 g, 1.82 mmol, 1.2 eq.), and DIPEA (665 µL, 7.5 mmol, 3 eq.) were added. The reaction mixture was stirred at room temperature for 10 minutes, then alanine tert-butyl ester hydrochloride (0.45 g, 1.2 eq.) was added to the reaction mixture and the mixture was stirred at room temperature overnight. After completion of the reaction, water (50 mL) was added to the reaction mixture. The solution was extracted with DCM and the organic layer was washed with water (5 mL). Then, the DCM layer was dried over anhydrous sodium sulfate, and concentrated on a rotary evaporator under reduced pressure at 40°C. The pale-yellow oil product obtained was purified through column chromatography using EtOAc over silica gel. Rf: 0.45. Yield: 0.60 mg, 1.86 mmol, 76%.[85]

^{1}H NMR (500 MHz, $CDCl_3$) δ (ppm) 8.05 (s, 1H), 7.82 (d, *J* = 2.2 Hz, 1H), 6.38 (t, *J* = 7.7 Hz, 1H), 5.39 – 5.35 (m, 1H), 4.61 (p, *J* = 7.2 Hz, 1H), 4.02 – 3.97 (m, 1H), 3.70 – 3.64 (m, 1H), 2.07 – 1.96 (m, 3H), 1.69 – 1.57 (m, 3H), 1.49 (s, 9H), 1.45 (d, *J* = 7.1 Hz, 3H).

Synthesis of compound 15A

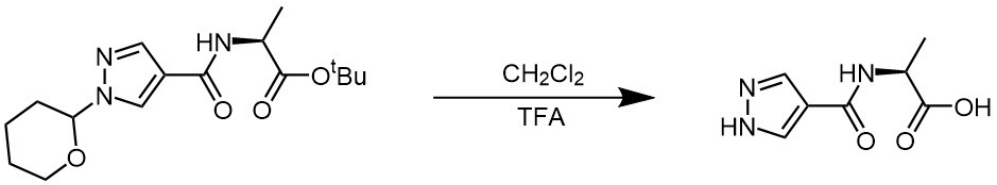

14A **15A**

Scheme B.5: Synthesis of compound **15A**

Compound **14A** (0.60 g, 1.86 mmol) was dissolved using 30 mL of DCM and cooled with an ice bath. To the above-stirred solution, trifluoroacetic acid (TFA) (14.2 mL, 185.6 mmol, 100 eq.) was added dropwise. After the addition was finished, the ice bath was removed. The reaction mixture was stirred at room temperature overnight. The reaction mixture turned very brown. The TLC showed most of the starting material was consumed and a new spot appeared. The solvent was removed on a rotary evaporator under reduced pressure to afford a dark brown oil. The product was partitioned between H_2O (5 mL) and DCM (5 mL). The impurity was partitioned to the DCM layer, while the product was partitioned to the H_2O layer. The H_2O was removed, to obtain colourless oil. The product was precipitated as a powder by sonicating it with Et_2O. Yield: 0.25 g, 1.36 mmol, 74%.[85]

^{1}H NMR (500 MHz, D_2O) δ (ppm) 8.06 (s, 2H), 4.47 (q, *J* = 22.07 Hz, 1H), 1.45 (d, *J* = 7.25 Hz, 3H).

B.4 NMR spectroscopic analysis for the H_2XPyr linkers and their precursors

B.4.1 H_2XPyr ligands precursor

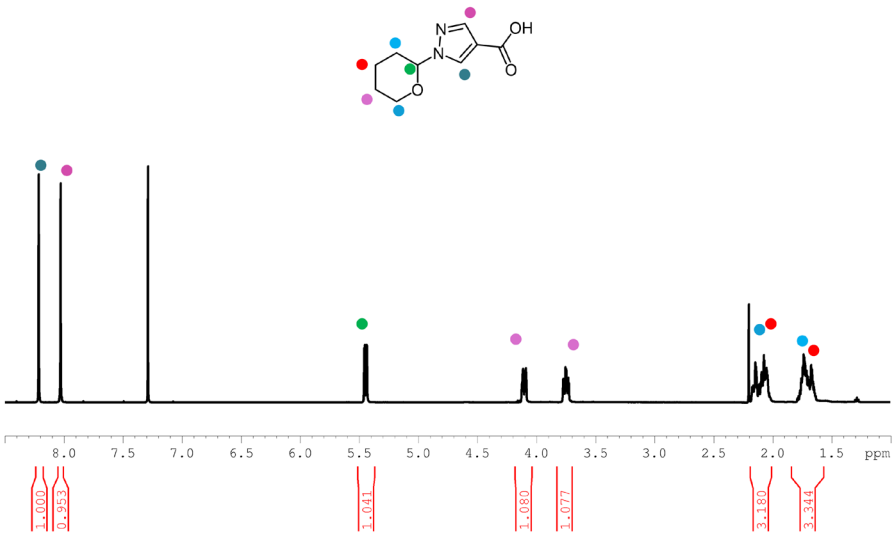

Figure B.1: ^{1}H NMR spectrum analysis of compound 3, the H_2XPyr ligands precursor in $CDCl_3$. The solvent protons were used as the internal standard**.**

B.4.2 H_2AlaPyr ligand intermediate ^{1}H NMR spectroscopic data

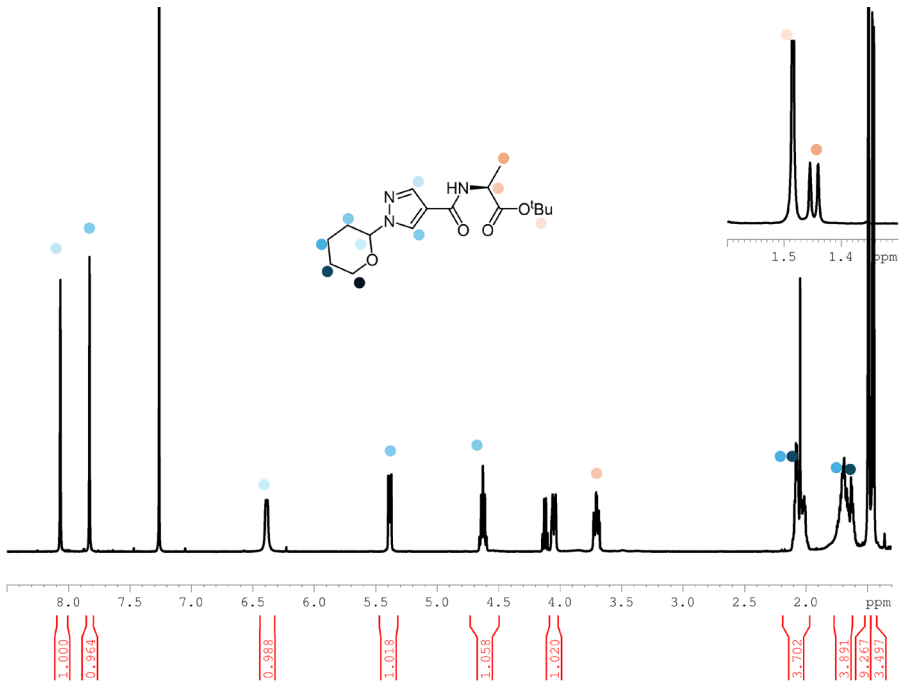

Figure B.2:^{1}H NMR spectrum of the H_2AlaPyr ligand intermediate in $CDCl_3$.

B.4.3 H_2AlaPyr ligand ^{1}H NMR spectroscopic data

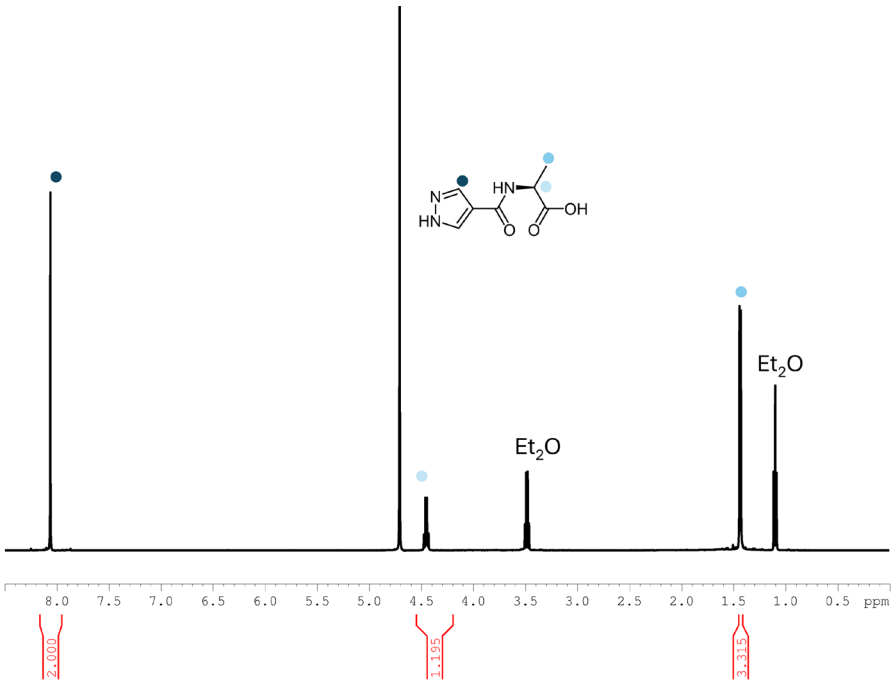

Figure B.3: ^{1}H NMR spectrum of the H_2AlaPyr ligand in D_2O.

B.4.4 H_2GlyPyr ligand intermediate ^{1}H NMR spectroscopic data

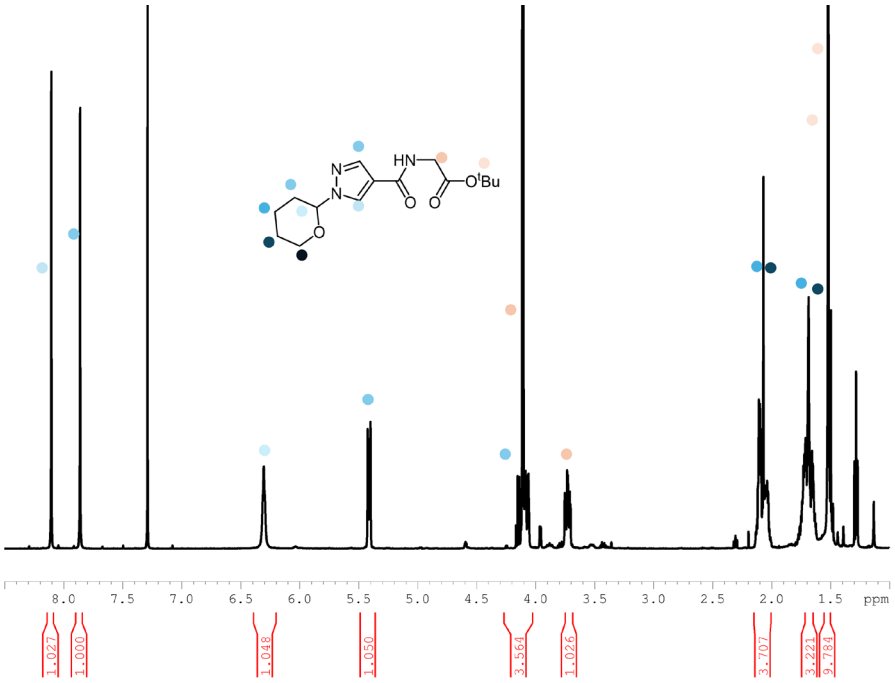

Figure B.4: ^{1}H NMR spectrum of the H_2GlyPyr ligand intermediate in $CDCl_3$.

B.4.5 H_2GlyPyr ligand ^{1}H NMR spectroscopic data

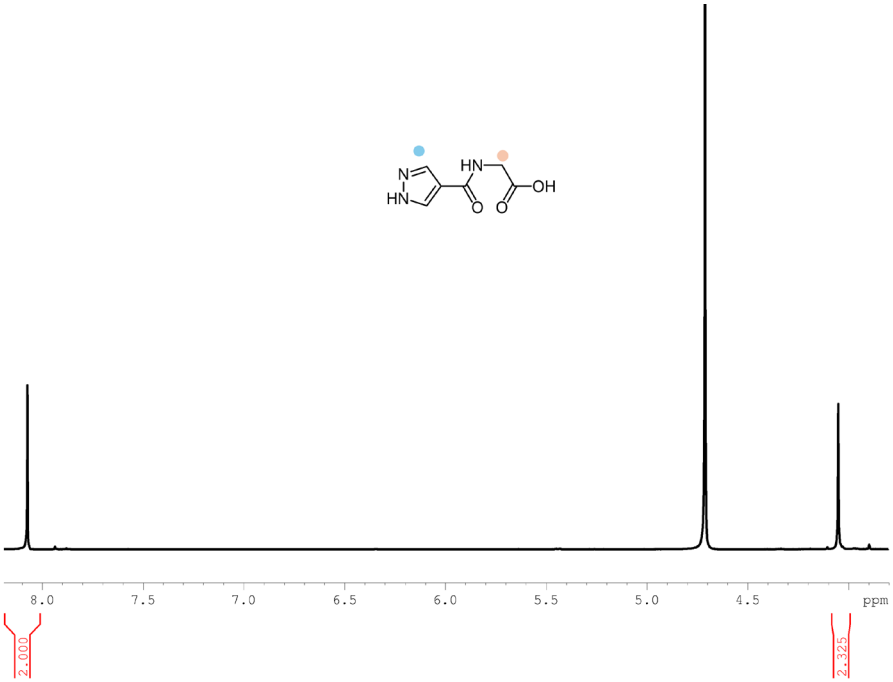

Figure B.5: ^{1}H NMR spectrum of H_2GlyPyr ligand in D_2O.

B.4.6 H_2ValPyr ligand intermediate ^{1}H NMR spectroscopic data

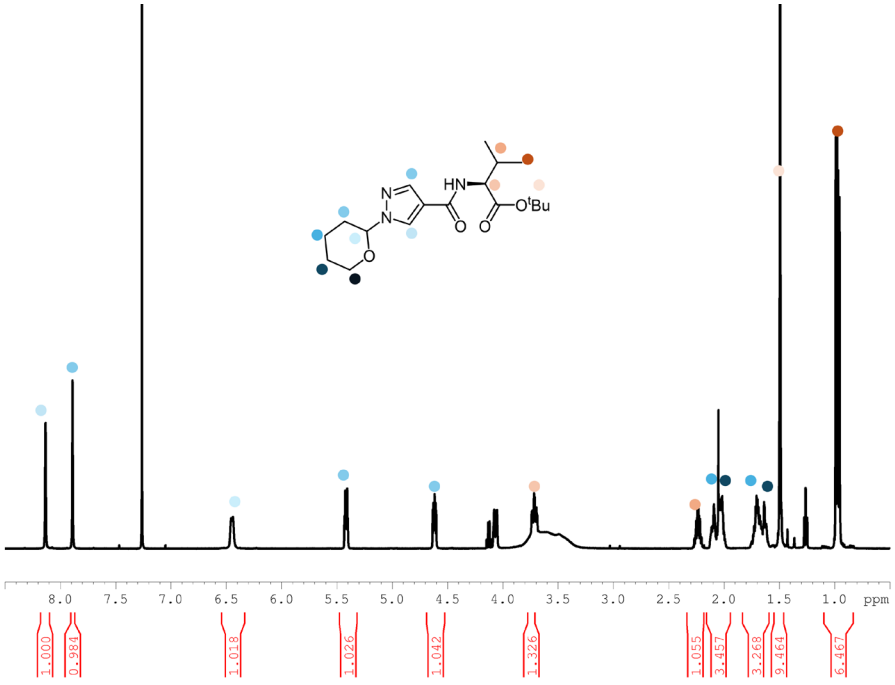

Figure B.6: ^{1}H NMR spectrum of H_2ValPyr ligand intermediate in $CDCl_3$.

B.4.7 H_2ValPyr ligand ^{1}H NMR spectroscopic data

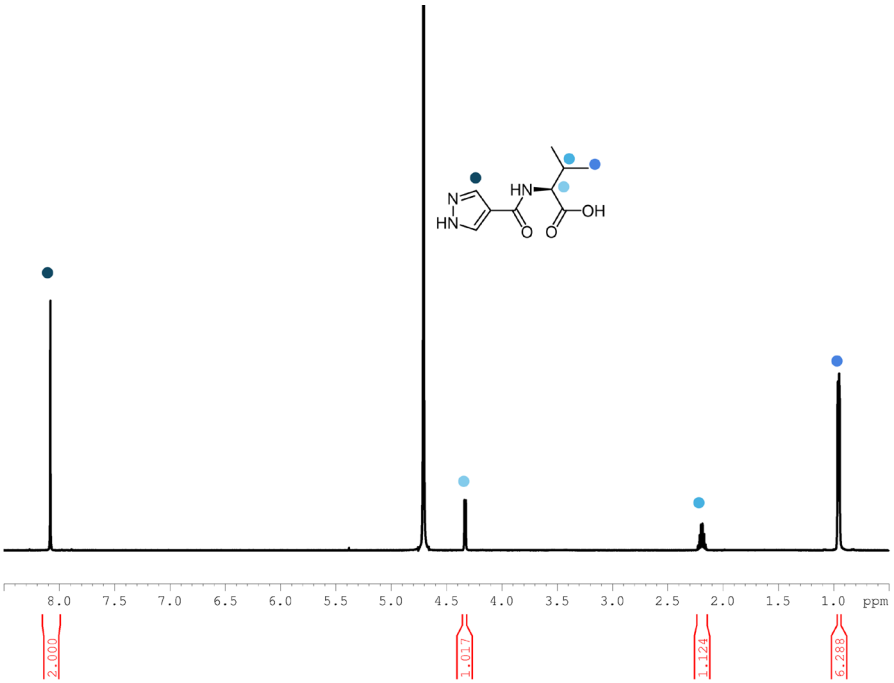

Figure B.7: ^{1}H NMR spectrum of the H_2ValPyr ligand in D_2O.

B.4.8 H_2ValPyr ligand ^{13}C NMR spectroscopic data

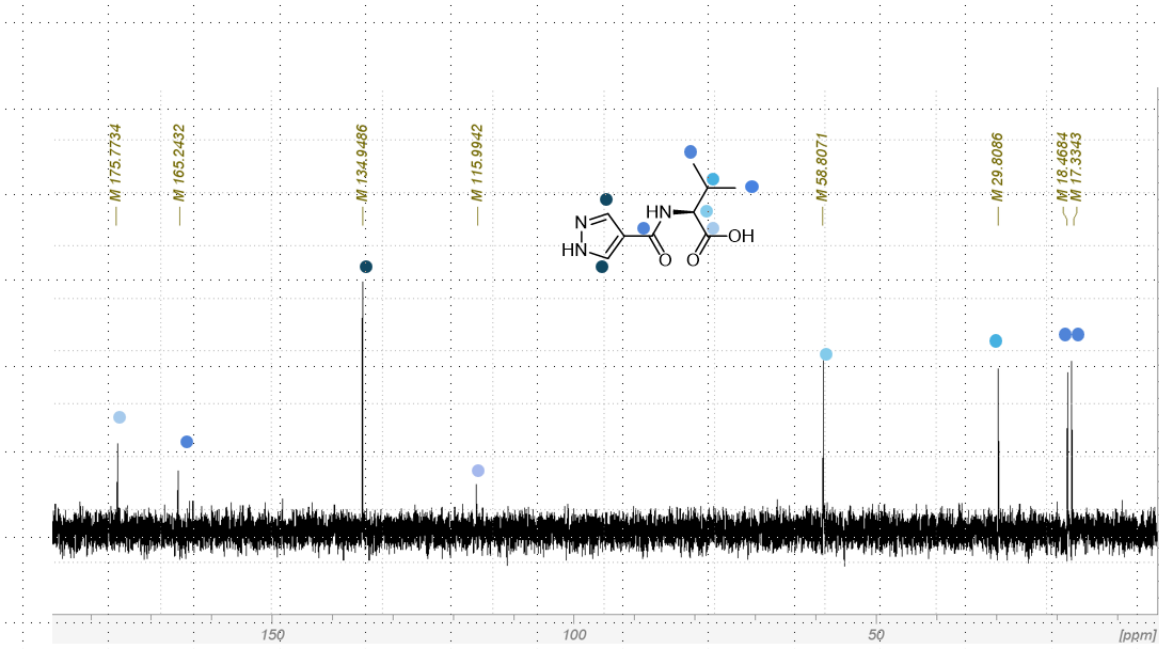

Figure B.8: ^{13}C NMR spectrum of the H_2ValPyr ligand in D_2O.

B.4.9 H_2SerPyr ligand intermediate ^{1}H NMR spectroscopic data

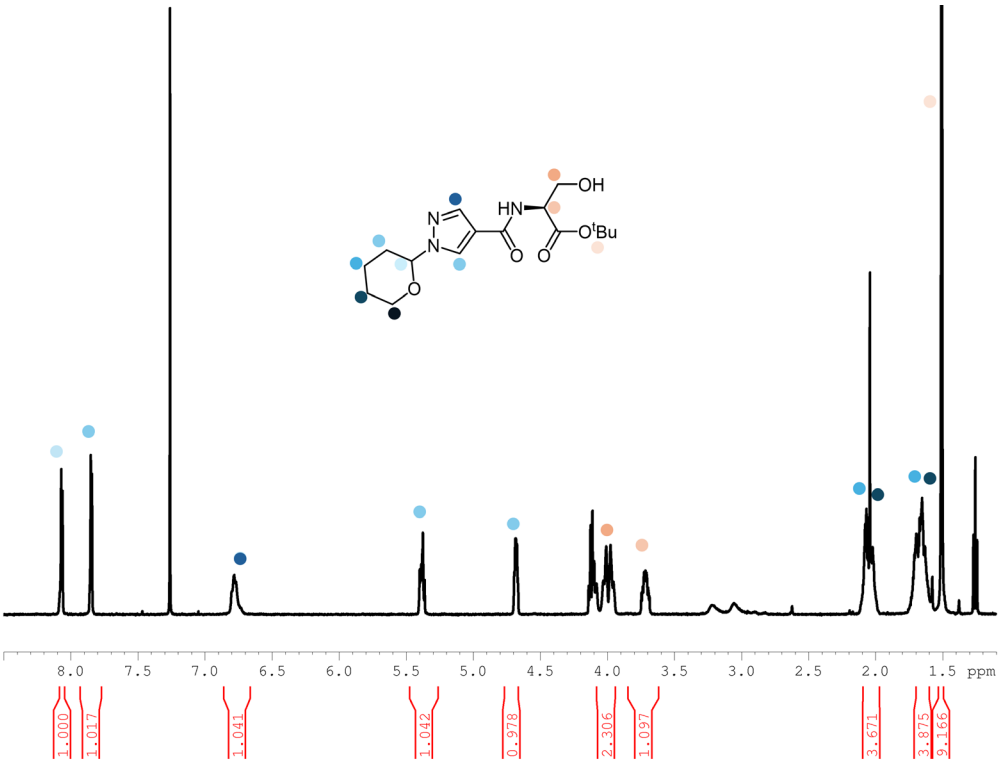

Figure B.9: ^{1}H NMR spectrum of the H_2SerPyr ligand intermediate in $CDCl_3$.

B.4.10 H_2SerPyr ligand ^{1}H NMR spectroscopic data

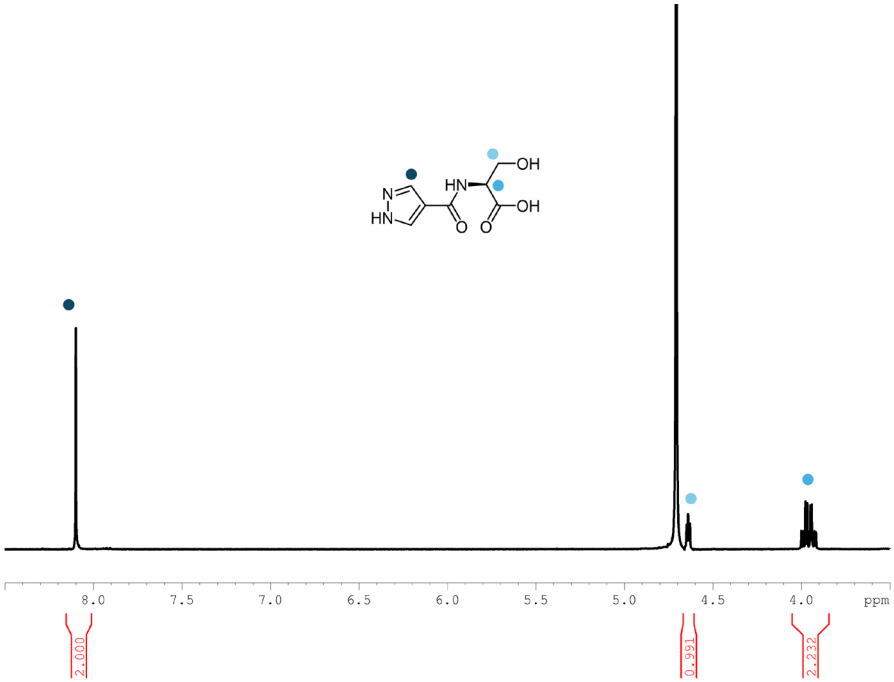

Figure B.10^{1}H NMR spectrum of H_2SerPyr ligand in D_2O.

B.4.11 H_2SerPyr ligand ^{13}C NMR spectroscopic data

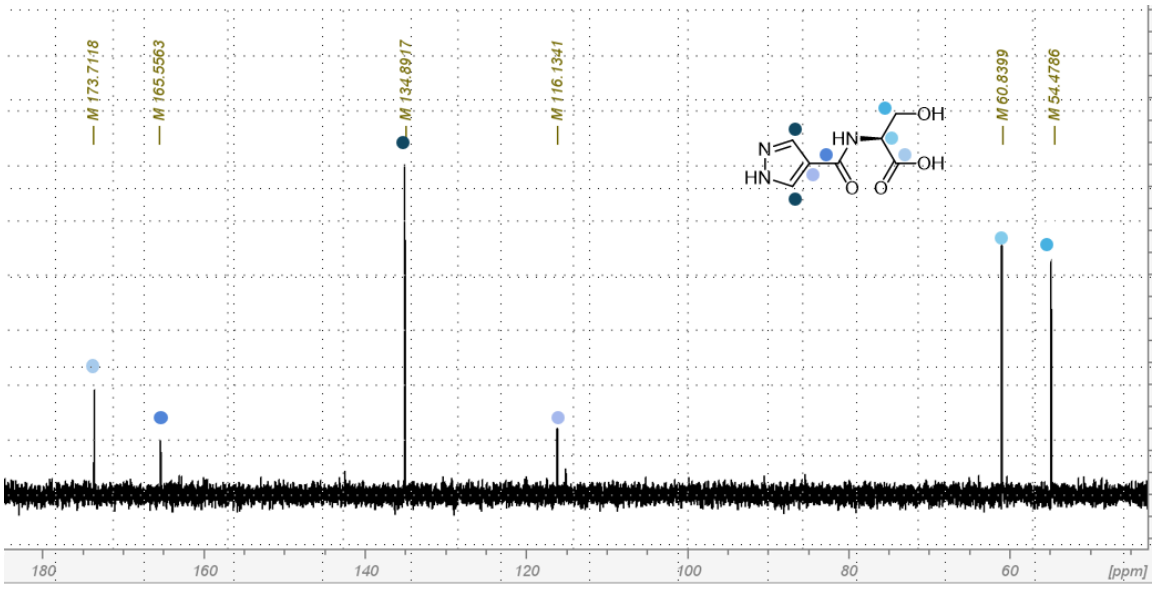

Figure B.11: ^{13}C NMR spectrum of H_2SerPyr ligand in D_2O.

B.4.12 H_2TyrPyr ligand intermediate ^{1}H NMR spectroscopic data

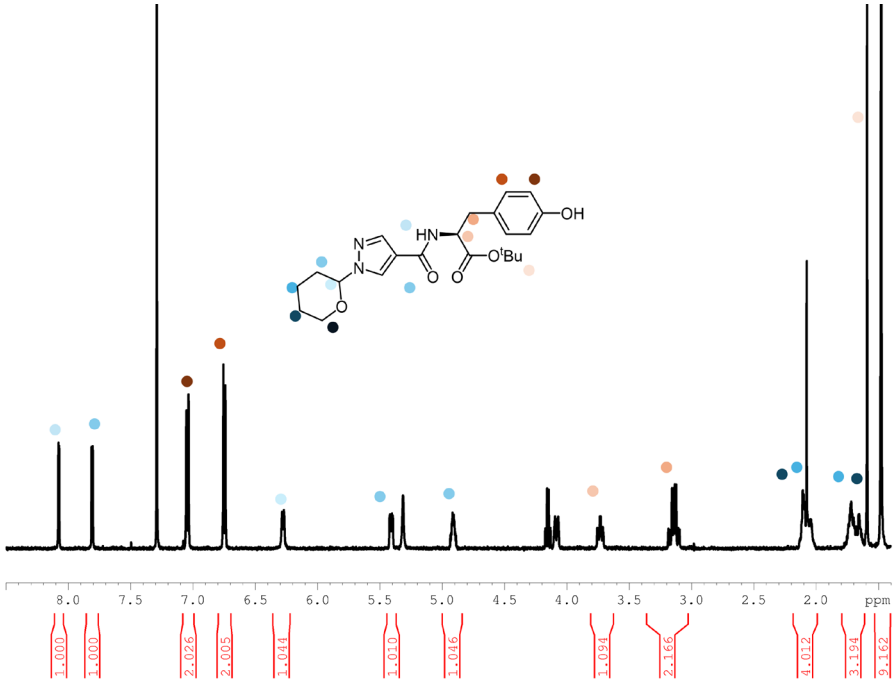

Figure B.12: ^{1}H NMR spectrum of H_2TyrPyr ligand intermediate in $CDCl_3$.

B.4.13 H_2TyrPyr ligand ^{1}H NMR spectroscopic data

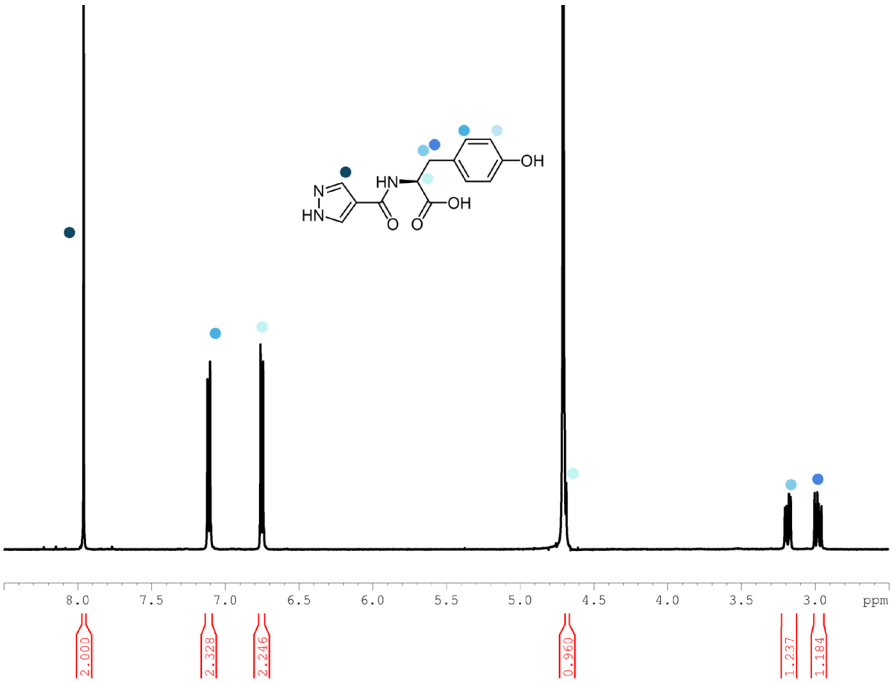

Figure B.13: ^{1}H NMR spectrum of H_2TyrPyr ligand in D_2O.

B.4.14 H_2TyrPyr ligand ^{13}C NMR spectroscopic data

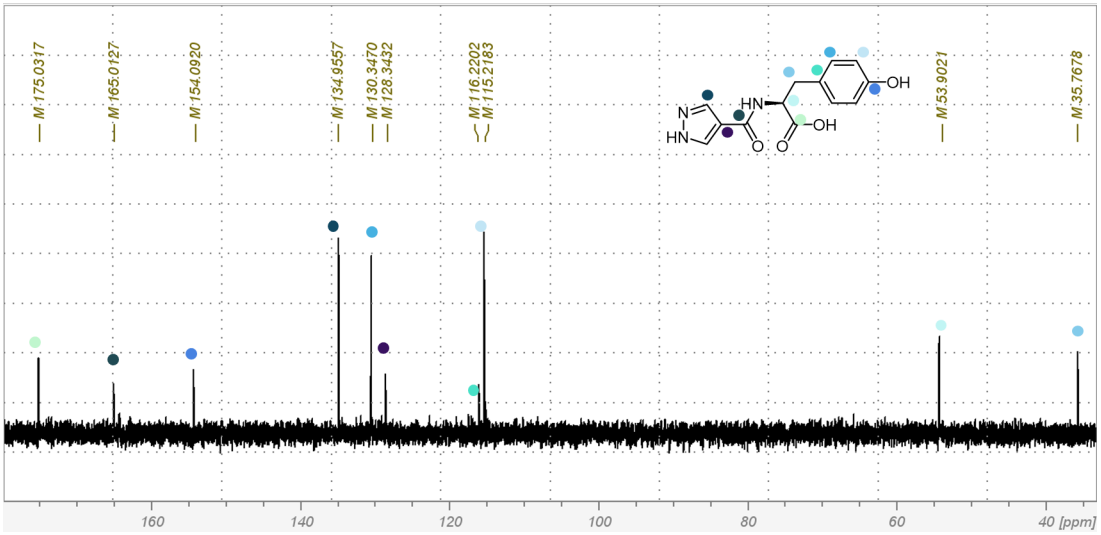

Figure B.14: ^{13}C NMR spectrum of H_2TyrPyr ligand in D_2O.

B.4.15 H_2PhePyr ligand intermediate ^{1}H NMR spectroscopic data

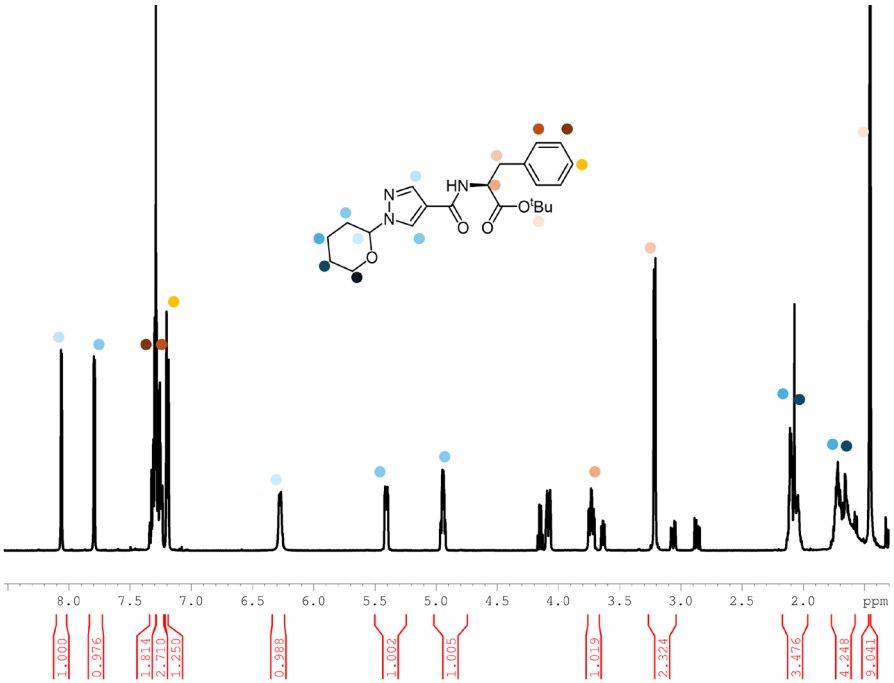

Figure B.15: ^{1}H NMR spectrum of H_2PhePyr ligand intermediate in $CDCl_3$.

B.4.16 H_2PhePyr ligand ^{1}H NMR spectroscopic data

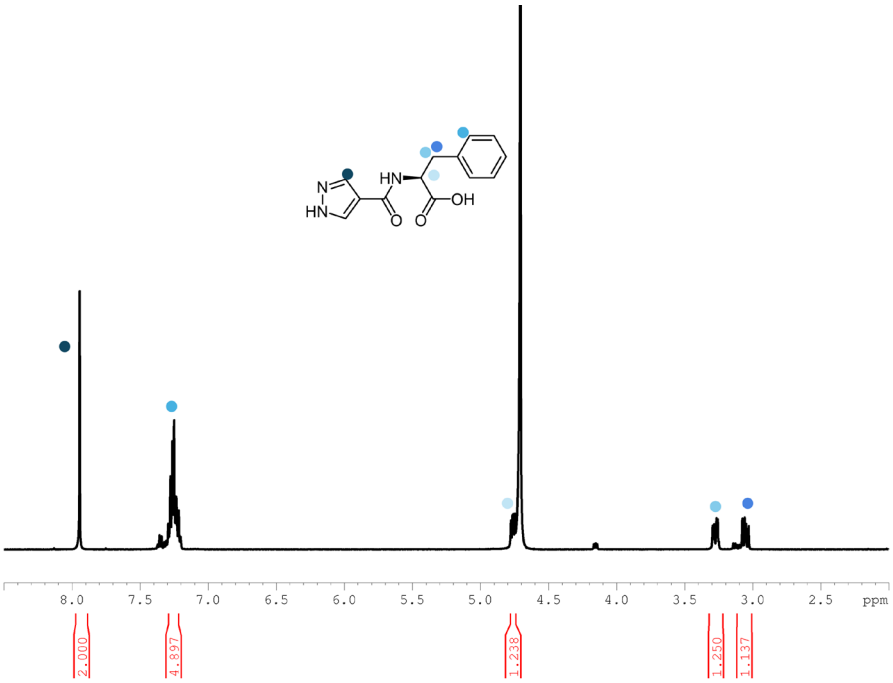

Figure B.16: ^{1}H NMR spectrum H_2PhePyr ligand in D_2O.

B.4.17 H_2PhePyr ligand ^{13}C NMR spectroscopic data

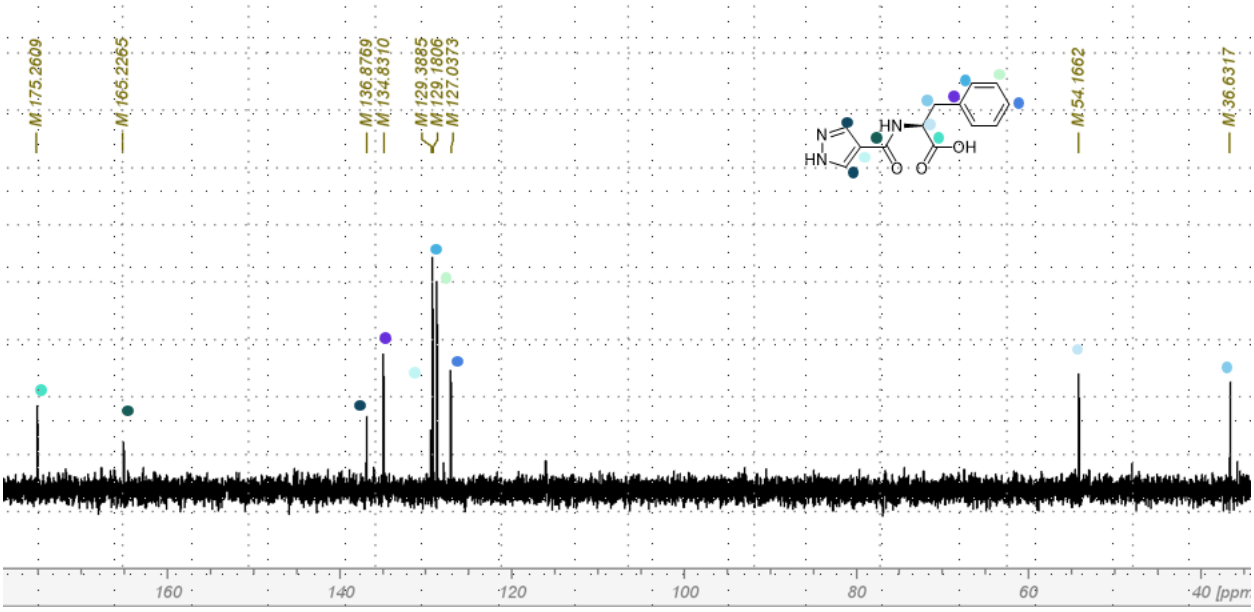

Figure B.17: ^{13}C NMR spectrum of H_2PhePyr ligand in D_2O.

Appendix C for Chapter 4

C.1 Bdc backbone synthesis

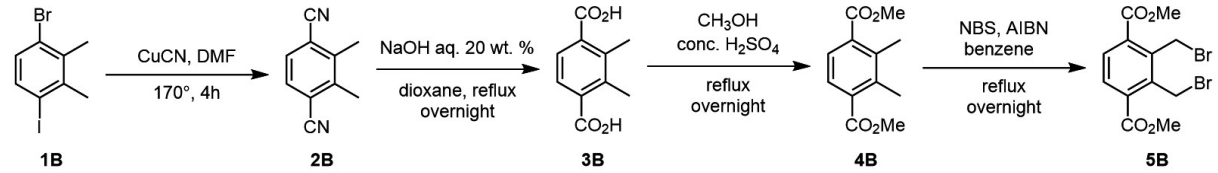

Scheme C.1: Bdc-backbone (5B) synthesis

Synthesis of compound 2B

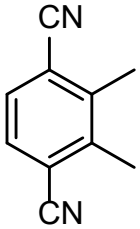

Compound **1B** (5.30 g, 17.09 mmol) was added to CuCN (6.32 g, 54.68 mmol, 3.2 eq.) in DMF (30 mL). The brown mixture was heated under N_2 at 170 ºC for 4 h. A separate solution was made of $FeCl_3 \cdot 6H_2O$ (6.54 g, 24.10 mmol), concentrated HCl (1.5 mL) and H_2O (10 mL). Once the refluxed mixture cooled down the $FeCl_3$ $6H_2O$ solution was added to the black mixture and stirred at r.t. for 1 h. The product was extracted with ethyl acetate and filtrated to remove the black solid. The combined organic layers were washed with H_2O (~100 mL). The solvent was removed under reduced pressure to give a brown solid. Yield: 2.52 g, 16.01 mmol, 94%. ^{1}H NMR (500 MHz, $CDCl_3$): 7.55(s, 2H), 2.55(s, 6H).

Synthesis of compound 3B

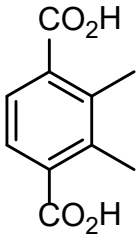

Compound **2B** (2.51 g, 16.01 mmol) was added to a NaOH aqueous solution (20 wt.%, 50 mL) and dioxane (4 mL). The cloudy solution was heated at 100 ºC overnight. After the yellow solution was cooled down to room temperature, Conc. HCl aq. was added while the solution was kept in an ice bath. When the pH was adjusted to around 2.0, a lot of white solid precipitated. The pure product was obtained as a white solid by filtration, washed with water, and dried under vacuum. Yield: 2.82 g, 14.40 mmol, 90%.^{1}H NMR (500 MHz, DMSO-d_6) δ (ppm) 7.35(s, 2H), 2.40(s, 6H).

Synthesis of compound 4B

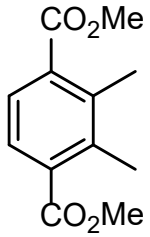

A white suspension of compound **3B** (2.49 g, 12.80 mmol) was dissolved in methanol (250 mL) and concentrated H_2SO_4 (37%, 4 mL) was added dropwise. After the addition, the solution was refluxed overnight. Some solid was filtered off, and methanol was removed under reduced pressure to give an oily substance that crashed out at r.t. to give a white precipitate. The white solid was washed with H_2O (x 3, 10 mL). Yield: 2.33 g, 12.10 mmol, 94%.

^{1}H NMR (500 MHz, $CDCl_3$) δ (ppm) 7.57(s, 2H), 3.85(s, 6H), 2.45(s, 6H).

Synthesis of compound 5B

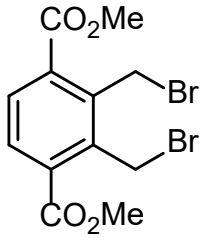

A suspension of compound **4B** (0.12 g, 0.53 mmol), AIBN (0.02 g, 0.11 mmol), NBS (0.20 mg, 1.10 mmol) in benzene was heated to reflux overnight to get a light-yellow suspension. The benzene was removed, and the reaction mixture was re-suspended in DCM. Then, it was washed with water (x 3, 20 mL). Then, the organic layers were collected and passed through a silica plug. The solvent was removed under reduced pressure, to give a yellow oily substance. Yield: 0.18 g, 0.46 mmol, 87%.

^{1}H NMR (500 MHz, $CDCl_3$) δ (ppm) 7.79(s, 2H), 5.35(s, 4H), 4.03(s, 6H).

C.2 Synthesis of ^{5}N-bdc-Val-OH

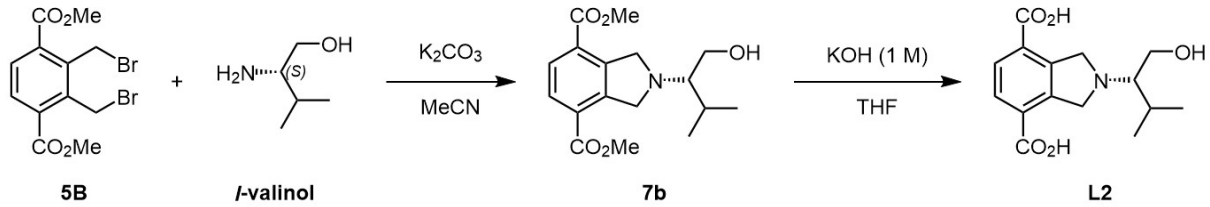

Scheme C.2: Synthesis of ^{5}N-bdc-Val-OH

Synthesis of compound 7B

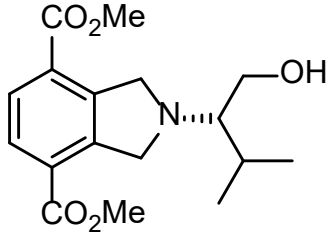

Compound **5B** (0.47 g, 1.2 mmol), and K_2CO_3 (0.52 g, 3.61 mmol) were suspended in MeCN (10 mL). S-Valinol (0.19 g, 1.80 mmol) was dissolved in MeCN (1 mL) and gradually added to the reaction mixture. The reaction mixture was stirred at room temperature for 24 hours. The base was filtered off, and the solvent was removed under reduced pressure. Then, the material was loaded into a silica column. The product was eluted using MeCN. Yield: 0.25 g, 0.82 mmol, 63%.

^{1}H NMR (500 MHz, DMSO-d$_6$) δ (ppm) 7.89 (s, 2H), 4.43 (q, *J* = 35.02 Hz, 4H), 3.98 (d, *J* = 16.20 Hz, 1H), 3.86 (s, 6H), 3.75 – 3.72(m, 1H), 3.60 – 3.57 (m, 1H), 1.96(m, *J* = 22.05 Hz, 1H), 0.98(d, *J* = 6.39 Hz, 3H), 0.93(d, *J* = 6.22, 3H).

HRMS **(**FTMS + p ESI Full) calculated for $[M + H]^+(C_{17}H_{24}NO_5)^+$ *m/z* 322.1646, found *m/z* .322.1649.

Synthesis of ligand L2

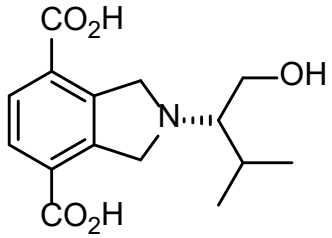

Compound **7B** (0.22 g, 0.71 mmol) was dissolved in 3 mL 1:1(V/V) THF/KOH (aq., 1M) and the solution was stirred at r.t. overnight. The pH was adjusted to ~2.0 using HNO_3 solution (0.20 M) to precipitate out the minor orange impurity, which was filtered off. Then, the aqueous layer was placed under a vacuum to remove all the residual organic solvents. Then, the pH was adjusted to 3.7, the product precipitated out (0.20 g, 0.68 mmol). Then, the product was filtered off and washed with H2O (x 3, 5 mL).

^{1}H NMR (500 MHz, NaOD/D$_2$O) δ (ppm) 7.49 (s, 2H), 4.15(s, 4H), 3.80 (dd, *J* = 4.23, 4.02 Hz, 1H), 3.68(dd, *J* = 4.94, 6.18 Hz, 1H), 2.53 (q, *J* = 12.11 Hz, 1H), 2.14 – 2.11(m, 1H), 0.97(d, *J* = 9.27 Hz, 2H), 0.84(d, *J* = 7.13 Hz, 2H).).^{13}C NMR (126 MHz, NaOD/D$_2$O) δ (ppm) 175.90, 139.50, 133.8, 126.8, 71.0, 61.1, 57.7, 28.4, 19.1, 16.0.

HRMS **(**FTMS + p ESI Full) calculated for $[M]^-(C_{15}H_{18}NO_5)^-$ *m/z* 292.1179, found *m/z* 292.1187.

C.3 Synthesis of ^{5}N-bdc-Ile-OH

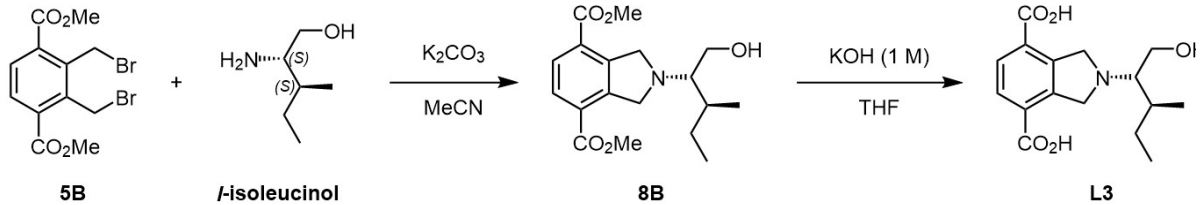

5B **/-isoleucinol** **8B** **L3**

Scheme C.3: Synthesis of ^{5}N-bdc-Ile-OH

Synthesis of compound 8B

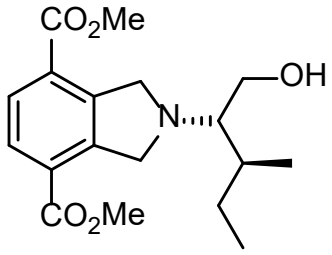

Compound **5B** (0.47 g, 1.23 mmol), and K_2CO_3 (0.41 g, 2.95 mmol) were suspended in MeCN (10 mL). *l*-Isoleucinol (0.16 g, 1.36 mmol, 1.1 eq.) was dissolved in MeCN (1 mL) and gradually added to the reaction mixture. The reaction mixture was stirred at r.t. for 24 hours. The base was filtered off, and the solvent was removed. Then, the sample was taken to de-esterification without any purification. R_f:(EtOAc: cyclohexane, 1:1, 0.48). Yield: 0.23 g, 0.68 mmol, 55%.

^{1}H NMR (500 MHz, $CDCl_3$) δ (ppm) 7.41 (s, 2H), 4.30 (s, 6H), 3.85 (s, 4H), 3.68-3.64 (m, 2H), 3.20-3.16 (m, 1H), 3.18-3.15 (m, 1H), 0.89-0.85 (m, 1H), 0.65-0.62 (m, 1H), 0.56 (dd, *J* = 4.94, 6.18 Hz, 6H).

HRMS **(**FTMS + p ESI Full) calculated for $[M]^+(C_{18}H_{26}NO_5)^+$ *m/z* 336.1805, found *m/z* 336.1800.

Synthesis of ligand L3

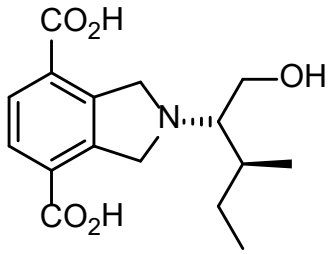

Compound **8B** (0.20 g, 0.59 mmol) was dissolved in 5 mL of 1:1(V/V) THF/KOH (aq., 1M) and the solution was stirred at r.t. overnight. The pH was adjusted to ~2.0 using HNO_3 solution (0.20 M) to precipitate out the orange impurity, which was filtered off. Then, the aqueous layer was placed under a vacuum to remove all the residual organic solvents. Then, the pH was adjusted to 4.07. The product was precipitated out gradually as a white solid. Yield: 169.87 mg, 0.55 mmol, 94%.

^{1}H NMR (500 MHz, NaOD/D_2O) δ (ppm) 7.15(s, 2H), 4.04(s, 4H), 3.69(d, J = 13.79 Hz, 1H), 3.54(dd, J = 5.75, 7.67 Hz, 1H), 2.52(d, J = 5.15 Hz, 1H), 1.74(d, J = 9.09 Hz, 1H), 1.30 – 1.27(m, 1H), 1.18 – 1.15(m, 1H), 0.79(d, J = 13.90 Hz, 3H), 0.71(d, J = 12.90 Hz, 3H).

^{13}C NMR (126 MHz, NaOD/D_2O) δ (ppm) 177.23, 139.60, 133.50, 127.00, 69.34, 61.10, 57.30, 35.60, 27.20, 13.30, 11.80.

HRMS **(**FTMS + p ESI Full) calculated for $[M]^-(C_{16}H_{20}NO_5)^-$ *m/z* 306.1336, found *m/z* 306.1348.

C.4 Synthesis of ^{5}N-bdc-Leu-OH

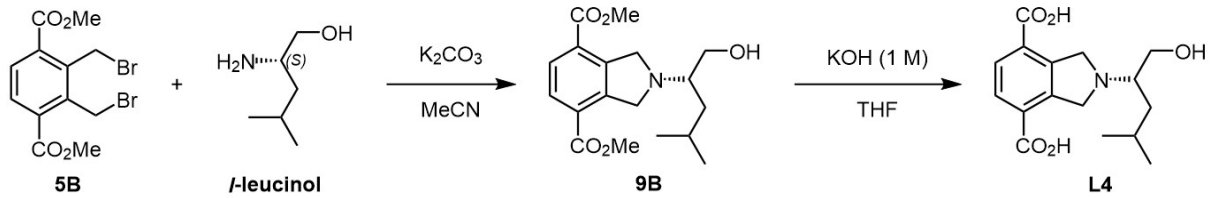

Scheme C.4: Synthesis of ^{5}N-bdc-Leu-OH.

Synthesis of compound 9B

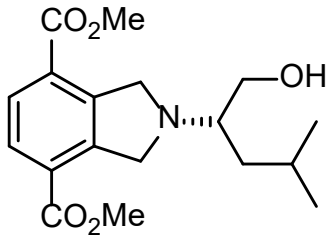

Compound **5B** (0.36 g, 0.93 mmol, 1 eq.), and TEA (1 mL) were suspended in THF (5 mL). *l*-Leucinol (2) (166.7 mg, 1.42 mmol, 1.5 eq.) was added to the reaction mixture. The reaction mixture was stirred at r.t. for 24 hours. The base was filtered off, and the solvent was removed. The reaction mixture was added to a silica column using EtOAc in cyclohexane (1:10). The product was eluted using EtOAc and cyclohexane (3:1). Then, the solvent was removed, and the product was placed in the freeze-dryer desiccator overnight. Yield: 0.11 g, 0.33 mmol, 35%.

^{1}H NMR (500 MHz, MeOD) δ (ppm): 7.91(s, 2H), 4.47 (t, J = 9.98 Hz, 1H), 4.40 (q, J = 40.60 Hz, 4H),3.62 (q, J = 15.60 Hz, 1H), 3.56 (q, J = 21.50 Hz, 1H), 2.86 – 2.83(m, 1H), 1.40 (m, 1H), 0.93 (d, J = 15.25 Hz, 6H).

HRMS (FTMS + p ESI Full) calculated for $[M+H]^{+}$ $(C_{18}H_{25}NO_5)^{+}$ *m/z* 336.1805, found *m/z* 336.1805.

Synthesis of ligand L4

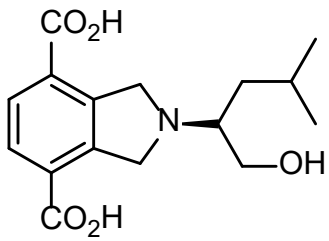

Compound **9B** (0.10 g, 0.29 mmol) was dissolved in 4 mL 1:1 (V/V) THF/KOH (aq., 1M) and the solution was stirred at r.t. overnight. The impurity was extracted with an EtOAc layer. Then, the aqueous layer was placed under a vacuum to remove all the residuals of the organic solvents. Then, the pH was adjusted to 4.66 using HNO_3 (0.1 M). Orange-whitish powder precipitated out. This powder was washed with H_2O (x 2, 2 mL) and dried in the desiccator connected to the freeze-dryer. Yield: 0.05 g, 0.16 mmol, 55%.

^{1}H NMR (500 MHz, NaOD/D_2O) δ (ppm) 7.48(s, 2H), 4.18(q, J = 34.59 Hz, 4H), 2.76(t, J = 29.31 Hz, 2H), 1.68(m, 1H), 1.43(t, J = 22.57 Hz, 1H), 0.85(d, J = 6.92 Hz, 6H).

^{13}C NMR(126 MHz, NaOD/D_2O) δ (ppm) 175.45, 139.81, 133.98, 127.17, 61.72, 55.72, 55.73, 37.42, 24.96, 22.96, 21.51.

HRMS (FTMS) calculated for $[M]^-$ $(C_{16}H_{20}NO_5)^-$ *m/z* 306.1336, found *m/z* 306.1348.

C.5 Synthesis of ^{5}N-bdc-Met-OH

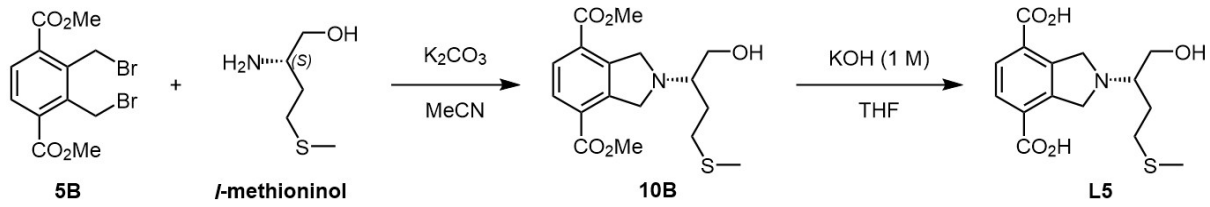

Scheme C.5: Synthesis of ^{5}N-bdc-Met-OH.

Synthesis of compound 10B

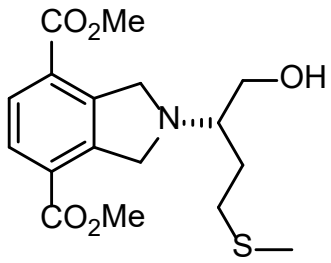

Compound **5B** (0.33 g, 0.86 mmol), and K_2CO_3 (0.36 g, 2.50 mmol) were suspended in MeCN (5 mL). *l*-Methioninol (0.17 g, 1.29 mmol) was dissolved in MeCN (1 mL) and gradually added to the reaction mixture. The reaction mixture was stirred at room temperature for 24 hours. The base was filtered off, and the solvent was removed. Then, the material was loaded into a silica column. The product was eluted with pure acetonitrile. Yield: 120.00 mg, 0.34 mmol, 40%.

^{1}H NMR (500 MHz, MeOD) δ (ppm).7.92(s, 2H), 4.44(s, 4H), 3.95(s, 6H), 3.83 – 3.80(m, 2H), 2.99 – 2.96(m, 1H), 2.72 – 2.59(m, 2H), 2.15 – 2.11(m, 2H), 2.03 – 1.98(m, 2H).

HRMS **(**FTMS + p ESI Full) calculated for $[M]^+(C_{17}H_{24}NO_5S)^+$ *m/z* 354.1370, found *m/z* 354.1368.

Synthesis of ligand L5

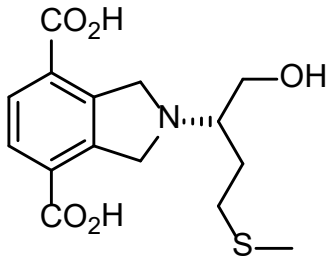

Compound **10B** (0.11 g, 0.28 mmol) was dissolved in 3 mL 1:1 (V/V) THF/KOH (aq., 1M) and the solution was stirred at r.t. overnight. The pH was adjusted to ~1.0 using HNO_3 solution (3 M). The orange impurity precipitated out, then filtered off. Then, the aqueous layer was placed under vacuum to remove all the residual of the organic solvents. Then, the pH was adjusted to 3.7 and the yellowish-white powder precipitated out. This powder was washed with H_2O (x 2, 5 mL). Yield: 50.90 mg, 0.15 mmol, 54%.

^{1}H NMR (500 MHz, NaOD/D_2O) δ (ppm) 7.50(s, 2H), 4.17(s, 4H), 3.77(dd, *J* = 5.04, 5.49 Hz, 1H), 3.70(dd, *J* = 4.60, 5.41 Hz, 1H), 2.81 – 2.78(m,1H), 2.60 – 2.58(m, 2H), 2.08(s, 3H), 1.89 – 1.86(m, 2H). ^{13}C NMR (126 MHz, NaOD/D_2O) δ (ppm) 175.69, 139.30, 134.04, 127.18, 63.03, 61.27, 56.33, 29.52, 27.77, 14.20 .

HRMS **(**FTMS + p ESI Full) calculated for $[M]^-(C_{15}H_{18}NO_5S)^-$ *m/z* 324.0900, found *m/z* 324.0908.

C.6 Synthesis of ^{5}N-bdc-Phe-OH

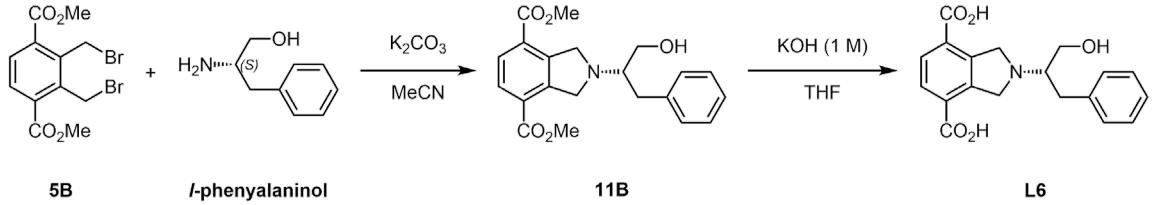

Scheme C.6: Synthesis of ^{5}N-bdc-Phe-OH.

Synthesis of compound 11B

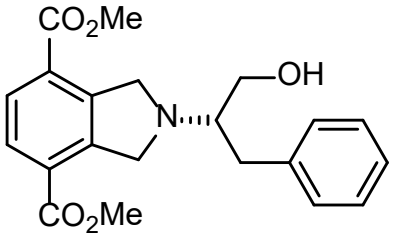

Compound **5B** (0.58 g, 0.70 mmol, 1 eq.), and K_2CO_3 (0.55 g, 4.08 mmol, 3 eq.) were suspended in MeCN (10 mL). *l*-Phenylalaninol (0.42 g, 2.70 mmol, 2.0 eq.) was added to the reaction mixture. The reaction mixture was stirred at r.t. for 24 hours. The base was filtered off, and the solvent was removed. The reaction mixture was added to a silica column using EtOAc in cyclohexane (1:10) to remove the unreacted starting material. The product was eluted using EtOAc and cyclohexane (1:1). Then, the solvent was removed, and the product was placed in the freeze-dryer desiccator overnight. yield: 0.16 g, 0.43 mmol, 61%.

^{1}H NMR (500 MHz, DMSO-d_6) δ (ppm) 7.91(s, 2H), 7.28(d, J = 4.80 Hz, 4H), 7.19 – 7.15(m, 1H), 4.54(t, J = 9.74 Hz, 1H), 4.41(s, 4H), 4.06(q, J = 20.08 Hz, 2H), 3.87(s, 6H), 3.54(t, J = 8.31 Hz, 2H). ESMS: $[M]/[Z]^{+}$ = 370.80.

Synthesis of ligand L6

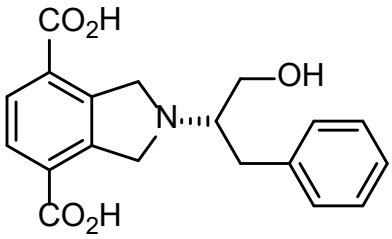

Compound **11B** (0.13 g, 0.35 mmol) was dissolved in 4 mL 1:1 (V/V) THF/KOH (aq., 1M) and the solution was stirred at r.t. overnight. The impurity was extracted with an EtOAc layer. Then, the aqueous layer was placed under a vacuum to remove all the residuals of the organic solvents. Then, the pH was adjusted to 3.94 and the orange powder precipitated out. This powder was washed with H_2O (x 2, 2 mL) and dried in the desiccator connected to the freeze-dryer. Yield: 110.0 mg, 0.29 mmol, 84%.

^{1}H NMR (500 MHz, NaOD/D_2O) δ (ppm) 7.51(s, 2H), 7.29(d, *J* = 5.17 Hz, 4H), 7.22 – 7.19(m, 1H), 4.27(q, *J* = 30.90 Hz, 4H), 3.68(dd, *J* = 4.17, 5.28 Hz, 1H), 3.57(dd, *J* = 4.89, 5.52 Hz, 1H), 3.04(m, *J* = 20.22 Hz, 2H), 2.80(q, *J* = 25.50 Hz, 1H). ^{13}C NMR (126 MHz, NaOD/D_2O) δ (ppm): 175.50, 139.57, 139.45, 133.82, 129.58, 128.64, 127.04, 126.32, 65.82, 60.81, 56.30, 34.60. ESMS: $[M]/[Z]^-$ = 340.10.

C.7 Synthesis of ^{5}N-bdc-Ser-OH

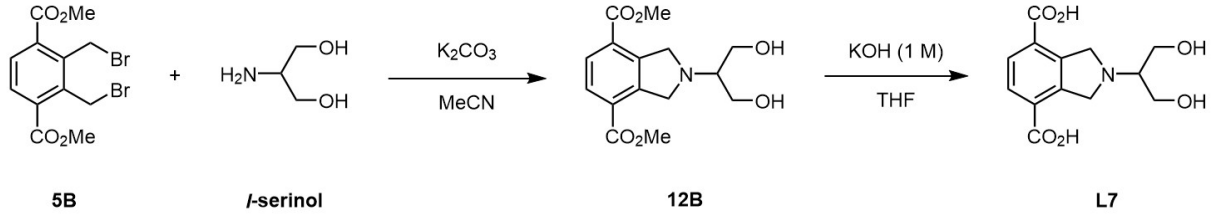

Scheme C.7: Synthesis of ^{5}N-bdc-Ser-OH (**L7**).

Synthesis of compound 12B

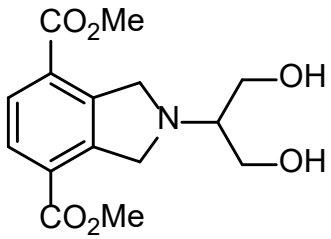

Compound **5B** (0.48 g, 0.86 mmol), and K_2CO_3 (0.58 g, 4.2 mmol) were suspended in MeCN (10 mL). S-Serinol (0.23 g, 2.54 mmol) was added. The reaction mixture was stirred at room temperature for 24 hours. The base adhered to the walls of the flask. TLC showed the product is very polar where it stayed at the baseline when polar solvents were used (EtOAc, MeCN). With the addition of MeOH (10%), it streaked a little. The reaction mixture was filtered, and the stuck base was washed with MeCN. The solvent was removed and ^{1}H NMR spectroscopy for the crude material was done. Yield: 240.0 mg. ESMS: $[M]/[Z]^+$ = 310.16

Synthesis of ligand L7

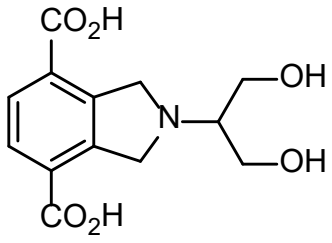

The reaction mixture was dissolved in 4 mL 1:1 (V/V) THF/KOH (aq., 1M) and the solution was stirred at r.t. overnight. The impurity was extracted with an EtOAc layer. Then, the aqueous layer was placed under a vacuum to remove all the residuals of the organic solvents. Then, the pH was adjusted to 4.00 and the yellowish-white powder precipitated out. This powder was washed with H_2O (x 2, 3 mL) and dried in the desiccator connected to the freeze-dryer. Yield: 0.05 g, 0.18 mmol.

^{1}H NMR (500 MHz, NaOD/D_2O) δ (ppm): 7.51(s, 2H), 4.19(s, 4H), 3.85(dd, J = 5.57, 4.02 Hz, 2H), 3.78(dd, J = 5.99 ,7.03 Hz, 2H), 2.77 – 2.74(m, 1H).

^{13}C NMR (126 MHz, NaOD/D_2O) δ (ppm) 175.29, 139.16, 133.98, 127.01, 65.77, 59.94, 55.73 ppm. ESMS: $[M]/[Z]^-$ = 280.13

C.8 ^{1}H NMR spectroscopic data for bdc backbone and bdc-x-OH

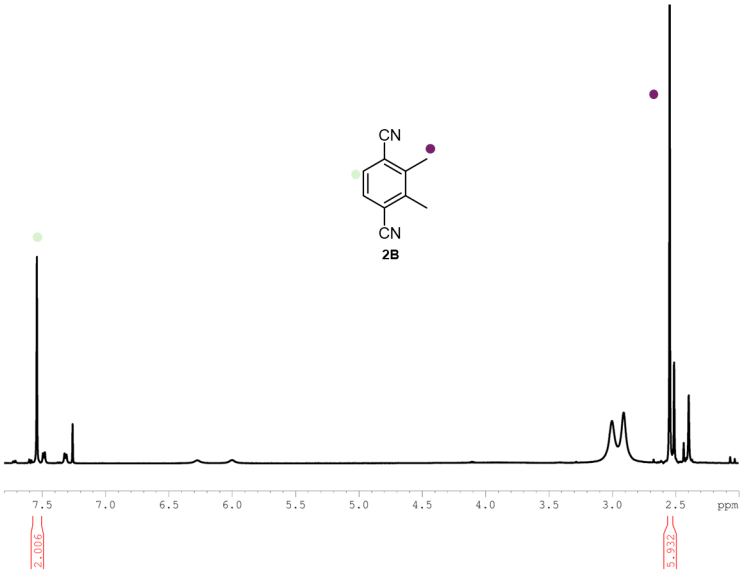

Figure C.1: ^{1}H NMR spectrum of compound 2B in DMSO-d$_6$

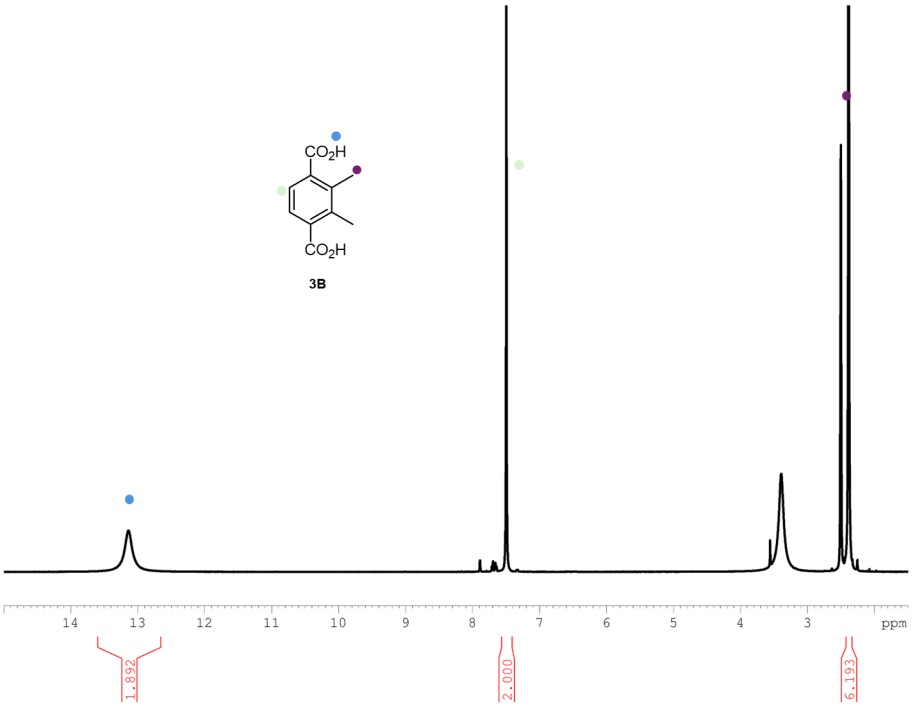

Figure C.2: ^{1}H NMR spectrum of compound 3B in DMSO-d$_6$

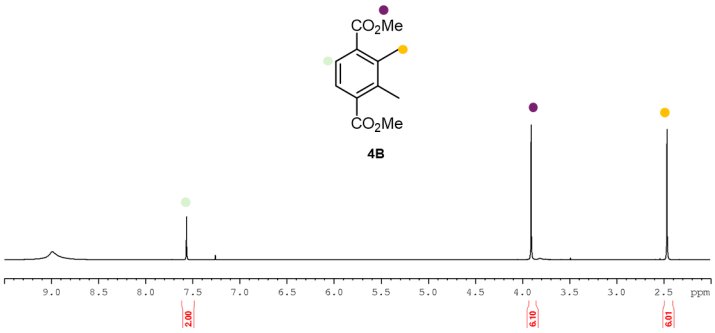

Figure C.3: ^{1}H NMR spectrum of compound 4B in $CDCl_3$

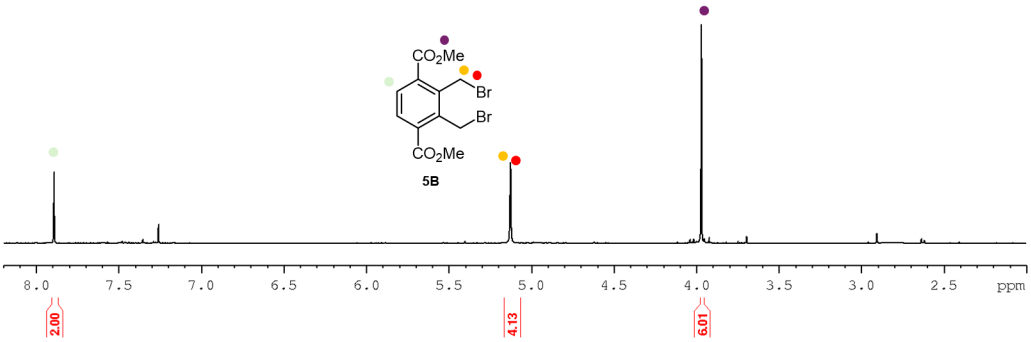

Figure C.4: ^{1}H NMR spectrum of compound 5B in $CDCl_3$

Synthesis of ^{5}N-bdc-Ala-OH NMR spectroscopic data

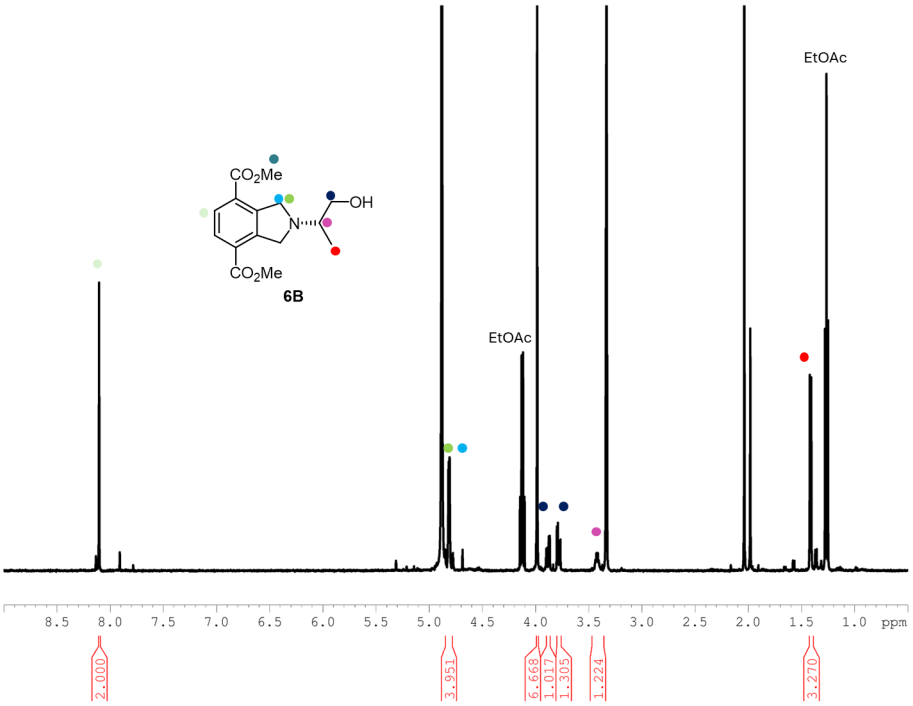

Figure C.5: ^{1}H NMR spectrum of compound 6B in MeOD.

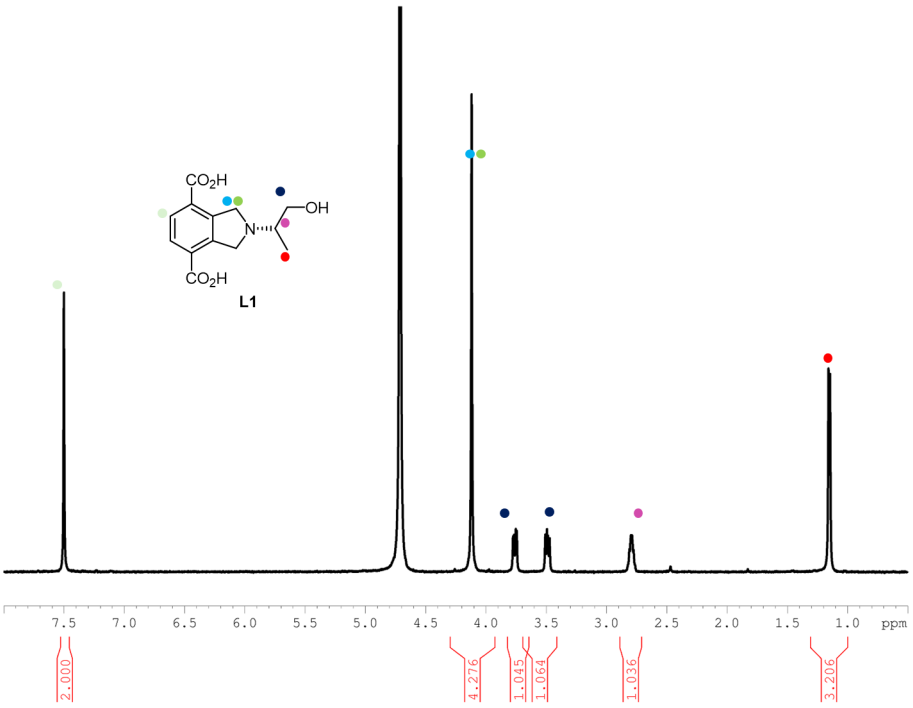

Figure C.6: ^{1}H NMR spectrum of ^{5}N-bdc-Ala-OH in NaOD/D_2O.

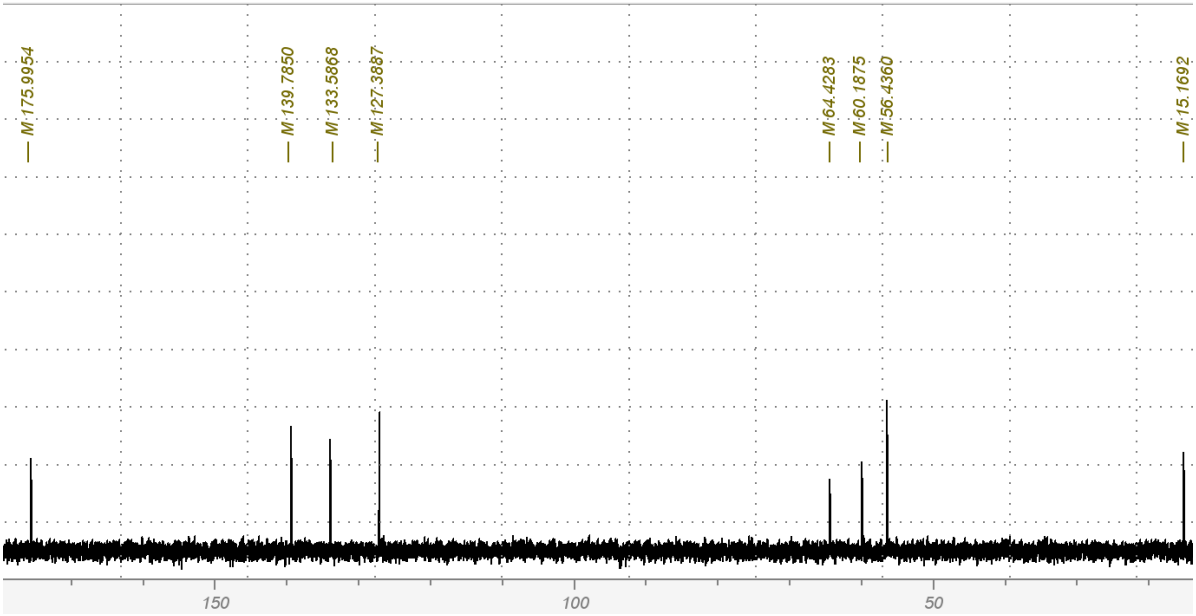

Figure C.7: ^{13}C NMR spectrum of ^{5}N-bdc-Ala-OH in NaOD/D_2O.

Synthesis of ^{5}N-bdc-Val-OH NMR spectroscopic data

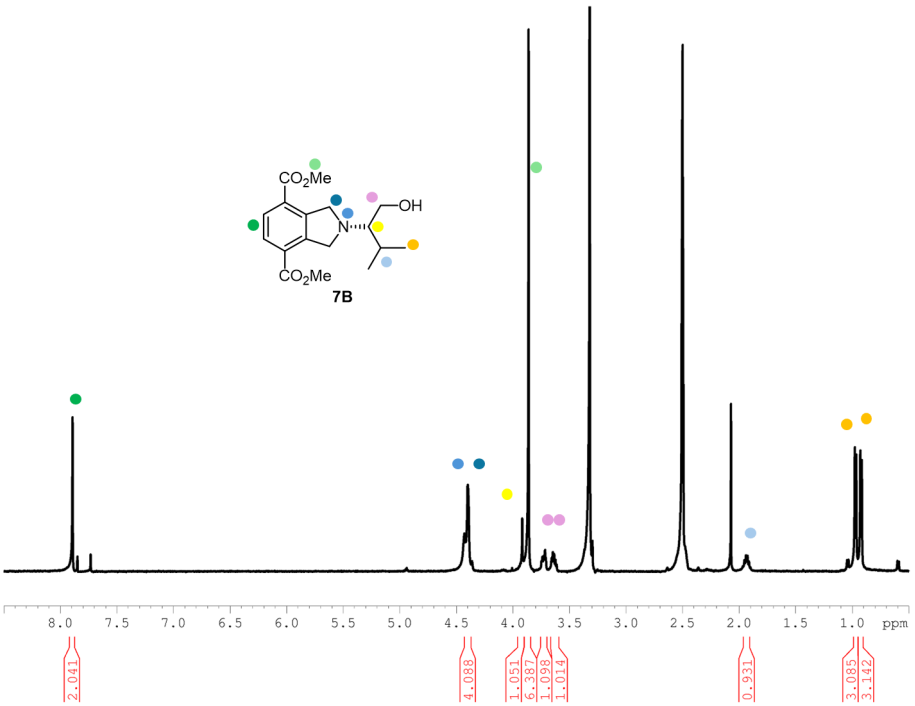

Figure C.8: ^{1}H NMR spectrum of compound 7B in DMSO-d$_6$.

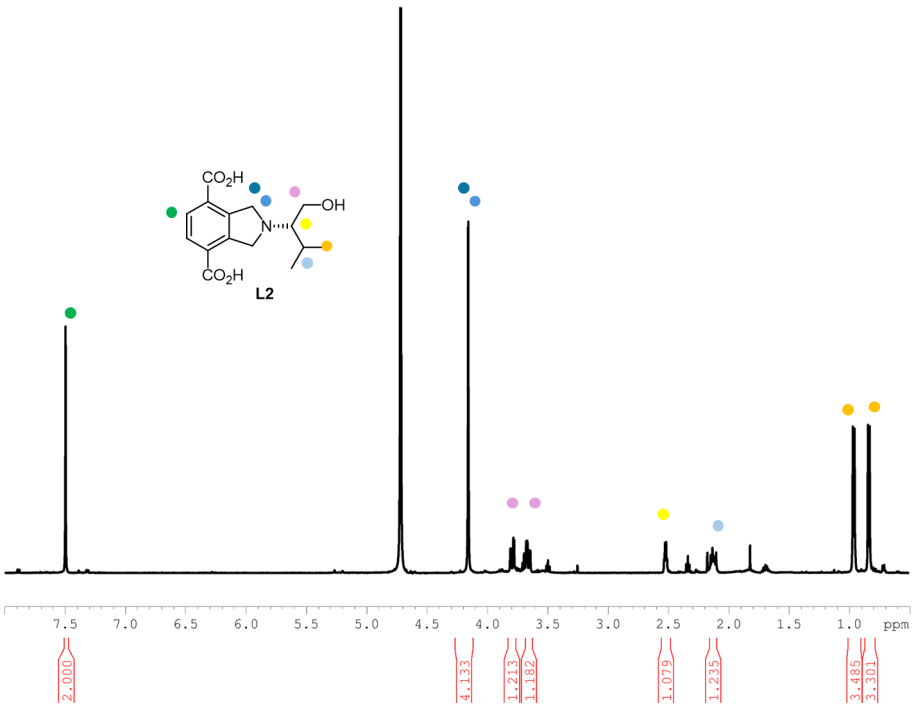

Figure C.9: ^{1}H NMR spectrum of ^{5}N-bdc-Vall-OH **(L2)** in NaOD/D$_2$O.

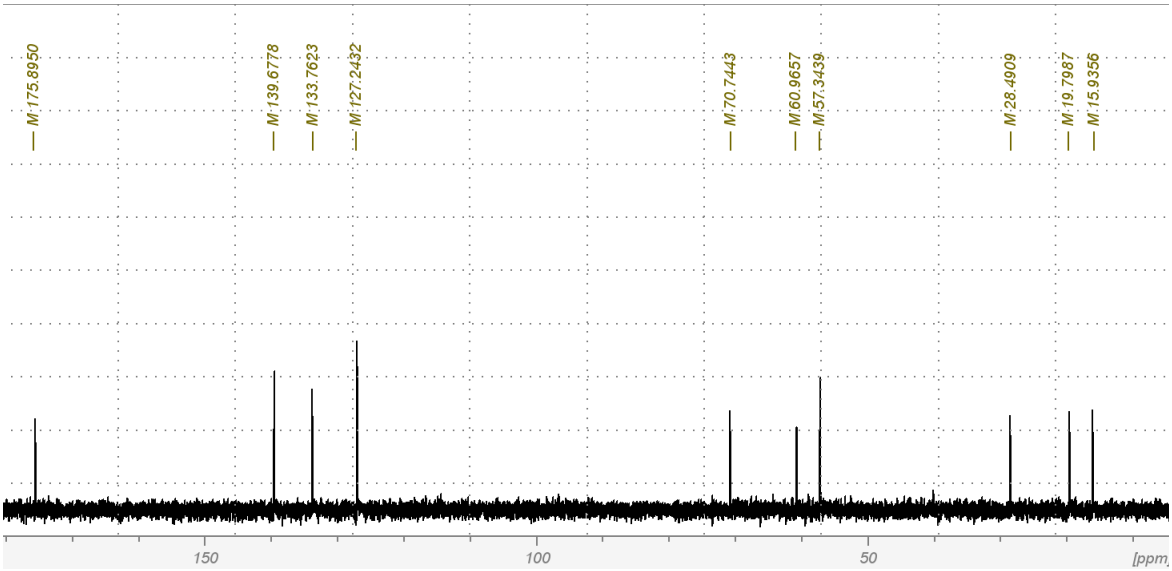

Figure C.10: ^{5}N-bdc-Val-OH ^{13}C NMR spectrum in NaOD/D_2O.

Synthesis of ^{5}N-bdc-Leu-OH NMR spectroscopic data

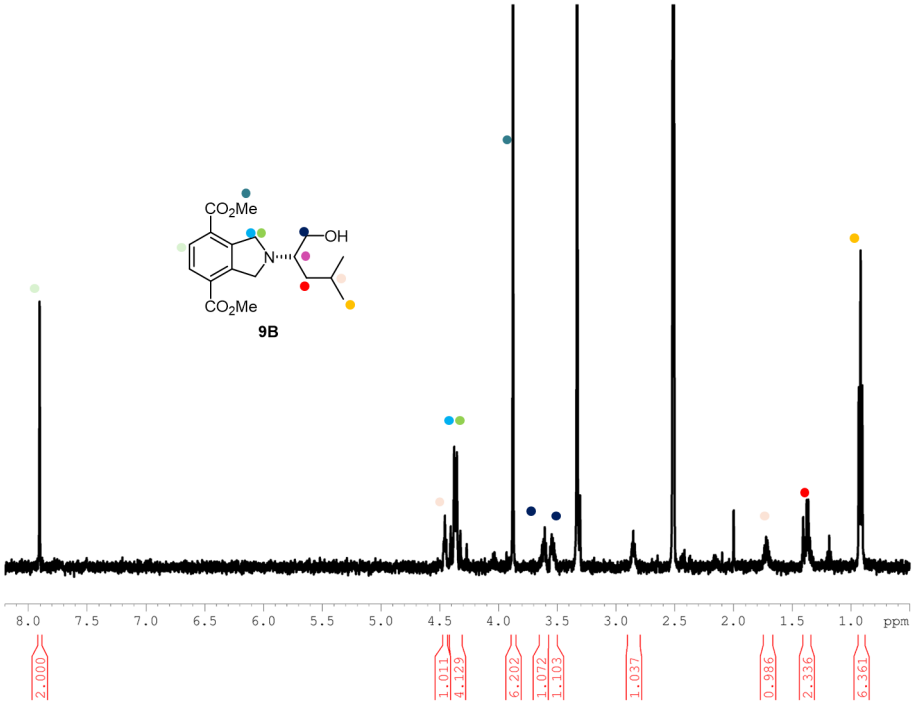

Figure C.11: ^{1}H NMR spectrum of compound 9B in MeOD

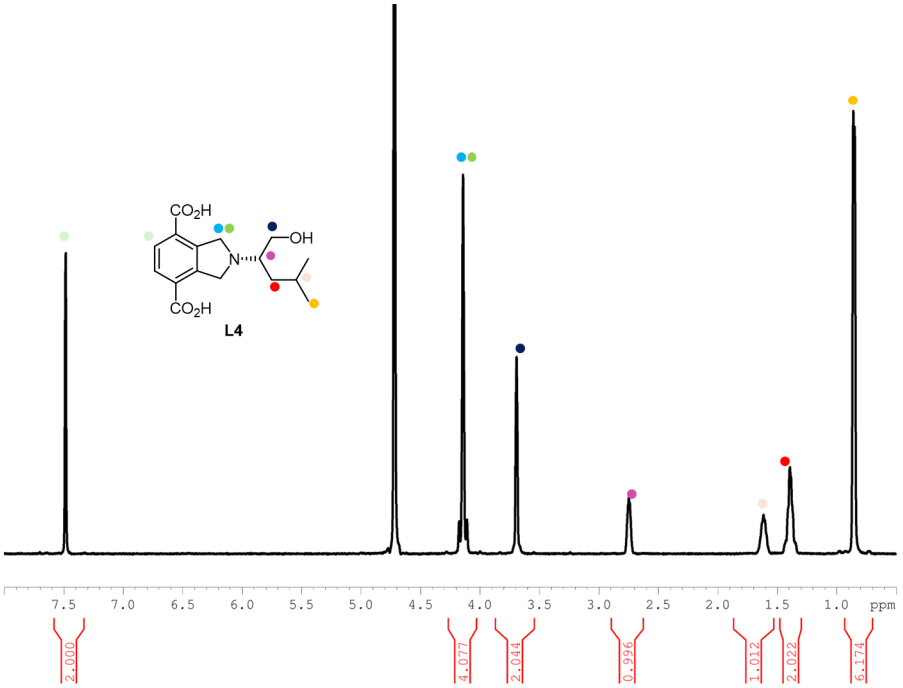

Figure C.12: ^{1}H NMR spectrum of ^{5}N-bdc-Leu (L4) in NaOD/D_2O.

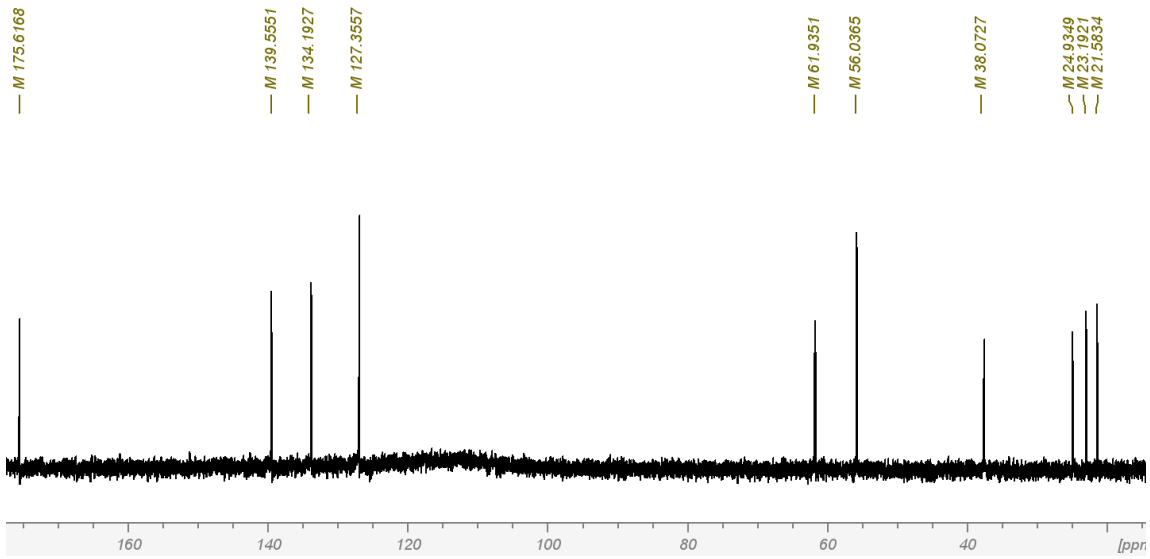

Figure C.13: ^{13}C NMR spectrum of ^{5}N-bdc-Leu in NaOD/D_2O.

Synthesis of ^{5}N-bdc-Ile-OH NMR spectroscopic data

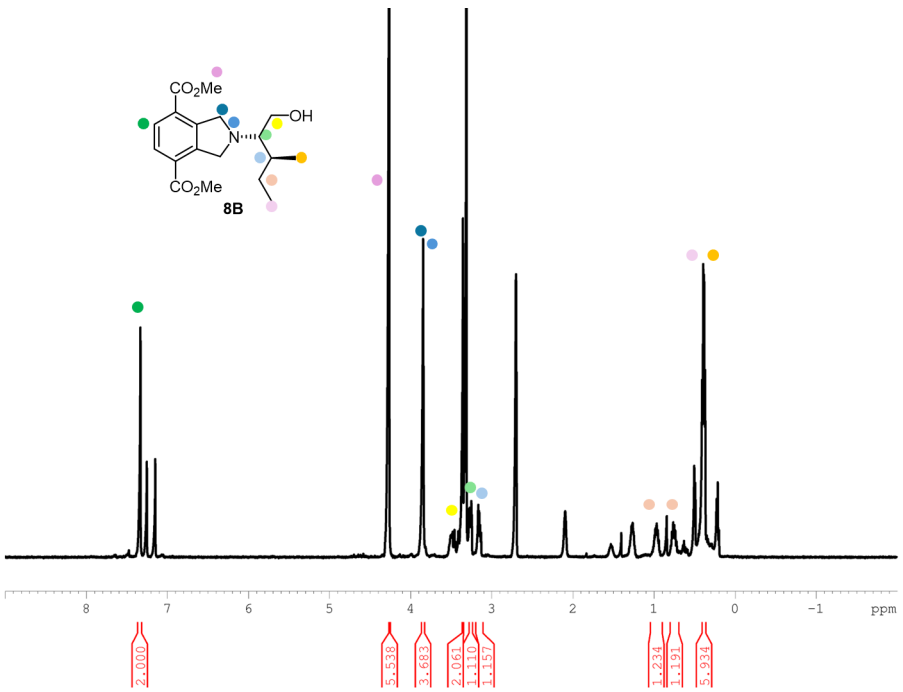

Figure C.14: ^{1}H NMR spectrum of crude 8B in MeOD.

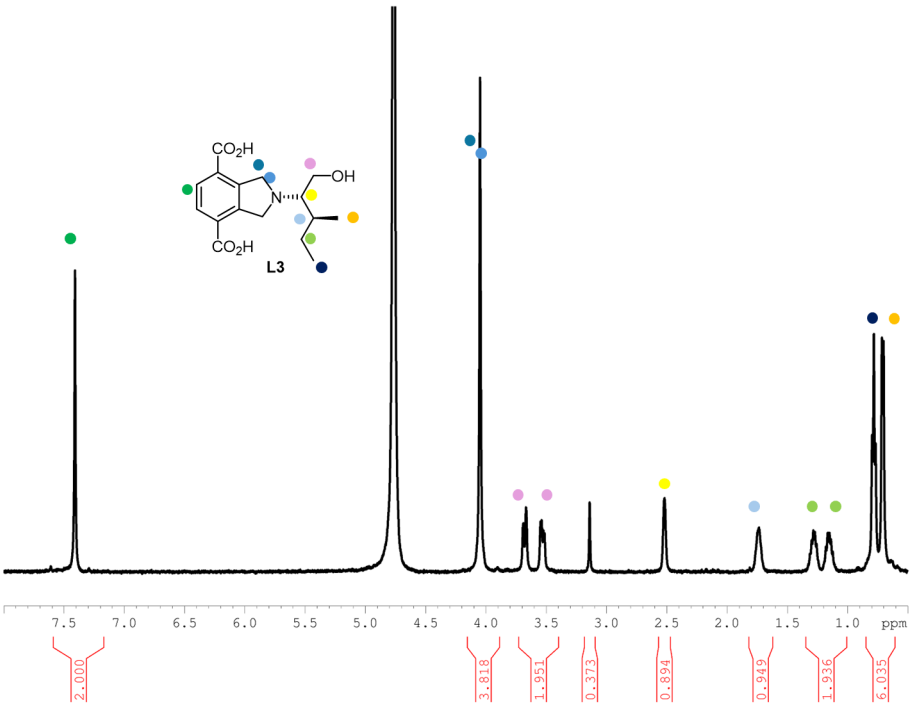

Figure C.15: ^{1}H NMR spectrum of ^{5}N-bdc-Ile-OH (L3) in NaOD/D_2O.

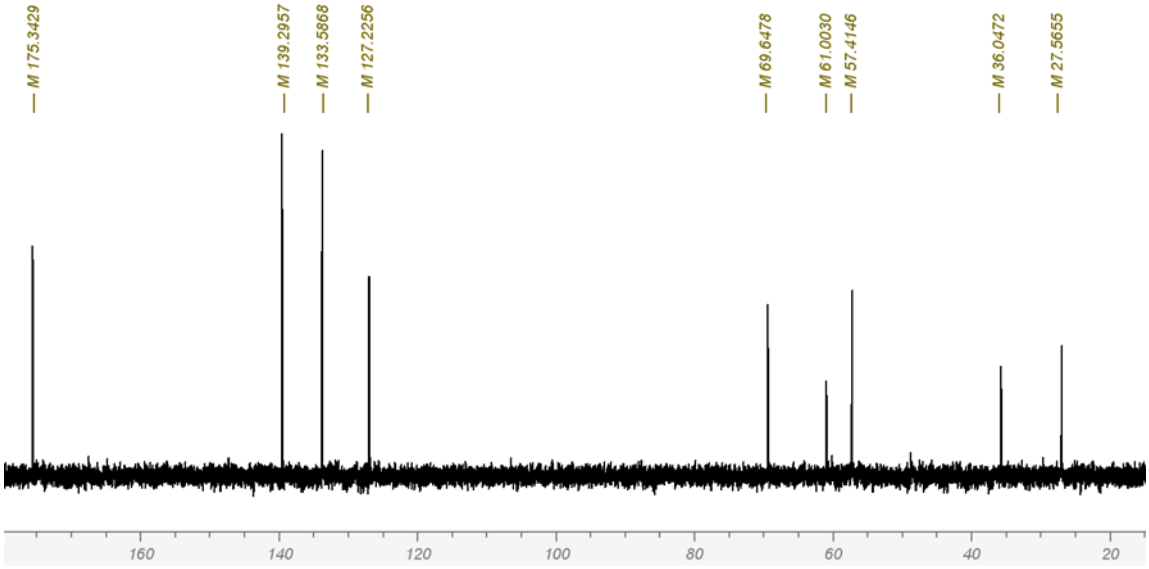

Figure C.16: ^{13}C NMR spectrum of ^{5}N-bdc-Ile-OH in NaOD/D_2O.

Synthesis of ^{5}N-bdc-Met-OH ^{1}H NMR spectroscopic data

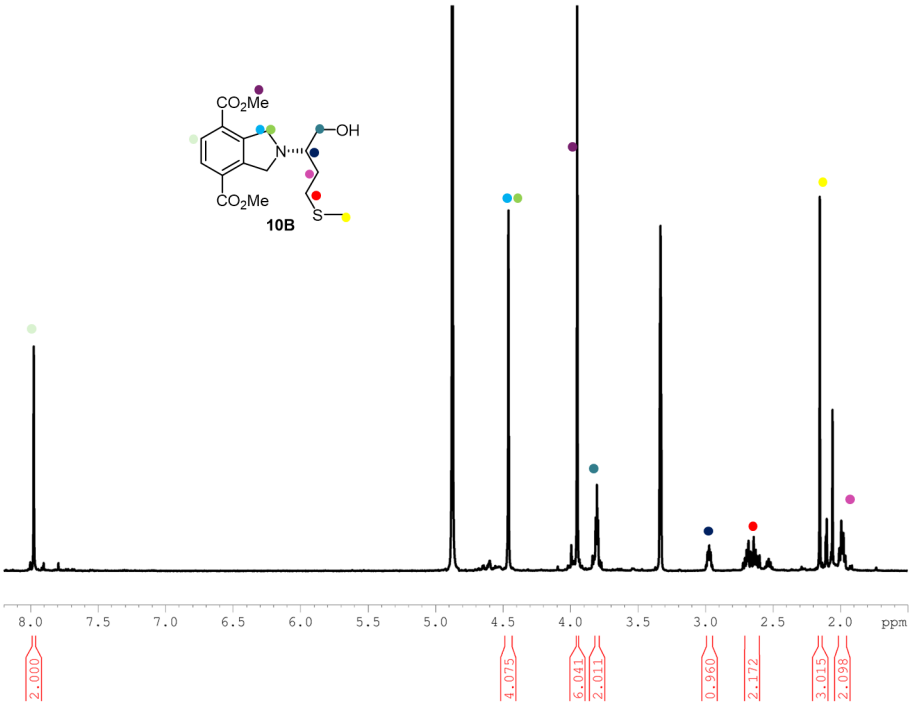

Figure C.17: ^{1}H NMR spectrum of compound 10B in MeOD.

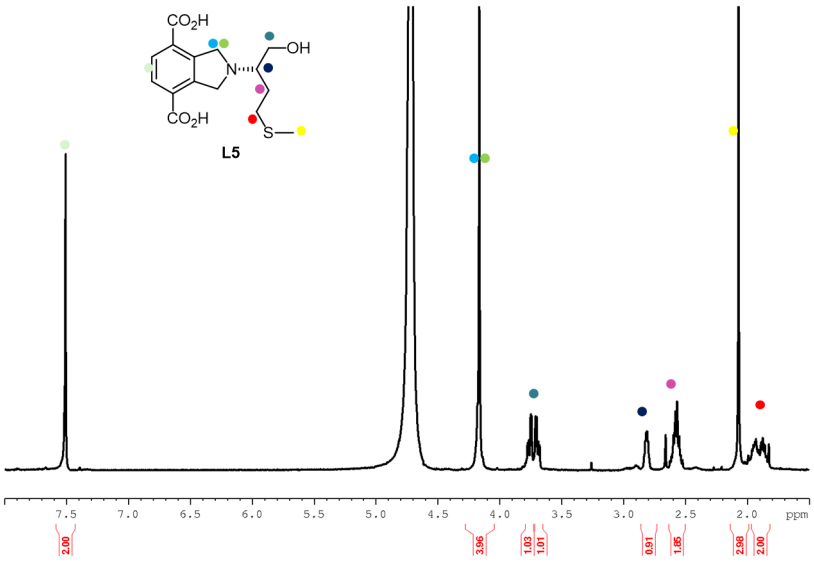

Figure C.18: ^{1}H NMR spectrum of ^{5}N-bdc-Met-OH (**L5**) in NaOD/D_2O.

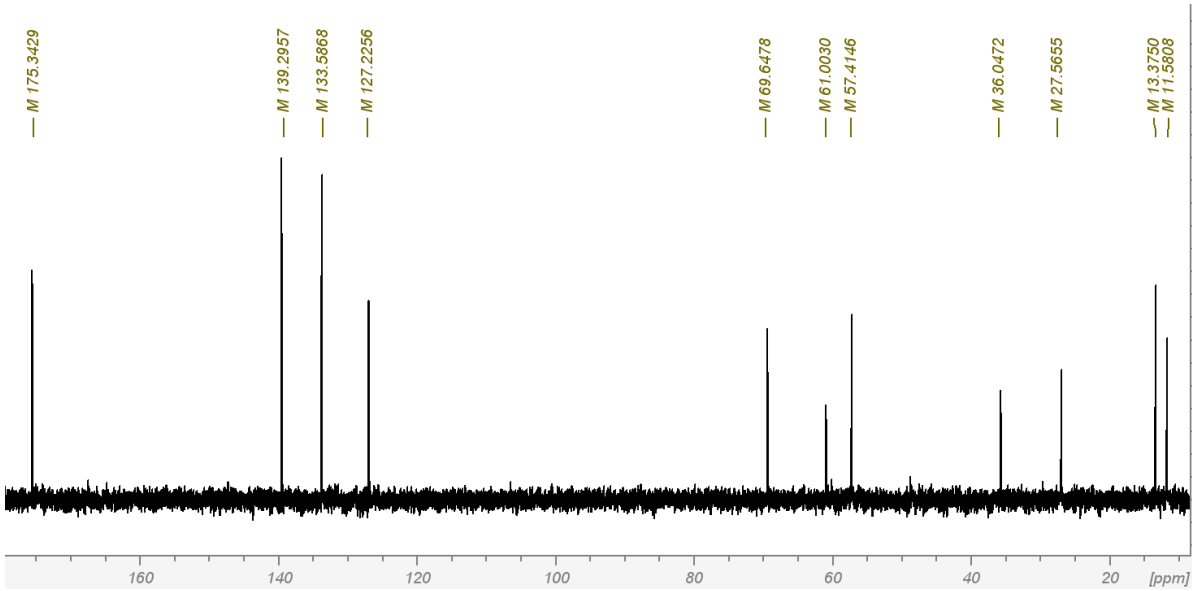

Figure C.19: ^{13}C NMR spectrum of ^{5}N-bdc-Met-OH in NaOD/D_2O.

Synthesis of ^{5}N-bdc-Phe-OH NMR spectroscopic data

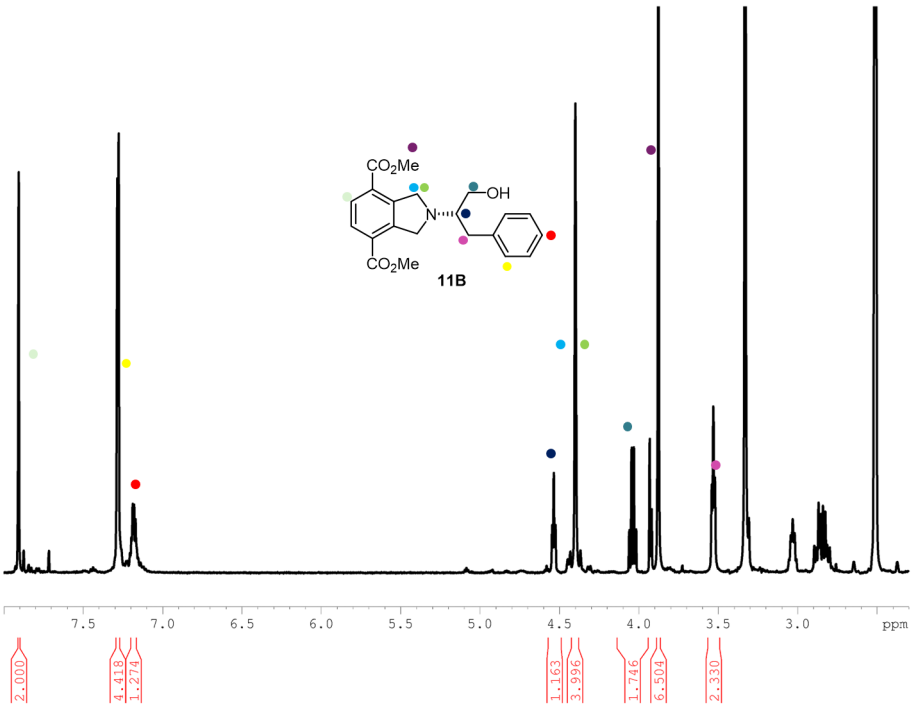

Figure C.20: ^{1}H NMR spectrum of compound 11B in DMSO-d_6.

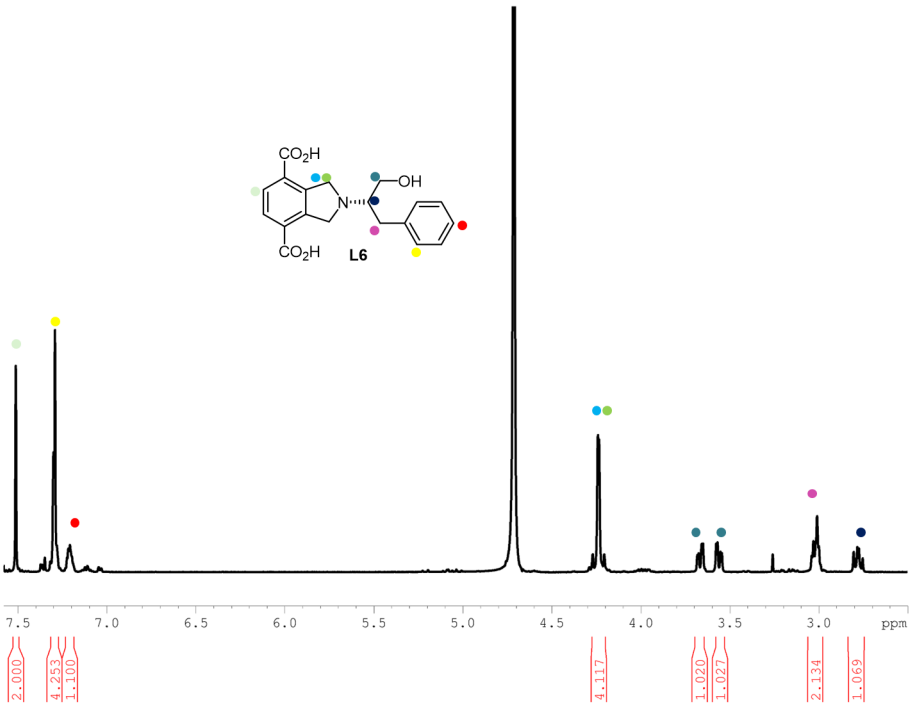

Figure C.21: ^{1}H NMR spectrum of ^{5}N-bdc-Phe-OH (**L6**) in NaOD/D_2O.

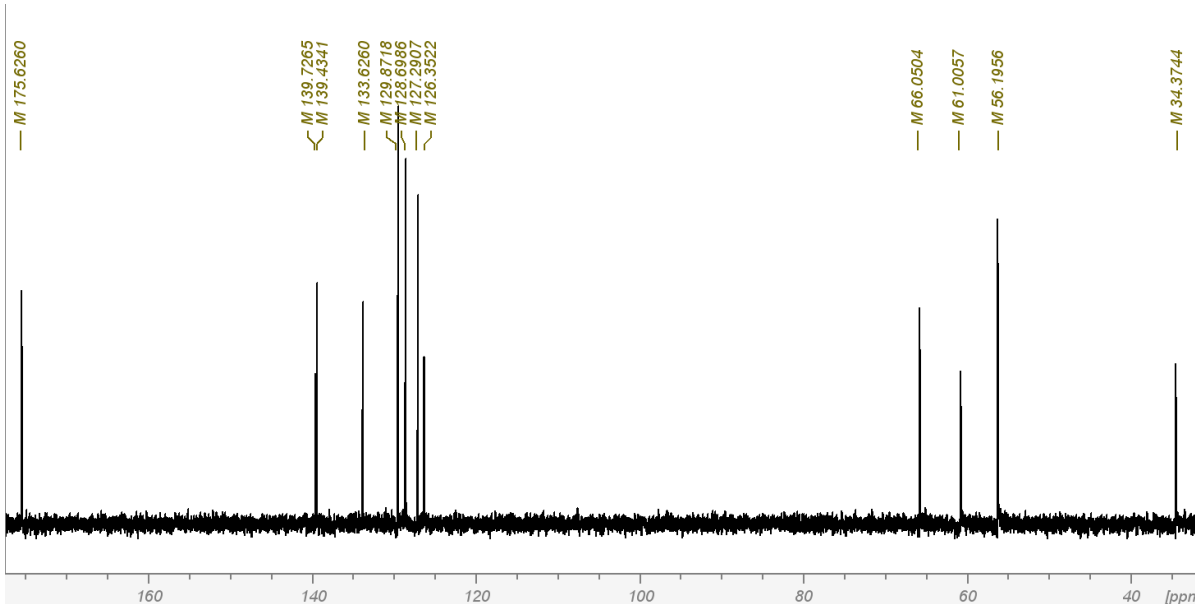

Figure C.22: ^{13}C NMR spectrum of ^{5}N-bdc-Phe-OH in NaOD/D_2O.

Synthesis of ^{5}N-bdc-Ser-OH NMR spectroscopic data

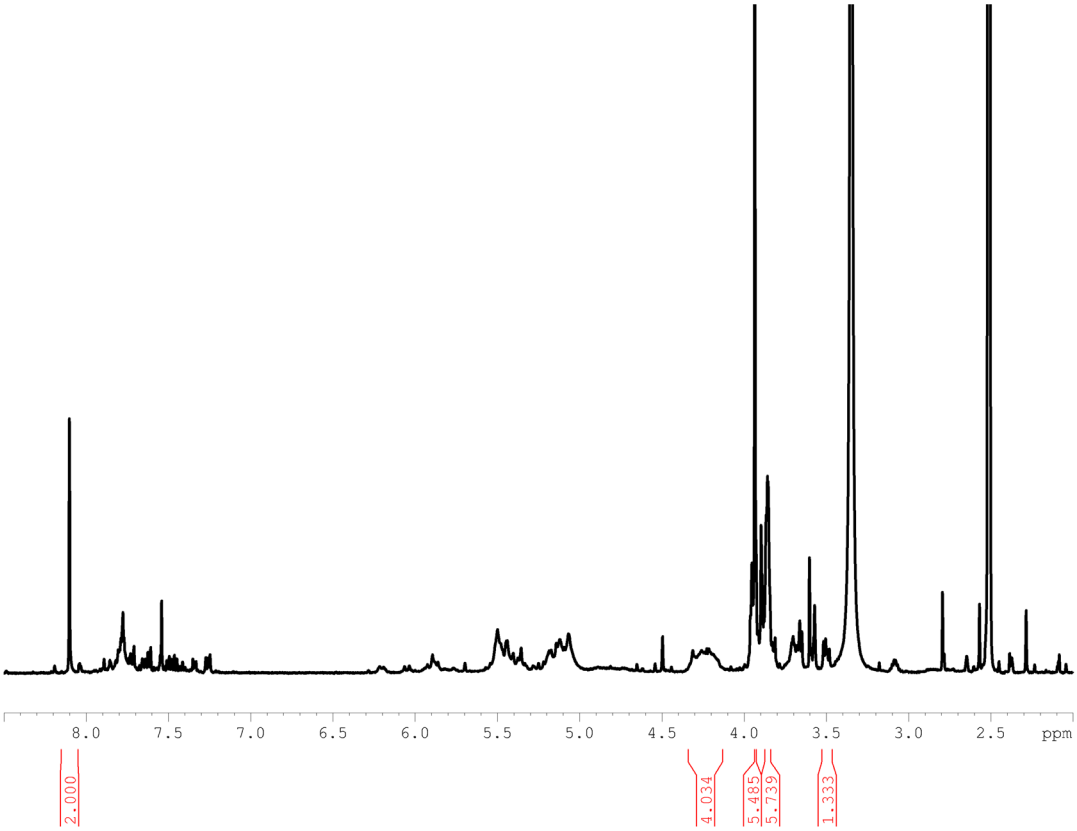

Figure C.23: ^{1}H NMR spectrum of crude ^{5}N-bdc-Ser-OH in DMSO-d$_6$.

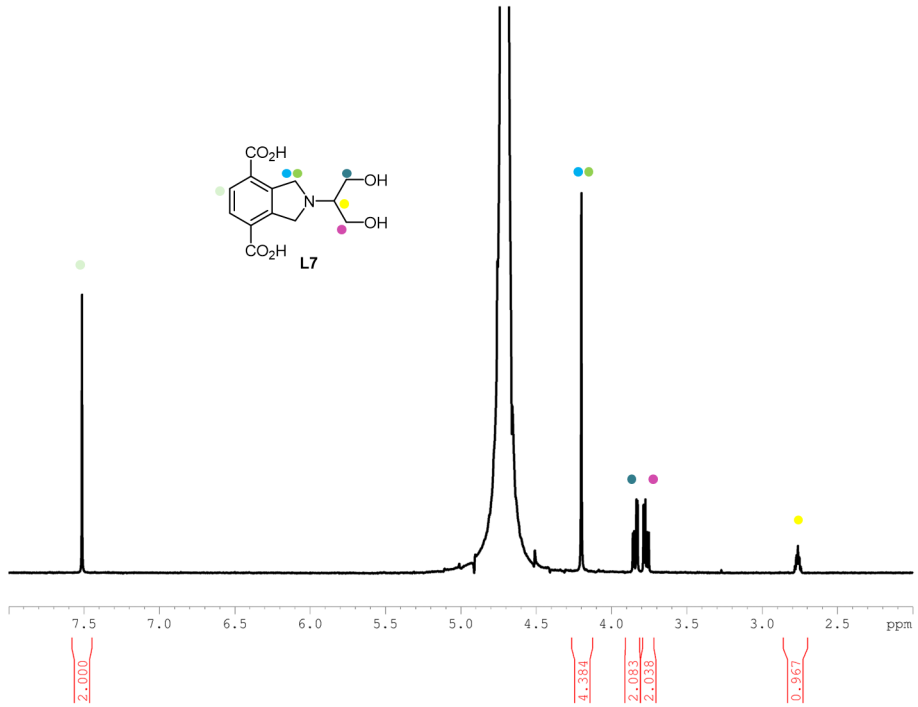

Figure C.24: ^{1}H NMR spectrum of ^{5}N-bdc-Ser-OH (**L7**) in NaOD/D$_2$O.

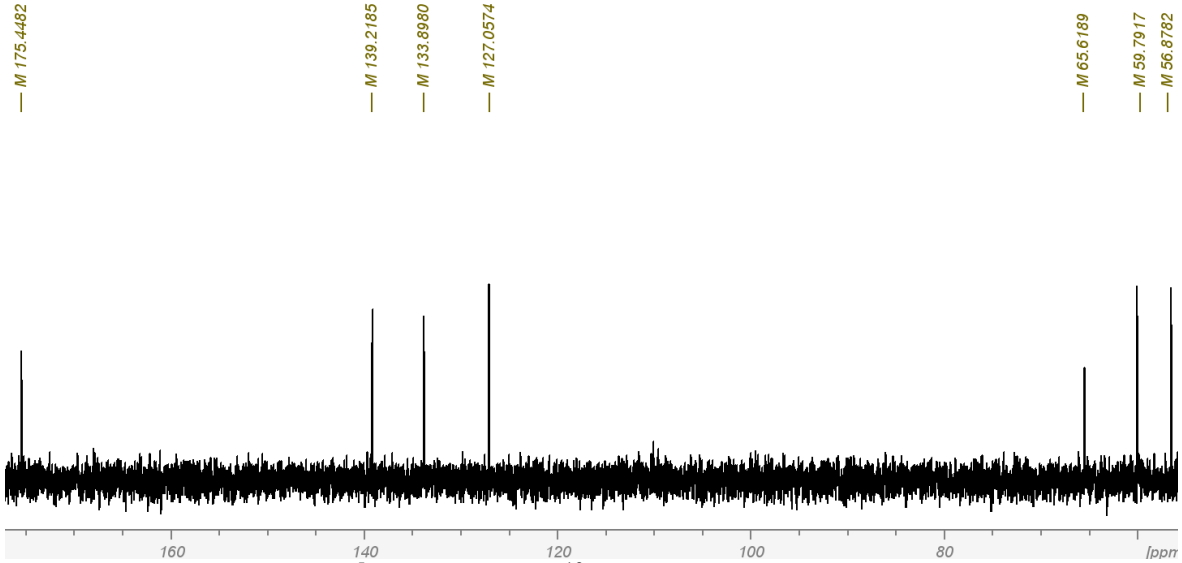

Figure C.25: ^{5}N-bdc-Ser-OH ^{13}C NMR spectrum in NaOD/D_2O.

C.9 Synthesis of bpdc backbone

Synthesis of compound 2C

4-Bromo-3-methyl-benzoic acid (**1C**) (5.00 g, 23.25 mmol, 1 eq.) was dissolved in a

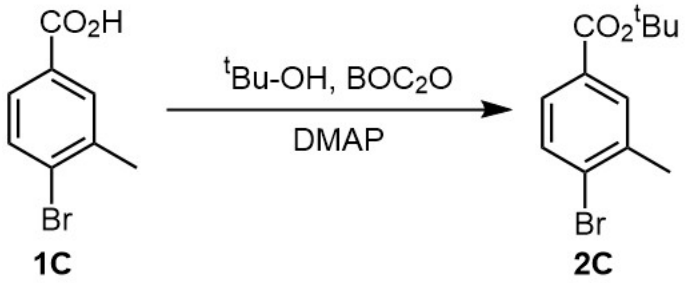

Scheme C.8: Synthetic pathway for Tert-butyl 4-bromo-3-methylbenzoate

mixture of *tert*-butanol/THF (20:1, 40 mL). Then, di-*tert*-butyl di-carbonate (10.2 mL, 46.5 mmol, 2 eq.) and 4-dimethylaminopyridine (4.26 g, 34.9 mmol, 1.5 eq.) were added. The colourless solution was stirred at 40 °C under N_2 overnight. Then, the reaction was stopped and the solvents were removed under reduced pressure. The substance was then dissolved in a solvent system of EtOAc in cyclohexane (1:10) and passed through silica plug. Then, the solvents were removed under reduced pressure. Yield: 5.90 g, 21.8 mmol, 94%.

^{1}H NMR (500 MHz, $CDCl_3$) δ (ppm) 2.39 (br s, 3H), 3.06 (s, 9H), 9.98 (d, J = 9.98 Hz, 1H), 7.18 (dd, J = 7.77 Hz, 1.5 Hz, 1H), and 7.98 (s,1H).

Synthesis of compound 3C

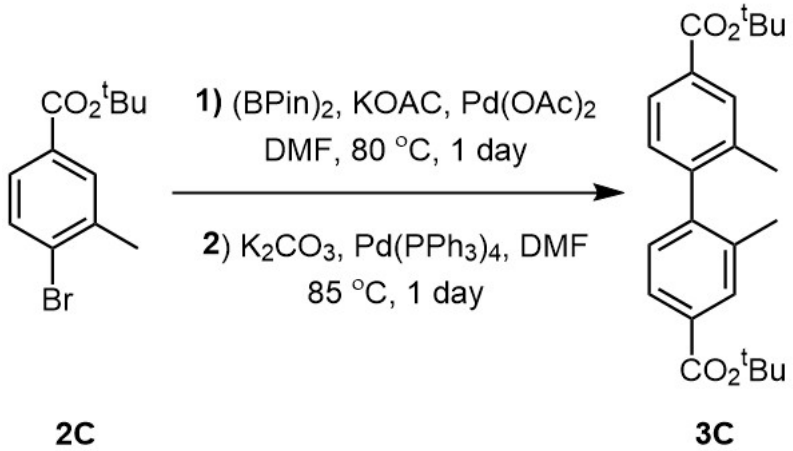

Scheme C.9: Synthetic pathway to compound 3C**.**

Tert-butyl 4-bromo-3-methylbenzoate (**2C**) (0.51 g,1.84 mmol, 1 eq.), $B(Pin)_2$ (0.47 g, 1.84 mmol, 1 eq.), KOAc (0.57 mg, 5.84 mmol, 3.2 eq.), and $Pd(OAc)_2$ (20.7 mg, 0.0922 mmol,

5 mol%) were suspended in DMF (10 mL). Then, the mixture was heated at 80 °C under N_2 overnight. Then, 10 % of the $B(Pin)_2$, KOAc, and $Pd(OAc)_2$ were added and left to react for another 6 hours. Then, the remaining starting material (0.51 g, 1.84 mmol, 1 eq.), K_2CO_3 (0.52 mg, 3.71 mmol, 2 eq.), and $Pd(PPh_3)_4$ (0.07 mg, 0.03 mmol, 0.05 eq.) to the black mixture. The mixture was heated under N_2 for 24 hours.

The reaction mixture was filtered through celite 100 and washed the substances with DCM. The solvent was removed under reduced pressure. Then, the dried material was dissolved in DCM and washed with water (x 3, 50 mL). The organic layers were combined and dried using $MgSO_4$, and the solvent was removed under reduced pressure. The product was dried using a vacuum oven. Yield: 0.64 g, 1.70 mmol, 91%.

^{1}H NMR (500 MHz, $CDCl_3$) δ (ppm): 1.62 (br s, 18H), 2.07 (s, 6H), 7.12 (d, J = 7.9 Hz, 2H), 7.85 (dd, J = 7.9 Hz, 1.5 Hz, 2H), and 7.90 (s, 2H)

Synthesis of compound 4C

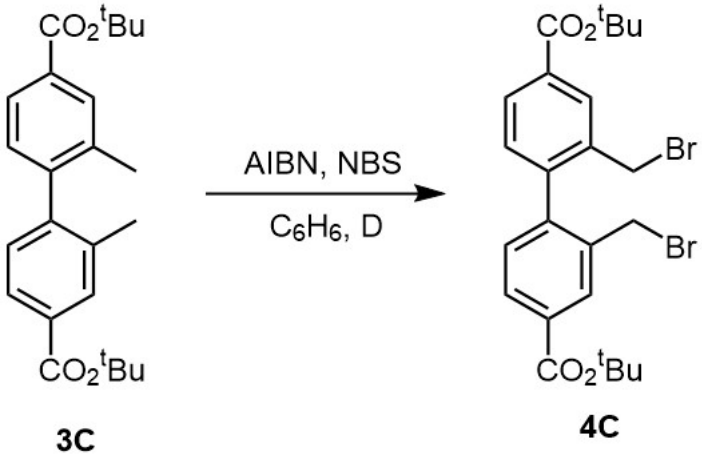

Scheme C.10: Synthetic pathway to product 4C**.**

Compound **3C** (0.20 g, 0.52 mmol) was dissolved in dry benzene (15 mL). Then, N-bromosuccinimide (194.3 mg, 1.09 mmol, 2.1 eq.) and AIBN (17.1 mg, 0.104 mmol, 0.2 eq.) were added. The reaction was refluxed overnight. The reaction was stopped, and the reaction mixture was dried using a rotary evaporator. Then, the substance was re-dissolved in DCM (300 mL), and washed with H_2O (x 3, 30 mL). The organic layers were combined, dried over $MgSO_4$, then passed through a silica plug. The solvent was removed under reduced pressure, the resulting product was a yellow, oily substance. This oil was transformed into a powder by adding hot methanol to the product gradually. The resulting crude powder (0.35 mg) was recrystallized from hot ethanol (3 mL) to get pure product **4C**. Yield: 0.25 g, 0.46 mmol, 89%.

^{1}H NMR: (500 MHz, $CDCl_3$) δ (ppm) 1.63 (br s, 18H), 4.17 (d, J = 10.3 Hz, 2H), 4.33 (d, J = 10.3 Hz, 2H), 7.32 (d, J = 8.0 Hz, 2H), 8.00 (dd, J = 8.0 Hz, 1.7 Hz, 2H), 8.16 (d, J = 1.7 Hz, 2H).

C.10 Synthesis of ^{7}N-bpdc-Val (L9)

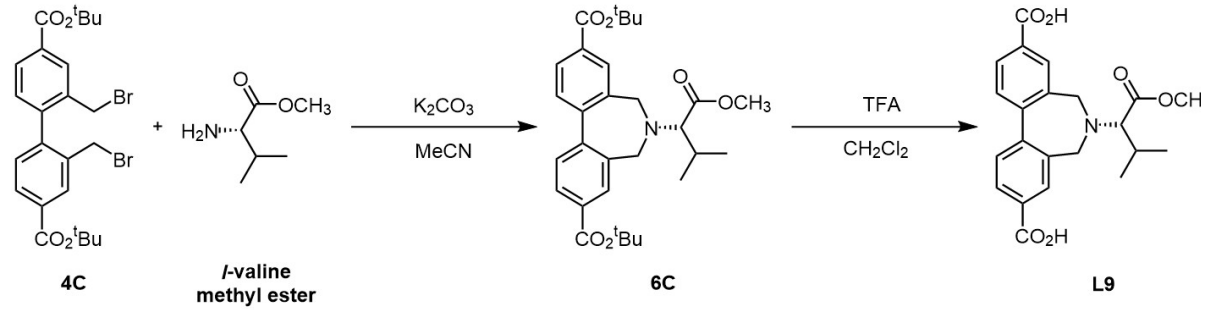

Scheme C.11: Synthesis of ^{7}N-bpdc-Val ligand.

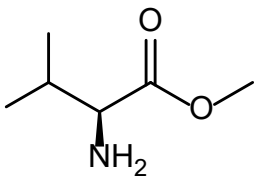

$SOCl_2$ (0.8 mL, 2 eq.) was added dropwise to the mixture of *l*-valine (1.00 g, 8.54 mmol) and methanol (10 mL) in an ice water bath with stirring. Then the temperature was gradually warmed up to r.t. and the mixture was stirred overnight. The solvent was removed by evaporation under reduced pressure. The product was an oil, then after drying under high vacuum the product precipitated as a powder. Yield: 1.11 g, 8.45 mmol, 99%:

^{1}H NMR (500 MHz, D_2O) δ (ppm) 4.16 (d, J = 4.98 Hz, 1H), 3.98 (s, 3H), 2.50 – 2.47 (m, 1H), 1.19 (dd, J = 6.58, 5.57 Hz, 2H).

Synthesis of compound 6C

Compound **4C** (0.25 g, 0.53 mmol, 1 eq.), and K_2CO_3 (0.54 g, xss.) were suspended in MeCN (10 mL). *l*-Valine methyl ester (209.8 mg, 1.6 mmol, 1.6 eq.) was added to the reaction mixture. The reaction mixture was stirred at 35 °C for 24 hours. The solvent was removed. Then, reaction mixture was suspended in EtOAc (15 mL) and washed with H_2O (x 3, 10 mL). EtOAc was removed and the substance was loaded into a flash silica column. The product was done using EtOAc/cyclohexane (1:10). R_f = 0.5 (1:10, EtOAc: cyclohexane). Yield: 130.0 mg, 0.26 mmol, 49%.

^{1}H NMR (500 MHz, $CDCl_3$) δ (ppm) 8.06 (d, J = 8.27 Hz, 2H), 7.97 (s, 2H), 7.55 (d, *J* = 8.22 Hz, 2H), 3.78 (dd, *J* = 12, 13.57 Hz, 4H), 3.59 (s, 3H), 3.07 (d, J = 9.91 Hz, 3H), 2.14 – 2.11 (m, 1H), 1.48 (s, br, 18H), 1.13 (d, J = 7.12 Hz, 3H), 0.96 (d, J = 6.15 Hz, 3H).

HRMS **(**FTMS + p ESI Full) calculated for $[M + H]^+$($C_{30}H_{40}NO_6)^+$ *m/z* 510.2850, found *m/z* 510.2841.

Synthesis of compound L9

Compound **6C** (0.12 g, 0.24 mmol) was dissolved in CH_2Cl_2 (3.0 mL). Then, TFA (1.5 mL, 100 eq.) was added, and the solution was stirred at r.t. overnight. Then, the reaction was stopped, and the solvent and TFA were removed under reduced pressure. Then, the product was dissolved in DCM and extracted with an aqueous NaOH solution (0.10 M). The extract was placed in an ice bath and HNO_3 solution (0.20 M) was added gradually. White powder precipitated out. The precipitated ligand was centrifuged and dried under high-vaccum. Yield: 0.85 g, 0.22 mmol, 91.7%.

^{1}H NMR (500 MHz, DMSO-d_6) δ (ppm) 8.04(d, *J* = 7.78 Hz, 2H), 7.94(s, 2H), 7.66(d, *J* = 7.89 Hz, 2H), 3.59(d, *J* =3.41, 2H), 3.44(d, *J* = 2.84 Hz, 2H), 3.36(s, 3H), 3.1(d, *J* = 13.44 Hz, 1H), 2.09(dd, *J* = 3.78, 8.33 Hz, 1H), 1.065(d, *J* = 7.90 Hz, 3H), 0.87(d, *J* = 6.83 Hz, 3H). ^{13}CNMR (126 MHz, DMSO-d_6): 173.5, 168.5, 144.9, 136.1, 132.1, 131.8, 130.1, 129.1, 73.5, 52.7, 51.6, 28.6, 20.4.

HRMS **(**FTMS + p ESI Full) calculated for $[M]^-(C_{22}H_{22}NO_6)^-$ *m/z* 396.1442, found *m/z* 396.1449.

C.11 Synthesis of ^{7}N-bpdc-Ser (L11)

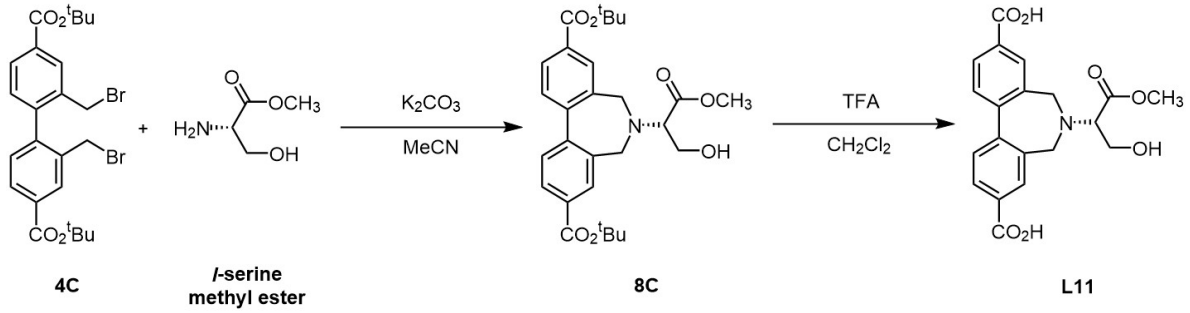

Scheme C.12: Synthesis of ^{7}N-bpdc-Ser.

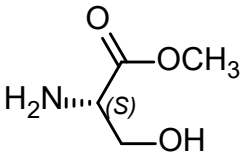

$SOCl_2$ (0.69 mL, 9.51 mmol, 2 eq.) was added dropwise to the mixture of *l*-serine (0.50 g, 4.76 mmol) and methanol (10 mL) in an ice water bath with stirring. Then the temperature was gradually warmed up to r.t. and the mixture was stirred overnight. The solvent was removed by evaporation under reduced pressure. The product was an oil, then after drying under high vacuum the product precipitated as a powder. Yield: 0.54 g, 4.52 mmol, 95%.

^{1}H NMR spectroscopy was done in D_2O. ^{1}H NMR (500 MHz, D_2O) δ (ppm) 4.3 (t, J = 8.30 Hz, 1H), 4.3 (dd, J = 4.98, 4.70 Hz, 1H), 4.03 (dd, J = 3.60, 4.16 Hz, 1H), 3.80 (s, 3H).

Synthesis of compound 8C

Compound **4C** (0.35 g, 0.65 mmol, 1 eq.), and K_2CO_3 (0.25 g, 2.0 mmol, 3 eq.) were suspended in MeCN (7 mL). *l*-Serine methyl ester (154.85 mg, 1.3 mmol,1.7 eq.) was added to the reaction mixture. The reaction mixture was stirred at 30 °C for 24 hours. The base was filtered off, and the solvent was removed. The substance was dissolved and loaded to a flash silica column. The product was eluted using EtOAc in cyclohexane (1:1). Yield: 0.19 g, 0.38 mmol, 58%.

^{1}H NMR (500 MHz, MeOD) δ (ppm) 8.092(d, J = 10.40 Hz, 2H), 8.02(s, 2H), 7.67(d, J = 8.29 Hz, 2H), 3.72(d, J = 12.89 Hz, 2H), 3.62(d, J = 9.21 Hz, 2H), 3.63(s, 3H), 3.62(t, J = 15.36 Hz, 3H), 1.67(s, br, 18H).

HRMS (FTMS + p ESI Full) calculated for $[M + H]^{+}(C_{28}H_{36}NO_7)^{+}$ *m/z* 498.248, found *m/z* 498.2478.

Synthesis of compound L11

Compound **8C** (0.14 g, 0.28 mmol) was dissolved in CH_2Cl_2 (7.0 mL). Then, TFA (2.14 mL, 28.1 mmol, 100 eq.) was added gradually while the solution is in ice bath. The solution was stirred overnight and allowed to warm at r.t. The reaction was stopped, the DCM and TFA were removed. The product was suspended in DCM and extracted with NaOH solution (0.1 M). The extracted substance was placed in an ie bath, and the product **L9** was precipitated by using HNO_3 (0.10 M).Then, the ligand was centrifuged and washed with H_2O (x 3, 2 mL). The resulting white powder was dried under high vacuum. Yield: 0.08 g, 0.22 mmol, 79%.

^{1}H NMR (500 MHz,NaOD/D_2O, 16 µL/1 mL) δ (ppm) 7.89(d, *J* = 9.96 Hz, 2H), 7.80(s, 2H), 7.57(d, , *J* = 7.54 Hz, 2H), 3.84(t, *J* = 7.68 Hz, 7.68), 3.49(d, *J* = 13.12 Hz, 2H), 3.40(d, *J* = 13.14 Hz, 2H), 3.24(s, 3H), 3.15(t, *J* = 11.10 Hz, 1H). ^{13}CNMR (126 MHz, NaOD/D_2O, 16 µL/1 mL) δ (ppm) 178.73, 175.29, 143.2, 136.1, 133.9, 130.5, 128.8, 127.3, 70.6, 60.2, 52.5, 49.1.

HRMS **(**FTMS + p ESI Full) calculated for $[M]^-(C_{20}H_{19}NO_7)^-$ *m/z* 384.1078, found *m/z* 384.1089.

C.12 Synthesis of ^{7}N-bpdc-Leu (L10)

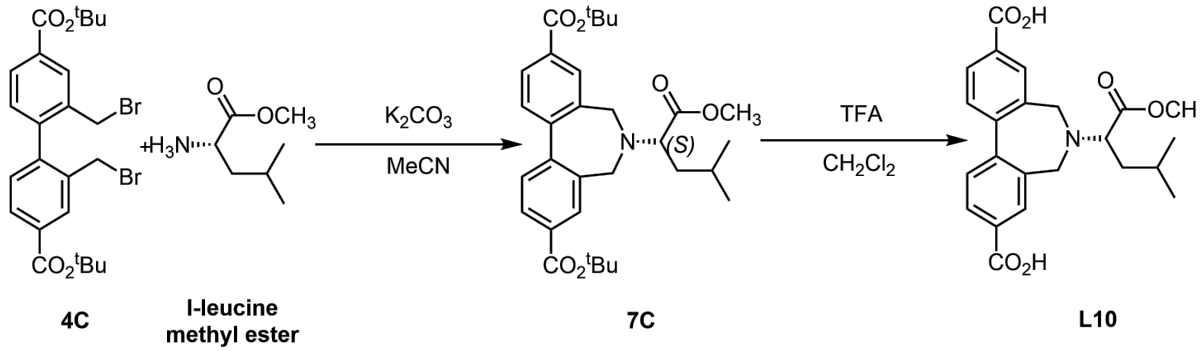

Scheme C.13: Synthesis of ^{7}N-bpdc-Leu.

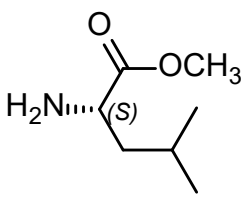

$SOCl_2$ (2.3 mL, 2 eq.) was added dropwise to the mixture of *l*-leucine (0.78 g, 5.95 mmol) and methanol (10 mL) in an ice water bath with stirring. Then the temperature was gradually warmed up to r.t. and the mixture was stirred overnight. The solvent was removed by evaporation under reduced pressure. The product was an oil, then after drying under high vacuum the product precipitated as a powder. Yield: 0.84 g, 0.58 mmol, 97%.

^{1}H NMR (500 MHz, D_2O) δ (ppm): 4.09 (t, *J* = 13.20 Hz, 1H), 3.77 (s, 3H), 1.79 – 1.75 (m, 1H), 1.66 – 1.63 (m, 1H), 0.88 (t, *J* = 8.73 Hz, 6H).

Synthesis of compound 7C

Compound **4C** (0.16 g, 0.29 mmol), and K_2CO_3 (0.67 g, excess.) were suspended in MeCN (7 mL). *l*-Leucine methyl ester (0.11 g, 0.59 mmol, 2.0 eq.) was added to the reaction mixture. The reaction mixture was stirred at 41°C overnight. The reaction was stopped, and the solvent was removed under reduced pressure. The substance was redissolved, and loaded into a flash silica column. The product was eluted using EtOAc and cyclohexane (1:10) and the solvents were removed under resuced pressure. Yield: 0.06 g, 0.10 mmol, 35%. Rf = 0.5 (1:10, EtOAc: cyclohexane).

^{1}H NMR (500 MHz, $CDCl_3$) δ (ppm) 8.07 (dd, *J* = 1.85, 2.01 Hz, 2H), 7.99 (d, *J* = 1.70 Hz, 2H), 7.56 (d, *J* = 8.0 Hz, 2H), 3.67 (s, 4H), 3.62 (s, 4 H), 3.57 (q, *J* = 15.57 Hz, 2 H), 1.81 – 1.79 (m, 1H), 1.65 (s, 18H), 1.02 (dd, J = 8.10, 5.20 Hz, 6H).

HRMS **(**FTMS + p ESI Full) calculated for $[M + H]^+(C_{31}H_{42}NO_6)^+$ *m/z* 524.3007, found *m/z* 524.3006.

Synthesis of ligand L10

Compound **7C** (0.05 g, 0.10 mol) was dissolved in CH_2Cl_2 (3.0 mL). Then, TFA (0.5 mL, 100 eq.) was added, and the solution was stirred overnight. TFA and DCM were removed, giving a yellow oily substance. The ligand was precipitated out as a white powder by sonicating the oily substance in DCM. The powder was washed with H_2O (x 2, 2 mL). Yield: 0.04 g, 9.72 mmol, 97%

^{1}H NMR (500 MHz, NaOD/D_2O) δ (ppm) 7.91(dd, *J* = 2.28, 2.11 Hz, 2H), 7.78(d, *J* = 2.31 Hz, 2H), 7.59(dd, J = 0.74, 0.25 Hz, 2H), 3.54(s, 3H), 3.45(dd, *J* = 12.75, 14.40 Hz, 4H), 1.76 – 1.73(m, 1H), 1.52 – 1.48(m, 1H), 1.38 – 1.34(m, 1H), 0.86(d, *J* = 7.39 Hz, 3H), 0.79(d, *J* = 6.38 Hz, 3H). ^{13}C NMR (126 MHz, NaOD/D2O) δ (ppm) 180.42, 174.96, 142.84, 135.75, 133.98, 130.86, 128.81, 127.46, 68.76, 52.16, 48.86, 39.95, 25.34, 25.34, 23.61, 20. 97.

HRMS **(**FTMS + p ESI Full) calculated for $[M]^-(C_{23}H_{24}NO_6)^-$ *m/z* 410.1598, found *m/z* 410.1612.

C.13 Synthesis of ^{7}N-bpdcThr (L12)

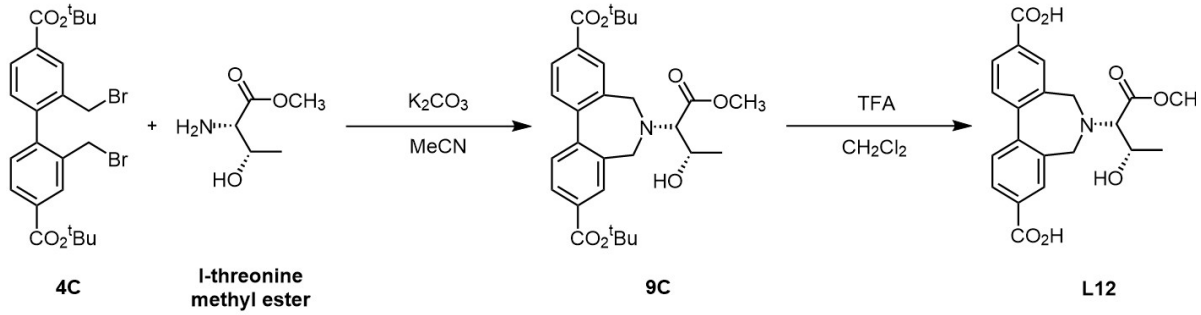

Scheme C.14: Synthesis of ^{7}N-bpdc-Thr

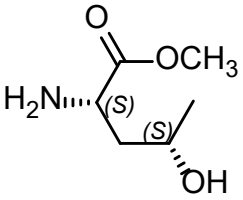

$SOCl_2$ (0.8 mL, 2 eq.) was added dropwise to the mixture of *l*-threonine (0.58 g, 4.36 mmol) and methanol (10 mL) in an ice water bath with stirring. Then the temperature was gradually warmed up to r.t. and the mixture was stirred overnight. The solvent was removed by evaporation under reduced pressure. The product was an oil, then after drying under high vacuum the product precipitated as a powder. Yield: 0.67 g, 3.86 mmol, 88%.

^{1}H NMR (500 MHz, D_2O) δ (ppm) 4.39-4.36 (m, H), 4.04 (d, J = 3.88 Hz, 1H), 3.79 (s, 3H), 1.27 (d, J = 6.61 Hz, 3H).

Synthesis of compound 9C

Compound **4C** (0.38 g, 0.70 mmol, 1 eq.), and K_2CO_3 (0.38 g, 3.50 mmol, 3 eq.) were suspended in MeCN (10 mL). *l*-Threonine methyl ester (477.2 mg, 3.5 mmol, 5 eq.) was added to the reaction mixture. The reaction mixture was stirred at 30 °C for 24 hours. The base was filtered off, and the solvent was removed. The reaction mixture was loaded to a silica column using EtOAc in cyclohexane (1:10). The product was eluted using EtOAc and cyclohexane (1:1). Then, the solvent was removed under reduced pressure. The product was dried in the freeze-dryer desiccator overnight. Yield: 0.23 g, 0.45 mmol, 64%.

^{1}H NMR (500 MHz, $CDCl_3$) δ (ppm) 8.11 (dd, J = 1.71 Hz, 1.84 Hz, 2H), 7.98 (s, 2H), 7.57 (d, J = 8.35 Hz, 2H), 4.16 – 4.13 (m, 1H), 3.79 (d, J = 13.26 Hz, 2H), 3.74 (d, J = 12.76 Hz, 2H), 3.54 (s, 3H), 3.19(d, J = 10.17 Hz, 1H), 1.67(s, *br*, 18H), 1.26 (d, J = 6.18 Hz, 3H).

HRMS (FTMS + p ESI Full) calculated for $[M + H]^+(C_{29}H_{38}NO_7)^+$ *m/z* 512.2643, found *m/z* 512.2633.

Synthesis of ligand L12

Compound **9C** (0.24 g, 0.45 mmol) was dissolved in CH_2Cl_2 (10.0 mL). Then, TFA (8.0 mL, 45.00 mmol, 100 eq.) was added gradually while the dissolved substance is in an ice bath. The solution was stirred overnight and allowed to warm at r.t. TFA and DCM were removed. Then, the resulting white substance was dissolved in NaOH (0.1 M, 2 mL), and washed with DCM (x 3, 2 mL). Then, HNO_3 (0.10 M) was used to precipitate the product (pH 4.3). A yellowish-white powder was obtained. The powder was washed with H_2O (x 2, 1 mL) and dried in the freeze-dryer desiccator. Yield: 0.12 g, 0.31 mmol, 69%.

^{1}H NMR (500 MHz, D_2O) δ (ppm) 7.80 (dd, *J* = 1.99 Hz, 1.77 Hz, 2H), 7.78 (s, 2H), 7.87 (d, *J* = 7.96 Hz, 2H), 4.24 – 4.21 (m, 1H), 3.61 (d, *J* = 12.65 Hz, 2H), 3.55 (d, *J* = 7.77 Hz, 2H), 3.53 (s, 3H), 3.42(d, *J* = 7.20 Hz, 1H), 1.19(d, *J* = 7.36 Hz, 3H). ^{13}C NMR (126 MHz, D_2O) δ (ppm) 178.12, 175.6, 142.93, 142.93, 136.2, 135.9, 134.4, 130.7, 128.5, 127.6, 57.5, 52.2, 48.5, 16.5.

HRMS **(**FTMS + p ESI Full) calculated for $[M]^-$($C_{21}H_{20}NO_7)^-$ *m/z* 398.1234, found *m/z* 398.1244.

C.14 Synthesis of ^{7}N-bpdc-Met

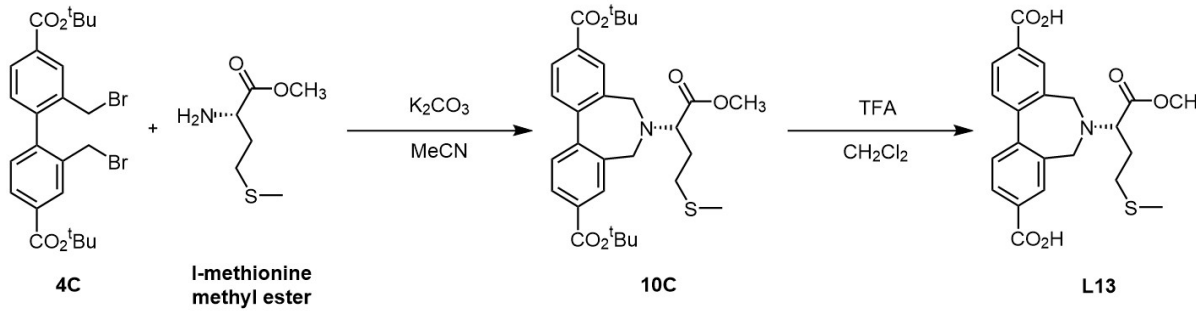

Scheme C.15: Synthesis of ^{7}N-bpdc-Met

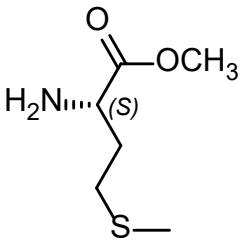

$SOCl_2$ (0.65 mL, 2 eq.) was added dropwise to the mixture of *l*-methionine (0.65 g, 4.37 mmol) and methanol (10 mL) in an ice water bath with stirring. Then the temperature was gradually warmed up to r.t. and the mixture was stirred overnight. The solvent was removed by evaporation under reduced pressure. The product was an oil, then after drying under high vacuum the product precipitated as a powder. Yield: 0.64 g, 3.93 mmol, 90%.^{1}H NMR spectroscopy was done in D_2O.

^{1}H NMR (500 MHz, D_2O) δ (ppm): 4.43 (t, *J* = 13.10 Hz, 1H), 3.95(s, 3H), 2.81 (t, *J* = 1.32 Hz, 2H), 2.45 – 2.41 (m, 1H), 2.35 –2.31 (m, 1H), 2.22 (s, 3H).

Synthesis of compound 10C

Compound **4C** (0.39 g, 0.72 mmol, 1 eq.), and K_2CO_3 (0.37 g, 2.70 mmol, 3.7 eq.) were suspended in MeCN (10 mL). *l*-Methionine methyl ester (0.30 g, 1.0 mmol, 1.5 eq.) was added to the reaction mixture. The reaction mixture was stirred at 30 °C for 24 hours. The base was filtered off, and the solvent was removed. The reaction mixture was loaded to a silica column was done using EtOAc in cyclohexane (1:10) The product was eluted with EtOAc in cyclohexane (1:1). Yield: 0.13 g, 0.24 mmol, 33%.

^{1}H NMR (500 MHz,MeOD) δ (ppm) 8.08 (dd, *J* = 1.90 Hz, 1.90 Hz, 2H), 7.89 (s, 2H), 7.65 (d, *J* = 8.10 Hz, 2H), 3.72 (d, *J* = 5.38 Hz, 2H), 3.70 (d, *J* = 10.10 Hz, 2H), 3.67 (d, *J* = 11.7 Hz, 2H), 3.57 (d, *J* = 5.38 Hz, 2H), 2.65 (m, *J* = 29.82 Hz, 2H), 2.14 (s, 3H), 2.15(d, *J* = 2.15 Hz, 1H),1.65 (s,br, 18H).

HRMS **(**FTMS + p ESI Full) calculated for $[M + H]^+(C_{30}H_{40}NO_6S)^+$ *m/z* 542.2571, found *m/z* 542.2563.

Synthesis of compound L13

Compound **10C** (0.13 g, 0.24 mmol) was dissolved in CH_2Cl_2 (7.0 mL). Then, TFA (1.8 mL, 23.00 mmol, 100 eq.) was added gradually while the solution was in ice bath. The solution was stirred overnight and allowed reach the r.t. TFA and DCM were removed. Then, the resulting white substance was dissolved in NaOH (0.10 M, 3.0 mL) and washed with DCM (x 3, 3 mL). Then, HCl (0.10 M) was used to precipitate the product. A white powder was obtained and washed with H_2O (x 3, 2 mL). Yield: 0.96 g, 0.23 mmol, 96%.

^{1}H NMR (500 MHz,D_2O) δ (ppm): 7.90(d, *J* = 8.09 Hz, 2H), 7.81 (s, 2H), 7.61 (d, *J* = 8.09 Hz, 2H), 3.49 (d, *J* = 13.21 Hz, 2H), 3.39 (d, *J* = 12.38 Hz, 2H), 3.14 (d, *J* = 14.92 Hz, 1H), 2.49 – 2.46 (m, 2H), 2.05(s, 3H), 1.97 – 1.94 **(**m, 2H). ^{13}C NMR (126 MHz, D_2O) δ (ppm): 179.5, 175.3, 143.2, 136.3, 134.2, 130.8, 129.0, 127.6, 69.0, 52.8, 49.7, 30.1, 49.7, 14.4.

HRMS **(**FTMS + p ESI Full) calculated for $[M]^-(C_{22}H_{22}NO_6S)^-$ *m/z* 428.1162, found *m/z* 428.1165.

C.15 Synthesis of ^{7}N-bpdc-Phe (L14)

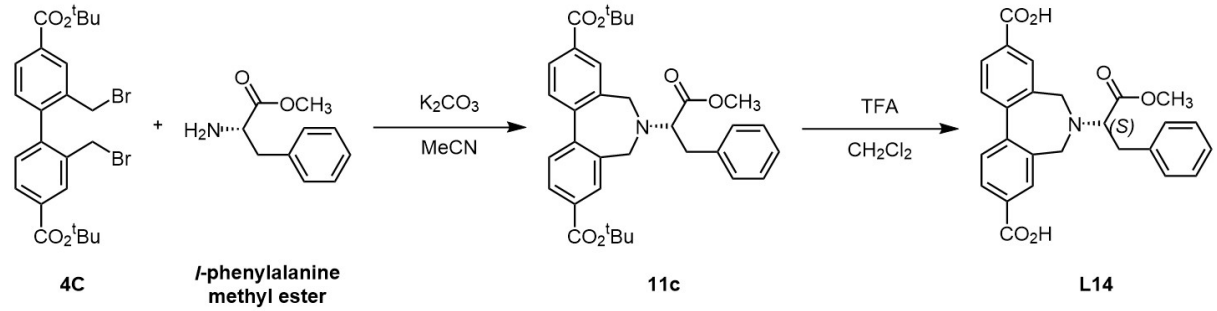

Scheme C.16: Synthesis pathway of ^{7}N-bpdc-Phe (**L14**).

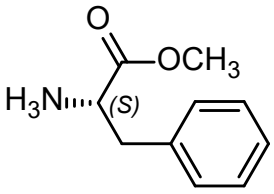

$SOCl_2$ (400.0 µL, 2 eq.) was added dropwise to the mixture of *l*-phenylalanine (0.45 g, 2.71 mmol) and methanol (10 mL) in an ice water bath with stirring. Then the temperature was gradually warmed up to r.t. and the mixture was stirred overnight. The solvent was removed by evaporation under reduced pressure. The product was an oil, then after drying under high vacuum the product precipitated as a powder. Yield: 0.44 g,0.25 mmol, 92%

^{1}H NMR (500 MHz, D_2O) δ (ppm): 7.38 – 7.35 (m, 3H), 7.24 (d, *J* = 9.42 Hz, 2H), 4.39 (q, *J* = 13.84 Hz, 1H), 3.78 (s, 3H), 3.31 (dd, *J* = 7.23, 11.18 Hz, 1H), 3.20 (dd, *J* = 9.20, 7.14 Hz, 1H).

Synthesis of compound 11C

Compound **4C** (0.20 g, 0.37 mmol, 1 eq.), and K_2CO_3 (0.54 g, excess) were suspended in MeCN (10 mL). *l*-Phenylalanine methyl ester (compound 2) (98.92 mg, 0.55 mmol, 1.6 eq.) was added to the reaction mixture. The reaction mixture was stirred at 41°C for 24 hours. The base was filtered off, and the solvent was removed. Then, reaction mixture was dissolved in EtOAc (5 mL) and washed with H_2O (3 mL, x 3). EtOAc was concentrated and the substance was loaded into a flash silica column. The column was done using EtOAc/cyclohexane (1:10). R_f: 0.3 (1:5, EtOAc: cyclohexane).Yield: 0.50 g, 0.09 mmol, 24%.

^{1}H NMR (500 MHz, $CDCl_3$) δ (ppm): 8.09 (dd, *J* = 1.81, 1.51 Hz, 2H), 8.01 (d, *J* = 2.75 Hz, 2H), 7.58 (d, *J* = 7.94 Hz, 2H), 7.33 – 7.30(m,2H), 7.26 (d, *J* = 7.34 Hz, 3H), 3.76 (q. *J* = 29.50 Hz, 5H), 3.51 (s, 3H), 3.27 (dd, *J* = 9.29, 11.80 Hz, 1H), 1.65 (s, 18H).

HRMS (FTMS + p ESI Full) calculated for $[M + H]^{+}(C_{34}H_{40}NO_6)^{+}$ *m/z* 558.2850, found *m/z* 558.2842.

Synthesis of ligand L14

Compound **D** (0.04 g, 0.07 mmol) was dissolved in CH_2Cl_2 (3.0 mL). Then, TFA (980.0 µL, 7.17 mmol) was added gradually into the solution in an ice bath. Then, the solution was stirred at r.t. overnight. The reaction was stopped, and the solvent and TFA were removed. The precipitated product was removed from the r.b.f , washed with H_2O (x 3, 1 mL), and dried using high-vaccum pump. Yield: 0.03 g, 0.07 mmol, 100%.

^{1}H NMR (500 MHz, DMSO-d_6) δ (ppm) 8.20 (d, *J* = 6.49 Hz, 4H), 7.86 (d, *J* = 11.54 Hz, 2H), 7.35 – 7.32(m, 5H), 4.47 (dd, *J* = 4.24, 5.15 Hz, H), 3.4 (s, 3H), 3.72 (t, *J* = 24.71 Hz, 1H), 3.25 (t, *J* = 29.85 Hz, 1H), 1.22 (s, 1H). ^{13}C NMR (126 MHz, DMSO-d_6) δ (ppm) 167.94, 166.98, 158.25, 158.46, 144.21, 1134.59, 133.51, 131.80, 131.48, 129.60, 129.17, 129.01, 66.92, 53.30, 34.34.

HRMS **(**FTMS + p ESI Full) calculated for $[M]^-(C_{26}H_{22}NO_6)^-$ *m/z* 444.1442, found *m/z* 444.1457.

C.16 Synthesis of ^{7}N-bpdc-His (L15)

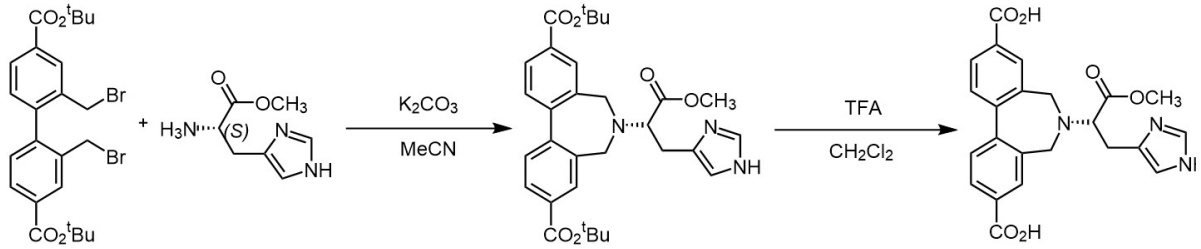

Scheme C.17: Synthesis of ^{7}N-bpdc-His.

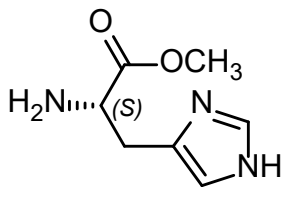

$SOCl_2$ (1.40 mL, 2 eq.) was added dropwise to the mixture of *l*-histidine (1.50 g, 9.67 mmol) and methanol (10 mL) in an ice water bath with stirring. Then the temperature was gradually warmed up to r.t. and the mixture was stirred overnight. The solvent was removed by evaporation under reduced pressure. The product was an oil, then after drying under high vacuum the product precipitated as a powder. Yield: 1.55, 9.18 mmol, 95%. ^{1}H NMR (500 MHz, D_2O) δ (ppm) 8.65 (s, 1H), 7.38 (s, 1H), 4.45 (t, *J* = 15.44 Hz, 1H), 3.79 (s, 3H), 3.46 – 3.42 (m, 2H).

Synthesis of compound 12C

Compound **B** (0.14 g, 0.26 mmol), and K_2CO_3 (668.5 mg, excess.) were suspended in MeCN (5 mL). *l*-Histidine methyl ester (0.23 g, 1.35 mmol, 2.0 eq.) was added to the reaction mixture. The reaction mixture was stirred at 35 °C overnight. The reaction was stopped, and the solvent was removed under reduced pressure. The substance was loaded into a flash silica column. The product was eluted using cyclohexane: EtOAc: EtOH (3:1:1) with R_f: 0.54.. Yield: 0.02 g, 36.50 µmol, 14%.

^{1}H NMR (500 MHz, DMSO-d_6) δ (ppm) 1.58 (s, br, 18H), 2.96 (dd, *J* = 5.90 Hz, 5.02 Hz, 1H), 3.08 (q, *J* =23.9Hz 1H), 3.41 (s,br, 3H), 3.63 (s,br, 4H), 3.83 (q, *J* = 15.20 Hz 1H), 6.82 (s,1H), 7.55 (s,1H), 7.68 (d, *J* = 8.37 Hz, 2H), 7.92 (d, *J* = 1.57 Hz, 2H), 8.27 (d, *J* = 14.11 Hz, 2H).

HRMS **(**FTMS + p ESI Full) calculated for $[M + H]^+(C_{31}H_{38}N_3O_6)^+$ *m/z* 548.2755, found *m/z* 548.2746.

Synthesis of ligand L15

Compound **D** (0.04 mg, 73.00 µmol) was dissolved in CH_2Cl_2 (3.0 mL). Then, TFA (0.50 mL, 100 eq.) was added gradually to the solution in an ice bath, then it was stirred overnight. TFA and DCM were removed, resulting in an oily substance. Then, the ligand precipitated out by sonicating it in DCM, then the ligand was filtered off and washed with water (x 2, 2 mL). The ligand was dried under high vacuum. Yield: 0.03 mg, 68.90 µmol, 94%.

^{1}H NMR (500 MHz, NaOD/D_2O, 16 µL/ 1 mL) δ (ppm) 2.97 (q, *J*= 26.11, 1H), 3.09 (dd *J*=6.4 HZ, 4.97 Hz, 1H), 3.26 (s, 3H), 3.35 (q, 14.61 Hz, 1H), 3.47 (d, *J* = 13.14 Hz, 2H), 3.54 (d, *J* = 14.28 Hz, 2H), 6.15(s,1H), 7.55 (s,1H), 7.61 (d, *J* = 7.90 Hz, 2H), 7.82 (S, 2H), 7.89 (d, *J* = 8.77 Hz, 2H). ^{13}C NMR (126 MHz, NaOD/D2O) δ (ppm) 28.12, 48.97, 52.07, 70.1, 127.57, 128.89, 130.71, 133.02, 134.04, 135.97, 136.03, 143.4, 150.3, 175.5, 179.3.

HRMS **(**FTMS + p ESI Full) calculated for $[M]^-(C_{23}H_{20}N_3O_6)^-$ *m/z* 434.1347, found *m/z* 434.1349.

C.17 Bpdc backbone, ^{7}N-bpdc-x intermediates and ligands ^{1}H and ^{13}C NMR spectroscopic data

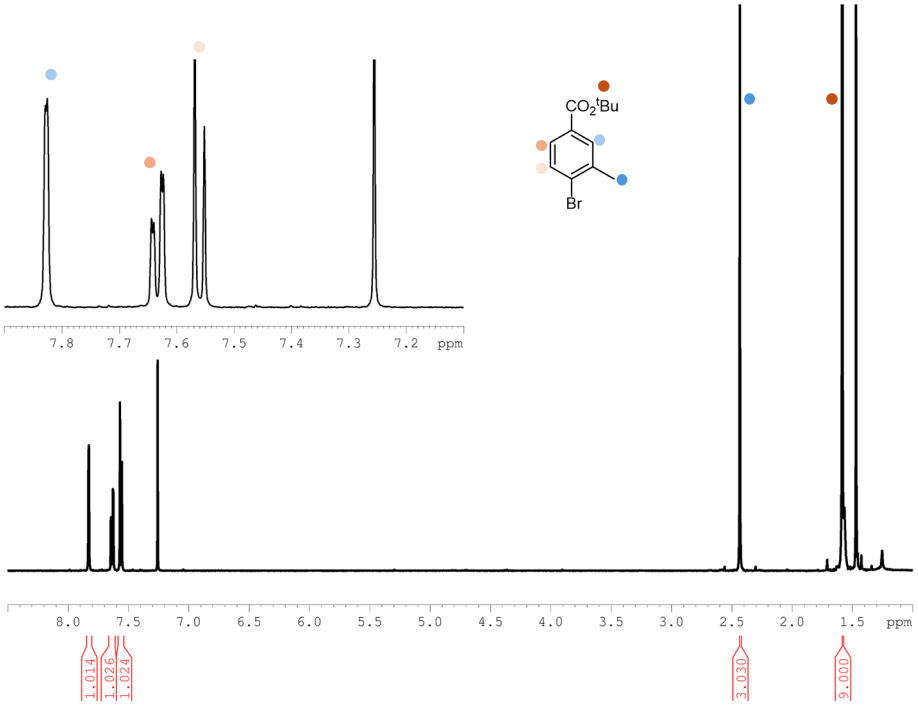

Figure C.26: ^{1}H NMR spectrum of ***t***ert-butyl 4-bromo-3-methylbenzoate in $CDCl_3$

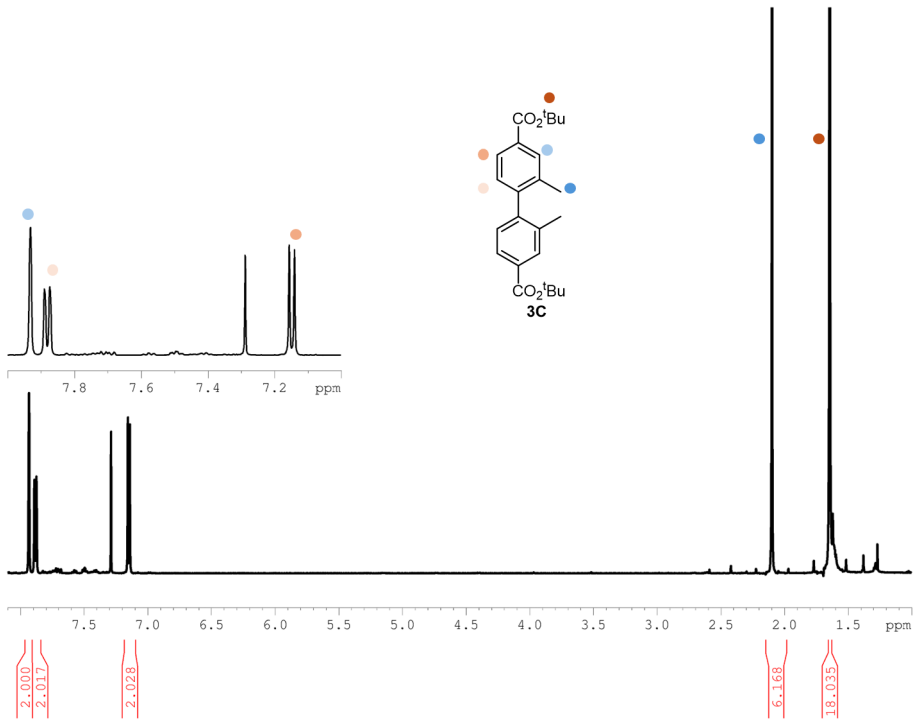

Figure C.27: ^{1}H NMR spectrum of compound 3C.

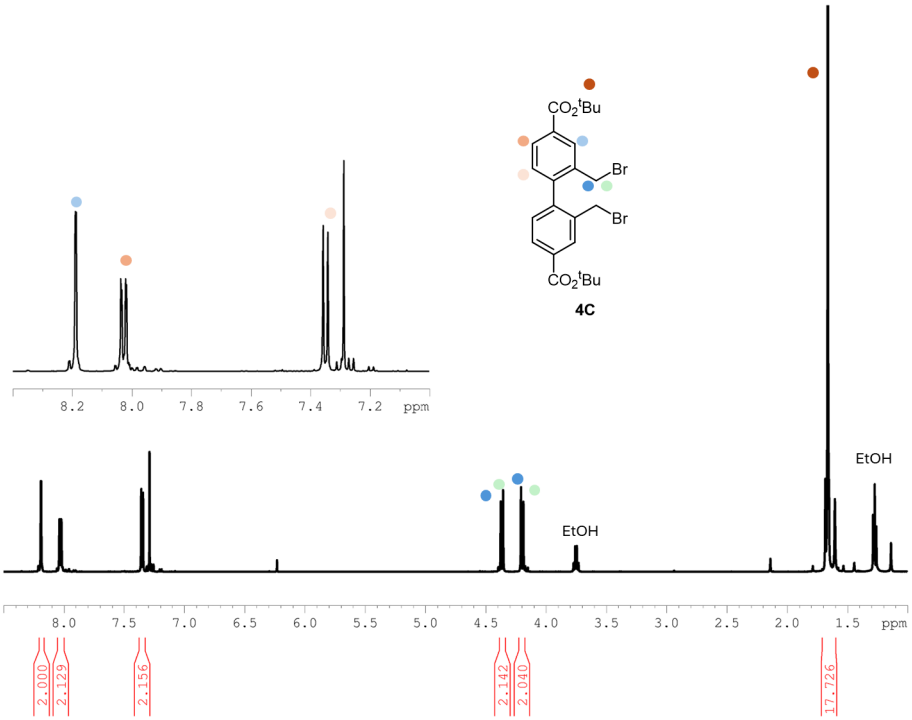

Figure C.28: ^{1}H NMR spectrum of compound 4C in $CDCl_3$.

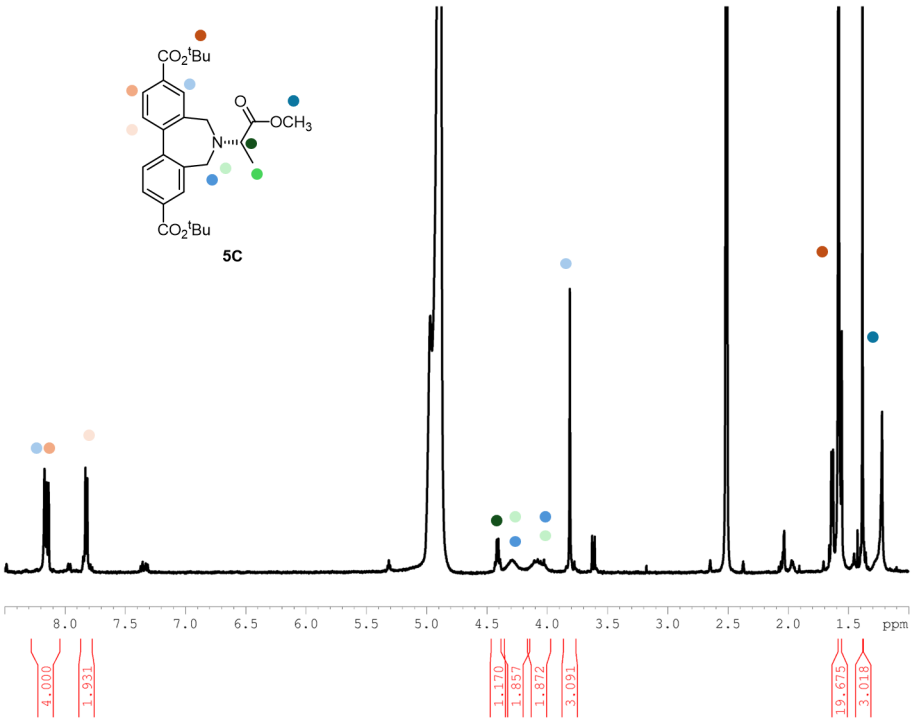

Figure C.29: ^{1}H NMR spectrum of the intermediate 5C in DMSO-d_6

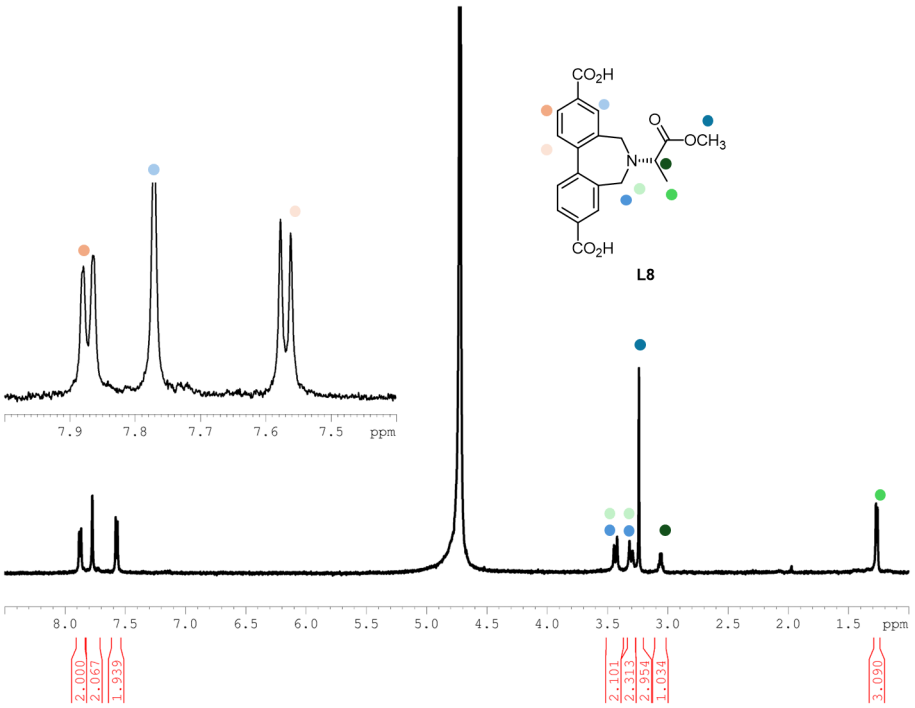

Figure C.30: ^{1}H NMR spectrum of the ^{7}N-bpdc-Ala in NaOD/D_2O

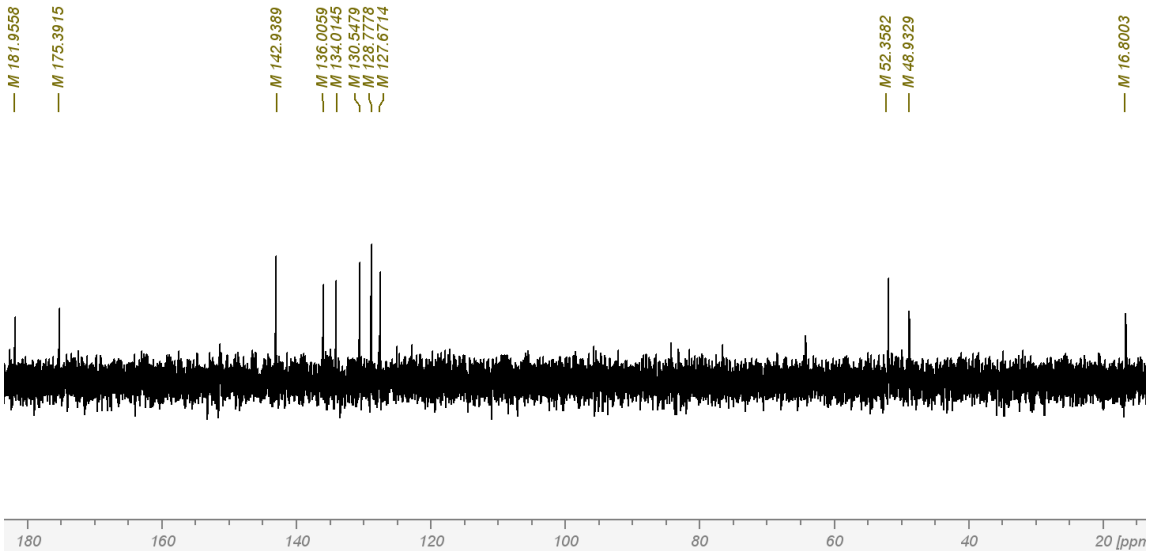

Figure C.31: ^{13}C NMR spectrum of the ^{7}N-bpdc-Ala in NaOD/D_2O

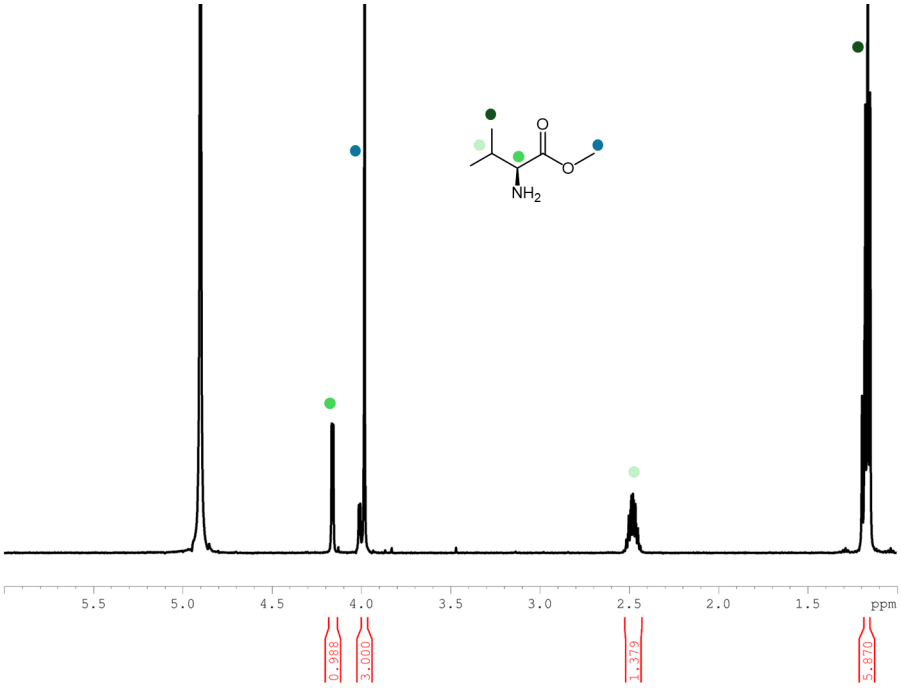

Figure C.32: ^{1}H NMR spectrum of Val-OMe in D_2O.

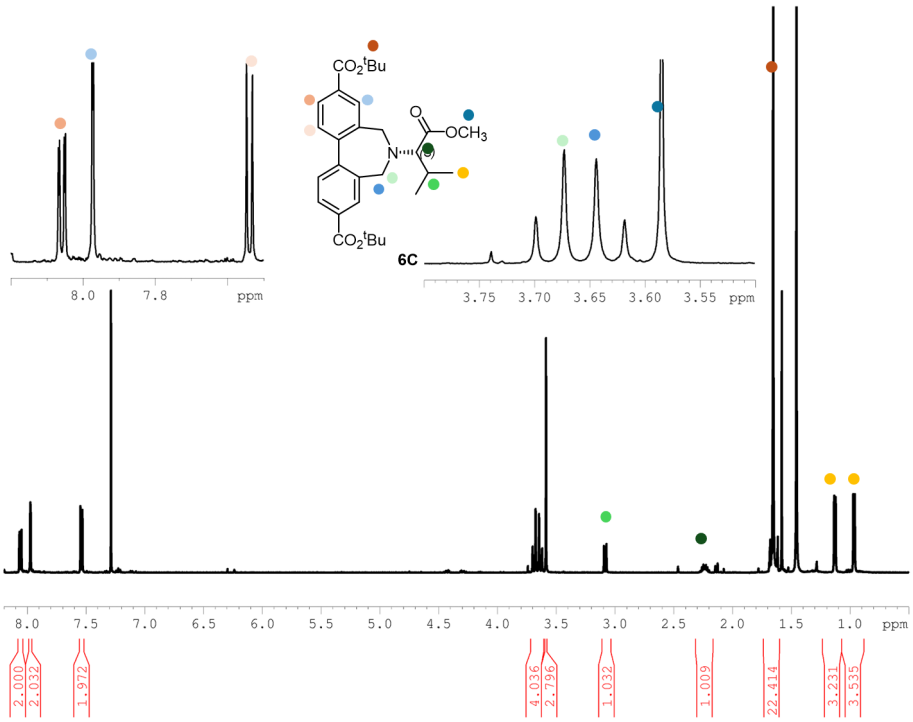

Figure C.33: ^{1}H NMR spectrum of the intermediate 6C in $CDCl_3$

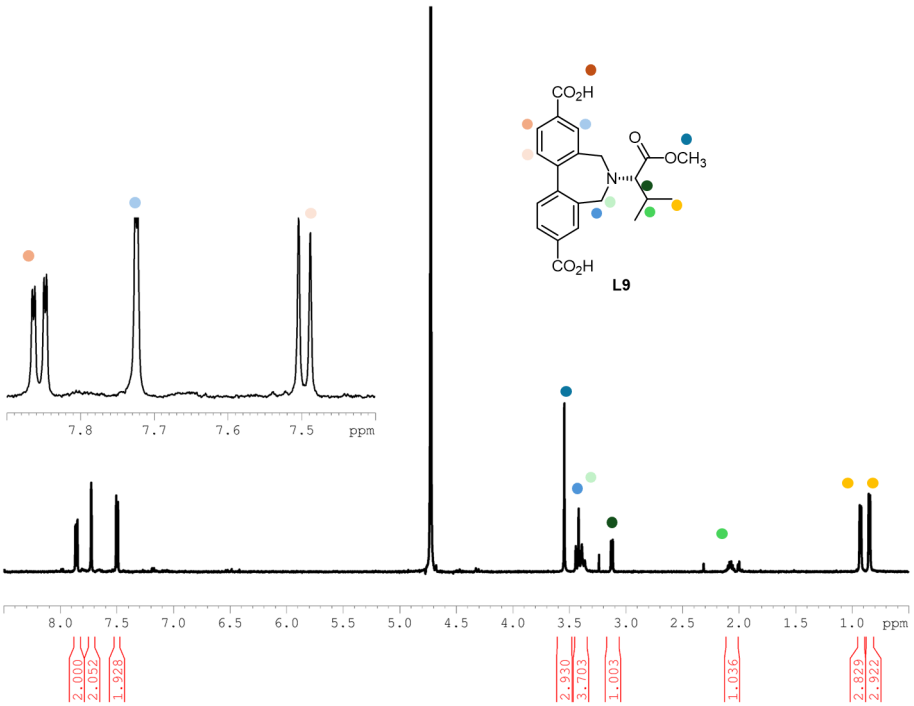

Figure C.34: ^{1}H NMR spectrum of the ^{7}N-bpdc-Val (**L9**) in NaOD/D_2O

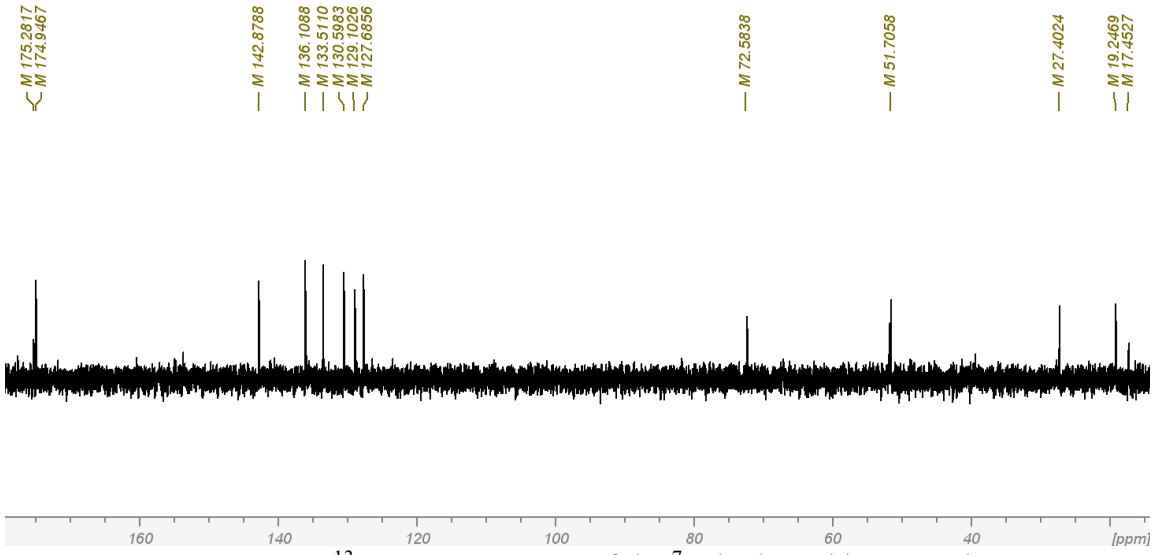

Figure C.35: ^{13}C NMR spectrum of the ^{7}N-bpdc-Val in NaOD/D_2O.

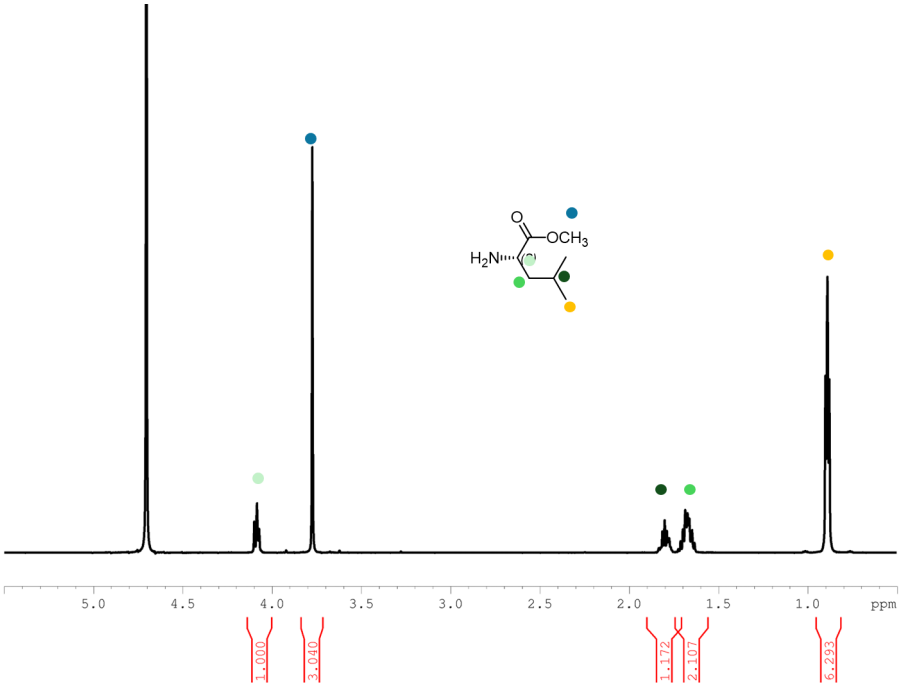

Figure C.36: ^{1}H NMR spectrum of Leu-OMe in D_2O.

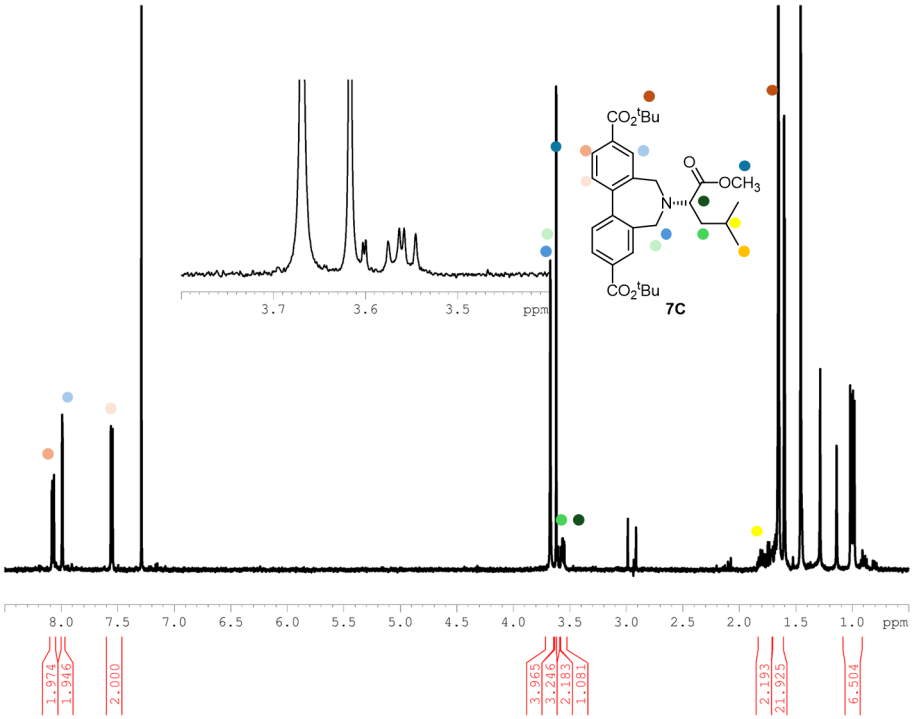

Figure C.37: ^{1}H NMR spectrum of the intermediate 7C in $CDCl_3$

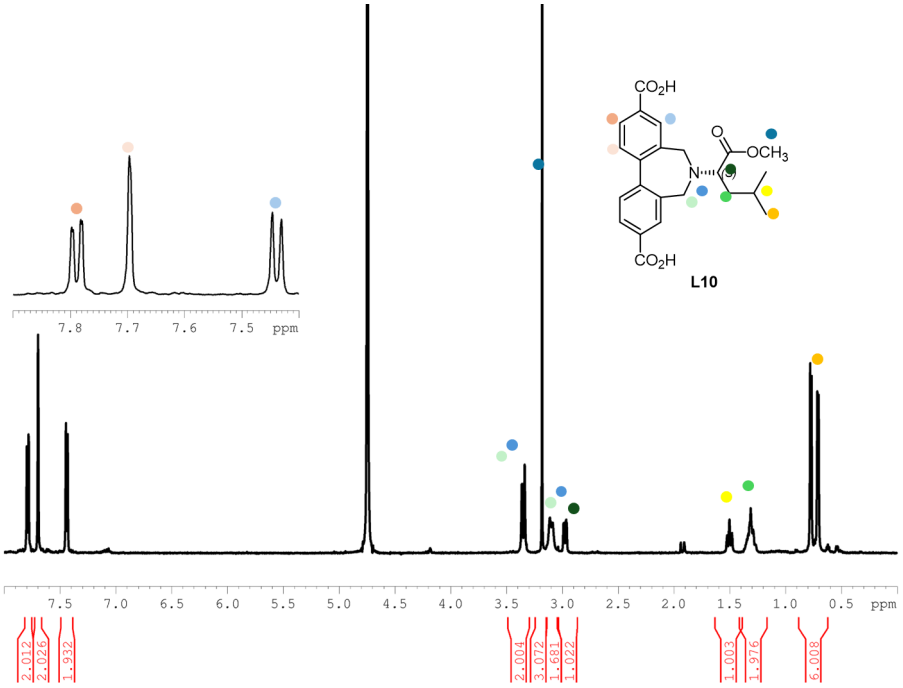

Figure C.38: ^{1}H NMR spectrum of the ^{7}N-bpdc-Leu (**L10**) in NaOD/D_2O

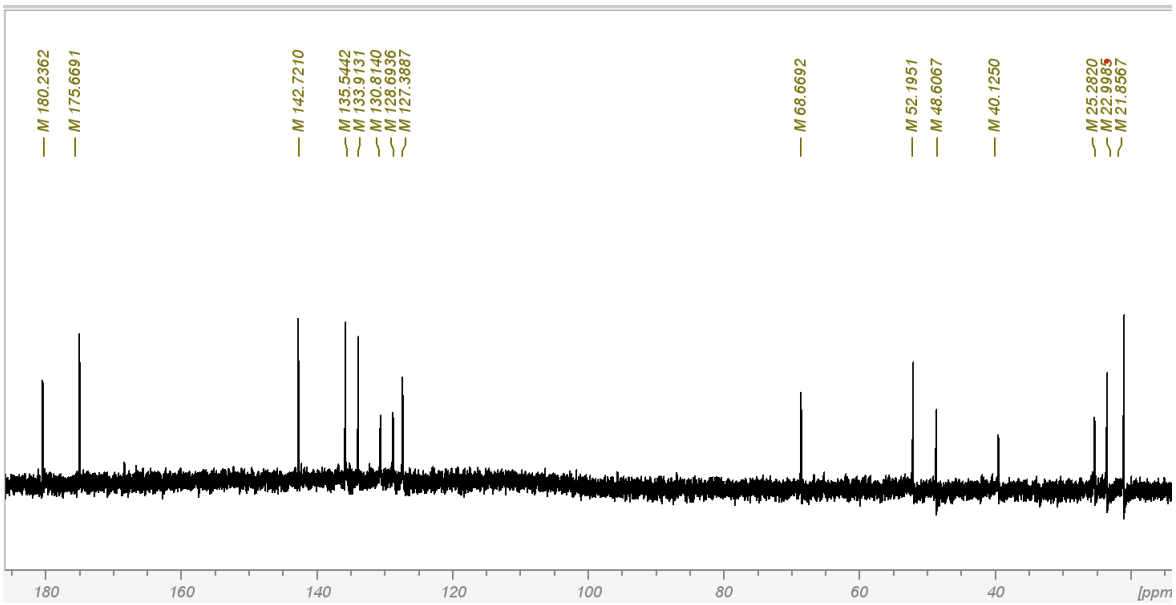

Figure C.39: ^{13}C NMR spectrum of the ^{7}N-bpdc-Leu (**L10**) in NaOD/D_2O.

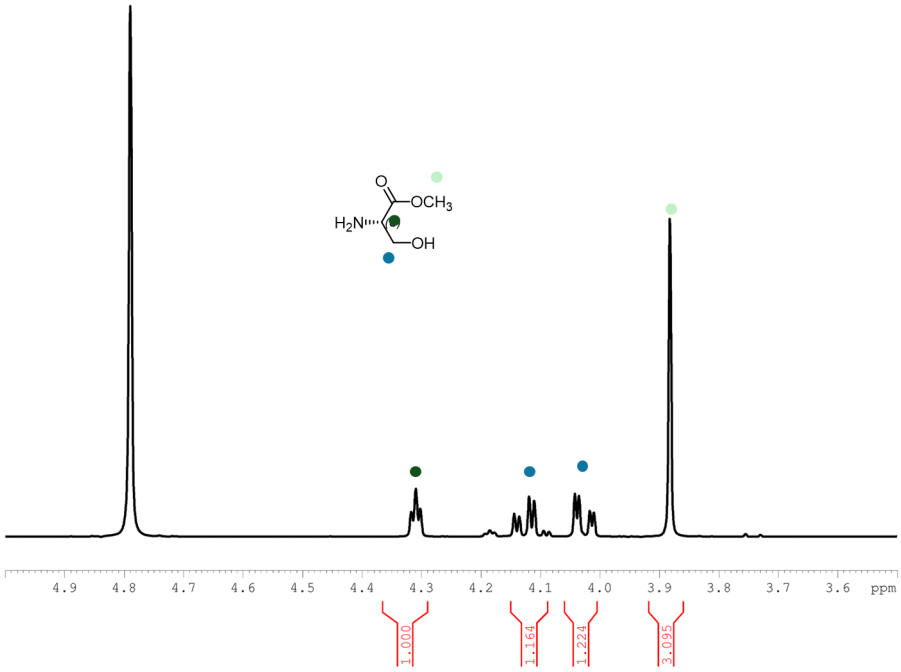

Figure C.40: ^{1}H NMR spectrum of Ser-OMe in D_2O.

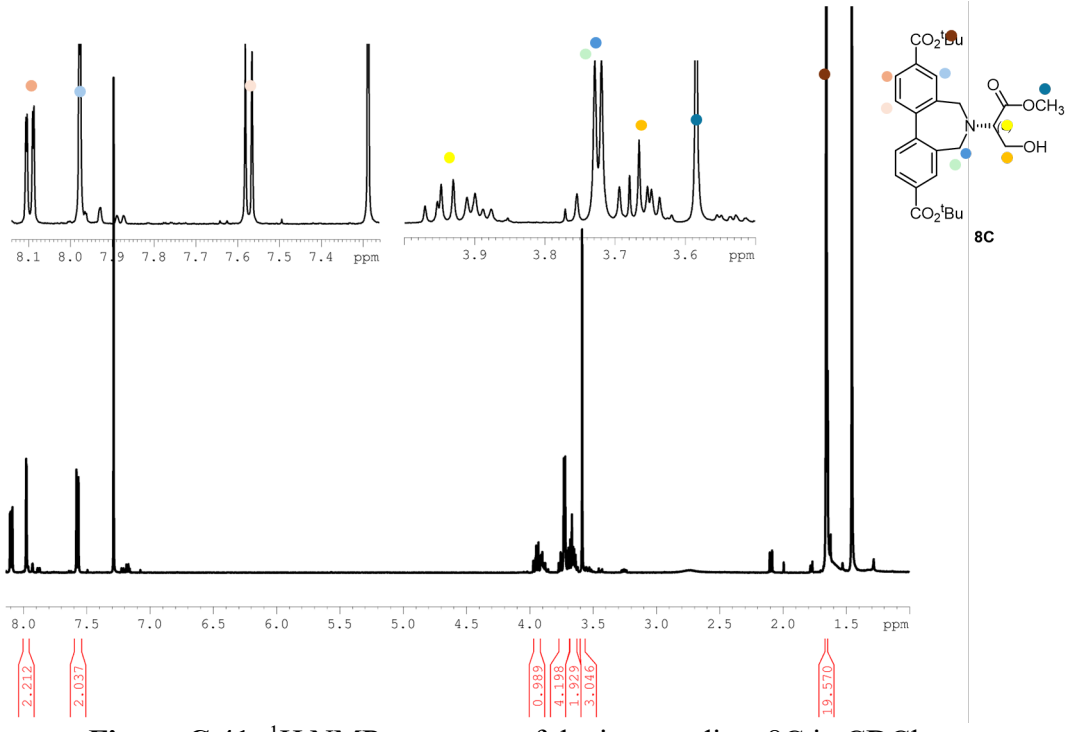

Figure C.41: ^{1}H NMR spectrum of the intermediate 8C in $CDCl_3$

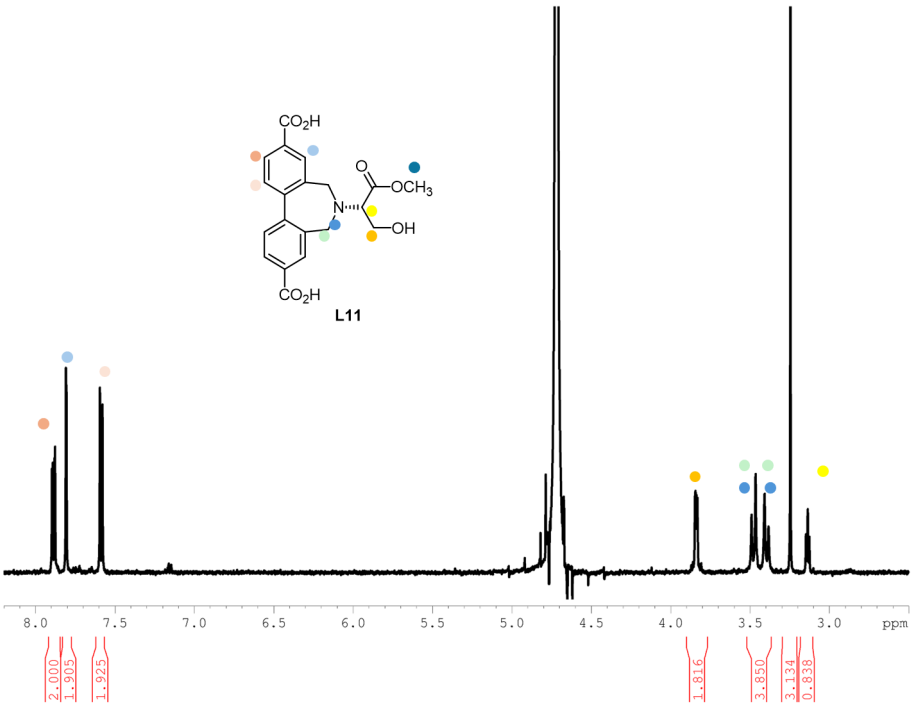

Figure C.42: ^{1}H NMR spectrum of the ^{7}N-bpdc-Ser (**L11**) in NaOD/D_2O

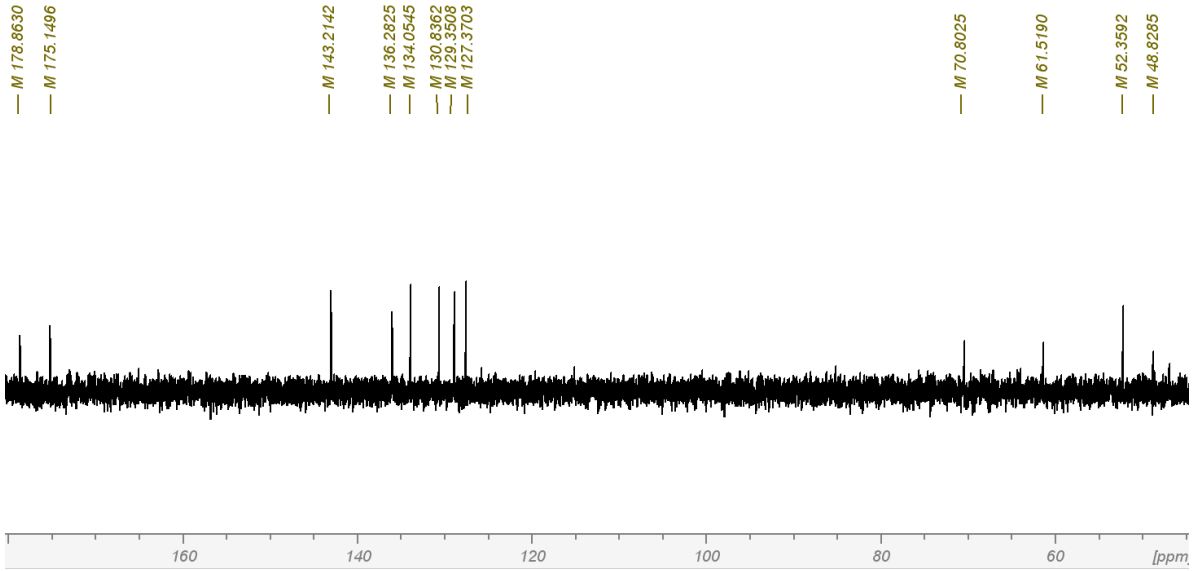

Figure C.43: ^{13}C NMR spectrum of the ^{7}N-bpdc-Ser in NaOD/D_2O.

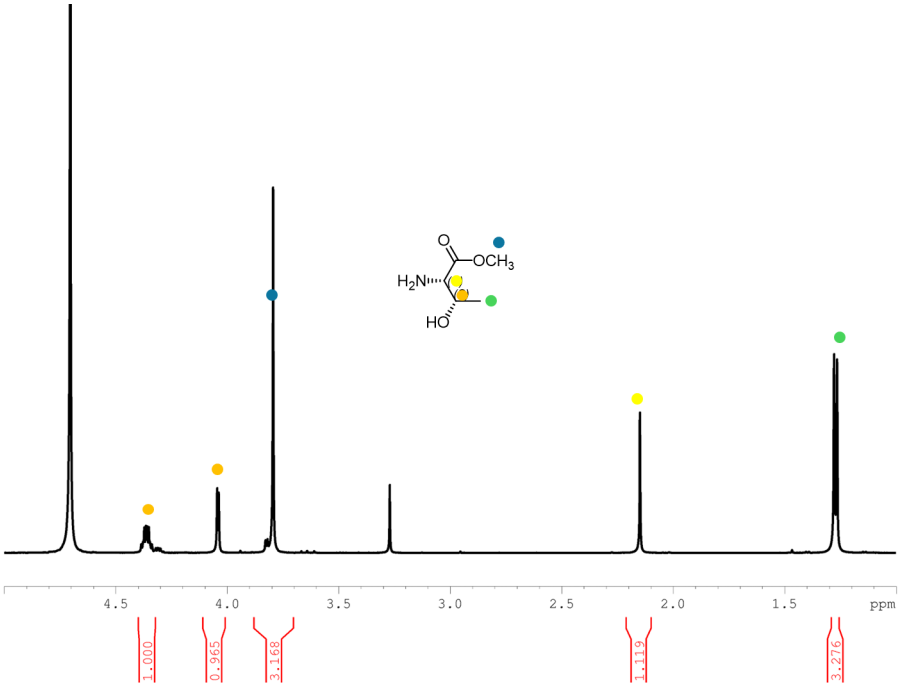

Figure C.44: ^{1}H NMR spectrum of Thr-OMe in D_2O.

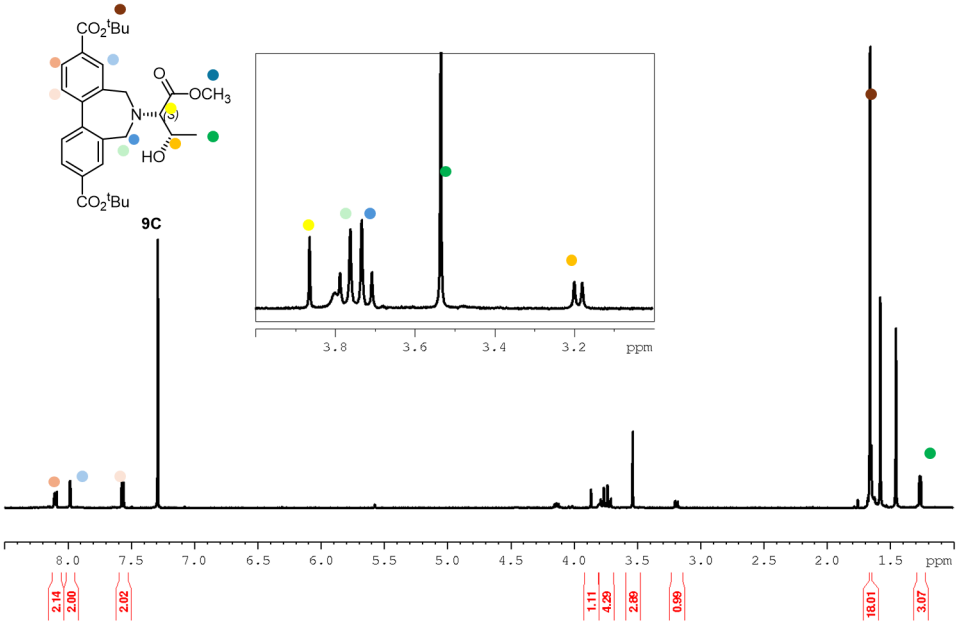

Figure C.45: ^{1}H NMR spectrum of the intermediate 9C in $CDCl_3$

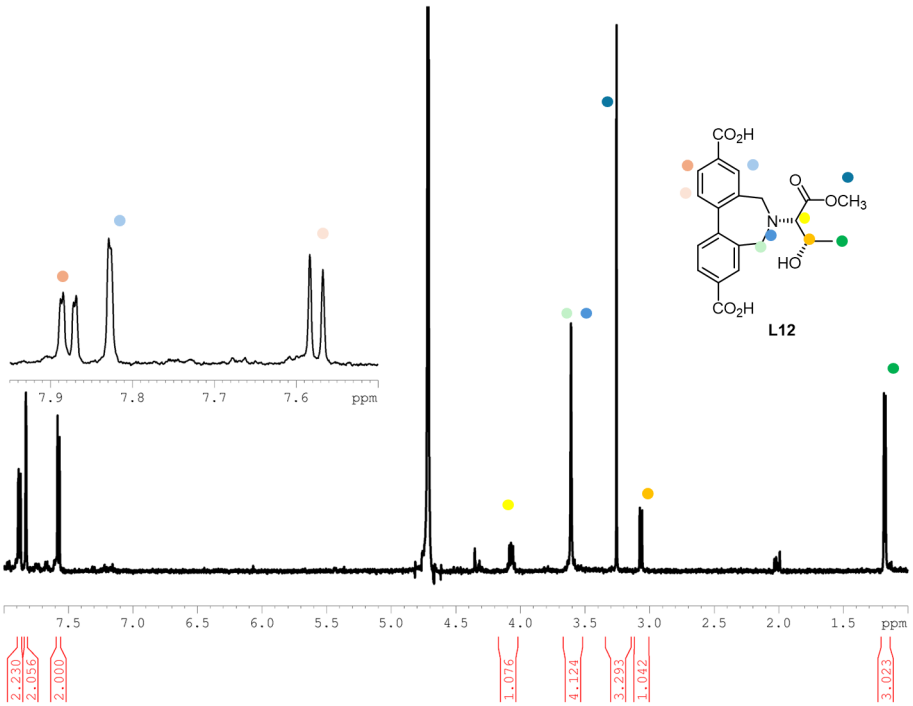

Figure C.46: ^{1}H NMR spectrum of the ^{7}N-bpdc-Thr (**L12**) in NaOD/D_2O

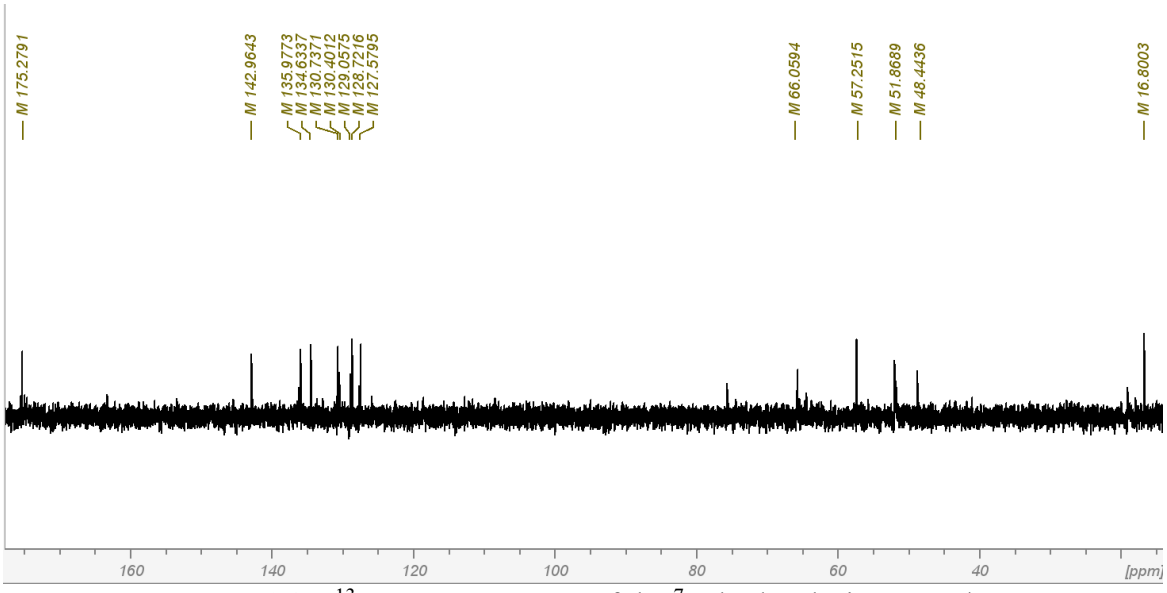

Figure C.47: ^{13}C NMR spectrum of the ^{7}N-bpdc-Thr in NaOD/D_2O

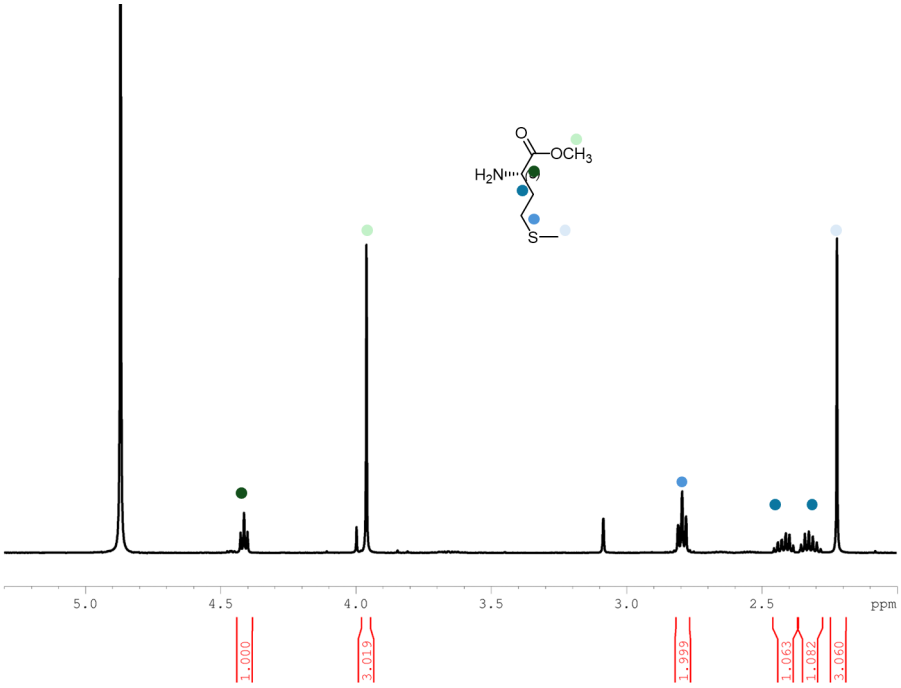

Figure C.48: ^{1}H NMR spectrum of Met-OMe in D_2O.

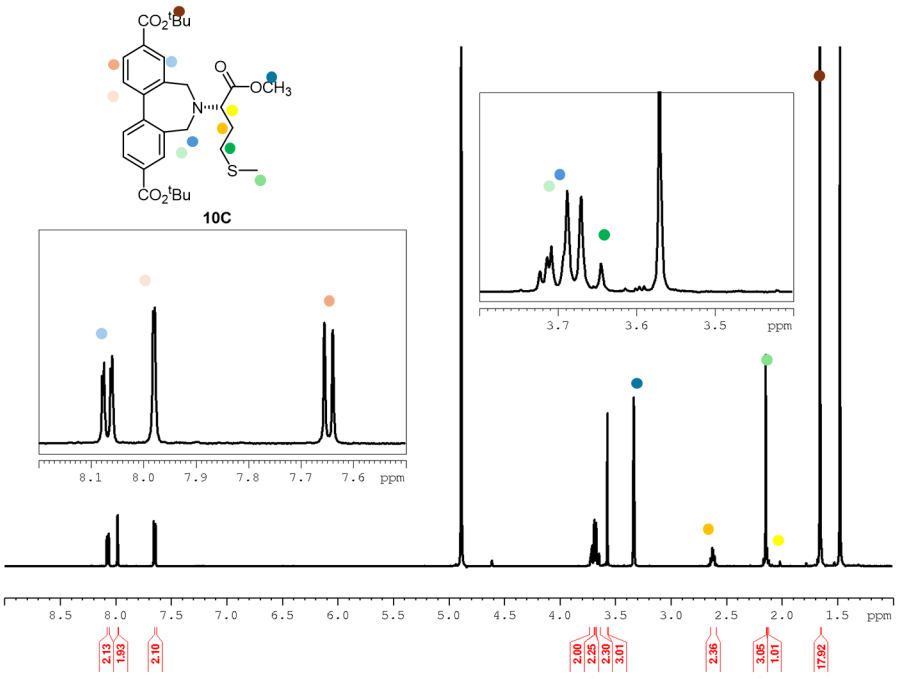

Figure C.49: ^{1}H NMR spectrum of the intermediate 10C in MeOD

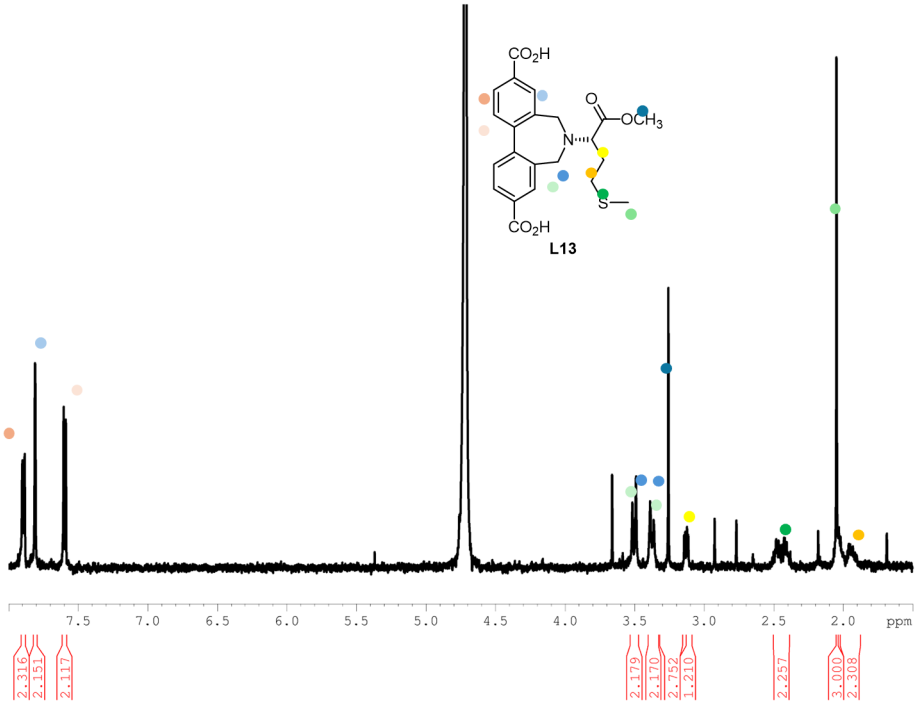

Figure C.50: ^{1}H NMR spectrum of the ^{7}N-bpdc-Met (**L13**) in NaOD/D_2O

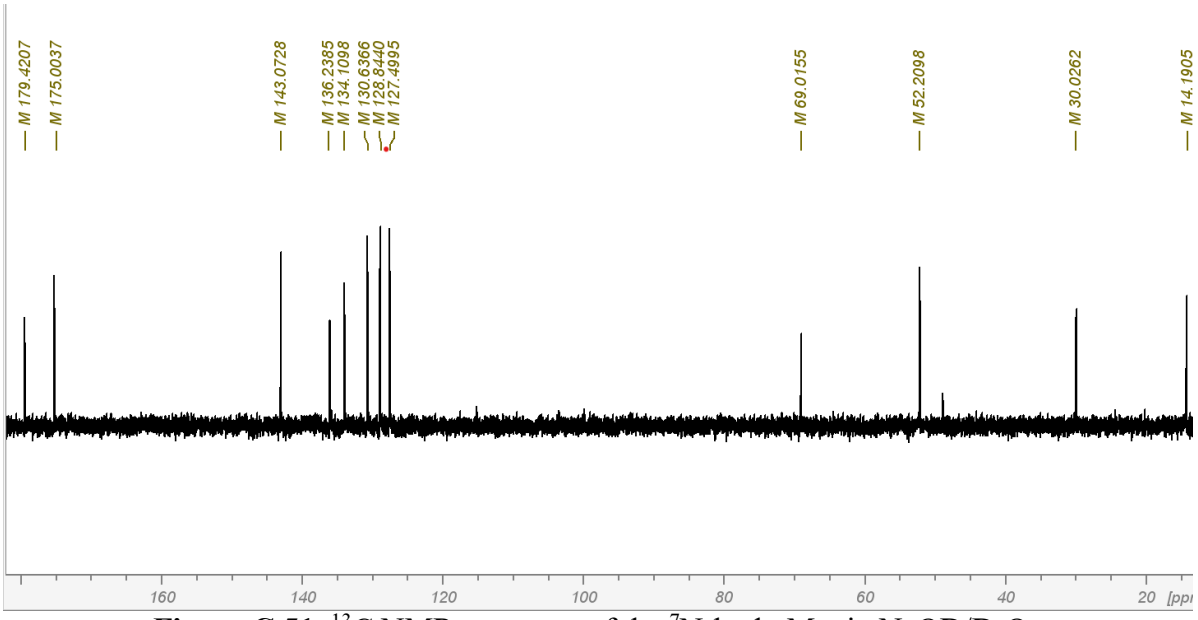

Figure C.51: ^{13}C NMR spectrum of the ^{7}N-bpdc-Met in NaOD/D_2O

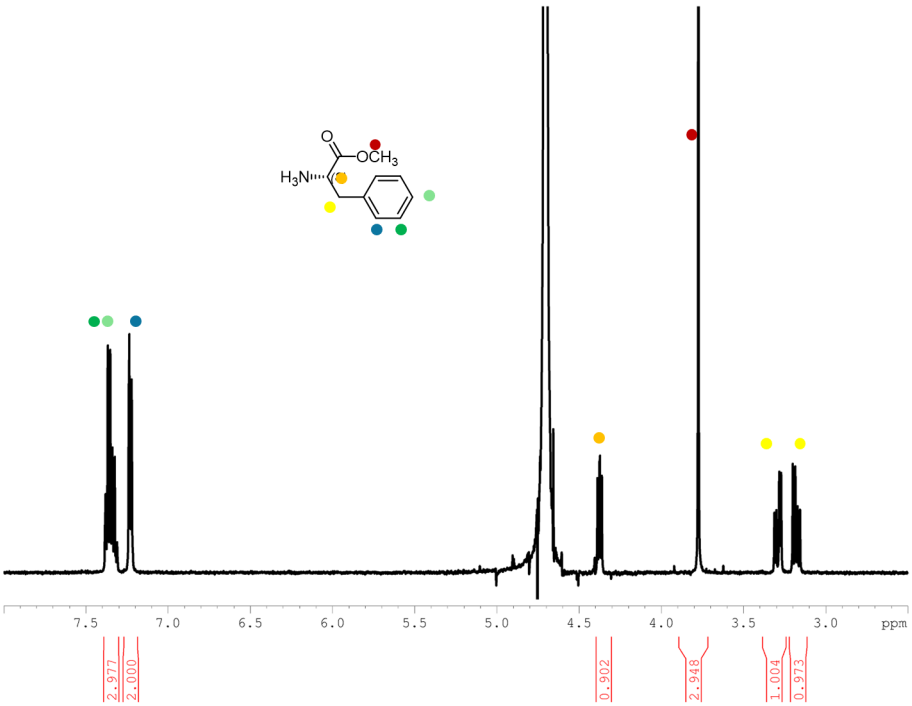

Figure C.52: ^{1}H NMR spectrum of Phe-OMe in D_2O.

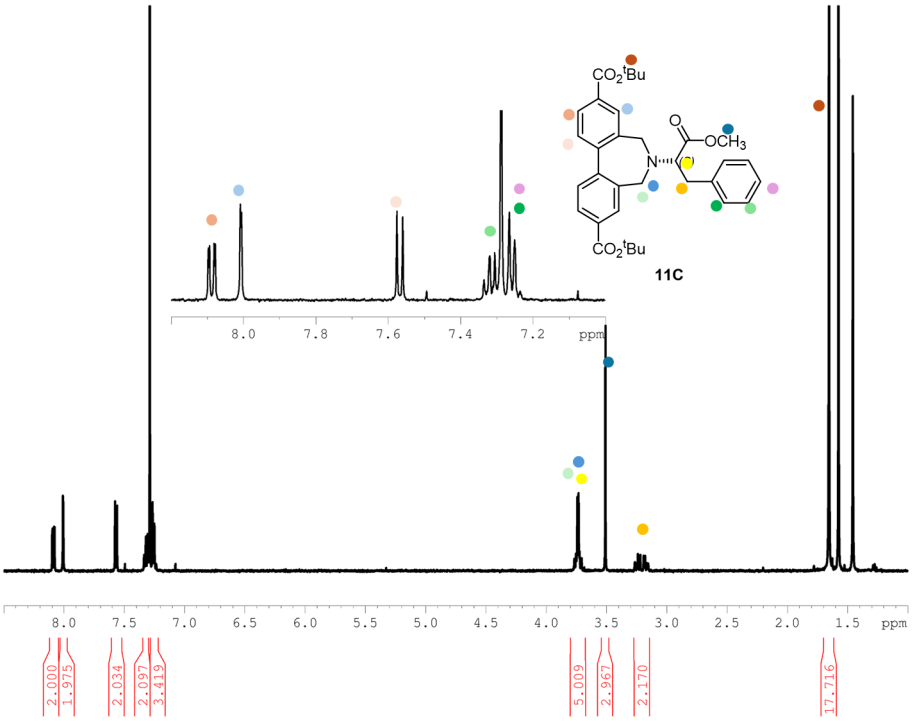

Figure C.53: ^{1}H NMR spectrum of compound 11C in D_2O.

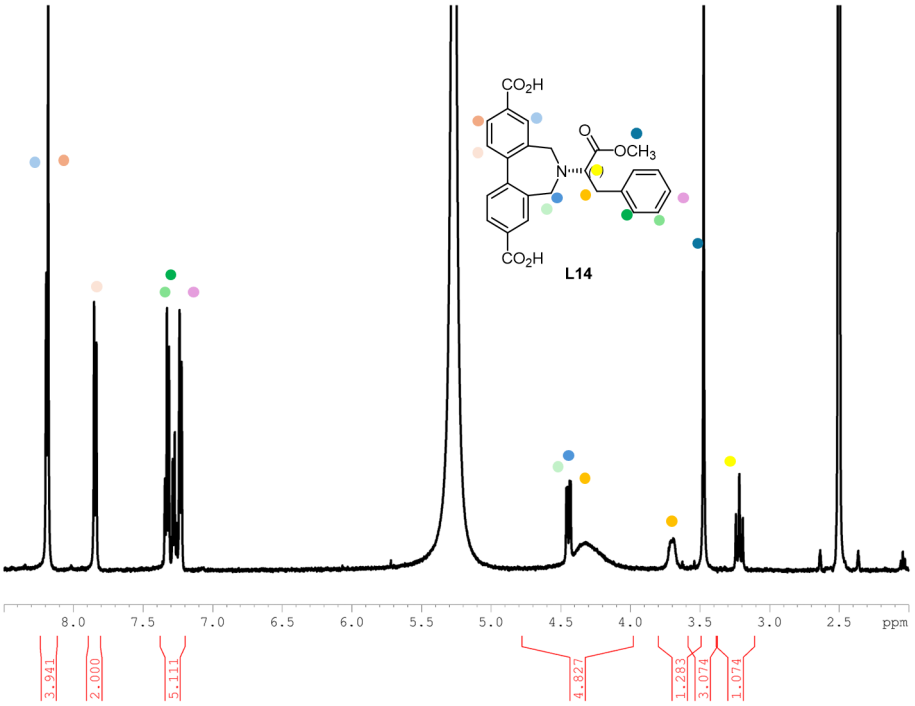

Figure C.54: ^{1}H NMR spectrum of the ^{7}N-bpdc-Phe in DMSO-d$_6$

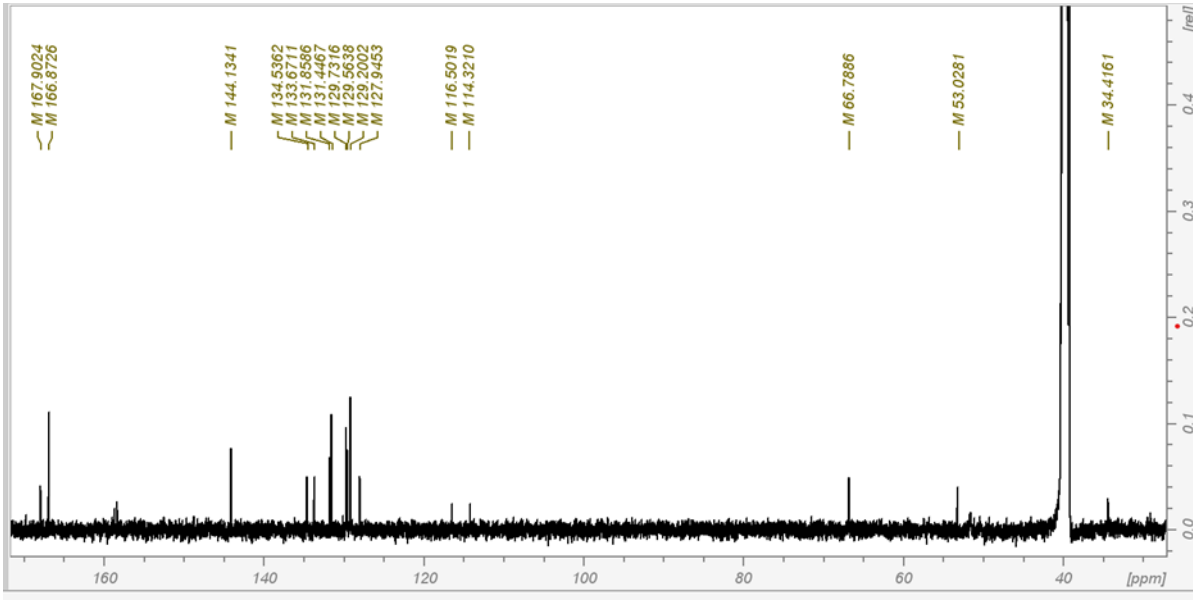

Figure C.55: ^{13}C NMR spectrum of the ^{7}N-bpdc-Phe in DMSO-d$_6$.

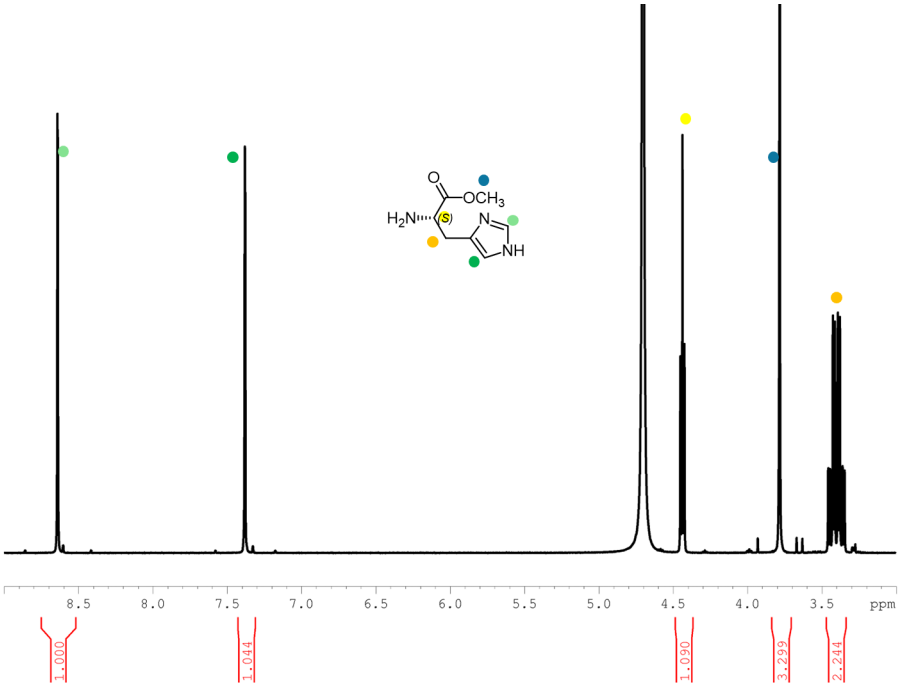

Figure C.56: ^{1}H NMR spectrum of His-OMe in D_2O.

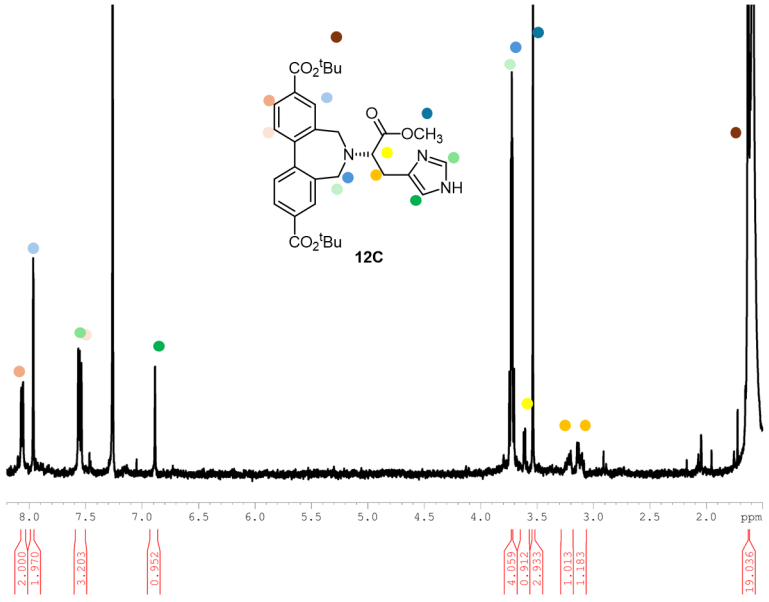

Figure C.57: ^{1}H NMR spectrum of compound 12C in $CDCl_3$

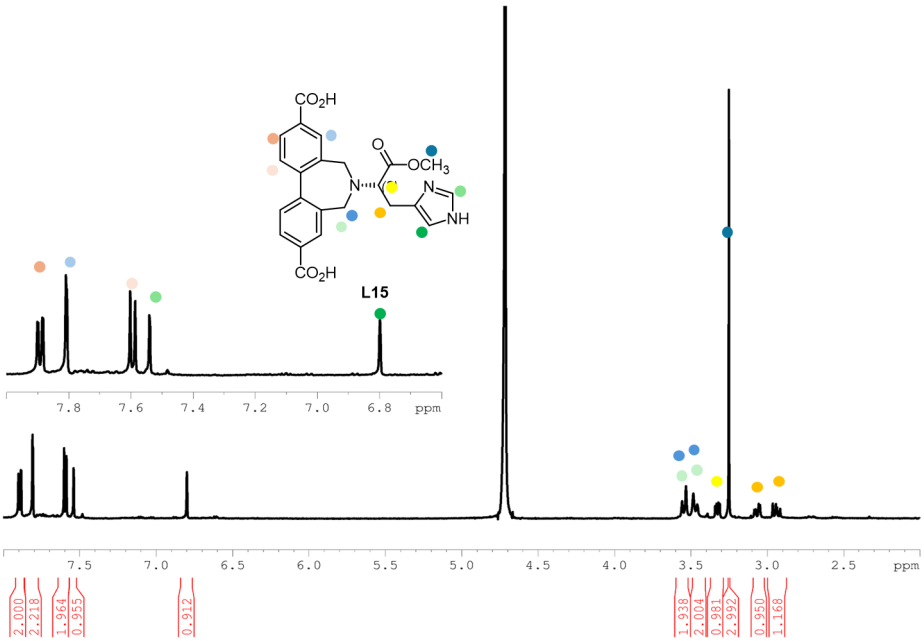

Figure C.58: ^{1}H NMR spectrum of the ^{7}N-bpdc-His in NaOD/D_2O

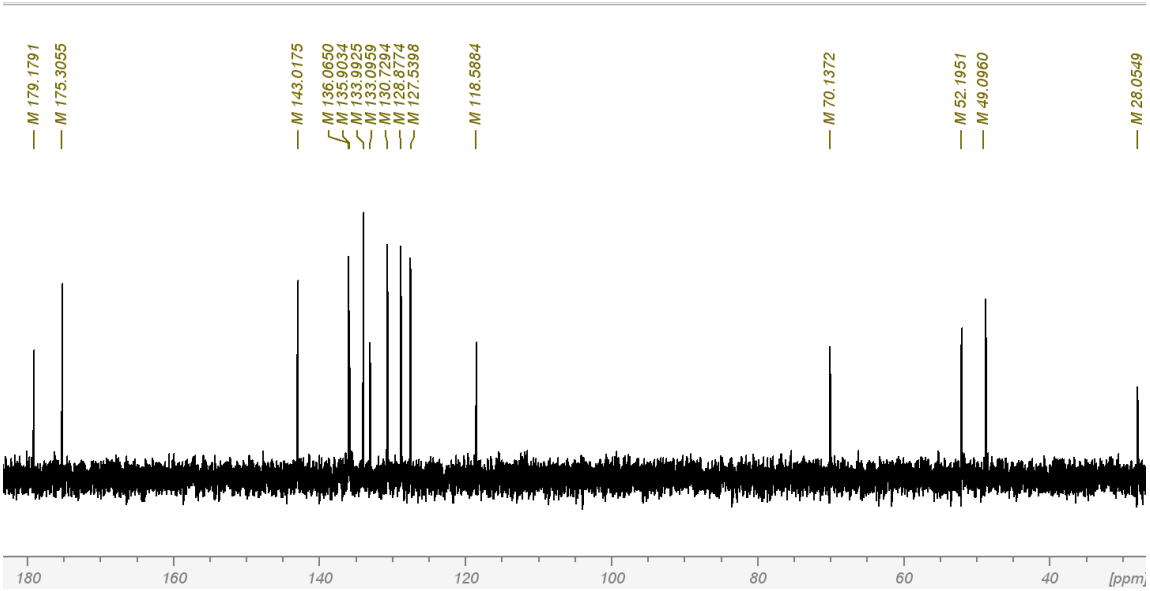

Figure C.59: ^{13}C NMR spectrum of the ^{7}N-bpdc-His in NaOD/D_2O

C.18 Synthesis of H_3hmtt

Synthesis of compound 1E

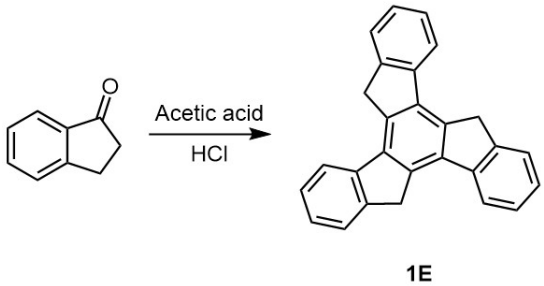

Figure C.60: Synthetic pathway to compound 1E

Acetic acid (20 mL) and conc. HCl (10 mL) were added to 1-indanone (5.0 g, 37.90 mmol), and the mixture was refluxed overnight. The solution was poured onto ice slurry and the brown precipitate was filtered off and successively washed with water, acetone, and CH_2Cl_2, and then dried to give a light-yellow powder (11.70 g, 34.16 mmol, 90%).

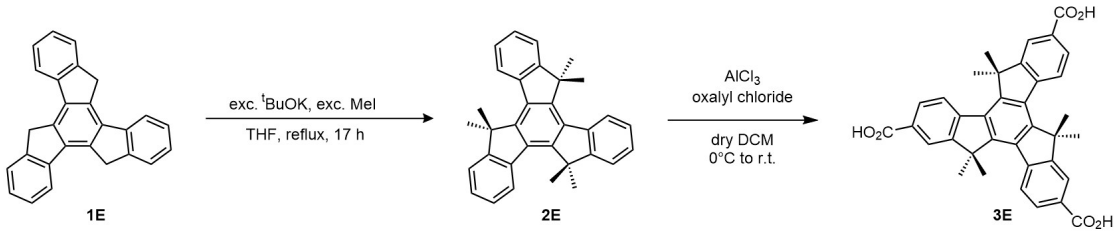

Figure C.61: Synthetic pathway to H_3hmtt.

Synthesis of compound 2E

Under inert atmosphere compound **1E** (2.72 g, 7.94 mmol, 1 eq.) and ^{t}BuOK (17.5 g, 14.3 mol, 18 eq.) were suspended in anhydrous THF (150 mL). Methyl iodide (9.9 mL, 0.158 mmol, 20 eq.) was added to the brown suspension, and the reaction mixture was refluxed for 17 h. The mixture was allowed to cool to room temperature; precipitates were filtered off and extracted with ethyl acetate (200 mL). The organic phase was washed with 0.2 M aqueous HCl (2 x 100 mL), sat. aqueous $NaHCO_3$ (2 x 100 mL) and distilled water (2 x 100 mL). The combined organic phases were dried over $MgSO_4$, and the solvent was concentrated at 45 °C. The forming precipitate was filtered off and dried at 50 °C to yield the product as a green crystalline solid. Yield: 2.70 g, 6.33 mmol, 80%

Ligand 3E synthesis

Under the N_2 atmosphere, $AlCl_3$ (1.77 g, 10.29Lmmol, 6.1 eq.) was suspended in anhydrous dichloromethane (7 mL). The yellow suspension was cooled to 0 °C, and oxalyl chloride (1.4 mL, 15.9 mmol, 9.4 eq.) was added dropwise. The reaction mixture was stirred for 30 min, and a solution of **2E** (720.0 mg, 1.69 mmol, 1.0 eq.) in anhydrous dichloromethane (10 mL) was added dropwise. The reaction was refluxed for 4 hours. Then, the dark suspension was cooled to 0 °C and water was slowly added. The reaction was allowed to warm to room temperature, and stirring was continued overnight. The DCM was removed under reduced pressure, and the solid was collected by filtration, washed with water, and air-dried overnight. DCM residues were still in the sample, so it was dried using the freeze-dry desiccator. Yield: 771.0 mg, 1.38 mmol, 82%.

C.19 H_3hmtt and its intermediates ^{1}H NMR spectroscopic data

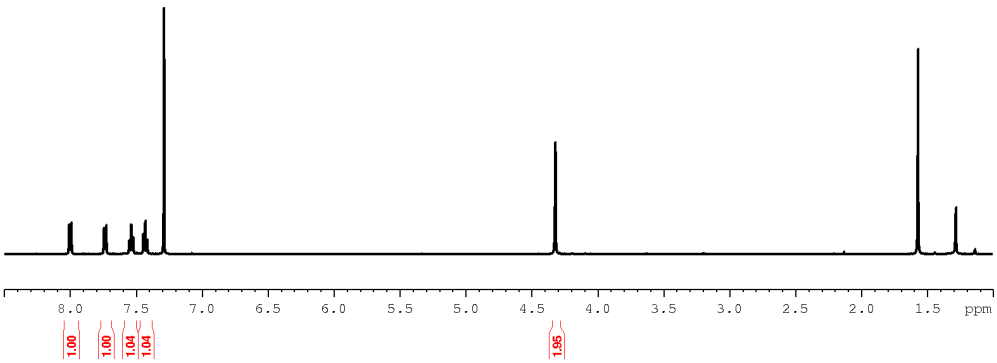

Figure C.62: ^{1}H NMR of compound **1E** in $CDCl_3$.

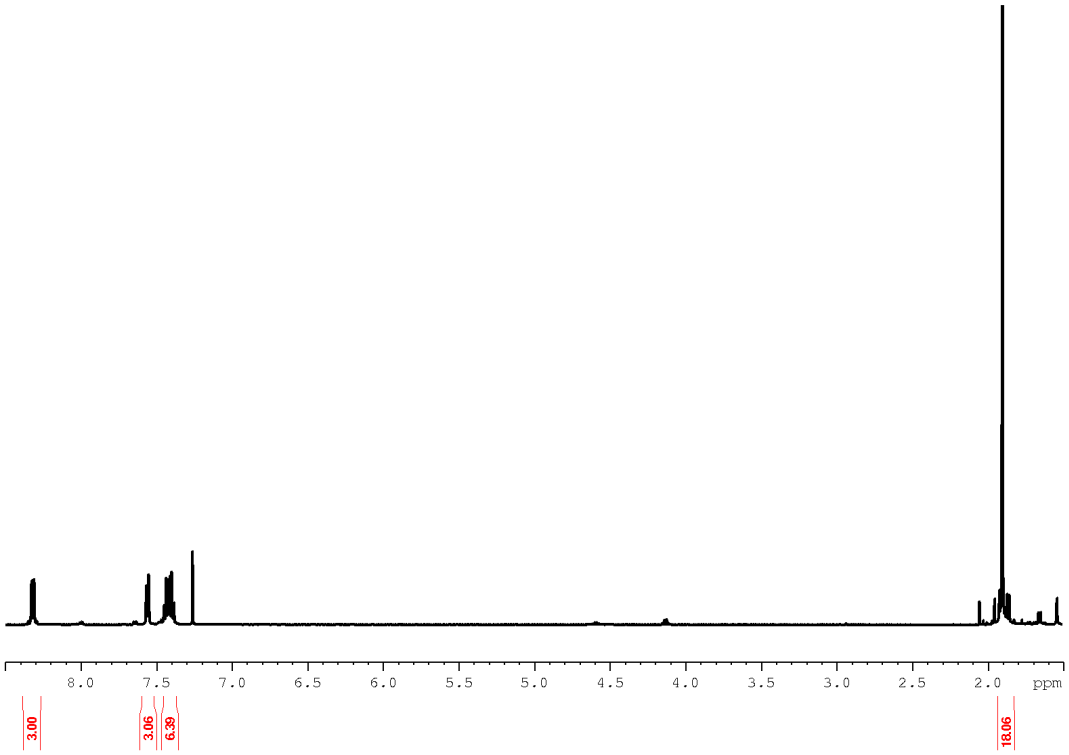

Figure C.63: ^{1}H NMR of compound **2E** in $CDCl_3$.

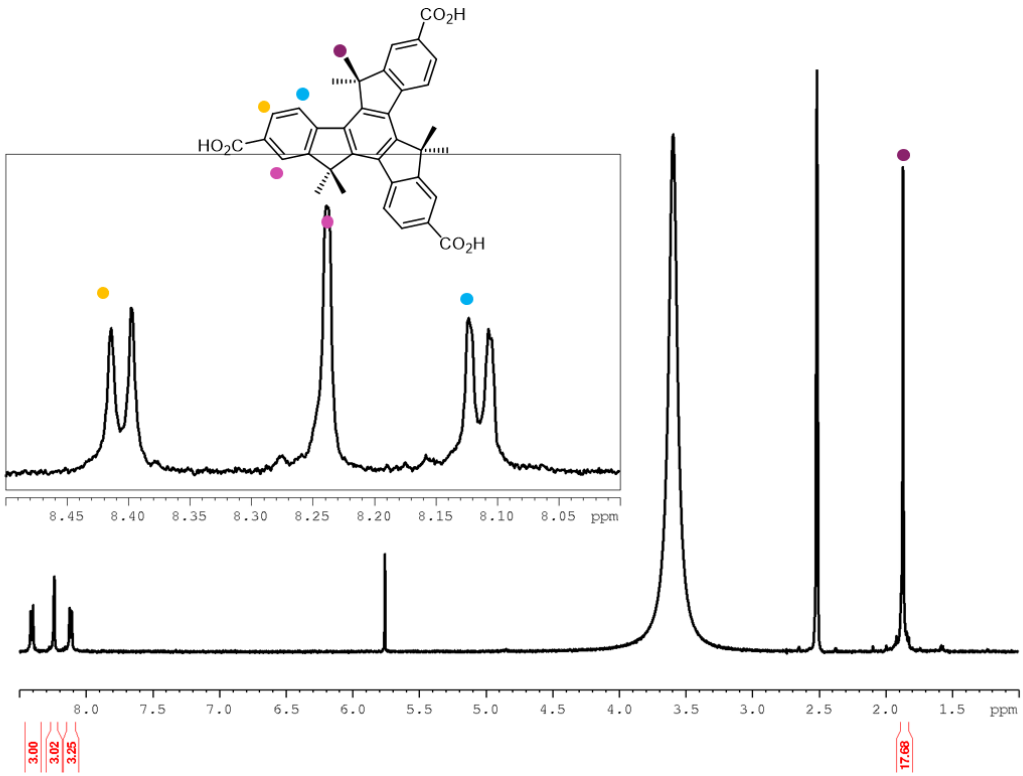

Figure C.64: ^{1}H NMR of ligand 3E (H_3hmtt) in DMSO-d_6.

C.20 $[Zn_4O(hmtt)_{4/3}(bpdc)_{1/2}(^{5}N\text{-bdc-X-OH})_{1/2}]$ MOFs ^{1}H NMR spectroscopic data

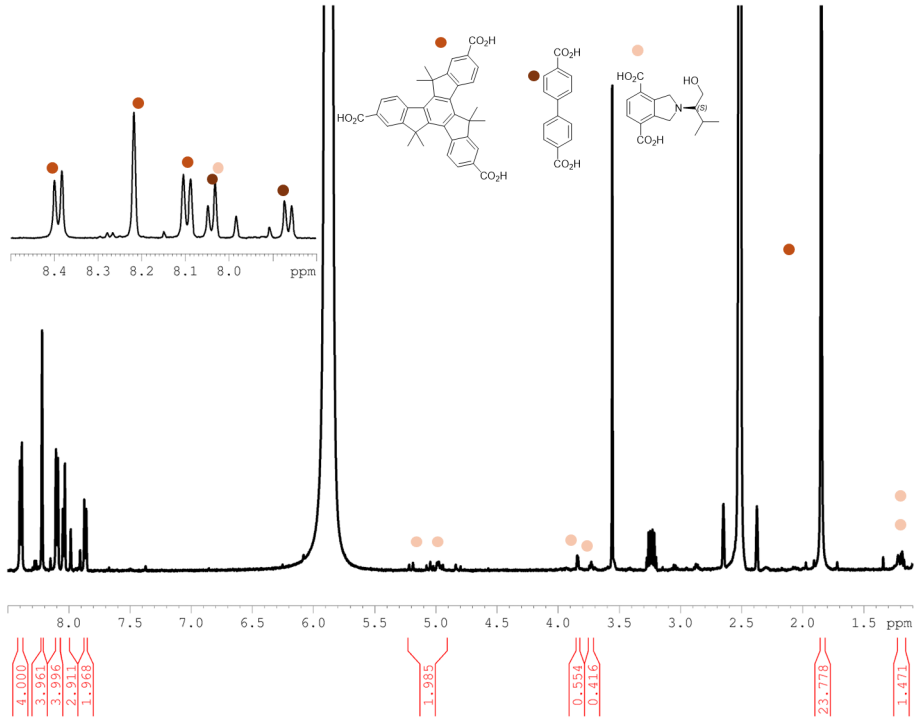

Figure C.65: ^{1}H NMR spectrum of $[(hmtt)_{4/3}(^{5}N\text{-bdc-Val-OH})_{1/2}(bpdc)_{1/2}]$ in DCl/DMSO-d_6 (23 µL/ 1 mL)

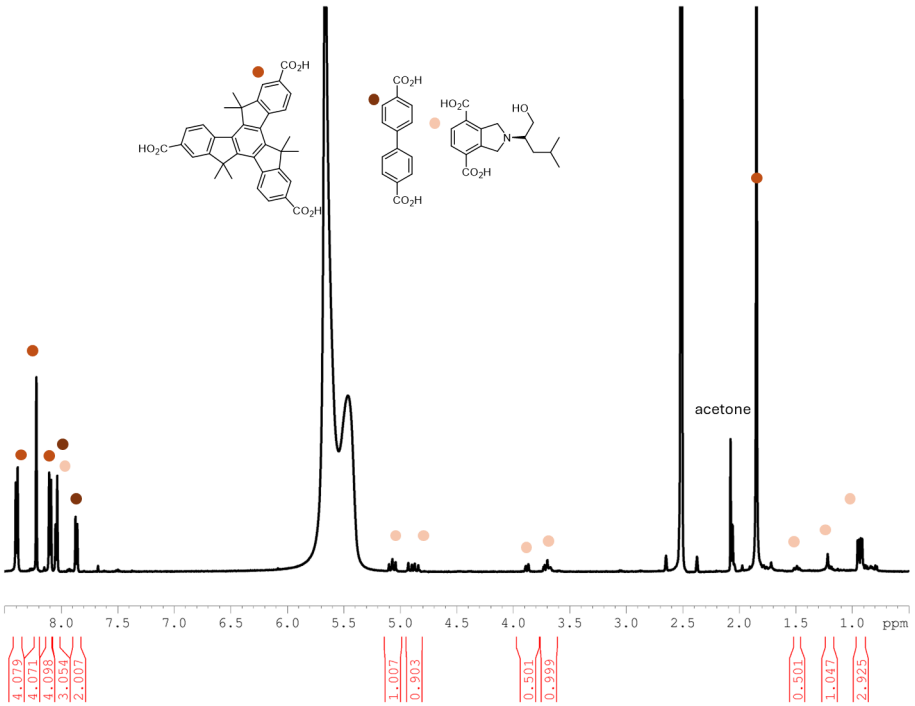

Figure C.66: ^{1}H NMR spectrum of $[(hmtt)_{4/3}(^{5}N\text{-bdc-Leu-OH})_{1/2}(bpdc)_{1/2}]$ in DCl/DMSO-d_6 (23 µL/ 1 mL)

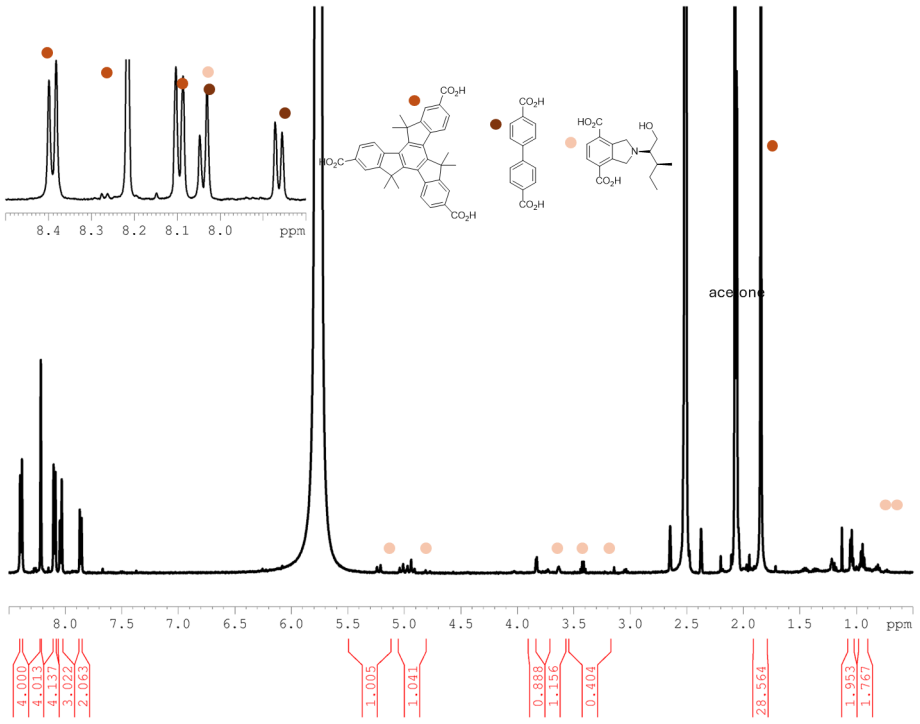

Figure C.67: ^{1}H NMR spectrum of $[(hmtt)_{4/3}(^{5}N\text{-bdc-Ile-OH})_{1/2}(bpdc)_{1/2}]$ in DCl/DMSO-d_6 (23 µL/ 1 mL)

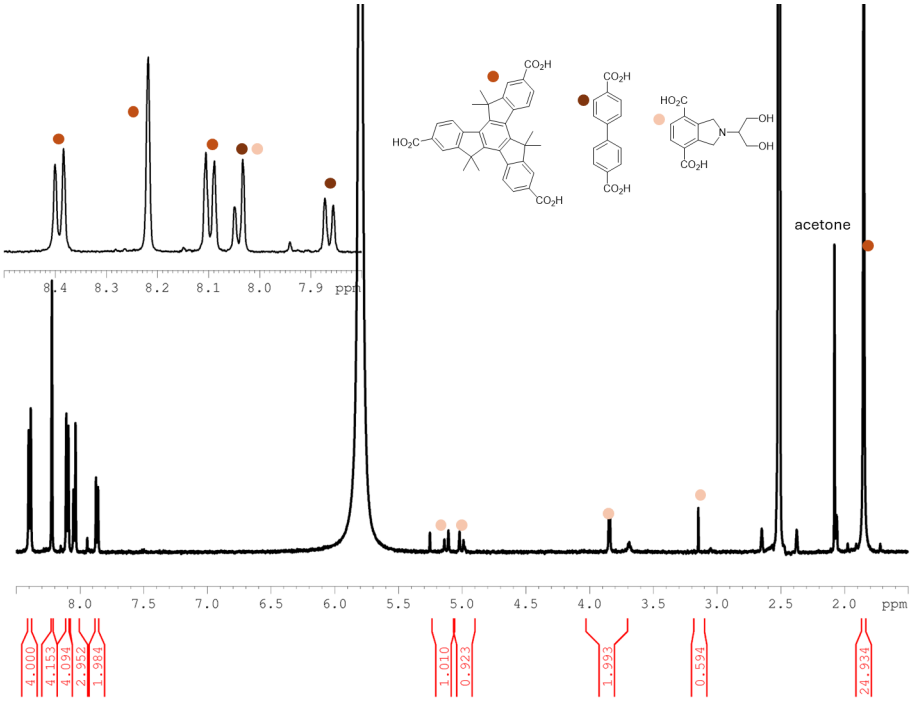

Figure C.68: ^{1}H NMR spectrum of $[(hmtt)_{4/3}(^{5}N\text{-bdc-Ser-OH})_{1/2}(bpdc)_{1/2}]$ in DCl/DMSO-d_6 (23 µL/ 1 mL).

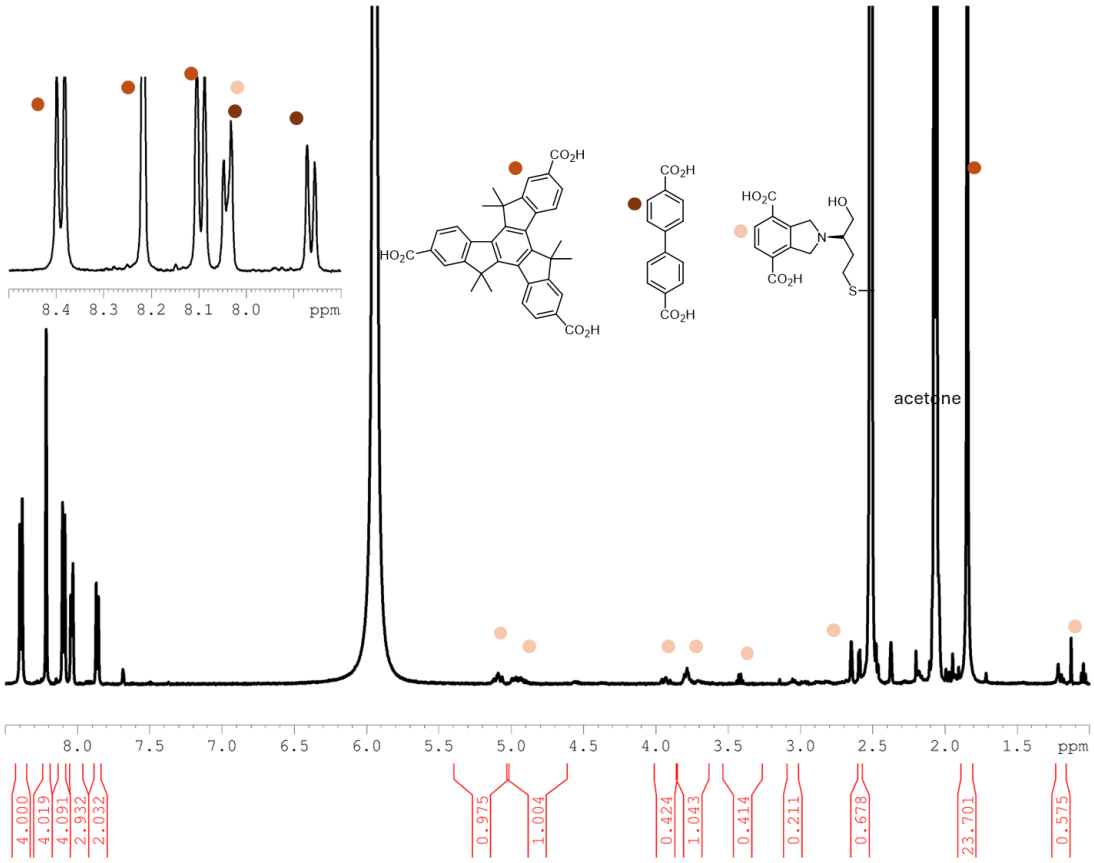

Figure C.69: ^{1}H NMR spectrum of $[(hmtt)_{4/3}(^{5}N\text{-bdc-Met-OH})_{1/2}(bpdc)_{1/2}]$ in DCl/DMSO-d_6 (23 µL/ 1 mL)

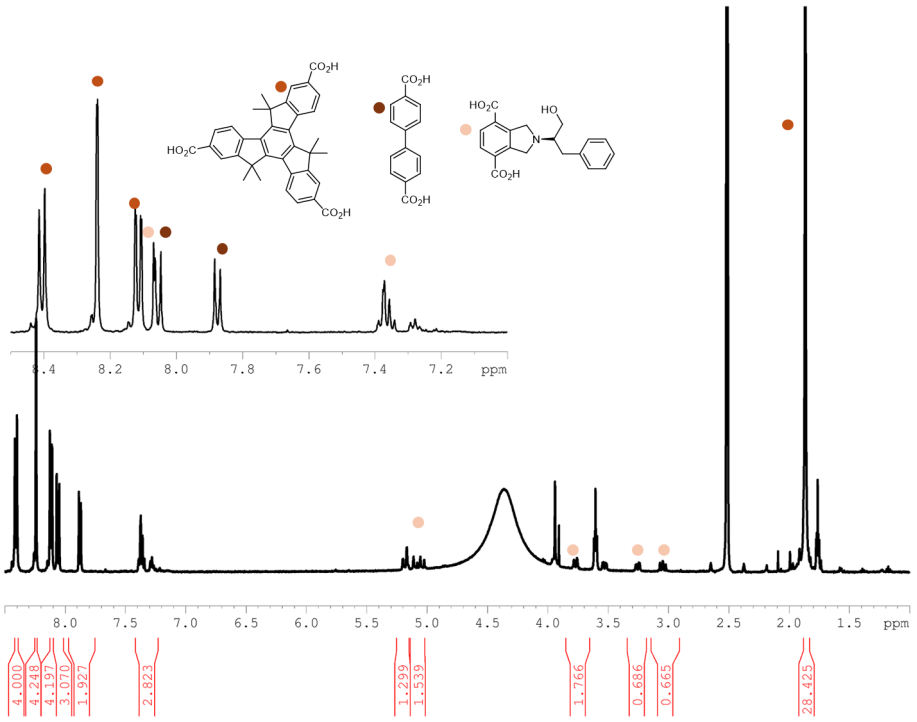

Figure C.70: ^{1}H NMR spectrum of [(hmtt)$_{4/3}$(^{5}N-bdc-Phe-OH)$_{1/2}$(bpdc)$_{1/2}$] in DCl/DMSO-d$_6$ (23 µL/ 1 mL)

C.21 [Zn$_4$O(hmtt)$_{4/3}$(^{7}N-bpdc-X)$_{1/2}$(bdc)$_{1/2}$] MOFs ^{1}H NMR spectra

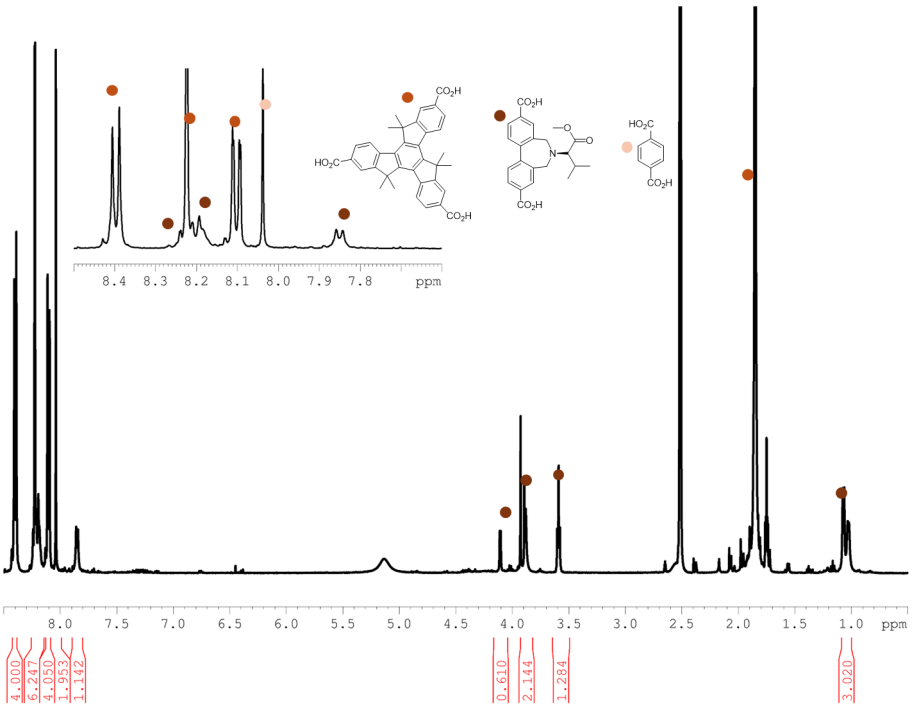

Figure C.71: ^{1}H NMR spectrum of [(hmtt)$_{4/3}$(bdc)$_{1/2}$(^{7}N-bpdc-Val)$_{1/2}$] in DCl/DMSO-d$_6$ (23 µL/ 1 mL)

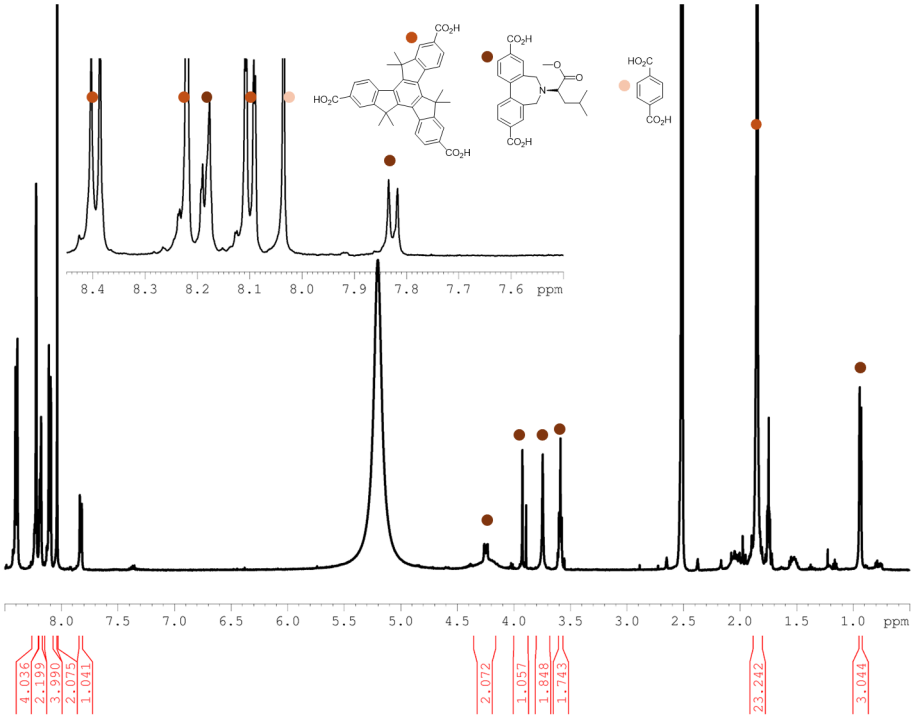

Figure C.72: ^{1}H NMR spectrum of $[(hmtt)_{4/3}(bdc)_{1/2}(^{7}N\text{-}bpdc\text{-}Leu)_{1/2}]$in DCl/DMSO-$d_6$ (23 µL/ 1 mL)

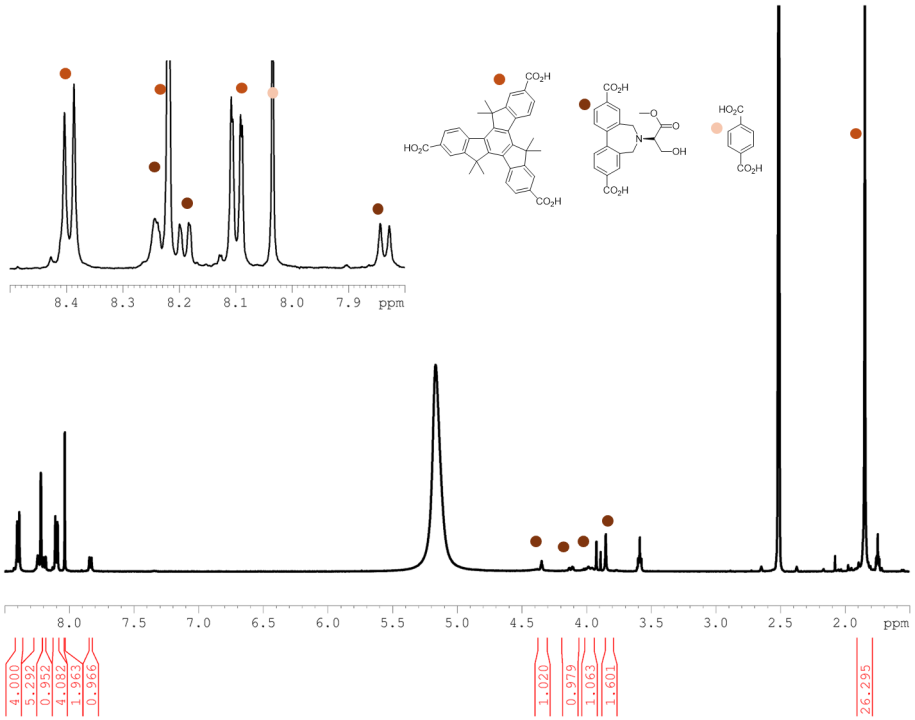

Figure C.73: ^{1}H NMR spectrum of $[(hmtt)_{4/3}(bdc)_{1/2}(^{7}N\text{-}bpdc\text{-}Ser)_{1/2}]$ in DCl/DMSO-d_6 (23 µL/ 1 mL)

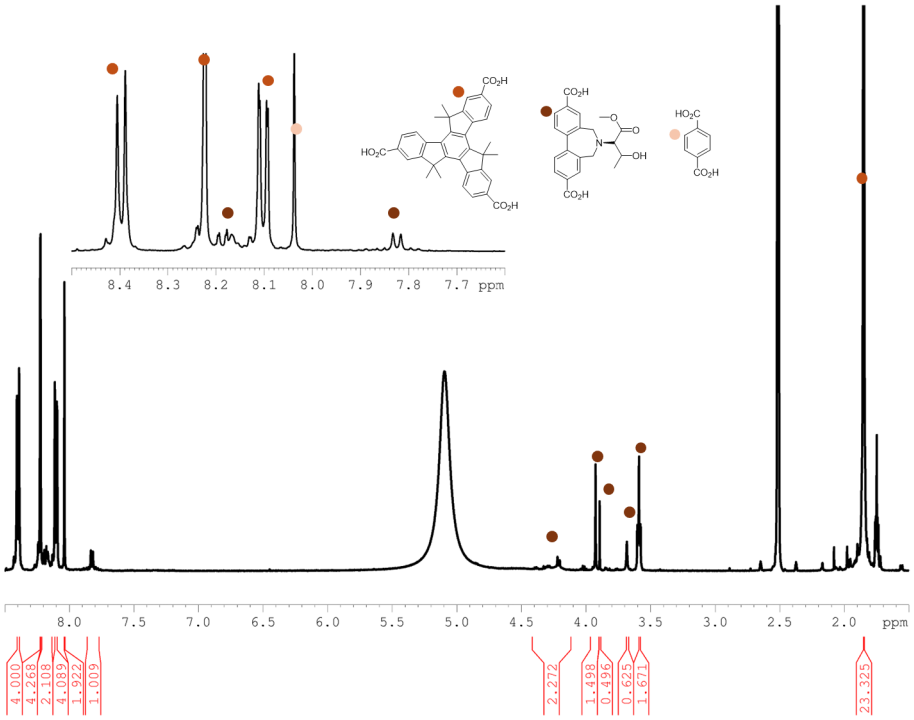

Figure C.74: ^{1}H NMR spectrum of [(hmtt)$_{4/3}$(bdc)$_{1/2}$(^{7}N-bpdc-Thr)$_{1/2}$] in DCl/DMSO-d$_6$ (23 µL/ 1 mL)

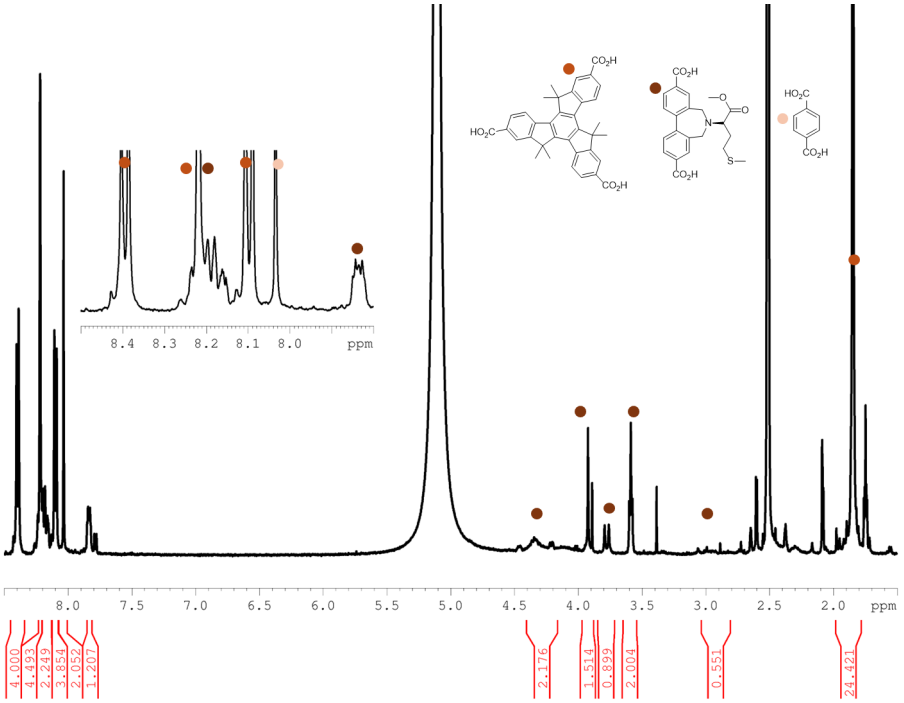

Figure C.75: ^{1}H NMR spectrum of [(hmtt)$_{4/3}$(bdc)$_{1/2}$(^{7}N-bpdc-Met)$_{1/2}$] in DCl/DMSO-d$_6$ (23 µL/ 1 mL)

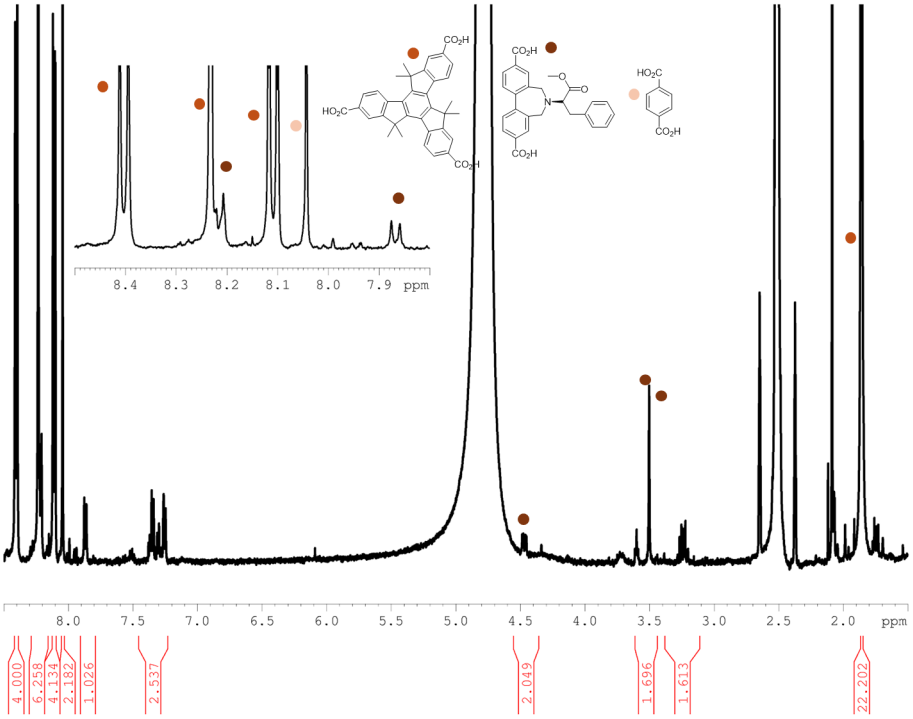

Figure C.76: ^{1}H NMR spectrum of [(hmtt)$_{4/3}$(bdc)$_{1/2}$(^{7}N-bpdc-Phe)$_{1/2}$] in DCl/DMSO-d$_6$ (23 µL/ 1 mL)

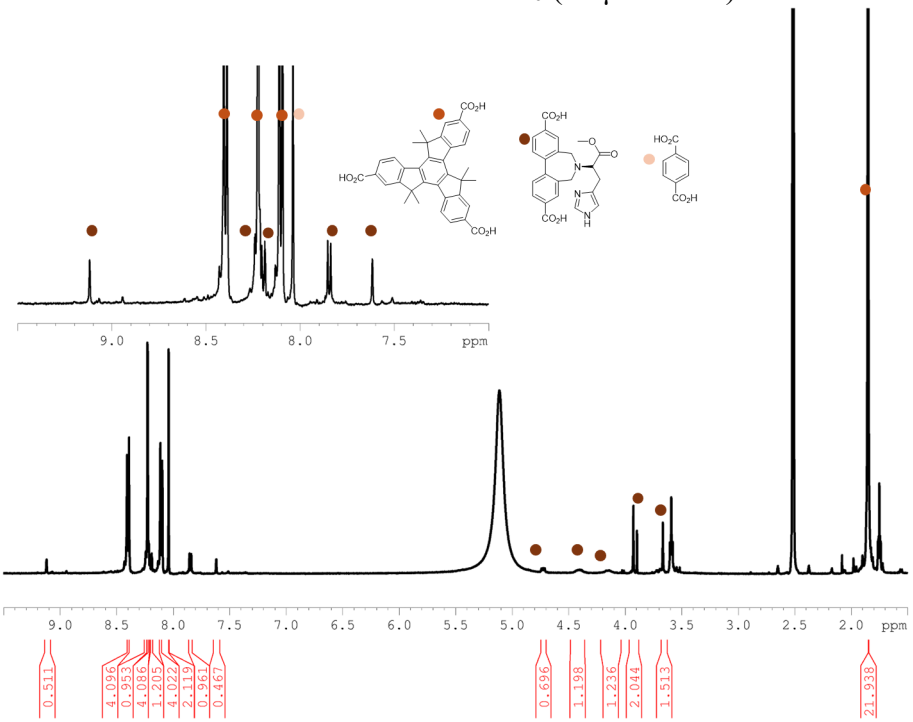

Figure C.77: ^{1}H NMR spectrum of [(hmtt)$_{4/3}$(bdc)$_{1/2}$(^{7}N-bpdc-His)$_{1/2}$] in DCl/DMSO-d$_6$ (23 µL/ 1 mL)

Appendix D for Chapter 5

D.1 Attempts to synthesise ^{7}N-Bpdc-Lys-BOC

Synthesis of $^{\varepsilon}$N-BOC-lysine

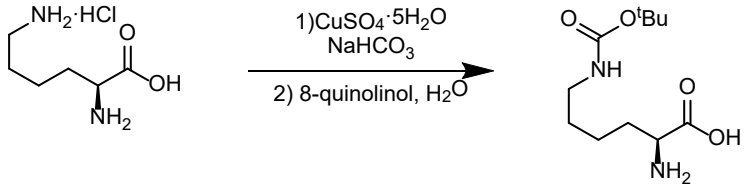

Lys-HCl **N-BOC-Lys**

Scheme D.1: Synthesis pathway of $^{\varepsilon}$N-BOC-Lys

BOC-protection of $^{\varepsilon}$N- lysine

l-Lysine-monohydrochloride (1.50 g, 8.2 mmol) was dissolved in $NaHCO_3$ solution (40 mL, 1 M). Then, $CuSO_4 \cdot 5H_2O$ (1.03 g, 4.1 mmol, 0.5 eq.) and solid $NaHCO_3$ (668.80 mg, 8.2 mmol, 1 eq.) were added. Then, Boc_2O (2.32 g, 10.66 mmol, 1.3 eq.) was dissolved in acetone (13 mL) and added to the mixture slowly. The solution was stirred at rt. Overnight. Then, a blue precipitate was formed over time. On the second day, the reaction was quenched by adding methanol (3.0 mL) and left to stir for 2 hours. Then, H_2O and EtOAc mixture (1:1, 20 mL) was added to the reaction mixture, then filtered off. The blue solid was washed with H_2O (x 2, 10 mL). The blue solid was dried and used directly in the next step reaction. H_2O (100 mL) and 8-quinolol (1.55 g, 1.3 eq.) were added to the blue solid. Then, the mixture was vigorously stirred overnight at rt. The green suspension was filtered off and the solids with H_2O (x 2, 10 mL). The solid was discarded, and the filtrate was washed with DCM (x 2, 100 mL). The aqueous layer was concentrated and a fluffy solid appeared. Yield: 1.0 g, 4.05 mmol, 50%.[194] $[M]/[Z]^{-} = 245.21$

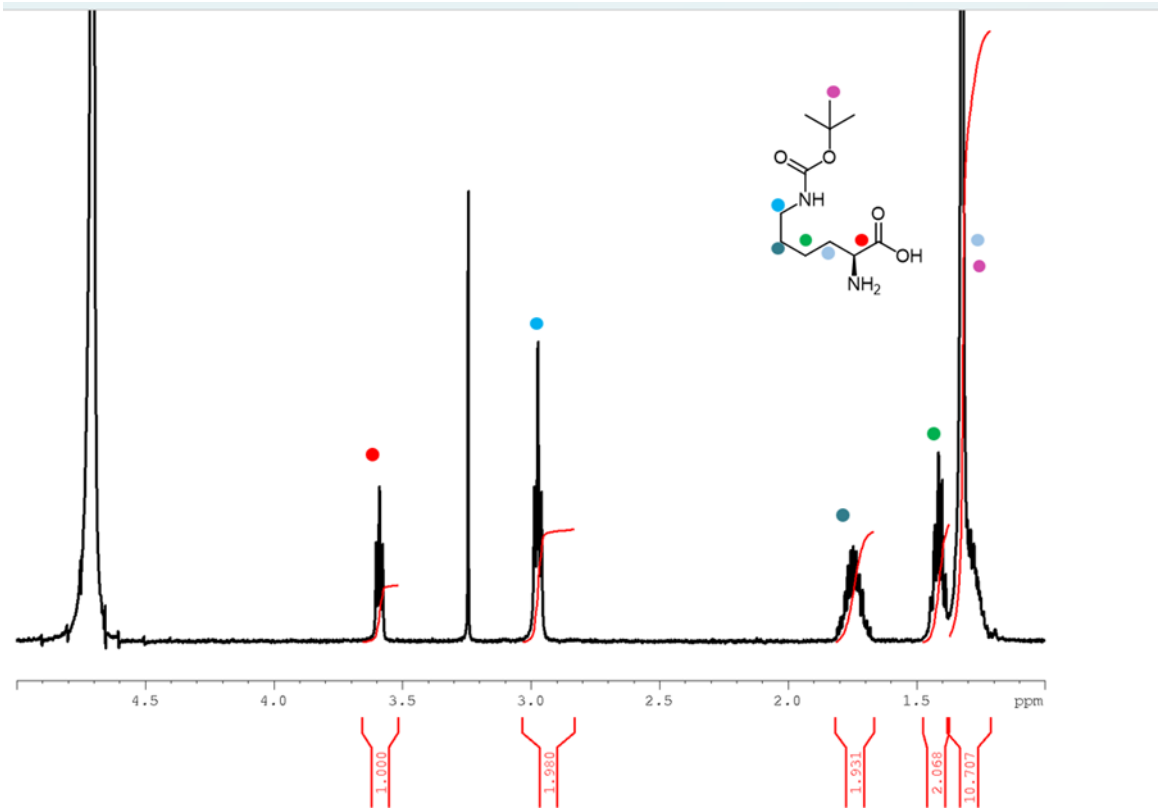

Figure D.1: $^{\varepsilon}$N-BOC-Lys ^{1}H NMR spectrum in D_2O.

D.2 Attempt to synthesize of compound 3D

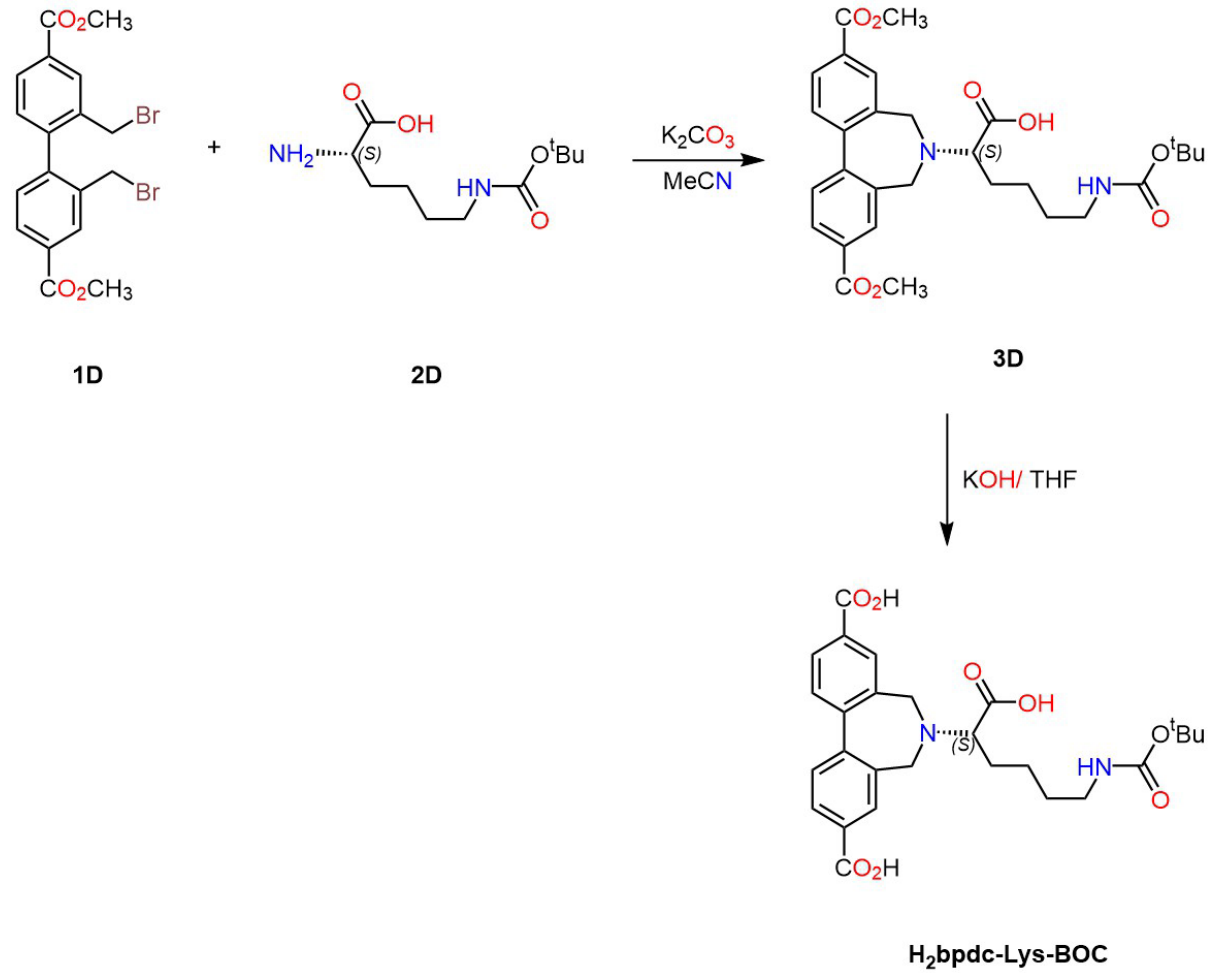

Figure D.2: Synthesis pathways targeted ligand H2bpdc-Lys-BOC

Compound **1D** (0.01g, 0.59 mmol, 1 eq.) was suspended in MeCN (5.00 mL) along with K_2CO_3 (200.00 mg, excess). Compound **2D** (0.08 g, 0.30 mmol, 2.0 eq.) was then added to the reaction mixture, which was stirred at 40 °C for 24 hours. After this, the base wasfiltered off, and the solvent was removed. The crude product was then loaded onto a silica flash column chromatography, and the product was eluted with a 1:1 mixture of EtOAc and cyclohexane. The R_f value for the product using EtOAc and hexane (1:1) was 0.5.
Yield: 20.0 mg.
Three different procedures were attempted to synthesise product **3**, varying the bases (DIPEA, TEA) and solvents (THF, MeCN). The products from each procedure were separated by flash silica column chromatography. Although a single spot was observed on TLC, analysis revealed that all samples contained a mixture of two products.

HRMS (FTMS + p ESI Full) calculated for $[M + H]^+(C_{29}H_{37}N_2O_8)^+$ *m/z* 541.2544, found *m/z* 541.2530.

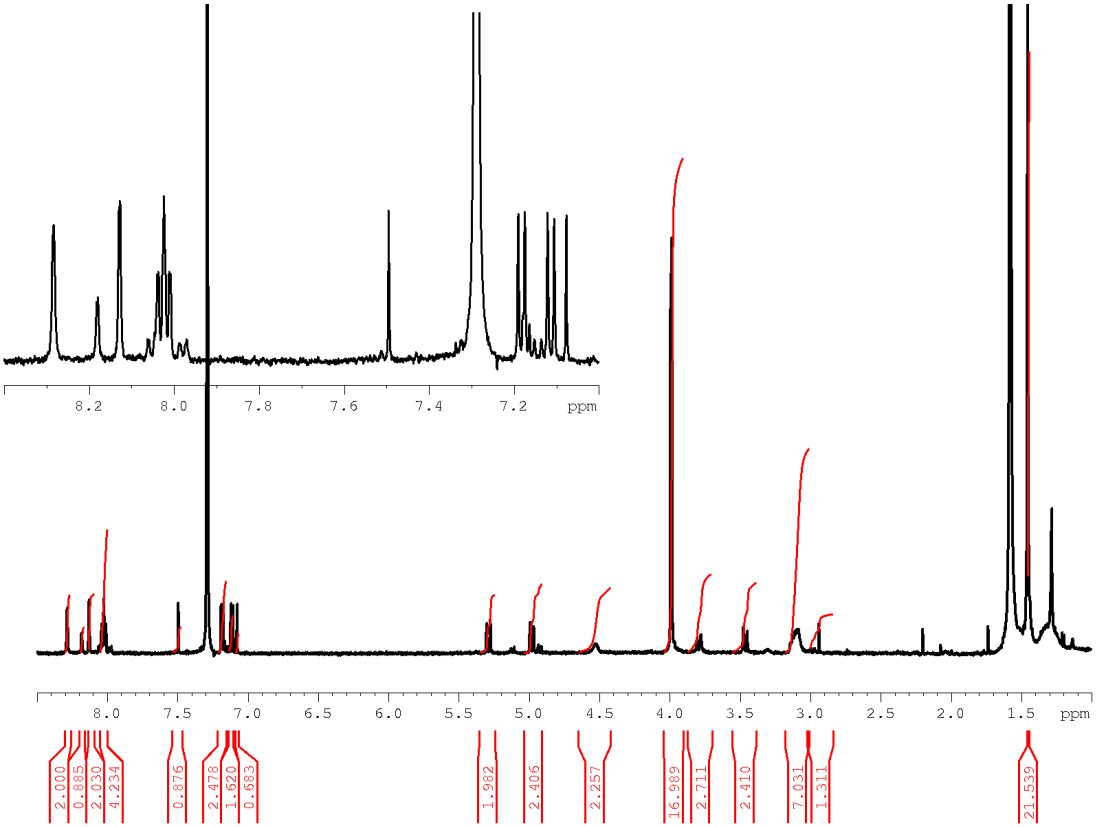

Figure D.3: ^{1}H NMR spectrum of material expected to be compound 3D

Synthesis of H_2bpdc-Lys-BOC

Compound 3D (20 mg) was dissolved in 2 mL 1:1 (V/V) THF/KOH (aq., 1M), and the solution was stirred at r.t. overnight. The product was precipitated using HNO_3 (0.5 M), centrifuged, washed with water and centrifuged again. The sample was dried using a freeze-dry desiccator. ^{1}H NMR spectroscopy was done in different solvents, and it showed that neither the precipitate nor the filtrate is the targeted product. MS did not show any sign of the product.

D.3 MOFs ^{1}H NMR spectroscopic data

The samples were prepared for NMR spectroscopy as described before in **4.4.6.**

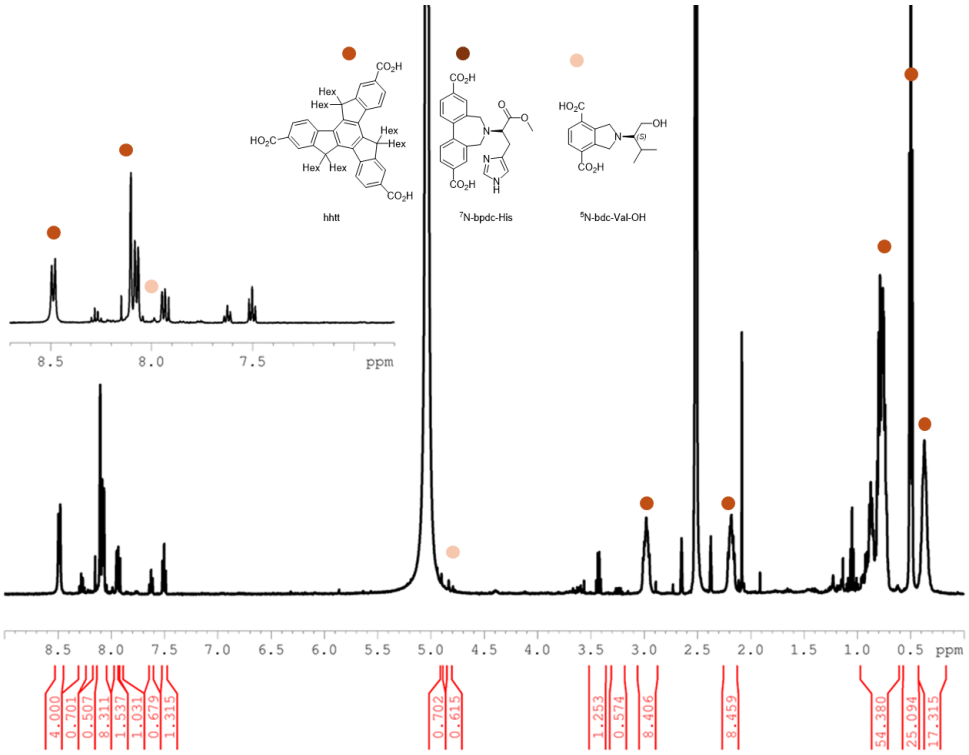

Figure D.4: ^{1}H NMR spectrum of crystals from the attempted incorporation of hhtt, ^{7}N-bpdc-His, and ^{5}N-bdc-Val-OH into MUF-77 using the standard synthesis procedure, after dissolution in DCl/DMSO-d_6 (23 µL/1 mL).

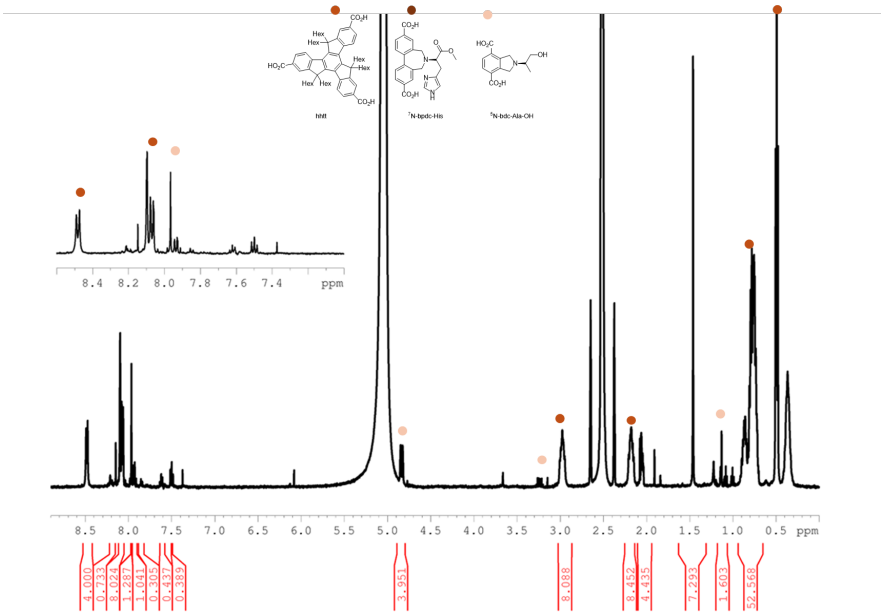

Figure D.5: ^{1}H NMR spectrum of crystals from the attempted incorporation of hhtt, ^{7}N-bpdc-His, and ^{5}N-bdc-Ala-OH into MUF-77 using the standard synthesis procedure, after dissolution in DCl/DMSO-d_6 (23 µL/1 mL).

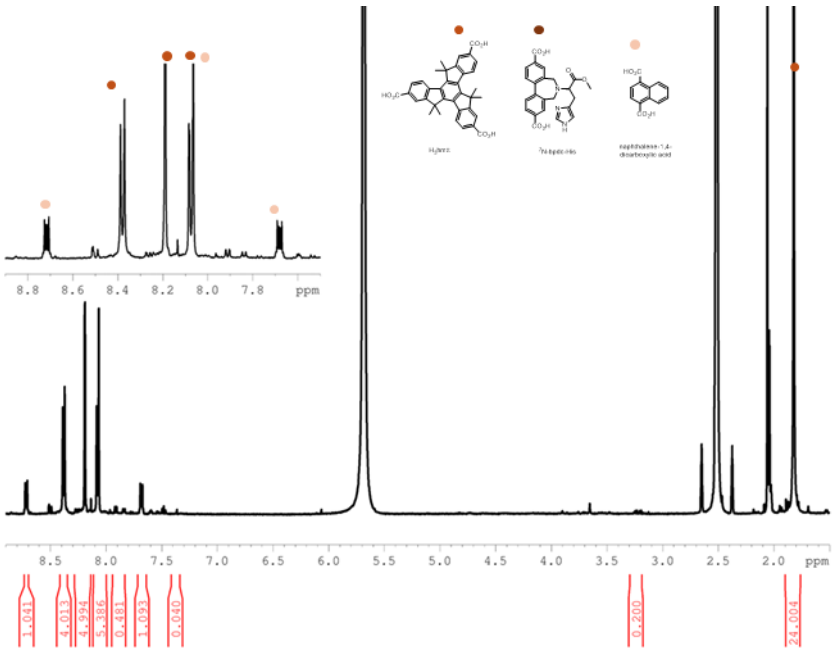

Figure D.6: ^{1}H NMR spectrum of crystals from the attempted incorporation of hmtt, ^{7}N-bpdc-His, and naphthalene-1,4-dicarboxylic acid into MUF-77 using the standard synthesis procedure, after dissolution in DCl/DMSO-d_6 (23 µL/1 mL).

D.4 Internal Reactions Manual

An internal reactions manual, developed within our research group, provided the standardised conditions employed to assess the activity of the MUF-77(^{7}N-bpdc–His) system toward these model reactions (**Table D.1**).

Table D.1: The Reactions internal manual

Reaction	Reagents → Product	TLC conditions and Result
Michael addition	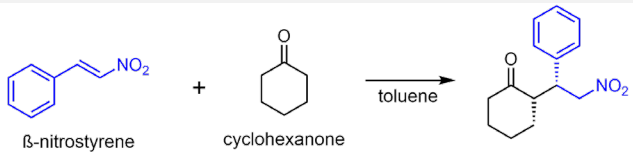 ß-nitrostyrene 0.12 mmol 17.9 mg + cyclohexanone 2.4 mmol 235.2 mg 250 µl	n-hex/EtOAc; 2/1 R_f = 0.4 No product was detected